Microbial assist for mixed plastic upcycling pp. 132 & 207

Tracking ultrafast neural activation pp. 139 & 160

Concerns over sharing data from community-engaged research p. 141

Science

$15
14 OCTOBER 2022
science.org

AAAS

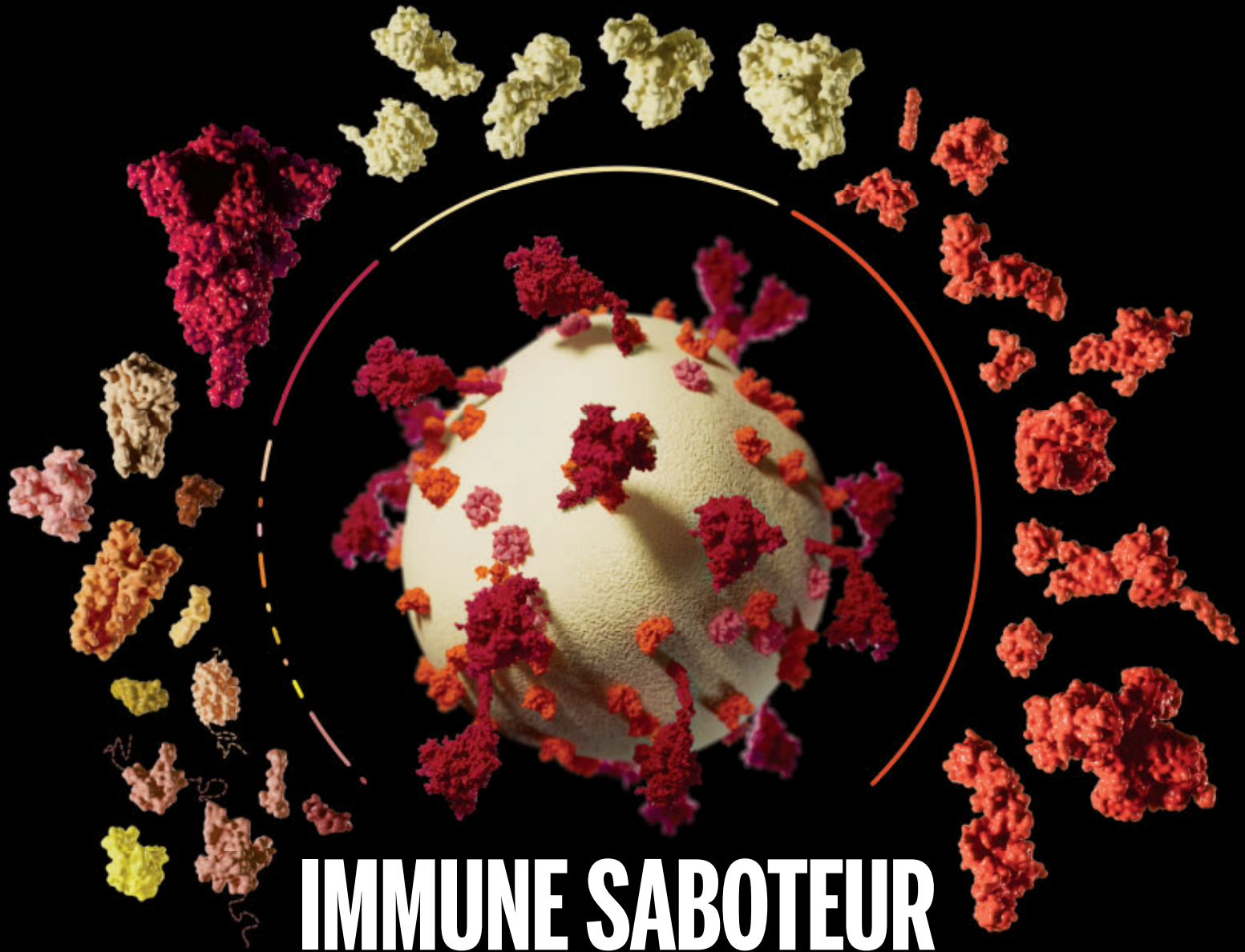

IMMUNE SABOTEUR

How SARS-CoV-2's proteins battle our immune system p. 128

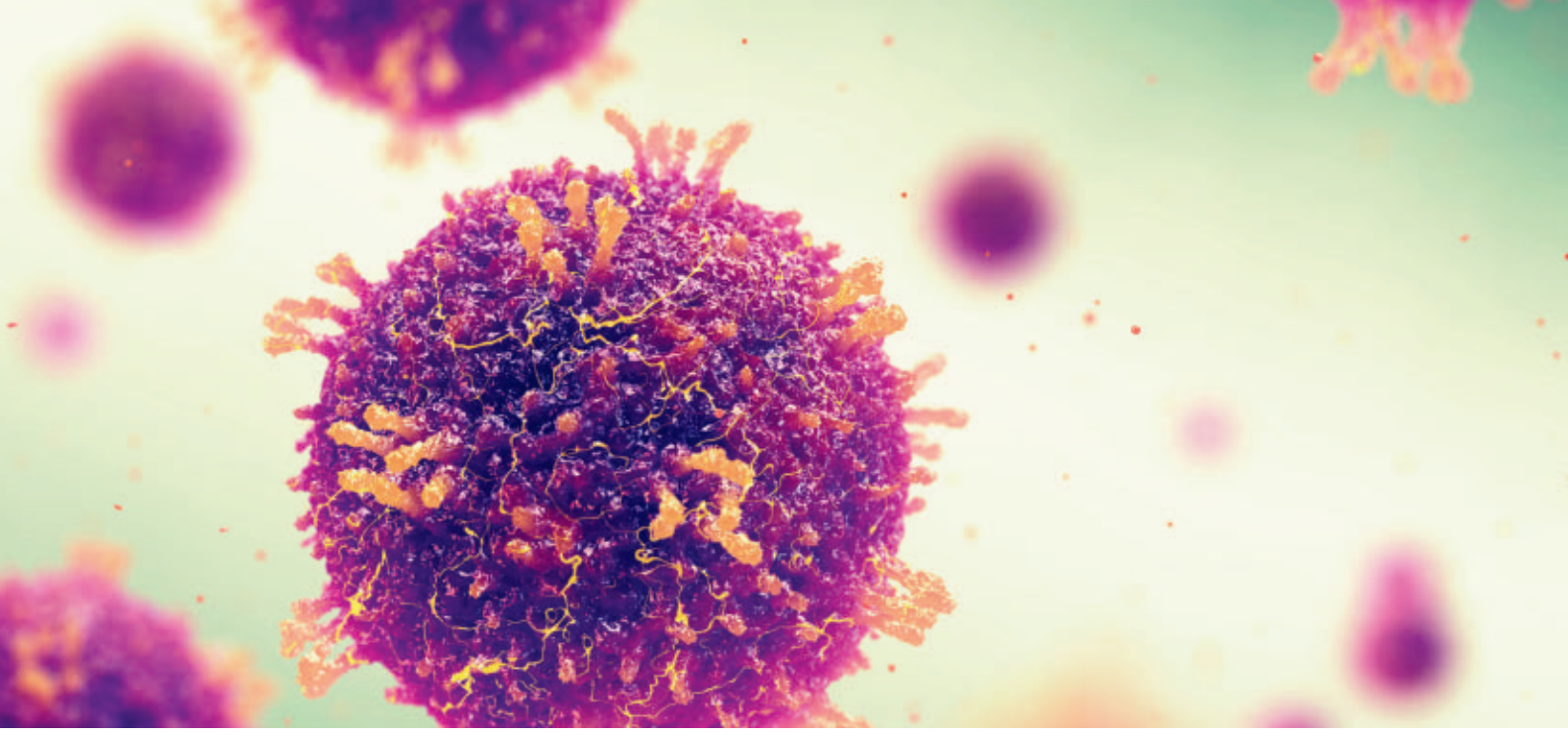

It's time to think differently.

Find out how NEB can support your infectious disease research and development.

Gaining a better understanding of infectious diseases, including their characterization, evolution and transmission, continues to be a priority, both from an R&D standpoint and as a public health issue. The COVID-19 pandemic has demonstrated the need for a wide range of tools to research infectious diseases, and has highlighted the importance of speed and the ability to pivot as new problems arise. This has emphasized the need for innovation and thinking differently about where to access those critical materials, including genomics reagents.

Many scientists know NEB as a trusted reagent supplier to the life science community, but what you may not know is that we also offer a portfolio of products that can be used in infectious disease research, development of diagnostics and therapies, and in epidemiological studies and disease surveillance. In fact, many of our products have supported the development of COVID-19 diagnostics and vaccines, and can also be utilized with other infectious diseases, such as influenza and malaria.

- Benefit from almost 50 years of experience in molecular biology & enzymology
- Partner with our OEM & Customized Solutions team to find the best solution for your needs
- Take advantage of our expanded manufacturing capabilities
- Access product formats, such as GMP-grade*, lyophilized, lyo-ready and glycerol-free
- Be confident in your product performance with our expanded quality and regulatory systems

Ready to get started? Learn more at
www.neb.com/InfectiousDiseases

"GMP-grade" is a branding term NEB uses to describe reagents manufactured at our Rowley, MA facility, where we utilize procedures and process controls to manufacture reagents in compliance with ISO 9001 and ISO 13485 quality management system standards. NEB does not manufacture or sell products known as Active Pharmaceutical Ingredients (APIs), nor do we manufacture products in compliance with all of the Current Good Manufacturing Practice regulations.

One or more of these products are covered by patents, trademarks and/or copyrights owned or controlled by New England Biolabs, Inc. For more information, please email us at busdev@neb.com. The use of these products may require you to obtain additional third party intellectual property rights for certain applications.

NEW ENGLAND BioLabs® Inc.

be INSPIRED
drive DISCOVERY
stay GENUINE

CONTENTS

14 OCTOBER 2022 • VOLUME 378 • ISSUE 6616

NEWS

IN BRIEF

IN DEPTH

PHOTOS: (TOP TO BOTTOM) REUTERS/HEO RAN; DASRIL ROSZANDI/ANADOLU AGENCY/GETTY IMAGES

A mother and baby Sumatran elephant at a conservation center in Indonesia. Just a few dozen are left in the wild.

FEATURES

INSIGHTS

PERSPECTIVES

BII | Prize for Science | Innovation

Bringing research to life–and science to market

Behind every life-changing solution is an entrepreneurial scientist–a creative mind who proved an idea in the lab and dared to carry it out in the world.

To encourage more scientists to translate their research, BioInnovation Institute (BII) and *Science* present a new annual award.

Our three winners will have their essays published in *Science* magazine and will be invited into BII's entrepreneurial ecosystem. In addition, the Grand Prize winner will receive a prize of USD 25,000, and each runner-up will receive USD 10,000 at a grand award ceremony in Copenhagen, Denmark.

The call for applications has just opened. Apply before November 1, 2022.
www.bii.dk/scienceprize

See film from the grand award ceremony 2022

Benedetto Marelli, Grand Prize Winner 2022

Presented by BII & *Science*

BII BioInnovation Institute Science

Apply before November 1, 2022
www.bii.dk/scienceprize

RESEARCH

ON THE COVER

Like many viruses, SARS-CoV-2 deploys a molecular arsenal to neutralize the host's immune response. Many of the viral proteins shown here suppress steps in the body's interferon response, for example (the arrangement and colors of the proteins indicate which genes encode them). An enhanced version of the News feature can be found online at https://scim.ag/ViralArsenal. See page 128. *Illustration: V. Altounian, C. Bickel, K. Franklin/*Science; *Data: see https://scim.ag/ViralArsenal*

SCIENCE (ISSN 0036-8075) is published weekly on Friday, except last week in December, by the American Association for the Advancement of Science, 1200 New York Avenue, NW, Washington, DC 20005. Periodicals mail postage (publication No. 484460) paid at Washington, DC, and additional mailing offices. The title SCIENCE is a registered trademark of the AAAS. Domestic individual membership, including subscription (12 months): $165 ($74 allocated to subscription). Domestic institutional subscription (51 issues): $2212; Foreign postage extra: Air assist delivery: $98. First class, airmail, student, and emeritus rates on request. Canadian rates with GST available upon request, GST #125488122. Publications Mail Agreement Number 1069624. **Printed in the U.S.A.**
Change of address: Allow 4 weeks, giving old and new addresses and 8-digit account number. **Postmaster:** Send change of address to AAAS, P.O. Box 96178, Washington, DC 20090–6178. **Single-copy sales:** $15 each plus shipping and handling available from backissues.science.org; bulk rate on request. **Authorization to reproduce** material for internal or personal use under circumstances not falling within the fair use provisions of the Copyright Act can be obtained through the Copyright Clearance Center (CCC), www.copyright.com. The identification code for *Science* is 0036-8075. *Science* is indexed in the *Reader's Guide to Periodical Literature* and in several specialized indexes.

ILLUSTRATION: ROBERT NEUBECKER

Science AAAS

Editor-in-Chief Holden Thorp, hthorp@aaas.org

Executive Editor Valda Vinson

Editor, Research Jake S. Yeston **Editor, Insights** Lisa D. Chong **Managing Editor** Lauren Kmec

DEPUTY EDITORS Gemma Alderton (UK),Stella M. Hurtley (UK), Phillip D. Szuromi, Sacha Vignieri **SR. EDITORS** Caroline Ash (UK), Michael A. Funk, Brent Grocholski, Pamela J. Hines, Di Jiang, Priscilla N. Kelly, Marc S. Lavine (Canada), Mattia Maroso, Yevgeniya Nusinovich, Ian S. Osborne (UK), L. Bryan Ray, Seth Thomas Scanlon (UK), H. Jesse Smith, Keith T. Smith (UK), Jelena Stajic, Peter Stern (UK), Valerie B. Thompson, Brad Wible, Yuen Yiu **ASSOCIATE EDITORS** Bianca Lopez, Corinne Simonti, Yury V. Suleymanov, Ekeoma Uzogara **LETTERS EDITOR** Jennifer Sills **LEAD CONTENT PRODUCTION EDITORS** Chris Filiatreau, Harry Jach **SR. CONTENT PRODUCTION EDITOR** Amelia Beyna **CONTENT PRODUCTION EDITORS** Julia Haber-Katris, Nida Masiulis, Abigail Shashikanth, Suzanne M. White **SR. EDITORIAL MANAGERS** Carolyn Kyle, Beverly Shields **SR. PROGRAM ASSOCIATE** Maryrose Madrid **EDITORIAL ASSOCIATE** Joi S. Granger **SR. EDITORIAL COORDINATORS** Aneera Dobbins, Jeffrey Hearn, Lisa Johnson, Shannon McMahon, Jerry Richardson, Hilary Stewart (UK), Alice Whaley (UK), Anita Wynn **EDITORIAL COORDINATORS** Maura Byrne, Alexander Kief, Ronmel Navas, Isabel Schnaidt, Qiyam Stewart, Brian White **RESEARCH & DATA ANALYST** Jessica L. Slater **ASI DIRECTOR, OPERATIONS** Janet Clements (UK) **ASI SR. OFFICE ADMINISTRATOR** Jessica Waldock (UK)

News Editor Tim Appenzeller

NEWS MANAGING EDITOR John Travis **INTERNATIONAL EDITOR** Martin Enserink **DEPUTY NEWS EDITORS** Shraddha Chakradhar, Elizabeth Culotta, Lila Guterman, David Grimm, Eric Hand (Europe), David Malakoff **SR. CORRESPONDENTS** Daniel Clery (UK), Jon Cohen, Jeffrey Mervis, Elizabeth Pennisi **ASSOCIATE EDITORS** Jeffrey Brainard, Kelly Servick **NEWS REPORTERS** Adrian Cho, Jennifer Couzin-Frankel, Jocelyn Kaiser, Rodrigo Pérez Ortega (Mexico City), Robert F. Service, Erik Stokstad, Paul Voosen, Meredith Wadman **INTERNS** Zack Savitsky, Viviana Flores, Katherine Irving **CONTRIBUTING CORRESPONDENTS** Warren Cornwall, Andrew Curry (Berlin), Ann Gibbons, Sam Kean, Eli Kintisch, Kai Kupferschmidt (Berlin), Andrew Lawler, Mitch Leslie, Eliot Marshall, Virginia Morell, Dennis Normile (Tokyo), Elisabeth Pain (Careers), Charles Piller, Gabriel Popkin, Michael Price, Joshua Sokol, Richard Stone, Emily Underwood, Gretchen Vogel (Berlin), Lizzie Wade (Mexico City) **CAREERS** Rachel Bernstein (Editor), Katie Langin (Associate Editor) **COPY EDITORS** Julia Cole (Senior Copy Editor), Morgan Everett, Cyra Master (Copy Chief) **ADMINISTRATIVE SUPPORT** Meagan Weiland

Creative Director Beth Rakouskas

DESIGN MANAGING EDITORS Marcy Atarod, Chrystal Smith **GRAPHICS MANAGING EDITOR** Chris Bickel **MULTIMEDIA MANAGING PRODUCER** Kevin McLean **WEB CONTENT STRATEGY MANAGER** Kara Estelle-Powers **PHOTOGRAPHY MANAGING EDITOR** Emily Petersen **DESIGNER** Christina Aycock **SENIOR SCIENTIFIC ILLUSTRATOR** Valerie Altounian **SCIENTIFIC ILLUSTRATORS** Austin Fisher, Kellie Holoski, Ashley Mastin **INTERACTIVE GRAPHICS EDITOR** Kelly Franklin **SENIOR GRAPHICS SPECIALISTS** Holly Bishop, Nathalie Cary **PHOTO EDITORS** Charles Borst, Kaitlyn Dolan **SENIOR PODCAST PRODUCER** Sarah Crespi **VIDEO PRODUCER** Meagan Cantwell **SOCIAL MEDIA STRATEGIST** Jessica Hubbard **SOCIAL MEDIA PRODUCER** Sabrina Jenkins **WEB DESIGNER** Jennie Pajerowski

Chief Executive Officer and Executive Publisher Sudip Parikh

Publisher, Science Family of Journals Bill Moran

DIRECTOR, BUSINESS SYSTEMS AND FINANCIAL ANALYSIS Randy Yi **DIRECTOR, BUSINESS OPERATIONS & ANALYSIS** Eric Knott **DIRECTOR OF ANALYTICS** Enrique Gonzales **MANAGER, BUSINESS OPERATIONS** Jessica Tierney **MANAGER, BUSINESS ANALYSIS** Cory Lipman **BUSINESS ANALYSTS** Kurt Ennis, Maggie Clark **FINANCIAL ANALYST** Isacco Fusi **BUSINESS OPERATIONS ADMINISTRATOR** Taylor Fisher **SENIOR PRODUCTION MANAGER** Jason Hillman **SENIOR MANAGER, PUBLISHING AND CONTENT SYSTEMS** Marcus Spiegler **CONTENT OPERATIONS MANAGER** Rebecca Doshi **SENIOR CONTENT & PUBLISHING SYSTEMS SPECIALIST** Jacob Hedrick **SENIOR PRODUCTION SPECIALIST** Kristin Wowk **PRODUCTION SPECIALISTS** Kelsey Cartelli, Audrey Diggs **DIGITAL PRODUCTION MANAGER** Lisa Stanford **CONTENT SPECIALIST** Kimberley Oster **ADVERTISING PRODUCTION OPERATIONS MANAGER** Deborah Tompkins **DESIGNER, CUSTOM PUBLISHING** Jeremy Huntsinger **SR. TRAFFIC ASSOCIATE** Christine Hall **SPECIAL PROJECTS ASSOCIATE** Sarah Dhere

ASSOCIATE DIRECTOR, BUSINESS DEVELOPMENT Justin Sawyers **GLOBAL MARKETING MANAGER** Allison Pritchard **DIGITAL MARKETING MANAGER** Aimee Aponte **JOURNALS MARKETING MANAGER** Shawana Arnold **MARKETING ASSOCIATES** Aaron Helmbrecht, Ashley Hylton, Mike Romano, Lorena Chirinos Rodriguez, Jenna Voris **SENIOR DESIGNER** Kim Huynh

DIRECTOR AND SENIOR EDITOR, CUSTOM PUBLISHING Sean Sanders **ASSISTANT EDITOR, CUSTOM PUBLISHING** Jackie Oberst **PROJECT MANAGER** Melissa Collins

DIRECTOR, PRODUCT & PUBLISHING DEVELOPMENT Chris Reid **DIRECTOR, BUSINESS STRATEGY AND PORTFOLIO MANAGEMENT** Sarah Whalen **ASSOCIATE DIRECTOR, PRODUCT MANAGMENT** Kris Bishop **PRODUCT DEVELOPMENT MANAGER** Scott Chernoff **PUBLISHING TECHNOLOGY MANAGER** Michael Di Natale **SR. PRODUCT ASSOCIATE** Robert Koepke **PRODUCT ASSOCIATE** Caroline Breul, Anne Mason **SPJ ASSOCIATE MANAGER** Samantha Bruno Fuller **SPJ ASSOCIATE** Casey Buchta

MARKETING MANAGER Kess Knight **BUSINESS DEVELOPMENT MANAGER** Rasmus Andersen **SENIOR INSTITUTIONAL LICENSING MANAGER** Ryan Rexroth **INSTITUTIONAL LICENSING MANAGER** Marco Castellan, Claudia Paulsen-Young **SENIOR MANAGER, INSTITUTIONAL LICENSING OPERATIONS** Judy Lillibridge **SENIOR OPERATIONS ANALYST** Lana Guz **SYSTEMS & OPERATIONS ANALYST** Ben Teincuff **FULFILLMENT ANALYST** Aminta Reyes

DIRECTOR, GLOBAL SALES Tracy Holmes **US EAST COAST AND MID WEST SALES** Stephanie O'Connor **US MID WEST, MID ATLANTIC AND SOUTH EAST SALES** Chris Hoag **US WEST COAST SALES** Lynne Stickrod **ASSOCIATE DIRECTOR, ROW** Roger Goncalves **SALES REP, ROW** Sarah Lelarge **SALES ADMIN ASSISTANT, ROW** Victoria Glasbey **DIRECTOR OF GLOBAL COLLABORATION AND ACADEMIC PUBLISHING RELATIONS, ASIA** Xiaoying Chu **ASSOCIATE DIRECTOR, INTERNATIONAL COLLABORATION** Grace Yao **SALES MANAGER** Danny Zhao **MARKETING MANAGER** Kilo Lan **ASCA CORPORATION, JAPAN** Rie Rambelli (Tokyo), Miyuki Tani (Osaka)

DIRECTOR, COPYRIGHT, LICENSING AND SPECIAL PROJECTS Emilie David **RIGHTS AND PERMISSIONS ASSOCIATE** Elizabeth Sandler **LICENSING ASSOCIATE** Virginia Warren **CONTRACT SUPPORT SPECIALIST** Michael Wheeler

MAIN HEADQUARTERS
Science/AAAS
1200 New York Ave. NW
Washington, DC 20005

SCIENCE INTERNATIONAL
Clarendon House
Clarendon Road
Cambridge, CB2 8FH, UK

SCIENCE CHINA
Room 1004, Culture Square
No. 59 Zhongguancun St.
Haidian District, Beijing, 100872

SCIENCE JAPAN
ASCA Corporation
Sibaura TY Bldg. 4F, 1-14-5
Shibaura Minato-ku
Tokyo, 108-0073 Japan

EDITORIAL
science_editors@aaas.org

NEWS
science_news@aaas.org

INFORMATION FOR AUTHORS
science.org/authors/
science-information-authors

REPRINTS AND PERMISSIONS
science.org/help/
reprints-and-permissions

MEDIA CONTACTS
scipak@aaas.org

MULTIMEDIA CONTACTS
SciencePodcast@aaas.org
ScienceVideo@aaas.org

INSTITUTIONAL SALES AND SITE LICENSES
science.org/librarian

PRODUCT ADVERTISING & CUSTOM PUBLISHING
advertising.science.org/
products-services
science_advertising@aaas.org

CLASSIFIED ADVERTISING
advertising.science.org/
science-careers
advertise@sciencecareers.org

JOB POSTING CUSTOMER SERVICE
employers.sciencecareers.org
support@sciencecareers.org

MEMBERSHIP AND INDIVIDUAL SUBSCRIPTIONS
science.org/subscriptions

MEMBER BENEFITS
aaas.org/membership/benefits

Science serves as a forum for discussion of important issues related to the advancement of science by publishing material on which a consensus has been reached as well as including the presentation of minority or conflicting points of view. Accordingly, all articles published in *Science*—including editorials, news and comment, and book reviews—are signed and reflect the individual views of the authors and not official points of view adopted by AAAS or the institutions with which the authors are affiliated.

EDITORIAL

Beyond nuclear deterrence

In October 1962, the United States and the Soviet Union squared off in what game theorist and Nobel laureate Thomas Schelling described as a nuclear game of "chicken" that threatened humanity's survival. The Cuban Missile Crisis spurred six decades of efforts to limit the spread of nuclear weapons and inspired a generation of scientists to think critically about reducing atomic risks. Russian President Vladimir Putin's recent nuclear threats during the war in Ukraine are an unambiguous reminder that such dangers have outlived the Cold War. A new wave of scientific research is urgently needed to understand conditions for making global nuclear disarmament desirable and feasible.

October 1962 and October 2022 are hardly comparable. There were four nuclear-armed states then—the United States, the Soviet Union, Britain, and France. Today, there are nine, with the additions of China, India, Israel, North Korea, and Pakistan. Success containing proliferation to just nine countries came about in no small part from the 1968 Nuclear Nonproliferation Treaty and subsequent International Atomic Energy Agency inspections. These initiatives were a direct result of the Cuban Missile Crisis, as were US–Soviet/Russian arms control agreements that reduced worldwide nuclear stockpiles from nearly 70,000 warheads in the 1980s to ~12,700 today.

> "...nuclear dangers are not speculative fiction."

Unfortunately, nuclear reductions have now been replaced by competition. China, Russia, and the US are modernizing their arsenals, ignoring disarmament commitments in the Nuclear Nonproliferation Treaty. Meanwhile, new actors, proliferation risks, and intersections between nuclear and emerging cyber and artificial intelligence technologies challenge existing deterrence and nonproliferation theories. Amid these developments, 68 countries have ratified the 2017 Treaty on the Prohibition of Nuclear Weapons, which seeks to ban all nuclear weapons–related activities. Nuclear-armed states reject the treaty, citing a lack of verification measures and a volatile security environment. Simultaneously, global research funding for nuclear risk reduction is shrinking rapidly, limiting opportunities for interested scientists.

Most social science research focuses on living with nuclear weapons rather than their elimination. Russian nuclear threats to deter intervention by the North Atlantic Treaty Organization in Ukraine may further entrench this status quo by hardening nuclear-armed states' resolve to maintain their arsenals and incentivizing proliferation among non-nuclear states hoping to avoid invasion. But deterrence, whether in 1962 or 2022, is a game of hostage taking. Adversaries point nuclear-tipped missiles at each other's population centers in the name of keeping the peace. Ironically, this existential gamble portrays vulnerability as protection. Polls have long shown that most people desire a world free from nuclear fears.

Still, academics have generally accepted nuclear deterrence as an eternal fact of life. Just as the Cuban Missile Crisis changed nuclear thinking, the war in Ukraine necessitates new research programs. Social scientists can draw on perspectives of nuclear and non-nuclear states alike to identify strategies for protecting populations and vital interests without nuclear risks to survival. After all, only a minority of states actually rely on nuclear weapons or protection pledges from nuclear-armed allies. These international political realities should be reflected in the scientific literature. Interrogating nuclear deterrence calls for rigorous scholarship on nuclear disarmament and alternative frameworks of security in public discourse, peer-reviewed journals, and academic syllabi.

Moving beyond nuclear deterrence requires research into nuclear disarmament's feasibility. An oft-repeated critique of complete disarmament is that it is desirable but ultimately unachievable. Yet, innovations in neutron detection, noble gas monitoring, and sensor technology offer ways to verify warhead dismantlement and the absence of fissile material production and nuclear test explosions. None of these methods are entirely foolproof, so increased resources for verification science should be a top priority for governments, universities, philanthropists, and other funders of peace and security research. Disarmament verification should mirror best practices of transparency and replicability in the natural sciences to win confidence from decision-makers.

The Cuban Missile Crisis may seem distant, but nuclear dangers are not speculative fiction. Thousands of cities are mere minutes away from nuclear destruction by weapons far more powerful than those dropped on Hiroshima and Nagasaki. This is the legacy of "protection" by nuclear deterrence. If scientists draw a lesson from October 1962, it is that existential risks demand novel thinking. Like climate change, solving the nuclear disarmament puzzle requires improved understanding of system-altering change. Putin's nuclear saber-rattling sends a clear message: Now is the time to fund and pursue scientific research for a world beyond nuclear deterrence.

–Stephen Herzog

PHOTO: CENTER FOR SECURITY STUDIES

Stephen Herzog is a senior researcher in nuclear arms control at the Center for Security Studies of ETH Zurich, Switzerland, and an associate of the Project on Managing the Atom of the Harvard Kennedy School's Belfer Center for Science and International Affairs, Cambridge, MA, USA. stephen.herzog@sipo.gess.ethz.ch; @HerzogSM

10.1126/science.adf2194

Your Legacy to Science

AN ESTATE GIFT TO THE
AMERICAN ASSOCIATION FOR THE ADVANCEMENT OF SCIENCE



Since 1848, our founding year, the American Association for the Advancement of Science (AAAS) has been deeply committed to advancing science, engineering and innovation around the world for the benefit of all people.

By making AAAS a beneficiary of your will, trust, retirement plan or life insurance policy, you become a member of our 1848 Society, joining Thomas Edison, Alexander Graham Bell and the many distinguished individuals whose vision led to the creation of AAAS and our world-renowned journal, *Science*, so many years ago.

Unlike many of its peers, *Science* is not for-profit. Your estate gift would provide long-term financial stability and durable annual income that will support operations and competitive innovation for years to come. **This support is vital.**

"As a teacher and instructor, I bear responsibility for the younger generations. If you have extra resources, concentrate them on organizations, like AAAS, that are doing work for all."

—Prof. Elisabeth Ervin-Blankenheim, 1848 Society member

If you intend to include AAAS in your estate plans, provide this information to your lawyer or financial adviser:

Legal Name: American Association for the Advancement of Science
Federal Tax ID Number: 53-0196568
Address: 1200 New York Avenue, NW, Washington, DC 20005

If you would like more information on making an estate gift to AAAS, cut out and return the form below or send an email to philanthropy@aaas.org. Additional details are also available online at **www.aaas.org/1848Society**.

1848 SOCIETY
AAAS

cut here

Yes, I would like more information about joining the AAAS 1848 Society.

PLEASE CONTACT ME AT:

Name: _____

Address: _____

City: _____ State: _____ Zip code: _____ Country: _____

Email: _____ Phone: _____

RETURN THIS FORM TO:
AAAS Office of Philanthropy and Strategic Partnerships • 1200 New York Avenue, NW • Washington, DC 20005 USA

EDITORIAL

Stop passing the buck on intro science

H. Holden Thorp
Editor-in-Chief, *Science* journals.
hthorp@aaas.org;
@hholdenthorp

The recent firing of Maitland Jones Jr. by New York University (NYU) has captured the attention of many quarters in higher education and science in the United States. Jones, a celebrated organic chemistry professor at Princeton University, who retired and became a contract professor at NYU, was dismissed after some of his students complained about their grades and the challenging level of the material in a large introductory class on organic chemistry. Even though the students never asked for Jones to be fired, NYU didn't renew his 1-year contract and sent him on his way. This reaction is illustrative of the problem of intro science, particularly at highly selective colleges: Universities would rather wash their hands of such matters than deal with all of the thorny issues revealed by stories like this. Until they do, many students will leave the courses disappointed and mistrustful of science, just at the time that science needs their support.

For sure, Jones's classes have always been taught at a high level, even higher than the already challenging level of organic chemistry. Many of his students went on to become scientists because of the deep insight they got into how organic reactions proceed, and his textbook is a tour de force in using molecular orbital theory to understand organic chemistry. But the vast majority of undergraduates who take organic chemistry are not on their way to becoming chemists. Most of them are taking it as a requirement for medical school or other health sciences. Very few faculty and research universities in the United States have the gumption to deal with this fact in a straightforward way.

The students at NYU wanted to get a good grade so that they could go to medical school. Faculty love to decry this fact as some kind of cheapening of the motivations of premed students, but why blame the students for this? Medical schools have decided that organic chemistry is a requirement and that a student can't get a good score on the Medical College Admissions Test without mastering some of the material.

The reaction to this disconnect is finger-pointing and buck-passing. The faculty torture the premeds with material they don't need. When I was the provost at Washington University in St. Louis, my chemistry colleagues were teaching graduate-level quantum mechanics in general chemistry, which sent students crying into the halls after the exams. Then the faculty would complain that the administration couldn't recruit undergraduates who were serious about science, even though their standardized test scores were outstanding and the university was admitting students from the same pool of applicants as that of other comparable institutions. Meanwhile, universities blame the faculty for not being good at teaching. The real problem is that universities are perfectly willing to collect tuition from premeds, but very few of these schools are doing the consensus building and hard work that are needed to build a relevant program for premeds that doesn't include the same breadth and depth of topics taught to other science students. And the institutions are also unwilling to take on the medical school regulatory bodies that set the admission requirements to begin with, as these bodies are huge drivers of revenue on the medical side of the research university.

> **"...the undergraduate education system that prepares students for medical school is broken."**

There are other problems underneath all of this. As *New York Times* columnist Tressie McMillan Cottom has pointed out, the fact that much of this teaching—including by Jones—is done by untenured faculty means that the universities can just throw folks overboard when things get hot. Although there has been some progress, many faculty still refuse to update their teaching methods in the face of copious data showing how teaching could be improved, particularly toward the success of women and underrepresented groups. Universities have failed to deal with gaps in learning caused by remote teaching due to COVID-19 in high school and early college, which is a temporary problem, but the inability to deal with it is a readout of the apathy that universities have for dealing with the general issues.

There's only one way out. Everyone in this system—the administrators, the faculty, the medical schools, and the medical regulatory bodies—need to state the plain truth that the undergraduate education system that prepares students for medical school is broken. Quit selling a bill of goods to ambitious young people and their parents that the research universities offer a value-adding path to a career in medicine.

–H. Holden Thorp

Published online 7 October 2022; 10.1126/science.adf2231

PHOTO: CAMERON DAVIDSON

NEWS

> “The stone is a symbol of cultural violence [and] ... cultural imperialism.”
>
> **Monica Hanna**, acting dean of a university’s College of Archaeology in Aswan, Egypt, to Reuters about the Rosetta Stone, now in the British Museum. Egyptian archaeologists are campaigning for its return to Egypt.

IN BRIEF

Edited by **Jeffrey Brainard**

DIVERSITY

In a first, Nobelists are out as LGBTQ+

Last week’s Nobel Prize recipients in the sciences included, for the first time, researchers who have publicly acknowledged they are members of the LGBTQ+ community. Ancient DNA pioneer Svante Pääbo, who bagged the Nobel Prize in Physiology or Medicine, has talked about his bisexuality in interviews and in his autobiography, *Neanderthal Man: In Search of Lost Genomes*. Stanford University chemist Carolyn Bertozzi, who was awarded the chemistry Nobel (see p. 125), is an out lesbian who has been lauded for her commitment to mentorship and promoting diversity in science. In February, she won AAAS’s Lifetime Mentor Award for mentoring more than 170 grad students and postdocs, including 73 women and 61 members of other underrepresented groups. “The diversity of people created an environment where we felt we didn’t have to play by the rules,” Bertozzi told an audience at Stanford last week. “If there weren’t the right chemistries to get the job done, we could invent new chemistries.” Although the inclusion of these laureates marked a milestone for diversity in science, this year’s science laureates were less diverse in other respects: Nine of the 10 are men, and all 10 are white.

Once-controversial fish delisted

CONSERVATION | A small fish famous for drawing the first U.S. Supreme Court ruling on the Endangered Species Act was removed last week by the U.S. Fish and Wildlife Service from the list of species under threat of extinction. In 1975, the agency declared the snail darter (*Percina tanasi*) endangered, concluding that construction of a dam on the Little Tennessee River would doom the 9-centimeter-long animals. Although the court upheld the listing in 1978, Congress allowed the dam to go ahead. The darter’s outlook improved after some were moved to other streams, more populations were discovered, and stream water became cleaner. Although the snail darter is the fifth fish species to recover and be removed from the list, some 400 other fish species across the United States remain listed as imperiled. The pace of recovery is slow mainly because species are listed only after they have declined to small populations that are difficult to rescue, and because conservation funding is inadequate, researchers report this week in *PLOS ONE*. Worldwide, populations of freshwater species have declined by 83% on average since 1970, according to the World Wildlife Fund’s *Living Planet Report*, released this week.

The snail darter became a symbol of the Endangered Species Act before its population increased.

PHOTO: JERRY A. PAYNE/USDA AGRICULTURAL RESEARCH SERVICE/BUGWOOD.ORG/CC BY

Asteroid deflected, NASA says

SPACE SCIENCE | The NASA spacecraft that hurtled into an asteroid 2 weeks ago significantly altered its target’s orbit around another asteroid, the agency announced this week—offering clear proof that humans could redirect future celestial threats to our planet. On 26 September, the Double Asteroid Redirection Test craft landed a 6-kilometer-per-second punch on Dimorphos, a 160-meter-wide moon of a larger asteroid, Didymos. To gauge the target’s deflection, Earth-based telescopes calculated its new orbital period by monitoring the dip in brightness of the two bodies as they pass in front of each other. Prior to impact, Dimorphos took 11 hours and 55 minutes to complete a lap around Didymos; now, the cycle is 32 minutes shorter. NASA had said before the impact that a reduction of at least 73 seconds would be a success.

Drug building blocks revealed

CHEMISTRY | By mining an existing database, researchers have identified an additional 1800 naturally occurring crystal compounds that could serve as building blocks for new, “one-handed” drugs. The newcomers join a smaller pool of about 250 starter compounds that are synthesized as mixtures of two mirror-image forms (much like a right and left hand), which spontaneously separate when the compounds crystallize. One of each pair can then be used to build more complex one-handed compounds that can be tested as drugs, which often require a specific handedness to be effective. Researchers at Durham University identified the 1800 compounds by analyzing the 1.2 million crystal structures in the Cambridge Structural Database, which had not been previously recognized as containing spontaneously separating crystals. The team reported its results on 23 September in *JACS Au*.

Aboriginal tree carvings recorded

ARCHAEOLOGY | Australia’s ancient rock art preserves images of what Aboriginal

Australians call the Dreaming, representing stories about the creation of their ancient culture and landscape. Now, researchers are studying another form of their art, preserved in the Tanami Desert in northwestern Australia: geometric symbols and figures of birds, serpents, and other animals carved into the soft, rippling bark of barrel-shaped boab trees. The archaeologists worked closely with Aboriginal Australians to document the carvings before they are lost, as the trees die of old age, lightning strikes, and bush fires. The authors, who include members of the Aboriginal Lingka (snake) clan, photographed and analyzed the artwork found on a dozen boabs and describe the work this week in *Antiquity*. One series of carvings depicts the winding path of the King Brown Snake, or Lingka Dreaming, who in traditional stories shaped the region's present dry, undulating landscape.

COVID-19 papers yanked faster

PUBLISHING | Retracted papers about COVID-19 have been pulled from journals faster than those on other topics, a study has found. Eighty-two percent of the flawed pandemic papers were removed within 6 months of publication compared with 58% of the other papers. Some scientists have suggested that too many COVID-19 findings were rushed into print with inadequate scrutiny, resulting in inferior quality. But the faster retractions for the COVID-19 papers indicate heightened scrutiny, at least after publication, the study's authors said in the 4 October issue of *JAMA Open Network*. The overall retraction rates for COVID-19 and other papers have been similar. In all, 138 original research papers about COVID-19 had been retracted by May—a small fraction of the total pandemic literature, which by some estimates has topped 500,000 articles.

Statistics gets $1 million award

SCIENTIFIC PRIZES | Five academic researchers will share an inaugural $1 million prize honoring pioneering work in statistical methodology that has become widely used and is socially relevant. The Rousseeuw Prize for Statistics, to be awarded biennially, is named for Peter Rousseeuw, a retired researcher from the hedge fund Renaissance Technologies and a statistics professor at KU Leuven, who funded it to bring more attention to his field. Announced this week, the award recognizes five collaborators for work on causal inference that has applications in medicine and public health. Their work influenced guidelines on when to initiate antiretroviral therapy in people with HIV, for example. James Robins of Harvard University will receive half the prize money, and Miguel Hernán of Harvard; Thomas Richardson of the University of Washington, Seattle; Andrea Rotnitzky of Torcuato Di Tella University; and Eric Tchetgen Tchetgen of the University of Pennsylvania will divide the other half.

EVOLUTION

Pesky plant bugs become pollinators

A Costa Rican flower has found a way to trick insects that damage it while feasting on its nectar into providing a benefit in return—pollination. *Syngonium hastiferum* is one of the first plants shown to have evolved to coax this service from a plant bug. Most species closely related to *Syngonium hastiferum* are pollinated by beetles, attracted by an evening perfume. But *Syngonium hastiferum* gives off a morning scent that attracts a plant pest—a nectar-robbing bug. The plants' usually smooth pollen has evolved spines that stick to the bugs of this species so they pollinate the female flowers, the researchers reported in the 4 October issue of *Current Biology*.

Bugs that provide pollination cover the plant *Syngonium hastiferum*.

PHOTO: FLORIAN ETL/UNIVERSITY OF VIENNA

U.S. agency's firing ruled illegal

LAB SAFETY | The U.S. Geological Survey (USGS) violated a federal law protecting whistleblowers when it fired a microbiologist in retaliation for reporting breaches in biosafety and animal welfare at a wildlife disease lab in Seattle, a federal judge ruled on 29 September. The judge decided that Eveline Emmenegger, a former lab manager at the Western Fisheries Research Center, is entitled to damages of up to $200,000. In 2017 and 2018 she reported problems, including leaks of wastewater containing hazardous, regulated pathogens and deficient care of lab animals. Emmenegger was fired in March 2021 for alleged poor performance, which she denied. She appealed and USGS reversed its decision the following month. Emmenegger returned to work in May 2021. USGS faces other allegations of lab safety problems at a facility in Wisconsin and data falsification at a lab in Colorado.

China launches solar observatory

ASTRONOMY | China this week launched the Advanced Space-based Solar Observatory (ASO-S), a satellite equipped to monitor the Sun's magnetic field while watching for solar flares and the titanic blasts known as coronal mass ejections. The simultaneous observations could yield clues to what triggers those eruptions and better predictions of when they will occur. Researchers hope those insights in turn may help lessen disruptions that the eruptions could cause to power grids and navigation systems on Earth. The platform—dubbed Kuafu-1 after a mythological Chinese Sun seeker—will orbit 720 kilometers from Earth. ASO-S joins NASA's Parker Solar Probe and the European Space Agency's Solar Orbiter in what are expected to be complementary solar observations.

IN DEPTH

RESEARCH POLICY

Indonesia tightens grip on conservation science

Five foreign scientists banned after critical op-ed; animal population estimates shelved

By **Dyna Rochmyaningsih**

Even before Dutch conservation scientist Erik Meijaard submitted an opinion piece to *The Jakarta Post* last month, he was worried about how the Indonesian government would react. In the article, he and four other Western scientists challenged the government's claims that orangutan populations in the country are thriving. Meijaard was aware that Indonesia is increasingly wary of "foreign interference" in conservation matters and had invited eight Indonesian collaborators to co-author the article. None agreed to do so.

After the piece ran on 14 September, the reaction was swift. In a letter issued that same day, Indonesia's Ministry of Forestry and Environmental Affairs (KLHK) said the authors had "discredited" the government and banned them from doing research in Indonesia. It also ordered national parks and KLHK offices around the country to tell the ministry's headquarters about any research conducted by foreign scientists. KLHK said that from now on, it would monitor and control all data from foreign researchers.

The move has no direct impact on the five authors' work. None of them is currently doing fieldwork in Indonesia, and all are based abroad. Meijaard runs a consulting company named Borneo Futures in nearby Brunei; his co-authors are based in the United States, Malaysia, Germany, and the United Kingdom. But the ban signals a deeper problem, Meijaard says. To head off interference in the government's ambitious development goals, KLHK has tightened control over research on the country's enormous biological diversity by both Indonesian and foreign scientists. Data on wildlife populations have been shelved and criticism of the government has been met with repercussions. "Our KLHK ban is not the issue," Meijaard says. "The real issue is the independence of Indonesian science in general and conservation science more specifically."

Many Indonesian scientists concur, but very few will talk about it publicly. "Our voices are silenced," says a conservationist in Sumatra who asked to remain anonymous for fear of reprisals.

There is little doubt about the threats to Indonesia's biodiversity. Sumatra, home to five critically endangered, iconic mammalian species found nowhere else—the Tapanuli orangutan, the Sumatran orangutan, the Sumatran tiger, the Sumatran rhinoceros, and the Sumatran elephant—has lost more than 80% of its lowland forests since the 1990s, to make room for pulpwood and oil palm plantations. Conflicts between humans and wildlife have become increasingly common. News stories frequently report elephants poisoned by angry farmers, tigers snared by poachers, and orangutans stranded in plantations.

Scientists and nongovernmental organizations (NGOs) say producing reliable population estimates and mapping remaining habitats are crucial to conservation. The environment ministry's provincial conservation agencies (BKSDA) and national park

PHOTO: CYRIL RUOSO/MINDEN PICTURES

Fewer than 50 Sumatran rhinos are left in the wild, the International Union for Conservation of Nature says. The Indonesian government insists the number is larger.

rangers have supported such work on the ground, for example by counting orangutan nests, collecting elephant dung samples, and setting camera traps for tigers. But researchers say KLHK's headquarters has kept data from such efforts under wraps.

Wulan Pusparini, an Indonesian wildlife conservationist at the University of Oxford, says her DNA-based population survey has shown the elephant population in a national park in southern Sumatra declined by 75% between 2001 and 2015. Provincial BKSDA officials were "very supportive" when she presented those data in 2018, she says, "but it got stuck in Jakarta." KLHK's central office has not allowed her to publish the findings, Pusparini says.

In 2020, the Sumatran Elephant Conservation Forum, a consortium of scientists and conservationists from various NGOs and BKSDA offices, produced what it called an Urgent Action Plan describing remaining elephant populations, the threats they face, and how they could be protected. KLHK's director of conservation signed and released the document, but the ministry retracted it a year later. Among the reasons was what KLHK called "a counterproductive statement against the government" in the plan.

> **"This fear is doing real damage to Indonesian science."**
> **Erik Meijaard**, Borneo Futures

Studies on other species have met a similar fate. KLHK has not approved a consortium's estimate for Indonesia's tiger population, submitted in 2016; the data remain unpublished. ("It is the best available knowledge so far," says an Indonesian member of the team.) The ministry also disputes a recent report from a specialist group at the International Union for Conservation of Nature that estimates there are fewer than 50 Sumatran rhinos left in the wild. KLHK says it's between 67 and 75.

As for orangutans, the op-ed by Meijaard and his colleagues took issue with an upbeat assessment by KLHK Minister Siti Nurbaya on World Orangutan Day, on 19 August. The minister stressed Indonesia's commitment to conservation and said all three species in the country—including the Tapanuli orangutan, whose existence is threatened by a hydropower project in North Sumatra—would continue to "grow and thrive." The authors countered in *The Jakarta Post* that "A wide range of scientific studies … show that all three orangutan species have declined in the past few decades and that nowhere are populations growing."

KLHK did not respond to queries from *Science*. In a response published by *The Jakarta Post* on 26 September, however, a ministry spokesperson said Meijaard's analysis was based on "outdated information" and ignored many steps KLHK had taken to protect orangutans, including ending some concessions for new plantations. Nurbaya's assessment "was intended to build optimism," the rebuttal said.

KLHK has also blocked conservation initiatives. In late 2019, the ministry unilaterally ended a joint program in forest conservation with the World Wildlife Fund (WWF) after the organization criticized the government's handling of forest fires. The move forced WWF to lay off about 400 staff at offices across Indonesia. That same year, KLHK asked the Center for International Forestry Research in Bogor to retract a sobering estimate of the area burned during the fire season. As *Science* has reported (14 February 2020, p. 722), the spat led to the deportation of David Gaveau, a French landscape ecologist who worked with the center.

Some NGOs have chosen to adapt. PanEco, a Swiss-based organization, once campaigned against the Batang Toru hydropower project in North Sumatra, which poses a threat to the 800 or so remaining Tapanuli orangutans. It did an about-face in 2019 and decided to work with the Indonesian government and the company building the dam (*Science*, 13 September 2019, p. 1064). But a new population estimate produced by the group since then has not yet been released; a PanEco representative says it's up to the BKSDA office in North Sumatra to do so.

Meijaard says the Indonesian government should open up about the state of its biodiversity by making results from population and habitat surveys public and storing them in Indonesian and international databases. But with foreign researchers squeezed out and their Indonesian colleagues increasingly fearful, that seems unlikely to happen.

One Indonesian scientist says criticizing the government publicly could mean losing their job. "And it's not only about me, but about hundreds of people working in the same organization," the researcher adds. Since the *Jakarta Post* article, at least one-third of the Indonesia-based co-authors on an upcoming paper about orangutan conservation have asked Meijaard to remove their names, he says: "This fear is doing real damage to Indonesian science." ■

Dyna Rochmyaningsih is a science journalist in Palembang, Indonesia.

EVOLUTIONARY BIOLOGY

Secrets of Tibet's hot-spring snakes revealed

Mutations helped animals adapt to extreme temperatures, low oxygen

By **Elizabeth Pennisi**

Jia-Tang Li knows firsthand how tough life can be on the Tibetan Plateau. The air at 4500 meters is so thin that just a few steps take one's breath away. Despite bitter cold, the Sun is intense enough to quickly burn the skin. Yet the small grayish brown snakes this herpetologist at the Chengdu Institute of Biology at the Chinese Academy of Sciences studies have been thriving in the plateau's northern reaches for millions of years. The Tibetan hot-spring snake, *Thermophis baileyi*, keeps from freezing to death by hanging around the region's geothermal pools, feasting on frogs and small fish living there.

Now, advances in genome sequencing are giving Li and others a more detailed look at how the snake has adapted to its extreme environment. In recent work, his team has pinpointed genetic adaptations that may help the snake find waters that are just warm enough and withstand the low oxygen and intense Sun. Li's team has also reconstructed the snake's evolutionary history, work that could guide efforts to save these reptiles as they face ever-greater threats from humans.

"This is a pretty extreme place for snakes to be living," says Sara Ruane, a herpetologist at the Field Museum. The work "just shows how adaptable snakes are." Says Alex Pyron, a herpetologist and evolutionary biologist at George Washington University: "For reptiles, we generally assume if it's too cold, there won't be any snakes or lizards. Not so fast, says *Thermophis*!"

Although the Tibetan Plateau has more than 100 species of snakes, *T. baileyi* is the only one that lives at about 4500 meters. Two other hot-spring snakes, the Sichuan hot-spring snake and the Shangri-La hot-spring snake, live at lower elevations and are less dependent on the hot springs, says Song Huang, a herpetologist at Anhui Nor-

Tibetan hot-spring snakes exploit geothermal pools to survive at a high altitude.

mal University. Other snakes, including a pit viper, exist even higher, "but the key difference is that they are predominantly found at lower elevations," says Anita Malhotra, a herpetologist and molecular ecologist at Bangor University.

For snakes, "The outside temperature is very influential on the body temperature," says Justin Bernstein, who studies snake evolution at the University of Kansas, Lawrence. To withstand air temperatures that can drop below –20°C, the snakes lurk near the edges of geothermal pools reaching 40°C and hibernate. But the warmth brings challenges of its own. "Being a hot snake at high altitude is physiologically challenging," says Raymond Huey, a physiological ecologist at the University of Washington, Seattle, because the warmth boosts the snakes' need for scarce oxygen.

Between 2015 and 2018, Li led teams to the plateau to capture snakes and collect blood or small bits of tissue from the tip of the tail for sequencing studies. Because the snakes are rare and typically active only between 11 a.m. and 3 p.m.—if the Sun is out—the researchers could go days without seeing one, Li recalls. Their initial, incomplete genome, published in 2018, revealed mutations in genes that enhance breathing, make red blood cells more efficient, and make the heart beat more powerfully—changes that may help the snakes cope with low oxygen. Some of the same genes have also changed in yaks, pikas, ground tits, and other species that live at high elevations, albeit in different ways, he and his colleagues reported later.

That study also identified genetic changes in response to intense sunlight on the plateau, including modifications to genes whose proteins help repair DNA damaged by ultraviolet radiation. More recent work, reported on 3 September in *The International Journal of Molecular Sciences*, builds on those findings by showing at least two of those genes—*ERCC6* and *MSH2*—are also altered in a lizard living on the Tibetan Plateau and other high-altitude animals. "There seems to be a very predictable subset of genes … involved in high altitude adaptation," says Todd Castoe, an evolutionary biologist at the University of Texas, Arlington.

A more complete genome published on 1 August in *Innovation* shows how the snakes cope with another challenge: finding bathing spots that are comfortable but not too hot. Li's team compared genes involved in temperature sensing in hot-spring snakes and other organisms, including snakes such as rattlesnakes and pythons that hunt by sensing heat. They found that a gene called *TRPA1* is mutated in both the hot-spring and heat-sensing snakes.

TRPA1 encodes an ion channel that opens and closes in response to temperature changes, setting off a cascade of signals that can be relayed to the brain or to other parts of the snake's body. In rattlesnakes and pythons, changes to *TRPA1* lower the activation temperature of the channel, improving the snakes' ability to detect warm prey. In hot-spring snakes, biochemical tests by Li's group revealed, different changes to the protein ensure the channel opens up very quickly and completely.

What this means for the snake isn't yet clear, but Li suspects the changes might help it orient toward warmth. In behavioral experiments reported in the new paper, his group found that given a choice between a cold rock and a warm one, hot-spring snakes chose the warm rock more often and more quickly than did two other snake species that don't live at high elevations.

"These snakes are probably walking a really fine line between not freezing to death and not boiling," Castoe points out. The threat of scalding seems to have shaped other genes: Li's group found heat shock proteins, which repair proteins damaged by heat, have undergone accelerated evolution in the hot-spring snakes.

Climate history has also left a mark on the snakes' DNA. Li's team sequenced the genomes of 58 Tibetan hot-spring snakes collected in 15 places spanning about 500 kilometers. DNA differences pointed to three distinct populations that roughly coincide with three geothermal regions across the northern plateau. The pattern is the handiwork of past ice ages, Li and colleagues argue in the 7 September issue of *Molecular Ecology*. The westernmost group split off from the rest of the species during a major ice age between half and three-quarters of a million years ago; then the central and eastern populations were divided 300,000 years ago when another ice age threw up a new barrier of cold, isolating each group or snakes near its hot springs. "The thermal springs allowed them to get through the ice ages," Ruane says.

The isolation also led to unique adaptations in each group. For example, several genes for processing selenium and for metabolizing sulfur have evolved rapidly in the western group, possibly to deal with the specific chemistry of hot springs there, Li suggests.

Even though the three groups intermix occasionally, they are unique enough that "I would consider each a species," says Frank Burbrink, a herpetologist at the American Museum of Natural History. (Li and Ruane aren't convinced they're that distinct.) Each, Burbrink thinks, needs to be conserved separately.

Yet populations are declining. "Human activities have seriously affected the survival of Tibetan hot-spring snakes," says Huang, who collaborated with Li on the *Molecular Ecology* paper. In some places, construction has destroyed dens where these reptiles spend the winters. In other places, development has ruined wetlands that act as nurseries for newly hatched snakes. In May 2023, Huang and colleagues hope to begin to build artificial snake dens, restoring the wetlands and fencing people out of these sensitive spots.

The snakes, it seems, are exquisitely adapted to harsh nature—but not to the pressures that humans bring. ■

PHOTO: JUN-FENG GUO

PLANETARY SCIENCE

Fireball is traced to far edge of Solar System

Rocky meteor suggests distant cloud of comets also contains asteroids

By **Eric Hand**

Just before dawn on 22 February 2021, a fireball lit up the skies across Canada's Alberta province when a 2-kilogram space rock vaporized as it plunged through Earth's atmosphere. Although the object hailed from the Oort Cloud—a conglomeration of comets at the edge of the Solar System—it wasn't a comet, researchers now say. Data collected during its fall suggest the object was made of rock rather than ice and behaved more like an asteroid.

Independent observers of the new work say the find sheds light on the processes that formed our Solar System and challenges the conventional wisdom that the Oort Cloud only holds icy comets. "It's telling us that there was scattering and depositing of material from all over the Solar System into the Oort Cloud," says Karen Meech, a planetary scientist at the University of Hawaii's Institute for Astronomy.

The discovery could provide support for models that suggest objects from the asteroid belt were dispersed into the Oort Cloud soon after the Solar System's birth 4.6 billion years ago, says Bill Bottke, a Solar System dynamicist at the Southwest Research Institute. "This is very exciting," he says. "Now, we have to see what we can do to explain it."

First proposed by Dutch astronomer Jan Oort in 1950, the Oort Cloud is a spherical halo of comets that stretches out halfway to Proxima Centauri, the Sun's nearest neighbor, well beyond the view of even the largest telescopes. "Everything we know about it is indirect," says Denis Vida, a meteor astronomer at Western University who led the new study.

Scientists presume the Oort Cloud became populated with comets when the gravitational muscle of Jupiter and the other giant planets scattered far and wide the icy objects left over from the formation of the outer Solar System. Occasionally, a passing star will gravitationally nudge an Oort Cloud object and send it plummeting into the inner Solar System. These objects are known as long-period comets, defined by the eccentric paths they follow, taking hundreds or even thousands of years to orbit the Sun.

In 2016, Meech and colleagues reported the discovery of an unusual long-period comet that was dark and lacked a bright tail of vaporized ice. In fact, the object seemed much more like an asteroid—a clue that the Oort Cloud's composition might not be so homogeneous. Meech called it a Manx comet, after a breed of cat without a tail. Although astronomers have since detected dozens more of these comets, they have yet to definitively demonstrate that the objects are asteroids because they are so faint and fast-moving.

A 2021 fireball that saturated security cameras across Alberta province in Canada hailed from the Oort Cloud, researchers say.

PHOTO: CYRIL RUOSO/MINDEN PICTURES

Now, with the Canadian fireball, researchers believe they have caught one of these rare objects crashing into Earth's atmosphere. "It was very bright, very fast, and it left a luminous train for several seconds," says Vida, who presented the work on 5 October at a meeting of the Division for Planetary Sciences of the American Astronomical Society.

In addition to hundreds of reports from witnesses who caught the fireball on dashboard and security cameras, Vida and his colleagues also worked with images from the Global Fireball Observatory, a network of high-precision sky cameras. Even a lightning monitor on an orbiting satellite caught the flare of the fireball. By combining these observations, the team calculated the object's trajectory and found it had a roughly 1000-year orbit—proof it came from the Oort Cloud.

Despite its provenance, the object was distinctly uncometlike. Most cometary fireballs are fragile; they fragment and burn up high in Earth's atmosphere. But this object, plunging at 62 kilometers per second, penetrated much deeper, Vida says, suggesting it was tough and rocky rather than icy. It also broke up in two phases at two discrete pressures—mirroring the breakup of a common kind of asteroid that drops meteorites to Earth.

Vida and colleagues turned to historical data to see whether other objects like this had been overlooked. They found that in 1979, a network of fireball cameras in Canada had tracked the demise of a 20-gram object that, like the Alberta object, was on a long-period orbit characteristic of an Oort Cloud object. It, too, fell through the atmosphere like rock, not ice. After comparing the 2021 and 1979 events with the total number of long-period comets caught by the two fireball networks, they calculated that between 1% and 20% of the Oort Cloud must be rocky.

Bottke, however, is skeptical about extrapolating from such a small number of events. He also thinks there might be a "survivability bias" toward detecting rocky objects because they're tougher than comets, skewing the true proportion of rocky objects in the Oort Cloud toward the low end of the estimate.

But even if the Oort Cloud is just 1% rocky, explaining how these objects got there from the asteroid belt will challenge theorists, says Alan Jackson, a planetary astronomer at Arizona State University, Tempe. He says the finding could lend support to one hypothesis called the Grand Tack, which suggests that just 3 million years after the Solar System's birth, Jupiter swooped inward toward the Sun, nearly to Earth's orbit, before moving back out to near to its current position. "As you can imagine, in the process of doing that, it stirs stuff up"—including flinging many of the rocky objects in its path out to the Oort Cloud, Jackson says.

Like Bottke, Meech is worried about making too much of two fireball events. But she's eager for Vida and his colleagues to capture more of these unusual streaks on the sky. "It's very interesting," she says. "I'm hoping they'll get more of them." ■

GLOBAL CHANGE

Climate change threatens supercomputers

Costly adaptations help stave off effects of wildfires, storms, and hot weather

By **Jacklin Kwan**

In 2018, during a savage drought, the California wildfire known as the Camp Fire burned 620 square kilometers of land, reducing several towns nearly to ashes and killing at least 85 people. The disaster also had a ripple effect far from the flames, at a supercomputer facility operated by Lawrence Berkeley National Laboratory (LBNL) 230 kilometers away. The National Energy Research Scientific Computing Center (NERSC) typically relies on outside air to help cool its hot electronics. But smoke and soot from the fire forced engineers to cool recirculated air, driving up humidity levels.

"That's when we discovered, 'Wow, this is a real event,'" says Norm Bourassa, an energy performance engineer at NERSC, which serves about 3000 users a year in fields from cosmology to advanced materials. Hot and dry weather took a toll again a year later. California utilities cut NERSC's power for fear that winds near LBNL might blow trees into power lines, sparking new fires. Although NERSC has backup generators, many machines were shut down for days, Bourassa says.

Managers at high-performance computing (HPC) facilities are waking up to the costly effects of climate change and the wildfires and storms it is intensifying. With their heavy demands for cooling and massive appetite for energy, HPC centers—which include both supercomputers and data centers—are vulnerable, says Natalie Bates, chair of an HPC energy efficiency working group set up by Lawrence Livermore National Laboratory (LLNL). "Weather extremes are making the design and location of supercomputers far more difficult."

Climate change can bring not only heat, but also increased humidity, reducing the efficiency of the evaporative coolers many HPC centers rely on. Humidity can also threaten the computers themselves, as NERSC discovered during a second fire. As interior air was recirculated, condensation inside server racks led to a blowout in one cabinet, Bourassa says. For its next supercomputer, set to open in 2026, NERSC is planning to install power-hungry chiller units, similar to air conditioners, that would both cool and dehumidify outside air.

The cost of such adaptations is motivating some HPC centers to migrate to cooler and drier climates, places like Canada and Finland, says Nicolas Dubé, chief technologist for Hewlett Packard Enterprise's HPC division. "We can't build in some locations going forward, it just doesn't make sense," he says. "We need to move north."

But some HPC facilities find themselves stuck. The supercomputers at LLNL are used to simulate the explosions of nuclear weapons. The cost of relocating specialized personnel could be prohibitive, and LLNL's California site is a highly secure facility, says Chief Engineer Anna-Maria Bailey. Instead, LLNL is studying the possibility of moving its computers underground. "Humidity and temperature control would be a lot easier," she says, "like a wine cave."

Running from climate change can be futile, however. In 2012, the National Center for Atmospheric Research opened a supercomputer site in Cheyenne, Wyoming, to take advantage of its cool, dry air. However, climate change has led to longer and wetter thunderstorm seasons there, hampering evaporative cooling. In response, the Wyoming center added a backup chiller. "Now you have to build your infrastructure to meet the worst possible conditions, and that's expensive," Bates says.

Climate change is also threatening the lifeblood of these HPC facilities: electricity. HPC centers consume up to 100 megawatts of power, as much as a medium-size town. Meanwhile, hotter temperatures can increase power demands by other users. During California's heat wave this summer, when air-conditioning use surged, LLNL's utility told the facility to prepare for power cuts of 2 to 8 megawatts. Although the cuts did not happen, it was the first time the laboratory was asked to prepare for nonvoluntary cuts, Bailey says.

Many HPC facilities are heavy users of water, too, which is piped around components to carry away heat—and which will grow scarcer in the western United States as droughts persist or worsen. A decade ago, Los Alamos National Laboratory in New Mexico invested in water treatment facilities so its supercomputers could use reclaimed wastewater rather than more precious municipal water, says Jason Hick, an LANL program manager.

Although droughts and rising temperatures may be the biggest threats, a RIKEN HPC facility in Kobe, Japan, must contend with power outages because of storms, which are expected to get more intense with global warming. A high-voltage substation was flooded in 2018, cutting RIKEN's power for more than 45 hours. Similarly, a lightning strike this year on a power line knocked the facility out for about 15 hours. The center's 200 projects span fields such as materials science and nuclear fusion, says Fumiyoshi Shoji, who directs operations and computer technologies. "If our system were unavailable, these research projects would stall," he says.

Bates says future supercomputers will need to be constructed in ways that will allow them to cut performance—and the need for cooling and power—during bouts of bad weather. "We're still building race cars, but we're building them with a throttle." ■

Jacklin Kwan is a science communications graduate student at Imperial College London.

ILLUSTRATION: ERHUI1979/GETTY IMAGES. ADAPTED BY M. ATAROD/*SCIENCE*

The winners of this year's Nobel Prize in Chemistry—Carolyn Bertozzi, Morten Meldal, and Barry Sharpless—on display at a press conference last week.

PHOTO: JONATHAN NACKSTRAND/AFP VIA GETTY IMAGES

NOBEL PRIZES

Molecular links snap up award

Trio of researchers pioneered "click chemistry" to design drugs and industrial materials

By **Daniel Clery** *and* **Robert F. Service**

Think of it as Lego for chemistry. A pioneering way to join molecules together, called click chemistry, last week earned its developers this year's Nobel Prize in Chemistry. The method hasn't quite turned chemistry into child's play, but it has made molecules from cancer drugs to industrial materials easier to assemble and allowed biologists to manipulate molecules in cells without disrupting their normal chemistry.

Carolyn Bertozzi of Stanford University, Morten Meldal of the University of Copenhagen, and Barry Sharpless of Scripps Research will share the 10 million Swedish kronor ($915,000) prize equally. Bertozzi was the lone woman to win a scientific Nobel this year (see p. 118), and Sharpless is the second scientist ever, after biochemist Frederick Sanger, to win two chemistry Nobels. (Sharpless earned a share of the 2001 prize for finding catalysts that create mirror-image molecules.) "Prizes aren't what I'm doing science for," Sharpless said last week at a press conference following the Nobel announcement. "I have to do it. It's kind of a compulsion."

The work of the three laureates has had "an enormous impact on science," said Olof Ramström, a chemist at Linnaeus University and a member of the Nobel Committee, at a press conference last week. "This discovery system can be used for almost everything," Ramström said. "So it has spread very widely, and it's been used, for example, to make new drug compounds to treat illness … [and make] all sorts of different materials like polymers, like gels."

The heart of chemistry is coaxing molecules to react and to form a specific product. But chemical reactions can be slow and generate a variety of products that must be separated before further study. In 2001, Sharpless and his colleagues sought to speed and simplify reactions by finding pairs of molecular linkers that reliably snap together when needed, while not reacting with anything else. Equipped with the right linkers, two reactants could form product more efficiently than ever before. Sharpless described his goal as click chemistry.

As linkers, Sharpless initially eyed an alkyne, which has two carbons linked by a triple bond, and an azide, which has a trio of nitrogen atoms in a line, each double bonded to its neighbor. In 1960, German chemist Rolf Huisgen discovered these two very different groups react reliably to create two closely related ring-shaped compounds with few unwanted side reactions. But the reaction was slow and required plenty of heat. "A lot of organic molecules couldn't take that," says Laura Kiessling, a chemist at the Massachusetts Institute of Technology. Chemists needed a way to click alkynes and azides together without destroying everything else in their flasks.

In 2002, Meldal and Sharpless independently hit on the same solution: sprinkling in a dash of copper. They added an alkyne to one molecule and an azide to another and used copper to snap the two molecules together. The copper dramatically sped the reaction, required no extra heat, and formed just one of the two possible combinations Huisgen had discovered, providing a dependable result every time. "It really opened the door to the whole field," Kiessling says.

Bertozzi, who came at the problem from a different direction, brought the system into biology. In the 1990s, she was studying glycans, complex sugars on the surface of cells that played a then–largely unknown role. Bertozzi was seeking a way to probe their functions, for example by adding a fluorescent or other marker that could be seen by imaging.

In 2000, she explored using an azide as a handle to link a marker to glycans. She attached the azide to sugars and fed the combo into cells, which incorporated the combined molecule into glycans on their surfaces. The alkyne developed by Sharpless and Meldal seemed the perfect way to attach other compounds to those azides. But copper is toxic to cells. So, in 2004, Bertozzi ditched the copper and remade alkynes, taking them from linear molecules to circular ones. "It's like you spring-load the bond," making it more reactive, Kiessling says.

Because azides and alkynes aren't common in living cells, the linkers only had eyes for each other and ignored the thousands of other molecules around them. They gave Bertozzi a powerful and precise way to study glycans and their biological role. Among other things, she learned that some tumor cells make protective glycans to shield themselves from immune cells—a discovery she and her colleagues have turned into an antitumor drug candidate. They attached enzymes that break down tumor-cell glycans to a glycan-specific antibody, which ferries the enzymes to their target. The drug is now in human trials.

In addition to anticancer compounds, click chemistry has already been used to make new antimicrobials, herbicides, diagnostics, corrosion retardants, tissue regeneration materials, gels, and polymers. All this, because chemists envisioned ways to craft simple, predictable reactions. Said Sharpless last week: "I find it very helpful to think like a molecule." ■

The origin of the pandemic that began in Wuhan, China, at the end of 2019 has been hotly debated.

PHOTO: HECTOR RETAMAL/AFP VIA GETTY IMAGES

COVID-19

Evidence backs natural origin for pandemic, report asserts

Authors were dropped from broader Lancet review

By **Jon Cohen**

The acrimonious debate over the origin of the COVID-19 pandemic flared up again this week with a report from an expert panel concluding that SARS-CoV-2 likely spread naturally in a zoonotic jump from an animal to humans—without help from a lab.

"Our paper recognizes that there are different possible origins, but the evidence towards zoonosis is overwhelming," says coauthor Danielle Anderson, a virologist at the University of Melbourne. The report, which includes an analysis that found the peer-reviewed literature overwhelmingly supports the zoonotic hypotheses, appeared in the *Proceedings of the National Academy of Sciences* (*PNAS*) on 10 October.

The expert panel's history reflects the debate's intensity. Originally convened as a task force of the Lancet COVID-19 Commission, a wide-reaching effort to derive lessons from the pandemic, it was disbanded by Columbia University economist Jeffrey Sachs, the commission's chair. Sachs alleged that several members had conflicts of interest that would bias them against the lab-origin hypothesis.

Sachs and others who contend scientists have ignored the lab-leak possibility aren't persuaded by the new analysis. Its literature analysis was a good idea, says Jesse Bloom, a virologist at the Fred Hutchinson Cancer Center who has pushed for investigating the lab-leak hypothesis. But he says zoonosis proponents have provided little new data. "What we've seen is mostly reanalysis and reinterpretation of existing evidence." And Sachs says the report did not "systematically address" the possible research-related origin of the pandemic. In September, *The Lancet* published a report from his commission that gave equal weight to both hypotheses.

When Sachs launched *The Lancet*'s origin task force in December 2020, he tapped conservation biologist Peter Daszak to lead it. Daszak heads the nonprofit EcoHealth Alliance, which has funded work on bat coronaviruses at China's Wuhan Institute of Virology (WIV). Because the first COVID-19 cases were reported in Wuhan some scientists suspect research conducted at WIV led to the spread of SARS-CoV-2. Sachs came to believe Daszak and other task force members who had links to WIV and the EcoHealth Alliance could not assess that possibility fairly and should step down. After fierce infighting over issues including transparency and access to information, Sachs pulled the plug on the task force in September 2021.

But the members continued to meet. "We had a distinguished, diverse group of experts … and we thought we had something to offer whether or not we were part of the commission," says Gerald Keusch, an infectious disease specialist at Boston University.

In assembling its report, the task force interviewed researchers who have different perspectives on the pandemic's origin. It also reviewed the history of other viruses that have an RNA genome, like SARS-CoV-2, and have made zoonotic jumps. And it combed through the scientific literature for papers addressing COVID-19's origin.

Their report overlaps with the wider ranging *Lancet* report. Both stress the need to address how forces such as deforestation and the illicit animal trade increase the risk of viral spillovers. And both emphasize the risk of lax safety measures, both in labs and field studies that hunt for pathogens.

But the two reports differ on the origin of the pandemic. The *PNAS* authors say their literature search revealed "considerable scientific peer-reviewed evidence" that SARS-CoV-2 moved from bats to other wildlife, then to people in the wildlife trade, finally causing an outbreak at the Huanan Seafood Market in Wuhan. In contrast, they say, relatively few peer-reviewed studies back the lab-leak idea, and Daszak notes that much of the argument has been advanced through opinion pieces. "The most parsimonious hypothesis is that the pandemic emerged through the animal market system," Daszak says. "And while the evidence could be a lot better, it's fairly good."

The *PNAS* perspective also stands apart for its recommendations on how to improve efforts to provide early warnings of a brewing pandemic. In a section called "looking forward," the authors promote "smart surveillance" that would focus on transmission hot spots where humans and wild animals mingle, using cutting-edge technologies to look for novel viruses. "For nearly 3 years we've been running in circles about different lab-leak scenarios, and nothing has really added to this hypothesis," says coauthor Isabella Eckerle, a virologist at the University of Geneva. "We have missed the chance to say … what can we do better the next time?"

Co-author Linda Saif, a coronavirus researcher at Ohio State University, Wooster, says studies of human and animal viral infections remain too siloed. But, "There's no source of funding" for combining them.

David Relman, a microbiome specialist at Stanford University who thinks the different origin scenarios are equally plausible, believes the *PNAS* and *Lancet* reports are "not at all contradictory or inconsistent with each other." And Relman, who was interviewed by the task force, compliments it for highlighting the need to better prepare for a new pandemic. "At the end of the day," he says, "this much is true: Spillovers, outbreaks, and pandemics are the result of human activities, for which much greater scrutiny, mindfulness, and insight are desperately needed." ■

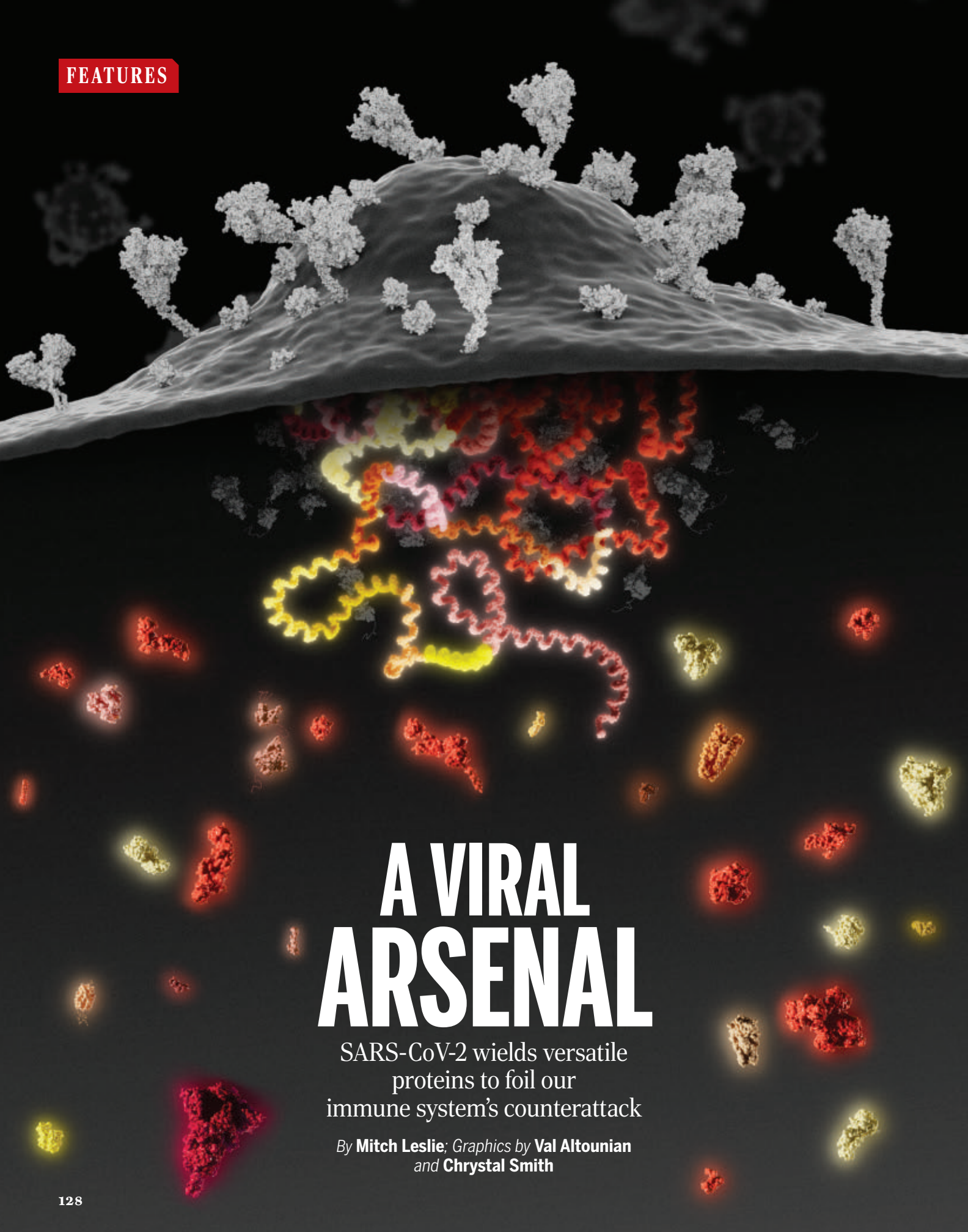

A VIRAL ARSENAL

SARS-CoV-2 wields versatile proteins to foil our immune system's counterattack

By **Mitch Leslie**; *Graphics by* **Val Altounian** *and* **Chrystal Smith**

Alpha, Beta, Delta, Omicron, BA.5—with each new SARS-CoV-2 variant or subvariant, the coronavirus seems to hone its ability to infect and spread between people. Although vaccines, drugs, and immunity from prior infections are allowing more and more people to dodge severe cases of COVID-19, the coronavirus has already killed more than 6 million people, according to the World Health Organization, and the true toll may exceed 18 million. Some virologists worry COVID-19 is here to stay, with SARS-CoV-2 potentially sickening people once or more a year as adenoviruses and other coronaviruses that cause the common cold do.

One key to the virus' success is its ability to neutralize the body's immune response, thanks to its arsenal of proteins. Over the past 3 years, investigators have begun to explore those viral countermeasures. They've shown that many of SARS-CoV-2's molecules manage to shield the virus—at least temporarily—from host immunity, allowing the invader to replicate and spread to more people.

A pitched battle between virus and host erupts when SARS-CoV-2 invades vulnerable body cells, transforming them into virus factories. The incursion, initiated when the spike proteins on the virus latch onto cellular targets, trips an alarm, provoking a sweeping counteroffensive by the multipronged immune system. Cells that are under attack begin to release potent immune proteins called interferons that boost resistance to the coronavirus. Once certain immune soldiers called CD8-positive T cells detect signs of SARS-CoV-2, they hunt down and destroy infected body cells, reducing the production of new viruses. Other immune warriors known as B cells begin to churn out antibodies that glom onto virus particles, locking them out of cells.

All too often, the virus manages to thwart these defenses. As it replicates ferociously in millions of people, its spike protein has picked up mutations that allow the virus to evade neutralizing antibodies evoked by vaccines or previous infection.

And like many viruses, SARS-CoV-2 is adept at blocking, dodging, and deceiving our immune protections in other ways. "Viruses are usually in an arms race with the host," says viral immunologist Adriana Forero of the Ohio State University College of Medicine. Their strategies elicit grudging admiration from virologist Stanley Perlman of the University of Iowa, who has been studying coronaviruses for more than 30 years. "Every time we discover something really cool in the immune system, we find a virus has already counteracted it," he says.

After SARS-CoV-2 infects a cell, it releases its RNA genome, which prompts the production of proteins that build fresh viruses and disrupt cellular defenses.

POTENT PROTEINS

Underpinning SARS-CoV-2's counterattack is the versatile suite of proteins that it coerces infected cells to manufacture from its RNA code. Researchers still disagree about how many proteins the virus' cellular victims make—estimates range from 26 to more than 30—but SARS-CoV-2 deploys more weapons than most other RNA viruses. The Ebola virus, for example, makes do with only seven proteins.

To probe how a particular SARS-CoV-2 protein upends our immune defenses, researchers typically engineer cells to produce unusually large amounts of the molecule. They then catalog the effects on cellular responses such as interferon output. Such studies suggest most proteins in the virus' arsenal play immune suppressing roles—even such unlikely actors as the membrane protein that helps new viral particles assemble and the editing enzyme that snips freshly made proteins down to size.

SCIENCE ONLINE

An enhanced version of this feature allows readers to examine how each SARS-CoV-2 protein may sabotage host defenses. Go to https://scim.ag/ViralArsenal.

Not all of these functions have been confirmed, however. Perlman cautions that overproducing just a single viral protein might not trigger the same cellular effects as a natural infection by the virus. Verifying the findings will require experiments with the virus itself, genetically tweaked to lack individual proteins, but researchers have performed few such studies, which require elaborate biosafety precautions. Immune-suppressing proteins may also rely on partnerships with one or more other viral molecules, virologist Susan Weiss of the University of Pennsylvania, Perlman, and colleagues recently revealed in a study of MERS-CoV, the relative of SARS-CoV-2 that causes Middle East respiratory syndrome.

It's already clear, however, that SARS-CoV-2 goes to great lengths to sabotage the body's interferon response, which is central to our defense against viruses. Interferons switch on hundreds of genes that can stymie every step in a virus' infection cycle. Some fortify cells' outer defenses and enable them to rebuff viruses that try to break in. Others boost the internal defenses of cells that become infected, curbing the production of viral molecules or preventing them from assembling into new viral particles. Still other interferon-stimulated genes stop newborn viruses from leaving an infected cell. Interferons also help recruit T and B cells to the body's battle with the virus.

Studies of COVID-19 patients have underscored the importance of interferons for fighting off SARS-CoV-2. For example, interferon responses are faulty in a sizable percentage of patients with severe disease. Up to 20% of the sickest people carry antibodies that latch onto and incapacitate their own interferons, researchers have found.

Many other pathogens, including the viruses that cause flu, Ebola, and hepatitis C, take aim at the interferon response. But SARS-CoV-2 stands out, Forero says. "What's unusual is how comprehensive the virus is." Its various proteins disrupt multiple steps, including a cell's detection of viral RNA, transmission of the alert signal to the nucleus, synthesis of interferons, and activation of interferon-stimulated genes. Moreover, multiple coronavirus proteins can block the same step.

Some SARS-CoV-2 proteins use trickery to circumvent the interferon response. Nonstructural protein 15 (Nsp15), for example, snips distinctive sequences out of newly made viral RNA molecules, helping disguise the RNA from cellular pathogen detectors that would otherwise trigger interferon production. Even some proteins whose main role is structural join the counteroffensive. For example, the nucleocapsid protein's day job is packing the pathogen's RNA into the interior of the viral particle. But a study this year revealed a cellular enzyme snips the nucleocapsid protein into fragments that can block interferon production by infected cells.

SARS-CoV-2 doesn't just interdict the interferon response, however. It may also stymie other immune defenses. Some studies suggest, for example, that viral proteins such as ORF3a, ORF7a, and the envelope protein hobble a process called autophagy, in which infected cells digest their own contents, breaking down viruses and individual viral proteins in the process. SARS-CoV-2 may also meddle with MHC-I, a protein that displays bits of the invader on the surface of infected cells and summons T cells. Viral proteins such as ORF6 and ORF8 may curb cells' production of MHC-I or block its transfer to the cell surface, preventing T cells from recognizing and killing infected cells.

MULTITASKING MOLECULES

The virus gets the most from its small repertoire of proteins, many of which do double or triple duty. Nsp14 typifies these multitasking molecules. Like many of the virus' other proteins, Nsp14 performs several tasks that have nothing to do with immune eva-

Sabotaging the immune response

Scientists are still deciphering how SARS-CoV-2 neutralizes immune responses, but its counterattack relies on many proteins. Some appear to interfere with antiviral molecules called interferons, whereas others keep a cell from making its own defensive proteins or stymie the recycling process of autophagy. (Colors reflect a protein's gene, with some genes encoding multiple proteins.)

Anti-immune action

■ Block protein synthesis ● Block interferon response ⬟ Disrupt autophagy
▲ Prevent T cell detection ◆ Other protective mechanisms

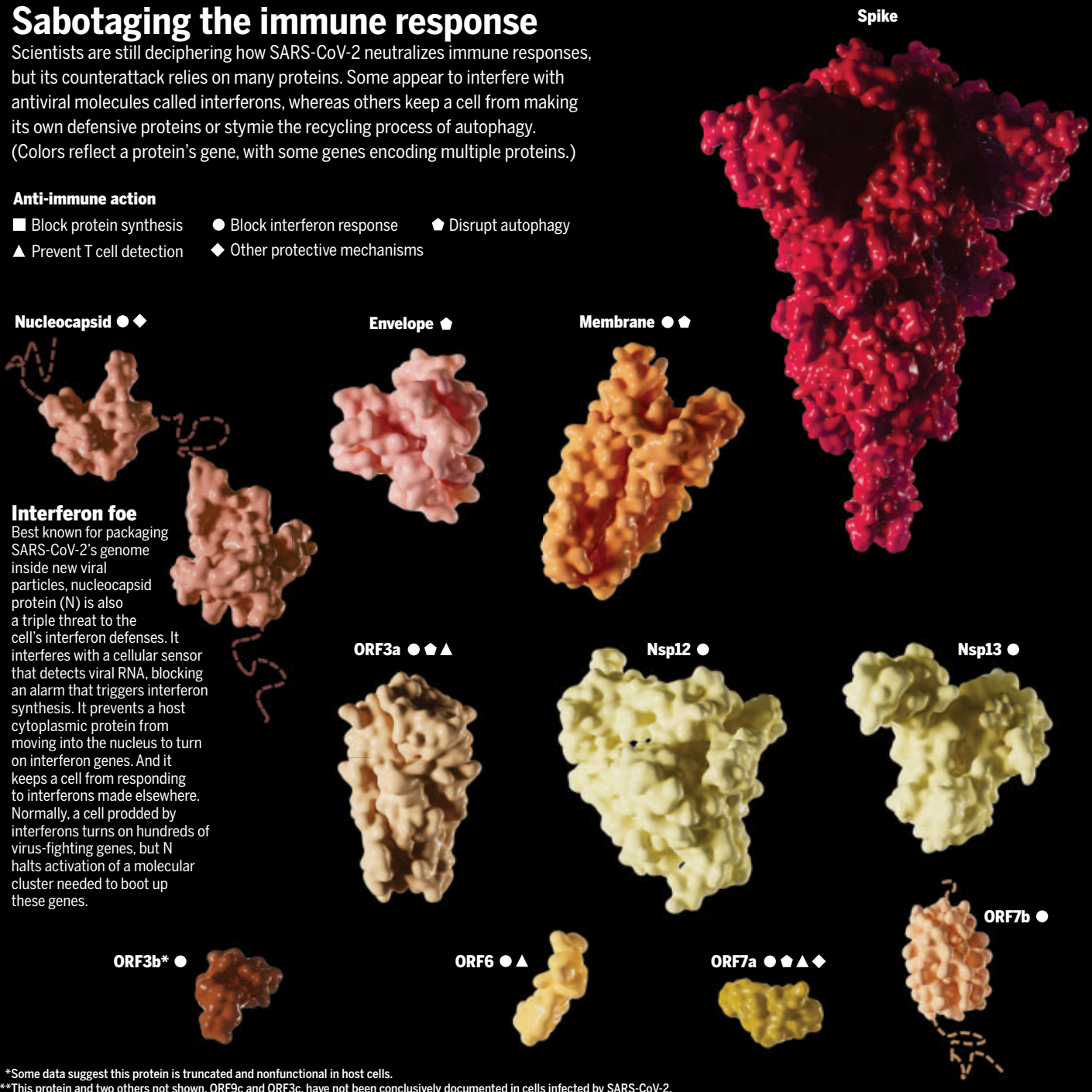

Interferon foe

Best known for packaging SARS-CoV-2's genome inside new viral particles, nucleocapsid protein (N) is also a triple threat to the cell's interferon defenses. It interferes with a cellular sensor that detects viral RNA, blocking an alarm that triggers interferon synthesis. It prevents a host cytoplasmic protein from moving into the nucleus to turn on interferon genes. And it keeps a cell from responding to interferons made elsewhere. Normally, a cell prodded by interferons turns on hundreds of virus-fighting genes, but N halts activation of a molecular cluster needed to boot up these genes.

*Some data suggest this protein is truncated and nonfunctional in host cells.
**This protein and two others not shown, ORF9c and ORF3c, have not been conclusively documented in cells infected by SARS-CoV-2.
CREDITS: (GRAPHIC) V. ALTOUNIAN AND C. SMITH/*SCIENCE*; (PROTEINS) HTTPS://SCIM.AG/VIRALARSENAL

sion. It teams up with Nsp10 to help the virus reproduce by correcting errors in newly synthesized copies of the viral RNA genome. Nsp14 also combines forces with other proteins, including Nsp9 and Nsp12, to tag the RNA with a molecular cap that allows ribosomes, the cell's proteinmaking factories, to read it and churn out viral proteins.

Those jobs should keep Nsp14 busy. But a 2021 study by immunologist Jack Chun-Chieh Hsu of Yale University and colleagues revealed yet another possible function: The molecule somehow shuts down an infected cell's production of its own proteins. Hsu says this blockade may benefit SARS-CoV-2 by forcing a cell to divert its resources into making viral proteins. It may also prevent the cell from turning on interferon-stimulated genes. "It's an important strategy to counter the production of these antiviral proteins," Hsu says. Another of SARS-CoV-2's weapons, Nsp1, also appears to induce a similar immunity-blocking effect by jamming ribo-

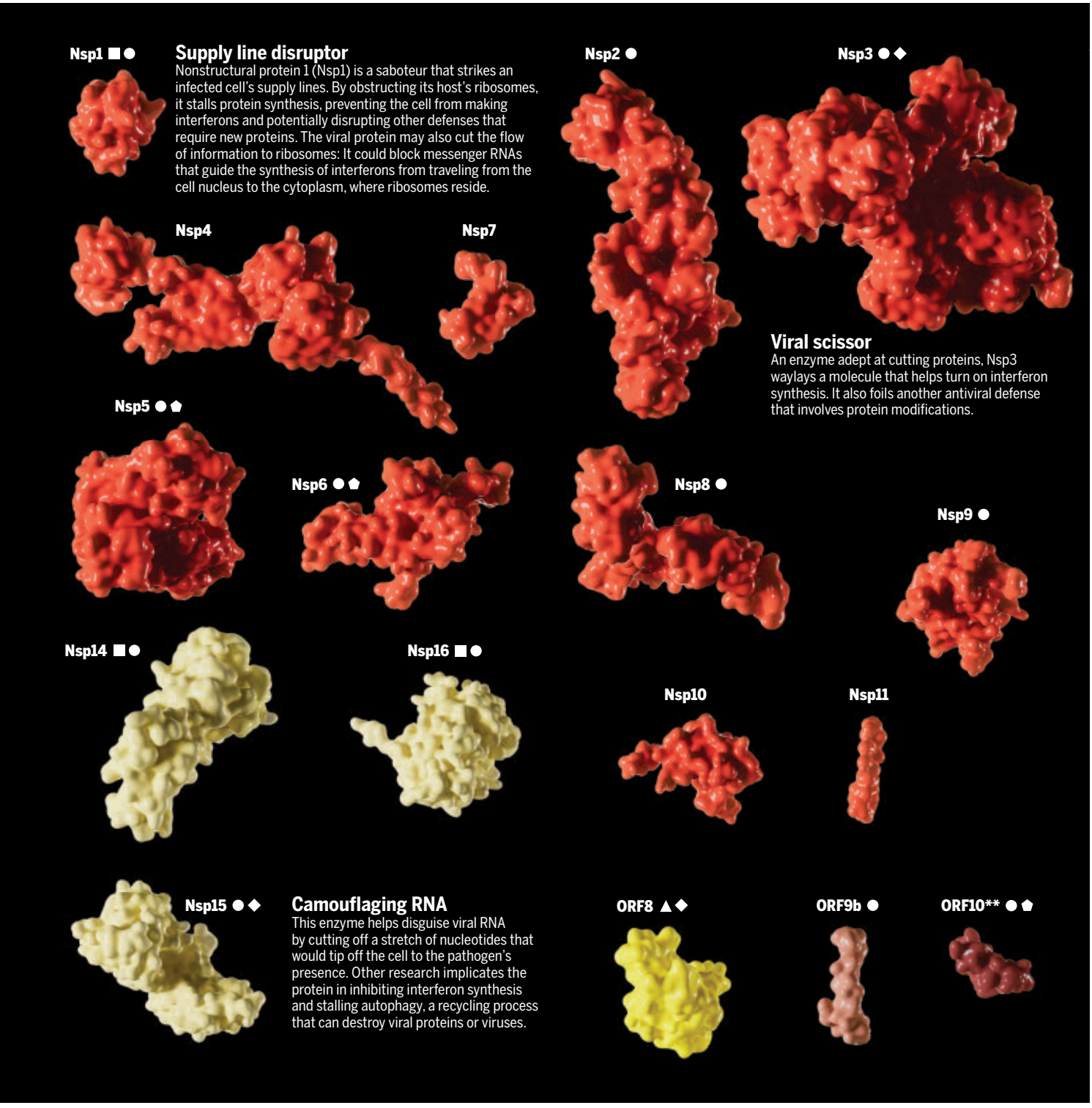

somes, keeping them from producing the host cell's own proteins. For reasons scientists don't understand, though, the cell is still able to make viral proteins.

Researchers may be able to turn their knowledge of SAR-CoV-2's anti-immune tactics against the virus. Several groups have screened existing compounds and drugs for activity against Nsp15. So far, however, no one has created drugs specifically designed to thwart SARS-CoV-2's anti-immune effects. (Pfizer's drug combo of nirmatrelvir and ritonavir, better known as Paxlovid, targets a viral enzyme, Nsp5, which has immune-thwarting properties, but the company's goal was instead to block the protein's central role in SARS-CoV-2's replication.)

Scientists don't yet have the full picture of SARS-CoV-2's ploys for eluding the body's defenses, but as the pandemic drags on, they will have plenty of opportunities—and plenty of urgency—to learn more. "We have built a nice foundation," Forero says, "but there is a lot of room to go further." ■

A two-step chemical and biological process can convert mixed plastics into useful chemicals.

PLASTIC RECYCLING

Recycling plastic using a hybrid process

Integrating oxidation and bioconversion provides a solution to recycle mixed plastics

By **Ning Yan**

Since the early 20th century, plastics have played an ever-increasing role in human society. There is polystyrene, a spongy material widely used in protective packaging, such as styrofoam. There is polyethylene, the most produced plastic today, whose different density variants have been used in everything from plastic bags to poolside furniture. There is also polyethylene terephthalate (PET), which is the main ingredient in many synthetic fibers and water bottles. The numerous advantages offered by these nondegradable plastics, such as versatile physical properties and low manufacturing costs, have yet to be meaningfully challenged by another class of materials in the marketplace. However, the accumulative environmental cost of plastic waste is increasingly becoming an irreversible global catastrophe. On page 207 of this issue, Sullivan *et al.* (*1*) report an expansion of the toolbox for recycling plastic mixtures into other useful chemicals through a process comprising chemical oxidation and biological conversion.

After reducing and reusing, recycling is the last option to prevent plastics from becoming forever waste. Unlike reducing and reusing, whose success is almost entirely governed by market forces, recycling presents some opportunities to be improved by chemistry. At present, plastic recycling is predominantly achieved using mechanical methods. Plastics recycled in this manner lack in quality and thus are often downcycled into lower-value implementations compared with their initial applications. To combat this one-way downcycling, researchers have been exploring chemical and biological processes to develop alternative recycling routes for converting plastic waste into commercially valuable chemicals. Within the past two years, polystyrene has been converted back to styrene monomers in the presence of table salt and an oxidized copper scrubber (*2*). Using alumina-supported platinum nanoparticles, polyethylene was turned into long-chain alkyl aromatics, which have broad uses as surfactants, lubricants, refrigeration fluids, and more (*3*). Furthermore, enzymes to convert PET back into its monomers, forming a closed-loop recycling process, have also been developed (*4*).

Each of these recently developed technologies is engineered to treat a single type of plastic waste. To tackle plastic mixtures, which exist widely in consumer products, such as electronics and home appliances, additional strategies must be developed to either physically deconstruct multicomponent materials into their constituent plastic polymers (*5*) or chemically deconstruct various plastics mixtures into small molecules that are able to be further refined (*6*).

With this goal in mind, Sullivan *et al.* report a two-step process to convert plastic mixtures into two simple products (see the figure). In their process, the mixed plastics are broken down into multiple organic acid intermediates by metal ion–promoted oxidation followed by biological conversion of oxygenated intermediates using an engineered bacterial strain, *Pseudomonas putida*. The two-step process can turn a mixture of polystyrene, polyethylene, and PET into β-ketoadipate—a monomer for making performance-enhanced polymers (*7*)—or polyhydroxyalkanoates—a type of bioplastic (*8*)—as the product.

Department of Chemical and Biomolecular Engineering, National University of Singapore, Singapore 117585, Singapore. Email: ning.yan@nus.edu.sg

PHOTO: REUTERS/HEO RAN

Improving on a previously developed method (*9*), which used a corrosive bromide cocatalyst, the method by Sullivan *et al.* uses a more benign *N*-hydroxyphthalimide. During the chemical oxidation step, polystyrene and PET are converted into benzoic acid and terephthalic acid with close to 70% yield, and polyethylene is broken down into a range of shorter-chain molecules ranging from C_4 to C_{22} dicarboxylic acids with a yield of >30%. Although the optimized reaction temperatures and durations for these plastics are not identical, the authors managed to identify conditions that are suitable to decompose different components simultaneously. Overall, a mixture of polystyrene, polyethylene, and PET was converted to ~60% benzoic acid and terephthalic acid and 20% dicarboxylic acids after 5.5 hours.

In the next step, the metal catalyst was recovered as metal hydroxides, and the remainder was digested within 36 hours by the genetically modified *P. putida*, which converts various types of organic acid salts into polyhydroxyalkanoates and aromatic acid salts into β-ketoadipate while consuming aliphatic acid salts as food. The ability of *P. putida* to perform this biological conversion is the result of the deactivation of the gene that encodes the enzyme that degrades β-ketoadipate.

The polymeric structure of plastics is often cited as the main reason that plastics are difficult to degrade; however, their low oxygen content arguably plays an equally important role. This is evident in the naturally occurring oxygen-enriched polymers, such as cellulose, hemicellulose, chitin, and lignin, which are readily degradable. This fact highlights that oxygen-containing functional groups in polymers are beneficial for biological conversion. In the study by Sullivan *et al.*, the oxygen content—in the form of carboxylic acids—is increased to 26% for polystyrene and to 17 to 54% for polyethylene after the oxidation treatment. These water-soluble, oxygen-enriched carboxylic acids derived from plastics provide substrates for more efficient bioconversion in the next step. With the combined oxidation and biological conversion, the molar yield of β-ketoadipate reached an impressive value of 57% for mixed polystyrene, polyethylene, and PET commercial plastics.

Sullivan *et al.* highlight how hybrid chemical and biological processes can enable plastic recycling that is otherwise unachievable. For instance, the chemical oxidation of plastics alone has little commercial value because of the formation of a highly diverse stream of products that are difficult to separate; yet, when combined with a downstream biological process, this purification hurdle is solved because all components are digested by microbes into a single product. In the future, researchers should seek to explore, design, and integrate other chemo- and bioconversion routes and to consider process optimization and cost analysis of said routes. ■

REFERENCES AND NOTES

1. K. P. Sullivan *et al.*, *Science* **378**, 207 (2022).
2. V. Kumar, A. Khan, M. Rabnawaz, *ACS Sustain. Chem. Eng.* **10**, 6493 (2022).
3. F. Zhang *et al.*, *Science* **370**, 437 (2020).
4. H. Lu *et al.*, *Nature* **604**, 662 (2022).
5. T. W. Walker *et al.*, *Sci. Adv.* **6**, eaba7599 (2020).
6. Y. Jing *et al.*, *Angew. Chem. Int. Ed.* **60**, 5527 (2021).
7. C. W. Johnson *et al.*, *Joule* **3**, 1523 (2019).
8. A. T. Adeleye *et al.*, *Process Biochem.* **96**, 174 (2020).
9. W. Partenheimer, *Catal. Today* **81**, 117 (2003).

ACKNOWLEDGMENTS

N.Y. acknowledges the National Research Foundation Singapore NRF Investigatorship (NRF-NRFI07–2021–0006). Thanks to M. Dickieson and D. Le for their assistance in preparing the manuscript.

10.1126/science.ade5658

A two-step process for recycling mixed plastics

Sullivan *et al.* developed a hybrid process for converting mixed plastic waste into commercially useful chemicals. The plastic mixtures are first converted into three types of organic acids, which are then transformed by the engineered bacterium *Pseudomonas putida* into β-ketoadipate or polyhydroxyalkanoates.

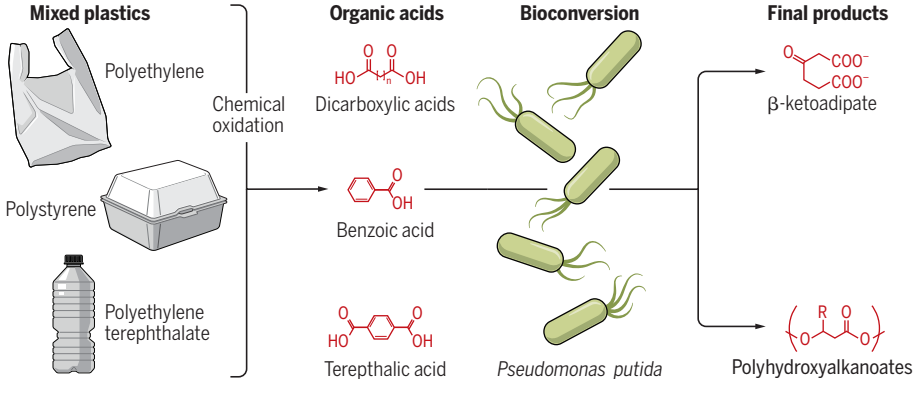

GRAPHIC: A. FISHER/*SCIENCE*

NANOPARTICLES

Counting charges per metal nanoparticle

Charges on a metal nanoparticle are measured with precision by electron holography

By **Chuanbo Gao**[1] *and* **Osamu Terasaki**[2]

Metal nanoparticles attached to metal oxide surfaces are an important family of catalysts with a wide range of applications, such as in organic synthesis, fuel production, and pollution cleanup (*1*). There have been efforts to better understand the catalytic properties of these nanoparticles as a function of their size, surface structure, electronic structure, and synergy with the metal oxide surface (*2*, *3*). For instance, the number of charges carried by the attached nanoparticles has a strong effect on their catalytic properties (*4*, *5*). Quantifying this "charge state," that is, the magnitude of this charge and whether it is positive or negative, is of fundamental importance for understanding the catalytic properties of the nanoparticle-surface system. On page 202 of this issue, Aso *et al.* (*6*) present a method to directly identify the charge state of a single platinum (Pt) nanoparticle sitting on a titanium dioxide (TiO_2) surface using electron holography.

The interaction between metal nanoparticles and the metal oxide substrate, or "support," has been studied for decades (*7*, *8*). In 1978, the concept of the "strong metal-support interaction" was proposed (*7*). The model considers a thin layer of the metal oxide material that either partially or fully covers the surfaces of the metal nanoparticles by interfacial chemical bonding. This explains the enhanced stability of metal nanoparticles and the blocked active sites for catalysis compared with the same metal nanoparticles without the support. More recently, researchers have reported another manifestation of the metal-support interaction—the "electronic metal-support interaction," which is associated with the charge transfer across the metal

and metal-oxide interface instead (*4*). This alternative interpretation helps explain the increased catalytic activity in some reactions, rather than the expected overall decreased activity caused by surface blockage. It also suggests that the charge carried by the metal nanoparticles can affect their catalytic properties. Because of this revelation, precise measurement of the charge state of the metal nanoparticles has since become an urgent challenge to address.

Microscopic techniques are powerful tools that have contributed to catalyst research at the atomic scale over the years (*9*–*12*). For example, through environmental transmission electron microscopy (TEM), the strong metal-support interaction can be seen in action by observing a metal nanoparticle being gradually covered up by a thin layer of the support material at high temperature. Aso *et al.* extended a TEM-based method called "electron holography". The method uses electrons to probe the electrostatic potential inside and outside the Pt nanoparticle. Considering the wave-particle duality of electrons, the wave phase of the electron probe is changed when it passes through the electrostatic field that is produced by the nanoparticle. Therefore, it is possible to measure the electrostatic potentials, and thus the charge state of the nanoparticle, through the phase shift of the electron probe.

Aso *et al.* used a 1.2-MV atomic-resolution holography microscope with an aberration corrector (*13*), which made it possible to measure this phase shift with atomic-level resolution (see the image). From these measurements, the authors calculated the number of electrons carried by the single Pt nanoparticle, or its charge state, by image processing and data fitting of the imaged phase-shift just outside the nanoparticle. This powerful measurement technique developed by Aso *et al.* allows them to determine how the charge states of the Pt nanoparticles are influenced by the TiO_2 support. In addition to the characteristic features at the interface between TiO_2 and Pt, the number of charges on a single Pt nanoparticle in contact with the TiO_2 support is related to the degree of structural distortion of the Pt nanoparticle from its otherwise perfect structure (i.e., face-centered cubic). And the more distorted the structure is, the more charges the nanoparticle carries. Whether the charges are positive or negative is dependent on the relative crystallographic orientation between the Pt nanoparticle and the TiO_2 support.

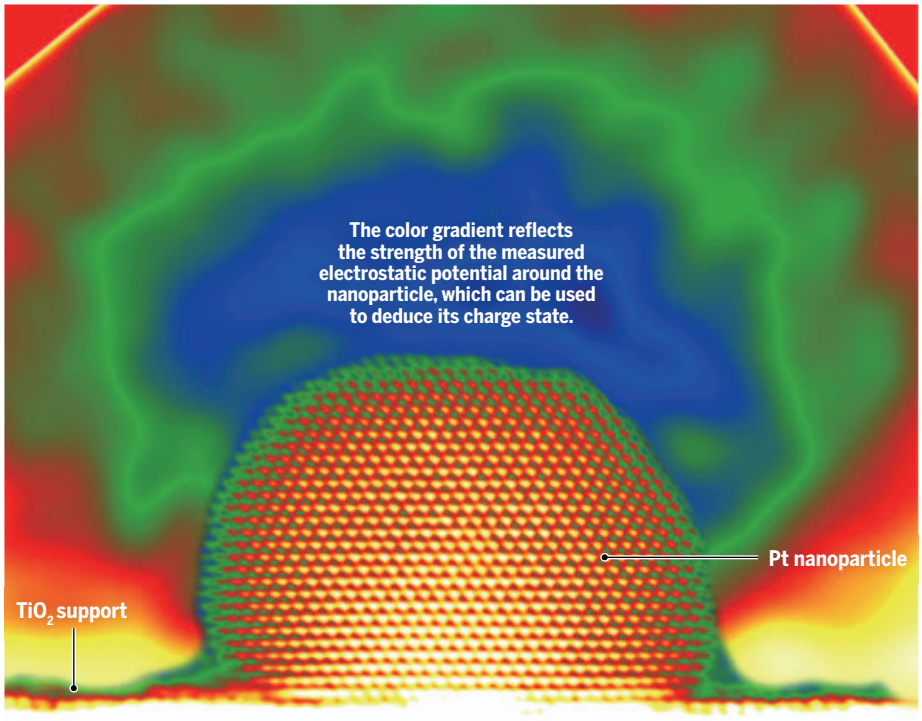

An electron holography technique has been developed for measuring the charge-state of a single platinum (Pt) nanoparticle on a titanium dioxide (TiO_2) support, which will help guide future designs for catalysts.

"...the technique introduced by Aso *et al.* may be used to measure other nanocomposite catalysts..."

These findings provide vital knowledge for understanding the physics of the charge state and the catalytic property of the supported metal nanoparticles. For researchers who are studying catalysts of supported metal nanoparticles, Aso *et al.* show how key experimental parameters for enhancing the catalytic performances can be obtained qualitatively by crystallographic characterization.

In addition to examining more metal-support systems, the technique introduced by Aso *et al.* may be used to measure other nanocomposite catalysts, such as those formed with metal nanoparticles and nanoporous crystals. These charge-state measurements will also improve understanding of the interaction between the nanoporous crystals and guest molecules—for example, hydrogen (H_2) and carbon dioxide (CO_2)—which have applications in the capture and release of these molecules.

Incident electrons, as waves, interact with the electromagnetic field along their travel paths. Therefore, besides the charge state, the spin state—that is, the local magnetic field inside and outside a sample—should also be obtainable using this method by placing the sample in a magnetic field–free condition. An improved ability to measure the spin state will be useful for enabling the detection of, for example, subnanometer-scale magnetic field distributions across magnetic domain boundaries inside nanocrystals and multilayered systems. These measurements will be key to advancing many problems in materials science applications such spintronics (*14*). ■

[1]State Key Laboratory of Multiphase Flow in Power Engineering, Frontier Institute of Science and Technology, Xi'an Jiaotong University, Xi'an, Shaanxi, China. [2]Center for High-resolution Electron Microscopy (ChEM) and Shanghai Key Laboratory of High-resolution Electron Microscopy, School of Physical Science and Technology, ShanghaiTech University, Shanghai, China. Email: gaochuanbo@mail.xjtu.edu.cn; osamuterasaki@mac.com

REFERENCES AND NOTES

1. L. Liu, A. Corma, *Chem. Rev.* **118**, 4981 (2018).
2. G. Chen *et al.*, *Science* **344**, 495 (2014).
3. Q. Fu *et al.*, *Science* **328**, 1141 (2010).
4. A. Bruix *et al.*, *J. Am. Chem. Soc.* **134**, 8968 (2012).
5. G. Pacchioni, H.-J. Freund, *Chem. Soc. Rev.* **47**, 8474 (2018).
6. R. Aso *et al.*, *Science* **378**, 202 (2022).
7. S. J. Tauster, *Acc. Chem. Res.* **20**, 389 (1987).
8. C. T. Campbell, *Nat. Chem.* **4**, 597 (2012).
9. J. H. K. Pfisterer *et al.*, *Nature* **549**, 74 (2017).
10. Y. Lykhach *et al.*, *Nat. Mater.* **15**, 284 (2016).
11. S. Zhang *et al.*, *Nano Lett.* **16**, 4528 (2016).
12. M. Tang *et al.*, *Angew. Chem. Int. Ed.* **60**, 22339 (2021).
13. T. Akashi *et al.*, *Appl. Phys. Lett.* **106**, 074101 (2015).
14. T. Tanigaki *et al.*, *Sci. Rep.* **7**, 16598 (2017).

10.1126/science.adeww6051

IMAGE: ASO *ET AL.*

MEDICINE

Developing pig-to-human organ transplants

Recent advances raise hope for a promising solution to the transplant organ shortage

By **Megan Sykes**

Over 100,000 people in the US are currently waiting for organ transplants. Because the human organ donor pool cannot keep pace with this demand, many patients die without receiving the life-saving transplant they need. Pigs are similar to humans in organ size and physiology, so the transplantation of pig organs to humans offers a potential solution to this problem and raises the prospect of scheduled, elective transplantation of quality-controlled organs, even for patients who would not currently meet the criteria for allocation of a scarce human organ. Although other technologies, such as tissue engineering, may eventually offer alternative solutions to this shortage, there is currently no substitute for transplantation of a fully formed, functioning organ. Several developments in the past year, most notably the first pig-to-human transplants, bring this promising solution closer to fruition, but challenges remain.

Transplants from one species to another are called xenotransplants. Because nonhuman primates (NHPs) are closest to humans phylogenetically, early human xenotransplantation efforts used NHP organs. However, graft survivals were short, and the use of NHPs for xenotransplantation was later deemed to be unsafe owing to potential virus transmission, impractical because of limited animal availability, and more ethically challenging than the use of pigs, which consequently became the xenograft source animal of choice. However, transplantation of pig organs into NHPs resulted in rapid "hyperacute" rejection (HAR) owing to the binding of preexisting "natural" antibodies (NAbs) in the NHP to targets on endothelial cells lining the transplant organ's blood vessels. Activation of complement and coagulation cascades then resulted in ischemic organ death within minutes to hours.

NAbs exist in the absence of any known exposure to pig tissues owing to cross-reaction with antigens that are shared by common microbes. During the 1990s, pigs transgenically expressing human complement regulatory proteins were developed, and it was discovered that most human and NHP anti-pig NAbs recognize a single carbohydrate, α-galactose-1,3-galactose (Gal) (*1*), making it possible to remove these antibodies by adsorption. These advances extended the survival of pig organs to days or weeks in NHPs. Enthusiasm for xenotransplantation was nevertheless dampened by the identification of porcine endogenous retroviruses (PERVs) and concerns about the possibility that new viral illnesses might arise in humans as a result.

With the advent of nuclear transfer–based methods for cloning large animals, in the 2000s pigs were produced that were deficient in the enzyme that produces Gal. Survival of pig-to-NHP xenografts was further prolonged, with some organs lasting months. Further advances have since improved immunosuppression of the recipient, and CRISPR-mediated editing has enabled additional genetic modification of pigs. Successful immunosuppression usually includes depletion of recipient T and B lymphocytes followed by post-transplant treatment with the antimetabolite mycophenolate mofetil and anti-inflammatory agents. Moreover, blockade of the CD40-CD154 pathway involved in B cell and antigen-presenting cell activation by T cells is an important component. Recently, several other carbohydrate moieties have been identified as targets of anti-pig non-Gal NAbs (*2*, *3*), and genes encoding the enzymes responsible for producing them have been deleted in pigs. Other genetic modifications to avoid rejection have included human transgenes to express complement regulatory proteins, modulators of coagulation, the macrophage-inhibitory protein CD47, and anti-inflammatory molecules. Although the need for each individual modification has not yet been demonstrated, survival of pig kidneys beyond 1 year has been achieved in NHPs. Ablating the gene encoding growth hormone receptor to prevent growth of pig hearts when in recipients has also been used to produce life-supporting pig heart grafts that survived for 9 months in NHPs (*4*).

Many of the organs transplanted to NHPs have shown evidence for rejection despite ongoing immunosuppressive medication. This suggests that inducing tolerance, which involves reeducating the immune system to regard the donor as "self," could be advantageous. Approaches to achieve immune tolerance include induction of "mixed chimerism," in which bone marrow–derived cells from

Advancing organ xenotransplantation

Source pigs for organ xenotransplantation are genetically modified to remove the immunogenic carbohydrate α-galactose-1,3-galactose (Gal), to avoid rejection. They can be further modified to eliminate other carbohydrates, growth hormone receptor, and porcine endogenous retroviruses. Additionally, human transgenes can be expressed to suppress rejection, including genes encoding complement and coagulation regulatory proteins, regulators of inflammation, and immunosuppressive molecules. Xenotransplantation can then be studied in nonhuman primates and humans to understand the factors that allow successful engraftment.

SYSTEM	INFORMATION TO BE GAINED	LIMITATIONS AND BARRIERS
Nonhuman primates	• Effects of genetic modification • Effective immunosuppression • Tolerance induction	• Need sequential modifications • Differences between nonhuman primates and humans • Reagent availability is limited for nonhuman primate studies • Ethics • Cost
Decedents	• Effects of genetic modifications and acceptable natural antibody levels for short-term survival with each type of pig • Early immune responses • Effective immunosuppression in the short term	• Ethics • Burden on families • Biosafety must be assured: Effective animal husbandry, surveillance, and recipient monitoring are required • Cost
Clinical trials	• Patient populations who can benefit • Human immune response over the life of the xenograft • Effective immunosuppression in the short and longer term	• Risk to recipient • Cost • Ethics and consent issues • Regulatory hurdles • Biosafety must be assured: Effective animal husbandry, surveillance, and recipient monitoring are required

Columbia Center for Translational Immunology, Department of Medicine, Department of Microbiology and Immunology and Department of Surgery, Columbia University Medical Center, Columbia University, New York, NY, USA. Email: ms3976@cumc.columbia.edu

the pig are transplanted into the recipient. This promoted tolerance among human T cells, B cells, and natural killer (NK) cells in humanized mouse models. Thymic transplantation, in which recipient T cells are educated in a pig thymus, also tolerizes T cells in NHPs and humanized mice (*5*–*7*).

Adding to this progress, guidelines have been developed to mitigate the risk of pathogen transmission from pigs to humans. Notably, PERV infection has not been detected in any pig-to-human or pig-to-NHP transplant recipient, although PERVs may have lower affinity for NHP forms of its receptor than of the human receptor. PERV loci have also been suppressed or deleted from some pigs, further improving safety. Consequently, there is broader acceptance of the likely safety of pig-to-human xenotransplantation with appropriate animal husbandry and microbial surveillance of the source animals, recipients, and their close contacts.

These encouraging developments have set the stage to proceed with clinical xenotransplantation. Although NHPs provide an outstanding transplantation model, they present some limitations. For example, one of the carbohydrate targets of human anti-pig NAbs, *N*-glycolylneuraminic acid (NeuGc), is also expressed by NHPs, which therefore do not produce NAbs against it. Indeed, deleting NeuGc in pigs increases NHP NAb binding to the xenograft (*8*) and rejection (*4*). The NHP model therefore cannot predict the impact of this modification for pig-to-human transplantation.

The first trials of pig-to-human organ xenotransplantation took place in 2021. Groups at New York University (NYU) and the University of Alabama at Birmingham (UAB) connected pig kidneys to the circulation of brain-dead human recipients. The NYU group circulated the blood of two decedents through a Gal-deleted pig kidney that was maintained outside of their bodies for 54 hours (*9*), whereas the UAB group transplanted pig kidneys with multiple genetic modifications to a nephrectomized decedent for 74 hours (*10*). Antibody-mediated rejection (AMR), coagulopathy, and clinical markers of a hyperactive immune response were not observed in any of the recipients, and there was no evidence of PERV transmission. In the two NYU cases, but not the UAB decedent, the pig kidneys were shown to function. Their short duration greatly limited the information obtained from these studies, and more could be learned from expanded studies with longer duration in more decedents. For example, the incidence of early AMR in recipients with different antibody levels against source pig organs with different genetic modifications might be identified, establishing standards for acceptable baseline anti-donor antibody levels in humans. However, these types of studies are extremely challenging, requiring careful attention to both the technical and ethical considerations involved in delaying the termination of life support.

In January 2022, surgeons at the University of Maryland transplanted a pig heart into a man with terminal heart failure who was dependent on life support and was not a candidate for a human heart transplant. The heart, which was from a pig with 10 genetic modifications (a "10-GE" pig), did not undergo rapid rejection and supported the patient's life for 7 weeks. Considering that pig hearts have sustained the lives of NHPs for much longer periods, this duration of support of a human life is perhaps not surprising from a scientific viewpoint, but it nevertheless represents a milestone in clinical xenotransplantation. The patient was returned to life support after 49 days and the precise cause of the heart's eventual failure remains to be determined. If porcine-specific cytomegalovirus (CMV) is found to have contributed to graft loss (*11*), this cause should be avoidable in the future with the development of more sensitive screening assays for effective elimination of CMV from the source pigs. It is encouraging that a pig heart has now been shown to be capable of sustaining human life.

"It is encouraging that a pig heart has now been shown to be capable of sustaining human life."

Contemplation of clinical xenotransplantation trials highlights the many questions and hurdles that remain. The optimal or even necessary genetic modifications of source pigs have not been determined. Some of the gene modifications in the 10-GE pig may be superfluous or even deleterious. Although inhibition of coagulation by expressing transgenic human thrombomodulin and other molecules in the transplant organ may delay graft loss due to AMR, such modifications may not be needed when AMR is prevented by selection of source animals and recipients or by tolerance induction. One transgene, human *CD47*, has been shown to mitigate macrophage-mediated clearance of porcine hematopoietic cells when mixed chimerism is attempted for tolerance induction in NHPs (*6*), but its utility in solid organ xenografts has not been demonstrated. Indeed, widespread human CD47 expression in pig kidneys may initiate systemic inflammation in NHP recipients (*12*). Further investment in NHP studies will therefore be critical, even as clinical trials in humans begin, to optimize future xenotransplantation outcomes.

Other questions surround the optimal patient populations for initiation of xenotransplantation trials. Patients unlikely to receive allografts because of presensitization, very young age, or other factors, though having a short life expectancy, have been suggested for initial cardiac and renal xenotransplantation trials (*13*). Identifying and meeting regulatory requirements will be facilitated by collaboration of regulators with scientists, professional organizations, and industry. The development of appropriately biosecure facilities and the ability to maintain pigs free of known and potential pathogens are critical. Pig-to-NHP xenotransplantation studies have revealed that source animals must be free of latent infections such as porcine CMV, which can reactivate and trigger graft loss when placed in a NHP, which, unlike the pig, has not previously been exposed to or immunized against porcine CMV (*14, 15*).

Many questions remain before xenotransplantation can be optimized in humans, but this should not prevent preliminary clinical studies from proceeding. If the quality and safety of the source animals can be assured, existing NHP studies with orthotopic heart and life-sustaining kidney transplantation are sufficient to justify such transplants. The courage of the trial volunteers and altruism of the families of decedent study subjects will allow generation of knowledge that improves future efforts. Concurrent with the initiation of clinical studies, there must be continuous attention to safety concerns for these patients and infectious risks to the community, along with vigorous pursuit of the preclinical studies that will further improve this enormously promising therapy (see the table). These commitments to xenotransplantation now will ultimately pay off in incalculable dividends for human health in the future. ■

REFERENCES AND NOTES

1. A. H. Good *et al.*, *Transplant. Proc.* **24**, 559 (1992).
2. G. W. Byrne, Z. Du, P. Stalboerger, H. Kogelberg, C. G. McGregor, *Xenotransplantation* **21**, 543 (2014).
3. A. Zhu, R. Hurst, *Xenotransplantation* **9**, 376 (2002).
4. M. M. Mohiuddin *et al.*, *Xenotransplantation* **29**, e12744 (2022).
5. M. Sykes, D. H. Sachs, *Sci. Immunol.* **4**, eaau6298 (2019).
6. H. Watanabe *et al.*, *Xenotransplantation* **27**, e12552 (2020).
7. E. E. Waffarn *et al.*, *Xenotransplantation* **28**, e12691 (2021).
8. Z. Y. Wang *et al.*, *Xenotransplantation* **21**, 376 (2014).
9. R. A. Montgomery *et al.*, *N. Engl. J. Med.* **386**, 1889 (2022).
10. P. M. Porrett *et al.*, *Am. J. Transplant.* **22**, 1037 (2022).
11. B. P. Griffith *et al.*, *N. Engl. J. Med.* **387**, 35 (2022).
12. Y. Ariyoshi *et al.*, *Xenotransplantation* **28**, e12642 (2021).
13. D. K. C. Cooper *et al.*, *Transplantation* **101**, 1551 (2017).
14. K. Yamada *et al.*, *Transplantation* **98**, 411 (2014).
15. J. Denner *et al.*, *Sci. Rep.* **10**, 17531 (2020).

ACKNOWLEDGMENTS

Thanks to D. H. Sachs for helpful comments and J. Cabrera for assistance. M.S. is supported by National Institutes of Health (grant P01AI045897). M.S. receives sponsored research support from Choironex, a subsidiary of Nephro Health.

10.1126/science.abo7935

Reconstructing CO_2 fixation from the past

Analysis of Rubisco evolution could inform how to engineer a better enzyme

By **Robert E. Sharwood**

Rubisco (ribulose-1,5-bisphosphate carboxylase/oxygenase) is the central CO_2-fixing enzyme of photosynthesis and often limits the rate of carbon assimilation for key agricultural crops. Rubisco is catalytically feeble because of its slow catalytic speed (1 to 9 catalytic cycles per second), low affinity for CO_2, and low specificity for CO_2 compared with O_2 (*1*). These catalytic parameters strongly influence crop water and nitrogen use required for efficient growth of photosynthetic organisms. The decline in CO_2 and the concomitant rise of O_2 in Earth's atmosphere led to the independent evolution of carbon-concentrating mechanisms across lineages of photosynthetic organisms to improve Rubisco catalysis by increasing CO_2 around the active site while effectively suppressing oxygenation (*1*). On page 155 of this issue, Schulz *et al.* (*2*) report the ancestral reconstruction of Rubisco to predict early isoforms and the functional adaptation that enabled sufficient carbon fixation in the face of rising O_2 in Earth's atmosphere.

The competitive inhibition of Rubisco by oxygen is perhaps one of the most difficult challenges to overcome because fixation of O_2 leads to photorespiration and decreases the efficiency of assimilating carbon. The form I isoforms of the Rubisco superfamily are present within terrestrial plants, algae, and bacteria. They are crucial for the regulation of flux through the Calvin-Benson-Bassham (CBB) cycle that produces the carbohydrate building blocks for the maintenance of productive growth (*1*). There exists a further divide between form I "red" and "green" enzymes, with structural and catalytic features underpinning this divergence but with both enzymes consisting of eight large subunits (LSUs; ~55 kDa) and eight small subunits (SSUs; ~15 to 17 kDa) (*1*) (see the figure). The large gaps in the fossil record have prevented the identification and catalytic characterization of early lineages of Rubisco.

Schulz *et al.* recreated the evolutionary tract of form I Rubisco using ancestral reconstruction (*3*) of extant metagenome Rubisco sequences and found that an ancestral LSU octamer (L_8) recruited the SSUs that provided new solutions for Rubisco catalysis. They resurrected both the LSU and SSU as well as the ancestral Rubisco that they formed in *Escherichia coli*, revealing that the hexadecamer was able to bind the transition-state analog carboxyaraibinitol bisphosphate (CABP), thereby demonstrating that the active site is functional. Furthermore, recruitment of the SSUs required key mutations at the LSU-SSU interface to enable stabilization of the L_8 core and prevent L_8-L_8 fiber formation. Notably, recruitment of the SSU improved catalytic efficiency fourfold and doubled the specificity for CO_2 as opposed to O_2. This event is hypothesized to have primed form I Rubisco before the Great Oxygenation Event 2.4 billion years ago (*4*). Moreover, this provides evidence for the elusive role of the Rubisco SSU in form I Rubisco catalysis and its requirement for stabilization of the hexadecamer and enhancing solubility.

Modern-day versions of form I L_8S_8 Rubisco are composed of four LSU antiparallel dimers encoded by the Rubisco large subunit (*rbcL*) gene and capped at either end by four SSUs encoded by the Rubisco small subunit (*RbcS*) gene (*5*). In photosynthetic bacteria and nongreen algae, *rbcL* and *RbcS* are often coexpressed in a bicistronic *rbcLS* operon. However, in higher plants and green algae, *RbcS* has been transferred to the nucleus, which requires complex coordination of gene expression between the nucleus and chloroplast (where *rbcL* is encoded) and extensive chaperone proteins to ensure subunit assembly (*5*). The recent discoveries of Rubisco auxiliary assembly factors, including Rubisco assembly factor 1 (Raf1) and Raf2, RbcX, and bundle sheath defective II (BSDII), as well as chaperonin 60/20 (Cpn60/20) highlight the importance of stabilizing the L_8 core before assembly with the SSUs and have made engineering versions of Rubisco into crops somewhat complicated (*6*). As Schulz *et al.* show, the L_8 core can form fibers that are catalytically deficient. In addition, the multigene families of *RbcS* in higher plants have made it more difficult to define the roles of individual SSUs. Moreover, individual subunits impart different kinetics to Rubisco, as shown by assembling individual potato (*Solanum tuberosum*) SSUs with LSU counterparts in tobacco (*Nicotiana tabacum*) (*7*).

The Rubisco active site resides within the LSUs without any direct contribution of SSU amino acids. Rubisco SSUs have been shown to be important for solubility and catalytic properties of *Synechococcus* Rubisco (*8*, *9*). Removal of SSUs by mild acid washing enabled the recovery of L_8 cores, which had depleted catalytic ac-

Structure-function of Rubisco during evolution

Rubisco is composed of four large subunit (LSU) dimers, which harbor the active sites, that are capped at either end by four small subunits (SSUs). Rubisco can react with O_2 as well as CO_2, which is used in photosynthesis. The specificity of Rubisco for CO_2 compared with O_2 ($S_{c/o}$) is shown for the form I Rubisco superfamily [based on data from (*2*, *15*)]. The resurrected ancestral Rubisco that does not contain SSUs (AncL) has less specificity for CO_2 than the ancestral version with SSUs (AncLS+AncS) and other family members that contain SSUs.

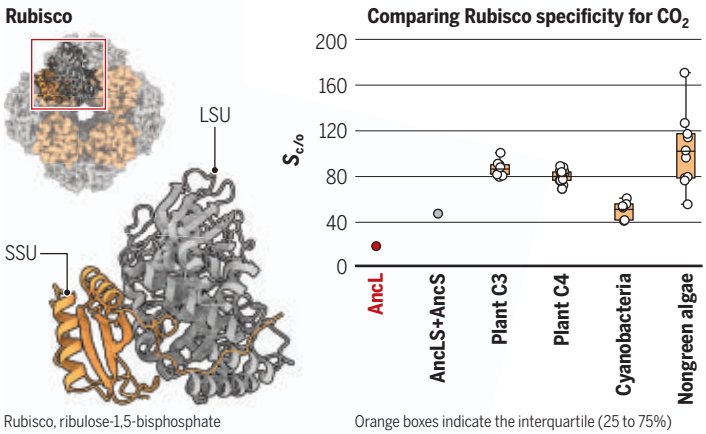

Rubisco, ribulose-1,5-bisphosphate carboxylase/oxygenase.

Orange boxes indicate the interquartile (25 to 75%) range. Horizontal bar represents the mean.

GRAPHIC: A. MASTIN/*SCIENCE*

Hawkesbury Institute for the Environment, Western Sydney University, Richmond, NSW, Australia.
Email: r.sharwood@westernsydney.edu.au

tivity but were still able to bind CABP (*9*). However, addition of *Synechoccous* SSUs or purified *Prochloron* SSUs enabled catalytic activity to be restored to the L_8 core (*10*). More recent studies interrogating the role of the Rubisco SSUs have shown that replacing the βA-βB loop of *Chlamydomonas* Rubisco SSUs with that of spinach (*Spinacia oleracea*) increased Rubisco specificity toward higher plant isoforms (*11*). Complete replacement of the rice (*Oryza sativa*) SSUs with sorghum (*Sorghum bicolor*) counterparts also shifted Rubisco catalysis closer to that of C_4 plant Rubisco (*12*).

The study by Schulz *et al.* provides crucial evidence for the role of SSUs in improving catalysis in the face of rising atmospheric O_2. Molecular dynamic modeling of Rubisco has shown previously that the SSUs may also be a reservoir for CO_2 for the active site, which may further explain the importance of the SSUs in increasing CO_2 fixation (*13*). Nevertheless, it is still largely unknown whether the SSUs alter the geometry of the Rubisco active site in a way that influences the positioning of the carbamate or the pockets that bind its substrate, RuBP (ribulose-1,5-bisphosphate), or that influences the reactivity of the catalytic intermediate, enediol, with CO_2 compared with O_2. Further studies are required to interrogate the precise changes to the catalytic mechanism of Rubisco to fully understand the adjustments in catalytic properties of the enzyme. In combination with directed evolution, new sequence space can now be interrogated to understand further Rubisco structure-function relationships to inform future Rubisco engineering strategies aimed at improving crop yields (*14*). The ability to simultaneously replace *rbcL* and *RbcS* genes in tobacco and other species amenable to chloroplast transformation could provide avenues for improving crop productivity in the future (*8*). ■

REFERENCES AND NOTES

1. R. E. Sharwood, *New Phytol.* **213**, 494 (2017).
2. L. Schulz *et al.*, *Science* **378**, 155 (2022).
3. M. A. Spence, J. A. Kaczmarski, J. W. Saunders, C. J. Jackson, *Curr. Opin. Struct. Biol.* **69**, 131 (2021).
4. A. L. Sessions, D. M. Doughty, P. V. Welander, R. E. Summons, D. K. Newman, *Curr. Biol.* **19**, R567 (2009).
5. A. Bracher, S. M. Whitney, F. U. Hartl, M. Hayer-Hartl, *Annu. Rev. Plant Biol.* **68**, 29 (2017).
6. H. Aigner *et al.*, *Science* **358**, 1272 (2017).
7. E. Martin-Avila *et al.*, *Plant Cell* **32**, 2898 (2020).
8. T. J. Andrews, *J. Biol. Chem.* **263**, 12213 (1988).
9. T. J. Andrews, B. Ballment, *J. Biol. Chem.* **258**, 7514 (1983).
10. T. J. Andrews, D. M. Greenwood, D. Yellowlees, *Arch. Biochem. Biophys.* **234**, 313 (1984).
11. R. J. Spreitzer, S. R. Peddi, S. Satagopan, *Proc. Natl. Acad. Sci. U.S.A.* **102**, 17225 (2005).
12. H. Matsumura *et al.*, *Mol. Plant* **13**, 1570 (2020).
13. M. van Lun, J. S. Hub, D. van der Spoel, I. Andersson, *J. Am. Chem. Soc.* **136**, 3165 (2014).
14. Y. Zhou, S. Whitney, *Int. J. Mol. Sci.* **20**, 5019 (2019).
15. R. E. Sharwood, B. M. Long, in *Photosynthesis, Respiration, and Climate Change*, K. M. Becklin, J. K. Ward, D. A. Way, Eds. (Springer, 2021), pp. 333–354.

10.1126/science.ade6522

FUEL CELLS

Hydrogen power gets a boost

A fuel cell gains more power from ion-conducting, porous covalent organic frameworks

By **Ting Ma**[1] *and* **Jodie L. Lutkenhaus**[1,2]

Fuel cells are an important energy technology for a low-carbon future. They convert oxygen and hydrogen into electricity through an electrochemical reaction. In contrast to battery cells, fuel cells can operate continuously so long as there is a supply of oxygen and hydrogen. Because no carbon-containing fuels are required, fuel cells offer the promise of low-carbon or zero-carbon electricity. The hydrogen and oxygen required for fuel cells can be obtained in an environmentally friendly manner such as from water-splitting and air separation, respectively. However, current fuel cell designs suffer from poor utilization of the platinum catalyst that speeds up the reaction, and the high cost of platinum. On page 181 of this issue, Zhang *et al.* (*1*) present a design that substantially improves fuel cell performance by using a type of porous material that promotes transport of the fuel to the catalyst and increases its utilization.

Proton exchange membrane fuel cells have been explored for decades in the pursuit of clean energy from hydrogen. The device consists of an electrode that reacts with oxygen, another electrode that reacts with hydrogen, and a proton-conducting membrane to divide the two. Without the membrane, the two electrodes could touch, leading to a short circuit and device failure. Instead, the membrane separates the electrodes and serves to control the transfer of protons, which are important ingredients for conversion reactions. Of these components, the largest inefficiency comes from the electrode that reacts with

A better electrode for fuel cells

A porous covalent organic framework (COF) material with 2.8- to 4.1-nm pores increases utilization of a platinum catalyst by 60%.

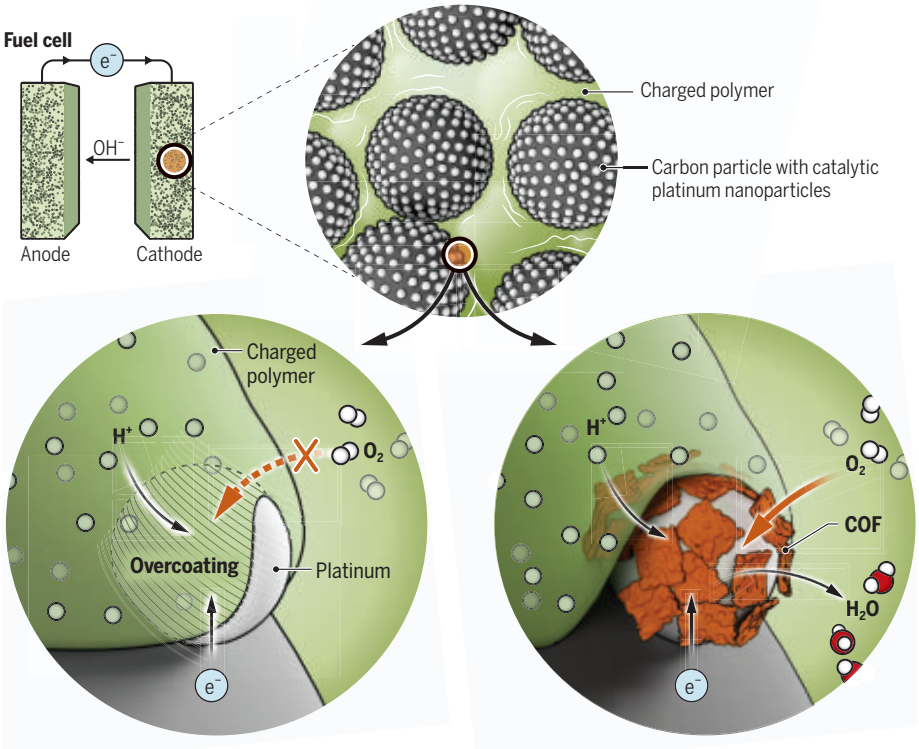

Without COF
A charged polymer conducts hydrogen atoms (protons) needed for the fuel cell reaction, but can also block oxygen access to a platinum catalyst.

With COF
A porous COF material still conducts protons while providing pathways for oxygen to reach a platinum catalyst.

GRAPHIC: V. ALTOUNIAN/*SCIENCE*

oxygen. There, oxygen molecules, protons, and electrons must all meet and interact at what is called a "three-phase boundary" (see the figure). Physically, this boundary is defined by the intersection of the platinum catalyst, the empty pore space for gas diffusion, and the proton-conducting-polymer, or "ionomer," of the membrane. If the pores are too small, then no oxygen can pass through. Under perfect conditions, the oxygen and protons would combine with electrons to form water at this boundary ($O_2 + 4H^+ + 4e^- \rightarrow 2H_2O$ + energy). Unfortunately, the ionomer can coat the platinum catalyst and block access of oxygen to the catalyst site during the manufacturing process.

Prior work has studied porous frameworks to improve gas diffusion at the three-phase boundary but faced challenges with chemical stability or small pore size (*2*–*4*). For example, metal-organic frameworks (MOFs), which consist of organic ligands and metal ions that organize into porous crystal lattices, have relatively small pores (<2 nm) that yield a relatively larger gas diffusion resistance. By contrast, covalent organic frameworks (COFs) have larger pores that allow for faster transport of oxygen to the catalyst (*5*, *6*). However, both MOFs and COFs face stability issues involving hydrolysis and temperature. MOFs, in particular, are susceptible to dissolution in water, as a by-product of the fuel cell reaction. By contrast, COFs can undergo thermally activated reversible reactions that cause dissolution. To overcome the stability issues and maintain proton conduction pathways and porous networks, several studies have examined COFs with more stable chemistries (*7*–*10*). These COFs incorporate polar or sulfonate groups to guide proton conduction through the pores.

Although each of these studies made singular advances, it is challenging to find a COF or MOF that addresses the multitude of challenges faced in the proton exchange membrane fuel cell environment. In the context of this prior work, Zhang *et al*. address the issues of porosity, stability, and performance all together in a single COF material. They improve the structure of the three-phase boundary by enhancing the accessibility for oxygen to reach the catalyst. They designed a COF with mesopores (2.8 to 4.1 nm) lined with sulfonate groups for use in conjunction with the ionomer in the electrode assembly. COFs contain organic building blocks that arrange into two- and three-dimensional porous crystalline lattices. These pores are just wide enough to allow oxygen molecules to reach the catalyst, and the sulfonate groups provide sites for proton transport. By exploring several COFs, the effect of pore size is revealed.

As a result of this improvement, the platinum utilization and the peak power increases by 60% relative to electrodes without the COF. Further, the sulfonate groups on the COF displace parts of the ionomer that would otherwise cover up the platinum catalysts, opening more surface area for oxygen to access by going through the pores in the COF.

This work bears some resemblance to a previous work that demonstrated advantageous proton conduction across porous channels in COFs, in which the larger pore size was advantageous (*11*). Recent work has shown that the void space could be better utilized by increasing ion exchange capacity through the introduction of multiple proton-conducting groups into the framework (*12*). These strategies could help future design in the pursuit of even more effective ion-conducting COFs for proton exchange membrane fuel cells. Zhang *et al*. address the multiple challenges faced by the oxygen reaction at the fuel cell electrode, which is currently a major limiting factor. The designed COF is porous enough to allow for oxygen diffusion, conductive toward protons, and stable in the extreme environment of the electrode. As a result, the electrode's platinum catalyst is more effectively utilized. The broader impact is that COFs such as these could lower the long-term price of fuel cells by minimizing the platinum required and improving the practicality and competitiveness of the hydrogen fuel cell. ■

"...covalent organic frameworks... could lower the long-term price of fuel cells..."

REFERENCES AND NOTES

1. Q. Zhang *et al*., *Science* **378**, 181 (2022).
2. S. Ott *et al*., *Nat. Mater.* **19**, 77 (2020).
3. J. A. Hurd *et al*., *Nat. Chem.* **1**, 705 (2009).
4. F. Yang *et al*., *Nat. Energy* **2**, 877 (2017).
5. X. Zhao, Y. Chen, Z. Wang, Z. Zhang, *Polym. Chem.* **12**, 4874 (2021).
6. R. Sahoo, S. Mondal, S. C. Pal, D. Mukherjee, M. C. Das, *Adv. Energy Mater.* **11**, 2102300 (2021).
7. Y. K. Im *et al*., *Angew. Chem. Int. Ed.* **61**, e202203250 (2022).
8. L. Liu *et al*., *Angew. Chem. Int. Ed.* **60**, 14875 (2021).
9. Z. Lu *et al*., *J. Am. Chem. Soc.* **144**, 9624 (2022).
10. Z. Meng, A. Aykanat, K. A. Mirica, *Chem. Mater.* **31**, 819 (2018).
11. H. Xu, S. Tao, D. Jiang, *Nat. Mater.* **15**, 722 (2016).
12. X. Wang *et al*., *Nat. Commun.* **13**, 1020 (2022).

10.1126/science.ade8092

[1]Artie McFerrin Department of Chemical Engineering, Texas A&M University, College Station, TX, USA. [2]Department of Materials Science and Engineering, Texas A&M University, College Station, TX, USA. Email: jodie.lutkenhaus@mail.che.tamu.edu

NEUROSCIENCE

Creating a window into the mind

A noninvasive imaging technique measures neuronal activity at a millisecond time scale

By **Timo van Kerkoerle**[1] *and* **Martijn A. Cloos**[2]

How does the brain generate the mind? For example, it remains a mystery how the neurons in our brain allow us to see these letters, understand this sentence, and decide whether to stop reading or continue. Finding answers to these questions could give an objective understanding of "self," as well as help clarify the mental disorders that affect large numbers of people, such as depression, schizophrenia, and autism. On page 160 of this issue, Toi *et al*. (*1*) describe a promising new magnetic resonance imaging (MRI) method that could measure the activity of neurons at time scales relevant to mental processes.

The development of functional MRI (fMRI) in the 1990s was revolutionary (*2*), offering a way to view activity patterns in the human brain noninvasively. This has made it possible to map regions in the brain that are involved in cognitive functions such as perception, understanding, and decision-making. However, fMRI is limited in its ability to pinpoint the time and place of neuronal activation (the temporal and spatial specificity). fMRI measures changes in the blood oxygenation level–dependent (BOLD) signal (*3*), which is a surrogate for neuronal activity (*4*). BOLD reflects the hemodynamic response of the brain, which comprises changes in blood circulation that are evoked by changes in neuronal activity. When viewed through this "hemodynamic lens," the inferred activation is blurred in space and time.

Spatial blurring in fMRI relates to the vascular architecture. Large veins near the surface of the brain, which drain large cortical areas, have great sensitivity but limited speci-

[1]Cognitive Neuroimaging Unit, Commissariat à l'Énergie Atomique et aux Énergies Alternatives, INSERM, Université Paris-Saclay, NeuroSpin, Gif-Sur-Yvette, France. [2]Centre for Advanced Imaging, University of Queensland, St. Lucia, Queensland, Australia. Email: timo@neuroscience.vision; m.cloos@uq.edu.au

ficity (*5*). One way to improve the specificity of fMRI is to focus on smaller veins by using stronger magnetic fields (*6*). This has led to a surge of "ultra-high-field" fMRI systems that allow an increase in resolution (see the photo). Fundamentally, the spatial specificity of BOLD is limited because the vessels form large networks where an increase in the size of vessels at one location will also cause changes in downstream vessels. So even the smallest vessels can change their size in response to the activity of faraway neurons (*7*). The spatial specificity of optical imaging of blood vessels is superior to that of fMRI (*8*), which suggests that fMRI systems with increased magnetic-field strength have much to offer.

The temporal specificity of fMRI is perhaps a more pressing limitation. Although hemodynamic fluctuations can be surprisingly fast (~1 s) (*9*), this is still too slow to follow neuron activation during cognitive processes such as perception and decision-making (~0.1 s) (*10*). The difficulties result from a delay in the hemodynamic response, which also remains increased for some time after neuronal activity has returned to baseline. Effectively, the hemodynamic response imposes a filter that suppresses the detection of rapid changes along the temporal dimension. This limited temporal specificity is also observed with optical imaging techniques (*11*).

The results of Toi *et al*. suggest that their method, called DIANA (direct imaging of neuronal activity), provides a signal that reflects the intracellular voltage of a population of neurons, avoiding indirect physiological limitations on the temporal and spatial specificity that can be reached. Furthermore, DIANA does not require contrast agents or new equipment; all that is needed is a simple modification to the control software used to operate existing ultra-high-field MRI systems. The exact biophysical underpinning of DIANA is not completely clear. The leading theory suggests that changes in neuronal membrane potential are reflected in the transverse relaxation time (T_2) of the MRI signal. Simply put, T_2 determines how quickly the MRI signal disappears. Initial estimates suggest that a ~0.1% signal increase can be observed during neuronal activity, which is caused by a membrane potential–induced lengthening of T_2. Although further study is needed to develop a better understanding of the DIANA contrast mechanism, the high spatial and temporal specificity of the activity patterns reported by Toi *et al*. could open a new window into the brain.

The 11.7-tesla magnetic resonance imaging (MRI) scanner at NeuroSpin in France (shown here) has, at present, the highest magnetic-field strength among MRI systems designed for human brain imaging.

fMRI studies have found that cognitive functions generally require networks of brain areas, but it has been challenging to disentangle the precise role of the different nodes in these networks (*12*). Notably, the temporal precision of DIANA could allow measurement of the small delays in the activation patterns across nodes, revealing how messages are relayed in networks (*13*). Toi *et al*. show that they can observe temporal delays between cortical layers in mouse brain (on the order of tens of milliseconds), which could even help to disentangle processing streams within an area (*14*). Furthermore, an exciting advantage of measuring intracellular voltage is that it enables distinction between excitatory and inhibitory signaling between neurons, something that is generally not even possible with highly invasive methods, such as electrodes implanted in the brain (*15*). As an example, Toi *et al*. provide results that suggest that neurons in superficial layers of mouse somatosensory cortex are hyperpolarized in response to the excitation of whiskers before deep and middle layers are activated, providing a glimpse of possible new ways to study the intricate communication between brain areas.

A major technical challenge for DIANA will likely be subject motion. Instead of collecting a series of complete images to follow the signal through time and space, like fMRI does, DIANA collects a series of partial images. This means that the stimulus must be repeated to collect the remaining parts of the image, and any motion that occurs between these time points can introduce artifacts. So far, Toi *et al*. have demonstrated DIANA in anesthetized mice, where motion artifacts are limited. The next major milestone will be to demonstrate that it can work in awake humans. In addition, because DIANA needs repeatable stimuli, it remains unclear whether and how DIANA can be applied to study spontaneous activation patterns of the brain that span multiple time scales. The ability of DIANA to lift the temporal and spatial hurdles that now limit BOLD fMRI holds the exciting potential to reveal the detailed computational mechanisms of mental processing at the fast pace at which it unfolds. ■

REFERENCES AND NOTES

1. P. T. Toi *et al*., *Science* **378**, 160 (2022).
2. J. W. Belliveau *et al*., *Science* **254**, 716 (1991).
3. S. Ogawa, T. M. Lee, A. R. Kay, D. W. Tank, *Proc. Natl. Acad. Sci. U.S.A.* **87**, 9868 (1990).
4. N. K. Logothetis, *Nature* **453**, 869 (2008).
5. J. R. Polimeni, B. Fischl, D. N. Greve, L. L. Wald, *Neuroimage* **52**, 1334 (2010).
6. K. Uğurbil, *Neuroimage* **168**, 7 (2018).
7. P. O'Herron *et al*., *Nature* **534**, 378 (2016).
8. J. M. Hu, X. M. Song, Q. Wang, A. W. Roe, *eLife* **9**, e57261 (2020).
9. L. D. Lewis, K. Setsompop, B. R. Rosen, J. R. Polimeni, *Proc. Natl. Acad. Sci. U.S.A.* **113**, E6679 (2016).
10. S. M. Crouzet, H. Kirchner, S. J. Thorpe, *J. Vis.* **10**, 16.1 (2010).
11. Y. B. Sirotin, E. M. C. Hillman, C. Bordier, A. Das, *Proc. Natl. Acad. Sci. U.S.A.* **106**, 18390 (2009).
12. S. M. Smith *et al*., *Proc. Natl. Acad. Sci. U.S.A.* **106**, 13040 (2009).
13. M. Siegel, T. J. Buschman, E. K. Miller, *Science* **348**, 1352 (2015).
14. M. W. Self, T. van Kerkoerle, R. Goebel, P. R. Roelfsema, *Neuroimage* **197**, 806 (2019).
15. G. Buzsáki, C. A. Anastassiou, C. Koch, *Nat. Rev. Neurosci.* **13**, 407 (2012).

ACKNOWLEDGMENTS

T.v.K. is the recipient of a Young Investigator award from the French National Research Agency (ANR-19-CE37-003-01). M.A.C. is the recipient of an Australian Research Council Future Fellowship award (FT200100329).

10.1126/science.ade4938

PHOTO: FRANCIS RHODES/COURTESY OF CEA

POLICY FORUM

DATA POLICY

Data sharing and community-engaged research

Data sharing must be accompanied by responsibility sharing

By **Maya Sabatello[1], Daphne O. Martschenko[2], Mildred K. Cho[2], Kyle B. Brothers[3]**

Research funders, professional associations, and scientific journals have increasingly endorsed positions and established policies that recognize data as a public good (*1*). In the health research context, the promise of data sharing is to accelerate health research across borders and improve patient care (*2*). But this raises ethical concerns for research participants, researchers, and marginalized communities, such as questions about data ownership, risk of reidentification (for example, genomic datasets), data security, and appropriate consent processes (*1*). Data sharing also raises distinctive ethical challenges for community-engaged research (CEnR), a term encompassing diverse research collaborations with communities, from community consultation to community-based participatory research. We discuss key rationales and goals of data sharing in health research and of CEnR and highlight three areas of potential tension between these two movements: incentives and benefit sharing; group harm and power structures; and researcher engagement and responsibility sharing.

This issue is particularly timely and important in light of the US National Institutes of Health (NIH) updated Data Management and Sharing Policy, which will enter into force in January 2023 ("the Policy") (*3*). The Policy "establishes the expectation for maximizing the appropriate sharing of scientific data generated from NIH-funded or conducted research," with a preference for sharing through established repositories. The Policy's shift from an aspirational culture of data sharing in scientific research to an established expectation to be documented in data sharing plans submitted with grant proposals (which may be perceived as a prerequisite for funding) creates new financial and nonfinancial incentives for researchers and research institutions. Though the Policy galvanizes the growing trend of recognizing health data as a public good, this transformation in its current form risks producing an excessively narrow understanding of public good.

[1]Center for Precision Medicine and Genomics at the Department of Medicine, Columbia University Irving Medical Center; Division of Ethics, Department of Medical Humanities and Ethics, Columbia University Irving Medical Center; New York, NY 10032, USA. [2]Stanford Center for Biomedical Ethics and Departments of Medicine and Pediatrics, Stanford Medicine, Stanford, CA 94305, USA. [3]Norton Children's Research Institute Affiliated with the University of Louisville School of Medicine, Louisville, KY 40202, USA. Email: ms4075@cumc.columbia.edu

TWO SCIENTIFIC MOVEMENTS

The data sharing and CEnR movements are both grounded in efforts to improve scientific research and health outcomes for marginalized populations. However, they differ in their locus of control and vision for how and who is entrusted to promote such efforts. The data sharing movement transfers scientific data from local and community ownership to global use and from individual researchers to institutionally controlled environments and the larger community of researchers. It aims to create larger and more diverse datasets for generating meaningful scientific findings (*2*), reducing biases, and enhancing scientific accuracy through data reuse, validation, and rigorous reproducibility (*4*). Data sharing further promotes the scientific enterprise by reducing redundancy in data collection and burden on research participants, creating training resources for emerging scientists, and spurring new research with existing data (*4*).

The CEnR movement promotes scientific progress through reliance on local rather than global knowledge and power sharing instead of researcher-led, top-down approaches to research. A fundamental tenet of CEnR is that researchers' expressions of responsibility to the community are inseparable from the study and the willingness of the community to contribute data for scientific endeavor. CEnR exists in various contexts (e.g., biodiversity studies) but is particularly illuminative in health research, where it intersects with laws, policies, and other commitments to promote equity and nondiscrimination in health. It empowers communities to work alongside researchers from the very beginning of the research process. Together, communities and researchers in CEnR set research priorities and identify—and proactively address—ways researchers might cause harm to the community (*5*). CEnR is geared toward equitable, justice-oriented partnerships, including a co-learning process between scientific researchers and communities, attention to sociopolitical contexts and power structures, and potential for identifying opportunities for benefit sharing (*5*, *6*). It is believed to enhance researchers' cultural humility, awareness of unconscious biases, and understanding of diverse health-related belief systems; it also serves as a tool to build rapport between researchers and participants and increase the trustworthiness of research institutions (*5*).

The elements comprising CEnR center attention on community well-being, the potential harms and benefits accruing to a community, and communities (not individuals) as the holders of rights and moral status. By contrast, the common practice of institutional review boards (IRBs) and informed consent forms is to emphasize individual research participants. The purpose of CEnR to create trust relationships gives rise to ethical obligations beyond those of non-CEnR studies and must extend to secondary users of CEnR-collected health data to uphold the goals, processes, and outcomes of CEnR.

INCENTIVES AND BENEFIT SHARING

The underpinnings of CEnR—i.e., high trust relationships and trustworthiness of researchers—are neither legally based nor transactional in nature. Trust relations between researchers and communities cannot be circumscribed in consent forms; they cannot be sold, bought, or transferred. However, data sharing plans commonly focus on individual (not community-level) consent and commodify data that were collected on the basis of community trust by allowing unrelated researchers to profit from them, regardless of community values and preferences. Some secondary data users may have even contributed to health disparities experienced by marginalized populations, making them untrustworthy to these communities. Blind community members, for example, expressed low will-

ingness to share health data with pharmaceutical companies (notwithstanding high interest in precision medicine research) because such companies commonly fail to assure that drug labels are provided in braille or large print as required by law (*7*)—inaccessibility that has negatively affected the health of blind people. The opportunity for secondary data users to utilize data that were collected through trusting relationships of CEnR obviates the need for secondary researchers to earn the community's trust and removes any incentive for them to alter their discriminatory practices.

Data sharing might also undermine efforts to protect marginalized communities from exploitation through extension of research benefits. CEnR in resource-poor settings, for example, has called for ensuring systemic and global-level benefit sharing as an ethical requirement of just research (*8*). Benefit sharing fulfills basic underpinnings of CEnR, including long-term, mutually beneficial partnerships, and transformative practices to redress past harms and existing power injustices (*6*). However, benefit sharing agreements that emerged in CEnR studies are not immediately applicable to secondary data users; viable approaches for extending benefit sharing responsibilities to secondary data users are needed (*8*). Although adding such conditionality to open-access repositories might complicate secondary data uses, it could facilitate changes toward socially responsible perceptions of the public good.

Lack of drug labeling in braille has fueled distrust among some blind people

GROUP HARM, POWER STRUCTURES

The NIH Policy acknowledges that data sharing is likely to be varied and contextual. In respect and recognition of Tribal sovereignty, the Policy specifically notes the data protection interests of Tribal Nations and commits to develop, with community input, additional guidelines for researchers that are responsive to and highlight the specific values, preferences, and data sharing concerns of American Indian and Alaska Native (AI/AN) communities (*3*).

Secondary data uses raise distinctive concerns for other marginalized communities that are engaged in research. In addition to conventional harms such as data uses in research that communities view as objectionable (for example, gene editing) (*9*), researchers have fused scientifically unfounded and socially demeaning constructs into publicly available data to analyze and interpret them in ways that harm the interests of marginalized racial and ethnic communities (*10*). Such secondary uses of data collected through community engagement add insult to injury: They circumvent a fundamental purpose of CEnR to empower communities to work with researchers to set health research priorities, assure appropriate processes for their implementation, and prevent group harm, and thus abuse the trust underpinning CEnR. However, acceptable secondary uses of data and how they will benefit communities at large are not necessarily subject to IRB review. Without broad oversight of secondary data uses and the inclusion of communities in such oversight, data sharing will dilute responsibility for community-informed and equitable research outcomes.

Secondary uses of data collected in CEnR also risk causing group harms, including dignitary harms. Researchers analyzing open data can reinterpret the data without attention to contexts or collapse the data into categories that deviate from community narratives and preferences. Aggregated data analyses are important for scientific findings to emerge (*2*). However, aggregate studies also objectify community members and remove their power to be actively involved in the research process—a key component of CEnR. Without bad intention, researchers may reinforce misperceptions of homogeneity, and invisibility, of marginalized populations—for example, in research with Asian American populations, who are often treated as a single racial category. Inappropriate aggregation of data could also mask health disparities or other phenomena in subpopulations and thus reduce the potential for the data to be used to benefit those subgroups (e.g., disproportionately high COVID-19 mortality rates among Chinese Americans and Filipino nurses) (*11*).

Moreover, contrary to the rigidity of informed consent forms that serve as the basis for data sharing (including in studies that engage communities), CEnR involves many additional informal agreements that evolve over time, reflect community-tailored expectations for respectful research collaborations, and are fundamental for ethical, socially just, and responsive research. For example, research engaging members of the Deaf community in the US have highlighted a preference for the use of identity-first ("Deaf individuals") rather than person-first ("person with deafness or hearing loss") language (*12*). This preference accentuates shared history, culture, and experiences of being deaf and challenges the medical model of disability that views being deaf as a deficit that requires treatment. Whereas researchers engaged in CEnR with the Deaf community would be or become educated about and be trusted to follow such community preferences, secondary data users are not required to share or follow such an obligation. Publications based on shared data thus risk perpetuating dignitary harms to communities (by, for example, misnaming them or falsely reinforcing harmful stereotypes), even when communities agreed to contribute data based on trust that primary researchers will not cause these harms.

RESEARCHER ENGAGEMENT, RESPONSIBILITY SHARING

An underlying assumption of data sharing is that data de-identification reduces common risks of research participation. Yet, as secondary research using de-identified data is no longer considered human subjects research, the ethical obligations of secondary users to participants could be considerably weakened. For example, institutional policies on data sharing do not commonly include assurances that data uses are aimed at benefiting communities that participated in CEnR. Data de-identification may have the unintended effects of dehumanizing research participants. Although this outcome may apply to various

PHOTO: JAMES KING-HOLMES/SCIENCE SOURCE

forms of data collection, it is particularly problematic in CEnR, where by design, participants are not mere "research subjects" but are "research partners" who are assured that their voices and preferences will be heeded. This, in turn, breaks the chain of trust-related obligations that underpinned the data collection in CEnR and enables secondary users to morally disengage from the context and communities involved (*13*). By contrast, CEnR encourages transparency and accountability toward research participants and communities throughout and after the study's life cycle. Ethical data sharing thus requires secondary data users to be morally engaged while developing research questions, conducting analyses, and disseminating findings by understanding both the data and the people and communities who donated them. Put differently: Data sharing must be accompanied by responsibility sharing.

Here, researchers conducting CEnR may find themselves caught in a catch-22. In CEnR, it is expected, and important, that some of the scientific researchers are also members of the studied community. Wearing their scientific hats, failure to share data might result in reduced knowledge about and potential health benefits to marginalized populations. Yet as members of the studied community, researchers might share the community's concerns over data sharing; even if not, they may be committed to a shared decision-making process—a common feature in CEnR (*5*)—and to upholding the ethical principle of solidarity (*6*). How to resolve such clashes of loyalties, especially in the absence of a legally recognized status as a community, has not yet been adequately considered.

POLICY IMPLICATIONS

The NIH Policy allows for "justified limitations or exemptions" to assure "appropriate" data sharing (*3*). Yet it primarily circumscribes these exemptions to existing regulations, including consent, and concerns about reidentification. Moreover, the Policy lays the burden of proof on the researchers and communities requesting limitations in how data will be shared without clarifying the evidence needed to secure such an exemption. Given the Policy's preference for maximizing data sharing, there is a risk that exemption decisions will be biased to reflect dominant cultural views.

Assuring appropriate representation on decision-making bodies will be critical but raises questions about which populations are considered "a community" that might merit exemption. Inclusion of "recognized" marginalized communities might be insufficient. Asian Americans, for example, are not recognized by the NIH as an underrepresented community, despite substantial health disparities experienced by its subpopulations (*11*). The disability community—the largest but least recognized health disparities group in the US (*14*)—might not be seen by some as fitting conventional notions of "a community," leading some to question who would be a legitimate representative to speak on its behalf. Notwithstanding heterogeneity within communities, it will be important to ensure that when requests for exemptions from data sharing requirements are being considered by funders, scientific journals, and other stakeholders, these processes consider the lived, shared, and intersectional experiences of the relevant communities and those contributing data as provided in data sharing plans—and celebrated in CEnR.

To address these tensions and ensure responsibility sharing to communities, the NIH could implement a mechanism for automatic exceptions to sharing data generated through CEnR when requested by communities. However, such an approach has faced challenges in implementation also with legally recognized Tribal Nations and communities. Despite the NIH's acknowledgement of their data protection interests and explicit allowance of exemption, researchers, institutions, and journal editors may neither understand nor follow it (*15*). It is therefore even less likely to be endorsed for nonsovereign and even currently unrecognized communities. Other approaches could require training reviewers on data sharing plans and the wider research community to recognize community nuances and measures to ensure that secondary data users understand, and commit to uphold, their own responsibility to the communities who contributed data. These efforts could include community consultation on data sharing plans; community review of individual data sharing requests, including a community veto of data sharing requests that raise concerns; raising the bar for standard "data use limitation statements" to assure benefit and responsibility sharing; requiring secondary data users to follow core formal and informal agreements reached with the community during the study, such as benefit sharing and culturally tailored, respectful communication of findings; and seeking feedback from the lead researchers in CEnR (who have first-hand knowledge and expertise on the community) on draft publications and other work products prior to their finalization. Fundamentally, it is critical to develop measures and processes to assure that data collected through trust relations in CEnR with marginalized communities are not used or disseminated in ways that are harmful to, or result in the restigmatization of, the community.

Community and public trust and accountability of secondary data users could also be enhanced by ensuring that all research databases under the Policy are documenting who is using data and for what purposes. Further, researchers requesting data derived from CEnR could be asked to detail how data uses intend to benefit communities and the public. Such transparency would allow NIH—and other entities involved in dissemination of scientific knowledge—to evaluate the extent to which the public good is being served by the data sharing policy.

There are key issues at stake: constructs of public good, justice and social responsibility in secondary data uses, and fairness in data sharing decisions. Research and multi-stakeholder engagement are needed to explore viable ethical, social, and policy solutions to the dilemmas that arise. Without appropriate protections for communities engaged in research, a data sharing expectation is likely to negatively affect marginalized communities, efforts to diversify enrollment, and researchers conducting CEnR. The critical role of CEnR for inclusive and equitable research requires addressing the tensions between these two scientific movements—for communities and science. ■

REFERENCES AND NOTES

1. C. Ohmann *et al.*, *BMJ Open* **7**, e018647 (2017).
2. H. L. Rehm *et al.*, *Cell Genom.* **1**, 100029 (2021).
3. Final NIH policy for data management and sharing (2020); https://grants.nih.gov/grants/guide/notice-files/NOT-OD-21-013.html.
4. *Nat. Commun.* **9**, 2817 (2018).
5. Clinical and Translational Science Awards Consortium, Community Engagement Key Function Committee Task Force on the Principles of Community Engagement, (2011); https://www.atsdr.cdc.gov/communityengagement/pdf/PCE_Report_508_FINAL.pdf.
6. B. Pratt, P. Y. Cheah, V. Marsh, *Am. J. Bioeth.* **20**, 43 (2020).
7. M. Sabatello *et al.*, *Genet. Med.* **21**, 2631 (2019).
8. A. Sudoi, J. De Vries, D. Kamuya, *BMC Med. Ethics* **22**, 102 (2021).
9. M. A. Rothstein, *J. Law Med. Ethics* **49**, 489 (2021).
10. A. Panofsky, K. Dasgupta, N. Iturriaga, *Am. J. Phys. Anthropol.* **175**, 387 (2021).
11. J. L. Young, M. K. Cho, *Am. J. Bioeth.* **21**, 100 (2021).
12. D. C. Garofalo *et al.*, *Genet. Med.* **24**, 712 (2022).
13. A. Bandura, C. Barbaranelli, G. V. Caprara, C. Pastorelli, *Am. Am. Psychol. Assoc.* **71**, 364 (1996).
14. G. L. Krahn, D. K. Walker, R. Correa-De-Araujo, *Am. J. Public Health* **105** (suppl. 2), S198 (2015).
15. S. R. Carroll *et al.*, *Front. Genet.* **13**, 823309 (2022).

ACKNOWLEDGMENTS

This work was partially supported by National Human Genome Research Institute (NHGRI)–NIH Office of the Director (OD) grant R01HG010868 (M.S.), NHGRI grant T32HG008953 (M.K.C., D.O.M.), and NHGRI grant U24 HG010733 (M.K.C.).

10.1126/science.abq6851

BOOKS *et al.*

Celebrating both Juneteenth and Independence Day is a way to embrace the complexity of US history.

PHOTO: ADREES LATIF/REUTERS IMAGES

SCIENCE AND SOCIETY

Justice meets social science

A pair of authors urge readers to confront society's shortcomings and build a better future

By **James M. Jones**

In 1917, William Tyler Page crystallized the conditions first specified in the preamble to the US Constitution that would be necessary to achieve "a more perfect union" (*1*). Those principles—freedom, equality, justice, and humanity—however exalted, have been eroded and undermined by white racism throughout the country's history. Two noteworthy new books confront this problem with an eye to what a more perfect union can look like and how we might achieve it.

Viral Justice, by sociologist Ruha Benjamin, is ultimately a manifesto for social change. It evolves from Benjamin's view that there are parallels between the COVID-19 pandemic and subjugating mechanisms such as racism, sexism, and colonialism, all of which, she argues, play a eugenicist role in constraining, if not eliminating, "unwanted" people. Justice, she maintains, requires us to go beyond sanctioned diversity, equity, and inclusion protocols to fundamentally transform the institutions and societies that purport to want to include marginalized people. What Benjamin calls "deep-rooted interdependence"—the notion that we are all connected to one another—is the centerpiece of her approach.

Benjamin argues that differential access to COVID-19 vaccines has widened the gap between "wanted" and "unwanted" humans and calls for the unwanted to rally to their own and others' benefit and spread justice and joy in the face of myriad perils. Here, Benjamin recounts numerous stories (many from her own life) of how individual dedication and community empowerment have acted as levers of social change. The stories she tells are at once heartbreaking, inspiring, and hopeful.

The book is organized into chapters that describe how marginalized people are worn down and made vulnerable to disease (the chapter titled "Weather"); how they are victimized by police and white supremacists ("Hunted"); how they are burdened by societal narratives that they are responsible for their unequal fate ("Lies"); how they struggle to make ends meet in a racialized capitalist system ("Grind"); how they are targets of social judgment, cruel treatment, and callous indifference ("Exposed"); and how they struggle with untrustworthy institutions ("Trust"). Benjamin's approach is undoubtedly radical, but it is not dogmatic or doctrinaire. The book illustrates how interdependence across boundaries of race, class, sex, and positionality can lead to meaningful change that transforms people, institutions, and societies in pursuit of justice.

In *A More Just Future,* social psychologist Dolly Chugh invites readers to reflect on US history and recognize the contradictions it entails. Failing to start there, Chugh argues, makes it difficult to unravel the paradoxes that make "justice for all" so elusive.

The three main sections of the book ask: "How do we start?," "What do we do?," and "Where do we go from here?" The undeniable starting point is to carefully and properly examine history through a racial lens. There, she argues, we find the igniter of current divisions.

US history is complicated, and divisions arise when we fail to recognize that two seemingly opposite ideas can both be true. Take, for example, two American holidays: Independence Day (4 July) and Juneteenth (19 June). "July 4 celebrates our purported ideals, sidelining our wrongs. June 19 celebrates our wrongs belatedly corrected to match our ideals," writes Chugh. "Together the two holidays epitomize our national—and human—condition: living in paradox. To be a patriot of this country is to learn to live with paradox."

We must be aware that racialized speech creates and condones racialized attitudes, that biased systems are self-perpetuating, and that trauma has a material effect on our psychological well-being, our chromosomes, and our communities, argues Chugh. We must also reject racial fables that simplify complex relationships. For a more just future, we must take responsibility—be informed; decolonize language, minds, and culture; and apologize when appropriate—and build grit, that is, perseverance and passion for reaching long-term goals.

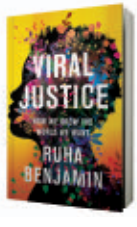

Viral Justice
Ruha Benjamin
Princeton University Press, 2022. 392 pp.

A More Just Future
Dolly Chugh
Atria Books, 2022. 224 pp.

Research shows how difficult it is to undo ingrained stereotypes and how beliefs persevere—even when facts clearly demonstrate their untenability. Psychological and cultural beliefs can only be altered when individuals commit to close examination and undertake actions dedicated to social change. Are people able or willing to do the work that is required? Some are and some are not.

Our actions must, as Benjamin argues, be predicated on a genuine belief in human interdependence. If we work together to create positive, interdependent relationships and to give voice to the marginalized, we can embark on a path that leads to a more just future. ■

The reviewer is a Trustees' Distinguished Professor Emeritus of Psychological and Brain Sciences and Africana Studies, University of Delaware, Newark, DE 19716, USA. Email: jmjones@udel.edu

REFERENCES AND NOTES

1. W. T. Page, "The American's Creed" (1917).

10.1126/science.add8003

DENDROCHRONOLOGY

Natural monuments

Reverence for old trees sparked early forest conservation efforts, even as ancient woodlands were cut with impunity

Elderflora: A Modern History of Ancient Trees
Jared Farmer
Basic Books, 2022.
448 pp.

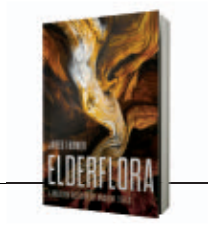

By **D. W. Stahle**

On 22 April 2022, US President Joe Biden issued an executive order to inventory mature and old-growth forests on public land. The order may prove to be particularly consequential because most of the oldest trees on Earth are found on federal land. Of the 10 species proven with tree-ring dating to include individual trees that have lived for at least 2000 years, eight are native to the United States, seven to the West, and five to California (*1*, *2*). *Elderflora*, by historian Jared Farmer, is a book about the giant, sacred, and exceptionally old trees that have achieved scientific interest and popular reverence.

Farmer describes the emergence of the cultural phenomenon of venerating "elderflora" (old trees), a tradition practiced in both Eastern and Western cultures around such specimens as Abraham's oak, an ancient tree in the West Bank with purported ties to the biblical Abraham; the dragon trees of the Canary Islands, which fascinated 19th-century European naturalists; and Montezuma bald cypress, respected in Indigenous and modern Mexico. Public veneration of exceptional trees has not always prevented destruction of the forests they inhabit, but Farmer argues that it may have helped sow the seeds of the modern conservation movement.

Elderflora describes in painful detail the cutting of the grandest forests on Earth. Some deforestation was colonial and capitalistic, some came out of a fear of the wild forest, and some arose from ideas about humankind's dominion over nature. The reader will note a little revisionist history in these pages, but the book succeeds as a cultural history of the conservation ideal that led society to forest preservation.

Alexander von Humboldt's vivid descriptions of megaflora, which he referred to as "monuments of nature," promoted Western thought on forest protection during the 19th century, an era that was characterized by serious overexploitation of natural resources. Before protection efforts finally succeeded, 95% of the coast redwood forests in California—the tallest conifer forests on Earth—were cut. This exploitation mindset was not restricted to the United States. As Farmer writes of the gigantic kauri forests in New Zealand, when "confronted with the rarest forests in creation…settlers could only imagine a wealth of pastures."

The astronomer A. E. Douglass invented the method of tree-ring cross dating in the early 1900s and used it to date the then "oldest known" trees on Earth: two giant sequoias in California, which Douglass determined to be more than 3000 years old. His student and colleague, Edmund Schulman, traveled widely across the semiarid United States seeking old conifers to develop exactly dated ring-width chronologies to document epic droughts and pluvials of the past.

Long-lived bristlecone pine trees thrive in cold, arid conditions.

In the 1950s, Schulman made a sensational discovery: bristlecone pine are more than 4000 years old in the White Mountains of California, which are still today the oldest-known living trees on Earth. Schulman cut down two of these exceptionally old trees for "detailed analysis." There are many old bristlecone pine, but the sacrifice of these ancient trees was doubly regrettable because it was not necessary (thin cores can be removed without harming the tree) and because it was subsequently used to justify the cutting of what turned out to be the oldest tree yet known to have lived—a 4900-year-old bristlecone pine on Wheeler Peak in Nevada.

Not coincidentally, many of the oldest trees still left on Earth are not valuable for lumber production. Unfortunately, this did not prevent the late-19th-century cutting and dynamiting of 8000 giant sequoias—a species with coarse, brittle wood of only marginal value as lumber—in the Converse Basin, "the densest, grandest expanse of *Sequoiadendron* ever known." Bristlecone pine is also "noncommercial" owing to its extremely slow growth in a cold, arid environment that perfectly illustrates Schulman's principle of "longevity under adversity."

The Pinyon-Juniper ecosystem covers 75,000 square miles of the American West (*3*), making it one of the largest areas of ancient woodland left on Earth. Yet this ecosystem rarely receives much respect and is featured in only one paragraph in this otherwise-great book. These austere, never-cut woodlands could, like the other marvelous forests that Farmer discusses, benefit from greater attention and stronger protection to slow the loss of biodiversity, the decline of vertebrate abundance, and the closing of open space. ■

The reviewer is at the Department of Geosciences, University of Arkansas, Fayetteville, AR 72701, USA. Email: dstahle@uark.edu

REFERENCES AND NOTES

1. P. M. Brown, in *Tree Rings, Environment and Humanity: Proceedings of the International Conference, Tucson, Arizona, 17–21 May 1994*, J. S. Dean, D. M. Meko, T. W. Swetnam, Eds. (Radiocarbon, Dept. of Geosciences, Univ. of Arizona, 1996), pp. 727–731.
2. Rocky Mountain Tree-Ring Research, OLDLIST, A Database of Old Trees; http://rmtrr.org/oldlist.htm.
3. R. M. Lanner, *The Piñon Pine: A Natural and Cultural History* (Univ. of Nevada Press, 1981).

10.1126/science.add7170

PHOTO: KATRINA BROWN/ALAMY STOCK PHOTO

CALL FOR PAPERS

SPJ
SCIENCE PARTNER JOURNALS

Health Data Science

Health Data Science is an online-only Open Access Science Partner Journal published in affiliation with **Peking University (PKU)** and distributed by the **American Association for the Advancement of Science (AAAS)**. This journal is committed to promoting the appropriate application of cutting-edge technologies and analytic approaches for the health field, translating the value of health data into practice for the benefit of patients' health and populations' well-being and advancing health data science. *Health Data Science* publishes innovative, scientifically-rigorous original research, comprehensive reviews, insightful perspectives, viewpoints and editorials. The topics of interest include but are not limited to: data management, governance and provenance; comparative effectiveness research; ethics issues; public health and health policies; and more.

Submit your research to *Health Data Science* today!

Learn more at **spj.sciencemag.org/hds**

The Science Partner Journal (SPJ) program was established by the American Association for the Advancement of Science (AAAS), the nonprofit publisher of the *Science* family of journals. The SPJ program features high-quality, online-only, Open Access publications produced in collaboration with international research institutions, foundations, funders and societies. Through these collaborations, AAAS furthers its mission to communicate science broadly and for the benefit of all people by providing top-tier international research organizations with the technology, visibility, and publishing expertise that AAAS is uniquely positioned to offer as the world's largest general science membership society.

Visit us at **spj.sciencemag.org**

@SPJournals **@SPJournals**

OPEN ACCESS

ARTICLE PROCESSING CHARGES WAIVED THROUGH DECEMBER 2024

LETTERS

Native tree plantations in rural areas of Chile are not sufficient compensation for urban development.

PHOTO: JUAN L. CELIS-DIEZ

Edited by **Jennifer Sills**

Expand native vegetation in Chile's cities

Globally, 56% of the population lives in cities (*1*). This trend is expected to continue, particularly in biodiversity-rich Latin American countries such as Chile, which have the highest percentage of urban population in the world (*1*, *2*). As in many other Latin American countries, urban parks in Chilean cities are small, rare (*3*), and dominated by exotic vegetation (*4*), whereas biodiversity-supporting remnants of native vegetation within city limits are confined in isolated and often vulnerable locations. Outside urban settings, extensive plantations of native tree species are grown in barren areas in an attempt to replace ecosystems that have been lost to development. Instead of creating more plantations, which may not be sustainable, Chile should prioritize the preservation of remnant native vegetation within its cities.

Continuous urban expansion that replaces natural ecosystems has negative effects on biodiversity (*5*). However, local geomorphology and urban development, driven mainly by the interests of the real estate market, have limited native vegetation to isolated hills, steep slopes, and ravines (*6*). Even in these areas, the vegetation is threatened by unregulated urban expansion, illegal logging, fires, drought, and, in the cases where unofficial landfills have been created, pollution (*6*).

The survival of native tree plantations, supported by the private sector as an easy solution to environmental degradation, depends on irrigation and herbivore protection (*7*). However, water scarcity, the limited maintenance period required by law, global economic instability, and climate change make the long-term survival of these plantations uncertain (*8*). Moreover, their capacity to serve as substitutes, in ecological or functional terms, for degraded ecosystems remains debated (*9*, *10*). Therefore, native tree planting should not be prioritized to the detriment of other initiatives (*9*).

Instead, Chile's policymaking should include the protection and restoration of remnant natural ecosystems in urban areas. Urban forests provide ecosystem services such as carbon sequestration, oxygen provision, reduction of heat islands and atmospheric pollution, water infiltration, and provision of habitat for biodiversity (*11*). Giving effective protection to natural remnants and increasing their connectivity to preserve native vegetation, including a network of urban parks, can bring together environmental conservation and human well-being. These measures could better offset biodiversity losses due to urban expansion, power generation, and mining activities. Given Chile's urban majority (*1*), and the emphasis the proposed new constitution places on common goods (*12*), the country is well positioned to address the challenge of increasing native biodiversity in urban landscapes.

Juan L. Celis-Diez[1,2]* and Nélida Pohl[2]
[1]Pontificia Universidad Católica de Valparaíso, Valparaíso, Chile. [2]Instituto de Ecología y Biodiversidad, Santiago, Chile.
*Corresponding author. Email: juan.celis@pucv.cl

REFERENCES AND NOTES

1. The World Bank, "Urban population (% of total population)" (2022); http://data.worldbank.org/indicator/SP.URB.TOTL.IN.ZS?order=wbapi_data_value_2012+wbapi_data_value+wbapi_data_value-last&sort=desc.
2. R. Rozzi, in *Earth Stewardship: Linking Ecology and Ethics in Theory and Practice*, R. Rozzi *et al.*, Eds. (Springer, 2015).
3. S. Reyes-Paecke, I. M. Figueroa, *EURE* **36**, 89 (2010).
4. L. Santilli *et al.*, *Gayana* **75**, 568 (2018).
5. A. Pauchard *et al.*, *Biol. Conserv.* **127**, 272 (2006).
6. I. C. Fernández *et al.*, *Landsc. Urban Plan.* **187**, 181 (2019).
7. M. Holmgren *et al.*, *Glob. Chang. Biol.* **12**, 2263 (2006).
8. J. Bannister *et al.*, *Restor. Ecol.* **26**, 1039 (2018).
9. K. D. Holl, P. H. S. Brancalion, *Science* **368**, 580 (2020).
10. K. M. S. Kemppinen *et al.*, *Conserv. Biol.* **34**, 1221 (2020).
11. Food and Agriculture Organization of the United Nations, "Benefits of urban trees" (2016); www.fao.org/documents/card/es/c/C0024E/.
12. E. Rodríguez Mega, *Nature*, 10.1038/d41586-022-02069-0 (2022).

10.1126/science.ade6402

Chile's monoculture plantations must adapt

On 30 May, the Chilean Climate Change Framework Law was enacted to address climate change challenges and decrease Chile's greenhouse gases with a goal of emissions neutrality by 2050 (*1*). The framework includes climate change mitigation through nature-based solutions such as carbon sinks (i.e., trees and soils that absorb more carbon than they release) in native forests and plantations with native species, but it discourages monoculture plantations. The strategies in the law underestimate the potential environmental value of monocultures.

The exclusion of plantation monocultures in the new law reflects some of the known negative effects of Chile's pervasive *Pinus radiata* and *Eucalyptus spp*. plantations. Plantations formed by these species are associated with environmental degradation which occurs when they cover continuous landscapes where trees are clearcut and replanted in short rotations (less than 25 years) (*2*–*4*). The plantations have also caused social harms such as rural poverty and conflicts with Indigenous peoples (*3*, *5*). However, better plantation management could provide the benefits of afforestation while avoiding these damaging consequences.

To maximize the benefits of *P. radiata*, *Eucalyptus spp*., and other monoculture plantations, Chile should promote changes that increase the ability of plantations to contribute to climate goals. Trees should be planted according to an extended rotation schedule, and instead of clearcutting, some trees or groups of trees should be retained and allowed to

grow old (*6*). Plantations should include fast-growing native species (*7*, *8*) and incorporate a variety of species instead of just one (*8*–*10*). Almost all plantations start as monocultures for financial reasons, but their diversity and carbon sinks should be increased within several decades (*6*, *9*, *10*). Plantations that meet some of the above criteria should be acknowledged in the Climate Change Framework Law as beneficial.

In Chile, monoculture plantations constitute almost all carbon removal contributions from harvested wood products (*11*), and they are considered in the national plan to cut emissions and adapt to climate impacts (*12*). Given their prominence, Chile's new law cannot discount them from future strategic planning. Instead, the law should provide guidance that allows the plantation sector to transition to standards that better meet the mitigation needs associated with climate change goals.

Pablo J. Donoso[1]*, Daniel P. Soto[2], Celso Navarro[3], Yasna Rojas[4]

[1]Universidad Austral de Chile, Facultad de Ciencias Forestales y Recursos Naturales, Instituto de Bosques y Sociedad, Isla Teja s/n, Valdivia, Chile. [2]Departamento de Ciencias Naturales y Tecnología, Universidad de Aysén, Coyhaique, Chile. [3]Universidad Católica de Temuco, Departamento de Ciencias Ambientales, Temuco, Chile. [4]Instituto Forestal, Valdivia, Chile.
*Corresponding author. Email: pdonoso@uach.cl

REFERENCES AND NOTES

1. Ministerio del Medio Ambiente, Ley 21455 Ley Marco de Cambio Climático (2022); www.bcn.cl/leychile/navegar?idNorma=1177286 [in Spanish].
2. C. Echeverría *et al.*, *Biol. Conserv.* **130**, 481 (2006).
3. C. Salas-Eljatib *et al.*, *J. For.* **114**, 562 (2016).
4. A. P. Durán, O. Barbosa, *Science* **365**, 1388 (2019).
5. G. Anríquez *et al.*, *Environ. Develop. Econ.* **26**, 51 (2020).
6. T. N. McFadden, R. Dirzo, *For. Ecol. Manag.* **425**, 75 (2018).
7. F. P. Cubbage *et al.*, *New For.* **33**, 237 (2007).
8. P. Ojeda-González *et al.*, *New Zealand J. For. Sci.* **50**, 11 (2020).
9. C. Messier *et al.*, *Conserv. Lett.* **15**, e12829 (2021).
10. B. Waring *et al.*, *Front. For. Glob. Change* **3**, 1 (2020).
11. Ministerio del Medio Ambiente, "Informe del Inventario Nacional de Chile 2020: Inventario nacional de gases de efecto invernadero y otros contaminantes climáticos 1990-2018" (Oficina de Cambio Climático, Santiago, Chile, 2021) [in Spanish].
12. Gobierno de Chile, "Contribución determinada a nivel nacional (NDC) de Chile, Actualización 2020" (2020). [in Spanish].

10.1126/science.ade7898

Lessons from extinctions of dugong populations

The dugong (*Dugong dugon*) is one of four living sirenians. Its closest modern relative, Steller's sea cow (*Hydrodamalis gigas*), was hunted to extinction in the 18th century (*1*). A dugong population near Okinawa, Japan became extinct in 2019 (*2*), and now dugongs are likely functionally extinct in China (*3*). The disappearance of these populations follows dugong losses in the Mascarenes, Maldives, Lakshadweep Islands, and Spermonde Islands (*4*, *5*). These extinctions provide crucial lessons for ongoing and future conservation of surviving dugong populations and other marine megafauna.

Extirpated dugong populations were lost through deliberate hunting, accidental bycatch, and destruction of their seagrass habitat (*2*–*6*). Hundreds of individuals were harvested between 1893 and 1916 in Japan and the 1960s in China, resulting in substantial declines that may have pushed populations below sustainable thresholds (*2*, *3*). Incidental captures in fishing gear in both regions caused continued mortality in remnant populations (*5*, *7*), and degradation of seagrass meadows through coastal development and habitat disturbance greatly reduced food availability (*6*–*8*). In 1986, a Chinese National Nature Reserve was established for dugongs in Beihai, Guangxi, and dugongs were listed as Grade 1 National Key Protected Animals in 1988 to ban hunting, trade, and consumption (*6*). However, sightings in China were already rare by the 1980s (*3*, *6*), indicating that these actions were implemented too late to be effective (*2*).

Dugongs persist in other shallow tropical and subtropical marine environments, but most populations are threatened (*4*). Understanding the factors responsible for recent dugong losses highlights the steps needed to prevent further extinctions of surviving dugong populations and other vulnerable marine mammals (*9*, *10*). Restrictions against deliberate hunting should be enforced across sirenian and other marine mammal ranges. Evidence-based decision-making is essential for population protection, reserve planning, and seagrass conservation (*11*, *12*). Ongoing dugong extirpations emphasize the crucial need to act early, before efforts to recover populations or locate surviving individuals become too challenging (*2*, *3*).

Mingli Lin[1], Samuel T. Turvey[2], Mingming Liu[1], Heidi Ma[2], Songhai Li[1,3]*

[1]Marine Mammal and Marine Bioacoustics Laboratory, Institute of Deep-Sea Science and Engineering, Chinese Academy of Sciences, Sanya 572000, China. [2]Institute of Zoology, Zoological Society of London, Regent's Park, London NW1 4RY, UK. [3]Center for Ocean Mega-Science, Chinese Academy of Sciences, Qingdao 266071, China.
*Corresponding author. Email: lish@idsse.ac.cn

REFERENCES AND NOTES

1. S. T. Turvey, C. L. Risley, *Biol. Lett.* **2**, 94 (2006).
2. H. Kayanne *et al.*, *Sci. Rep.* **12**, 6151 (2022).
3. M. Lin *et al.*, *Roy. Soc. Open Sci.* **9**, 211994 (2022).
4. H. Marsh, S. Sobtzick, *Dugong dugon* (The IUCN Red List of Threatened Species, 2019).
5. A. M. Moore, R. Ambo-Rappe, Y. Ali, *Front. Mar. Sci.* **4**, 284 (2017).
6. P. Wang *et al.*, *Acta Theriol. Sinica* **27**, 68 (2007).
7. H. Marsh, H. Penrose, C. Eros, J. Hugues, "Dugong status report and action plans for countries and territories," (UN Environment Programme Early Warning and Assessment Report, 2002).
8. R. Wu, H. Zhang, *Chin. Sci. Technol. Inform.* **22**, 68 (2018).
9. J. Panyawai, A. Prathep, *Aquat. Mamm.* **48**, 203 (2022).
10. H. Marsh, G. De'ath, N. Gribble, B. Lane, *Ecol. Appl.* **15**, 481 (2005).
11. E. D'Souza *et al.*, *PLOS ONE* **10**, 0141224 (2015).
12. A. Preen, *Environ. Manag.* **22**, 173 (1998).

10.1126/science.ade9750

PHOTO: SONGHAI LI

A stranded dugong on Hainan Island, China, in 2008 may have been the last of the country's now functionally extinct population.

RESEARCH

IN *SCIENCE* JOURNALS

Edited by **Michael Funk**

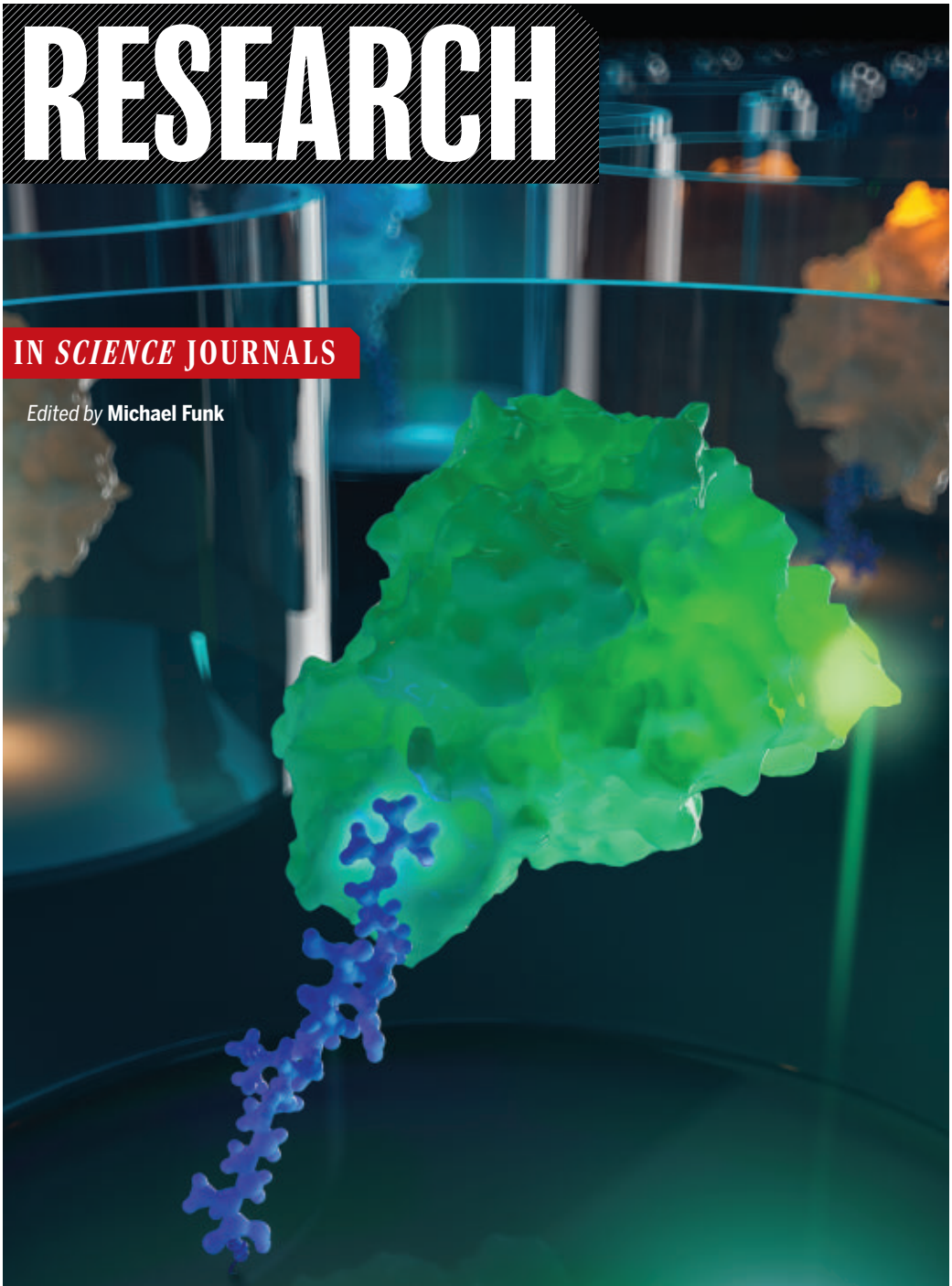

PEPTIDE SEQUENCING

Single-molecule reading of proteins

Modern DNA-sequencing methods can interrogate single molecules in extremely high throughput, but protein sequencing typically uses ensemble techniques and requires larger amounts of relatively pure material. Reed *et al*. generated a set of labeled proteins that recognize the first few amino acids at the N terminus of a peptide immobilized on an optical chip. Transient binding yields spectral signals and association and dissociation rates that can be used to identify the terminal amino acid. Multiple amino acids on a single molecule can then be read by adding a protease that gradually reveals the next amino acid at the terminus. —MAF

Science, abo7651, this issue p. 186

Artist's conception of an array of fluorescently labeled recognizer proteins binding to the end of surface-attached peptides

ILLUSTRATION: QUANTUM-SI, INC. -B

NEUROSCIENCE

Millisecond neural activation tracking

Functional magnetic resonance imaging (fMRI) has made profound contributions to our understanding of the human brain. However, limitations in the temporal and spatial resolution of the underlying signal have prevented this technique from providing information about how cognitive functions emerge from communication between different brain regions. Toi *et al*. developed a method that allows for direct imaging of neuronal activity by fMRI (see the Perspective by van Kerkoerle and Cloos). Retaining the original benefit of high spatial resolution of MRI, the temporal resolution of this method is on the order of milliseconds. Detecting sequential propagation of neuronal activity through functionally defined networks in the brain is thus possible. The ability to image a direct correlate of neuronal spiking is a game changer for noninvasive neuroimaging. —PRS

Science, abh4340, this issue p. 160; see also ade4938, p. 139

THERMAL MANAGEMENT

A one-way street for heat

For most materials, reversing the direction of the thermal gradient does not change the thermal conductivity. The difficulty in finding thermal rectifiers impedes the development of thermal diodes that would be important for managing heat flow. Y. Zhang *et al*. found that a heterostructure made of molybdenum diselenide and tungsten diselenide rectifies both electricity and heat. The magnitude of the effect depends on the relative geometry of the interface and the thermal gradient. The discovery provides the opportunity to develop more effective heat dissipation in highly integrated circuits. —BG

Science, abq0883, this issue p. 169

CELL BIOLOGY

Senescence marker revisited

Searching for cells that express the *p16*^{INK4a} tumor suppressor,

which is often used as a marker of senescence during aging, Reyes *et al*. identified a population of fibroblasts within the stem cell niche in the lungs of young mice. When lung epithelial cells were injured with a toxic compound, they appeared to increase secretion and stimulate airway stem cells to regenerate the epithelium. The findings raise questions about whether all $p16^{INK4a}$-expressing cells are senescent, and if strategies to remove such cells (because senescent cells can be harmful) could interfere with previously unappreciated beneficial effects. —LBR

Science, abf3326, this issue, p. 192

PLANT SCIENCE

Balancing growth and stress responses

A collection of small, sulfated peptides act as growth-promoting hormones in the model plant *Arabidopsis thaliana*. Ogawa-Ohnishi *et al*. characterized the structures of several of these PLANT PEPTIDE CONTAINING SULFATED TYROSINE (PSY) family peptides and identified their receptors among subfamily XI of the *Arabidopsis* leucine-rich repeat receptor kinases (LRR-RKs). These functionally redundant receptors repress plant growth and activate stress-response genes when they are not repressed by their peptide hormone ligands. From this branched signaling point, plant cells deprived of their sustaining signal as they face abiotic or biotic stress can divert resources from growth to stress responses. —PJH

Science, abq5735, this issue p. 175

POLYMERS

A reactive way to make a composite

Blending different materials to form a composite is a way to tune properties to achieve something not possible in a single material. However, it can be challenging to mix or pattern dissimilar materials. Rylski *et al*. developed a way to produce multimaterials by patterning a strong domain within an elastic domain. They used a dual-catalyst system that polymerizes *cis*-polycyclooctene in the dark but forms *trans*-polycyclooctene when exposed to light. This approach led to a polyoctenamer with cohesively connected viscoelastic (soft) and semicrystalline (hard) domains and provided the ability to spatially control the properties of the polymer. —MSL

Science, add6975, this issue p. 211

DEVICES

Ventilators at the ready

There remains a need for easy-to-use ventilators that can be rapidly deployed to provide respiratory support in response to crises or in low-resource environments. Pritchard *et al.* evaluated miniature in-line ventilators in swine models of acute lung injury. The three-dimensional–printed ventilators were designed to use compressed oxygen and to operate in specific pressure ranges, with three models corresponding to mild, moderate, and severe injury. Testing in swine showed that the devices provided adequate support for acute mild and moderate lung injury but were insufficient for severe injury, resulting in elevated respiratory rate and reduced tidal volume. With further optimization and testing, these ventilators could be a simple yet powerful tool. —CC

Sci. Transl. Med. **14**, eabm8351 (2022).

PHOTOTRANSDUCTION

Endocannabinoids light the way

The *Drosophila* eye is a model system for phototransduction. Light exposure of photoreceptors stimulates the generation of signaling lipids that elicit calcium influx through the cation channels TRP and TRPL. Sokabe *et al.* identified the endocannabinoids produced in response to light that activate TRP and TRPL. One of the endocannabinoids also activated the related mammalian channels TRPC5 and TRPC6. These results suggest that a role for endocannabinoids in phototransduction could be evolutionarily conserved. —WW

Sci. Signal. **15**, eabl6179 (2022).

IN OTHER JOURNALS

Edited by **Caroline Ash** *and* **Jesse Smith**

DEVELOPMENT

Making a planthopper fly

In a single population of the brown planthopper, a destructive rice pest in Asia, some juvenile insects mature into long-winged migratory individuals. Long-winged forms disperse seasonally from tropical to subtropical areas, causing severe rice yield losses across Asia. Other individuals mature into relatively sedentary, short-winged forms that invest heavily in reproduction. Crowding, host plant quality, photoperiod, and temperature influence phenotype; however, we still do not know much about how morph fate is decided. Zhang *et al.* identified a zinc finger homeodomain transcription factor called Zfh1 that acts like a molecular switch activating the wing-growing program. Disabling this switch genetically, the authors were able to give juveniles destined to become short-winged a full set of long wings. —DJ *Nat. Commun.* 13, 5670 (2022).

The brown rice planthopper, *Nilaparvata lugens*, is a devastating pest of rice in Asia that has different morphs; a long-winged migratory form is shown.

PHOTO: NIGEL CATTLIN/SCIENCE SOURCE

ECONOMICS

The market for discrimination

Analysis of all nondiscriminatory US hotels, restaurants, and gas stations listed in the *Negro Motorist Green Book* between 1936 and 1966 supports the idea that racial discrimination by businesses, initially a profit-maximizing response to white consumers' preference for discrimination, lessened in

response to the changing racial composition of local consumers. Cook *et al*. integrated data from these travel guides for Black motorists with data on white mortality in World War II and data on Black migration. An increase in the Black population in a community led to slight increases in nondiscriminatory businesses, but market forces alone would have been insufficient to bring about full equal access, which eventually required legal intervention in the form of the Civil Rights Act of 1964. —BW

Q. J. Econ. 10.1093/qje/qjac035 (2022).

PAIN

Lift away the pain

Exercise is often advised to reduce muscle pain in humans. Resistance training is also known to prevent or reverse activity-dependent muscle pain in rodents, but how this works is not well understood. Lesnak *et al*. developed a mouse model of activity-induced muscle hyperalgesia in which the animals showed an elevated sensitivity to pain. Preceding the hyperalgesia-induction protocol with 8 weeks of resistance training prevented the mice from developing pain. Resistance training after the establishment of activity-induced pain also reduced established hyperalgesia. Inhibiting the androgen receptor during resistance training blocked the analgesic effects of resistance training in the mice. —MM

PAIN **163**, 1879 (2022).

INFLAMMATION

Gut disease and bone loss

Inflammatory bowel disease represents a group of disorders marked by chronic inflammation of the gastrointestinal tract. In many individuals, this disease can also affect parts of the body outside of the gut, including the skin, kidneys, liver, and bone. Peek *et al*. investigated the association between systemic inflammation and bone loss using mouse models of gastrointestinal inflammation. The authors found increased numbers of osteoclast precursor cells, the cells that initiate bone "eating" and remodeling, and pro-osteoclastogenic cytokines within the bone. Alterations in cell surface receptors involved in osteoclast function, including the pro-osteoclastogenic co-receptor myeloid DNAX activation protein 12-associating lectin (MDL-1), provided a therapeutic target for monoclonal antibodies. Treating mice with antibodies reduced osteoclast numbers and the bone loss associated with intestinal inflammation. —PNK

Cell Mol. Gastroenterol. Hepatol. **14**, 731 (2022).

MARINE MICROBIOLOGY

Enzymes of the central Pacific Ocean

Marine microbes of the open ocean vary greatly in their metabolic capacity depending on what nutrients are available. Saunders *et al.* conducted a metaproteomic study across 5000 kilometers of the central Pacific Ocean to catalog the various enzymes found from the surface down to a depth of 1250 meters. Consistent with geochemical measurements, proteomic data showed signatures of poor nutrient availability north of the equator and more abundant nutrients, higher productivity, and elevated oxidative stress to the south. Enzymes involved in nitrogen cycling and energy metabolism also exhibited patterns of correlation. —MAF

Proc. Natl. Acad. Sci. U.S.A. **119**, e2200014119 (2022).

HUMAN BEHAVIOR

Vaccine jackpot

During the COVID-19 vaccine rollout in May 2021, scientists and politicians believed that vaccine lotteries (with jackpots of $50,000 USD or more) would motivate more people to get vaccinated, but was this strategy effective? Milkman *et al.* tested it in an experiment in one US city, Philadelphia, as part of a partnership with "Philly Vax Sweepstakes" for adults over age 18. This experiment included 587,508 people across 20 Philadelphia zip codes where an average of one-third of adults received the vaccine. Of the 20 zip codes, 17 acted as control groups, whereas in the other three, adults were given an elevated chance to win the lottery. Only one of three treatment zip codes showed an initial uptick in vaccinations, but this uptake was not sustained. The results indicate that the lottery only promoted a small boost in vaccinations, and only in the zip codes that had had more media coverage of the sweepstakes. —EEU

Nat. Hum. Behav. 10.1038/s41562-022-01437-0 (2022).

QUANTUM SIMULATION

Selectively localizing atoms

Strong correlations between electrons can cause a nominally metallic material to become an insulator through the so-called Mott transition. If the electrons also have another degree of freedom, such as an orbital, then the localization can involve some of the orbitals more than others. This phenomenon has been studied in solids, but simulating it with ultracold atoms would add a degree of control not present in solid-state physics. Tusi *et al.* used interacting ^{173}Yb atoms in a mixture of three nuclear-spin states that played the role of orbitals. Starting with equal numbers of atoms in each state and introducing coupling between two of the three states, the researchers achieved selective localization. —JS

Nat. Phys. 10.1038/s41567-022-01726-5 (2022).

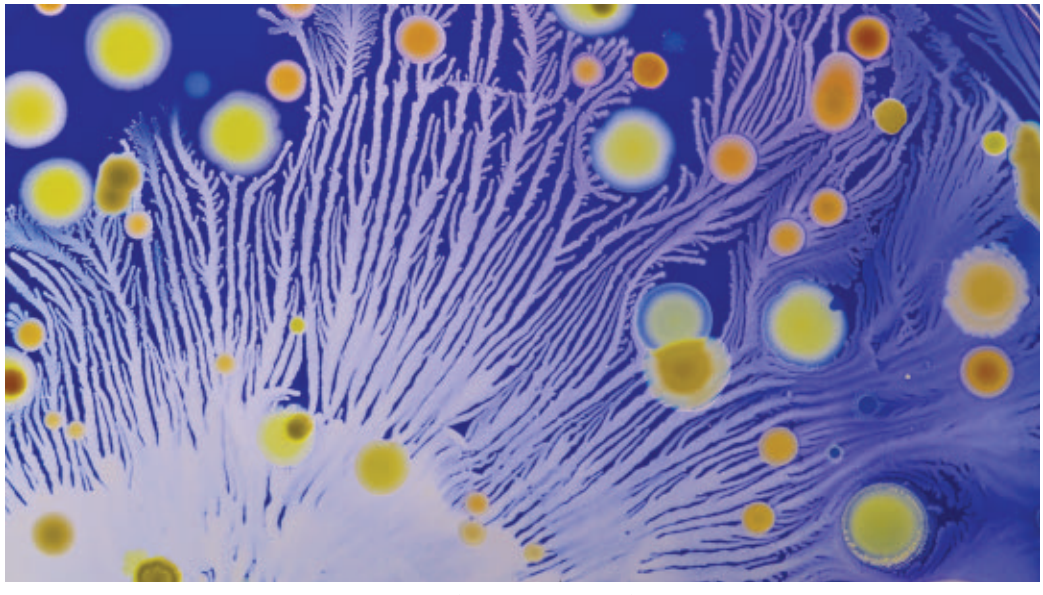

PHOTO: CHARLOTTE RAYMOND/SCIENCE SOURCE

Marine microbes, such as the bacteria Actinomycetes (pictured in a culture), produce the bulk of the enzymatic proteins that act as biological catalysts in the oceans.

ALSO IN *SCIENCE* JOURNALS

Edited by **Michael Funk**

CELLULAR BARCODING

Tracing cell lineages during disease

Cellular barcoding techniques have been widely used to study developmental biology, and now they are being used to study human diseases, helping us gain unanticipated insights into disease mechanisms. In a review, Sankaran *et al*. provide an overview of current cellular barcoding approaches. They describe applications in clonality analysis and lineage tracing in human hematopoiesis and cancer and discuss potential future applications. —SMH

Science, abm5874, this issue p. 152

MEDICINE

Pig organ transplants

Recent research has demonstrated the potential for xenotransplants of organs from pigs to humans, which could address the demand for organ replacement. In a Perspective, Sykes discusses the progress in our understanding of how to effectively and safely transplant pig organs into nonhuman primates. The first pig-to-human transplants have revealed the promise of this approach, as well as the challenges that still need to be overcome. One issue is ensuring that pigs have the necessary alterations to reduce rejection in humans and that they are free from viruses that could infect hosts. The author argues that, although research still needs to be performed in model systems, trials of this potentially life-saving therapy should also continue in humans. —GKA

Science, abo7935, this issue p. 135

MICROBIOLOGY

How a pathogen inhibits pyroptosis

Pyroptosis is a proinflammatory form of programmed cell death adopted by mammalian hosts to control infections, but how pathogens evade this immune response remains largely unexplored. Chai *et al*. found that PtpB, a known protein phosphatase secreted by *Mycobacterium tuberculosis*, acts as a phospholipid phosphatase that dephosphorylates host plasma membrane phosphoinositides upon activation by ubiquitin to inhibit pyroptosis. These findings reveal a delicate strategy by which pathogens suppress pyroptosis by altering host membrane composition, and provide a potential tuberculosis treatment by targeting the PtpB-ubiquitin interacting interface. —SMH

Science, abq0132, this issue p. 153

ION CHANNELS

Chilly reception

The sensation of cold stimuli in mammals is mediated by transient receptor potential melastatin 8 (TRPM8) channels that also respond to various chemicals (think of the frosty feel of menthol). The molecular basis for channel activation by cooling agonists has not been clear, in part because prior efforts have used suboptimal agonists or avian channels that cannot be fully opened during structural experiments. Using a combination of cooling agents that does not induce desensitization, Yin *et al*. determined cryo–electron microscopy structures of the mouse channel in an open state, revealing changes in the pore and gate that are consistent with ion conduction and are supported by electrophysiology and molecular dynamics experiments. The lipid phosphotidylinositol 4,5-bisphosphate plays an important role in sensitizing the channel, revealed in part by closed and intermediate states with one or both agonists absent. —MAF

Science, add1268, this issue p. 154

ENZYME EVOLUTION

Origins of Rubisco's small subunit sidekick

Maintaining the correct activity, specificity, and stability is a challenge faced by metabolic enzymes that is often solved by forming multimeric complexes. The large, catalytic subunit of form I Rubisco, the carbon-fixing enzyme found in aerobic photosynthetic organisms such as plants and cyanobacteria and in some nonphotosynthetic bacteria, makes such a complex with an essential small subunit. Using ancestral sequence reconstruction, Schulz *et al*. investigated how recruiting this small subunit contributed to Rubisco evolution and, in particular, its specificity for carbon dioxide (see the Perspective by Sharwood). Enzyme activity assays and macromolecular structures revealed that the small subunit quickly became essential and opened the door to broader functional changes within the large subunit, including increased activity and specificity for carbon dioxide. —MAF

Science, abq1416, this issue p. 155; see also ade6522, p. 137

FUEL CELLS

Helping fuel cells breathe

In proton exchange membrane fuel cells, the Nafion ionomer usually overencapsulates and inhibits the platinum catalyst and can impede gas transport in the catalyst layer. Q. Zhang *et al*. showed that adding a sulfonated covalent organic framework (COF) to Nafion could improve the activity based on platinum by up to 60% (see the Perspective by Ma and Lutkenhaus). The hexagonal pores of the COF improve gas transport, and the sulfonic acid groups anchored on the pore walls decrease binding to platinum, which inhibits its activity. —PDS

Science, abm6304, this issue p. 181; see also ade8092, p. 138

ELECTRON HOLOGRAPHY

Visualizing metal nanoparticle charging

Charging of metal nanoparticles supported on metal oxides can occur during catalytic reactions and can be measured as an average charge with x-ray photoemission spectroscopy or as anomalies in surface potential with scanning probe microscopy. Aso *et al*. used ultra-high-precision electron holography to directly identify the charge state of single platinum nanoparticles supported on a titanium dioxide crystal (see the Perspective by Gao and Terasaki). A phase-shift analysis visualized slight changes that resulted from charging around the parts of the platinum nanoparticle that extended out from the surface into the vacuum. A platinum nanoparticle could gain or lose one to six electron charges depending on the nanoparticle structure (lattice strain) or its orientation on the titanium dioxide support. —PDS

Science, abq5868, this issue p. 202; see also ade6051, p. 133

PLASTIC WASTE

Funneling mixed waste with microbes

Current plastic recycling methods require sorting by chemical composition, a method that is expensive and results in products that are of lower quality and value than the starting plastic. If plastic waste could instead be converted to valuable chemical intermediates, then economical use of mixed waste as a feedstock might be feasible. Sullivan *et al*. developed a two-stage oxidation and biological funneling approach that can break down and reform mixtures of common consumer plastics (see the Perspective by Yan). The end products can be adjusted by metabolic engineering of the microbes in the second step, which should enable tailored

conversion into various platform or specialty chemicals. —MAF

Science, abo4626, this issue p. 207; see also ade5658, p. 132

AUTOIMMUNITY

Engineering CAR T cells to target autoimmunity

Autoimmune diseases, including multiple sclerosis (MS), are driven by pathogenic $CD4^+$ T cells that recognize self-antigens. Yi *et al.* engineered chimeric antigen receptor (CAR) T cells to recognize and kill self-reactive T cells by introducing a peptide–major histocompatibility complex class II (pMHCII) domain. Their original pMHCII-CAR design efficiently deleted T cells bearing a higher-affinity T cell receptor, whereas further modifications to enhance pMHCII stability and in vivo survival enabled simultaneous targeting of lower-affinity T cells. In a mouse experimental autoimmune encephalomyelitis model of MS-like disease, deletion of higher-affinity T cells was sufficient to prevent disease onset, whereas targeting lower-affinity T cells was necessary to reverse ongoing disease. These findings highlight potential strategies for designing CAR T cells to target distinct stages of autoimmune diseases. —CO

Sci. Immunol. **7**, eabo0777 (2022).

REVIEW SUMMARY

CELLULAR BARCODING

Cellular barcoding to decipher clonal dynamics in disease

Vijay G. Sankaran*, Jonathan S. Weissman*, Leonard I. Zon*

BACKGROUND: Cellular barcodes are nucleic acid sequences that enable cells to be tracked across space and time. These barcodes can occur naturally in cells within the nuclear or mitochondrial genomes. Alternatively, they can also be synthetically introduced into cells through engineering approaches applied in model systems. These barcodes can allow clones to be followed while also enabling the opportunity for lineage tracing, with which cellular genealogies can be deduced. Cellular barcoding may occur at a single time point, and fate mapping can then be performed on those clones that are marked. Alternatively, newer barcoding approaches allow for tracking of each division with evolution of barcodes over time. Medicine has traditionally lacked clonal precision to enable most diagnostic and therapeutic decisions.

ADVANCES: Advances in the ability to detect natural barcodes at single-cell resolution with measurements of the cell state, as well as advances in applying synthetic barcodes in model systems, provide the opportunity to gain insights into the cellular hierarchies composing a range of healthy and diseased tissues. Such maps can lead to an improved understanding of how altered clonal contributions in tissues can give rise to disease or could enable earlier detection of disease. We discuss specific applications that have led to an improved understanding of blood cell production and cancer pathogenesis. The contributions of stem and progenitor cells to production of specific blood cell lineages have been refined through the use of barcoding approaches. In the context of cancer models, distinct subclonal contributions to malignancies and pathways to clonal evolution have become evident through the use of cellular barcoding. Clonal expansions may not only be important in the context of cancer, in which the role of specific malignant clones has been well established, but also appear across a range of other tissues, even in the absence of malignancy. Tissues where this has been reported include the blood, skin, bronchial epithelium, bladder, endometrium, prostate, colon, liver, pancreas, and brain. These expansions may contribute to disease predisposition or pathogenesis in some circumstances. In most instances, this somatic mosaicism has only been characterized at the bulk level, and a greater extent of clonal complexity may become apparent with the increasing use of single-cell genomic methods. In some instances, these clonal expansions may be a response to disease, as is evident in some inflammatory disorders in which the emergence of resistant clones occurs. The opportunity to use the latest cellular barcoding approaches could improve our understanding of how these clonal expansions contribute to disease while also identifying opportunities for early diagnosis or therapeutic intervention based on this information.

OUTLOOK: A number of further technological developments could enable broader use and application of cellular barcodes beyond lineage tracing. For example, molecular recording of specific cell state transitions or other historical events that a cell experiences could be recorded with barcodes to provide a higher-resolution view of cell dynamics in health and disease. This could include not only information about the lineage history and genealogies of a cell but also past transcriptional states of a cell, as well as other events that may occur to a cell, such as viral infections. With further improvements for detecting natural or synthetic barcodes in diseased tissues or model systems, along with multimodal measurements of cell state at single-cell resolution, an improved understanding of how human disease arises will emerge. These insights may reveal how our current understanding of clonal contributions in disease is overly simplistic and may necessitate refinement of existing models of disease pathogenesis. Opportunities for therapeutic intervention may arise from this higher-resolution lens on disease. For example, some diseases may have precursor states with altered clonal contributions to a tissue, which would enable earlier detection of disease and potential prevention. The broader application of these approaches to a range of biomedical fields will likely catalyze advances across diverse areas, much in the way that cancer and blood research have already seen advances through the application of cellular barcoding. ■

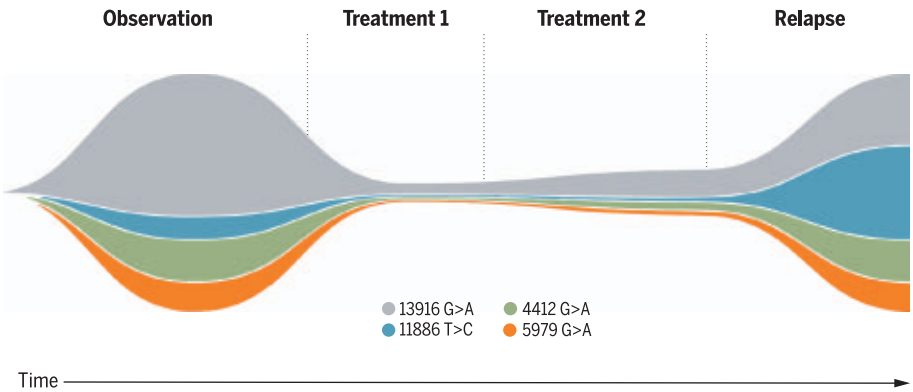

An image depicting how clonal tracking can help resolve distinct subclones in the context of cancer progression, which illustrates the value of cellular barcoding for therapeutic purposes. This example depicts a group of mitochondrial DNA mutation–based cellular barcodes marking distinctly colored subclones and is adapted from data of an actual patient followed over the course of their treatment for chronic lymphocytic leukemia. During treatment, bottlenecks to clonal contributions emerge and alter the subclonal composition of the malignancy.

The list of author affiliations is available in the full article online.
*Corresponding author. Email: sankaran@broadinstitute.org (V.G.S.); weissman@wi.mit.edu (J.S.W.); zon@enders.tch.harvard.edu (L.I.Z.)
Cite this article as V. G. Sankaran *et al.*, *Science* **378**, eabm5874 (2022). DOI: 10.1126/science.abm5874

REVIEW

CELLULAR BARCODING

Cellular barcoding to decipher clonal dynamics in disease

Vijay G. Sankaran[1,2,3,4]*, Jonathan S. Weissman[5,6,7,8]*, Leonard I. Zon[1,2,3,4,6,9,10]*

Cellular barcodes are distinct DNA sequences that enable one to track specific cells across time or space. Recent advances in our ability to detect natural or synthetic cellular barcodes, paired with single-cell readouts of cell state, have markedly increased our knowledge of clonal dynamics and genealogies of the cells that compose a variety of tissues and organs. These advances hold promise to redefine our view of human disease. Here, we provide an overview of cellular barcoding approaches, discuss applications to gain new insights into disease mechanisms, and provide an outlook on future applications. We discuss unanticipated insights gained through barcoding in studies of cancer and blood cell production and describe how barcoding can be applied to a growing array of medical fields, particularly with the increasing recognition of clonal contributions in human diseases.

Tracing back the origins of tissues and organs has long been a fascination of developmental biologists and more recently has become an important component of medicine. Historically, lineage tracing has involved coating with or injection of dyes to follow cells as they contribute to embryos. In the modern era, techniques involving recombinases that drive fluorescent colors have elucidated precise populations of cells that give rise to their differentiated progeny. Recently, the next version of tracing cell origins has involved cellular barcoding, a technique that uses distinct DNA sequences to mark each cell and to follow the process of differentiation or self-renewal. Coupling this DNA marking with single-cell profiling technologies to measure gene expression or epigenetic marks has generated rich datasets that define the lineage tree and cell state of each differentiated cell in a tissue. Medicine has traditionally lacked the precision of lineage tracing to inform patient decisions. Even excellent animal models of disease could only examine populations of cells and tell which tissues are formed from a group of cells. Recently, cellular barcoding technologies have begun to provide the medical and biotechnology communities tools for enabling the reconstruction of high-resolution lineage trees and their application to clinically relevant questions.

Two medical fields have already begun leveraging the insights of cellular barcoding studies: cancer and blood formation. For the oncologist, the concept of clones of cancer cells having distinct behaviors for tumor initiation, therapy resistance, and metastasis may help with treatment design (*1*). Currently, somatically acquired cancer driver mutations are used as a proxy for clonality (*2*, *3*), the number of cells that participate in tissue growth. However, multiple clones and subclones can arise with the exact same oncogenic mutation, making it difficult to identify the "offending" clones. Now, cellular barcoding can examine a cancer, find the DNA barcode for many cells of the tumor, draw lineage trees to find the cell of origin, calculate the timing of that origin, examine growth rates of clones, and evaluate the transcriptional and chromatin state of each cell. Cellular barcoding has also been extensively applied to hematopoiesis, the process by which blood cells are made. The use of barcoding has begun to refine our understanding of the relative contributions of blood stem cells and progenitors to the maintenance of blood and immune cell production at steady state and under various stresses (*4*–*8*). Using barcoding to follow these stem cells and progenitors to examine the onset of blood cancers, such as myelodysplastic syndrome and leukemia, becomes possible (*9*–*11*). By combining lineage trees with gene expression or other functional readouts (*12*, *13*), informed decisions can be made about when to treat patients and which drugs to give them. For example, therapy-resistant clones may harbor different expression signatures that separate them from the majority of cells in a tumor. Understanding such heterogeneity in cell states and behavior could lead to improved and more targeted therapeutic approaches.

In this Review, we provide a brief overview of cellular barcoding approaches that either take advantage of engineering in model systems or rely on the detection of naturally occurring somatic DNA changes, we discuss medical insights that have emerged from cellular barcoding studies, and we provide an outlook on further advances that will affect this field.

Cellular barcoding: An overview of technology and approaches

Barcoding techniques can determine the genealogy of related cells, providing a critical tool for exploring the phylogenetic principles of biological processes such as metazoan development, cancer progression and metastasis, and hematopoiesis (*14*–*16*). Historically, these efforts have often been categorized as "prospective" lineage tracing strategies, which involve labeling of individual cells (for example, with synthetic DNA sequence barcodes or fluorescent markers) and then following their descendants. Alternatively, "retrospective" lineage tracing strategies have been used and involve sequencing natural DNA variations that occur during the life of an organism (for example, single-nucleotide polymorphisms, copy-number variants, or short tandem repeats) (*17*, *18*). Whereas prospective approaches can be used to study clonal dynamics in model systems (for example, the clonal progeny of a given cell type), retrospective approaches are particularly valuable for studying subclonal dynamics in patient-derived samples, such as elucidating which mutations contribute to tumor metastasis and when they occur (Fig. 1) (*19*–*22*). The resolution of such approaches has been limited by technical challenges, including sample heterogeneity (*23*, *24*) and the slow rate and disperse nature of naturally occurring mutations. These technical limitations are now being mitigated by using single-cell resolution measurements or whole-genome sequencing (*25*–*28*).

A key recent advance in retrospective lineage tracing has been the use of naturally occurring mutations of the mitochondrial genomes as an evolving barcode (*11*, *29*). Critically, it is possible to exploit the high level of mitochondrial DNA, which is a natural byproduct of single-cell chromatin accessibility "ATAC-seq" (assay for transposase-accessible chromatin with high-throughput sequencing) approaches, to monitor the accumulation of mitochondrial mutations at single-cell resolution. This, together with the much more rapid (10- to 100-fold) rate of accumulation of mutations in the mitochondrial versus nuclear genomes, makes it possible to follow far more cells than is possible by using single-cell analysis of nuclear genome mutations.

[1]Division of Hematology and Oncology, Boston Children's Hospital, Harvard Medical School, Boston, MA 02115, USA. [2]Department of Pediatric Oncology, Dana-Farber Cancer Institute, Harvard Medical School, Boston, MA 02115, USA. [3]Broad Institute of MIT and Harvard, Cambridge, MA 02142, USA. [4]Harvard Stem Cell Institute, Cambridge, MA 02138, USA. [5]Whitehead Institute for Biomedical Research, Massachusetts Institute of Technology, Cambridge, MA 02142, USA. [6]Howard Hughes Medical Institute, Chevy Chase, MD 20815, USA. [7]David H. Koch Institute for Integrative Cancer Research, Massachusetts Institute of Technology, Cambridge, MA 02142, USA. [8]Department of Biology, Massachusetts Institute of Technology, Cambridge, MA 02142, USA. [9]Stem Cell Program, Boston Children's Hospital, Harvard Medical School, Boston, MA 02115, USA. [10]Harvard Department of Stem Cell and Regenerative Biology, Harvard University, Cambridge, MA 02138, USA. ***Corresponding author. Email: sankaran@broadinstitute.org (V.G.S.); weissman@wi.mit.edu (J.S.W.); zon@enders.tch.harvard.edu (L.I.Z.)**

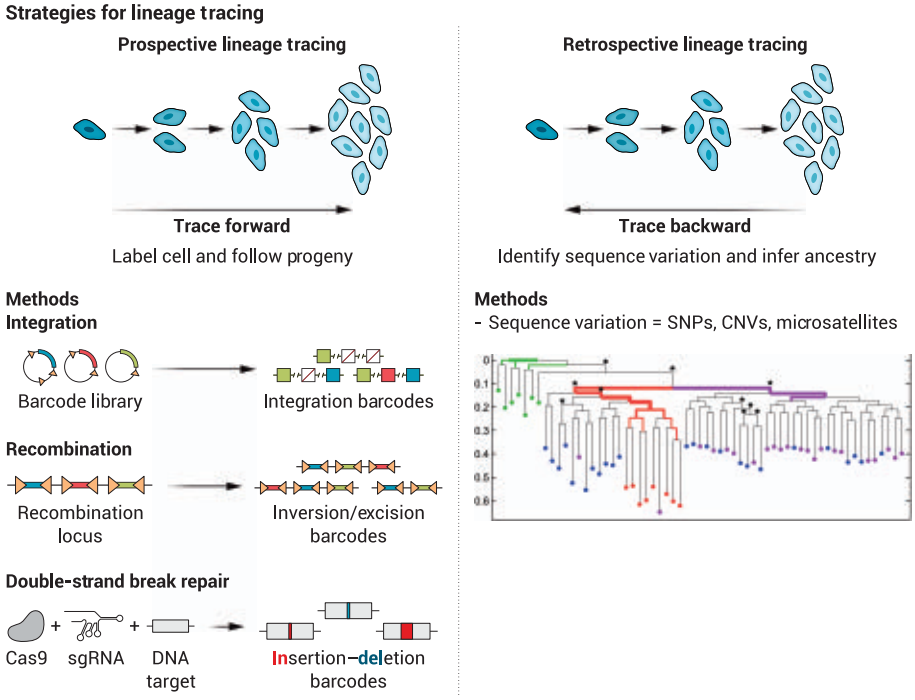

Fig. 1. An overview of strategies for lineage tracing. (**Left**) Some strategies for prospective lineage tracing. These approaches rely on engineered barcodes that are introduced through integration of the barcode into DNA, recombination of modified alleles that can evolve over time, or genome editing–mediated scar formation that can either occur at a single time point or evolve over time. This enables all the descendants of a particular marked cell to be tracked. (**Right**) The concept of retrospective lineage tracing, which uses the detection of natural barcodes in cells (such as single-nucleotide variants or other types of mutations) to track back and generate phylogenetic relationships between different cells. Such approaches can be made even more powerful by combining this barcoding with measurements of the cell state at single-cell resolution.

This approach allows for cellular barcoding of human cells without having to create a synthetic barcoding system and has been applied already to clonal tracking in human cancers. The current methods for mitochondrial DNA analyses are limited by the difficulty in accurately detecting mutations, particularly rarer variants, and by the challenges in linking the cell lineages with a detailed description of the cellular state (such as transcriptional or epigenomic states) (*30*, *31*).

Some of the earliest contributions to the use of cellular barcodes encoded in DNA started with the classic analysis of hematopoietic stem cell clones after retroviral marking, which took advantage of each clone harboring a distinct retroviral insertion site in the genome (*32*). Such approaches have been advanced further more recently and provided an initial approach to assess the behavior of stem and progenitor cell populations (*33*, *34*). These methods have even been applied to infer clonal dynamics after lentiviral gene therapy, providing key insights into clonal contributions to blood and immune reconstitution in these clinical settings (*35*). But these strategies also have limitations because they rely on a barcode being introduced at only a single time point upon retroviral insertion into the genome and cannot undergo further modification. These static barcodes can track clones but fail to provide further information as clones evolve.

The recent development of Cas9-enabled lineage tracing techniques with single-cell RNA readouts (*36*–*39*) provides the potential to explore phylogenetic relationships in cancer progression and normal development at a vastly larger scale and finer resolution than was previously possible with methods involving static barcodes or fluorescent markers (*33*, *40*–*45*). These newer methods most commonly rely on similar technical principles [reviewed in (*15*, *16*)]. Briefly, Cas9 targets and cuts a defined, synthetic genomic locus introduced into a cell type of interest (“scratch pad” or “target site”), resulting in a stable insertion-deletion (indel) allele that is inherited over subsequent generations. As cells divide, they accrue more Cas9-induced indels at additional sites that further distinguish successive clades of cells (Fig. 2) (*46*). At the end of the lineage tracing experiment, the indel alleles are collected from each individual cell by means of single-cell sequencing. Lineage information can be paired with single-cell gene expression profiles or other measures of the cell state to relate the phylogenetic history of a cell with its present state. Then, as in retrospective tracing approaches, various computational approaches (*47*, *48*) can reconstruct a phylogenetic tree that best models subclonal cellular relationships (such as by maximum parsimony) from the observed alleles, although this remains a challenging problem for complex trees (*49*–*52*). By progressively introducing indel “scars” into the genomes of living cells by use of CRISPR-Cas9, it is possible to record in vivo and reconstruct high-depth lineage trees over months-long time scales that detail cellular parentage with single-cell resolution. Moreover, by pairing lineage information with the transcriptional state, it is possible to relate the phylogenetic history of a cell with its present state. Thus far, Cas9-enabled tracing has been successfully applied to study important aspects of metazoan biology, such as the cellular progenitor landscape in early mammalian embryogenesis (*37*, *53*) and neural development in zebrafish (*36*, *54*); the rates, routes, and drivers of tumor metastases (*55*); and the evolution of a tumor from initial acquisition of oncogenic mutations to formation of an aggressive and ultimately metastatic cancer (*56*).

Beyond simple barcoding information, the DNA scratch pad approach can in principle be used to develop multichannel molecular recorders that record critical information about the history of the cell [for example, the states a cell has passed through, whether a cell has been infected with a virus, or a cell’s three-dimensional (3D) environment]. Critically, such records can be made in an animal under normal physiological conditions or in disease states. Along this line, a number of strategies have been devised for recording in DNA scratch pads past transcriptional states of the cell (*57*, *58*), including clever approaches that allow for recording the temporal order in which such cellular transcriptional programs occur (*59*, *60*). As such approaches advance further, it will be interesting to assess to what extent past changes in cell state (such as the gene expression of a precursor) may contribute to alterations in lineage contributions in more differentiated cells (*61*). When such linkages are made, questions about how more recent cell states relate to earlier cell states can be addressed.

A key goal for lineage tracing efforts is to reconstruct the complete 3D cell fate map of a developing mammalian embryo analogous to the seminal studies of *Caenorbhabditis elegans* (*62*). In principle, the Cas9 DNA scratch pad approaches have the capacity to specifically mark every cell even in a complex animal such as a mouse. Moreover, current droplet-based (such as Chromium X) and split pool [such as Sci and SHARE-seq (simultaneous high-throughput ATAC and RNA expression with sequencing)] single-cell approaches now make it

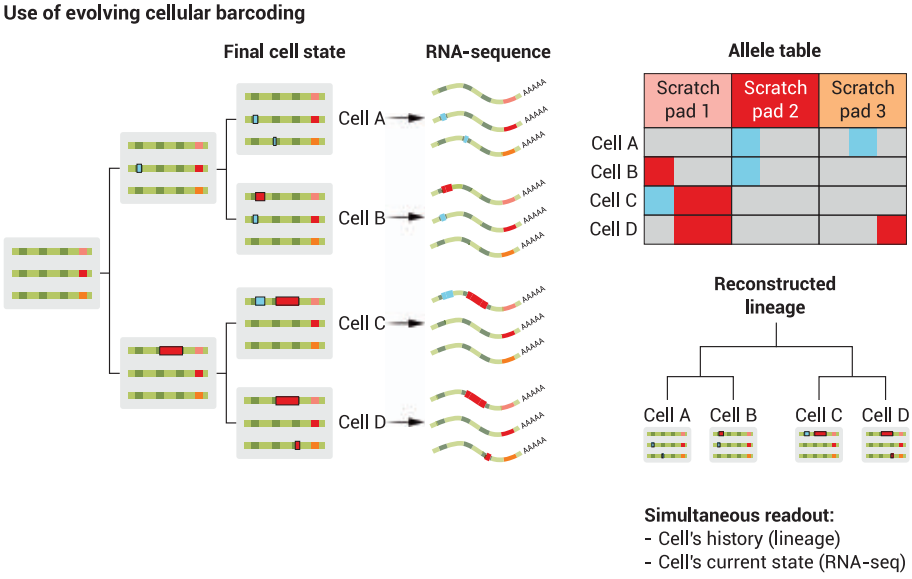

Fig. 2. A simplified example of the use and value of evolving cellular barcoding. Advances in cell barcoding now enable the use of evolving barcodes. In the simplified example shown, there are three independent integrated barcode regions that can each be modified at every cell division (for example, through genome editing–mediated scar formation). The combination of these different barcodes allows cellular hierarchies to be reconstructed. At the same time, other measurements of cell state can be obtained (such as the transcriptome or epigenome), providing rich information into the evolution of tissues in healthy and disease states.

possible to routinely analyze millions of cells. However, the spatial information relating these cells is lost when using these approaches. Advances in spatial transcriptomic approaches may circumvent this problem, but achieving true single-cell resolution or preserving the spatial interactions between cells is currently not possible (*63*, *64*). Parallel efforts by use of microscopy-based approaches hold great promise for simultaneous profiling of single-cell lineage and high-dimensional cellular information. For example, in the MEMOIR (memory by engineered mutagenesis with optical in situ readout) approach, information recorded in the DNA scratch pads is read out through microscopy by using fluorescent in situ hybridization (FISH), making it possible to visualize cell lineage relationships directly within their native tissue context (*65*, *66*). However, the nature of DNA alterations that can be readily assayed by using current microscopy-based lineage tracing modalities limits the resolution of reconstructed trees and the time scales over which lineages can be recorded relative to what has been achieved with Cas9-based lineage tracing systems. In addition, FISH can currently only assess relatively small tissue sections, which limits applications.

Opportunities to gain insights into disease through barcoding

Cellular barcoding may have a major use in disease detection and prevention. Lineage has been brought to the forefront of medicine with the discovery that mutations occur in humans with clonal hematopoiesis during aging. Aging is also associated with *TP53* mutant clones that lead to eyelid wrinkles (*67*), esophageal clones with *NOTCH* mutations (*68*), and colon clonal expansions (DNA mutations induced by a bacterial protein) (*69*, *70*). Such changes are a natural process in aging, but the clonal expansions can predispose to disease. Following such expanding clones with cellular barcoding would allow for disease monitoring and could lead to earlier treatments with surgery or chemotherapy. Consider the current care of Barrett's esophagus, which has a prevalence of 1.6% in the United States (*71*). Patients are followed with repeat biopsies to detect cancer, but currently, there are no lineage trees to predict the "offending" clones that could occur years before. Cellular barcoding would give the physician a precise detail of the activity of clones that lead to disease. Similarly, clonal hematopoiesis has been shown to be an inflammatory condition and associated with cardiovascular events (*72*). There is interest in diagnosing clones of cells that promote inflammation to be able to give individuals therapies that prevent the cardiovascular manifestations by identifying synthetic lethal vulnerabilities in the expanded clones. Other human disorders can be probed by using cellular barcoding. Somatic mosaicism accounts for substantial symptomatology. It is estimated that 2 to 3% of all Down syndrome cases are mosaic (*73*). Following patients by means of barcoding could establish genotypes associated with clone expansion that leads to pathophysiology.

Given that altered clonal architecture may underlie the etiology of a number of human diseases, there are emerging opportunities to study this process more deeply with both natural and synthetic barcoding to enable a higher-resolution view of disease pathology. Perhaps the clearest opportunity to apply such approaches is in the study of cancers, which are characterized by clonal evolutionary processes driven by both genetic and epigenetic alterations (*74*–*76*). Naturally occurring somatic mutations have been used for retrospective phylogenetic inference of the clonal dynamics in cancers (*77*, *78*). Although many of the somatic mutations that have been used in such studies may be drivers of the malignancy (*79*), some somatic changes—including passenger single-nucleotide variants, copy number alterations, and mitochondrial DNA mutations—have shown value as innocuous cell barcodes by which to reconstruct cancer clonal hierarchies (*11*, *80*, *81*). Such retrospective analyses have elucidated subclonal genetic and epigenetic alterations, factors contributing to metastatic spread of these diseases, and drivers of therapy resistance. Coupling such analyses with insights into transcriptional or epigenetic states has provided valuable insights into the drivers of clonal diversity, as exemplified by studies of human gliomas, leukemias, and cell lines that illuminate nongenetic drivers of clonal evolution and dominance (*13*, *82*, *83*).

Although the study of natural mutations has improved our knowledge of cancer evolution, many aspects of this process remain poorly understood and are challenging to validate experimentally beyond the observed associations. This has motivated the use of cell barcoding in tractable cancer model systems. Recent studies that used static barcoding of cancer cells have revealed how there can be substantial clonal diversity driven by nongenetic mechanisms that underlie properties observed in these cell populations, including subclonal therapy resistance and dominance (*13*, *41*, *84*). These findings highlight the potential insights that will likely emerge through studies of primary cancers with higher-resolution assessment of natural variants concomitant with cell state measurements, particularly if used over a span of time. In addition, the use of evolving engineered barcodes is providing a refined view of the clonal dynamics in disease, including in studies that have introduced these barcodes into cancer cell lines that are then transplanted into mice to track variable behavior in vivo (*55*, *85*, *86*) or through the use of engineered faithful cancer mouse models (*56*). For example, the use of evolving barcodes in a lung cancer mouse model has revealed how perturbation of additional tumor suppressors, including *Lkb1* or *Apc*, can accelerate clonal evolution through distinct

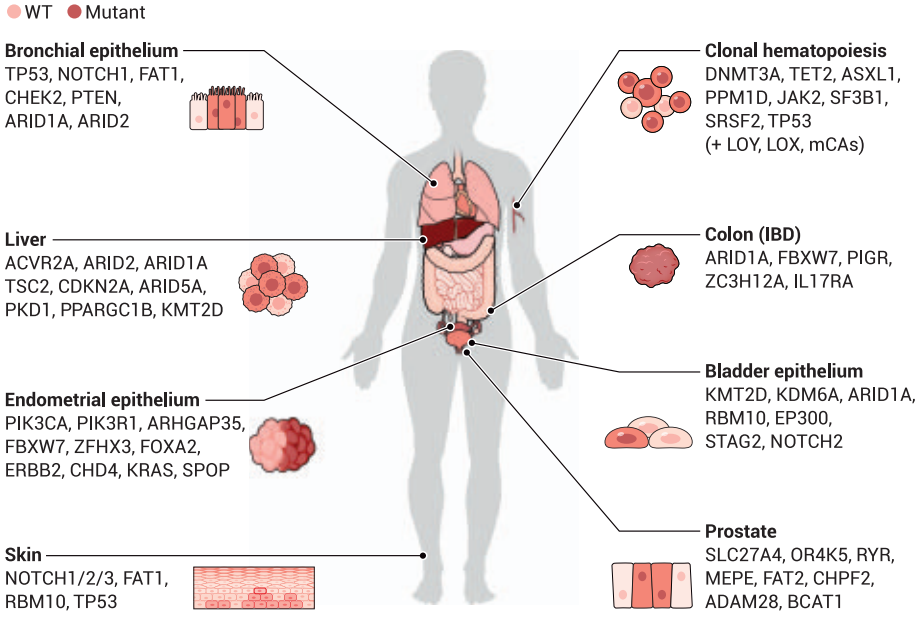

Fig. 3. Nonmalignant clonal expansions can be found across a range of human tissues and organs. A variety of human tissues and organs, including those highlighted here, have been shown to have age-related clonal expansions that are often driven by somatic mutations found in cancer. Examples of the affected tissues and some genes frequently mutated in these expansions are highlighted. The majority of these studies have relied on the use of bulk sequencing approaches, and with improved resolution of barcoding approaches, the implications of such clonal dynamics and its impact on disease will likely become clearer. IBD, inflammatory bowel disease.

evolutionary mechanisms compared with what is seen in the absence of these perturbations (*56*).

Although the applications of cell barcoding in cancer have been in many ways a natural progression in a field that has been thinking about clonal evolution for decades (*75*), genome sequencing is providing clues on how clonal dynamics may have a broader scope of implications across a range of human tissues, even in conditions that are conventionally thought to be nonmalignant (*87*). For example, as individuals age, the hematopoietic system can be dominated by specific clones harboring somatic driver mutations that overlap with what is observed in blood cancers—a condition that is termed clonal hematopoiesis of indeterminate potential (CHIP) (*72*, *88*). Although CHIP can predispose to acquisition of blood cancers, most individuals do not undergo such transformation. These observations have largely emerged from detection of somatic driver mutations in bulk populations of cells, but assessment of such mutations at the resolution of single cells will likely provide further critical insights into this process and how often such events can occur, as well as variation in properties between distinct clones (*28*). Cell barcoding in such states may also reveal cooperating pathways that are required to achieve clonal outgrowth, as illuminated through a recent study revealing how zebrafish *asxl1* mutations that promote clonal hematopoiesis require resistance to inflammatory pathways to achieve clonal dominance (*89*). Interestingly, CHIP has been linked to a variety of age-related conditions beyond the risk for acquiring blood cancers, and higher-resolution studies of this process may provide an improved understanding of the mechanisms through which these risks emerge (*90*–*94*).

Clonal growths in nonmalignant states are not only a feature of the hematopoietic system, in which the measures of such states have been facilitated through the frequent sampling of blood, but also appear in a variety of other tissues (Fig. 3). Somatic driver mutations found in cancer have been identified in nonmalignant samples from the skin (*95*), bronchial epithelium (*96*), bladder (*97*), endometrium (*98*), prostate (*99*), colon (*69*), liver (*100*, *101*), pancreas (*102*), and brain (*103*). In some cases, the expansion of such clones can be promoted in diseased states such as inflammatory bowel disease for the colon (*104*) or cirrhosis for the liver (*100*, *101*). The precise risk of disease conferred by these clonal populations requires further study across this diverse group of tissues. Critically, such clonal populations that harbor somatic mutations may not always predispose to acquisition of a malignancy, and in some instances, these clonal expansions could prevent the outgrowth of malignant clones, as shown in the context of mouse models in the esophageal epithelium (*105*). Such findings may also be relevant in clinical scenarios, as suggested by individuals who have clonal hematopoiesis that involves *DNMT3A* mutations being less likely to have a disease relapse after blood stem cell transplantation (*106*). Further studies of these observations are needed to fully understand the mechanisms underlying the reduced risk of relapse.

Although somatic driver mutations can promote clonal outgrowths that are readily measured in bulk, single-cell monitoring of natural or synthetic barcodes provides an opportunity to gain a higher-resolution view of clonal dynamics that may contribute both to normal development and to disease predisposition. As our understanding of developmental processes continues to expand (*25*, *27*, *107*), we are learning more about how mosaic mutations acquired early during development could contribute to a range of human diseases, including cancer predisposition (*108*) and neurodevelopmental disorders (*109*). Even in normal development in zebrafish, there appear to be examples of limited clonal contributions, as exemplified by studies of early heart development (*110*). However, in some ways this may only be the tip of the iceberg for understanding clonal contributions to development and disease. Although the somatic mutations detected may be drivers of or confer predisposition to disease, they could also serve as markers of clonality, and variation in this process itself may alter disease risk. For example, a range of estimates for clonal contributions to physiologic processes such as human hematopoiesis suggests that there may be tens to several hundred thousand distinct clones composing this process in healthy individuals (*28*, *111*, *112*). It is possible that a greater number of hematopoietic stem cell clones contribute to increased risks for blood cancers, as suggested through functional follow-up of genetic studies (*113*), or that a reduced amount of such stem cells could predispose to conditions such as aplastic anemia (*114*). Our ability to better detect natural barcodes or to engineer improved disease models with evolving barcodes will facilitate our knowledge of how disease arises and provide a higher-resolution view of this process. Moreover, although specific somatic changes such as T cell receptor rearrangements can facilitate assessment of clonal diversity in immune cell populations, the use of higher-resolution barcodes could enable the tracking of subclonal dynamics, particularly with findings emerging from therapeutic use of such cells (*115*).

Future innovations and application to diseases

There is clearly tremendous promise for cellular barcoding to enable a deeper understanding of human disease. Here, we highlight both technological innovations that will enable further insights as well as potential clinical applications that we envision will come to fruition in the future. There are some limitations of existing cellular barcoding approaches for both

prospective and retrospective lineage tracing. Improvements in barcode detection, cell recovery, and avoidance of allelic dropout will enable higher-fidelity lineage reconstruction, which will be improved with advanced computational approaches that take advantage of the rich set of data generated (*48*, *50*, *51*). Increased throughput, which can be enabled through both droplet-based or split-pool approaches, will enable data to be generated on a greater diversity and larger number of cells and will enable more faithful lineage reconstruction in the context of disease. In particular, a major challenge relates to inferring lineage information from smaller clones that may be more poorly sampled by using existing methods, and with improved detection of barcodes in a greater number of cells, this issue can be overcome. The opportunity to integrate cellular barcodes with further data could illuminate the pathologic mechanisms that underlie disease. This includes the use of multichannel recorders, including those that enable temporal resolution, as well as multimodal analysis of cells (*116*).

We foresee there being two areas in which advances are likely to enable substantial progress. First, the development of spatial genomic analyses can be advanced by integrating barcode detection into these methods, including through adaptation of existing lineage tracing methods in single-cell spatial genomics or through the further development of microscopy-based approaches. This could not only enable insights into clonal hierarchies in disease contexts such as tumors but also enable the determination of how lineage relationships occur in 3D space. Such insights could refine therapeutic approaches, as exemplified by the use of traditional histology for determining tumor margins—an approach that could be improved and made more accurate through spatial genomic analyses. Second, we have focused almost entirely on cellular barcoding to elucidate cellular relationships in either primary disease samples or model systems. However, integration of perturbation approaches along with these cellular barcodes could enable insights into therapeutic targets or pathways that could alter the clonal composition in disease contexts (*117*). For example, if models of premalignant clonal states were analyzed with barcodes, this could enable newer regulators of clonal dominance to more accurately be identified and validated (*89*).

As these approaches advance further and as more data are generated, it is likely that limitations inherent to these approaches will become apparent. For example, the use of mitochondrial DNA mutations as natural cellular barcodes assumes that most mutations would not alter cellular metabolism or differentiation (*11*, *30*). However, studies of specific mutations demonstrate how these variants are selected against in specific immune cell populations, including in T lymphocytes (*118*). As we obtain larger datasets, the impact of markers used as cellular barcodes may reveal that some of these do indeed affect the processes being studied, as has been clearly demonstrated through the study of somatic cancer driver mutations. Although we think that mutation rates may be constant in a cell and depend on cell division rates, recent studies have revealed how conditions such as inflammation can substantially alter the rate of mutation accrual in the nuclear genome (*104*) and have also revealed how nuclear mutations can arise in postmitotic tissues (*119*).

Beyond the technological advances, there are a number of highly promising clinical applications. At the moment, most cellular barcoding approaches are focused on helping to decipher the etiology and progression of disease. However, it may be possible to apply these approaches for prospective diagnostics. For example, if a patient was known to have a predisposition to acquiring cancer or had a premalignant condition, such diagnostics could be applied in a routine clinic visit to enable risk stratification or prediction that could tailor further clinical management on the patient's likelihood of progressing to have a malignancy. Even in ongoing clinical studies, such as experimental gene therapy or genome editing trials, the malignancies observed in patients, such as those with sickle cell disease (*120*, *121*), suggest a critical need to use these approaches both to study the basis for these cancers and to try to predict those patients who might develop such complications. From a therapeutic perspective, understanding subclonal properties of populations contributing to disease may enable the development of targeting approaches based on the concept of synthetic lethality that selectively target those clonal populations (for example, the drivers of clonal expansion may confer specific vulnerabilities to the dominant subclonal population).

The applications of cellular barcoding approaches in clinical medicine are likely to grow considerably, particularly with the increasing use of cellular therapies. For example, although clonal tracking of chimeric antigen receptor (CAR)–T cell clones has been valuable to detect durable persistence of this therapy for more than a decade (*115*), advances in molecular recording in the future could provide insights into the activities of these cellular therapies and enable the development of even more effective and targeted therapies in the future. In the setting of replacement of diseased epidermis by gene-modified cells, cellular barcodes from viral insertion demonstrated the limited contributions to regeneration by a subset of the stem cells introduced, suggesting opportunities for further clinical improvement as a result of insights from barcoding (*122*).

Conclusions

The advances in cellular barcoding in both primary human tissues and model systems offer an unprecedented opportunity to gain new insights into the mechanisms of disease. We have reviewed some advances in our understanding of cancer and hematopoiesis by dissecting the cellular hierarchies involved in these processes. Further applications of these approaches will undoubtedly advance a number of other medical fields, particularly with the growing recognition of clonal contributions in a diverse array of human diseases. Moreover, with further technological innovations, the opportunities to apply these approaches more broadly and prospectively in clinical medicine will continue to blossom. Barcoding provides us with a lens to define how clonal contributions can play a role in and help predict the outcome of disease.

REFERENCES AND NOTES

1. A. Kreso *et al*., Variable clonal repopulation dynamics influence chemotherapy response in colorectal cancer. *Science* **339**, 543–548 (2013). doi: 10.1126/science.1227670; pmid: 23239622
2. L. I. Shlush *et al*., Tracing the origins of relapse in acute myeloid leukaemia to stem cells. *Nature* **547**, 104–108 (2017). doi: 10.1038/nature22993; pmid: 28658204
3. M. Jan *et al*., Clonal evolution of preleukemic hematopoietic stem cells precedes human acute myeloid leukemia. *Sci. Transl. Med.* **4**, 149ra118 (2012). doi: 10.1126/scitranslmed.3004315; pmid: 22932223
4. J. Sun *et al*., Clonal dynamics of native haematopoiesis. *Nature* **514**, 322–327 (2014). doi: 10.1038/nature13824; pmid: 25296256
5. W. Pei *et al*., Resolving fates and single-cell transcriptomes of hematopoietic stem cell clones by PolyloxExpress barcoding. *Cell Stem Cell* **27**, 383–395.e8 (2020). doi: 10.1016/j.stem.2020.07.018; pmid: 32783885
6. J. Carrelha *et al*., Hierarchically related lineage-restricted fates of multipotent haematopoietic stem cells. *Nature* **554**, 106–111 (2018). doi: 10.1038/nature25455; pmid: 29298288
7. A. E. Rodriguez-Fraticelli *et al*., Clonal analysis of lineage fate in native haematopoiesis. *Nature* **553**, 212–216 (2018). doi: 10.1038/nature25168; pmid: 29323290
8. J. Feng *et al*., Clonal lineage tracing reveals shared origin of conventional and plasmacytoid dendritic cells. *Immunity* **55**, 405–422.e11 (2022). doi: 10.1016/j.immuni.2022.01.016; pmid: 35180378
9. D. Van Egeren *et al*., Reconstructing the lineage histories and differentiation trajectories of individual cancer cells in myeloproliferative neoplasms. *Cell Stem Cell* **28**, 514–523.e9 (2021). doi: 10.1016/j.stem.2021.02.001; pmid: 33621486
10. N. Williams *et al*., Life histories of myeloproliferative neoplasms inferred from phylogenies. *Nature* **602**, 162–168 (2022). doi: 10.1038/s41586-021-04312-6; pmid: 35058638
11. L. S. Ludwig *et al*., Lineage tracing in humans enabled by mitochondrial mutations and single-cell genomics. *Cell* **176**, 1325–1339.e22 (2019). doi: 10.1016/j.cell.2019.01.022; pmid: 30827679
12. C. Umkehrer *et al*., Isolating live cell clones from barcoded populations using CRISPRa-inducible reporters. *Nat. Biotechnol.* **39**, 174–178 (2021). doi: 10.1038/s41587-020-0614-0; pmid: 32719478
13. K. A. Fennell *et al*., Non-genetic determinants of malignant clonal fitness at single-cell resolution. *Nature* **601**, 125–131 (2022). doi: 10.1038/s41586-021-04206-7; pmid: 34880496
14. T. Stadler, O. G. Pybus, M. P. H. Stumpf, Phylodynamics for cell biologists. *Science* **371**, eaah6266 (2021). doi: 10.1126/science.aah6266; pmid: 33446527
15. D. E. Wagner, A. M. Klein, Lineage tracing meets single-cell omics: Opportunities and challenges. *Nat. Rev. Genet.* **21**, 410–427 (2020). doi: 10.1038/s41576-020-0223-2; pmid: 32235876

16. S. VanHorn, S. A. Morris, Next-generation lineage tracing and fate mapping to interrogate development. *Dev. Cell* **56**, 7–21 (2021). doi: 10.1016/j.devcel.2020.10.021; pmid: 33217333
17. S. S. Wu, J.-H. Lee, B.-K. Koo, Lineage tracing: Computational reconstruction goes beyond the limit of imaging. *Mol. Cells* **42**, 104–112 (2019). pmid: 30764600
18. L. Tao *et al*., Retrospective cell lineage reconstruction in humans by using short tandem repeats. *Cell Rep Methods* **1**, 100054 (2021). doi: 10.1016/j.crmeth.2021.100054; pmid: 34341783
19. M. Jamal-Hanjani *et al*., Tracking genomic cancer evolution for precision medicine: The lung TRACERx study. *PLOS Biol.* **12**, e1001906 (2014). doi: 10.1371/journal.pbio.1001906; pmid: 25003521
20. Z. Hu *et al*., Quantitative evidence for early metastatic seeding in colorectal cancer. *Nat. Genet.* **51**, 1113–1122 (2019). doi: 10.1038/s41588-019-0423-x; pmid: 31209394
21. M. Gerlinger *et al*., Intratumor heterogeneity and branched evolution revealed by multiregion sequencing. *N. Engl. J. Med.* **366**, 883–892 (2012). doi: 10.1056/NEJMoa1113205; pmid: 22397650
22. D. J. H. Shih *et al*., Genomic characterization of human brain metastases identifies drivers of metastatic lung adenocarcinoma. *Nat. Genet.* **52**, 371–377 (2020). doi: 10.1038/s41588-020-0592-7; pmid: 32203465
23. W. S. Hong, M. Shpak, J. P. Townsend, Inferring the origin of metastases from cancer phylogenies. *Cancer Res.* **75**, 4021–4025 (2015). doi: 10.1158/0008-5472.CAN-15-1889; pmid: 26260528
24. S. Turajlic, C. Swanton, Metastasis as an evolutionary process. *Science* **352**, 169–175 (2016). doi: 10.1126/science.aaf2784; pmid: 27124450
25. S. Park *et al*., Clonal dynamics in early human embryogenesis inferred from somatic mutation. *Nature* **597**, 393–397 (2021). doi: 10.1038/s41586-021-03786-8; pmid: 34433967
26. M. Spencer Chapman *et al*., Lineage tracing of human development through somatic mutations. *Nature* **595**, 85–90 (2021). doi: 10.1038/s41586-021-03548-6; pmid: 33981037
27. T. H. H. Coorens *et al*., Extensive phylogenies of human development inferred from somatic mutations. *Nature* **597**, 387–392 (2021). doi: 10.1038/s41586-021-03790-y; pmid: 34433963
28. E. Mitchell *et al*., Clonal dynamics of haematopoiesis across the human lifespan. *Nature* **606**, 343–350 (2022). doi: 10.1038/s41586-022-04786-y; pmid: 35650442
29. J. Xu *et al*., Single-cell lineage tracing by endogenous mutations enriched in transposase accessible mitochondrial DNA. *eLife* **8**, e45105 (2019). doi: 10.7554/eLife.45105; pmid: 30958261
30. C. A. Lareau *et al*., Massively parallel single-cell mitochondrial DNA genotyping and chromatin profiling. *Nat. Biotechnol.* **39**, 451–461 (2021). doi: 10.1038/s41587-020-0645-6; pmid: 32788668
31. T. E. Miller *et al*., Mitochondrial variant enrichment from high-throughput single-cell RNA sequencing resolves clonal populations. *Nat. Biotechnol.* **40**, 1030–1034 (2022). doi: 10.1038/s41587-022-01210-8; pmid: 35210612
32. I. R. Lemischka, D. H. Raulet, R. C. Mulligan, Developmental potential and dynamic behavior of hematopoietic stem cells. *Cell* **45**, 917–927 (1986). doi: 10.1016/0092-8674(86)90566-0; pmid: 2871944
33. R. Lu, N. F. Neff, S. R. Quake, I. L. Weissman, Tracking single hematopoietic stem cells in vivo using high-throughput sequencing in conjunction with viral genetic barcoding. *Nat. Biotechnol.* **29**, 928–933 (2011). doi: 10.1038/nbt.1977; pmid: 21964413
34. R. Lu, A. Czechowicz, J. Seita, D. Jiang, I. L. Weissman, Clonal-level lineage commitment pathways of hematopoietic stem cells in vivo. *Proc. Natl. Acad. Sci. U.S.A.* **116**, 1447–1456 (2019). doi: 10.1073/pnas.1801480116; pmid: 30622181
35. L. Biasco *et al*., In vivo tracking of human hematopoiesis reveals patterns of clonal dynamics during early and steady-state reconstitution phases. *Cell Stem Cell* **19**, 107–119 (2016). doi: 10.1016/j.stem.2016.04.016; pmid: 27237736
36. B. Raj *et al*., Simultaneous single-cell profiling of lineages and cell types in the vertebrate brain. *Nat. Biotechnol.* **36**, 442–450 (2018). doi: 10.1038/nbt.4103; pmid: 29608178
37. M. M. Chan *et al*., Molecular recording of mammalian embryogenesis. *Nature* **570**, 77–82 (2019). doi: 10.1038/s41586-019-1184-5; pmid: 31086336
38. A. Alemany, M. Florescu, C. S. Baron, J. Peterson-Maduro, A. van Oudenaarden, Whole-organism clone tracing using single-cell sequencing. *Nature* **556**, 108–112 (2018). doi: 10.1038/nature25969; pmid: 29590089
39. B. Spanjaard *et al*., Simultaneous lineage tracing and cell-type identification using CRISPR-Cas9-induced genetic scars. *Nat. Biotechnol.* **36**, 469–473 (2018). doi: 10.1038/nbt.4124; pmid: 29644996
40. S. H. Naik *et al*., Diverse and heritable lineage imprinting of early haematopoietic progenitors. *Nature* **496**, 229–232 (2013). doi: 10.1038/nature12013; pmid: 23552896
41. Y. Oren *et al*., Cycling cancer persister cells arise from lineages with distinct programs. *Nature* **596**, 576–582 (2021). doi: 10.1038/s41586-021-03796-6; pmid: 34381210
42. B. A. Biddy *et al*., Single-cell mapping of lineage and identity in direct reprogramming. *Nature* **564**, 219–224 (2018). ; doi: 10.1038/s41586-018-0744-4; pmid: 30518857
43. C. Weinreb, A. Rodriguez-Fraticelli, F. D. Camargo, A. M. Klein, Lineage tracing on transcriptional landscapes links state to fate during differentiation. *Science* **367**, eaaw3381 (2020). doi: 10.1126/science.aaw3381; pmid: 31974159
44. J. Livet *et al*., Transgenic strategies for combinatorial expression of fluorescent proteins in the nervous system. *Nature* **450**, 56–62 (2007). doi: 10.1038/nature06293; pmid: 17972876
45. H. J. Snippert *et al*., Intestinal crypt homeostasis results from neutral competition between symmetrically dividing Lgr5 stem cells. *Cell* **143**, 134–144 (2010). doi: 10.1016/j.cell.2010.09.016; pmid: 20887898
46. A. McKenna *et al*., Whole-organism lineage tracing by combinatorial and cumulative genome editing. *Science* **353**, aaf7907 (2016). doi: 10.1126/science.aaf7907; pmid: 27229144
47. H. Zafar, C. Lin, Z. Bar-Joseph, Single-cell lineage tracing by integrating CRISPR-Cas9 mutations with transcriptomic data. *Nat. Commun.* **11**, 3055 (2020). doi: 10.1038/s41467-020-16821-5; pmid: 32546686
48. M. G. Jones *et al*., Inference of single-cell phylogenies from lineage tracing data using Cassiopeia. *Genome Biol.* **21**, 92 (2020). doi: 10.1186/s13059-020-02000-8; pmid: 32290857
49. I. Salvador-Martínez, M. Grillo, M. Averof, M. J. Telford, Is it possible to reconstruct an accurate cell lineage using CRISPR recorders? *eLife* **8**, e40292 (2019). doi: 10.7554/eLife.40292; pmid: 30688650
50. N. Konno *et al*., Deep distributed computing to reconstruct extremely large lineage trees. *Nat. Biotechnol.* **40**, 566–575 (2022). doi: 10.1038/s41587-021-01111-2; pmid: 34992246
51. S.-W. Wang, M. J. Herriges, K. Hurley, D. N. Kotton, A. M. Klein, CoSpar identifies early cell fate biases from single-cell transcriptomic and lineage information. *Nat. Biotechnol.* **40**, 1066–1074 (2022). doi: 10.1038/s41587-022-01209-1; pmid: 35190690
52. W. Kong *et al*., Capybara: A computational tool to measure cell identity and fate transitions. *Cell Stem Cell* **29**, 635–649. e11 (2022). doi: 10.1016/j.stem.2022.03.001; pmid: 35354062
53. R. Kalhor *et al*., Developmental barcoding of whole mouse via homing CRISPR. *Science* **361**, eaat9804 (2018). doi: 10.1126/science.aat9804; pmid: 30093604
54. B. Raj *et al*., Emergence of neuronal diversity during vertebrate brain development. *Neuron* **108**, 1058–1074.e6 (2020). doi: 10.1016/j.neuron.2020.09.023; pmid: 33068532
55. J. J. Quinn *et al*., Single-cell lineages reveal the rates, routes, and drivers of metastasis in cancer xenografts. *Science* **371**, eabc1944 (2021). doi: 10.1126/science.abc1944; pmid: 33479121
56. D. Yang *et al*., Lineage tracing reveals the phylodynamics, plasticity, and paths of tumor evolution. *Cell* **185**, 1905–1923. e25 (2022). doi: 10.1016/j.cell.2022.04.015; pmid: 35523183
57. W. Tang, D. R. Liu, Rewritable multi-event analog recording in bacterial and mammalian cells. *Science* **360**, eaap8992 (2018). doi: 10.1126/science.aap8992; pmid: 29449507
58. R. U. Sheth, H. H. Wang, DNA-based memory devices for recording cellular events. *Nat. Rev. Genet.* **19**, 718–732 (2018). doi: 10.1038/s41576-018-0052-8; pmid: 30237447
59. T. B. Loveless *et al*., Lineage tracing and analog recording in mammalian cells by single-site DNA writing. *Nat. Chem. Biol.* **17**, 739–747 (2021). doi: 10.1038/s41589-021-00769-8; pmid: 33753928
60. J. Choi *et al*., A time-resolved, multi-symbol molecular recorder via sequential genome editing. *Nature* **608**, 98–107 (2022). doi: 10.1038/s41586-022-04922-8; pmid: 35794474
61. J. S. Packer *et al*., A lineage-resolved molecular atlas of *C. elegans* embryogenesis at single-cell resolution. *Science* **365**, eaax1971 (2019). doi: 10.1126/science.aax1971; pmid: 31488706
62. J. E. Sulston, E. Schierenberg, J. G. White, J. N. Thomson, The embryonic cell lineage of the nematode *Caenorhabditis elegans*. *Dev. Biol.* **100**, 64–119 (1983). doi: 10.1016/0012-1606(83)90201-4; pmid: 6684600
63. A. Rao, D. Barkley, G. S. França, I. Yanai, Exploring tissue architecture using spatial transcriptomics. *Nature* **596**, 211–220 (2021). doi: 10.1038/s41586-021-03634-9; pmid: 34381231
64. S. R. Srivatsan *et al*., Embryo-scale, single-cell spatial transcriptomics. *Science* **373**, 111–117 (2021). doi: 10.1126/science.abb9536; pmid: 34210887
65. K. L. Frieda *et al*., Synthetic recording and in situ readout of lineage information in single cells. *Nature* **541**, 107–111 (2017). doi: 10.1038/nature20777; pmid: 27869821
66. K. K. Chow *et al*., Imaging cell lineage with a synthetic digital recording system. *Science* **372**, eabb3099 (2021). doi: 10.1126/science.abb3099; pmid: 33833095
67. A. S. Jonason *et al*., Frequent clones of p53-mutated keratinocytes in normal human skin. *Proc. Natl. Acad. Sci. U.S.A.* **93**, 14025–14029 (1996). doi: 10.1073/pnas.93.24.14025; pmid: 8943054
68. M. P. Alcolea *et al*., Differentiation imbalance in single oesophageal progenitor cells causes clonal immortalization and field change. *Nat. Cell Biol.* **16**, 615–622 (2014). doi: 10.1038/ncb2963; pmid: 24814514
69. H. Lee-Six *et al*., The landscape of somatic mutation in normal colorectal epithelial cells. *Nature* **574**, 532–537 (2019). doi: 10.1038/s41586-019-1672-7; pmid: 31645730
70. C. Pleguezuelos-Manzano *et al*., Mutational signature in colorectal cancer caused by genotoxic pks$^+$ E. coli. *Nature* **580**, 269–273 (2020). doi: 10.1038/s41586-020-2080-8; pmid: 32106218
71. E. W. Gilbert, R. A. Luna, V. L. Harrison, J. G. Hunter, Barrett's esophagus: A review of the literature. *J. Gastrointest. Surg.* **15**, 708–718 (2011). doi: 10.1007/s11605-011-1485-y; pmid: 21461873
72. A. G. Bick *et al*., Inherited causes of clonal haematopoiesis in 97,691 whole genomes. *Nature* **586**, 763–768 (2020). doi: 10.1038/s41586-020-2819-2; pmid: 33057201
73. M. Shin, C. Siffel, A. Correa, Survival of children with mosaic Down syndrome. *Am. J. Med. Genet. A.* **152A**, 800–801 (2010). doi: 10.1002/ajmg.a.33295; pmid: 20186777
74. J.-C. Marine, S.-J. Dawson, M. A. Dawson, Non-genetic mechanisms of therapeutic resistance in cancer. *Nat. Rev. Cancer* **20**, 743–756 (2020). doi: 10.1038/s41568-020-00302-4; pmid: 33033407
75. P. C. Nowell, The clonal evolution of tumor cell populations. *Science* **194**, 23–28 (1976). doi: 10.1126/science.959840; pmid: 959840
76. T. Prieto, D. A. Landau, A heritable, non-genetic road to cancer evolution. *Nature* **601**, 31–32 (2022). doi: 10.1038/d41586-021-03606-z; pmid: 34880486
77. J. Nangalia, P. J. Campbell, Genome sequencing during a patient's journey through cancer. *N. Engl. J. Med.* **381**, 2145–2156 (2019). doi: 10.1056/NEJMra1910138; pmid: 31774959
78. I. Cortés-Ciriano, D. C. Gulhan, J. J.-K. Lee, G. E. M. Melloni, P. J. Park, Computational analysis of cancer genome sequencing data. *Nat. Rev. Genet.* **23**, 298–314 (2022). doi: 10.1038/s41576-021-00431-y; pmid: 34880424
79. M. Gerstung *et al*., The evolutionary history of 2,658 cancers. *Nature* **578**, 122–128 (2020). doi: 10.1038/s41586-019-1907-7; pmid: 32025013
80. R. Gao *et al*., Delineating copy number and clonal substructure in human tumors from single-cell transcriptomes. *Nat. Biotechnol.* **39**, 599–608 (2021). doi: 10.1038/s41587-020-00795-2; pmid: 33462507
81. R. Schwartz, A. A. Schäffer, The evolution of tumour phylogenetics: Principles and practice. *Nat. Rev. Genet.* **18**, 213–229 (2017). doi: 10.1038/nrg.2016.170; pmid: 28190876
82. R. Chaligne *et al*., Epigenetic encoding, heritability and plasticity of glioma transcriptional cell states. *Nat. Genet.* **53**, 1469–1479 (2021). doi: 10.1038/s41588-021-00927-7; pmid: 34594037
83. S. M. Shaffer *et al*., Memory Sequencing Reveals Heritable Single-Cell Gene Expression Programs Associated with Distinct Cellular Behaviors. *Cell* **182**, 947–959.e17 (2020). doi: 10.1016/j.cell.2020.07.003; pmid: 32735851
84. Y. Goyal, I. P. Dardani, G. T. Busch, B. Emert, D. Fingerman, A. Kaur, N. Jain, I. A. Mellis, J. Li, K. Kiani, M. E. Fane, A. T. Weeraratna, M. Herlyn, A. Raj, Pre-determined diversity in resistant fates emerges from homogenous cells after

anti-cancer drug treatment. bioRxiv 471833 [Preprint] (2021). doi: 10.1101/2021.12.08.471833
85. W. Zhang *et al*., The bone microenvironment invigorates metastatic seeds for further dissemination. *Cell* **184**, 2471–2486.e20 (2021). doi: 10.1016/j.cell.2021.03.011; pmid: 33878291
86. K. P. Simeonov *et al*., Single-cell lineage tracing of metastatic cancer reveals selection of hybrid EMT states. *Cancer Cell* **39**, 1150–1162.e9 (2021). doi: 10.1016/j.ccell.2021.05.005; pmid: 34115987
87. S. Mustjoki, N. S. Young, Somatic mutations in "benign" disease. *N. Engl. J. Med.* **384**, 2039–2052 (2021). doi: 10.1056/NEJMra2101920; pmid: 34042390
88. S. Jaiswal, B. L. Ebert, Clonal hematopoiesis in human aging and disease. *Science* **366**, eaan4673 (2019). doi: 10.1126/science.aan4673; pmid: 31672865
89. S. Avagyan *et al*., Resistance to inflammation underlies enhanced fitness in clonal hematopoiesis. *Science* **374**, 768–772 (2021). doi: 10.1126/science.aba9304; pmid: 34735227
90. S. Jaiswal *et al*., Clonal hematopoiesis and risk of atherosclerotic cardiovascular disease. *N. Engl. J. Med.* **377**, 111–121 (2017). doi: 10.1056/NEJMoa1701719; pmid: 28636844
91. P. G. Miller *et al*., Association of clonal hematopoiesis with chronic obstructive pulmonary disease. *Blood* **139**, 357–368 (2022). doi: 10.1182/blood.2021013531; pmid: 34855941
92. P. G. Kim *et al*., Dnmt3a-mutated clonal hematopoiesis promotes osteoporosis. *J. Exp. Med.* **218**, e20211872 (2021). doi: 10.1084/jem.20211872; pmid: 34698806
93. S. M. Zekavat *et al*, Hematopoietic mosaic chromosomal alterations increase the risk for diverse types of infection. *Nat. Med.* **27**, 1012–1024 (2021). doi: 10.1038/s41591-021-01371-0; pmid: 34099924
94. K. L. Bolton *et al*., Clonal hematopoiesis is associated with risk of severe Covid-19. *Nat. Commun.* **12**, 5975 (2021). doi: 10.1038/s41467-021-26138-6; pmid: 34645798
95. I. Martincorena *et al*., Tumor evolution. High burden and pervasive positive selection of somatic mutations in normal human skin. *Science* **348**, 880–886 (2015). doi: 10.1126/science.aaa6806; pmid: 25999502
96. K. Yoshida *et al*., Tobacco smoking and somatic mutations in human bronchial epithelium. *Nature* **578**, 266–272 (2020). doi: 10.1038/s41586-020-1961-1; pmid: 31996850
97. A. R. J. Lawson *et al*., Extensive heterogeneity in somatic mutation and selection in the human bladder. *Science*; **370**, 75–82 (2020). doi: 10.1126/science.aba8347; pmid: 33004514
98. L. Moore *et al*., The mutational landscape of normal human endometrial epithelium. *Nature* **580**, 640–646 (2020). doi: 10.1038/s41586-020-2214-z; pmid: 32350471
99. C. S. Cooper *et al*., Analysis of the genetic phylogeny of multifocal prostate cancer identifies multiple independent clonal expansions in neoplastic and morphologically normal prostate tissue. *Nat. Genet.* **47**, 367–372 (2015). doi: 10.1038/ng.3221; pmid: 25730763
100. S. F. Brunner *et al*., Somatic mutations and clonal dynamics in healthy and cirrhotic human liver. *Nature* **574**, 538–542 (2019). doi: 10.1038/s41586-019-1670-9; pmid: 31645727
101. M. Zhu *et al*., Somatic mutations increase hepatic clonal fitness and regeneration in chronic liver disease. *Cell* **177**, 608–621.e12 (2019). doi: 10.1016/j.cell.2019.03.026; pmid: 30955891
102. M. Enge *et al*., Single-cell analysis of human pancreas reveals transcriptional signatures of aging and somatic mutation patterns. *Cell* **171**, 321–330.e14 (2017). doi: 10.1016/j.cell.2017.09.004; pmid: 28965763
103. J. Ganz *et al*., Rates and patterns of clonal oncogenic mutations in the normal human brain. *Cancer Discov.* **12**, 172–185 (2022). doi: 10.1158/2159-8290.CD-21-0245; pmid: 34389641
104. S. Olafsson *et al*., Somatic evolution in non-neoplastic IBD-affected colon. *Cell* **182**, 672–684.e11 (2020). doi: 10.1016/j.cell.2020.06.036; pmid: 32697969
105. B. Colom *et al*., Mutant clones in normal epithelium outcompete and eliminate emerging tumours. *Nature* **598**, 510–514 (2021). doi: 10.1038/s41586-021-03965-7; pmid: 34646013
106. C. J. Gibson *et al*., Donor clonal hematopoiesis and recipient outcomes after transplantation. *J. Clin. Oncol.* **40**, 189–201 (2022). doi: 10.1200/JCO.21.02286; pmid: 34793200
107. R. Li *et al*., A body map of somatic mutagenesis in morphologically normal human tissues. *Nature* **597**, 398–403 (2021). doi: 10.1038/s41586-021-03836-1; pmid: 34433965
108. F. Pareja *et al*., Cancer-causative mutations occurring in early embryogenesis. *Cancer Discov.* **12**, 949–957 (2022). doi: 10.1158/2159-8290.CD-21-1110; pmid: 34949653
109. S. Bizzotto, C. A. Walsh, Genetic mosaicism in the human brain: From lineage tracing to neuropsychiatric disorders. *Nat. Rev. Neurosci.* **23**, 275–286 (2022). doi: 10.1038/s41583-022-00572-x; pmid: 35322263
110. V. Gupta, K. D. Poss, Clonally dominant cardiomyocytes direct heart morphogenesis. *Nature* **484**, 479–484 (2012). doi: 10.1038/nature11045; pmid: 22538609
111. L. A. Liggett, V. G. Sankaran, Unraveling hematopoiesis through the lens of genomics. *Cell* **182**, 1384–1400 (2020). doi: 10.1016/j.cell.2020.08.030; pmid: 32946781
112. H. Lee-Six *et al*., Population dynamics of normal human blood inferred from somatic mutations. *Nature* **561**, 473–478 (2018). doi: 10.1038/s41586-018-0497-0; pmid: 30185910
113. E. L. Bao *et al*., Inherited myeloproliferative neoplasm risk affects haematopoietic stem cells. *Nature* **586**, 769–775 (2020). doi: 10.1038/s41586-020-2786-7; pmid: 33057200
114. N. S. Young, Aplastic anemia. *N. Engl. J. Med.* **379**, 1643–1656 (2018). doi: 10.1056/NEJMra1413485; pmid: 30354958
115. J. J. Melenhorst *et al*., Decade-long leukaemia remissions with persistence of CD4$^+$ CAR T cells. *Nature* **602**, 503–509 (2022). doi: 10.1038/s41586-021-04390-6; pmid: 35110735
116. A. S. Nam, R. Chaligne, D. A. Landau, Integrating genetic and non-genetic determinants of cancer evolution by single-cell multi-omics. *Nat. Rev. Genet.* **22**, 3–18 (2021). doi: 10.1038/s41576-020-0265-5; pmid: 32807900
117. L. Tian *et al*., Clonal multi-omics reveals Bcor as a negative regulator of emergency dendritic cell development. *Immunity* **54**, 1338–1351.e9 (2021). doi: 10.1016/j.immuni.2021.03.012; pmid: 33862015
118. M. A. Walker *et al*., Purifying selection against pathogenic mitochondrial DNA in human T cells. *N. Engl. J. Med.* **383**, 1556–1563 (2020). doi: 10.1056/NEJMoa2001265; pmid: 32786181
119. F. Abascal *et al*., Somatic mutation landscapes at single-molecule resolution. *Nature* **593**, 405–410 (2021). doi: 10.1038/s41586-021-03477-4; pmid: 33911282
120. L. A. Liggett *et al*., Clonal hematopoiesis in sickle cell disease. *J. Clin. Invest.* **132**, e156060 (2022). doi: 10.1172/JCI156060; pmid: 34990411
121. J. Kaiser, Gene therapy trials for sickle cell disease halted after two patients develop cancer. *Science* (2021). doi: 10.1126/science.abh1106
122. T. Hirsch *et al*., Regeneration of the entire human epidermis using transgenic stem cells. *Nature* **551**, 327–332 (2017). doi: 10.1038/nature24487; pmid: 29144448

ACKNOWLEDGMENTS

We thank members of the Sankaran, Weissman, and Zon laboratories, particularly C. Weng, J. D. Martin-Rufino, L. A. Liggett, L. Koblan, C. Baron, J. Henninger, and S. Avagyan, as well as A. Schier and C. Trapnell, for valuable comments and advice on this work. **Funding:** The work in V.G.S.'s laboratory is supported by the New York Stem Cell Foundation (NYSCF), a gift from the Lodish Family, the Edward P. Evans Foundation, the MPN Research Foundation, and National Institute of Health (NIH) grants R01 DK103794, R01 CA265726, and R01 HL146500. J.S.W.'s laboratory is supported by NIH grants 1RM1 HG009490-01 and 1U01 CA217882-01, the Milkyway Research Foundation, the Jameel Clinic at MIT, and the Ludwig Institute for Cancer Research. L.I.Z.'s laboratory is supported by NIH grants P01HL131477, P01HL032262, U54DK110805, R24DK092760, R24OD017870, U01 HL134812, and R01HL144780-01; the Edward P. Evans Foundation; and the Alex's Lemonade Stand Fund. V.G.S. is a NYSCF-Robertson Investigator. J.S.W. and L.I.Z. are investigators of the Howard Hughes Medical Institute. **Competing Interests:** V.G.S. declares outside interest in Branch Biosciences, Ensoma, Novartis, Forma, Sana Biotechnology, and Cellarity. J.S.W. declares outside interest in 5 AM Ventures, Amgen, Chroma Medicine, KSQ Therapeutics, Maze Therapeutics, Tenaya Therapeutics, and Tessera Therapeutics. L.I.Z. declares outside interest in Branch Biosciences, Fate Therapeutics, CAMP4Therapeutics, and Scholar Rock.

Submitted 19 April 2022; accepted 26 August 2022
10.1126/science.abm5874

RESEARCH ARTICLE SUMMARY

MICROBIOLOGY

A bacterial phospholipid phosphatase inhibits host pyroptosis by hijacking ubiquitin

Qiyao Chai†, Shanshan Yu†, Yanzhao Zhong†, Zhe Lu, Changgen Qiu, Yang Yu, Xinwen Zhang, Yong Zhang, Zehui Lei, Lihua Qiang, Bing-Xi Li, Yu Pang, Xiao-Bo Qiu*, Jing Wang*, Cui Hua Liu*

INTRODUCTION: Pyroptosis is a proinflammatory form of programmed cell death characterized by membrane pore formation that allows the release of intracellular inflammatory mediators, a process that is elicited by the inflammasome-mediated cleavage and activation of gasdermin D (GSDMD). Growing evidence supports a critical role for pyroptosis in the control of infections by mammalian hosts, but how pathogens evade this immune response remains largely unexplored.

RATIONALE: *Mycobacterium tuberculosis* (Mtb), an ancient pathogen that causes tuberculosis (TB), has developed numerous intracellular survival strategies to evade host immunity and to drive the occurrence and development of TB. One notable feature evolved by Mtb is a set of eukaryotic-like effectors, but their host targets and regulatory roles in pathogen–host interactions remain largely unclear. In this study, we sought to identify the key pathogenic regulators of inflammasome-pyroptosis pathways from Mtb eukaryotic-like effectors, information that could improve our understanding of TB pathogenesis and provide potential targets for novel anti-TB treatment.

RESULTS: We examined the whole genome of Mtb to predict its secreted eukaryotic-like proteins possessing eukaryotic-like motifs or domains that might target host factors directly. These Mtb effector proteins were then subjected to further experimental analyses using an inflammasome reconstitution system for screening inhibitors of inflammasome-pyroptosis pathways. Out of 201 predicted Mtb-secreted eukaryotic proteins, six Mtb proteins (Rv0153c, Rv0561c, Rv0824c, Rv0861c, Rv1515c, and Rv1679) exhibited strong inhibitory effects on both NOD-like receptor protein 3 (NLRP3) and absent in melanoma 2 (AIM2) inflammasome pathways. Among these proteins, PtpB (i.e., Rv0153c) was most abundantly secreted by Mtb during infection. We thus focused on PtpB and further confirmed its inhibitory effect on AIM2 or NLRP3 inflammasome-mediated interleukin-1β (IL-1β) secretion. Subsequent experiments demonstrated that PtpB inhibited gasdermin D (GSDMD)–dependent cytokine release and pyroptosis to promote Mtb intracellular survival in macrophages. Mechanistically, Mtb-secreted PtpB could target and dephosphorylate host plasma membrane phosphatidylinositol-4-monophosphate (PI4P) and phosphatidylinositol-(4,5)-bisphosphate [PI(4,5)P_2] to inhibit the membrane localization of the N-terminal cleavage fragment of GSDMD (GSDMD-N), thus preventing GSDMD-mediated immune responses. This phosphoinositide phosphatase activity requires binding of PtpB to ubiquitin. Accordingly, disrupting phospholipid phosphatase activity or the unusual ubiquitin-interacting motif (UIM)–like domain of PtpB markedly enhanced host innate immune responses and reduced intracellular pathogen survival in mice in a GSDMD-dependent manner.

CONCLUSION: We demonstrate that GSDMD-mediated pyroptosis and inflammatory cytokine release play a critical role in host anti-infection immunity, which is counteracted by Mtb effector protein PtpB. Our data reveal a role of the pathogen-derived phospholipid phosphatase in the regulation of GSDMD-dependent pyroptosis and cytokine releases, extending our understanding of the elaborate regulatory mechanism of cellular inflammasome-pyroptosis signaling pathways during pathogen infection. The present study also presents a strategy by which pathogens hijack ubiquitin to inhibit host pyroptosis by altering the phospholipid composition of the host membrane. Our discovery of the PtpB UIM-like domain, which is not homologous to any human protein, may provide potential selectivity for the development of anti-TB therapies. ■

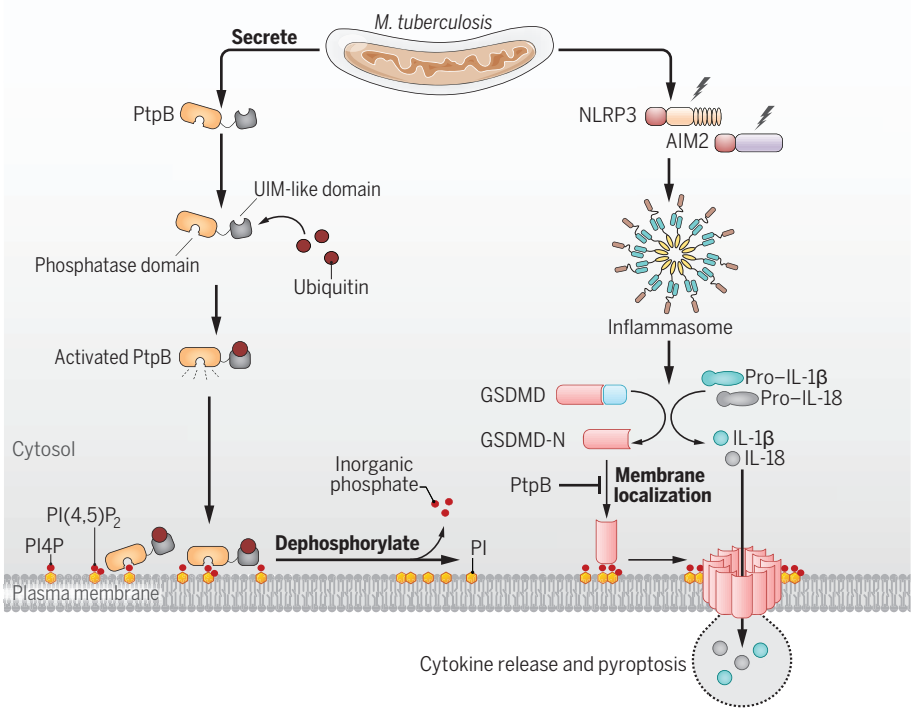

***M. tuberculosis* PtpB hijacks host ubiquitin to inhibit pyroptosis through altering host membrane phospholipid composition.** *M. tuberculosis*–secreted phospholipid phosphatase PtpB is activated by interacting with host ubiquitin through a UIM-like domain, by which it dephosphorylates host plasma membrane phosphoinositides PI4P and PI(4,5)P_2 to inhibit the membrane targeting of GSDMD-N, thus disrupting the inflammatory cytokine release and pyroptosis upon activation of *M. tuberculosis* infection–triggered inflammasome activation in macrophages.

The list of author affiliations is available in the full article online.
*Corresponding author. Email: xqiu@bnu.edu.cn (X.-B.Q.); wangj6@im.ac.cn (J.W.); liucuihua@im.ac.cn (C.H.L.)
†These authors contributed equally to this work.
Cite this article as Q. Chai *et al.*, *Science* **378**, eabq0132 (2022). DOI: 10.1126/science.abq0132

READ THE FULL ARTICLE AT
https://doi.org/10.1126/science.abq0132

RESEARCH ARTICLE

MICROBIOLOGY

A bacterial phospholipid phosphatase inhibits host pyroptosis by hijacking ubiquitin

Qiyao Chai[1]†, Shanshan Yu[2]†, Yanzhao Zhong[1,3]†, Zhe Lu[1,3], Changgen Qiu[1,3], Yang Yu[1,3], Xinwen Zhang[1,3], Yong Zhang[1], Zehui Lei[1,3], Lihua Qiang[1,3], Bing-Xi Li[1], Yu Pang[2], Xiao-Bo Qiu[4,5]*, Jing Wang[1]*, Cui Hua Liu[1,3]*

The inflammasome-mediated cleavage of gasdermin D (GSDMD) causes pyroptosis and inflammatory cytokine release to control pathogen infection, but how pathogens evade this immune response remains largely unexplored. Here we identify the known protein phosphatase PtpB from *Mycobacterium tuberculosis* as a phospholipid phosphatase inhibiting the host inflammasome-pyroptosis pathway. Mechanistically, PtpB dephosphorylated phosphatidylinositol-4-monophosphate and phosphatidylinositol-(4,5)-bisphosphate in host cell membrane, thus disrupting the membrane localization of the cleaved GSDMD to inhibit cytokine release and pyroptosis of macrophages. Notably, this phosphatase activity requires PtpB binding to ubiquitin. Disrupting phospholipid phosphatase activity or the ubiquitin-interacting motif of PtpB enhanced host GSDMD-dependent immune responses and reduced intracellular pathogen survival. Thus, pathogens inhibit pyroptosis and counteract host immunity by altering host membrane composition.

Tuberculosis (TB) is a highly infectious disease caused by *Mycobacterium tuberculosis* (Mtb), which remains the leading cause of death from a single infectious agent, accounting for ~1.5 million deaths each year (*1*). This situation is being exacerbated by the emergence and spread of drug-resistant Mtb, which renders patients untreatable with currently available drugs. This is particularly troublesome as the pathogenesis of TB remains poorly understood, impeding the rational development of new anti-TB therapies (*2*). As an adaptable intracellular pathogen that coexists and coevolves within the human host, Mtb has developed numerous strategies to establish prolonged infection. One interesting feature of Mtb is a set of eukaryotic-like effectors (*3*–*5*), but their host cellular targets and regulatory roles in pathogen–host interactions remain largely unexplored.

The inflammasome is a multiprotein cytoplasmic complex composed of cytosolic immune sensors such as absent in melanoma 2 (AIM2) and NOD-like receptor protein 3 (NLRP3), inflammatory caspases (especially caspase-1), and apoptosis-associated speck-like protein containing a CARD (ASC). The inflammasome mediates the secretion of inflammatory cytokines (e.g., interleukins IL-1β and IL-18) in response to infection by pathogens including Mtb (*6*). The inflammasome-mediated activation of caspase-1 leads to cleavage of gasdermin D (GSDMD), resulting in the formation of membrane pores and the induction of pyroptosis. Pyroptosis is an inflammatory form of cell death that features cytoplasmic swelling, DNA fragmentation, and leakage of cytosolic contents (*7*). Cellular membrane phospholipids, especially phosphoinositides, have recently been linked to pyroptosis and IL-1β release by macrophages (*8*–*10*). The distribution and abundance of phosphoinositides are regulated by cellular phosphoinositide kinases and phosphatases and may be disturbed by invading pathogens (*11*). However, it is unclear whether pathogens remodel cellular phospholipid homeostasis to manipulate host inflammasome-mediated immune responses. Here, we demonstrate that the known protein tyrosine phosphatase B (PtpB, also called Rv0153c) from Mtb alters the phospholipid composition of the host membrane by binding ubiquitin (Ub) to inhibit pyroptosis and counteract host immunity.

[1]CAS Key Laboratory of Pathogenic Microbiology and Immunology, Institute of Microbiology, Chinese Academy of Sciences, Beijing 100101, China. [2]Beijing Tuberculosis and Thoracic Tumor Research Institute, Beijing Chest Hospital, Capital Medical University, Beijing 101149, China. [3]Savaid Medical School, University of Chinese Academy of Sciences, Beijing 101408, China. [4]State Key Laboratory of Natural Medicines, China Pharmaceutical University, Nanjing, Jiangsu 211198, China. [5]Ministry of Education Key Laboratory of Cell Proliferation and Regulation Biology, College of Life Sciences, Beijing Normal University, Beijing 100875, China.
***Corresponding author. Email: xqiu@bnu.edu.cn (X.-B.Q.); wangj6@im.ac.cn (J.W.); liucuihua@im.ac.cn (C.H.L.)**
†These authors contributed equally to this work.

Results

Identification of Mtb PtpB as an inhibitor of NLRP3 and AIM2 inflammasome pathways

To predict Mtb-secreted eukaryotic-like proteins that might target host factors directly, we examined the whole genome of Mtb H37Rv and found 540 genes (accounting for ~13.8% of Mtb protein-encoding genes) that encode proteins harboring eukaryotic-like motifs or domains. Of these, 201 proteins were classified as Mtb-secreted molecules (fig. S1A and data S1). These proteins were then subjected to an enzyme-linked immunosorbent assay (ELISA) to determine their effects on the AIM2 and NLRP3 inflammasome pathways in human embryonic kidney 293T (HEK293T) cells with a reconstituted inflammasome system (Fig. 1A). Inflammasome assembly induces autoproteolytic activation of caspase-1, which then proteolytically cleaves pro–IL-1β and GSDMD, followed by the release of mature IL-1β through cell membrane pores generated by the N-terminal cleavage fragment of GSDMD (GSDMD-N) (*7*). Our data showed that six Mtb proteins (Rv0153c, Rv0561c, Rv0824c, Rv0861c, Rv1515c, and Rv1679) exhibited strong inhibitory effects on the secretion of IL-1β from both AIM2 and NLRP3 inflammasome-reconstituted HEK293T cells [relative activation rate < 0.2; data S2]. Among these proteins, PtpB (i.e., Rv0153c) was most abundantly secreted by Mtb during infection (fig. S1B). Thus, we focused on PtpB and further confirmed its inhibitory effect on AIM2 or NLRP3 inflammasome-mediated IL-1β secretion through ELISA and immunoblotting analyses (Fig. 1B and fig. S1, C and D). Accordingly, the Mtb mutant strain with the deletion of *ptpB* (Δ*ptpB*) showed stronger pyroptosis-inducing effect in macrophages than the wild-type (WT) Mtb strain (fig. S1E and movies S1 and S2). Together, these results suggest that PtpB is an important bacterial inhibitor of the host inflammasome-pyroptosis pathway.

PtpB inhibits GSDMD-dependent cytokine release and pyroptosis

We then sought to define the specific mechanism(s) of suppression of the inflammasome pathway by Mtb PtpB. Because ASC speck formation is a marker for inflammasome assembly, we examined whether PtpB affects this process. Deletion of *ptpB* did not show significant effects on ASC speck formation in Mtb-infected macrophages (fig. S2, A and B). Proximity ligation assays confirmed that PtpB had no significant effect on the interaction between ASC and caspase-1 (fig. S2, C to E), suggesting that PtpB does not affect inflammasome assembly (*7*). PtpB also did not affect the interaction between Mtb and caspase-1 (fig. S2, F and G), indicating that certain mycobacterial proteins might interact with host caspase-1 during Mtb infection, even though this interaction is independent of PtpB. We then found that Mtb Δ*ptpB* infection resulted in lower intracellular amounts of mature IL-1β, caspase-1 (p20), and the C-terminal cleavage fragment of GSDMD (GSDMD-C) but higher supernatant amounts of these molecules compared with WT or *ptpB*-complemented (Δ*ptpB:ptpB*) Mtb strains (fig. S2H). Mature IL-1β, caspase-1 (p20), and GSDMD-C are released from the pyroptotic cells upon inflammasome activation

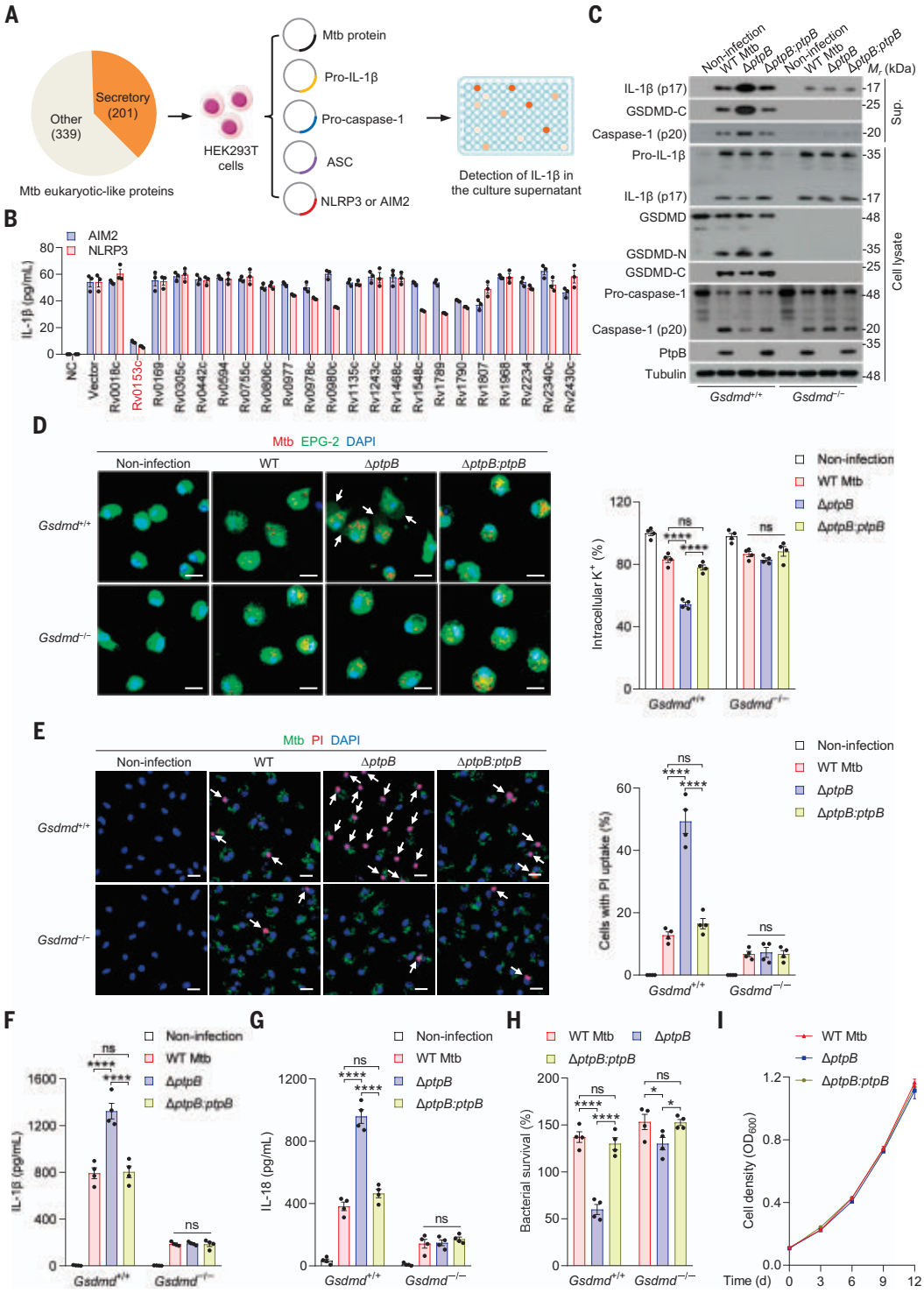

Fig. 1. PtpB inhibits GSDMD-dependent cytokine release and pyroptosis. (**A**) Schematic diagram of the procedure to screen Mtb inhibitors of AIM2 and NLRP3 inflammasome pathways. (**B**) Representative results of the effects of Mtb proteins on IL-1β secretion from inflammasome-reconstituted HEK293T cells. PtpB (i.e., Rv0153c) is indicated in red. NC, negative control. (**C**) Immunoblotting of the indicated proteins in the culture supernatants (Sup.) and cell lysates of *Gsdmd*$^{+/+}$ or *Gsdmd*$^{-/-}$ BMDMs. (**D**) Measurement of the K^+ concentrations in BMDMs using Enhanced Potassium Green-2 (EPG-2). Arrows indicate the pyroptotic cells. Scale bars, 10 μm. (**E**) Membrane integrity analysis of BMDMs. Arrows indicate propidium iodide (PI)–positive cells. Scale bars, 10 μm. (**F** and **G**) ELISA of supernatant IL-1β (F) and IL-18 (G) from BMDMs. (**H**) Intracellular survival analysis of Mtb in BMDMs. (**I**) In vitro growth kinetics of the indicated Mtb strains. For (C) to (H), cells were infected with the indicated Mtb strains for 48 hours. $P > 0.05$, not significant (ns); $^*P < 0.05$; $^{****}P < 0.0001$ (two-way ANOVA with Tukey's post-hoc test). Data are shown as mean ± SEM [$n = 3$ in (B) and $n = 4$ in (D) to (I)]. Data are representative of at least three independent experiments.

(*10*, *12*). Deletion of *ptpB* in Mtb increased intracellular amounts of GSDMD-N (fig. S2H), which binds to the cell membrane rather than being released into the supernatant upon inflammasome activation (*12*). Deletion of *ptpB* in Mtb decreased intracellular amounts of pro–IL-1β, probably owing to the acceleration of pro–IL-1β cleavage by enhanced inflammasome activation (fig. S2H). These observations indicate that PtpB might target GSDMD, which is required for cell membrane pore formation to allow the release of intracellular small-diameter proteins and to promote K^+ efflux that further facilitates inflammasome activation (*10*, *13*).

Next, we obtained bone marrow–derived macrophages (BMDMs) from *Gsdmd*-deficient ($Gsdmd^{-/-}$) and WT ($Gsdmd^{+/+}$) mice to confirm whether GSDMD is required for PtpB-mediated inhibition of the inflammasome-pyroptosis pathway. We found that deletion of *ptpB* increased the secretion of matured IL-1β, caspase-1 (p20), and GSDMD-C in $Gsdmd^{+/+}$ BMDMs but not in $Gsdmd^{-/-}$ BMDMs (Fig. 1C). PtpB deletion also decreased the concentrations of K^+ in $Gsdmd^{+/+}$ BMDMs and induced a higher proportion of $Gsdmd^{+/+}$ BMDMs with swelling bubbles, which are a marker of pyroptosis; these effects were abolished in $Gsdmd^{-/-}$ BMDMs (Fig. 1D). In addition, deletion of *ptpB* in Mtb increased pyroptosis in $Gsdmd^{+/+}$ BMDMs but not in $Gsdmd^{-/-}$ BMDMs (Fig. 1E). Furthermore, PtpB suppressed the secretion of IL-1β and IL-18, two vital inflammatory cytokines released by macrophages upon inflammasome activation (*10*) in a GSDMD-dependent manner (Fig. 1, F and G). In contrast, PtpB inhibited the production of tumor necrosis factor α (TNF-α) and IL-6, but not IL-12 (p40) or IL-10, by macrophages in a GSDMD-independent manner (fig. S3, A to D). Accordingly, PtpB decreased mRNA levels of *Tnf* and *Il6* at various time points after Mtb infection independent of GSDMD (fig. S3, E to J), supporting the notion that PtpB is involved in Mtb suppression of several non-inflammasome immune pathways (*14*, *15*). We then examined the effects of PtpB-suppressed GSDMD-dependent inflammasome cytokine release and pyroptosis on Mtb intracellular survival and found that Mtb Δ*ptpB* exhibited a more pronounced attenuation of intracellular survival in $Gsdmd^{+/+}$ BMDMs than in $Gsdmd^{-/-}$ BMDMs (Fig. 1H), but Mtb Δ*ptpB* did not exhibit any growth defects in the absence of host cells (Fig. 1I). Further, we used cytokine antagonists and/or neutralizing antibodies to confirm that both GSDMD-mediated inflammatory cytokine release and pyroptosis promoted the PtpB-promoted Mtb intracellular survival (fig. S3K). We also observed that PtpB-suppressed production of TNF-α and IL-6 weakly promoted Mtb intracellular survival (fig. S3K). Next, we exogenously expressed Mtb PtpB in $Gsdmd^{+/+}$ and $Gsdmd^{-/-}$ BMDMs to validate the inhibitory effect of PtpB on inflammasome pathways (fig. S4A). PtpB inhibited the GSDMD-dependent release of IL-1β and IL-18 and pyroptosis upon activation of the AIM2 and NLRP3 inflammasome pathways stimulated by poly(deoxyadenylic-deoxythymidylic) acid [poly(dA:dT)] and nigericin, respectively, in lipopolysaccharide (LPS)–primed macrophages (fig. S4, B to I). PtpB also suppressed GSDMD-independent production of TNF-α and IL-6 in LPS-stimulated macrophages (fig. S4, D and E). Taken together, these data suggest that PtpB inhibits the GSDMD-dependent inflammasome cytokine release and pyroptosis to facilitate Mtb intracellular survival, although PtpB may also impair other innate immune pathways, for example, macrophage production of TNF-α and IL-6, in a GSDMD-independent manner.

PtpB disrupts membrane localization of GSDMD-N

GSDMD-N is the functional domain of GSDMD that mediates cytokine release and pyroptosis. We examined the role of GSDMD-N in PtpB-mediated inhibition of inflammasome pathways by generating $Gsdmd^{-/-}$ immortalized BMDMs (iBMDMs) stably expressing WT human GSDMD (hGSDMD) or hGSDMD 4A mutant, where Arg^{137}, Lys^{145}, Arg^{151}, and Arg^{153} were all mutated to Ala to inactivate GSDMD-N (Fig. 2A) (*10*). $Gsdmd^{-/-}$ iBMDMs complemented with WT hGSDMD, but not the hGSDMD 4A mutant, restored the phenotype of macrophages infected with Mtb Δ*ptpB*, as indicated by increased amounts of supernatant IL-1β and IL-18, increased cell cytotoxicity, and reduced bacterial viability compared with the WT Mtb and Δ*ptpB:ptpB* infection groups (Fig. 2, B to E). Furthermore, expression of PtpB prominently reduced the membrane localization of GSDMD-N and cell cytotoxicity of HeLa cells (Fig. 2, F to H). Accordingly, deletion of *ptpB* markedly increased the translocation of GSDMD-N to the plasma membrane (PM) of macrophages during Mtb infection (Fig. 2I). Notably, PtpB secreted by the WT and *ptpB*-complemented strains was also detected in the PM fraction. Thus, PtpB impedes macrophage cytokine secretion and pyroptosis via GSDMD-N, whose membrane localization can be disrupted by PtpB.

PtpB impairs membrane localization of GSDMD-N depending on its lipid phosphatase activity

GSDMD-N shows a strong affinity for cell membrane lipids, particularly phosphoinositides phosphatidylinositol-4-monophosphate (PI4P) and phosphatidylinositol-(4,5)-bisphosphate [$PI(4,5)P_2$]. This affinity enables it to localize to the inner leaflet of the PM to form pores (*9*, *10*). Mtb PtpB is a eukaryotic-like protein tyrosine phosphatase that exhibits weak phosphoinositide phosphatase activity in vitro (*16*, *17*). The Cys^{160}→Ser (C160S) mutation abolishes the phosphotyrosine and phosphoinositide phosphatase activities of PtpB, whereas the K164A mutation only eliminates the phosphotyrosine phosphatase activity of PtpB (*16*). To test whether PtpB dephosphorylates host membrane phosphoinositides to disrupt GSDMD-N membrane localization, we complemented Mtb Δ*ptpB* with the *ptpB* C160S or K164A mutant. Confocal microscopy analysis showed that PtpB and its mutants, including C160S and K164A, were secreted by Mtb and then localized to the PM of macrophages during infection (Fig. 3, A and B). PtpA, the only other protein tyrosine phosphatase identified in Mtb, did not show obvious membrane localization (*18*). Similar to the membrane lipid–binding behavior of GSDMD-N (*9*, *10*), PtpB showed strongest affinity to PI4P, followed by $PI(4,5)P_2$, whereas its binding affinity to sulfatides and cardiolipins was much weaker (Fig. 3C). When incubated with liposomes containing phosphatidylcholine as the skeleton lipid, PtpB and its C160S or K164A mutants were precipitated by liposomes containing 20% PI4P or $PI(4,5)P_2$ (Fig. 3D). Similar to *ptpB* deletion, the PtpB C160S, but not K164A, mutation increased the translocation of GSDMD-N to the PM of macrophages during Mtb infection (Fig. 3, E to G). Accordingly, the PtpB C160S mutation, but not the K164A mutation, enhanced the secretion of IL-1β and IL-18 from Mtb-infected macrophages with increased cell cytotoxicity (Fig. 3, H to J) and reduced Mtb intracellular survival, reaching a level comparable to that of Mtb Δ*ptpB* (Fig. 3K). These results demonstrate that PtpB is a membrane lipid–binding protein whose Cys^{160}-dependent lipid phosphatase activity is essential for impairing GSDMD-N membrane localization.

PtpB reduces the concentrations of plasma membrane PI4P and PI(4,5)P_2 to impair GSDMD-mediated immune functions

Next, we tested whether PtpB dephosphorylates host membrane phosphoinositides. PtpB exhibited the strongest binding to PI4P and relatively weaker affinity for PI3P, $PI(3,5)P_2$, and $PI(4,5)P_2$ in vitro (fig. S5A). We then tested whether the PtpB-induced subversion of GSDMD functions in macrophages could be restored by supplementing these phosphoinositides (fig. S5B). In both WT and *ptpB*-complemented Mtb-infected macrophages, treatment with exogenous PI4P promoted IL-1β and IL-18 secretion with increased cytotoxicity and reduced bacterial intracellular survival, reaching levels similar to those of Mtb Δ*ptpB* and Δ*ptpB:ptpB* C160S-infected macrophages (Fig. 4, A to D). Meanwhile, treatment with $PI(4,5)P_2$, but not PI3P or $PI(3,5)P_2$, partially diminished the differences among the four infection groups. $PI(4,5)P_2$ and its synthetic precursor PI4P are the two major phosphoinositides in the PM, whereas PI3P and $PI(3,5)P_2$ are primarily found

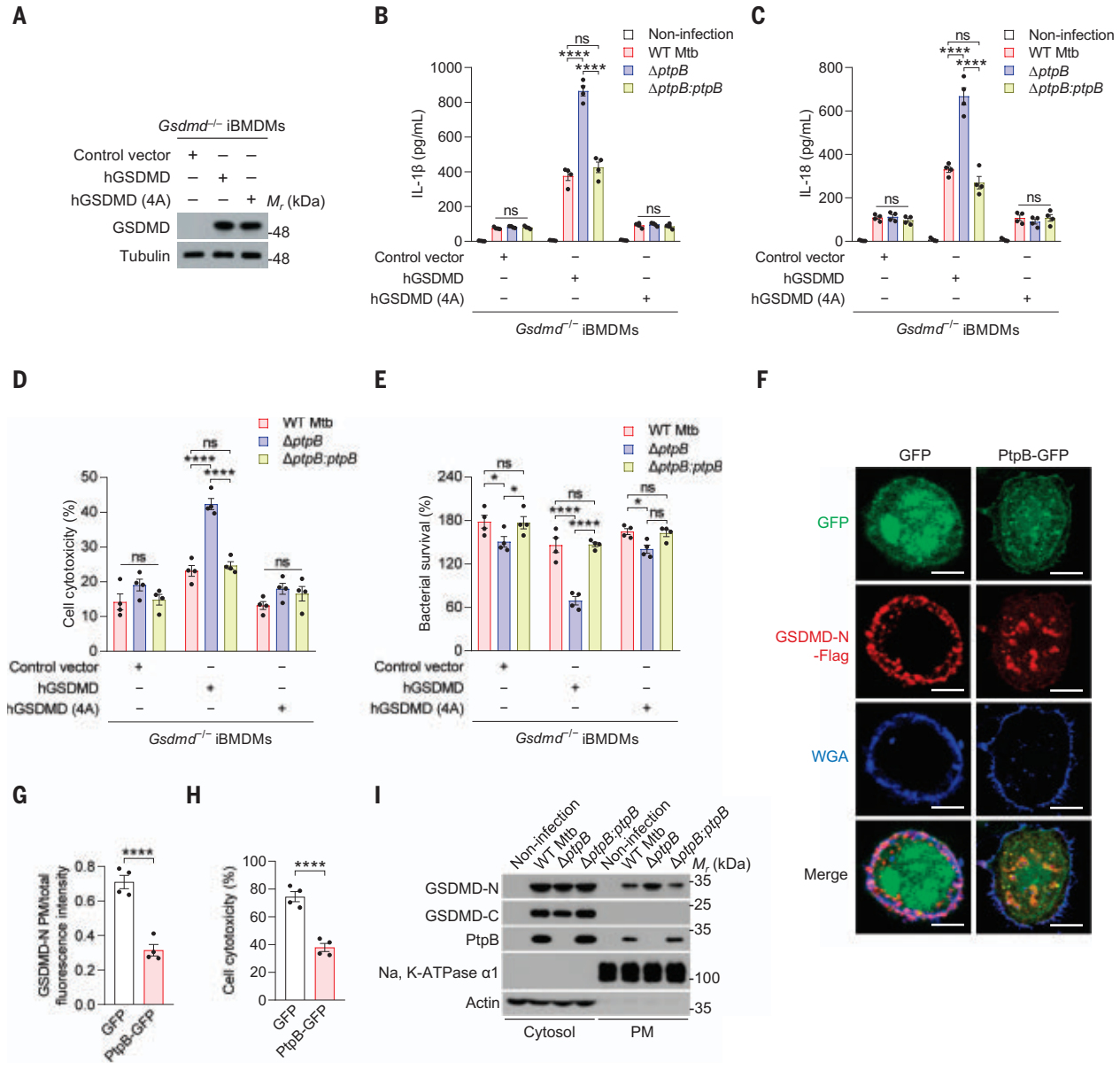

Fig. 2. PtpB disrupts membrane localization of GSDMD-N. (**A**) Immunoblotting of hGSDMD in *Gsdmd*$^{-/-}$ iBMDMs complemented with or without WT hGSDMD or hGSDMD 4A mutant. (**B** and **C**) ELISA of supernatant IL-1β (B) and IL-18 (C) from iBMDMs treated as in (A). (**D** and **E**) Analysis for cell cytotoxicity (D) and intracellular bacterial survival (E) in iBMDMs treated as in (A). (**F**) Confocal microscopy of HeLa cells cotransfected with GSDMD-N-Flag and GFP or PtpB-GFP for 24 hours. The plasma membrane (PM) was stained with wheat germ agglutinin (WGA). Scale bars, 5 μm. (**G** and **H**) Quantitation of GSDMD-N PM/total fluorescence intensity (G) and cell cytotoxicity (H) of HeLa cells treated as in (F). (**I**) Immunoblotting of the indicated proteins in subcellular fractions of BMDMs. For (B) to (E), and (I), cells were infected with or without the indicated Mtb strains for 48 hours; $P > 0.05$, not significant (ns); $^{*}P < 0.05$; $^{****}P < 0.0001$ (two-way ANOVA with Tukey's post-hoc test). For (G) and (H), $^{****}P < 0.0001$ (unpaired two-tailed *t* tests). Data are shown as mean ± SEM [$n = 4$ in (B) to (E), (G), and (H)]. Data are representative of at least three independent experiments.

in intracellular vesicles (*19*, *20*). Upon Mtb infection, PtpB markedly reduced the concentrations of PI4P and PI(4,5)P_2 in the PM, whereas it had much less effects on the concentrations of PI4P and PI(4,5)P_2 in the internal membrane (IM), which is derived from intracellular organelles (Fig. 4, E and F). Meanwhile, Mtb-secreted PtpB showed little Golgi localization in macrophages (fig. S6A). Deletion of *ptpB* had no significant effect on the Golgi pool of PI4P, Golgi morphology, or the Golgi-mediated trafficking of Ras-related protein Rab-11A (RAB11A) and α-mannosidase II, two markers of Golgi-derived vesicles (fig. S6, B to F) (*21*, *22*). Thus, PtpB impairs GSDMD-mediated immune responses, probably by depleting host PM PI4P and PI(4,5)P_2. To verify this result, we monitored PM concentrations of PI4P and GSDMD-N during Mtb infection using immunocytochemistry (*19*). Deletion or C160S mutation of *ptpB* resulted in comparably increased PI4P concentrations in the PM (fig. S7, A and B). In vitro analyses further confirmed the Cys^{160}-dependent phosphatase activity of PtpB toward PI4P (fig. S7C). When macrophages were treated with phenylarsine oxide (PAO) or Pik-93 to deplete cellular PI4P, the difference in membranous GSDMD-N concentrations between WT and Δ*ptpB:ptpB* (C160S) strains was reduced (fig. S7, D to F). Accordingly, depletion of PM PI4P also diminished the differences

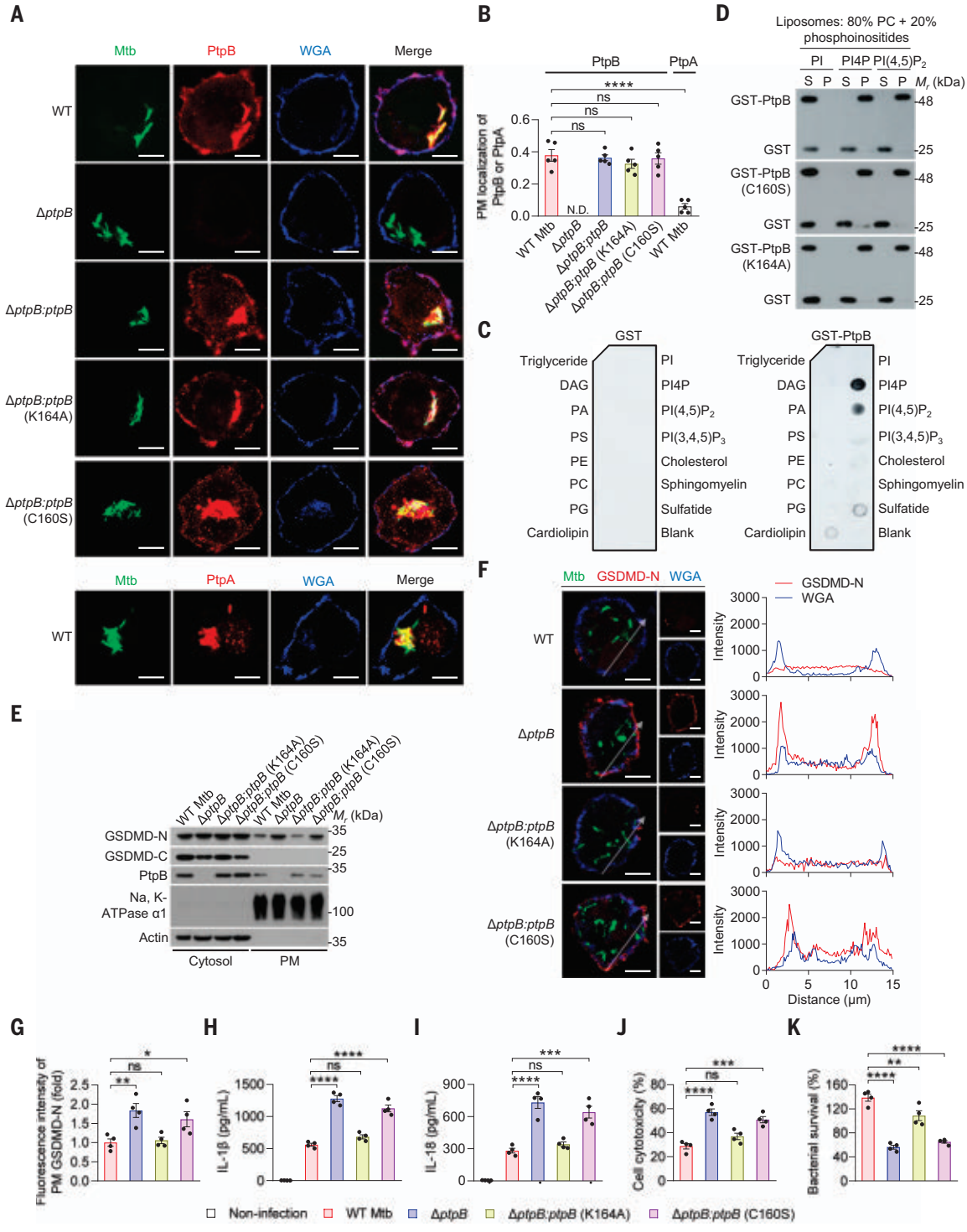

Fig. 3. PtpB impairs membrane localization of GSDMD-N depending on its lipid phosphatase activity. (**A**) Subcellular localization of PtpB and PtpA in BMDMs. The PM was stained with WGA. Scale bars, 5 μm. (**B**) Quantitation of PM PtpB and PtpA. N.D., not detectable. (**C**) Membrane lipid-binding assay of PtpB. DAG, diacylglycerol; PA, phosphatidic acid; PS, phosphatidylserine; PE, phosphatidylethanolamine; PC, phosphatidylcholine; PG, phosphatidylglycerol. (**D**) Immunoblotting of the indicated proteins in the liposome-free supernatant (S) and liposome pellet (P) after their incubation with liposomes. (**E**) Immunoblotting of the indicated proteins in subcellular fractions of BMDMs. (**F**) Confocal microscopy of PM GSDMD-N in BMDMs with fluorescence intensity plotted along the arrows. Scale bars, 5 μm. (**G**) Quantitation of PM GSDMD-N in BMDMs. (**H** and **I**) ELISA of supernatant IL-1β (H) and IL-18 (I) from BMDMs. (**J** and **K**) Analysis for cell cytotoxicity (J) and intracellular bacterial survival (K) in BMDMs. For (A), (B), and (E) to (K), cells were infected with or without Mtb strains for 48 hours. $P > 0.05$, not significant (ns); $^{*}P < 0.05$; $^{**}P < 0.01$; $^{***}P < 0.001$; $^{****}P < 0.0001$ (one-way ANOVA with Dunnett's post-hoc test). Data are shown as mean ± SEM [$n = 5$ in (B) and $n = 4$ in (G) to (K)]. Data are representative of three independent experiments.

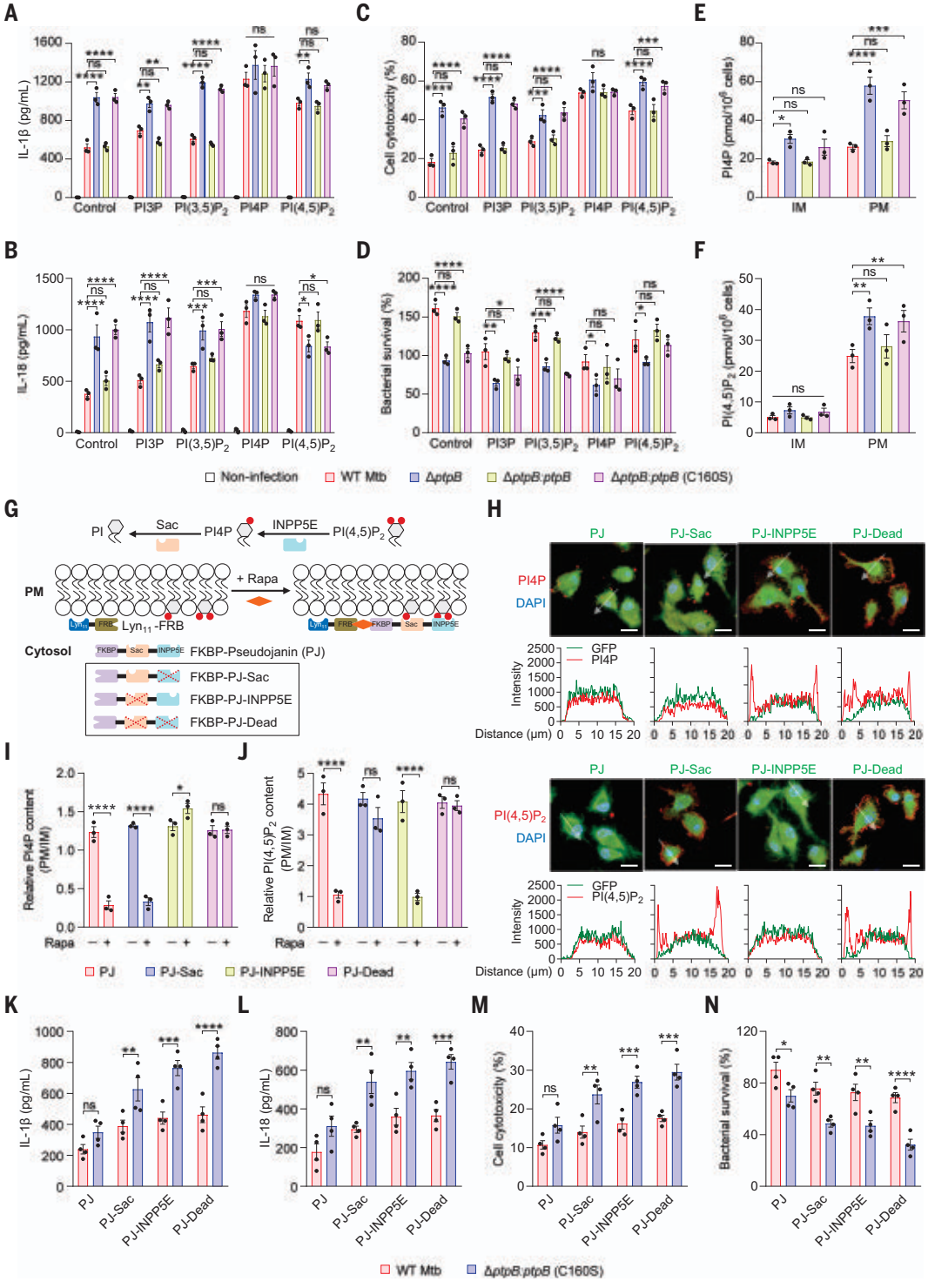

Fig. 4. PtpB reduces PM concentrations of PI4P and PI(4,5)P_2 to impair GSDMD-mediated immune functions. (**A** and **B**) ELISA of supernatant IL-1β (A) and IL-18 (B) from BMDMs. (**C** and **D**) Cell cytotoxicity (C) and intracellular bacterial survival (D) in BMDMs. (**E** and **F**) ELISA of IM- and PM-derived PI4P (E) and PI(4,5)P_2 (F) from BMDMs. (**G**) Schematic diagram of the rapamycin-induced recruitment of FKBP-PJ to PM-targeted Lyn_{11}-FRB for PI4P and PI(4,5)P_2 depletion. (**H** to **J**) Confocal microscopy (H) and ELISA of cellular PI4P (I) and PI(4,5)P_2 (J) in BMDMs after PM recruitment of PJ, PJ-Sac, PJ-INPP5E, or PJ-Dead for 10 min with 0.5 μM rapamycin. Fluorescence intensity was plotted along the arrows. Scale bars, 10 μm. (**K** and **L**) ELISA of supernatant IL-1β (K) and IL-18 (L) from BMDMs. (**M** and **N**) Cell cytotoxicity (M) and intracellular bacterial survival (N) in BMDMs. For (A) to (F), cells were infected with Mtb strains for 24 hours with or without the treatment of phosphoinositides (10 μM). For (K) to (N), cells were treated with 0.5 μM rapamycin for 10 min before infection with Mtb for 8 hours. $P > 0.05$, not significant (ns); $^*P < 0.05$; $^{**}P < 0.01$; $^{***}P < 0.001$; $^{****}P < 0.0001$ (two-way ANOVA with Dunnett's post-hoc test). Data are shown as mean ± SEM [$n = 3$ in (A) to (F), (I), and (J), and $n = 4$ in (K) to (N)]. Data are representative of at least three independent experiments.

in IL-1β and IL-18 release, cell cytotoxicity, and bacterial survival in macrophages between the WT Mtb and Mtb Δ*ptpB:ptpB* C160S infection groups (fig. S7, G to J). Likewise, the C160S mutation abolished the PtpB-mediated reduction in PM $PI(4,5)P_2$ concentrations in Mtb-infected macrophages (fig. S8, A and B). The depletion of cellular $PI(4,5)P_2$ using ionomycin partially diminished the differences in IL-1β and IL-18 release, cell cytotoxicity, and bacterial intracellular survival between WT Mtb and Mtb Δ*ptpB:ptpB* C160S infection groups (fig. S8, C to F). To exclude the possibility that the inhibitory effect of PtpB on GSDMD functions might be due to its pleiotropic phosphatase activity in depleting both PM and IM PI4P and $PI(4,5)P_2$, and to avoid the undesired effects of PAO, Pik-93, and ionomycin on other phosphoinositides, we turned to a rapamycin-inducible PM phosphoinositide depletion approach using two constructs including PM-targeted Lyn_{11}-FRB and cytosolic FKBP-Pseudojanin (PJ), which dephosphorylates PI4P and $PI(4,5)P_2$ (Fig. 4G; see table S1 for details) (*23*). The recruitment of PJ to the PM decreased PM PI4P and $PI(4,5)P_2$ concentrations in response to rapamycin, while PJ-Sac (which dephosphorylates PI4P) and PJ-INPP5E [which dephosphorylates $PI(4,5)P_2$], but not PJ-Dead [which dephosphorylates neither PI4P nor $PI(4,5)P_2$], selectively reduced PM PI4P and $PI(4,5)P_2$ concentrations, respectively (Fig. 4, H to J). These results demonstrate the feasibility of this approach in depriving PM PI4P and/or $PI(4,5)P_2$ in macrophages. We then found that the PM recruitment of PJ, but not of PJ-Dead, partially reduced the amounts of membranous GSDMD-N (L192D) (which retards pyroptosis to enable monitoring) (*10*), concurrent with decreased cell cytotoxicity (fig. S9). Meanwhile, the PM recruitment of either PJ-Sac or PJ-INPP5E alone had little, if any, effect on the membranous GSDMD-N (L192D) concentrations and cell cytotoxicity (fig. S9). These data indicate that the PM PI4P and $PI(4,5)P_2$ have synergistic effects on PM localization of GSDMD-N. The remaining undissociated PM GSDMD-N is probably due to their stable membrane insertion after oligomerization with drastic conformational changes (*10*). Finally, the PJ-induced depletion of PM PI4P and $PI(4,5)P_2$ significantly reduced the differences in IL-1β and IL-18 release, cell cytotoxicity, and bacterial survival in macrophages between the WT Mtb and Mtb Δ*ptpB:ptpB* C160S infection groups (Fig. 4, K to N). Together, these findings suggest that PtpB can dephosphorylate and therefore reduce the PM concentrations of PI4P and $PI(4,5)P_2$ to impair GSDMD-mediated immune responses.

Ubiquitin binding is required for PtpB to disrupt GSDMD-mediated immune responses

We next investigated how PtpB efficiently reduces host PM PI4P and $PI(4,5)P_2$ abundance to impair GSDMD function, given that its lipid phosphatase activity is not easily detectable in vitro (fig. S7C) (*16*, *24*). The structure of PtpB features a buried active site with a phosphate-binding loop (or P-loop; Cys^{160}-X_5-Arg^{166}) covered by a flexible two-helix "lid," suggesting that the phosphatase activity of PtpB is regulable in vivo (*25*). We have previously shown that another Mtb protein tyrosine phosphatase, PtpA, can exploit host Ub (*5*). Structure-based analysis of the interaction between PtpB and Ub revealed that PtpB harbors a Ub-interacting motif (UIM)–like region with a hydrophobic surface including three key UIM residues (Ala^{240}–Ala^{242}) on an α helix (i.e., helix α9) that potentially bind the Ile^{44} residue in Ub (Fig. 5A) (*26*). To confirm whether this UIM-like region mediates the interaction between PtpB and Ub, we generated a PtpB mutant with Ala^{240}–Ala^{242} to Glu mutations (PtpB 3E), which predictably disrupts the hydrophobic surface but reserves helix α9 (fig. S10, A and B). PtpB bound to Ub directly in vitro and also interacted with Ub in the cells, whereas the PtpB 3E (but not C160S) or Ub I44A mutation subverted their interaction (Fig. 5B and fig. S10C). Moreover, PtpB could only interact with mono-Ub, not poly-Ub chains (fig. S10, D and E). Helix α9 of PtpB is adjacent to α8, which constitutes a structurally dynamic lid together with α7. Thus, the binding of Ub to the UIM-like region might induce a conformational change in PtpB to expose the P-loop and promote its substrate turnover (*25*). As expected, Ub increased the catalytic efficiency of WT PtpB, but not its 3E mutant, toward PI4P and the phosphotyrosine peptides of the epidermal growth factor receptor (EGFR) or insulin-like growth factor 1 receptor (IGF1R) (Fig. 5C and fig. S10F). However, Ub-like proteins, including neural precursor cell–expressed developmentally down-regulated protein 8 (NEDD8), human leukocyte antigen F-associated transcript 10 (FAT10), interferon-stimulated gene 15 (ISG15), small ubiquitin-related modifier 1 (SUMO1), ubiquitin-fold modifier 1 (UFM1), autophagy-related protein 12 (ATG12), autophagy-related protein 8 (ATG8), and ubiquitin-related modifier 1 (URM1), did not interact with PtpB and thus had no effects on PtpB activity (fig. S10G). During infection, the PtpB 3E mutation did not affect PtpB secretion by Mtb or its PM localization but did markedly increase the abundance of PI4P, $PI(4,5)P_2$, and GSDMD-N in the PM of the infected macrophages (Fig. 5, D to F, and fig. S10, H and I). Likewise, both the 3E and C160S mutation attenuated the PtpB-induced inhibition of GSDMD-N membrane localization and cytotoxicity in HeLa cells (fig. S11). In vitro kinetic analyses further supported that the addition of Ub markedly increases the catalytic efficiency of WT PtpB, but not of its C160S or 3E mutant, toward PI4P (Fig. 5G and fig. S12). However, the effect of Ub was relatively weaker for $PI(3,5)P_2$ and $PI(4,5)P_2$ and negligible for PI3P and PI5P. Hence, Ub binding appears to be critical for PtpB to dephosphorylate host phosphoinositides to inhibit GSDMD-mediated immune responses. To further confirm this hypothesis, we infected $Gsdmd^{+/+}$ or $Gsdmd^{-/-}$ BMDMs with each of the aforementioned Mtb *ptpB* variant strains. Similar to Mtb Δ*ptpB* and Δ*ptpB:ptpB* C160S strains, Mtb Δ*ptpB:ptpB* 3E enhanced secretion of IL-1β and IL-18, increased cell cytotoxicity, and reduced intracellular viability in $Gsdmd^{+/+}$ BMDMs but not $Gsdmd^{-/-}$ BMDMs (Fig. 5, H to K). These data demonstrate that Ub binding is required for PtpB to disrupt the GSDMD-dependent immune responses in macrophages during Mtb infection.

PtpB–ubiquitin interaction is required for Mtb to evade host GSDMD-dependent immunity

We then sought to determine the role of PtpB in GSDMD-dependent host immunity during Mtb infection in a mouse model. Similar to *ptpB* deletion, *ptpB* C160S and 3E mutations markedly reduced Mtb-induced inflammatory infiltration in the lungs and livers of $Gsdmd^{+/+}$ mice (Fig. 6, A and B, and fig. S13, A and B). However, each Mtb *ptpB* variant strain caused comparable histopathological changes in $Gsdmd^{-/-}$ mice. Notably, $Gsdmd^{-/-}$ mice showed diffused cellular infiltration rather than the typical granulomatous lesions in the lungs (Fig. 6A), which supports the recently proposed notion that the activation of inflammasome pathways is critical for inflammatory cytokine–mediated granuloma formation (*27*). In $Gsdmd^{+/+}$ mice, *ptpB*-deleted or *ptpB*-mutated Mtb strains induced comparable numbers of, but much smaller, lung granulomatous lesions than those caused by *ptpB*-sufficient strains at 3 weeks after infection (Fig. 6A). Accordingly, deletion or mutation of *ptpB* in Mtb comparably reduced bacterial loads both in the lungs and spleens of mice at 3 and 12 weeks after infection in a *Gsdmd*-dependent manner (Fig. 6, C and D, and fig. S13, C and D). Furthermore, deletion or mutation of *ptpB* in Mtb led to significantly increased amounts of IL-1β and IL-18 in bronchoalveolar lavage fluid (BALF) obtained from $Gsdmd^{+/+}$ mice at 3 weeks after infection (Fig. 6E). In addition, *ptpB*-deleted or *ptpB*-mutated Mtb strains caused increased amounts of interferon-γ (IFN-γ) in both BALF and lungs of $Gsdmd^{+/+}$ mice (Fig. 6E). Interestingly, the amounts of these inflammatory cytokines in $Gsdmd^{+/+}$ mice caused by *ptpB*-deleted or *ptpB*-mutated Mtb strains decreased slightly at 12 weeks after infection, whereas the *ptpB*-sufficient strain-induced inflammatory cytokines in $Gsdmd^{+/+}$ mice drastically increased at 12 weeks after infection (Fig. 6E). Moreover, the deletion of

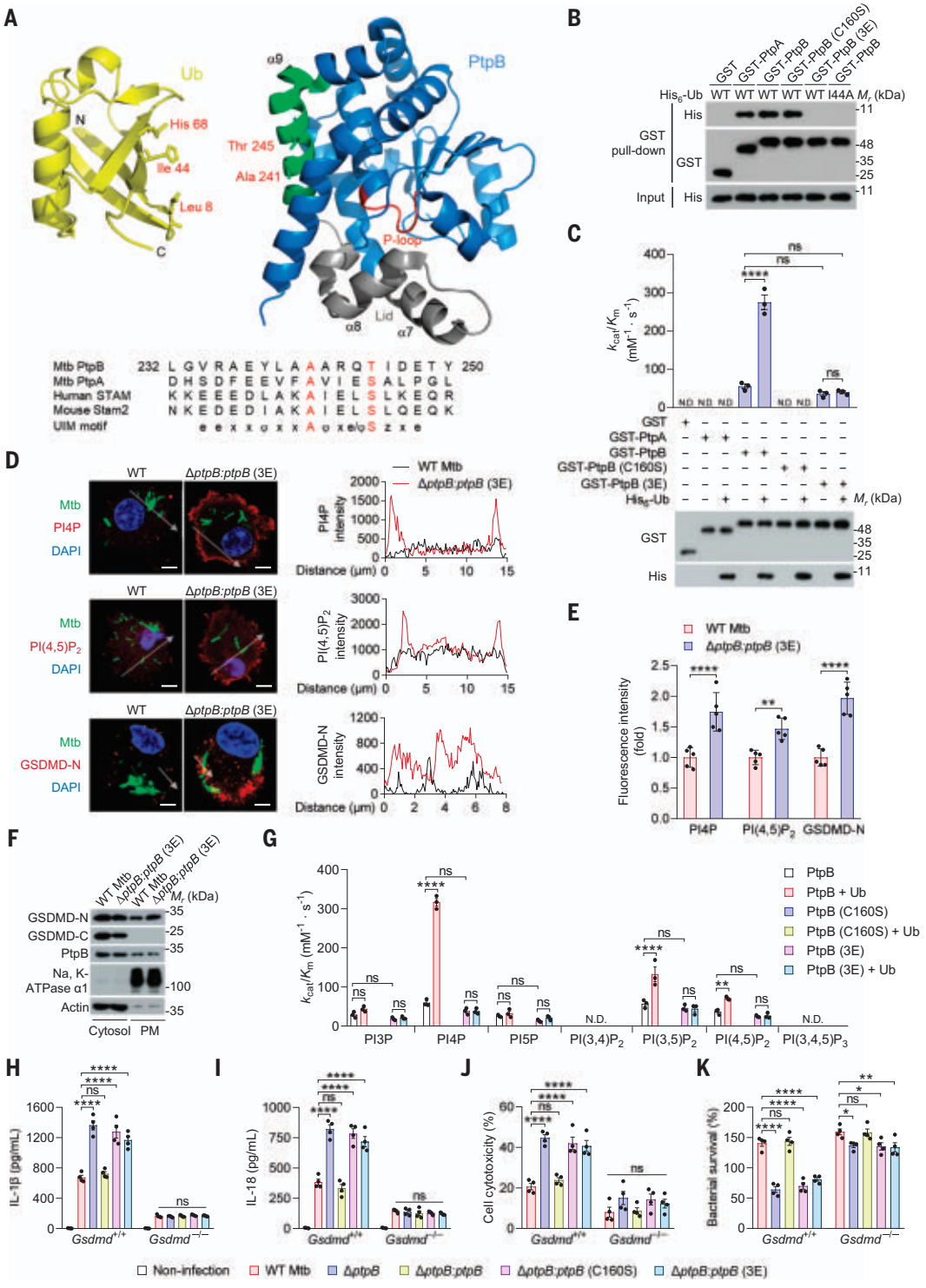

Fig. 5. Ubiquitin binding is required for PtpB to disrupt GSDMD-mediated immune responses. (**A**) Interfaces between PtpB and ubiquitin. Lower panel, alignment of PtpB UIM-like region with the related region of the indicated proteins. Single-letter abbreviations for the amino acid residues are as follows: A, Ala; C, Cys; D, Asp; E, Glu; F, Phe; G, Gly; H, His; I, Ile; K, Lys; L, Leu; M, Met; N, Asn; P, Pro; Q, Gln; R, Arg; S, Ser; T, Thr; V, Val; W, Trp; and Y, Tyr. (**B**) GST pull-down analysis for the PtpB-ubiquitin interaction. (**C**) PI4P phosphatase activity and immunoblotting of PtpB and its mutants with or without ubiquitin. N.D., not detectable. (**D** and **E**) Confocal microscopy (D) and quantitation (E) of PM PI4P, PI(4,5)P_2, and GSDMD-N in BMDMs. Fluorescence intensity was plotted along the arrows. Scale bars, 5 μm. (**F**) Immunoblotting of the indicated proteins in subcellular fractions of BMDMs. (**G**) Phosphoinositide phosphatase activity analysis of PtpB and its mutants. N.D., not detectable. (**H** and **I**) ELISA of supernatant IL-1β (H) and IL-18 (I) from BMDMs. (**J** and **K**) Analysis for cell cytotoxicity (J) and intracellular bacterial survival (K) in BMDMs. Cells were infected with Mtb strains for 48 hours in (D) to (F), and (H) to (K). $P > 0.05$, not significant (ns); $^{*}P < 0.05$; $^{**}P < 0.01$; $^{****}P < 0.0001$. One-way ANOVA with Tukey's post-hoc test for (C); two-way ANOVA with Tukey's post-hoc test for (E) and (G), and with Dunnett's post-hoc test for (H) to (K). Data are shown as mean ± SEM [$n = 3$ in (C) and (G), $n = 5$ in (E), and $n = 4$ in (H) to (K)]. Data are representative of at least three independent experiments.

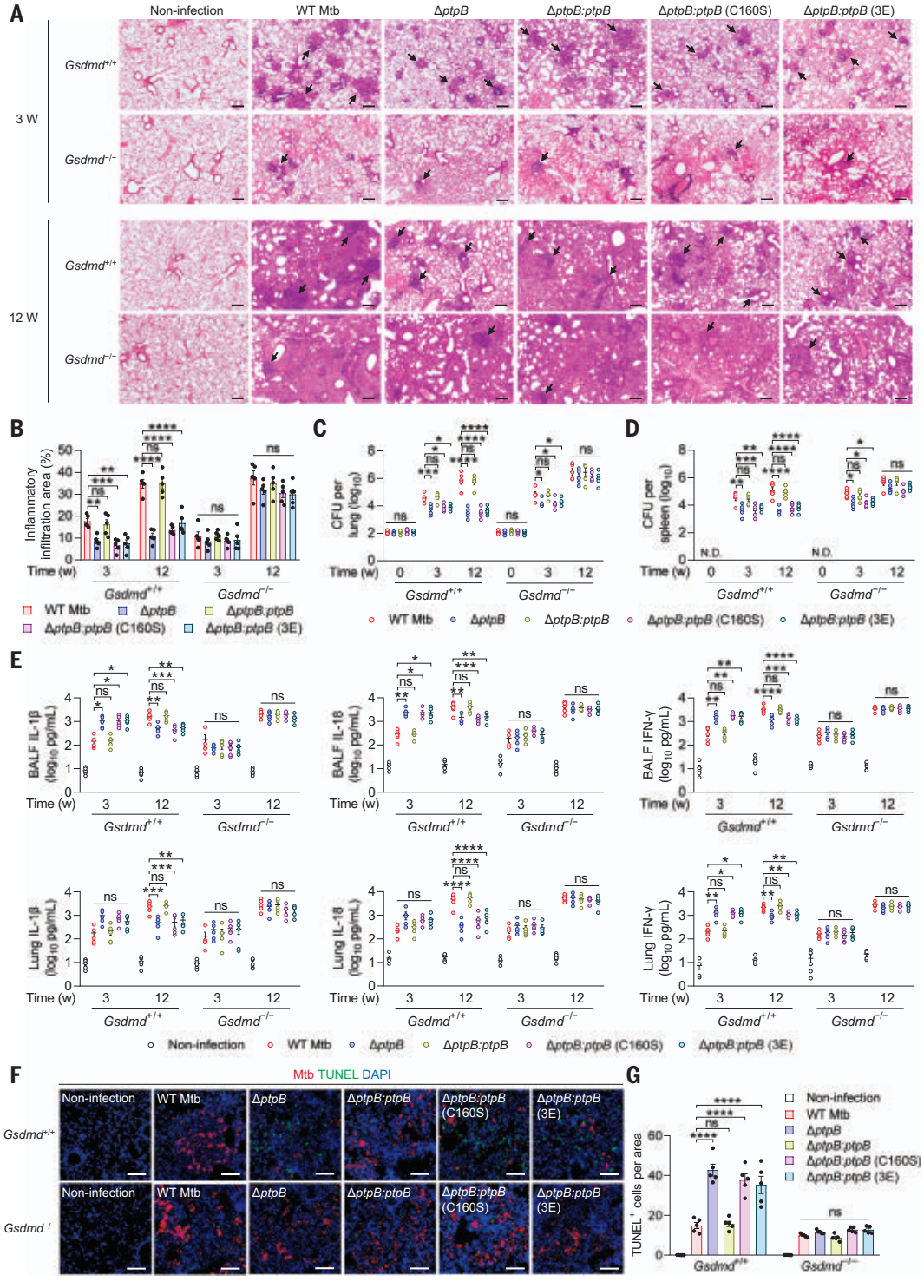

Fig. 6. PtpB-ubiquitin interaction is required by Mtb to evade host GSDMD-dependent immunity. (**A**) Histopathology of lung sections from *Gsdmd*$^{+/+}$ or *Gsdmd*$^{-/-}$ mice infected with or without the indicated Mtb strains by aerosol (~ 100 CFUs) for 0 to 12 weeks. Arrows indicate foci of cellular infiltration. Scale bars, 200 μm. (**B**) Quantitation of inflammatory areas in the lungs of mice infected with Mtb as in (A). (**C** and **D**) Bacterial CFUs in lungs (C) and spleens (D) of mice infected with Mtb as in (A). N.D., not detectable. (**E**) ELISA of cytokines (IL-1β, IL-18, and IFN-γ) in bronchoalveolar lavage fluid (BALF; upper) or lung homogenates (lower) of mice infected with Mtb as in (A). (**F**) TUNEL staining of lung sections from *Gsdmd*$^{+/+}$ or *Gsdmd*$^{-/-}$ mice at 3 weeks after infection with Mtb. Scale bars, 100 μm. (**G**) Quantitation of TUNEL-positive cells in lungs of mice infected with Mtb as in (F). $P > 0.05$, not significant (ns); $^{*}P < 0.05$; $^{**}P < 0.01$; $^{***}P < 0.001$; $^{****}P < 0.0001$ (two-way ANOVA with Dunnett's post-hoc test). Data are shown as mean ± SEM of $n = 5$. Data are representative of at least three independent experiments.

Gsdmd in mice abolished the differences in cytokine amounts in the BALF and lungs of mice infected with different Mtb strains (Fig. 6E). Accordingly, the *ptpB*-deleted or *ptpB*-mutated Mtb strain, but not the *ptpB*-sufficient strain, caused higher mRNA levels of *Il1b*, *Il18*, and *Ifng* in *Gsdmd*$^{-/-}$ mice than those in *Gsdmd*$^{+/+}$ mice at 12 weeks after infection (fig. S13E). The elevated amounts of inflammatory cytokines in *Gsdmd*$^{-/-}$ mice at 12 weeks after infection are probably due to excessive bacterial loads of different Mtb strains. Finally, compared with the WT and *ptpB*-complemented strains, *ptpB*-deleted and *ptpB*-mutated Mtb strains induced more TUNEL-positive cells with decreased bacterial staining in mouse lungs in a *Gsdmd*-dependent manner (Fig. 6, F and G), indicating enhanced host GSDMD-mediated pyroptosis and antibacterial immunity (*28*). Taken together, our results suggest that PtpB is required by Mtb to evade host GSDMD-mediated immune responses, depending on the Ub-activated lipid phosphatase activity of PtpB.

Discussion

Mtb represents an extraordinary paradigm of intracellular pathogens that deliver multiple

effectors into host cells for immune evasion (*3*, *29*). Our data indicate that nearly one-seventh of Mtb genes encode proteins containing eukaryotic-like functional domains or motifs, demonstrating the astute adaptation of Mtb to its human host after eons of coevolution (*30*). Among these potential pathogenic factors, we identified PtpB as a potent inhibitor of host pyroptosis that subverts GSDMD functions to facilitate Mtb intracellular survival. Recently, the emerging role of pyroptosis in host anti-infection and tumor immunity has attracted increasing attention, and gasdermin family members have been considered as key immune factors targeted by pathogens such as *Shigella* (*31*–*34*). However, their exact roles in TB pathogenesis remain unclear. We showed that GSDMD-mediated pyroptosis and inflammatory cytokine release play critical roles in host anti-infection immunity, which is counteracted by the Mtb effector protein PtpB. When Mtb lacks functional PtpB, it cannot counteract host GSDMD-mediated immunity, meaning that GSDMD could confer prompt and robust host protective immune responses against infection in the early stage of infection, thus restricting bacterial survival to avoid host excessive pathogenic inflammatory responses at a later stage. Therefore, PtpB may be an attractive target for improving the immune efficacy of Bacille Calmette-Guérin, the only licensed TB vaccine whose genome harbors a PtpB-encoding gene identical to that of Mtb (*35*).

Disordered cellular lipid metabolic homeostasis has recently been linked to TB pathogenesis but is not fully understood (*36*–*38*). Phosphoinositides are a group of cellular membrane lipids involved in pyroptosis (*10*, *11*). However, whether and how they are regulated by invading pathogens during this immune process remains largely unclear. Mtb PtpB has been linked to host cell death and innate immune pathways (*14*, *15*). Here, we showed that PtpB can dephosphorylate host cell membrane PI4P and PI(4,5)P_2 upon activation by Ub to efficiently suppress GSDMD-mediated inflammatory responses. Our data reveal a regulatory role of pathogen-derived phospholipid phosphatase in the GSDMD-dependent pyroptosis and cytokine release, extending our understanding of the elaborate regulatory mechanism of cellular inflammasome signaling pathways during pathogen infection.

The mammalian Ub system subtly modulates diverse immune responses by controlling protein ubiquitination; thus, it is a common target of effectors from pathogens, including Mtb (*4*, *39*). In this study, we revealed that Mtb-secreted PtpB localizes to the host cell membrane, where it efficiently dephosphorylates phosphoinositides upon hydrophobic interaction with cytosolic Ub to impair GSDMD-mediated immunity. A structural study revealed that PtpB harbors a buried phosphatase active site covered by a dynamic lid (*25*). Therefore, the activation of PtpB through Ub binding suggests a delicate strategy by which Mtb precisely controls the catalytic activity of PtpB to counteract the host immune system. Our data elucidate a strategy by which pathogens hijack Ub to inhibit host pyroptosis by altering the phospholipid composition of the host membrane. Our discovery of the PtpB UIM-like domain, which is not homologous to any human protein, may provide potential selectivity for the development of anti-TB therapies.

Materials and methods

Bacterial strains and plasmids

Escherichia coli DH5α were grown in flasks using LB medium for genetic manipulations. Mtb H37Rv strains were grown in Middlebrook 7H9 broth (7H9) supplemented with 10% oleic acid-albumin-dextrose-catalase (OADC) and 0.05% Tween-80, or on Middlebrook 7H10 agar supplemented with 10% OADC. Mtb with deletion of *ptpB* (NCBI gene ID: 886842; Δ*ptpB*) was created using the pJV53 system (*40*). pMV306 plasmid (kindly provided by W. R. Jacobs, Albert Einstein College of Medicine, Yeshiva University) was used to complement the strain Mtb Δ*ptpB* with WT *ptpB* or create variant strains Mtb Δ*ptpB:ptpB* (C160S) and Mtb Δ*ptpB:ptpB* (3E). pSC300 plasmid was used for expression of Mtb proteins with C-terminal green fluorescent protein (GFP) in Mtb. The mammalian expression plasmids for hemagglutinin (HA)–tagged ubiquitin (Ub); Myc-tagged human AIM2, ASC, and IL-1β; and Flag-tagged human caspase-1, NLRP3, and GSDMD-N were kindly provided by F. Shao (National Institute of Biological Sciences, Beijing). HA-tagged K6 only, K11 only, K27 only, K29 only, K33 only, K48 only, and K63 only Ub were kind gifts from L. Zhang (Beijing Institute of Lifeomics, Beijing). The full-length cDNA of PtpB was amplified from Mtb H37Rv genomic DNA, and those of human GSDMD, NEDD8, and ATG12 were amplified from U937 cDNA. Nucleotide sequences for expressing OSH2-PH×2, Lyn_{11}-FRB, and FKBP-Pseudojanin (PJ) were designed on the basis of previous studies (*23*, *41*) and were synthesized by GenScript Biotechnology (Nanjing) (see table S1 for details). The sequence information of these recombinant genes (GenBank accession numbers OP056760, OP056761, and OP056762, respectively) has been deposited at GenBank (https://www.ncbi.nlm.nih.gov/genbank/) and is publicly available as of the date of publication. For expression in mammalian cells, genes were cloned into the vector pcDNA6A, pEGFP-N1, pEGFP-C1, or pmCherry-N1. Prokaryotic expression plasmids were constructed by inserting the genes into the vector pGEX-6p-1 or pET30a. Point mutations were generated by using Fast Mutagenesis Kit V2 (Vazyme Biotech). All of the strains, plasmids, and primers used in this study are detailed in table S1.

Antibodies and reagents

Rabbit antibodies against Mtb PtpB or PtpA were prepared and purified as described previously (*5*, *18*). Briefly, a total of 5 mg of glutathione *S*-transferase (GST)–PtpB or GST-PtpA fusion proteins were purified and solubilized in Freund's complete adjuvant for injection into rabbits. The antibodies specific to PtpB or PtpA were isolated by passaging the immunized rabbit serum on protein A agarose (Santa Cruz). All of the antibodies used in this study are listed in table S2. Phosphoinositides including PI3P, PI4P, PI5P, PI(3,4)P_2, PI(3,5)P_2, PI(4,5)P_2, and PI(3,4,5)P_3 were purchased from Echelon Biosciences (Cat# P-3016, P-4016, P-5016, P-3416, P-3516, P-4516, and P-3916, respectively). Phosphotyrosine peptides pTyr-EGFR (DADE-pY-LIPQQG) and pTyr-IGF1R (TRDI-pY-ETDYYRK) were synthesized by GenScript Biotechnology (Nanjing). Lipopolysaccharide from *E. coli* 0111:B4 (Cat# tlrl-eblps), nigericin (Cat# tlrl-nig), and poly(dA:dT) (Cat# tlrl-patc) were purchased from InvivoGen. Pik-93 (Cat# S1489) and rapamycin (Cat# S1039) were purchased from Selleck. Phenylarsine Oxide (PAO) was purchased from Shanghai Yuanye Bio-Technology (Cat# Y17991). Ionomycin was purchased from Abcam (Cat# ab120116). Recombinant mouse IL-1 receptor antagonist (IL-1RA; Cat# 769702) and IL-18 binding protein (IL-18BP; Cat# HY-P75841) were purchased from BioLegend and MedChemExpress, respectively. Human Ub_4 WT Chains (K48-linked), Human Ub_4 WT Chains (K63-linked), and Human Ub_4 WT Chains (M1-linked) were purchased from Boston Biochem (Cat# UC-210B, UC-310B, and UC-710B, respectively).

Cell lines

HEK293T (ATCC, Cat# CRL-3216) and HeLa (ATCC, Cat# CCL-2) cells were obtained from the American Type Culture Collection (ATCC). Immortalized murine bone marrow–derived macrophages (iBMDMs) derived from *Gsdmd*$^{-/-}$ mice on C57BL/6 genetic background were kindly provided by F. Shao (National Institute of Biological Sciences, Beijing, China). HEK293T, HeLa, and iBMDMs were cultured in Dulbecco's modified Eagle's medium (DMEM; Gibco) with 10% fetal bovine serum (FBS; Gemini Bioproducts). Cells were cultured at 37°C in a 5% CO_2 incubator.

Mice

WT (*Gsdmd*$^{+/+}$) C57BL/6 mice were purchased from Beijing Vital River Laboratory Animal Technology. *Gsdmd*-deficient (*Gsdmd*$^{-/-}$) mice on C57BL/6 genetic background were a kind gift of F. Shao (National Institute of Biological Sciences, Beijing, China). *Gsdmd*$^{-/-}$ mice were bred with C57BL/6 mice to obtain *Gsdmd*$^{+/-}$

heterozygotes. *Gsdmd*$^{-/-}$ mice and littermate controls obtained from heterozygote crosses were used for all experiments. All mice were housed in a specific pathogen–free (SPF) facility according to standard humane animal husbandry protocols, which were approved by the animal care and use committee of the Institute of Microbiology (Chinese Academy of Sciences).

Prediction of Mtb-secreted eukaryotic-like proteins

The entire genome sequence and information of Mtb H37Rv were obtained from National Center for Biotechnology Information (NCBI; RefSeq: NC_000962.3). Each corresponding sequence of encoded proteins was downloaded from UniProt database (https://www.uniprot.org/proteomes/UP000001584/), and their harboring functional domains were predicted with the SMART database (http://smart.embl-heidelberg.de/). Each protein-encoding gene was then functionally classified using the PANTHER database (http://www.pantherdb.org/). Mtb proteins that contain one or more eukaryotic-like domains or motifs identified from Effective DB (https://effectivedb.org/) were considered as eukaryotic-like proteins. The subcellular localization of each Mtb protein was annotated according to the published articles (see data S1). Circos plot that depicts Mtb genome features was generated with Circos 0.69-8 (http://www.circos.ca/soft-ware/) using the information of Mtb H37Rv genome location from Mycobrowser (https://mycobrowser.epfl.ch/).

Screening for Mtb inhibitors of inflammasome pathway

The full-length cDNAs of 201 Mtb proteins were amplified from Mtb H37Rv genomic DNA (see data S3) and were cloned into the vector p3× Flag-CMV-14 (Sigma-Aldrich). HEK293T cells in 24-well cluster plates were transfected with pCS2-Myc-ASC (50 ng), pCS2-Flag-caspase-1 (50 ng), and pCS2-Myc-IL-1β (325 ng) in combination with pCS2-Myc-AIM2 or pCS2-Flag-NLRP3 (75 ng), and a Mtb protein expression plasmid or the control empty plasmid (250 ng) using Hieff Trans Liposomal Transfection Reagent (Yeasen). At 24 hours after transfection, cell-free supernatants were collected, and IL-1β concentrations were measured by ELISA. For inflammasome reconstitution assay, cells were collected and lysed for immunoblotting with the indicated antibodies to analyze the expression of each transfected plasmid.

In vitro growth kinetics of Mtb strains

To determine the in vitro growth kinetics, Mtb strains were inoculated into Middlebrook 7H9 broth supplemented with 10% OADC and 0.05% Tween-80 at OD_{600} of ~0.1 and cultivated at 37°C. Growth of the cultures was followed by measuring the light absorbance at 600 nm every 3 days.

Preparation of BMDMs

BMDMs were collected from tibiae and femurs of 6-week-old male mice. After lysis of red blood cells, BMDMs were cultured in DMEM supplemented with 10% FBS, 1% penicillin-streptomycin solution (Caisson) and murine macrophage colony-stimulating factor (Pepro Tech) for 4 to 6 days. For each experimental design, at least two *Gsdmd*$^{-/-}$ mice and littermate controls were chosen to prepare the BMDM cells for analysis.

Macrophage infection and colony-forming unit counting

For macrophage infection, Mtb in Middle brook 7H9 medium (BD Biosciences) with 0.05% Tween-80 and 10% OADC enrichment (BD Biosciences) were grown to midlogarithmic phase at OD_{600} of ~0.6. Macrophages were seeded in six-well plates at a density of 5.0×10^5 cells per well and precultured in DMEM medium supplemented with 10% FBS for 12 hours before infection. Mtb were collected and washed twice in 1× phosphate-buffered saline (PBS) containing 0.05% Tween-80 and were then pelleted and thoroughly resuspended using DMEM medium with 0.05% Tween-80. Macrophages were then infected with Mtb strains at a multiplicity of infection (MOI) of 5 for 1 hour at 37°C to allow bacterial entry into cells. Thereafter, the culture media were discarded, and the cells were washed three times with 1× PBS to exclude noninternalized bacteria and were then incubated again with the fresh medium. At each designated time point, the cells and culture supernatants were collected for different analyses. To measure Mtb survival in macrophages, cells were lysed in 7H9 broth containing 0.05% SDS for 10 min. Bacterial colony-forming units (CFUs) were determined by serial-dilution plating on 7H10 agar plates, and the percent survival of Mtb was calculated by dividing the bacterial CFUs at the designated time point by that at time 0.

Cell transfection and retroviral transduction

Transient transfection of plasmid DNA in HEK293T cells or HeLa cells was carried out with Hieff Trans Liposomal Transfection Reagent (Yeasen) according to the manufacturer's instructions. To generate *Gsdmd*$^{-/-}$ iBMDMs stably expressing hGSDMD, the gene encoding hGSDMD was cloned into the retroviral plasmid pMSCVpuro. 293T cells were cotransfected with this retroviral construct and two packaging plasmids, pCMV-VSV-G and pCL-Eco, for 48 hours. The retroviral supernatant was then collected and filtered through a 0.45-μm filter and was used to transduce *Gsdmd*$^{-/-}$ iBMDMs in the presence of 4 μg/ml polybrene (Santa Cruz). Transduced cells were selected using 1 μg/ml puromycin (InvivoGen), and the expression of hGSDMD was verified by immunoblotting with anti-GSDMD antibody. For expression of exogenous PtpB or Lyn_{11}-FRB-GFP and GFP-FKBP-PJ in macrophages, in vitro transcribed mRNAs that encode these reconstituted proteins were transfected into the cells, as described previously (*42*, *43*). Briefly, pCDNA6A and pCDNA6A-PtpB vectors were used to generate the linearized DNA templates for transcription of the control and *ptpB* mRNAs, respectively, with a forward primer containing the T7 promotor sequence ahead of the start codon and a reverse primer located downstream of the stop codon; likewise, recombinant pEGFP-N1-Lyn_{11}-FRB and pEGFP-C1-FKBP-PJ vectors were used to generate the DNA templates for Lyn_{11}-FRB-GFP and GFP-FKBP-PJ, respectively (see table S1 for primers). The indicated mRNAs were then generated in vitro using the HiScribe T7 ARCA mRNA Kit (New England BioLabs, Cat# E2060), with incorporation of the modified nucleosides 5-methyl-CTP and pseudo-UTP (APExBIO, Cat# B7972 and B7967, respectively) to minimize the immunogenicity and enhance the stability (*44*). The transcribed mRNA was then dephosphorylated by Antarctic phosphatase (New England BioLabs, Cat# M0289) to avoid recognition by the cytoplasmic RNA sensors in macrophages (*45*, *46*). Finally, the transcribed mRNA was purified using MEGAclear Transcription Clean-Up Kit (Thermo Fisher Scientific, Cat# AM1908). The purified mRNA was then transfected into BMDMs cultured in 6-well plates (500 ng for a total of 2.5×10^5 cells per well) using jetMESSENGER (Polyplus-transfection, Cat# 101000056) in accordance with the manufacturer's instructions. After transfection for 8 hours, the expression of the indicated proteins was verified by immunoblotting with anti-PtpB or anti-GFP antibodies or was examined by confocal microscopy.

Immunoblotting analysis and immunoprecipitation

Cells were lysed in the Cell Lysis Buffer for Western and Immunoprecipitation (IP) (Beyotime) or Radioimmunoprecipitation Assay (RIPA) Lysis Buffer (Beyotime) supplemented with 1 mM phenylmethanesulfonyl fluoride (PMSF). Proteins were separated by SDS–polyacrylamide gel electrophoresis (SDS-PAGE) and transferred to polyvinylidene difluoride membranes (Millipore). The membranes were blocked with 5% skimmed milk powder in tris-buffered saline with 0.1% Tween-20 (TBST) for 1 hour at room temperature (RT) and subsequently incubated with primary antibodies overnight at 4°C. The membranes were then incubated with goat anti-mouse IgG or goat anti-rabbit IgG conjugated to horseradish peroxidase (HRP) for 1 hour at RT after three washes of 10 min each with TBST. Finally, the membranes were developed by Immobilon Western Chemiluminescent HRP Substrate (Millipore) after three washes with TBST and exposed to x-ray film.

For immunoprecipitation, cells were lysed in a lysis buffer containing 50 mM Tris-HCl

(pH 7.4), 150 mM NaCl, 1 mM ethylenediaminetetraacetic acid (EDTA), 1% Triton X-100, and 1% protease inhibitor cocktail (Bimake). Cell lysates were incubated with Monoclonal Anti-HA Agarose (Sigma-Aldrich) for immunoprecipitation of HA-tagged protein in a vertical rotator at 4°C for 4 hours. After five washes with lysis buffer, the immunocomplexes bound in affinity beads were analyzed by SDS-PAGE and blotted with indicated antibodies.

Protein purification

E. coli BL21 (DE3) strain was used for bacterial expression of GST-fused Mtb PtpA and PtpB and its mutants (using pGEX-6P-1 vector), and of His_6-tagged NEDD8, ATG12, and Ub and its mutant (using pET30a vector). The bacterial strains were grown in LB medium at 37°C until OD_{600} = 0.6. For GST-PtpB, GST-PtpA, His_6-Ub, and their mutants, isopropyl-β-D-thiogalactopyranoside (IPTG) was subsequently added to a final concentration of 400 μM, and cultures were shaken for further growing at 16°C for 16 hours. For His_6-tagged NEDD8 and ATG12, IPTG was used at 600 μM, and the cultures were shaken at 37°C for 4 hours. Cells were then harvested by centrifugation at 6,500*g* for 10 min and suspended in a buffer containing 20 mM Tris-HCl (pH 7.5) and 150 mM NaCl for cell-breaking with using Low-temperature Ultra-high Pressure Continuous Flow Cell Disrupters (JNBIO) or an Ultrasonic Homogenizer (Scientz Biotechnology). Glutathione Sepharose 4B (GE Healthcare) and Nickel Nitrilotriacetic Acid Agarose (Qiagen) were used, respectively, for purification of GST-fused proteins or His_6-tagged proteins by means of affinity chromatography, followed by size exclusion chromatography on a Superose 6 Increase 10/300 GL column (GE Healthcare).

In vitro precipitation assay

For the precipitation assay, 10 μg of GST or GST-protein fusions were immobilized onto 20 μl of Glutathione Sepharose 4B resins in 1 ml binding buffer (50 mM Tris, pH 7.5, 150 mM NaCl, 5 mM dithiothreitol, and 0.1% NP-40) supplemented with 1% protease inhibitor cocktail for 1 hour at 4°C. The resins were then washed three times with binding buffer and incubated with 10 μg of purified His_6-Ub, His_6-Ub (I44A), K48-linked poly-Ub (Ub_4), K63-linked poly-Ub (Ub_4), or M1-linked poly-Ub (Ub_4) in 1 ml binding buffer supplemented with 0.1 mg/ml bovine serum albumin (BSA). For analysis of the interactions between PtpB and Ub-like proteins (including NEDD8, FAT10, ISG15, SUMO1, UFM1, ATG12, ATG8, and URM1), GST-PtpB and His_6-tagged Ub (as control) or Ub-like proteins were used at 0.3 and 0.6 μM, respectively. Except that NEDD8 and ATG12 were expressed and purified from *E. coli* (as described above), His_6-tagged recombinant Ub-like proteins including human FAT10 (Cat# ab113594), ISG15 (Cat# ab268685), SUMO1 (Cat# ab140417), UFM1 (Cat# ab104461), and URM1 (Cat# ab105598) were purchased from Abcam, and ATG8 (Cat# 14549-H07E) was purchased from Sino Biological. After 4 hours of incubation at 4°C, beads were extensively washed, and the bound protein complexes were subjected to SDS-PAGE and blotted with indicated antibodies.

Immunofluorescence microscopy

Alexa Fluor (488, 594, or 350) succinimidyl esters (Invitrogen) were used for Mtb staining before infection, as described previously (*47*). HeLa cells or macrophages were seeded on poly-lysine–coated coverslips and transfected or infected, as described above. For cell membrane staining, cells were gently washed with Hank's balanced salt solution (HBSS; Beyotime), and 50 μg/ml CF350-conjugated wheat germ agglutinin (Biotium) was applied to the cells on ice for 5 min in HBSS. Cells were then washed three times in HBSS and fixed in 4% paraformaldehyde (PFA) for 15 min at RT. Thereafter, cells were washed in 1× PBS and permeabilized with 0.5% Triton X-100 for 5 min. After three washes, the cells were blocked with 2% BSA for 30 min, subsequently incubated in indicated primary antibodies (anti-ASC: 1:400; anti-Flag: 1:400; anti-PtpA: 1:200; anti-PtpB: 1:800) diluted in 2% BSA for 1 hour. Cells were then washed in 1× PBS again and incubated with Alexa Fluor 594 or fluorescein isothiocyanate (FITC)–labeled secondary antibody (1:200; ZSGB-BIO) for another hour. After successive washing with 1× PBS and deionized water, the coverslips were mounted onto glass slides using 4′,6-diamidino-2-phenylindole (DAPI) Staining Solution (Beyotime). Confocal images were taken with Olympus FV1000 confocal microscope and analyzed by FV10-ASW 4.2 (Olympus; https://www.olympus-global.com/).

For live-cell imaging, cells were plated in 20-mm glass-bottom dishes (NEST), which were placed in a humidified chamber supplemented with 5% CO_2 at 37°C during imaging. Images were acquired on an Olympus FV3000RS confocal laser scanning microscope equipped with a 60× silicone oil objective and were analyzed by FV31S-SW 2.3.1.163 (Olympus; https://www.olympus-global.com/).

Proximity ligation in situ assay

Proximity ligation assay (PLA) was performed using Duolink In Situ Detection Reagents Red (Sigma-Aldrich, Cat# DUO92008) according to Duolink PLA Fluorescence Protocol provided by the manufacturers. Briefly, ~1×10^5 BMDM cells were seeded on poly-lysine–coated coverslips and were infected with the indicated Mtb strains stained with Alexa Fluor 488 succinimidyl esters at a MOI of 5 for 24 hours. Cells were then washed, fixed, and permeabilized, as described above, and blocked with Duolink Blocking Solution for 1 hour at 37°C. Thereafter, cells were incubated with mouse anti-mCaspase-1 antibody (diluted at 1:400) and rabbit anti-mASC (diluted at 1:400) or anti-Mtb (diluted at 1:800) antibody, in the Duolink Antibody Diluent for 1 hour at 37°C. For controls that determine the specificity of PLA, the anti-mCaspase-1 antibody was replaced by Mouse IgG1 Isotype Control (AdipoGen; Cat# AG-35B-0003PF), or the anti-mASC or anti-Mtb antibody was replaced by Normal Rabbit IgG (Cell Signaling Technology, Cat# 2729). After two washes, cells were further incubated with Duolink In Situ PLA probes (Anti-Mouse PLUS and Anti-Rabbit MINUS; Sigma-Aldrich, Cat# DUO92001 and DUO92005, respectively) diluted at 1:5 in the Duolink Antibody Diluent for another 1 hour at 37°C, allowing hybridization of PLA probes only if they were in close proximity (<40 nm). After two washes, cells were then incubated with a DNA ligase diluted at 1:50 in the Ligation Buffer for 30 min at 37°C. Next, cells were washed twice and incubated with a DNA polymerase at a 1:80 dilution in the Amplification Buffer for 90 min at 37°C. Finally, the coverslips were mounted onto glass slides using Duolink PLA Mounting Medium with DAPI and were subjected to confocal microscopy.

Plasma membrane and internal membrane staining

Immunocytochemistry for detection of PM PI4P and GSDMD-N was performed as previously described in detail (*19*). Briefly, cells were plated on poly-lysine–coated coverslips (for microscopy analysis) or collected in a 1.5-ml Eppendorf tube (for flow cytometer) and were fixed by 1× PBS containing 4% formaldehyde (FA) and 0.2% glutaraldehyde for 15 min at RT. After rinsing three times with 1× PBS containing 50 mM NH_4Cl, cells were chilled on ice for 5 min. Cells were then blocked and permeabilized with a piperazine-N,N′-bis(2-ethanesulfonic acid) (PIPES)–buffered saline (20 mM PIPES, pH 6.8, 137 mM NaCl, 2.7 mM KCl, 50 mM NH_4Cl) containing 5% normal goat serum (NGS; Yeasen) and 0.5% saponin (Sigma-Aldrich) on ice for 45 min. Primary antibodies (anti-PI4P: 1:200; anti-GSDMD-N: 1:100) were applied in PIPES-buffered saline with 5% NGS and 0.1% saponin on ice for 1 hour. Cells were then washed thrice in PIPES-buffered saline followed by incubation with Alexa Fluor 594 secondary antibody (1:200; ZSGB-BIO) in PIPES-buffered saline containing 5% NGS and 0.1% saponin on ice for 45 min. Cells were then rinsed four times with PIPES-buffered saline and were postfixed for 10 min on ice and 5 min at RT with 2% FA in 1× PBS. Thereafter, cells were washed thrice in 1× PBS containing 50 mM NH_4Cl and rinsed once in distilled water. Cells were then stained with DAPI for microscopy

analysis, as described above, or were resuspended in 1× PBS for flow cytometer analysis on a Fortessa flow cytometer (BD Biosciences). For IM PI4P staining, all steps were performed at RT, and a similar protocol was used, except that cells were fixed with 2% FA, and saponin was omitted, with the cells instead permeabilized with 20 μM digitonin (Abcam) for 5 min before staining (*19*).

Quantitative image analysis

For measurement of PM localization of PtpA or PtpB, the colocalizations of WGA with PtpA or PtpB were measured with FV10-ASW 4.0 (Olympus). Briefly, a line was drawn along the boundary of the cell to fully surround the cell. Then, the integrated intensity of each channel of interest and the Pearson's correlation coefficient between the channels of interest were determined. The fluorescence intensity of each fluorescent protein or lipid of interest was determined using the drawing/selection tool with the same software. Data are shown as mean ± SEM of at least four biological replicates, and ~100 cells were examined for each biological replicate. Results are representative of at least three independent experiments.

Intracellular potassium measurement

BMDM cells were seeded on poly-lysine–coated coverslips and infected with or without Mtb strains at a MOI of 5. At 48 hours after infection, medium was replaced with FBS-free DMEM containing 10 μM of Enhanced Potassium Green-2 (EPG-2) AM (Shanghai Maokang Biotechnology), which is a potassium-specific probe, and 0.5% (w/v) pluronic acid F-127, which aids in efficient permeation of EPG-2 AM into the cells. After 1 hour of incubation at 37°C, cells were extensively washed with 1× PBS followed by immunofluorescence microscopy analysis using anti-Mtb antibody. For fluorescence measurement, BMDM cells were plated in 96-well clear bottom black plates and were infected with Mtb strains as described above. After incubation with EPG-2 AM, the fluorescence was determined with a Cytation 5 Plate Reader (BioTek, USA).

Cell membrane integrity assay

BMDM cells were seeded on poly-lysine–coated coverslips and infected with or without Mtb strains pre-stained with Alexa Fluor 488 succinimidyl ester at a MOI of 5. At 48 hours after infection, 15 μM of propidium iodide (PI; Beyotime) was added to the medium for monitoring cell membrane integrity. After 20 min of incubation at 37°C, cells were washed with 1× PBS thrice followed by immunofluorescence microscopy analysis as described above. Approximately 100 cells were examined for quantitative analysis of PI-positive cells, and results are represented as mean ± SEM from four independent experiments.

Cell fractionation assay

For separation of the cytosol and PM fractions of BMDMs, cells were seeded in 10-cm plates and infected with indicated Mtb strains for 48 hours as described above. Approximately 2×10^7 cells were then harvested for separation of total cellular components into different fractions with Minute Plasma Membrane Protein Isolation and Cell Fractionation Kit (Invent Biotechnologies) according to the manufacturers' instructions. Finally, the cytosol and PM fractions were collected, and ~100 μg cytosolic and PM proteins were separately dissolved in 100 μl SDS sample buffer for analysis by SDS-PAGE and blotted with indicated antibodies.

For separation of the bacterial and macrophage cytosolic fractions of Mtb-infected BMDMs, cells were lysed in hypotonic lysis buffer (containing 10 mM HEPES, pH 7.9, 1.5 mM $MgCl_2$, 10 mM KCl, 0.34 M sucrose, 10% glycerol, 0.1% Triton X-100, and 1% protease inhibitor cocktail) as described previously (*5*). The lysis mixture was then centrifuged at 4°C, 1300*g* for 10 min to pellet the bacteria with macrophage nuclei. The supernatant was collected as the cytosolic fraction of macrophages. The bacteria (with macrophage nuclei) and macrophage cytosolic fraction were dissolved in SDS sample buffer for analysis by SDS-PAGE and blotted with indicated antibodies.

Enzyme-linked immunosorbent assay and cell cytotoxicity analysis

Cell culture media, mouse bronchoalveolar lavage fluid (BALF), or cell-free supernatants from mouse lung homogenates were collected for quantitative detection of cytokines including IL-1β, IL-18, TNF-α, IL-6, IL-12 (p40), IL-10, or IFN-γ with commercial ELISA kits according to the manufacturers' instructions. Human and mouse IL-1β ELISA kits and mouse IL-18, TNF-α, IL-6, IL-12 (p40), and IL-10 ELISA kits were purchased from RayBiotech, and mouse IFN-γ ELISA kit was purchased from CloudClone Corp.

Quantitative analysis of cellular phosphoinositides

To determine the concentrations of PM- and IM-derived PI4P and $PI(4,5)P_2$ from BMDMs, ~2×10^7 cells were collected for cell fractionation to obtain the PM and IM fractions using Minute Plasma Membrane Protein Isolation and Cell Fractionation Kit (Invent Biotechnologies). The separated membrane fractions were then resuspended in ice-cold 0.5 M trichloroacetic acid (TCA) in conical glass centrifuge tubes (Kimble) and incubated on ice for 5 min, followed by centrifugation at 1500*g* for 7 min at 4°C. The pellet was then washed two times with 5% TCA containing 1 mM EDTA at RT and was resuspended in MeOH:$CHCl_3$ (2:1) with 10-min vortex to extract neutral lipids (twice). The supernatant (containing neutral lipids) was discarded after centrifugation at 1500*g* for 5 min at RT, and the pellet was resuspended in 750 μl MeOH:$CHCl_3$:HCl (80:40:1) with 25-min vortex to extract acidic lipids. The supernatant (containing acidic lipids) was then collected after centrifugation at 1500*g* for 5 min at RT and was mixed with 250 μl of $CHCl_3$ and 450 μl of 0.1 M HCl. After 30-s vortex, the mixture was centrifuged at 1500*g* for 5 min at RT, and the organic (lower) phase was collected into the screw-cap glass vials (Thermo Fisher Scientific) and was dried in a vacuum dryer. The dried lipid abstracts were stored at −80°C until use, or immediately reconstituted in relevant detecting buffer with sonication for 10 min at RT using a water bath sonicator, and were then subjected to quantitative detection of PI4P and $PI(4,5)P_2$ using PI4P and $PI(4,5)P_2$ Mass ELISA Assay Kits (Echelon Biosciences), respectively, according to the manufacturers' instructions.

Quantitative PCR analysis

Mtb-infected macrophages or mouse lung homogenates were used for total RNA extraction with RNeasy Plus Mini Kit according the manufacturers' instructions (Qiagen). The reverse transcription of RNA was accomplished by using a 1st Strand cDNA Synthesis Kit (Yeasen) and performed to quantitative PCR (qPCR) analysis with Hieff qPCR SYBR Green Master Mix (Yeasen) on ABI 7500 system (Applied Biosystems). Quantitative expression of targeted gene was normalized to *Gapdh*. All qPCR primers are listed in table S1.

Protein-liposome binding assay

Liposomes were prepared as previously described (*10*). Briefly, phosphatidylcholine (PC; Avanti Polar Lipids, Cat# 850457), phosphatidylinositol (Avanti Polar Lipids, Cat# 850149), PI4P (Avanti Polar Lipids, Cat# 840045), and $PI(4,5)P_2$ (Avanti Polar Lipids, Cat# 850155) were dissolved in MeOH:$CHCl_3$ (20:9). Thereafter, 0.4 μmol of PC was mixed with 0.1 μmol of phosphatidylinositol, PI4P, or $PI(4,5)P_2$ in the screw-cap glass vials (Thermo Fisher Scientific), and the mixture was dried in a vacuum dryer. The dried lipids were then reconstituted in 500 μl binding buffer (20 mM HEPES, pH 7.5 and 150 mM NaCl). Liposomes were produced by extrusion of the hydrated lipids through a 0.1-μm polycarbonate filter 35 times using the Mini-Extruder device (Avanti Polar Lipids). For liposome-binding assay, purified GST-fused PtpB or its mutants (0.5 μM) were incubated with the indicated liposomes (containing 0.5 mM lipids) at RT for 1 hour in a total volume of 100μl. The mixtures were then centrifuged at 100,000*g* for 20 min at 4°C in a Beckman Optima MAX-XP ultracentrifuge. The liposome-free supernatant was collected, and

the liposome pellets were further washed twice with 100 μl binding buffer by re-centrifugation before collection. The supernatant and pellet fractions were then analyzed by SDS-PAGE and blotted using anti-GST antibody.

Protein-lipid binding assay

GST or GST-fused PtpB proteins were spotted on PIP strips or membrane lipid strips (Echelon Biosciences) according to the manufacturer's instructions. Briefly, lipid strips were blocked with 1× PBS containing 0.1% Tween-20 (PBST) and 3% fatty acid–free bovine serum albumin (BSA; Biotopped) for 1 hour at RT. The strips were then incubated with 2 μg/ml protein diluted in PBST buffer containing 3% BSA for 1 hour at RT, followed by three washes with PBST buffer. Membrane-bound proteins were detected by incubating the lipid strips with anti-GST-tag HRP-DirecT antibody (MBL International) diluted 1: 2000 in PBST buffer containing 3% BSA for 1 hour at RT. After washing three times with PBST buffer, proteins were visualized using Immobilon Western Chemiluminescent HRP Substrate (Millipore) and exposed to x-ray film.

Intracellular delivery of phosphoinositides

Shuttle PIP Kits purchased from Echelon Biosciences were used for intracellular delivery of phosphoinositides according to their protocols. In brief, 2×10^5 BMDM cells were cultured in 500 μl DMEM with 10% FBS in 24-well plates and infected with or without Mtb strains for 1 hour as described above. Phosphoinositides and polyamine carriers were reconstituted in DMEM and combined with a ratio of 1:1 (100 μM final concentration each) for 10 min at RT. Then the mixtures were diluted with DMEM and were used for incubation of cells for 4 hours at 37°C. The final phosphoinositide and carrier concentrations on cells were both 10 μM. For the negative control, cells were treated with carriers only according to this procedure. After treatment, the culture media were discarded, and the cells were incubated again with the fresh medium. At 24 hours after infection, the cells and supernatants were collected for CFU counting, cell cytotoxicity assay, or ELISA. The exogenous phosphoinositide uptake efficiency of cells was verified by flow cytometer analysis on FACS Calibur (BD Biosciences) using fluorescent phosphoinositides labeled with the green fluorophore BODIPY-FL (Echelon Biosciences) for intracellular delivery according to the same protocol.

Phosphatase activity assay and kinetic determination

Malachite Green Phosphate Detection Kit (Cell Signaling Technology) was used for quantitation of free phosphate during the dephosphorylation of phosphoinositide according to the manufacturer's protocol. The PI4P phosphatase activity assay was carried out using a 50 μl reaction mixture containing reaction buffer (20 mM Tris-Base, pH 7.4, 150 mM NaCl and 1 mM EDTA), 80 μM of diC16-PI4P (Echelon Biosciences), and various concentrations (0.01 to 2 μM) of purified proteins (GST, GST-fused PtpB or PtpB mutants). The reaction mixtures were incubated at 37°C for 15 min before the addition of 50 μl of Malachite Green Reagent. After further incubation for 30 min at RT, the absorbance was measured at 630 nm on a spectrophotometer. Control reactions containing no proteins were included to measure the background level of phosphate. The concentration of released inorganic phosphate was determined using a phosphate standard curve created with Phosphate Standard. For kinetic analysis, the initial dephosphorylation rate (V_0) of each phosphoinositide catalyzed by PtpB or its mutants (0.5 μM each) was determined from reactions with various concentrations (0 to 200 μM) of PI3P, PI4P, PI5P, PI(3,4)P_2, PI(3,5)P_2, PI(4,5)P_2, and PI(3,4,5)P_3 (Echelon Biosciences) in the presence or absence of His_6-Ub (0.5 μM) according to the same procedure. Similarly, the V_0 of protein substrates catalyzed by PtpB or its mutants (0.5 μM each) was determined using 0 to 1000 μM of phosphotyrosine peptides, pTyr-EGFR and pTyr-IGF1R. The Lineweaver-Burk plots were used to determine the Michaelis-Menten kinetic parameters (k_{cat} and K_m).

Mouse infection

For in vivo Mtb H37Rv infection, 6- to 8-weeks-old female mice were infected via the aerosol route using an inhalation exposure system (Glas-Col Inc.) as previously described (*48*). Briefly, log-phase Mtb cultures were washed twice with 1× PBS and were sonicated to generate single cell suspension. Bacteria were then resuspended in 10 ml 1× PBS at an OD_{600} of 0.1, and 5 ml of this inoculum was loaded into the inhalation exposure nebulizer. The aerosol unit was programmed to deliver ~100 CFUs per animal, as determined by plating whole lung homogenates from five mice on Middlebrook 7H10 agar for CFU counting within 24 hours of infection. At each designated time point, lungs were homogenized with a FastPrep-24 System (MP Biomedicals) for ELISA, qPCR analysis, or CFU counting or subjected to section along with livers for further analysis. BALF was obtained by washing the lung airways with 1 ml 1× PBS per mouse according to a previously detailed protocol (*49*), and after centrifugation, the cell-free supernatants were assayed by ELISA. All animal studies were approved by the Biomedical Research Ethics Committee of Institute of Microbiology (Chinese Academy of Sciences).

Histopathology and tissue immunofluorescence

Lungs or livers from Mtb-infected or control mice were fixed by inflating the tissues with 4% formaldehyde, sectioned, and stained with hematoxylin and eosin or by the Ziehl-Neelsen method to visualize acid-fast mycobacteria. Slides containing histological sections were scanned with Aperio CS2 (Leica Biosystems), and quantitation of the inflammation area in each tissue section was performed using ImageJ 1.50e with an IHC Toolbox plugin (National Institutes of Health; https://imagej.nih.gov/ij/). For lung immunofluorescence analysis, Mtb was detected using anti-Mtb antibody (1:200) with a Two-step IHC Detection Kit (ZSGB-BIO), followed by amplification with tyramide (1:200) using Opal 570 Reagent Pack (AKOYA) according to the manufacturer's instructions. Slides were then rinsed three times with 1× PBS and were subjected to TUNEL assay using One-step TUNEL Assay Kit (KeyGEN BioTECH) according to the manufacturer's protocol. DAPI Staining Solution (Beyotime) was used to visualize the nuclei and to mount the slides. Slides were scanned using Aperio Versa 200 (Leica Biosystems) and quantitation of the $TUNEL^+$ cells in each lung section was performed using Imaris 9.6 (Bitplane; https://imaris.oxinst.com/).

Structure analysis

The structure information of PtpB and Ub was retrieved from Protein Data Bank (PDB IDs 1YWF and 1UBQ, respectively; https://www.rcsb.org/). Multiple sequence alignments were performed using MUSCLE (*50*). The secondary structure of PtpB 3E mutant was predicted using the SOPMA algorithm (https://npsa-prabi.ibcp.fr/) or AlphaFold2 (https://github.com/deepmind/alphafold) (*51*, *52*). All structural figures were generated in PyMOL (http://www.pymol.org).

Statistics

Two-way analysis of variance (ANOVA) was used for analysis of experiments with multiple groups and multiple independent variables, and one-way ANOVA was used for analysis of multiple groups with a single independent variable. The Tukey and Dunnett tests were used as follow-up tests to the ANOVAs, where the Tukey test was used to compare every mean with every other mean, and the Dunnett test was used when comparing every mean to a control mean. Unpaired two-tailed Student's *t* tests were used for single comparison of two groups. The quantified data with statistical analysis were performed using GraphPad Prism 8.0 (https://www.graphpad.com/). $P > 0.05$, not significant (ns); $^*P < 0.05$; $^{**}P < 0.01$; $^{***}P < 0.001$; $^{****}P < 0.0001$. Data are shown as mean ± SEM of at least three biological replicates, and results are representative of at least three independent experiments unless otherwise designated in figure legends.

REFERENCES AND NOTES

1. S. Bagcchi, Dismal global tuberculosis situation due to COVID-19. *Lancet Infect. Dis.* **21**, 1636 (2021). doi: 10.1016/S1473-3099(21)00713-1; pmid: 34838229
2. J. P. Ernest *et al*., Development of new tuberculosis drugs:Translation to regimen composition for drug-sensitive and multidrug-resistant tuberculosis. *Annu. Rev. Pharmacol. Toxicol.* **61**, 495–516 (2021). doi: 10.1146/annurev-pharmtox-030920-011143; pmid: 32806997
3. M. A. Forrellad *et al*., Virulence factors of the *Mycobacterium tuberculosis* complex. *Virulence* **4**, 3–66 (2013). doi: 10.4161/viru.22329; pmid: 23076359
4. Q. Chai, L. Wang, C. H. Liu, B. Ge, New insights into the evasion of host innate immunity by *Mycobacterium tuberculosis*. *Cell. Mol. Immunol.* **17**, 901–913 (2020). doi: 10.1038/s41423-020-0502-z; pmid: 32728204
5. J. Wang *et al*., *Mycobacterium tuberculosis* suppresses innate immunity by coopting the host ubiquitin system. *Nat. Immunol.* **16**, 237–245 (2015). doi: 10.1038/ni.3096; pmid: 25642820
6. S. M. Man, T. D. Kanneganti, Regulation of inflammasome activation. *Immunol. Rev.* **265**, 6–21 (2015). doi: 10.1111/imr.12296; pmid: 25879280
7. D. E. Place, T. D. Kanneganti, Recent advances in inflammasome biology. *Curr. Opin. Immunol.* **50**, 32–38 (2018). doi: 10.1016/j.coi.2017.10.011; pmid: 29128729
8. R. Kang *et al*., Lipid peroxidation drives gasdermin D-mediated pyroptosis in lethal polymicrobial sepsis. *Cell Host Microbe* **24**, 97–108.e4 (2018). doi: 10.1016/j.chom.2018.05.009; pmid: 29937272
9. X. Chen *et al*., Pyroptosis is driven by non-selective gasdermin-D pore and its morphology is different from MLKL channel-mediated necroptosis. *Cell Res.* **26**, 1007–1020 (2016). doi: 10.1038/cr.2016.100; pmid: 27573174
10. J. Ding *et al*., Pore-forming activity and structural autoinhibition of the gasdermin family. *Nature* **535**, 111–116 (2016). doi: 10.1038/nature18590; pmid: 27281216
11. T. K. Phan, G. K. Bindra, S. A. Williams, I. K. H. Poon, M. D. Hulett, Combating human pathogens and cancer by targeting phosphoinositides and their metabolism. *Trends Pharmacol. Sci.* **40**, 866–882 (2019). doi: 10.1016/j.tips.2019.09.006; pmid: 31677918
12. K. Wang *et al*., Structural mechanism for GSDMD targeting by autoprocessed caspases in pyroptosis. *Cell* **180**, 941–955.e20 (2020). doi: 10.1016/j.cell.2020.02.002; pmid: 32109412
13. I. Banerjee *et al*., Gasdermin D restrains type I interferon response to cytosolic DNA by disrupting ionic homeostasis. *Immunity* **49**, 413–426.e5 (2018). doi: 10.1016/j.immuni.2018.07.006; pmid: 30170814
14. B. Zhou *et al*., Targeting mycobacterium protein tyrosine phosphatase B for antituberculosis agents. *Proc. Natl. Acad. Sci. U.S.A.* **107**, 4573–4578 (2010). doi: 10.1073/pnas.0909133107; pmid: 20167798
15. L. Fan *et al*., MptpB promotes mycobacteria survival by inhibiting the expression of inflammatory mediators and cell apoptosis in macrophages. *Front. Cell. Infect. Microbiol.* **8**, 171 (2018). doi: 10.3389/fcimb.2018.00171; pmid: 29888212
16. N. Beresford *et al*., MptpB, a virulence factor from *Mycobacterium tuberculosis*, exhibits triple-specificity phosphatase activity. *Biochem. J.* **406**, 13–18 (2007). doi: 10.1042/BJ20070670; pmid: 17584180
17. A. Koul *et al*., Cloning and characterization of secretory tyrosine phosphatases of *Mycobacterium tuberculosis*. *J. Bacteriol.* **182**, 5425–5432 (2000). doi: 10.1128/JB.182.19.5425-5432.2000; pmid: 10986245
18. J. Wang *et al*., The mycobacterial phosphatase PtpA regulates the expression of host genes and promotes cell proliferation. *Nat. Commun.* **8**, 244 (2017). doi: 10.1038/s41467-017-00279-z; pmid: 28811474
19. G. R. Hammond, G. Schiavo, R. F. Irvine, Immunocytochemical techniques reveal multiple, distinct cellular pools of PtdIns4P and PtdIns(4,5)P_2. *Biochem. J.* **422**, 23–35 (2009). doi: 10.1042/BJ20090428; pmid: 19508231
20. X. Li *et al*., Genetically encoded fluorescent probe to visualize intracellular phosphatidylinositol 3,5-bisphosphate localization and dynamics. *Proc. Natl. Acad. Sci. U.S.A.* **110**, 21165–21170 (2013). doi: 10.1073/pnas.1311864110; pmid: 24324172
21. N. Vashi, S. B. Andrabi, S. Ghanwat, M. Suar, D. Kumar, Ca^{2+}-dependent focal exocytosis of Golgi-derived vesicles helps phagocytic uptake in macrophages. *J. Biol. Chem.* **292**, 5144–5165 (2017). doi: 10.1074/jbc.M116.743047; pmid: 28174296
22. T. Welz, J. Wellbourne-Wood, E. Kerkhoff, Orchestration of cell surface proteins by Rab11. *Trends Cell Biol.* **24**, 407–415 (2014). doi: 10.1016/j.tcb.2014.02.004; pmid: 24675420
23. G. R. Hammond *et al*., PI4P and PI(4,5)P_2 are essential but independent lipid determinants of membrane identity. *Science* **337**, 727–730 (2012). doi: 10.1126/science.1222483; pmid: 22722250
24. I. Vergne *et al*., Mechanism of phagolysosome biogenesis block by viable *Mycobacterium tuberculosis*. *Proc. Natl. Acad. Sci. U.S.A.* **102**, 4033–4038 (2005). doi: 10.1073/pnas.0409716102; pmid: 15753315
25. C. Grundner, H. L. Ng, T. Alber, *Mycobacterium tuberculosis* protein tyrosine phosphatase PtpB structure reveals a diverged fold and a buried active site. *Structure* **13**, 1625–1634 (2005). doi: 10.1016/j.str.2005.07.017; pmid: 16271885
26. S. Hirano *et al*., Double-sided ubiquitin binding of Hrs-UIM in endosomal protein sorting. *Nat. Struct. Mol. Biol.* **13**, 272–277 (2006). doi: 10.1038/nsmb1051; pmid: 16462748
27. C. Huppertz *et al*., The NLRP3 inflammasome pathway is activated in sarcoidosis and involved in granuloma formation. *Eur. Respir. J.* **55**, 1900119 (2020). doi: 10.1183/13993003.00119-2019; pmid: 31949113
28. I. Jorgensen, E. A. Miao, Pyroptotic cell death defends against intracellular pathogens. *Immunol. Rev.* **265**, 130–142 (2015). doi: 10.1111/imr.12287; pmid: 25879289
29. Q. Chai, Y. Zhang, C. H. Liu, *Mycobacterium tuberculosis*: An adaptable pathogen associated with multiple human diseases. *Front. Cell. Infect. Microbiol.* **8**, 158 (2018). doi: 10.3389/fcimb.2018.00158; pmid: 29868514
30. S. Gagneux, Ecology and evolution of *Mycobacterium tuberculosis*. *Nat. Rev. Microbiol.* **16**, 202–213 (2018). doi: 10.1038/nrmicro.2018.8; pmid: 29456241
31. Y. Liu *et al*., Gasdermin E-mediated target cell pyroptosis by CAR T cells triggers cytokine release syndrome. *Sci. Immunol.* **5**, eaax7969 (2020). doi: 10.1126/sciimmunol.aax7969; pmid: 31953257
32. Z. Zheng *et al*., The lysosomal Rag-Ragulator complex licenses RIPK1– and caspase-8–mediated pyroptosis by *Yersinia*. *Science* **372**, eabg0269 (2021). doi: 10.1126/science.abg0269; pmid: 35058659
33. Y. Wang *et al*., Chemotherapy drugs induce pyroptosis through caspase-3 cleavage of a gasdermin. *Nature* **547**, 99–103 (2017). doi: 10.1038/nature22393; pmid: 28459430
34. G. Luchetti *et al*., Shigella ubiquitin ligase IpaH7.8 targets gasdermin D for degradation to prevent pyroptosis and enable infection. *Cell Host Microbe* **29**, 1521–1530.e10 (2021). doi: 10.1016/j.chom.2021.08.010; pmid: 34492225
35. A. Ahmed *et al*., A century of BCG: Impact on tuberculosis control and beyond. *Immunol. Rev.* **301**, 98–121 (2021). doi: 10.1111/imr.12968; pmid: 33955564
36. M. Ouimet *et al*., *Mycobacterium tuberculosis* induces the miR-33 locus to reprogram autophagy and host lipid metabolism. *Nat. Immunol.* **17**, 677–686 (2016). doi: 10.1038/ni.3434; pmid: 27089382
37. J. Daniel, H. Maamar, C. Deb, T. D. Sirakova, P. E. Kolattukudy, *Mycobacterium tuberculosis* uses host triacylglycerol to accumulate lipid droplets and acquires a dormancy-like phenotype in lipid-loaded macrophages. *PLOS Pathog.* **7**, e1002093 (2011). doi: 10.1371/journal.ppat.1002093; pmid: 21731490
38. D. G. Russell, P. J. Cardona, M. J. Kim, S. Allain, F. Altare, Foamy macrophages and the progression of the human tuberculosis granuloma. *Nat. Immunol.* **10**, 943–948 (2009). doi: 10.1038/ni.1781; pmid: 19692995
39. H. Hu, S. C. Sun, Ubiquitin signaling in immune responses. *Cell Res.* **26**, 457–483 (2016). doi: 10.1038/cr.2016.40; pmid: 27012466
40. J. C. van Kessel, G. F. Hatfull, Recombineering in *Mycobacterium tuberculosis*. *Nat. Methods* **4**, 147–152 (2007). doi: 10.1038/nmeth996; pmid: 17179933
41. A. Balla *et al*., Maintenance of hormone-sensitive phosphoinositide pools in the plasma membrane requires phosphatidylinositol 4-kinase IIIα. *Mol. Biol. Cell* **19**, 711–721 (2008). doi: 10.1091/mbc.e07-07-0713; pmid: 18077555
42. M. Herb *et al*., Mitochondrial reactive oxygen species enable proinflammatory signaling through disulfide linkage of NEMO. *Sci. Signal.* **12**, eaar5926 (2019). doi: 10.1126/scisignal.aar5926; pmid: 30755476
43. H. Zhang *et al*., 5-Hydroxymethylfurfural alleviates inflammatory lung injury by inhibiting endoplasmic reticulum stress and NLRP3 inflammasome activation. *Front. Cell Dev. Biol.* **9**, 782427 (2021). doi: 10.3389/fcell.2021.782427; pmid: 34966742
44. M. S. Kormann *et al*., Expression of therapeutic proteins after delivery of chemically modified mRNA in mice. *Nat. Biotechnol.* **29**, 154–157 (2011). doi: 10.1038/nbt.1733; pmid: 21217696
45. V. Hornung *et al*., 5′-Triphosphate RNA is the ligand for RIG-I. *Science* **314**, 994–997 (2006). doi: 10.1126/science.1132505; pmid: 17038590
46. A. Pichlmair *et al*., RIG-I-mediated antiviral responses to single-stranded RNA bearing 5′-phosphates. *Science* **314**, 997–1001 (2006). doi: 10.1126/science.1132998; pmid: 17038589
47. Q. Chai *et al*., A *Mycobacterium tuberculosis* surface protein recruits ubiquitin to trigger host xenophagy. *Nat. Commun.* **10**, 1973 (2019). doi: 10.1038/s41467-019-09955-8; pmid: 31036822
48. A. J. Wolf *et al*., *Mycobacterium tuberculosis* infects dendritic cells with high frequency and impairs their function *in vivo*. *J. Immunol.* **179**, 2509–2519 (2007). doi: 10.4049/jimmunol.179.4.2509; pmid: 17675513
49. L. Van Hoecke, E. R. Job, X. Saelens, K. Roose, Bronchoalveolar lavage of murine lungs to analyze inflammatory cell infiltration. *J. Vis. Exp.* **2017**, e55398 (2017). doi: 10.3791/55398; pmid: 28518083
50. R. C. Edgar, MUSCLE: Multiple sequence alignment with high accuracy and high throughput. *Nucleic Acids Res.* **32**, 1792–1797 (2004). doi: 10.1093/nar/gkh340; pmid: 15034147
51. C. Geourjon, G. Deléage, SOPMA: Significant improvements in protein secondary structure prediction by consensus prediction from multiple alignments. *Comput. Appl. Biosci.* **11**, 681–684 (1995). doi: 10.1093/bioinformatics/11.6.681; pmid: 8808585
52. K. Tunyasuvunakool *et al*., Highly accurate protein structure prediction for the human proteome. *Nature* **596**, 590–596 (2021). doi: 10.1038/s41586-021-03828-1; pmid: 34293799
53. Q. Chai, A bacterial phospholipid phosphatase inhibits host pyroptosis by hijacking ubiquitin, version 1, Mendeley Data (2022); https://doi.org/10.17632/r53vh3tdmg.1.
54. LuShuYangMing, LuShuYangMing/Function_annotation_of_MTB_Genome: Function annotation of MTB genome, version 1.0.0, Zenodo (2022); https://doi.org/10.5281/zenodo.7021021.

ACKNOWLEDGMENTS

We thank F. Shao (National Institute of Biological Sciences, Beijing) for *Gsdmd*$^{-/-}$ mice and multiple plasmids; L. Zhang (Beijing Institute of Lifeomics, Beijing) for multiple plasmids; T. Zhao (Institute of Microbiology, Chinese Academy of Sciences, Beijing) for help with flow cytometry; J. Hao (Core Facility for Protein Research, Institute of Biophysics, Chinese Academy of Sciences, Beijing) for help with histological analysis; Y. Teng, D. Duo, and X. Jia (Center for Biological Imaging, Institute of Biophysics, Chinese Academy of Sciences, Beijing) for help with live-cell imaging. **Funding:** This work was supported by the National Natural Science Foundation of China (81825014 and 31830003 to C.H.L., 82171744 to Q.C., and 82022041 to J.W.), the National Key Research and Development Program of China (2017YFA0505900 to C.H.L. and 2019YFA0802100 to X.-B.Q.), the Strategic Priority Research Program of the Chinese Academy of Sciences (XDB29020000 to C.H.L.), the Youth Innovation Promotion Association CAS (2018118 to J.W.), the China National Postdoctoral Program for Innovative Talents (BX2021347 to Q.C.), and the China Postdoctoral Science Foundation (2021M693358 to Q.C.). **Author contributions:** C.H.L. conceived of the project. Q.C., S.Y., Y.Zho., and J.W. designed and executed the experiments. Z.Lu., C.Q., Y.Y., X.Z., Y.Zha., Z.Le., L.Q., and B.-X.L. assisted with experiments. X.-B.Q. performed structural analysis of the interaction between Mtb PtpB and ubiquitin. Y.P. contributed critical experimental materials. Q.C., X.-B.Q., and C.H.L. wrote the manuscript, with critical input from all other authors. All authors read and approved the final version of the manuscript. **Competing interests:** The authors declare that they have no competing interests. **Data and materials availability:** The unprocessed immunoblots, images, and source data for the main figures and supplementary figures in this study have been deposited at Mendeley Data (*53*) and are publicly available as of the date of publication. The sequence information of recombinant genes encoding OSH2-PH×2, Lyn_{11}-FRB, and FKBP-Pseudojanin (GenBank accession numbers: OP056760, OP056761, and OP056762, respectively) has been deposited at GenBank (https://www.ncbi.nlm.nih.gov/genbank/). The source code used for the Circos plot is available on Zenodo (*54*), where brief instructions are attached.

SUPPLEMENTARY MATERIALS

science.org/doi/10.1126/science.abq0132
Figs. S1 to S13
Tables S1 and S2
MDAR Reproducibility Checklist
Movies S1 and S2
Data S1 to S3

Submitted 12 March 2022; resubmitted 31 July 2022
Accepted 14 September 2022
10.1126/science.abq0132

1848 SOCIETY
AAAS

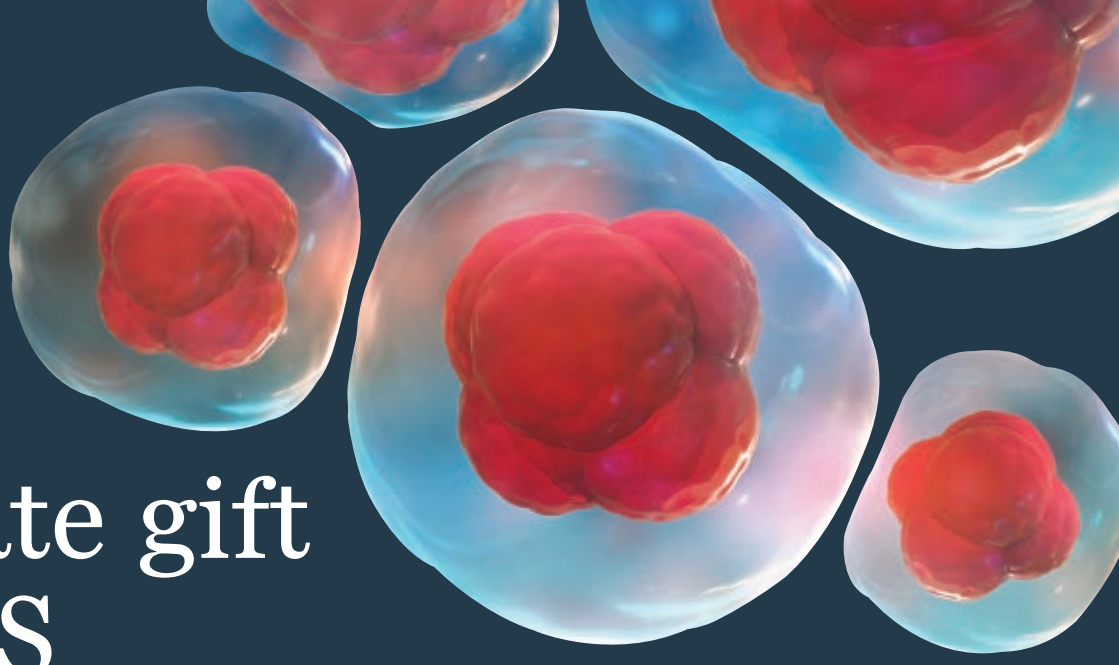

An estate gift to AAAS

Going all the way back to 1848, our founding year, the American Association for the Advancement of Science (AAAS) has been deeply committed to advancing science, engineering and innovation around the world for the benefit of all people.

Today, we are dedicated to advocating for science and scientific evidence to be fully and positively integrated into public policy and for the community to speak with one voice to advance science and engineering in the United States and around the world.

By making AAAS a beneficiary of your will, trust, retirement plan or life insurance policy, you will become a member of our 1848 Society and will help fuel our work on behalf of science and society – including publishing the world's most promising, innovative research in the *Science* family of journals and engaging in the issues that matter locally, nationally and around the world.

"As a teacher and instructor, I bear responsibility for the younger generations. If you have extra resources, concentrate them on organizations, like AAAS, that are doing work for all."

—Prof. Elisabeth Ervin-Blankenheim, 1848 Society member

If you intend to include AAAS in your estate plans, provide this information to your lawyer or financial adviser:

Legal Name: American Association for the Advancement of Science
Federal Tax ID Number: 53-0196568
Address: 1200 New York Avenue, NW, Washington, DC 20005

If you would like more information on making an estate gift to AAAS, cut out and return the form below or send an email to philanthropy@aaas.org. Additional details are also available online at **www.aaas.org/1848Society**.

AMERICAN ASSOCIATION FOR THE ADVANCEMENT OF SCIENCE

cut here

Yes, I would like more information about joining the AAAS 1848 Society.

1848 SOCIETY
AAAS

PLEASE CONTACT ME AT:

Name: _____

Address: _____

City: _____ State: _____ Zip code: _____ Country: _____

Email: _____ Phone: _____

RETURN THIS FORM TO:
AAAS Office of Philanthropy and Strategic Partnerships • 1200 New York Avenue, NW • Washington, DC 20005 USA

RESEARCH ARTICLE SUMMARY

ION CHANNELS

Activation mechanism of the mouse cold-sensing TRPM8 channel by cooling agonist and PIP_2

Ying Yin, Feng Zhang, Shasha Feng, Kevin John Butay, Mario J. Borgnia, Wonpil Im, Seok-Yong Lee*

INTRODUCTION: Mammals sense cold through drops in temperature or by exposure to particular compounds, such as the menthol found in peppermint. The basis for this cold sensation is through activation of the transient receptor potential melastatin member 8 (TRPM8) ion channels. These channels are expressed in sensory neurons and function as the primary transducer for cool sensation in humans. Channel opening can be achieved by either physical or chemical stimuli, but both modes of stimulation require allosteric binding of the membrane signaling lipid phosphatidylinositol-4,5-bisphosphate (PIP_2).

RATIONALE: Most previous structural studies were limited to avian TRPM8, which exhibits differential thermal and chemical sensitivities compared with mammalian TRPM8 despite high sequence identity. These studies revealed that PIP_2 and cooling compounds bind in the transmembrane channel region but the structures all exhibit nonconducting conformations. How exactly agonist- and PIP_2-binding to TRPM8 induces channel opening has therefore remained a mystery. The lack of an open state structure—particularly of mammalian TRPM8—has hampered not only our understanding of cold sensing in humans but also therapeutic developments targeting this important sensory receptor.

RESULTS: We use single particle cryo–electron microscopy to capture snapshots of mouse TRPM8 structures in closed (C_0, C_1), intermediate (C_2), and open (O) states. We open the channel through application of PIP_2 and two types of agonists [type I, cryosim-3 (C3) and type II, allyl isothiocyanate (AITC)]. We show that avian and mammalian TRPM8 employ a common conformational path necessary for PIP_2- and ligand-activation but differ in the binding affinity for PIP_2 and/or the sensitivity to PIP_2-induced structural rearrangements. We reveal that the binding sites for PIP_2 and agonists are strategically positioned surrounding the transmembrane helix 4b (S4b), which connects other structural elements critical for channel gating. Our structures, electrophysiology, and molecular dynamics analysis reveal that small local structural changes triggered by PIP_2 and cooling agonist binding are propagated and amplified as large rearrangements in the pore domain. During the gating transition, the pore undergoes noncanonical conformational changes that lead to the open state: The pore cavity progressively decreases in size, the surface charge electrostatics gradually becomes more electronegative, and the selectivity filter gradually forms. Concomitantly, the pore-forming helix S6 undergoes substantial helical rotation and translation and a C-terminal coil-to-helix transition, which lead to changes in the intracellular S6 gate positions and dynamics.

CONCLUSION: In this study, we investigated the mechanism of chemically induced cool sensation in mammals by visualizing the conformational landscape of mouse TRPM8 channel gating as it opens. Our study reveals a molecular mechanism for PIP_2- and cooling agonist-mediated TRPM8 activation and clarifies the structural basis for the differential PIP_2 sensitivities between TRPM8 orthologs. We unveil noncanonical conformational rearrangements in the pore domain accompanied by substantial state-dependent changes at the intracellular gate positions during TRPM8 gating. We speculate that this design could underlie the sensitivity of TRPM8 toward both physical (cold) and chemical (cooling agonist) stimuli. ■

The list of author affiliations is available in the full article online.
*Corresponding author. Email: seok-yong.lee@duke.edu
Cite this article as Y. Yin *et al.*, *Science* **378**, eadd1268 (2022).
DOI: 10.1126/science.add1268

READ THE FULL ARTICLE AT
https://doi.org/10.1126/science.add1268

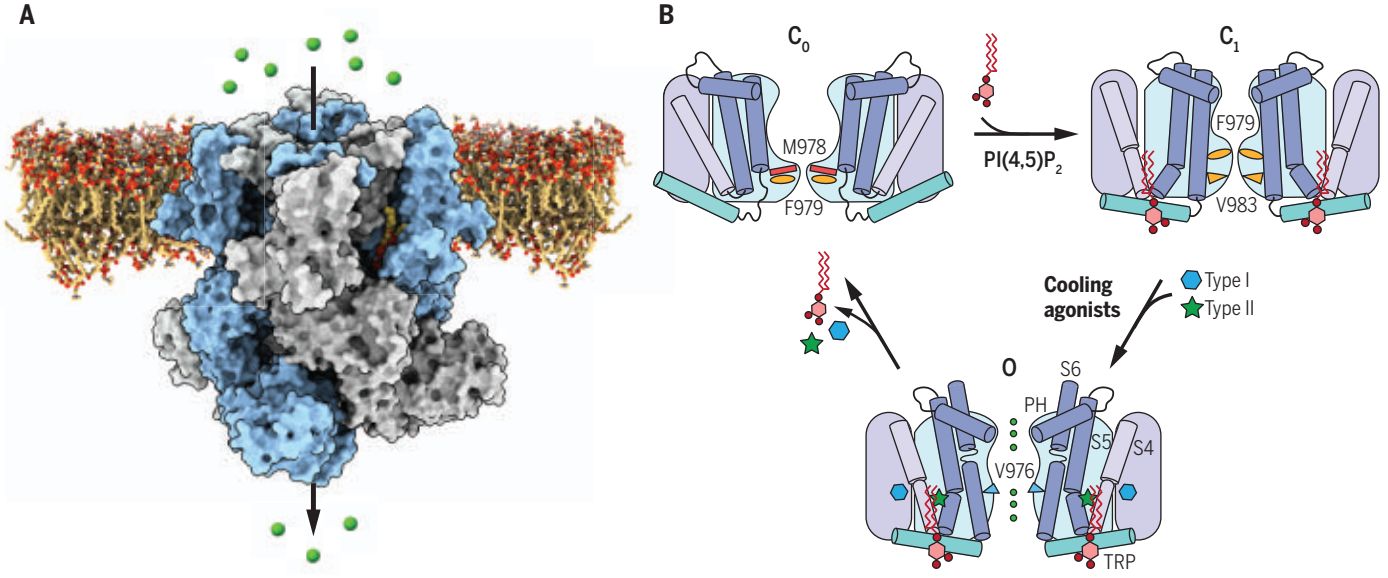

PIP_2- and cooling agonist-dependent activation of TRPM8. (**A**) The homotetrameric mouse TRPM8 channel embedded in the membrane bilayer. (**B**) Schematic diagrams illustrating the conformational rearrangements in the pore cavity and the intracellular gate position during TRPM8 gating.

RESEARCH ARTICLE

ION CHANNELS

Activation mechanism of the mouse cold-sensing TRPM8 channel by cooling agonist and PIP_2

Ying Yin[1], Feng Zhang[1], Shasha Feng[2], Kevin John Butay[3], Mario J. Borgnia[1,3], Wonpil Im[2], Seok-Yong Lee[1]*

The transient receptor potential melastatin 8 (TRPM8) channel is the primary molecular transducer responsible for the cool sensation elicited by menthol and cold in mammals. TRPM8 activation is controlled by cooling compounds together with the membrane lipid phosphatidylinositol 4,5-bisphosphate (PIP_2). Our knowledge of cold sensation and the therapeutic potential of TRPM8 for neuroinflammatory diseases and pain will be enhanced by understanding the structural basis of cooling agonist- and PIP_2-dependent TRPM8 activation. We present cryo–electron microscopy structures of mouse TRPM8 in closed, intermediate, and open states along the ligand- and PIP_2-dependent gating pathway. Our results uncover two discrete agonist sites, state-dependent rearrangements in the gate positions, and a disordered-to-ordered transition of the gate-forming S6—elucidating the molecular basis of chemically induced cool sensation in mammals.

The transient receptor potential melastatin member 8 (TRPM8) is a menthol and cold receptor expressed in dorsal root ganglia and trigeminal ganglia neurons (*1*, *2*). It is required for sensing cold temperatures as TRPM8-knockout mice show severe behavioral deficiency in response to cold stimuli (*3*–*5*). Recent studies show that TRPM8 is also critical for warm sensing, as TRPM8-deficient mice are unable to perceive warmth (*6*). TRPM8 is the principal mediator in menthol-induced analgesia of acute and inflammatory pain (*7*). In sensory fibers innervating the ocular surface, this channel regulates basal tear secretion by sensing evaporation-induced cooling and changes in osmolality (*8*, *9*). In addition to its critical role in human temperature sensing, increasing evidence suggests that TRPM8 is a promising therapeutic target of dry eye disease, migraines, cold-related pain, chronic pain, and chronic cough (*10*–*16*).

TRPM8 is a polymodal calcium-permeable cation channel whose gating is controlled by various physical and chemical stimuli (*17*, *18*). It is activated by innocuous cold temperatures and by "cooling" compounds, such as menthol found in peppermint and the synthetic super-cooling agonist icilin. TRPM8 activation requires the signaling phospholipid phosphatidylinositol 4,5-bisphosphate (PIP_2); the depletion of PIP_2 causes desensitization of channel activity (*19*–*21*). Channel function is also activated by voltage (*22*). However, the molecular bases underlying channel opening by the interplay of these stimuli remain elusive.

Previous structural studies on avian TRPM8 channels from flycatcher *Ficedula albicollis* and great tit *Parus major* ($TRPM8_{FA}$ and $TRPM8_{PM}$, respectively) revealed the architecture of TRPM8 and the binding sites for PIP_2, the cooling agonists icilin and menthol derivative WS-12 ($TRPM8_{FA}$) (*18*, *23*, *24*), and the antagonist AMTB ($TRPM8_{PM}$) (*25*). All reported ligand-bound TRPM8 structures adopt nonconducting states; thus, it is unclear how ligand binding is transduced to opening of the ion conduction pathway of TRPM8. Moreover, despite the high sequence identity (~80%) between avian and mammalian TRPM8 orthologs, it is well known that they exhibit substantial differences in chemical and thermal sensitivity (*26*, *27*).

In this study, we used PIP_2 and type I and type II agonists to open the mouse (*Mus musculus*) TRPM8 channel ($TRPM8_{MM}$), capturing distinct closed, intermediate, and open states by single-particle cryo–electron microscopy (cryo-EM). We observed notable mobility and structural rearrangements in the pore domain along with unexpected changes in the state-dependent intracellular gate. Our study combines mutagenesis, electrophysiology, and molecular dynamics (MD) simulations to elucidate the molecular basis of ligand-dependent gating of a mammalian TRPM8 channel.

Synergistic TRPM8 activation by C3 and AITC

A dialkylphosphorylalkane cooling agent, 1-diisopropylphosphorylnonane [also called cryosim-3 (C3)] (Fig. 1A), was reported to relieve dry eye disease by inducing cooling to promote tear secretion through TRPM8 activation (*15*). We characterized the agonist effects of C3 using two-electrode voltage clamp (TEVC) recordings on *Xenopus laevis* (African clawed frog) oocytes expressing TRPM8 channels (Fig. 1B). Independent of Ca^{2+} (fig. S1), C3 elicited robust outward-rectifying currents with a half-maximal effective concentration (EC_{50}) of 10.3 ± 0.4 μM (Fig. 1B). In contrast to menthol or icilin (*27*, *28*), no appreciable Ca^{2+}-dependent desensitization of $TRPM8_{MM}$ by C3 was observed either in the TEVC recordings (fig. S1A) or in the inside-out patch recordings at the concentrations tested (500 and 200 μM, respectively) (fig. S1B). C3 is therefore a good chemical tool for structural studies of ligand gating in TRPM8 as a result of its apparent independence of Ca^{2+} in activation and desensitization.

Janssens *et al.* (*29*) defined two distinct agonist types for TRPM8 based on kinetic analysis: type I (menthol-like) agonists stabilize the open state, whereas type II [allyl isothiocyanate (AITC)-like] agonists destabilize the closed state. C3-activated TRPM8 slows voltage-dependent deactivation substantially, a feature of the type I agonist (fig. S1, C and D). We hypothesized that combining a type I and a type II agonist should synergistically increase the TRPM8 channel open probability. In TEVC recordings, coapplication of 300 μM C3 and 2 mM AITC increased the inward current by ~50% compared with the current elicited by 300 μM C3 alone and increased the relative conductance at 0 mV (Fig. 1, C and D). AITC produced very weak agonistic effects at low millimolar concentrations (0.5 mM in Fig. 1C). We formed a strategy to coapply C3 and AITC to enhance the open probability of $TRPM8_{MM}$ to visualize the ligand-dependent conformational changes leading to the open state.

Structure determination of mouse TRPM8

$TRPM8_{MM}$ shares 82 and 94% sequence identity with $TRPM8_{FA}$ and human TRPM8, respectively (fig. S2). We determined six structures (five $TRPM8_{MM}$ and one $TRPM8_{FA}$) structures capturing four distinct conformational states along the gating pathway (Fig. 1, E and F): ligand-free $TRPM8_{MM}$ (apo-$TRPM8_{MM}$) and PIP_2-bound $TRPM8_{FA}$ (PIP_2-$TRPM8_{FA}$) in the closed (C) C_0 state, PIP_2-bound $TRPM8_{MM}$ (PIP_2-$TRPM8_{MM}$) and $TRPM8_{MM}$ in the C_1 state, PIP_2- and C3-bound $TRPM8_{MM}$ (PIP_2-C3-$TRPM8_{MM}$) in the intermediate C_2 state, and the open (O) state $TRPM8_{MM}$ in complex with PIP_2, C3, and AITC (PIP_2-C3-AITC-$TRPM8_{MM}$). The three-dimensional (3D) reconstructions for the six structures were determined to overall resolutions of 3.07 to 3.59 Å (figs. S3 and S4). The high-quality electron microscopy (EM) densities for the pore lining S6 helices and the TRP domains enabled us to unambiguously model the register and assign the gating residues (Fig. 1G and fig. S5). The outer pore is typically less well resolved as a result of its intrinsic flexibility. Particle subtraction followed by focused 3D classification on the transmembrane

[1]Department of Biochemistry, Duke University School of Medicine, Durham, NC 27710, USA. [2]Departments of Biological Sciences, Chemistry, and Bioengineering, Lehigh University, Bethlehem, PA 18015, USA. [3]Genome Integrity and Structural Biology Laboratory, National Institute of Environmental Health Sciences, National Institutes of Health, Department of Health and Human Services, Research Triangle Park, NC 27709, USA.
*Corresponding author. Email: seok-yong.lee@duke.edu

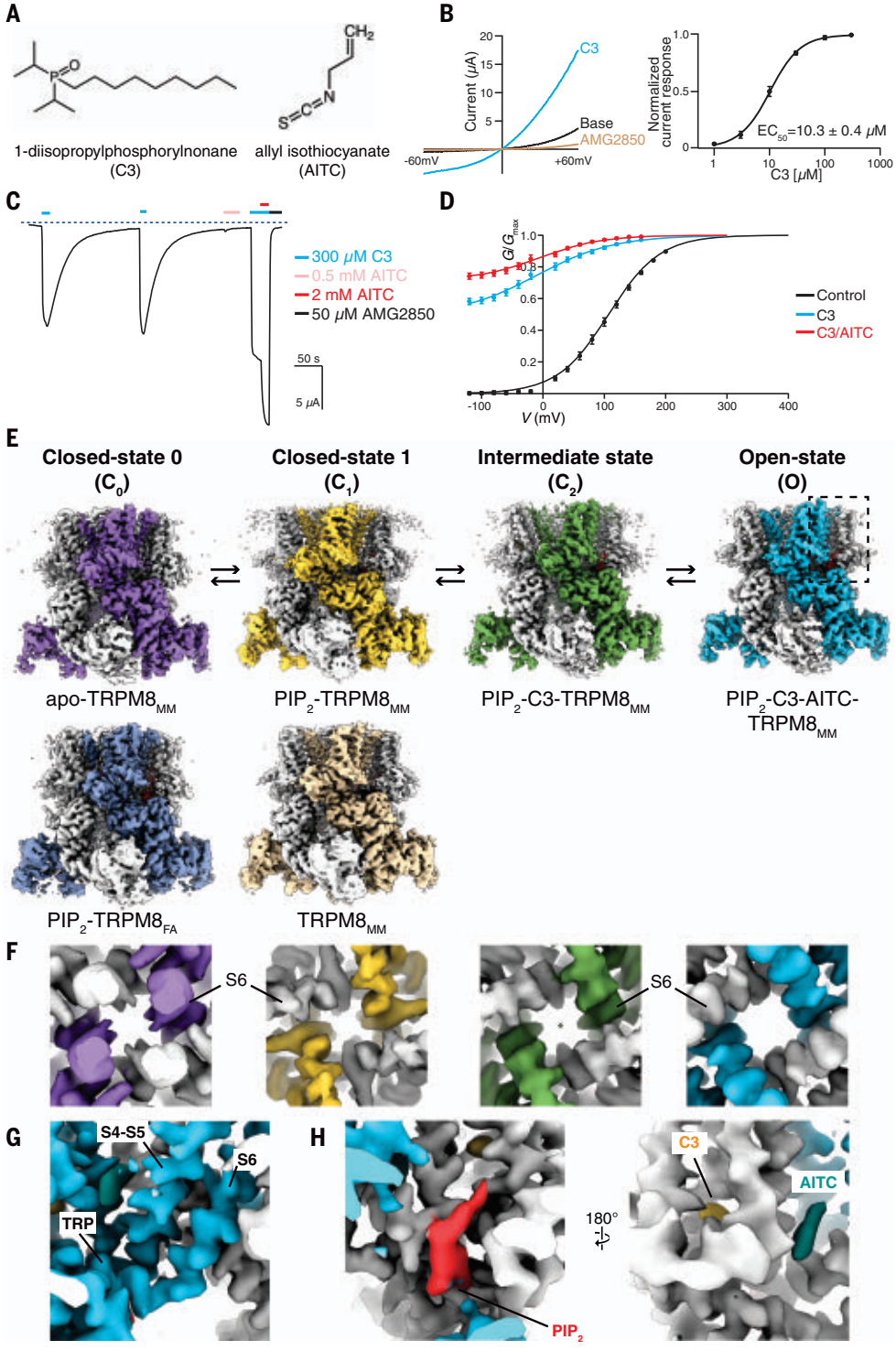

Fig. 1. Functional characterization and structure determination of the mouse $TRPM8_{MM}$ channel. (**A**) Chemical structures of 1-diisopropylphosphorylnonane (C3) and allyl isothiocyanate (AITC). (**B**) (Left) $TRPM8_{MM}$ current-voltage (*I-V*) plots obtained from 600-ms voltage ramps, following the sequential application of 300 μM C3 then 50 μM TRPM8 antagonist AMG2850. (Right) Mean normalized concentration-response relations for C3. Data are shown as mean ± SEM (n = 6). The curves are fit to the Hill equation with EC_{50} = 10.3 ± 0.4 μM, and s (slope) = 1.59 ± 0.1. (**C**) Representative time course recording of $TRPM8_{MM}$ currents elicited by 300 μM C3, 0.5 mM AITC, 300 μM C3/2 mM AITC, and 50 μM AMG2850, as indicated by the colored horizontal lines. The dotted line indicates the zero-current level. The voltage was initially held at −60 mV and ramped to +60 mV over 300 ms every 2 seconds; plotted here are the currents at −60 mV. (**D**) Conductance-voltage (*G-V*) relationships of $TRPM8_{MM}$ in the absence of agonist (control, black; n = 5) and in the presence of 300 μM C3 only (blue; n = 7) and 300 μM C3/2 mM AITC (red; n = 7), respectively. Error bars indicate SEM. (**E**) Cryo-EM reconstructions of $TRPM8_{MM}$ and $TRPM8_{FA}$ channels in the C_0, C_1, C_2, and O states, as indicated. Thresholding, 0.25 (purple), 0.36 (silver-gray), 0.22 (orange), 0.2 (light orange), 0.24 (green), and 0.22 (blue). (**F**) Close-up view at the S6 gate of 3D reconstructions from (E), viewed from the intracellular side, at thresholding 0.24, 0.25, 0.18, and 0.22, respectively. (**G**) Close-up view of the EM densities for the S4-S5 junction, S6, and TRP domain in the O state from (E), at thresholding 0.24. (**H**) Close-up view of the EM densities for PIP_2 (red), C3 (yellow), AITC (teal) from the dashed box in the O state from (E), at thresholding 0.25. All thresholding values were obtained at the isosurface level.

region (see fig. S6 and methods) facilitated model building for the outer pore region. The $TRPM8_{MM}$ channel adopts a three-layered homotetrameric architecture (fig. S7A). The transmembrane channel region at the top layer constitutes the pre-S1 domain, the transmembrane domain (TMD), and the TRP domain (fig. S7B). The TMD consists of the voltage-sensor–like domain (VSLD), formed by transmembrane helices S1 to S4, and the pore domain, constituting the S4-S5 junction, S5, pore helix (PH), and the pore-lining helix S6.

For the PIP_2-C3-AITC-$TRPM8_{MM}$ dataset, we resolved two 3D classes (fig. S6A): Class 1 contains strong EM densities for PIP_2, C3, and AITC (Fig. 1H) whereas class 2 shows EM densities for PIP_2 and C3 but not for AITC. Importantly, this class 2 adopts a nearly identical conformation to the EM map for the PIP_2-C3-$TRPM8_{MM}$ structure (map correlation 0.98; fig. S6B). We define both the class 2 and the PIP_2-C3-$TRPM8_{MM}$ dataset as the intermediate C_2 state because its conformation is between the C_1 and the O states (see discussion below). PIP_2-C3-$TRPM8_{MM}$ was used for structural analysis of the C_2 state owing to its better map quality around S6.

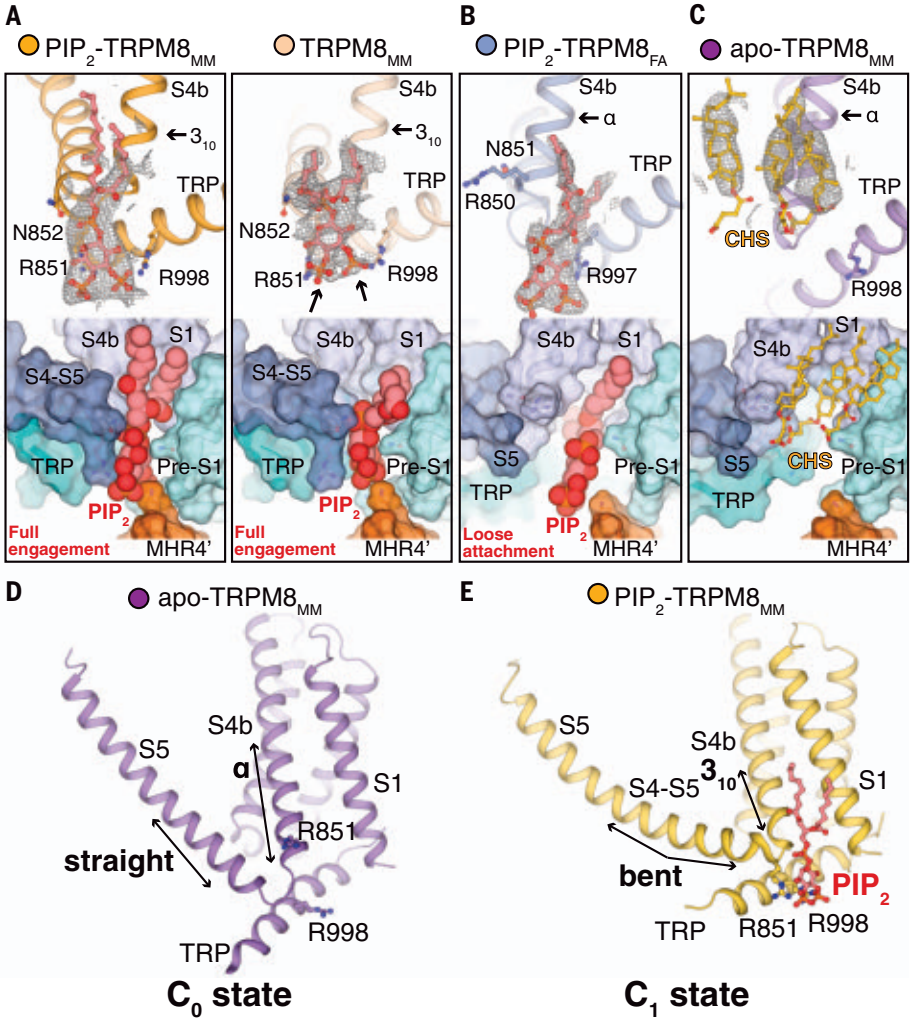

Fig. 2. PIP_2 binding primes the $TRPM8_{MM}$ channel. (**A** to **C**) (Top) EM densities (gray mesh) for PIP_2 (red sticks) in PIP_2-$TRPM8_{MM}$, $TRPM8_{MM}$ (A), and PIP_2-$TRPM8_{FA}$ (B). CHS (yellow sticks) binds to apo-$TRPM8_{MM}$ (C) at the interfacial cavity. Densities are contoured at 0.16 and 0.15 (A), 0.31 (B), and 0.22 to 0.24 (C) thresholding, respectively. Residue side chains are shown in sticks. (Bottom) Surface representations showing the two PIP_2 binding modes [(A) and (B)] and CHS (C) in the interfacial cavity. PIP_2 is shown as red spheres. (**D** and **E**) Conformations of S4b and S5 in apo-$TRPM8_{MM}$ (D) and PIP_2-$TRPM8_{MM}$ (E). Arrows indicate key structural differences. PIP_2 (red) and residues are shown in sticks.

PIP_2 binding sensitizes mouse TRPM8

PIP_2 is essential for TRPM8 function (*19*–*21*). Our previous $TRPM8_{FA}$ study showed that PIP_2 binds to the interfacial cavity at the S4b, TRP domain, and pre-S1. $TRPM8_{FA}$ exhibits two PIP_2-associated conformations: (i) loose attachment to a wider binding site formed by α-helical S4b and straight S5, also observed in apo-$TRPM8_{FA}$ and (ii) full engagement with the cavity consisting of 3_{10}-helical S4b and bent S5 (fig. S8, A and B) (*23*). In the current study, we determined two $TRPM8_{MM}$ structures with PIP_2 bound: PIP_2-$TRPM8_{MM}$ and $TRPM8_{MM}$. Strong EM density for PIP_2 was present at the interfacial cavity of PIP_2-$TRPM8_{MM}$ (Fig. 2A). In the $TRPM8_{MM}$ structure, an EM density consistent with the shape of PIP_2 was resolved, although no PIP_2 was included, suggesting that endogenous PIP_2 is copurified with the channel (Fig. 2A). The two structures are very similar (fig. S8C; TMD Cα RMSD = 0.6 Å), exhibiting the fully PIP_2 engaged conformation with 3_{10}-helical S4b and bent S5, and revealing drastic conformational differences with those of the apo or the loose attachment mode of avian TRPM8 (fig. S8D; TMD Cα RMSD = 6.0 Å).

Because we do not observe the loose attachment mode in mouse TRPM8 in the presence of PIP_2, we hypothesized that distinct from avian orthologs, mammalian TRPM8 channels are readily primed by PIP_2 binding and undergo TMD rearrangement. To test this proposal, we first determined the $TRPM8_{FA}$ structure in complex with PIP_2 alone (PIP_2-$TRPM8_{FA}$), which closely resembles the conformation of avian apo TRPM8 (Fig. 2B and fig. S8E; TMD Cα RMSD = 1.0 Å). PIP_2 binds in the loosely attached mode in $TRPM8_{FA}$, in contrast to its binding mode in PIP_2-$TRPM8_{MM}$ (fig. S8F; TMD Cα RMSD = 4.9 Å). Second, we posited that the removal of endogenous PIP_2 copurified with mouse TRPM8 would convert the channel conformation to that of the apo-$TRPM8_{FA}$ structure. For channel purification, we included cholesteryl hemisuccinate (CHS), a detergent that was shown to occupy the interfacial cavity in the TRPM8 structures determined in the presence of CHS (*25*, *30*). From this cryo-EM dataset, we resolved three subclasses with distinct conformations (fig. S9A). Class I (defined as apo-$TRPM8_{MM}$), the interfacial cavity of which is occupied by CHS molecules in place of PIP_2, resembles the apo-$TRPM8_{FA}$ conformation (Fig. 2C). Class II shows residual PIP_2 density at the binding site and resembles PIP_2-$TRPM8_{MM}$ (fig. S9, B and C). Class III resembles the Ca^{2+}-bound and PIP_2-depleted desensitized TRPM8 structures (*25*, *30*), which is likely a result of the additional interaction of the CHS molecule with the outer pore region (fig. S9, B and D). Our results suggest that, in the absence of PIP_2, apo-$TRPM8_{MM}$ adopts the same conformation as apo-$TRPM8_{FA}$, which we define as the C_0 state. PIP_2 binding triggers conformational transition to a fully engaged mode in PIP_2-$TRPM8_{MM}$, which we define as the C_1 state (Fig. 2, D and E). Our data show that both avian and mammalian TRPM8s share a common PIP_2- and agonist-dependent gating landscape with distinct differences in the energetic barriers for PIP_2 binding, resulting in different preferred ground states between avian (C_0 state) and mammalian (C_1 state) TRPM8.

Synergistic agonist and lipid binding centered at helix S4b

Inside the VSLD cavity, we resolved a pronounced EM density consistent with the shape of the diisopropylphosphoryl head group of C3 positioned below Tyr^{745} on S1 and near Arg^{842}, His^{845} on S4b (Fig. 3A and fig. S10, A and B). Tyr^{745} is critical for menthol binding (*31*), and the diisopropylphosphoryl head group position with respect to Tyr^{745} is similar to that of the menthol analog WS–12 in $TRPM8_{FA}$ (*23*). Based on MD simulations, we modeled a headgroup binding pose that enables C3 to interact with polar residues and water molecules at the base of the VSLD (fig. S10, C and D). Mutations Tyr^{745}His, Arg^{842}Ala, and His^{845}Ala all suppress TRPM8 activation by C3 relative to AITC (Fig. 3B). Based on the binding pose, the mutational effects, and the kinetics of C3 deactivation (fig. S1, C and D), we conclude that C3 is a type I agonist.

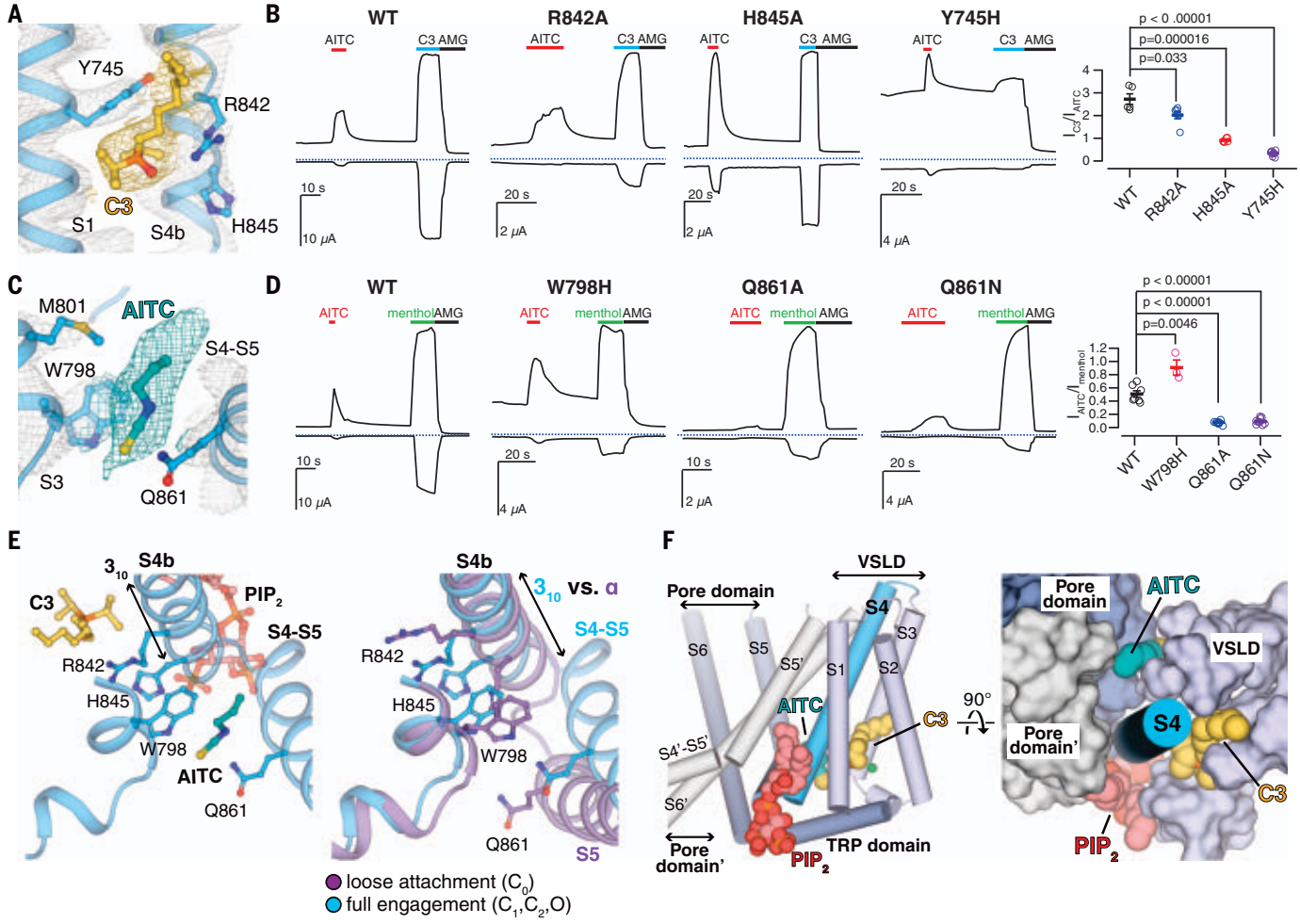

Fig. 3. Ligand binding to TRPM8$_{MM}$. (**A** and **C**) EM densities for C3 [(A) yellow] and AITC [(C) (teal)] in the O state PIP_2-C_3-AITC-TRPM8$_{MM}$ structure. Ligands and residue side chains are shown as sticks. Densities are contoured at thresholding 0.11 for C3 [(A) yellow mesh], 0.200 for AITC [(C) teal mesh], and 0.27 for TRPM8$_{MM}$ channel (gray mesh), respectively. (**B** and **D**) Representative TEVC recordings on wild-type (WT) and mutant TRPM8$_{MM}$ channels at −60 mV (lower traces) and +60 mV (upper traces). Horizontal colored lines denote the application of 2 mM AITC (red), 300 μM C3 (blue), and 50 μM AMG2850 (AMG) (black). The dotted lines denote the zero current. Summary of the current magnitudes in response to 300 μM C3 relative to 2 mM AITC at +60 mV from experiments in the left panels [(B) rightmost panel] and the current magnitudes in response to 2 mM AITC relative to 1 mM menthol at +60 mV [(D) rightmost panel], respectively. Values for individual oocytes are shown as open circles along with mean ± SEM (n = 3 to 10 oocytes). P values are calculated by two-tailed Student's t test. (**E**) Comparison of conformational changes at S4b and S5 upon PIP_2, C3, and AITC binding reveals that AITC cannot bind to TRPM8 in the C_0 state (right). Ligands and residue side chains are shown in sticks. (**F**) PIP_2, C3, and AITC bind surrounding the S4b helix (blue cylinder). TMD helices are shown in either cylinder (left) or surface (right). The neighboring pore domain (indicated by an apostrophe) is colored gray. Single-letter abbreviations for the amino acid residues are as follows: A, Ala; C, Cys; D, Asp; E, Glu; F, Phe; G, Gly; H, His; I, Ile; K, Lys; L, Leu; M, Met; N, Asn; P, Pro; Q, Gln; R, Arg; S, Ser; T, Thr; V, Val; W, Trp; and Y, Tyr.

In the 3D reconstruction of the O state structure, we observed a strong EM density consistent with the size and shape of AITC in front of the S4-S5 junction (Fig. 3C). The isothiocyanate group of AITC is sandwiched between Trp^{798} on S3 and Gln^{861} at the S4-S5 junction and mutation of Gln^{861} abolished AITC activation. The Trp^{798}Ala mutant could not be activated by C3 or AITC, but substitution of Trp^{798} to His increased the efficacy of AITC activation (Fig. 3D). MD simulations are consistent with weak AITC binding at this site (fig. S10, E and F), which we term the type II agonist site. Type II agonist binding is possible only in the full engagement mode (the 3_{10}-helix of S4b), which is induced by PIP_2 and C3 binding (Fig. 3E).

Taken together, the binding sites for PIP_2 and cooling agonists (C3 and AITC) required for TRPM8 activation are positioned at three different sides surrounding the S4b helix, which is the nexus of structural elements important for gating: the VSLD, the pore domain (S5), and the TRP domain (Fig. 3F). The effects of the individual compounds can thus allosterically enhance each other and provide synergistic transmission of the effects toward the gate to increase the open probability of the channel.

Pore conformation changes during gating

The C_0 conformation of TRPM8$_{FA}$ and the current apo-TRPM8$_{MM}$ structures have a wide-set pore and selectivity filter, unlike other TRP channels (*23*–*25*, *32*–*34*). It was not previously clear how ions would be coordinated in such a large radius pore. Our structures now offer a clue to this question. In the mouse structures, we find that extensive conformational rearrangements take place in the pore during gating (Fig. 4A). Analysis of pore cavity volumes (Fig. 4, B and C) reveals a noticeable decrease as the channel transitions from the C_0 to the C_1/C_2 state, and then to the O state. When the channel is liganded by PIP_2 and agonists, the pore-lining S6 helices rotate and the pore helices move toward the center of the pore. The pore cavity progressively decreases in size while the selectivity filter gradually forms, as illustrated in the HOLE plot (Fig. 4B), changing shape to become a canonical ion conduction pathway

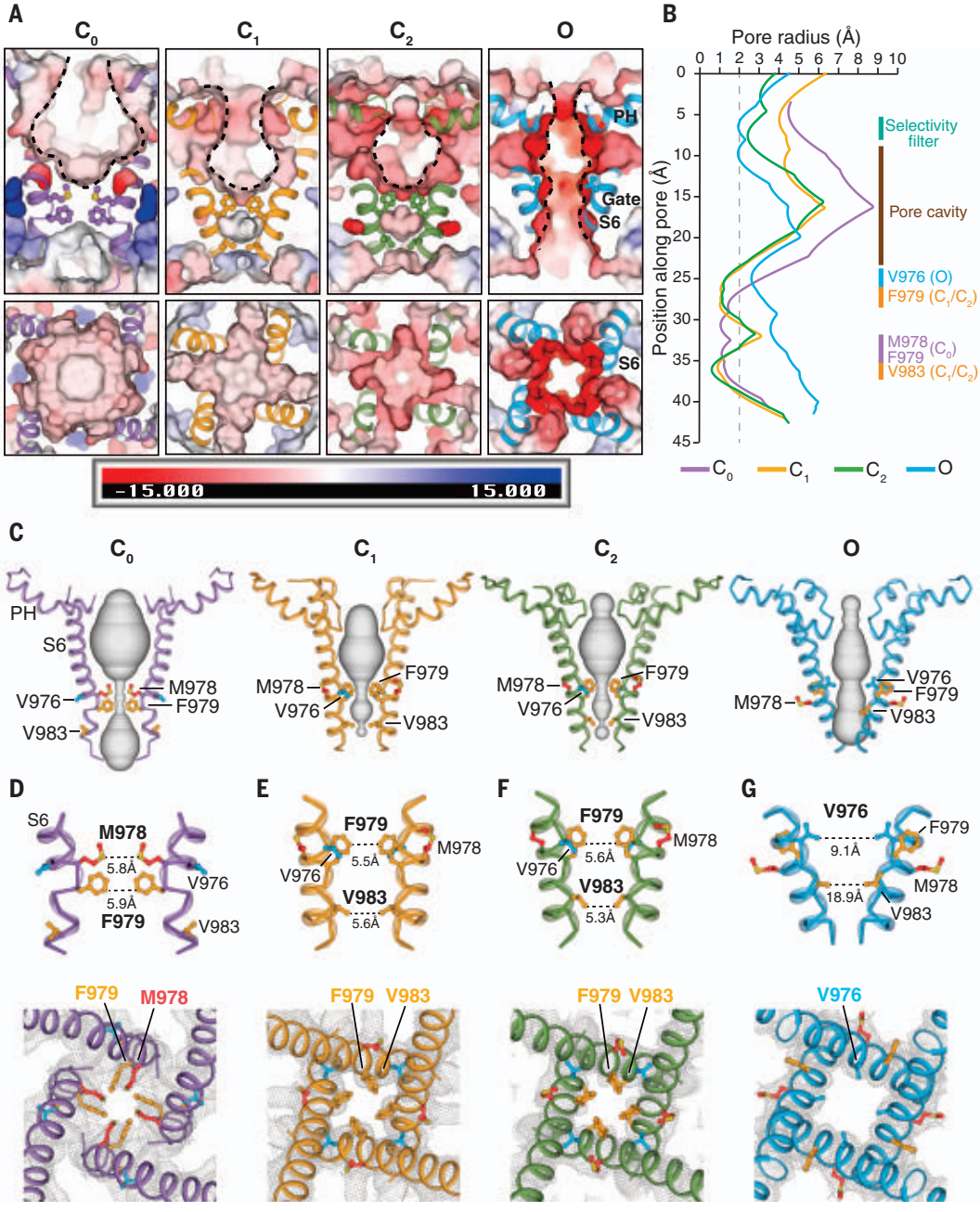

Fig. 4. Structural changes in the pore domain and S6 gate position during gating. (**A**) Viewed from the membrane plane (top) and from the extracellular side (bottom), electrostatic potential of the pore-lining surface in the C_0, C_1, C_2, and O states, calculated by APBS (*74*) implemented in PyMOL. S6 helices are shown in the illustration and gating residues are shown as sticks. The scale bar indicates electrostatics from −15 to +15 kT/e. (**B**) Pore radii calculated using the HOLE program (*75*) as colored in (A) (see methods). Regions spanning the selectivity filter, pore cavity, and S6 gate in distinct conformation states are denoted. The dotted line denotes a 2.0 Å-radius. (**C**) Ion permeation pathway in the C_0, C_1, C_2, and O states shown as gray surfaces. (**D** to **G**) Close-up views of the S6 gate from the membrane plane (top panels) and from the extracellular side (bottom panels) for the C_0 state [(D) purple], C_1 state [(E) orange], C_2 state [(F) green], and O state [(G) blue]. Diagonal distances in Å between opposing gating residues are labeled in the top panels. Gray meshes represent EM densities at the S6 gate region, contoured at 0.19 (D), 0.16 (E), 0.16 (F), and 0.16 (G) thresholding, respectively. Gating residues are shown in sticks and colored red for Met^{978}, orange for Phe^{979} and Val^{983}, and blue for Val^{976}. The apo-$TRPM8_{MM}$ (purple), PIP_2-$TRPM8_{MM}$ (orange), PIP_2-C3-$TRPM8_{MM}$ (green), and PIP_2-C3-AITC-$TRPM8_{MM}$ (blue) structures are used for illustration and analysis.

akin to that of other homotetrameric cation channels. The surface charge distribution in the pore changes as a result of conformational changes in S6 in response to ligand gating. Namely, the hydrophobic or charge neutral S6 residues, which face the center of the pore in C_0, are replaced by negatively charged or polar residues in the C_1/C_2 and O states (Fig. 4A and fig. S11). Concomitant reduction in pore size and a progressive increase in electronegative surface potential of the pore cavity likely facilitate the conduction of cations through the pore.

S6 gate changes upon opening

Comparing structures of the different conformations along the gating pathway reveals spatial alterations of the narrowest constriction point at the intracellular S6 gate (Figs. 4, D to G and 5A). In the C_0 state structure,

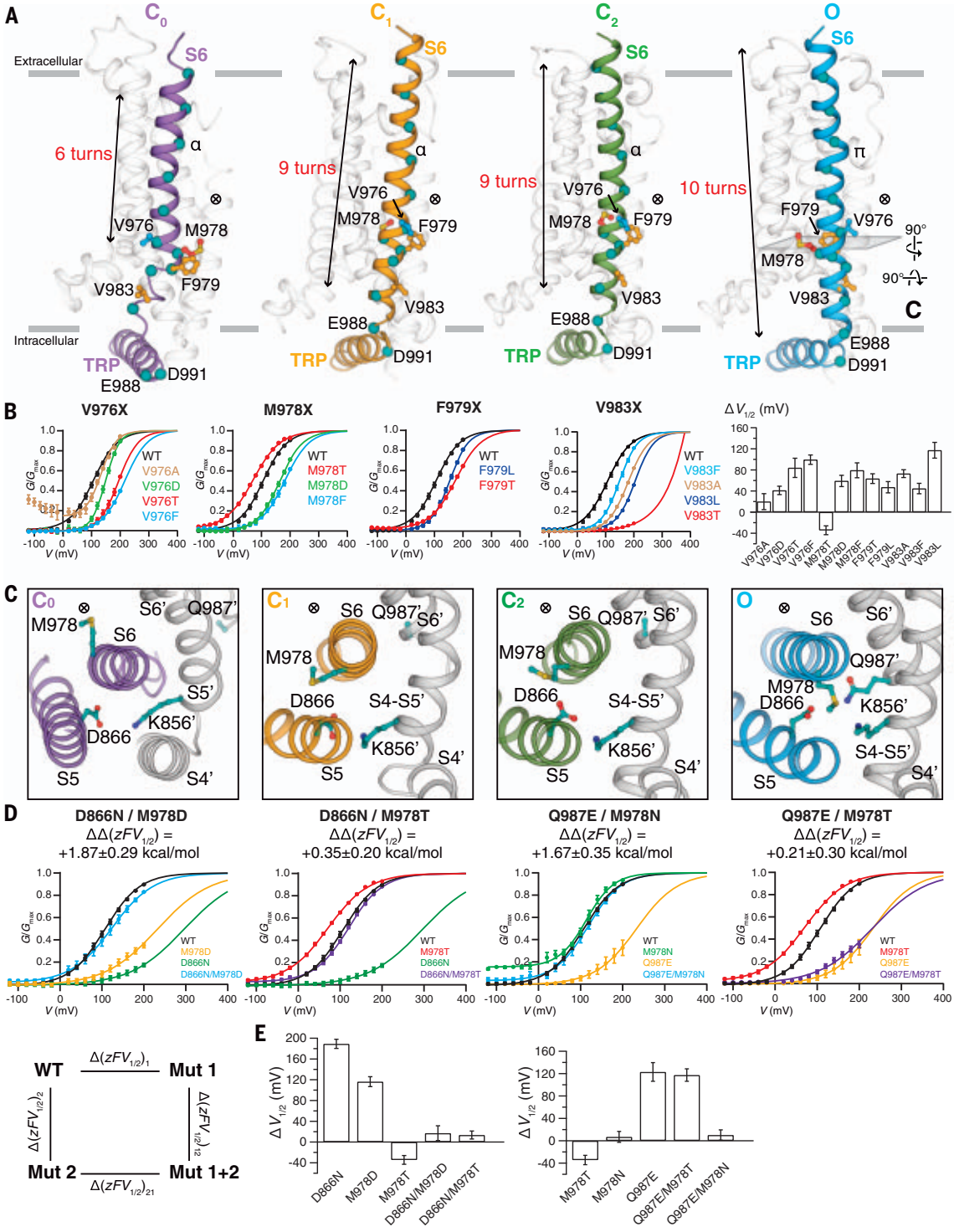

Fig. 5. State-dependent interface in the O state of TRPM8$_{MM}$. (**A**) Side-by-side comparison of the S6 rearrangement in the C_0, C_1, C_2, and O state structures viewed from the membrane plane. Gating residues are shown as sticks and colored as in Fig. 4. The ⊗ symbol next to the gate residue indicates the location of the pore. Teal-colored spheres represent residues from every helical turn along S6. S1 to S5 and PH are colored transparent gray for clarity. Gray bars indicate the membrane bilayer position. The number of helical turns in S6 is denoted. (**B**) *G-V* relationships of gating residue mutants. The data were fit with Boltzmann functions, with extrapolation to +400 mV. Bar chart (rightmost panel) quantifying the effect of mutations on the $V_{1/2}$ of activation with respect to wild type ($\Delta V_{1/2}$) as mean ± SEM (n = 4 to 11 oocytes). $V_{1/2}$ of V983T is far right-shifted so its $\Delta V_{1/2}$ is omitted in the bar chart. (**C**) Close-up extracellular view at the MDQK interface sliced from (A). Gray illustration and (′) represent structural domains from the neighboring protomer. ⊗ indicates the location of the ion conduction pore. (**D**) *G-V* relationship for the double-mutant cycle analysis. *G-V* curves for D866N, M978D, Q987E, Q987E/M978T were obtained with G_{max} values measured in the presence of menthol (fig. S14). Coupling energy $\Delta\Delta zFV_{1/2}$ (mean ± SEM) was calculated using Equations 2 to 7 in methods. (**E**) Bar chart quantifying the difference of $V_{1/2}$ between mutant and wild type ($\Delta V_{1/2}$) as mean ± SEM (n = 4 to 11 oocytes).

Met^{978} and Phe^{979} protrude toward the channel lumen and constitute a double-layered hydrophobic seal of 5.8 Å and 5.9 Å in diameter (Fig. 4D). Upon the binding of PIP_2 and/or C3 in the C_1 and C_2 states, Met^{978} rotates about 90° counterclockwise away from the pore, whereas Phe^{979} and Val^{983} subsequently rotate in and form a second double-layered hydrophobic gate distinct from that in the C_0 state (Fig. 4, E and F). This structure reveals the role of Phe^{979} and Val^{983} as gating residues. In the O state, Met^{978} and Phe^{979} rotate another 90° counterclockwise away from the pore, whereas Val^{976} swings into the ion pathway forming a wider conduction point of ~9.1 Å in diameter, permitting passage of hydrated cations (Fig. 4G) (*35*).

The S6 gate transition is accompanied by rotation, vertical and lateral translation, and secondary structural changes in the pore-lining S6 helix (Fig. 5A). From the C_0 to C_1/C_2 states the entire S6 rotates along the vertical axis by ~90° counterclockwise, followed by an additional 90° rotation from the C_1/C_2 states to the O state, which is associated with an α- to π-helical transition in S6 (*36*). As a result Met^{978}, which gates the C_0 state, flips nearly 180° in the O state to interact with residues on the intrasubunit S5 and the neighboring S4-S5 junction and S6. The side chain of Val^{976} must also rotate 180° from the C_0 state to gate the channel in the O state. These 90° to 180° rotations result in solvent-accessibility changes of the pore-lining S6 residues between the solvent-accessible lumen and the solvent-inaccessible membrane bilayer.

Besides rotation, S6 is coupled to S5 movement away from the channel lumen during channel activation (fig. S12, A and B). In going from C_1/C_2 to O, a ~2 to 5 Å shift in residue position indicates the downward movement of S6 (Fig. 5A and fig. S12, B and C). Notably, coils at the N- and C-termini of S6 in the C_0 state become partially helical in the C_1/C_2 state and adopt fully α-helical structures in the O state (Fig. 5A and fig. S12C). These cumulative effects thereby extend S6 by four helical turns (Fig. 5A) accompanied by a subdomain structure shift at the linkage between S6 and the TRP domain, where the N-terminal Glu^{988} on the TRP domain in the C_0 state relocates to the C terminus of the S6 helix in the O state (Fig. 5A and fig. S12C).

To further probe the O state structure, we performed MD simulations. Based on the wetting or dewetting status at the gate inside the pore domain, the O state was stable in five out of the total eight simulation replicates (200 nanoseconds each), whereas transient opening and closure were observed in two, and gate closure was observed in one (fig. S13). Transient opening and closing are typically observed for TRPM8 at the single channel level (*2*). To further interrogate the observed pore conformation, we systematically mutated the four gate residues (Val^{976}, Met^{978}, Phe^{979}, and Val^{983}) to Ala, Thr/Ser (polar), Asp (charged), and Phe/Leu (nonpolar), respectively, then measured the conductance-voltage (*G-V*) relationships in response to voltage activation (Fig. 5B). The channel function is highly sensitive to mutagenesis at these positions: (i) Mutation of Val^{976} to Asp, Thr, and Phe; Met^{978} to Asp and Phe; Phe^{979} to Thr and Leu; and Val^{983} to Ala, Thr, Phe, and Leu profoundly shifted *G-V* curves to more positive membrane potentials compared with the wild type (>~42 mV). Val^{976}Ala showed increased basal currents at negative potential. (ii) We could not detect appreciable currents for Phe^{979}Ala, Phe^{979}Asp, and Val^{983}Asp mutants. There appears to be no correlation in side chain properties (size and polarity) of mutated residues, likely because these gate residues are involved in the interaction networks of multiple states.

An O state–dependent interface at the S6 gate region

The observed state-dependent changes of the S6 gate rearrange Met^{978} on S6 to form an interface with Asp^{866} on S5, Gln^{987} on S6′, and Lys^{856} on the S4′-S5′ junction from the neighboring pore domain in the O state. This is an unusual interface arrangement as hydrophobic Met^{978} faces three hydrophilic residues (Fig. 5C). This interface indicates that mutation of Met^{978} to Thr would introduce hydrogen bonding with Asp^{866} and/or Gln^{987}, thus stabilizing the O state conformation. Consistent with this idea, we observed an appreciable left-shift of the *G-V* curve ($\Delta V_{1/2}$ = −34.41 ± 8.37 mV) in the Met^{978}Thr mutant (Fig. 5B).

We used double-mutant cycle analysis to further examine the coupling between paired residues among Met^{978}, Asp^{866}, and Gln^{987} (Fig. 5, D and E). We first probed Asp^{866} and its coupling with Met^{978}. The $V_{1/2}$ values of Asp^{866}Asn and Met^{978}Asp right-shifted about 189 mV and 116 mV, respectively, compared with that of the wild type, indicating that these point mutations destabilize the O state. However, the $V_{1/2}$ of the double mutant Asp^{866}Asn/Met^{978}Asp is similar to that of the wild type ($\Delta V_{1/2}$ = +13.63 ± 14.14 mV) with a large coupling energy ($\Delta\Delta zFV_{1/2}$) of >1.87 ± 0.29 kcal/mol, corroborating that these two sites are energetically coupled in the O state (see methods). For mutants with large $V_{1/2}$ shifts, additional *G-V* curves were measured in the presence of menthol to obtain more accurate G_{max} (fig. S14). We also found that Gln^{987}Glu and Met^{978}Asn are strongly energetically coupled (~1.67 ± 0.35 kcal/mol). However, the double mutant pairs Gln^{987}Glu and Met^{978}Thr, and Asp^{866}Asn and Met^{978}Thr did not show a substantial coupling energy, indicating the requirement for a specific set of interactions at the S6 interface.

Structural basis of ligand-induced TRPM8 activation

Comparisons of the C_1, C_2, and O state structures allow us to grasp the molecular basis of TRPM8 activation by agonists (Fig. 6 and figs. S15 and S16). A small local change at the ligand binding site in the VSLD propagates throughout the TMD and triggers conformational rearrangements in the pore domain for gate opening. Upon C3 binding, residues in the 3_{10}-helical S4b rotate slightly and stretch downward by ~1.4 Å (Fig. 6A). This minimal change at S4b is transduced through the connecting S4-S5 junction helix which rotates slightly closer to S3 and S4 (Fig. 6B). The bending point in S5 changes from Ile^{865} in the C_1 state to Phe^{868} in the O state, which amplifies the translation and rotation in S5. More importantly, S5 maintains extensive but differing interactions with S6; the movement in S5 being tightly coupled with the ~10.7 Å translocation of S6 away from the central axis, leading to the dilation of the ion conduction pore (Fig. 6B). This coupled movement is not a simple rigid body movement, as the interfacial residue contacts also change to accommodate the changes in the S6 gate (fig. S16A). The pore helix, located between S5 and the neighboring S6, is tilted and displaced toward the intracellular side by ~5.5 Å and moves closer to the neighboring protomer in the O state relative to the C_1 state (Fig. 6, B and C).

Contact analysis suggests there are three interfaces that undergo the most notable changes during TRPM8 activation (fig. S15). First, the lateral displacement and helical rotation in S6 from C_1 to O requires stabilization by intersubunit hydrophobic contacts with the neighboring S4 (S4′) plus an intrasubunit hydrogen bonding between Thr^{967} on S6 and Trp^{877} on S5 (Fig. 6, C and D, and fig. S16B). This network is absent in the intermediate C_2 state, where although PIP_2 and C3 binding is propagated to coupled movements of S5 and S6 (partially), the gate remains closed, suggesting that this interfacial contact is necessary to maintain the O state pore domain. Second, the interface amongst the TRP domain, S4b, and the S4-S5 junction rearranges during TRPM8 gating (Fig. 6E and fig. S16C). Compared with the C_1 state, the TRP domain packs tighter with the VSLD (S4b) and the S4-S5 junction in the O state. The hydrophilic side chain of Gln^{997} on the TRP domain flips inward and inserts into a hydrophobic groove formed by Ile^{857} and Ile^{858} on the S4-S5 junction and hydrogen bonds with Thr^{848} on S4b (Fig. 6E and fig. S16C), suggesting a change in solvent accessibility. Third, the S6-TRP connection region undergoes a coil-to-helix transition during channel gating, rearranging its interface with the S4-S5 junction and S5. In the C_1 state, Asn^{990} on the N-terminal end of the TRP domain hydrogen bonds with Arg^{862}

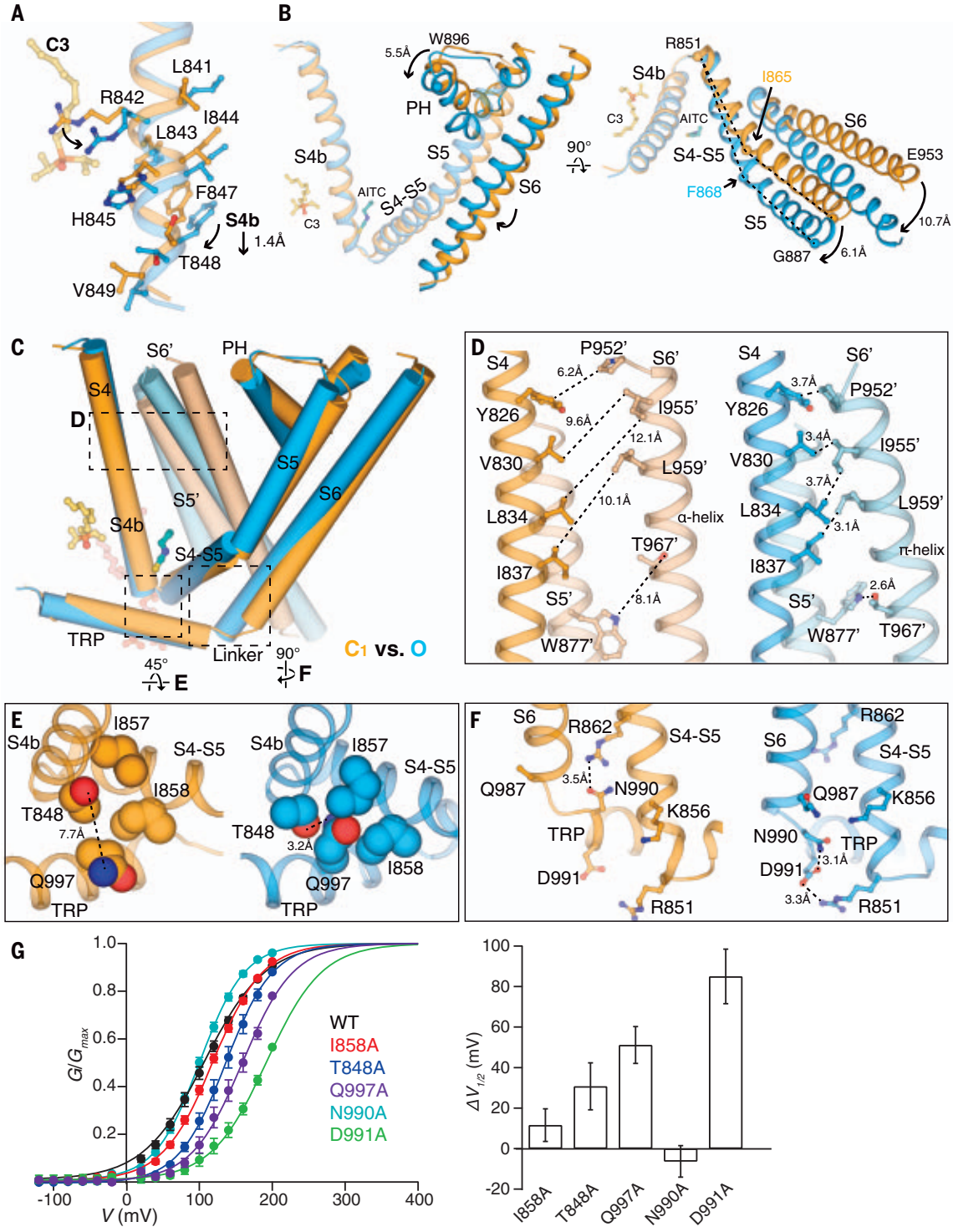

Fig. 6. Structural basis of ligand-dependent gating of TRPM8$_{MM}$. (**A**) Structural overlay of the C_1 (orange) and O (blue) states at S4b. C3 (yellow) and residue side chains are shown in sticks. Arrows indicate downward movement and side chain rotations. (**B**) Comparison of the C_1 (orange) and O (blue) state structures at the TMD, aligned at the VSLD. Arrows indicate movement in S5, PH, and S6 by the marked distances. Key residues for comparison are shown as spheres. Dashed lines (right panel) compare the change in the bending points (Ile^{865} and Phe^{868} as spheres) on S5. C3 and AITC are shown as sticks for orientation reference. S1 to S3 are removed for clarity. (**C**) Comparison of two neighboring protomers in the C_1 (orange and light orange) and O state (blue and light blue) at the TMDs. The channel is shown as cylinders and ligands as sticks. S1 to S3 are removed in chain A and only S5 and S6 are shown in chain B for clarity. Dashed regions are zoomed in for comparison in (**D** to **F**). Alignment was done using the entire tetrameric channel. (D to F) Close-up views showing side-by-side comparison of the C_1 (orange) and O state (blue) structures at inter- and intra-subunit interfaces marked in (C). Side chains are shown in sticks [(D) and (F)] or spheres (E). Dashed lines indicate the minimum distances between the corresponding residues. (**G**) (Left) *G-V* relationship of mutants at interfaces as indicated. (Right) Bar chart quantifying the difference of $V_{1/2}$ between mutant and wild type ($\Delta V_{1/2}$) as mean ± SEM (n = 4 to 6 oocytes).

on the S4-S5 junction. During activation this interaction breaks and Asn^{990} and Asp^{991} on the TRP domain and Arg^{851} on S5 (which also binds to PIP_2) form an interaction triad involving hydrogen bonding and a salt bridge, thus stabilizing the helical formation at the S6-TRP linkage in the O state (Fig. 6F and fig. S16D). Mutations of many residues involved in these interfaces lead to substantial changes in the *G-V* curves (Fig. 6G). Our findings are consistent with a previous study that reported residues Val^{986} to Asn^{990} on the C-terminal end of S6 mediate interactions with the TRP domain and the S4-S5 junction and are critical for TRPM8 activation (*37*). Notably, the C_2 state conformation is between those of the C_1 and O states along the conformational pathway toward gating (fig. S16, E and F). In contrast to the TMD, the cytoplasmic domain (CD) does not undergo substantial conformational changes during channel activation (fig. S16, H to K).

Discussion

Our open, closed, and intermediate structures show that mammalian and avian TRPM8 share the allosteric networks necessary for ligand activation but differ in their PIP_2 binding affinity and/or propensity for PIP_2-induced conformational changes. Under physiological conditions, the more populated ground state is likely the C_1 state for mammalian TRPM8 and the C_0 state for avian TRPM8. Mammalian and avian TRPM8 have distinct temperature and chemical sensitivities with mammalian orthologs substantially more sensitive to cold and exhibiting stronger cold-induced responses (*26*). Higher cold sensitivity in mammals may thus be caused by a higher sensitivity to PIP_2 or enhanced allosteric coupling between PIP_2 and temperature sensing.

Our structural data reveal noncanonical changes in the pore domain during TRPM8 channel gating. The pore helices move concomitantly with a decrease in pore cavity size and increased electronegativity. This transition at the pore in TRPM8 gating (Fig. 4A) is distinct from TRPV1, in which the selectivity filter and intracellular gate dilate for pore opening with minimal change in the pore cavity (*38*, *39*), or potassium channels, in which no change in the selectivity filter and minimal change in the pore cavity occur during gating (*40*, *41*). It is still unclear why TRPM8 undergoes such noncanonical changes in the pore domain. Quallo *et al*. showed that TRPM8 is an osmosensor in corneal afferent neurons, where it activates in response to hyperosmolality (*9*). When extracellular osmolality increases, water molecules in the pore cavity are driven out down the gradient and the cavity size decreases. Although it will require experimental testing to evaluate, we speculate that the pore cavity of TRPM8 could potentially act as a sensor to detect osmolality change.

We observe large, state-dependent conformational changes in the key interfaces as well as coil-to-helix transition in the pore-forming S6 helix of TRPM8 for ligand and PIP_2 gating, which are associated with electrostatics and solvent accessibility changes in the pore. Because TRPM8 is a polymodal sensor for both thermally and chemically induced cooling, the conformational changes observed in ligand activation may also play a role in TRPM8 cold sensing. For example, lowering temperature would favor the coil-to-helix transition in the S6 helix for TRPM8 activation (*42*). Our study thus provides structural and mechanistic insights into the interplay of diverse chemical and physical stimuli on TRPM8 functions.

Materials and Methods

Protein expression and purification

The cDNA sequence for the full-length WT mouse TRPM8 ($TRPM8_{MM}$) was cloned into a modified pEG BacMam vector (*43*) in frame with a preScission Protease cleavage site, a FLAG tag, and a 10x His tag at the C terminus. $TRPM8_{MM}$ channel was expressed by baculovirus-mediated transduction of the human embryonic kidney (HEK) 293F suspension cells. Cells were cultured in Freestyle 293 medium (Life Technologies) and maintained at 37°C in the presence of 8% CO_2. The baculovirus was generated and amplified in accordance with the standard protocol for the Bac-to-Bac® Baculovirus Expression System (Life Technologies). 3–4% P2 virus for $TRPM8_{MM}$ was added to HEK293F cells at a cell density of ~2.5 M mL^{-1}. After 18 hours, 10 mM sodium butyrate was added to the cell culture and the growth temperature was lowered to 30°C. After ~45-48 hours of expression, cells were harvested, resuspended in buffer A (50 mM Tris-HCl pH 8, 150 mM NaCl, 12 μg mL^{-1} leupeptin, 12 μg mL^{-1} pepstatin, 12 μg mL^{-1} aprotinin, 1.2 mM phenylmethylsulfonyl fluoride, and DNase I), and lysed by a Dounce tissue grinder. 1% glycol-diosgenin (GDN; Anatrace) and 0.2 mg ml^{-1} soybean polar lipid extract (Avanti Polar Lipids) was added to the cell lysate and protein was solubilized at 4°C by gentle agitation for 2 hours. Insoluble materials were removed by centrifugation at 8,000*g* for 30 min at 4°C. The supernatant was incubated with anti-FLAG M2 resin (Sigma-Aldrich) for 40 min at 4°C with gentle agitation. The resin was harvested, packed into a gravity-flow column (Bio-Rad), and washed with 10 column volumes (CV) of buffer B (20 mM Tris-HCl pH 8, 150 mM NaCl, 0.02% GDN, 5 mM ATP, 10 mM $MgCl_2$) followed by 10 CV of buffer C (20 mM Tris-HCl pH 8, 150 mM NaCl, 0.02% GDN). Protein was eluted by 5 CV of buffer C supplemented with 0.128 mg mL^{-1} FLAG peptide. Protein elution was concentrated and further purified on a Superose 6 Increase column (Cytiva Life Science) equilibrated with buffer C at 4°C.

To determine the $TRPM8_{MM}$ and PIP_2-$TRPM8_{MM}$ structures in the C_1 state, protein was solubilized in buffer A supplemented with 1% GDN and 5 mM EDTA (pH 8) at 4°C for 2 hours. After anti-FLAG M2 resin binding, the column was washed with 10 CV buffer D (20 mM Tris-HCl pH 8, 300 mM NaCl, 0.02% GDN, 5 mM ATP, 10 mM $MgCl_2$, 5 mM EDTA) and 10 CV buffer E (20 mM Tris-HCl pH 8, 150 mM NaCl, 0.02% GDN, 5 mM EDTA), followed by 5 CV elution in buffer E with FLAG peptide. Protein elution was further purified on a Superose 6 Increase column equilibrated with buffer E at 4°C.

To determine the apo-$TRPM8_{MM}$ structure in the C_0 state, protein was solubilized in buffer A supplemented with 1% GDN and 5 mM EDTA (pH 8) at 4°C for 2 hours. After anti-FLAG M2 resin binding, the column was washed with 10 CV of buffer F [20 mM Tris-HCl pH 8, 300 mM NaCl, 0.02% GDN, 0.004% cholesteryl hemisuccinate (CHS; Anatrace), 5 mM ATP, 10 mM $MgCl_2$, 5 mM EDTA], 10 CV of buffer G (20 mM Tris-HCl pH 8, 300 mM NaCl, 0.02% GDN, 0.004% CHS, 5 mM EDTA), 10 CV of buffer H (20 mM Tris-HCl pH 8, 150 mM NaCl, 0.02% GDN, 0.004% CHS, 5 mM EDTA), and eluted with 5 CV of buffer H plus FLAG peptide. Protein elution was further purified on a Superose 6 Increase column equilibrated with buffer H at 4°C.

For the collared flycatcher TRPM8 ($TRPM8_{FA}$), a codon-optimized gene for the full-length channel with mutations Phe^{535}Ala, Tyr^{538}Asp, and Tyr^{539}Asp was synthesized and cloned into the same pEG expression vector (Bio Basic Inc.). The functional integrity of this mutant $TRPM8_{FA}$ was confirmed previously (*24*). The protein expression and purification methods were identical to the previous report (*23*). In brief, the $TRPM8_{FA}$ channel was expressed in HEK293S GnTi$^-$ cells and solubilized and purified in digitonin detergent (Sigma-Aldrich).

All mammalian cell lines were authenticated and tested negative for mycoplasma by the Duke Cell Culture Facility. All mutations in the current study were introduced using the QuikChange mutagenesis kit (Agilent) and verified by Sanger sequencing (Genewiz Inc. and Azenta Life Science).

Cryo-EM specimen preparation

The peak fractions of $TRPM8_{MM}$ and $TRPM8_{FA}$ proteins eluted from size exclusion chromatography in distinct buffer conditions as described above were pooled and concentrated to 0.6–0.8 mg mL^{-1} for cryo-EM analysis. Protein was equilibrated at ambient temperature (20°C) for ~5 min followed by incubation with different ligand conditions at 20°C for 2–5 min. For the apo-$TRPM8_{MM}$ and $TRPM8_{MM}$ samples, no ligand was added to the purified protein. For the PIP_2-$TRPM8_{MM}$ sample, protein was incubated with 1 mM water-soluble

diC8-PIP_2 (Echelon Biosciences). For the PIP_2-C3-$TRPM8_{MM}$ sample, protein was incubated with 1 mM diC8-PIP_2 and 1 mM C3. For the PIP_2-C3-AITC-$TRPM8_{MM}$ sample, protein was incubated with 1 mM diC8-PIP_2, 1 mM C3, and 500 μM AITC (Sigma-Aldrich). For the PIP_2-$TRPM8_{FA}$ sample, protein was incubated with 1 mM diC8-PIP_2 at 4°C.

3 μL of protein was applied to freshly glow-discharged Quantifoil R 1.2/1.3 300-mesh Cu holey carbon grids with a 2 nm continuous carbon layer (Quantifoil). For the apo-$TRPM8_{MM}$, $TRPM8_{MM}$, PIP_2-$TRPM8_{MM}$, and PIP_2-C3-$TRPM8_{MM}$ samples, 100 μM fluorinated octyl maltoside (FOM; Anatrace) was quickly mixed with protein before applying to grids. Grids were prepared with a Mark IV Vitrobot (FEI) at 20°C and 100% humidity. Grids were blotted for 2.5–6 s at blot force 0 followed by immediate plunge freezing in liquid ethane. The blotting time varied depending on the specific ligand conditions to achieve optimal image quality for data collection. Cryo-EM grids were stored in liquid nitrogen before data acquisition.

Cryo-EM data acquisition

Grids were screened on a Talos Arctica (FEI) operated at 200 keV equipped with a Ceta, K2, or K3 detector.

Cryo-EM datasets for the apo-$TRPM8_{MM}$, $TRPM8_{MM}$, and PIP_2-C3-AITC-$TRPM8_{MM}$ structures were collected on a Titan Krios (FEI) operating at 300 keV equipped with a K3 detector (Gatan) with GIF BioQuantum energy filter (20 eV slit width; Gatan) in counting mode, using the Latitude-S automated data acquisition software (Gatan). Movies were collected at a nominal magnification of 81,000× with a physical pixel size of 1.08 Å $pixel^{-1}$ using a nominal defocus range of -0.7 to -2.2 μm. Each movie stack (60 frames) was acquired with a total dose of ~60 e^- $Å^{-2}$. The exposure time and dose rate were 3.7 s and ~20 e^- $pixel^{-1}$ s^{-1}, 3.7 s and ~20 e^- $pixel^{-1}$ s^{-1}, 4.6 s and ~15 e^- $pixel^{-1}$ s^{-1}, respectively.

Cryo-EM datasets for the PIP_2-$TRPM8_{MM}$ and PIP_2-C3-$TRPM8_{MM}$ structures were collected on a Titan Krios (FEI) operating at 300 keV equipped with a K3 detector (Gatan) with GIF BioQuantum energy filter (20 eV slit width; Gatan), using the Serial-EM automated data acquisition software (*44*). Movies were acquired at a nominal magnification of 81,000× in super-resolution mode with a pixel size of 0.528 Å $pixel^{-1}$ and 0.535 Å $pixel^{-1}$, respectively, using a nominal defocus range of -0.8 to -2.2 μm. For the PIP_2-$TRPM8_{MM}$ data, each movie stack (50 frames) was acquired over 3.1 s exposure time, using a dose rate of 17.5 e^- $pixel^{-1}$ s^{-1} and a total dose of ~50 e^- $Å^{-2}$. For the PIP_2-C3-$TRPM8_{MM}$ data, each movie stack (40 frames) was acquired over 3.5 s exposure time, using a dose rate of 17 e^- $pixel^{-1}$ s^{-1} and a total dose of ~50 e^- $Å^{-2}$.

The PIP_2-$TRPM8_{FA}$ dataset was collected on a Titan Krios (FEI) operating at 300 keV equipped with a Falcon III detector in counting mode, using the EPU automated data-acquisition program. Movies were acquired at a nominal magnification of 75,000× with a physical pixel size of 1.08 Å $pixel^{-1}$ using a nominal defocus range of -1.25 to -3 μm. Each movie (30 frames) was acquired with a dose rate of 0.8 e^- $pixel^{-1}$ s^{-1} with a total dose of ~42 e^- $Å^{-2}$.

Cryo-EM data processing

A total of 4283, 10147, 9536, 12071, 9135, and 13218 movies were collected for the PIP_2-$TRPM8_{FA}$, apo-$TRPM8_{MM}$, $TRPM8_{MM}$, PIP_2-$TRPM8_{MM}$, PIP_2-C3-$TRPM8_{MM}$, and PIP_2-C3-AITC-$TRPM8_{MM}$ structures, respectively. All six datasets were processed in a similar format as illustrated in fig. S3B using RELION 3.1 and 4.0 (*45*, *46*) and CryoSPARC (*47*). Beam-induced motion correction and dose-weighting were performed using MotionCor2 (*48*) in RELION. For PIP_2-$TRPM8_{MM}$ and PIP_2-C3-$TRPM8_{MM}$ data, the movies were Fourier-binned 2×2 to a physical pixel size of 1.056 Å/pixel and 1.07 Å/pixel, respectively. Gctf (*49*) was used for CTF estimation of non–dose-weighted summed images. Micrographs were selected based on the astigmatism, CTF fit quality, and defocus values. Particles were auto-picked for the entire dataset using template-free Laplacian-of-Gaussian (LoG) algorithm in RELION after optimizing the picking threshold with a small subset of micrographs. 2D templates from manual particle picking were used for template-based auto-picking the PIP_2-$TRPM8_{FA}$ dataset in RELION. Typically, there were on average ~350–400 particles per micrographs. Particles were re-centered and re-extracted Fourier-binned 4×4 (64- or 80-pixel box size) and imported to CryoSPARC. After one or two round(s) of 2D classification (100 classes), false picks and chaperone or ice contaminant classes were excluded. The remaining particles were transferred back to RELION and input to 3D auto-refinement with C4 symmetry imposed. The published EM map of apo-$TRPM8_{FA}$ (EMD-7127) was rescaled and low-pass filtered to 30 Å as the initial reference without a mask. The refined particles, if the reconstruction resolution reached Nyquist, were re-centered, re-extracted Fourier binned 2×2 for 3D auto-refinement with a soft mask covering the entire channel. If not, 3D classification with alignment (K=3, T=8) was performed, from which the class showing clear shape of TRPM8 channel was selected and proceeded in the same manner. Refined particles at 2x2 Fourier binning were classified by 3D classification without image alignment (K=2–4, T=8 or 16). Particles from the class with the best resolved density for transmembrane helices were re-centered and re-extracted without binning and were input to 3D auto-refinement with a soft full mask. The refined particles were subject to CTF refinement (*50*) and Bayesian polishing (*51*) to yield a decent consensus 3D reconstruction. Furthermore, to sort out higher-resolution 3D classes with stronger density at the TMD and to dissect conformational heterogeneity, we performed particle subtraction followed by focused 3D classification. In brief, a tight mask (fig. S6A) was made to subtract out signals of detergent belt and cytoplasmic domains (CDs; including MHR1-4 and post-TRP domain CTD) from the consensus 3D. Next, the subtracted particles were subject to a masked 3D classification without image alignment (K=2–4, T=8 or 16). Particles comprising the best resolved class or distinct conformations at TMD were reverted to original full particles, which were input to 3D auto-refinement with a full mask. Additional CTF refinement and Bayesian polishing were done to improve the map quality. This particle subtraction, along with focused 3D classification, were reiterated as necessary. Finally, particles yielding the best 3D reconstruction from RELION were transferred to CyroSPARC and input to non-uniform (NU) refinement (*52*) and local refinement. To improve the EM density quality at the pore helix and outer pore region for the PIP_2-C3-$TRPM8_{MM}$ and PIP_2-C3-AITC-$TRPM8_{MM}$ structures, we performed focused refinement at the TMD after subtracting signals of detergent belt and the CDs. The subtracted particles were refined using local refinement in CryoSPARC. A detailed data processing flowchart for the O state PIP_2-C3-AITC-$TRPM8_{MM}$ structure is depicted in fig. S6A. Local resolution estimation and the Fourier shell correlation (FSC) validation of the final 3D reconstruction were calculated using the gold-standard 0.143 FSC (*53*) in CryoSPARC (*47*).

Model building, refinement, and validation

The published PIP_2-icilin-Ca^{2+}-$TRPM8_{FA}$ structure (PDB 6NR3) was docked into the cryo-EM map for the O state PIP_2-C3-AITC-$TRPM8_{MM}$ structure followed by manual model building in Coot (*54*). The residue sequence was replaced with the WT mouse TRPM8 sequence. Secondary structures were first rigid body fit into the EM densities. Side chains were adjusted to optimal rotamer conformations and loops were rebuilt to fit into the density. Residues with bulky side chains guided the correct registers of helices and β-strands. Residues and side chains missing in the previous structure but resolved in the current data were built in. The high-quality EM density at the TRP domain and its linkage with S6 facilitated register assignment at the S6 gate (Fig. 1G and fig. S5F). Ideal geometry restraints were imposed on secondary structures and rotamer conformation as much as

possible during the initial manual model building in Coot.

The PIP_2-C3-AITC-$TRPM8_{MM}$ structure served as the initial reference for model building of the $TRPM8_{MM}$, PIP_2-$TRPM8_{MM}$, and PIP_2-C3-$TRPM8_{MM}$ structures. The published PIP_2-WS–12-$TRPM8_{FA}$ structure (PDB 6NR2) was used as the initial model for building the PIP_2-$TRPM8_{FA}$ and apo-$TRPM8_{MM}$ structures. Subsequent manual model building in Coot was performed following the procedure described above. In addition, to facilitate model building of the pore helices (PHs) and the selectivity filters (SFs), the TMD focused EM maps were used for the PIP_2-C3-AITC-$TRPM8_{MM}$ and PIP_2-C3-$TRPM8_{MM}$ structures.

Ligand geometry restraint files were generated from isomeric or canonical SMILES strings using the eLBOW tool (*55*) in PHENIX using fixed bond lengths and angles. For the $TRPM8_{MM}$, PIP_2-$TRPM8_{MM}$, and PIP_2-$TRPM8_{FA}$ structures, a PIP_2 molecule was modeled into the PIP_2 density in each protomer of the structure, respectively (Fig. 2, A and B). For the apo-$TRPM8_{MM}$ structure, three CHS molecules were modeled into the elongated shape densities at the interfacial cavity per protomer (Fig. 2C and fig. S9B). For the PIP_2-C3-$TRPM8_{MM}$ structure, a PIP_2 molecule, a C3 molecule, and a Ca^{2+} ion were modeled into each protomer (fig. S10B). For the PIP_2-C3-AITC-$TRPM8_{MM}$ structure, a PIP_2 molecule, a C3 molecule, an AITC molecule, and a Ca^{2+} ion were modeled into each protomer (Fig. 3, A and C, fig S10A).

The manually built structure models were subjected to real-space refinement in PHENIX against cryo-EM maps along with ligand restraints, using global minimization, rigid body refinement, and B-factor refinement with secondary structure restraints (*56*). Geometry outliers in the real-space refined models were identified by the Molprobity server (http://molprobity.biochem.duke.edu/) (*57*) and were further manually fixed in Coot. The FSCs between the structure model against the full map and both half-maps were calculated in PHENIX (*56*), and showed good agreement to each other, indicating the models were not over-refined.

Structure analysis and illustration were performed in Coot and PyMOL (Schrödinger) (*58*). The Cα RMSD values in fig. S8 were calculated in PyMOL, using the "align" command and specifying Cα-only alignment at TMD residues 721 to 1027. Analysis and presentation of cryo-EM 3D reconstructions and EM densities were performed in UCSF Chimera (*59*), UCSF ChimeraX (*60*), and PyMOL. For the HOLE plot in Fig. 4B, to ensure a similar vertical position along the ion conduction pore, structures were aligned at the tetrameric TMD level. Gly^{913}, Pro^{916}, Val^{919}, Asp^{918} were chosen as the starting point and Thr^{982}, Glu^{988}, Glu^{988}, and Glu^{988} as the ending point for the C_0, C_1, C_2, O state structures, respectively.

Structure-based analysis of protein interfacial contact

The analysis of intra- and inter-subunit residue contact was performed using the CONTACT/ACT program supported in the CCP4 suite (*61*) for the PIP_2-$TRPM8_{MM}$, PIP_2-C3-$TRPM8_{MM}$, and PIP_2-C3-AITC-$TRPM8_{MM}$ structures. Hydrogen atoms in the structure coordinates were first removed by the PDB Tools in PHENIX (*56*) before inputting to CCP4. Inter-chain contacts were probed between residues 502–1026 (covering MHR4 to CTDH1 domains in TRPM8 structures) from chain A and chain B. Contacts between any atom type within 0.0–4.1 Å distance were reported. The list of contacts was visually inspected. Source atom from residues in chain A and target atom from residues in chain B were selected when the distance between the two atoms allows for prominent interactions: maximum 3.3 Å for hydrogen bonding, maximum 4.0 Å for salt bridge interaction, and maximum 4.0 Å for hydrophobic interactions (van der Waals interactions). Interacting residue pairs which are located on S1–S6, PH, PL, and the TRP domain were highlighted and plotted in fig. S15. For intra-chain contacts, contact distances within 0.0–4.1 Å range for all residues were calculated. The list of contact for atoms from residue 502–1026 in chain A only was visually inspected using the same criteria described above. Interacting residue pairs from S4, the pore domain, and the TRP domain were illustrated in fig. S15.

Molecular dynamics (MD) simulation

Eight replicates of the O state PIP_2-C3-AITC-$TRPM8_{MM}$ structure with AITC, C3, and PIP_2 bound were embedded in a mixed membrane of POPC: POPE: Cholesterol = 2:1:1. The 8 replicates started with the exact same atom configuration with exception of two atoms in the C3 ligand. In 4 replicates, the P=O bond of C3 was oriented upward toward Tyr^{745}; in the remaining 4 replicates, the P=O bond was oriented downward away from Tyr^{745}, to study the proper ligand binding pose. Sodium and chloride ions were added to neutralize the charge of the entire system and maintain a salt concentration of ~0.15 M. PIP_2 was modeled as SAPI24, phosphatidylinositol-4,5-bisphosphate with protonation on 4′-phosphate group and stearic (18:0) and arachidonic (20:4) acid as tails. The simulations were performed using the CHARMM36m force field (lipid and protein) (*62*–*65*), TIP3P water model (*66*), and CGenFF (AITC and C3) (*67*). The initial simulation system was assembled in CHARMM-GUI Membrane Builder (*68*–*71*) and equilibrated using the standard CHARMM-GUI six-step protocol. After that, additional restrained simulation of 30 ns was performed for protein backbone in each replicate to relax the whole protein, with the harmonic force constant gradually reducing from 50 to 0 kJ mol^{-1} nm^{-2}. A 1-fs time step was used for production using OpenMM (*72*). The van der Waals interactions were cut off at 12 Å with a force-switching function between 10 and 12 Å. Each system was held at a constant particle number, 1 bar pressure, and 300.15 K temperature (NPT) with hydrogen mass repartitioning (*73*), and simulated for 200 ns.

For C3 ligand orientation analysis, the tilting angle between the P=O bond in C3 regarding the membrane bilayer plane was calculated along the time course. For characterizing the pore opening state, the region spanning from Asn^{973} to Ala^{977} was selected. The number of water molecules in this region was counted and averaged across the 10 frames for every ns.

Two-electrode voltage-clamp electrophysiology in Xenopus laevis oocytes

The full-length WT mouse TRPM8 gene was cloned into a pGEM-HE vector. The plasmid was linearized with XbaI restriction enzyme and complementary RNA (cRNA) was synthesized by in vitro transcription using T7 RNA polymerase (Thermo Fisher). All defolliculated oocytes were ordered from Xenocyte. cRNAs were injected into *Xenopus laevis* oocytes and were incubated at 17°C for 2–4 days in ND*96* solution [*96* mM NaCl, 2 mM KCl, 1 mM $MgCl_2$, 1.8 mM $CaCl_2$ and 5 mM HEPES, pH 7.6 (with NaOH)]. Oocyte membrane voltage was controlled using an OC-725C oocyte clamp (Warner Instruments). Data were filtered at 1–3 kHz and digitized at 20 kHz using pClamp software (Molecular Devices) and a Digidata 1440A digitizer (Axon Instruments). Microelectrode resistances were 0.1–0.3 MΩ when filled with 3 M KCl. The external recording solution contained 100 mM KCl, 2 mM $MgCl_2$, 5 mM HEPES, pH 7.6 (with KOH). All TRPM8 agonists (AITC, menthol, WS–12 from Sigma-Aldrich and C3 from Edward Wei at U.C. Berkeley) and antagonist AMG2850 (Alomone Labs) were applied using a gravity-fed perfusion system. For time course recording, the voltage was initially held at -60 mV and ramped to +60 mV for 300 ms every second.

For the conductance-voltage (*G-V*) recording, a voltage-step protocol covering the voltage range from –120 to +200 mV with +20 mV increment was used. After initial recording, 50 μM AMG2850 was applied to the chamber to block TRPM8 currents; then the same voltage-step protocol was repeated to measure background endogenous currents, which were subtracted from the initial recording to obtain TRPM8-speficic currents. For Val^{976}Ala mutant, 200 μM AMG2850 was used. The

steady-state currents at different test potentials were quantified and the apparent channel open probability (P_o) was determined as G/G_{max}. The maximum conductance G_{max} values were obtained by extrapolating G-V curves to +400 mV. For mutants M978D, D866N, Q987E, Q987E/M978T, and V983T (fig. S14) which showed strongly right-shifted G-V relationships, additional G-V recordings in the presence of 200-500 μM menthol were done to measure their G_{max} values. The steady state conductance G measured in the absence of menthol was normalized to G_{max}.

The G-V curves were constructed by fitting the conductance from measured current amplitudes and voltages to a two-state Boltzmann equation:

$$\frac{G}{G_{max}} = \frac{1}{1+\exp\left(-\frac{z}{k_BT}\left(V-V_{\frac{1}{2}}\right)\right)} \quad (1)$$

where G/G_{max} is the normalized channel conductance, z is the number of equivalent gating charge, k_B is the Boltzmann constant, T is the absolute temperature, V is voltage, and $V_{1/2}$ is the voltage for half-maximal activation.

Double-mutant cycle analysis and coupling energy

Structure-based design of double mutations and relevant single mutations were created by site-directed mutagenesis. A total of 10 constructs (Fig. 5D) were expressed in *Xenopus laevis* oocytes. The G-V relationships of mutant and WT channels were measured following the methods in the previous section and the $V_{1/2}$ and z values were extracted. The free energy change for the channel to transition from the closed to the open state was calculated as

$$\Delta G = -zFV_{1/2} \quad (2)$$

The perturbation in free energy change upon mutation was calculated as

$$\Delta\Delta G_1 = -F\left(z_{mut1}V_{\frac{1}{2},mut1} - z_{WT}V_{\frac{1}{2},WT}\right) \quad (3)$$

$$\Delta\Delta G_{21} = -F\left(z_{mut2+1}V_{\frac{1}{2},mut2+1} - z_{mut2}V_{\frac{1}{2},mut2}\right) \quad (4)$$

Finally, the nonadditive coupling free energy was calculated as

$$\Delta\Delta\Delta G = -F\left[\left(z_{WT}V_{\frac{1}{2},WT} - z_{mut1}V_{\frac{1}{2},mut1}\right) - \left(z_{mut2}V_{\frac{1}{2},mut2} - z_{mut2+1}V_{\frac{1}{2},mut2+1}\right)\right] \quad (5)$$

The standard error in ΔG was calculated as

$$\sigma = F\left(V_{\frac{1}{2}}^2\sigma_z^2 + z^2\sigma_{V_{1/2}}^2\right)^{1/2} \quad (6)$$

The propagated standard errors in $\Delta\Delta G$ were calculated as

$$\sigma_{mut1-WT} = \left(\sigma_{WT}^2 + \sigma_{mut1}^2\right)^{1/2}$$

$$\sigma_{mut21-mut2} = \left(\sigma_{mut21}^2 + \sigma_{mut2}^2\right)^{1/2} \quad (7)$$

The standard errors in coupling energy $\Delta\Delta\Delta G$ were calculated by linear error propagation as above in (7).

Cell culture and transfection

HEK293T cells up to passage 25 were grown in DMEM culture medium supplemented with 10% fetal bovine serum (FBS; Gibco) and 1% Antibiotic-Antimycotic (Gibco), and were maintained at 37°C in the presence of 5% CO_2. Cells seeded in 6-well plates (Genesee Scientific) were transiently transfected at ~50% confluency using X-tremeGENE 9 DNA transfection reagent (Sigma-Aldrich) at a 1:3 DNA: transfection reagent ratio (3 μL reagent for every 1 μg DNA). 800 ng of $TRPM8_{MM}$ DNA and 200 ng eGFP DNA were transfected for each well. About 24 hours following transfection, $TRPM8_{MM}$-expressing cells were trypsinized and plated onto 12mm-dimater coverslips precoated with 0.1 mg mL^{-1} Poly-L-lysine (PLL; Sigma-Aldrich) and 50 μg mL^{-1} laminin (Sigma-Aldrich) inside 12-well culture plates. Cells were used for inside-out patch clamp ~24 hours after split onto coverslips. The same $TRPM8_{MM}$ construct cloned in pEG vector for cryo-EM study was used for HEK293T cell transfection.

For whole-cell recording, cells seeded in 6-well plates were transiently transfected at ~20% confluency using FuGENE® 6 DNA transfection reagent (Promega) at a 1:3 of DNA: transfection reagent ratio (0.3 μL reagent for every 0.1 μg DNA). 100 ng of $TRPM8_{MM}$-GFP fusion cloned in a pcDNA4 vector were transfected for each well and cells were used 16–24 hours after transfection.

Patch clamp electrophysiology

All patch-clamp recordings were performed at ambient temperature (20–24°C). Pipettes were pulled from borosilicate glass with resistances between 2 to 2.5 MΩ. Current responses were lowpass filtered at 2 kHz (Axopatch 200B), digitally sampled at 5–10 kHz (Digidata 1440A), and converted to digital files in Clampex10.4 (Clampfit10.4, Molecular Devices; Igor Pro 6.34A, Wavemetrics). Electrodes were filled with an intracellular solution containing 140 mM NaCl, 5 mM $MgCl_2$, 10 mM HEPES, 5 mM EGTA and adjusted to pH 7.4 (NaOH). For inside-out patch-clamp recordings, extracellular solutions contained 140 mM NaCl, 5 mM HEPES pH 7.4 (NaOH), and 200 μM Ca^{2+}. Following formation of giga-ohm seal, inside-out configuration was formed by excising the membrane patches from cells co-expressing TRPM8 and eGFP. TRPM8 currents were elicited by focal perfusion of test solutions containing 300 μM C3 in the presence of 200 μM Ca^{2+} to the cytoplasmic side of the excised patches for 2 min, followed by application of 50 μM of TRPM8 specific antagonist AMG2850. For time course recording of TRPM8 channels, a repeated ramp protocol from -120 mV to +120 mV at a 2-s interval was used to elicit channel activity, and the membrane was held at 0 mV. Peak currents at ±120 mV were used for data analysis presented in the right panel in fig. S1B.

For whole cell recording (fig. S1, C and D), the intracellular solution contained 140 mM NaCl, 5 mM $MgCl_2$, 5 mM EGTA, and 10 mM HEPES pH 7.4 (NaOH), and the extracellular solution contained 140 mM NaCl and 10 mM HEPES pH 7.4 (NaOH). The published methods (*29*) was used to characterize TRPM8 activation by type I and type II agonists. TRPM8 current was recorded using voltage steps from -80 to +120 mV, in the absence of agonist, as well as in the presence of 3 mM AITC, 10 μM C3, 30 μM menthol, and 10 μM C3/ 3mM AITC. To analyze the gating kinetics during TRPM8 activation and deactivation in the presence of different agonist conditions, mono-exponential function was used to fit current traces, which yielded the time constants (τ) of current relaxation at +120 mV and -80 mV voltage, respectively.

Statistical analysis

Statistical analyses were performed in Igor 6.0, using two-tailed Student's t test for single comparisons between two data groups. Comparisons with p-values <0.05 are considered statistically significant. Data in summary graphs are presented as mean ± SEM, where each data point presents an individual recording. p-values are denoted in the figures.

REFERENCES AND NOTES

1. A. M. Peier *et al.*, A TRP channel that senses cold stimuli and menthol. *Cell* **108**, 705–715 (2002). doi: 10.1016/S0092-8674(02)00652-9; pmid: 11893340
2. D. D. McKemy, W. M. Neuhausser, D. Julius, Identification of a cold receptor reveals a general role for TRP channels in thermosensation. *Nature* **416**, 52–58 (2002). doi: 10.1038/nature719; pmid: 11882888
3. D. M. Bautista *et al.*, The menthol receptor TRPM8 is the principal detector of environmental cold. *Nature* **448**, 204–208 (2007). doi: 10.1038/nature05910; pmid: 17538622
4. A. Dhaka *et al.*, TRPM8 is required for cold sensation in mice. *Neuron* **54**, 371–378 (2007). doi: 10.1016/j.neuron.2007.02.024; pmid: 17481391
5. R. W. Colburn *et al.*, Attenuated cold sensitivity in TRPM8 null mice. *Neuron* **54**, 379–386 (2007). doi: 10.1016/j.neuron.2007.04.017; pmid: 17481392
6. R. Paricio-Montesinos *et al.*, The Sensory Coding of Warm Perception. *Neuron* **106**, 830–841.e3 (2020). doi: 10.1016/j.neuron.2020.02.035; pmid: 32208171
7. B. Liu *et al.*, TRPM8 is the principal mediator of menthol-induced analgesia of acute and inflammatory pain. *Pain* **154**, 2169–2177 (2013). doi: 10.1016/j.pain.2013.06.043; pmid: 23820004
8. A. Parra *et al.*, Ocular surface wetness is regulated by TRPM8-dependent cold thermoreceptors of the cornea. *Nat. Med.* **16**, 1396–1399 (2010). doi: 10.1038/nm.2264; pmid: 21076394
9. T. Quallo *et al.*, TRPM8 is a neuronal osmosensor that regulates eye blinking in mice. *Nat. Commun.* **6**, 7150 (2015). doi: 10.1038/ncomms8150; pmid: 25998021

10. I. Alcalde *et al*., Morphological and functional changes in TRPM8-expressing corneal cold thermoreceptor neurons during aging and their impact on tearing in mice. *J. Comp. Neurol.* **526**, 1859–1874 (2018). doi: 10.1002/cne.24454; pmid: 29664111
11. D. I. Chasman *et al*., Genome-wide association study reveals three susceptibility loci for common migraine in the general population. *Nat. Genet.* **43**, 695–698 (2011). doi: 10.1038/ng.856; pmid: 21666692
12. D. B. Horne *et al*., Discovery of TRPM8 Antagonist (S)-6-(((3-Fluoro-4-(trifluoromethoxy)phenyl)(3-fluoropyridin-2-yl) methyl)carbamoyl)nicotinic Acid (AMG 333), a Clinical Candidate for the Treatment of Migraine. *J. Med. Chem.* **61**, 8186–8201 (2018). doi: 10.1021/acs.jmedchem.8b00518; pmid: 30148953
13. A. D. Weyer, S. G. Lehto, Development of TRPM8 Antagonists to Treat Chronic Pain and Migraine. *Pharmaceuticals* **10**, 37 (2017). doi: 10.3390/ph10020037; pmid: 28358322
14. W. M. Knowlton *et al*., A sensory-labeled line for cold: TRPM8-expressing sensory neurons define the cellular basis for cold, cold pain, and cooling-mediated analgesia. *J. Neurosci.* **33**, 2837–2848 (2013). doi: 10.1523/JNEUROSCI.1943-12.2013; pmid: 23407943
15. J. M. Yang *et al*., A novel TRPM8 agonist relieves dry eye discomfort. *BMC Ophthalmol.* **17**, 101 (2017). doi: 10.1186/s12886-017-0495-2; pmid: 28651550
16. E. Millqvist, TRPV1 and TRPM8 in Treatment of Chronic Cough. *Pharmaceuticals* **9**, 45 (2016). doi: 10.3390/ph9030045; pmid: 27483288
17. D. D. McKemy, in *TRP Ion Channel Function in Sensory Transduction and Cellular Signaling Cascades*, W. B. Liedtke, S. Heller, Eds. (CRC Press, 2007), Chapter 13.
18. Y. Yin, S. Y. Lee, Current View of Ligand and Lipid Recognition by the Menthol Receptor TRPM8. *Trends Biochem. Sci.* **45**, 806–819 (2020). doi: 10.1016/j.tibs.2020.05.008; pmid: 32532587
19. T. Rohács, C. M. Lopes, I. Michailidis, D. E. Logothetis, PI(4,5) P2 regulates the activation and desensitization of TRPM8 channels through the TRP domain. *Nat. Neurosci.* **8**, 626–634 (2005). doi: 10.1038/nn1451; pmid: 15852009
20. E. Zakharian, C. Cao, T. Rohacs, Gating of transient receptor potential melastatin 8 (TRPM8) channels activated by cold and chemical agonists in planar lipid bilayers. *J. Neurosci.* **30**, 12526–12534 (2010). doi: 10.1523/JNEUROSCI.3189-10.2010; pmid: 20844147
21. B. Liu, F. Qin, Functional control of cold- and menthol-sensitive TRPM8 ion channels by phosphatidylinositol 4,5-bisphosphate. *J. Neurosci.* **25**, 1674–1681 (2005). doi: 10.1523/JNEUROSCI.3632-04.2005; pmid: 15716403
22. T. Voets *et al*., The principle of temperature-dependent gating in cold- and heat-sensitive TRP channels. *Nature* **430**, 748–754 (2004). doi: 10.1038/nature02732; pmid: 15306801
23. Y. Yin *et al*., Structural basis of cooling agent and lipid sensing by the cold-activated TRPM8 channel. *Science* **363**, eaav9334 (2019). doi: 10.1126/science.aav9334; pmid: 30733385
24. Y. Yin *et al*., Structure of the cold- and menthol-sensing ion channel TRPM8. *Science* **359**, 237–241 (2018). doi: 10.1126/science.aan4325; pmid: 29217583
25. M. M. Diver, Y. Cheng, D. Julius, Structural insights into TRPM8 inhibition and desensitization. *Science* **365**, 1434–1440 (2019). doi: 10.1126/science.aax6672; pmid: 31488702
26. M. Pertusa, B. Rivera, A. González, G. Ugarte, R. Madrid, Critical role of the pore domain in the cold response of TRPM8 channels identified by ortholog functional comparison. *J. Biol. Chem.* **293**, 12454–12471 (2018). doi: 10.1074/jbc.RA118.002256; pmid: 29880642
27. H. H. Chuang, W. M. Neuhausser, D. Julius, The super-cooling agent icilin reveals a mechanism of coincidence detection by a temperature-sensitive TRP channel. *Neuron* **43**, 859–869 (2004). doi: 10.1016/j.neuron.2004.08.038; pmid: 15363396
28. F. J. Kühn, C. Kühn, A. Lückhoff, Inhibition of TRPM8 by icilin distinct from desensitization induced by menthol and menthol derivatives. *J. Biol. Chem.* **284**, 4102–4111 (2009). doi: 10.1074/jbc.M806651200; pmid: 19095656
29. A. Janssens *et al*., Definition of two agonist types at the mammalian cold-activated channel TRPM8. *eLife* **5**, e17240 (2016). doi: 10.7554/eLife.17240; pmid: 27449282
30. C. Zhao *et al*., Structures of a mammalian TRPM8 in closed state. *Nat. Commun.* **13**, 3113 (2022). doi: 10.1038/s41467-022-30919-y; pmid: 35662242
31. M. Bandell *et al*., High-throughput random mutagenesis screen reveals TRPM8 residues specifically required for activation by menthol. *Nat. Neurosci.* **9**, 493–500 (2006). doi: 10.1038/nn1665; pmid: 16520735
32. L. Zubcevic *et al*., Conformational ensemble of the human TRPV3 ion channel. *Nat. Commun.* **9**, 4773 (2018). doi: 10.1038/s41467-018-07117-w; pmid: 30429472
33. M. Hirschi *et al*., Cryo-electron microscopy structure of the lysosomal calcium-permeable channel TRPML3. *Nature* **550**, 411–414 (2017). doi: 10.1038/nature24055; pmid: 29019979
34. Y. Suo *et al*., Structural Insights into Electrophile Irritant Sensing by the Human TRPA1 Channel. *Neuron* **105**, 882–894.e5 (2020). doi: 10.1016/j.neuron.2019.11.023; pmid: 31866091
35. S. Rao, G. Klesse, P. J. Stansfeld, S. J. Tucker, M. S. P. Sansom, A heuristic derived from analysis of the ion channel structural proteome permits the rapid identification of hydrophobic gates. *Proc. Natl. Acad. Sci. U.S.A.* **116**, 13989–13995 (2019). doi: 10.1073/pnas.1902702116; pmid: 31235590
36. L. Zubcevic, S. Y. Lee, The role of π-helices in TRP channel gating. *Curr. Opin. Struct. Biol.* **58**, 314–323 (2019). doi: 10.1016/j.sbi.2019.06.011; pmid: 31378426
37. F. J. Taberner, A. López-Córdoba, G. Fernández-Ballester, Y. Korchev, A. Ferrer-Montiel, The region adjacent to the C-end of the inner gate in transient receptor potential melastatin 8 (TRPM8) channels plays a central role in allosteric channel activation. *J. Biol. Chem.* **289**, 28579–28594 (2014). doi: 10.1074/jbc.M114.577478; pmid: 25157108
38. D. H. Kwon *et al*., Heat-dependent opening of TRPV1 in the presence of capsaicin. *Nat. Struct. Mol. Biol.* **28**, 554–563 (2021). doi: 10.1038/s41594-021-00616-3; pmid: 34239123
39. E. Cao, M. Liao, Y. Cheng, D. Julius, TRPV1 structures in distinct conformations reveal activation mechanisms. *Nature* **504**, 113–118 (2013). doi: 10.1038/nature12823; pmid: 24305161
40. C. H. Lee, R. MacKinnon, Activation mechanism of a human SK-calmodulin channel complex elucidated by cryo-EM structures. *Science* **360**, 508–513 (2018). doi: 10.1126/science.aas9466; pmid: 29724949
41. S. B. Hansen, X. Tao, R. MacKinnon, Structural basis of PIP2 activation of the classical inward rectifier K+ channel Kir2.2. *Nature* **477**, 495–498 (2011). doi: 10.1038/nature10370; pmid: 21874019
42. C. Y. Huang, J. W. Klemke, Z. Getahun, W. F. DeGrado, F. Gai, Temperature-dependent helix-coil transition of an alanine based peptide. *J. Am. Chem. Soc.* **123**, 9235–9238 (2001). doi: 10.1021/ja0158814; pmid: 11562202
43. A. Goehring *et al*., Screening and large-scale expression of membrane proteins in mammalian cells for structural studies. *Nat. Protoc.* **9**, 2574–2585 (2014). doi: 10.1038/nprot.2014.173; pmid: 25299155
44. D. N. Mastronarde, Automated electron microscope tomography using robust prediction of specimen movements. *J. Struct. Biol.* **152**, 36–51 (2005). doi: 10.1016/j.jsb.2005.07.007; pmid: 16182563
45. J. Zivanov *et al*., New tools for automated high-resolution cryo-EM structure determination in RELION-3. *eLife* **7**, e42166 (2018). doi: 10.7554/eLife.42166; pmid: 30412051
46. D. Kimanius, L. Dong, G. Sharov, T. Nakane, S. H. W. Scheres, New tools for automated cryo-EM single-particle analysis in RELION-4.0. *Biochem. J.* **478**, 4169–4185 (2021). doi: 10.1042/BCJ20210708; pmid: 34783343
47. A. Punjani, J. L. Rubinstein, D. J. Fleet, M. A. Brubaker, cryoSPARC: Algorithms for rapid unsupervised cryo-EM structure determination. *Nat. Methods* **14**, 290–296 (2017). doi: 10.1038/nmeth.4169; pmid: 28165473
48. S. Q. Zheng *et al*., MotionCor2: Anisotropic correction of beam-induced motion for improved cryo-electron microscopy. *Nat. Methods* **14**, 331–332 (2017). doi: 10.1038/nmeth.4193; pmid: 28250466
49. K. Zhang, Gctf: Real-time CTF determination and correction. *J. Struct. Biol.* **193**, 1–12 (2016). doi: 10.1016/j.jsb.2015.11.003; pmid: 26592709
50. J. Zivanov, T. Nakane, S. H. W. Scheres, Estimation of high-order aberrations and anisotropic magnification from cryo-EM data sets in *RELION*-3.1. *IUCrJ* **7**, 253–267 (2020). doi: 10.1107/S2052252520000081; pmid: 32148853
51. J. Zivanov, T. Nakane, S. Scheres, A Bayesian approach to beam-induced motion correction in cryo-EM single-particle analysis. *IUCRJ* **17**, (2019). doi: 10.1107/S2052252520000081; pmid: 32148853
52. A. Punjani, H. Zhang, D. J. Fleet, Non-uniform refinement: Adaptive regularization improves single-particle cryo-EM reconstruction. *Nat. Methods* **17**, 1214–1221 (2020). doi: 10.1038/s41592-020-00990-8; pmid: 33257830
53. S. H. Scheres, S. Chen, Prevention of overfitting in cryo-EM structure determination. *Nat. Methods* **9**, 853–854 (2012). doi: 10.1038/nmeth.2115; pmid: 22842542
54. P. Emsley, K. Cowtan, Coot: Model-building tools for molecular graphics. *Acta Crystallogr. D* **60**, 2126–2132 (2004). doi: 10.1107/S0907444904019158; pmid: 15572765
55. N. W. Moriarty, R. W. Grosse-Kunstleve, P. D. Adams, electronic Ligand Builder and Optimization Workbench (eLBOW): A tool for ligand coordinate and restraint generation. *Acta Crystallogr. D* **65**, 1074–1080 (2009). doi: 10.1107/S0907444909029436; pmid: 19770504
56. P. D. Adams *et al*., PHENIX: A comprehensive Python-based system for macromolecular structure solution. *Acta Crystallogr. D* **66**, 213–221 (2010). doi: 10.1107/S0907444909052925; pmid: 20124702
57. V. B. Chen *et al*., MolProbity: All-atom structure validation for macromolecular crystallography. *Acta Crystallogr. D* **66**, 12–21 (2010). doi: 10.1107/S0907444909042073; pmid: 20057044
58. W. L. Delano, *The PyMol Molecular Graphics System*. (DeLano Scientific, 2002).
59. T. D. Goddard, C. C. Huang, T. E. Ferrin, Visualizing density maps with UCSF Chimera. *J. Struct. Biol.* **157**, 281–287 (2007). doi: 10.1016/j.jsb.2006.06.010; pmid: 16963278
60. E. F. Pettersen *et al*., UCSF ChimeraX: Structure visualization for researchers, educators, and developers. *Protein Sci.* **30**, 70–82 (2021). doi: 10.1002/pro.3943; pmid: 32881101
61. M. D. Winn *et al*., Overview of the CCP4 suite and current developments. *Acta Crystallogr. D* **67**, 235–242 (2011). doi: 10.1107/S0907444910045749; pmid: 21460441
62. R. B. Best *et al*.., Optimization of the additive CHARMM all-atom protein force field targeting improved sampling of the backbone φ, ψ and side-chain χ(1) and χ(2) dihedral angles. *J. Chem. Theory Comput.* **8**, 3257–3273 (2012). doi: 10.1021/ct300400x; pmid: 23341755
63. J. Huang, A. D. MacKerell Jr., CHARMM36 all-atom additive protein force field: Validation based on comparison to NMR data. *J. Comput. Chem.* **34**, 2135–2145 (2013). doi: 10.1002/jcc.23354; pmid: 23832629
64. J. B. Klauda *et al*., Update of the CHARMM all-atom additive force field for lipids: Validation on six lipid types. *J. Phys. Chem. B* **114**, 7830–7843 (2010). doi: 10.1021/jp101759q; pmid: 20496934
65. J. Huang *et al*., CHARMM36m: An improved force field for folded and intrinsically disordered proteins. *Nat. Methods* **14**, 71–73 (2017). doi: 10.1038/nmeth.4067; pmid: 27819658
66. S. R. Durell, B. R. Brooks, A. Ben-Naim, Solvent-Induced Forces between Two Hydrophilic Groups. *J. Phys. Chem.* **98**, 2198–2202 (1994). doi: 10.1021/j100059a038
67. K. Vanommeslaeghe *et al*., CHARMM general force field: A force field for drug-like molecules compatible with the CHARMM all-atom additive biological force fields. *J. Comput. Chem.* **31**, 671–690 (2010). pmid: 19575467
68. E. L. Wu *et al*., CHARMM-GUI Membrane Builder toward realistic biological membrane simulations. *J. Comput. Chem.* **35**, 1997–2004 (2014). doi: 10.1002/jcc.23702; pmid: 25130509
69. J. Lee *et al*., CHARMM-GUI Input Generator for NAMD, GROMACS, AMBER, OpenMM, and CHARMM/OpenMM Simulations Using the CHARMM36 Additive Force Field. *J. Chem. Theory Comput.* **12**, 405–413 (2016). doi: 10.1021/acs.jctc.5b00935; pmid: 26631602
70. S. Jo, T. Kim, V. G. Iyer, W. Im, CHARMM-GUI: A web-based graphical user interface for CHARMM. *J. Comput. Chem.* **29**, 1859–1865 (2008). doi: 10.1002/jcc.20945; pmid: 18351591
71. S. Jo, J. B. Lim, J. B. Klauda, W. Im, CHARMM-GUI Membrane Builder for mixed bilayers and its application to yeast membranes. *Biophys. J.* **97**, 50–58 (2009). doi: 10.1016/j.bpj.2009.04.013; pmid: 19580743
72. P. Eastman *et al*., OpenMM 7: Rapid development of high performance algorithms for molecular dynamics. *PLOS Comput. Biol.* **13**, e1005659 (2017). doi: 10.1371/journal.pcbi.1005659; pmid: 28746339
73. Y. Gao *et al*., CHARMM-GUI Supports Hydrogen Mass Repartitioning and Different Protonation States of Phosphates in Lipopolysaccharides. *J. Chem. Inf. Model.* **61**, 831–839 (2021). doi: 10.1021/acs.jcim.0c01360; pmid: 33442985
74. E. Jurrus *et al*., Improvements to the APBS biomolecular solvation software suite. *Protein Sci.* **27**, 112–128 (2018). doi: 10.1002/pro.3280; pmid: 28836357
75. O. S. Smart, J. G. Neduvelil, X. Wang, B. A. Wallace, M. S. Sansom, HOLE: A program for the analysis of the pore dimensions of ion channel structural models. *J. Mol. Graph.* **14**, 354–360, 376 (1996). doi: 10.1016/S0263-7855(97)00009-X; pmid: 9195488

ACKNOWLEDGMENTS

We thank E.T.F. Wei from U.C. Berkeley for providing the C3 compound and encouraging us to test it for structural studies. We thank A. Patapoutian from TSRI and M. Bandell from GNF for sharing unpublished data and the plasmid containing mouse TRPM8-GFP. Cryo-EM data were screened and collected at the Duke University Shared Materials Instrumentation Facility (SMIF), the Pacific Northwest Center for Cryo-EM (PNCC) at OHSU, National Center for CryoEM Access and Training (NCCAT), the Simons Electron Microscopy Center at the New York Structural Biology Center, the National Cancer Institute's National Cryo-EM Microscopy facility (NCEF) at the Frederick National Laboratory for Cancer Research, the National Institute of Environmental Health Sciences (NIEHS), and the UNC Cryo-EM Core. We thank J. Myers at PNCC; A. Wier and T. Fox at NCEF; M. Aragon, H. Wei, H. Kuang at NCCAT; E. Viverette at NIEHS; J. Peck and J. Strauss at UNC, and N. Bhattacharya at SMIF for assistance with the microscope operation. We thank L. Zubcevic, J. Grandl, and J. Fedor for critical manuscript reading and Y. Suo for assistance with data collection at SMIF. **Funding:** This work was supported by the National Institutes of Health (R35NS097241 and R01EY031698 to S.-Y.L. and R01GM138472 to W.I.) and by the National Institute of Health Intramural Research Program; US National Institutes of Environmental Health Science (ZIC ES103326 to M.J.B.). Some of this research was supported by NIH grant U24GM129547 and performed at the PNCC at OHSU and accessed through EMSL (grid.436923.9), a DOE Office of Science User Facility sponsored by the Office of Biological and Environmental Research, by the NIH Common Fund Transformative High Resolution Cryo–Electron Microscopy program (U24 GM129539), grants from the Simons Foundation (SF349247) and NY State Assembly, by the contract 75N91019D00024 (NCEF), and by NIH grant P30CA016086 (UNC). **Author contributions:** Y.Y. conducted all biochemical preparation, cryo-EM experiments, and single-particle 3D reconstruction under the guidance of S.-Y.L. Y.Y. and S.-Y.L. performed model building. F.Z. carried out all electrophysiological recordings under the guidance of S.-Y.L. S.F. performed all molecular dynamics simulations under the guidance of W.I. K.J.B. helped with part of cryo-EM sample screening under the guidance of M.J.B. Y.Y. and S.-Y.L. wrote the paper. **Competing interests:** The authors declare no competing interests. **Data and materials availability:** For PIP_2-$TRPM8_{FA}$, apo-$TRPM8_{MM}$, $TRPM8_{MM}$, PIP_2-$TRPM8_{MM}$, PIP_2-C3-$TRPM8_{MM}$, and PIP_2-C3-AITC-$TRPM8_{MM}$ structures, the coordinates are deposited in the Protein Data Bank with the accession codes 8E4Q, 8E4P, 8E4O, 8E4N, 8E4M, 8E4L; the cryo-EM density maps are deposited in the Electron Microscopy Data Bank (EMDB) with the accession codes EMD-27896, EMD-27895, EMD-27894, EMD-27893, EMD-27892, and EMD-27891. The cryo-EM maps for the Class II C_1-state and the Class III putative desensitized state from $TRPM8_{MM}$ purified in ligand- and PIP_2-free condition are deposited in EMDB with accession codes EMD-27889 and EMD-27890.

SUPPLEMENTARY MATERIALS

science.org/doi/10.1126/science.add1268
Figs. S1 to S16
Tables S1 and S2
MDAR Reproducibility Checklist

Submitted 23 May 2022; accepted 15 September 2022
10.1126/science.add1268

RESEARCH ARTICLES

ENZYME EVOLUTION

Evolution of increased complexity and specificity at the dawn of form I Rubiscos

Luca Schulz[1], Zhijun Guo[2], Jan Zarzycki[1], Wieland Steinchen[3,4], Jan M. Schuller[3,4], Thomas Heimerl[3,5], Simone Prinz[6], Oliver Mueller-Cajar[2], Tobias J. Erb[1,3]*, Georg K. A. Hochberg[3,4,7]*

The evolution of ribulose-1,5-bisphosphate carboxylase/oxygenases (Rubiscos) that discriminate strongly between their substrate carbon dioxide and the undesired side substrate dioxygen was an important event for photosynthetic organisms adapting to an oxygenated environment. We use ancestral sequence reconstruction to recapitulate this event. We show that Rubisco increased its specificity and carboxylation efficiency through the gain of an accessory subunit before atmospheric oxygen was present. Using structural and biochemical approaches, we retrace how this subunit was gained and became essential. Our work illuminates the emergence of an adaptation to rising ambient oxygen levels, provides a template for investigating the function of interactions that have remained elusive because of their essentiality, and sheds light on the determinants of specificity in Rubisco.

Ribulose-1,5-bisphosphate carboxylase/oxygenases (Rubiscos) that are paired with oxygenic photosynthesis are responsible for most inorganic carbon assimilation on Earth today (*1*, *2*). Rubisco ancestrally evolved in anaerobic environments, predating the emergence of oxygenic photosynthesis (*3*, *4*). As oxygenic photosynthesis evolved, Rubisco faced molecular oxygen, which acts as an undesired side substrate during catalysis. Reaction with O_2 produces 2-phosphoglycolate (2PG), a metabolite that inhibits carbon metabolism and causes a loss of carbon from metabolism (*5*, *6*). To reduce the buildup of 2PG and enable its conversion, several mitigation strategies evolved: recycling of 2PG through photorespiration (*6*, *7*), carbon-concentrating mechanisms that concentrate CO_2 around Rubisco (*8*), and the use of Rubiscos with higher specificity for CO_2 (*9*–*11*). Although the exact strategies used for photorespiration and carbon concentration vary, all aerobic phototrophs, in particular algae and plants, use high-specificity Rubiscos (*9*, *11*). Their evolution was an important ingredient in the rise of oxygenic photosynthesis. Yet, how and when Rubisco evolved high specificity remain unknown despite extensive research and speculation (*4*, *12*–*14*).

[1]Department of Biochemistry and Synthetic Metabolism, Max Planck Institute for Terrestrial Microbiology, 35043 Marburg, Germany. [2]School of Biological Sciences, Nanyang Technological University, Singapore 637551, Singapore. [3]Center for Synthetic Microbiology (SYNMIKRO), Philipps University Marburg, 35043 Marburg, Germany. [4]Department of Chemistry, Philipps University Marburg, 35043 Marburg, Germany. [5]Department of Biology, Philipps University Marburg, 35043 Marburg, Germany. [6]Central Electron Microscopy Facility, Max Planck Institute of Biophysics, 60438 Frankfurt am Main, Germany. [7]Evolutionary Biochemistry Group, Max Planck Institute for Terrestrial Microbiology, 35043 Marburg, Germany.
*Corresponding author. Email: toerb@mpi-marburg.mpg.de (T.J.E.); georg.hochberg@mpi-marburg.mpg.de (G.K.A.H.)

The defining structural feature of all known high-specificity form I Rubiscos is their assembly into a complex of eight catalytic large subunits (LSUs) and eight noncatalytic small subunits (SSUs) (total stoichiometry: L8S8) (*1*). This stoichiometry evolved from simpler ancestors that did not interact with SSUs, as evidenced by modern-day SSU-independent form I′, II, and III Rubiscos (*3*, *13*). Because the SSU was previously shown to influence Rubisco catalysis (*15*–*20*) and because it is the most obvious structural difference between form I and other Rubiscos, it is thought to be at least partly responsible for increased specificity toward CO_2 (*10*, *17*). However, it has so far not been possible to directly test this hypothesis because the SSU is essential for both catalytic activity and solubility of form I Rubiscos (*15*, *21*, *22*). Studies on its effect have therefore been limited to in silico calculations (*23*), homolog shuffling experiments (*16*–*19*), and small-scale mutational perturbations (*17*, *20*), which have not been conclusive and have shown relatively small, mostly deleterious effects on specificity.

In this work, we overcome this challenge using ancestral sequence reconstruction (*24*) to recapitulate the evolution of form I Rubiscos. We identify the genetic and structural causes for the recruitment of the SSU, show that the SSU was indirectly responsible for an increase in specificity, and reveal how the solubility of form I Rubiscos became dependent on the SSU. Notably, our experiments suggest that form I Rubiscos increased their specificity for CO_2 over O_2 even before oxygen was abundant (*25*–*28*).

SSU gain coincided with rising specificity

To determine when Rubisco gained the SSU, we inferred maximum-likelihood phylogenies of Rubisco's LSU and SSU (Fig. 1A and figs. S1 and S2). On the LSU phylogeny, three clades of orthologs branch on the stem lineage toward form I Rubiscos (form I-α, form I′, and form I″) (*13*, *29*). These orthologs were identified from metagenome-assembled genomes (MAGs), which do not encode SSUs (fig. S3A). We also identified a fourth clade of true form I Rubiscos from MAGs that do encode SSUs (form I Anaero). This clade branches close to the last common ancestor (LCA) of known cyanobacterial and plant form I AB and proteobacterial and red algal form I CD Rubiscos (see the supplementary text).

These Rubisco-encoding MAGs were sampled in hot environments and belong to organisms related to anaerobic, thermophilic *Chloroflexaeota* (*30*) and *Firmicutes* (fig. S3, A, B, and C). For further characterization, we purified Rubiscos of clades branching close to the SSU's appearance and measured their oligomerization state using mass photometry (MP). Form I-α Rubiscos assembled into dimers, form I′ Rubiscos into octamers (*13*), and form I Anaero variants into L8S8 hexadecamers (Fig. 1B and fig. S3D). Furthermore, form I Anaero Rubiscos exhibited high thermal stability (>80°C), a high catalysis temperature optimum of 55° to 70°C (k_{catC} ~ 5 s^{-1}), and low specificity for CO_2 over O_2 for form I Rubiscos (specificity < 27; fig. S3, E, F, and G, and Table 1).

Together, the stoichiometry measurements and the absence of SSU genes in the MAGs of form I″–encoding organisms suggest that Rubisco began to interact with the SSU after branching of the form I″ clade. Furthermore, the MAG's origin in hot, anaerobic environments and the thermophilicity of form I Anaero Rubiscos suggest that the SSU first evolved in thermophilic anaerobes that existed before crown cyanobacteria diverged and thus before atmospheric oxygen levels rose substantially during the Great Oxygenation Event (GOE) (*25*–*28*). We cannot rule out that yet-unsampled organisms carry forms of Rubisco that conflict with these inferences. However, the phylogenetic interval in question is bracketed by three separate Rubisco clades with similar characteristics that derive from multiple sampling sites and sequencing projects. An anaerobic, thermophilic origin of form I Rubiscos is thus the most parsimonious scenario based on current data.

We next investigated how the evolution of Rubisco's L8S8 assembly influenced its function. To do this, we inferred sequences of ancestral Rubisco LSUs that existed before (AncL) and after (AncLS) the gain of the SSU (Fig. 1A and fig. S4, A and B). We also resurrected an ancestral small subunit (AncSSU). Because the SSU phylogeny has no outgroup, we reconstructed a deep node within the form I Anaero SSUs as a surrogate that existed close to the presumed root. MP of purified proteins showed that AncL formed a homo-octamer and that AncLS formed an L8S8 heterocomplex with

AncSSU (Fig. 1C). Both complexes were able to bind the active site inhibitor carboxyarabinitol-1,5-bisphosphate (CABP) and were stable to >75°C (fig. S4, C and D).

We quantified AncL and AncLS+AncSSU's carboxylation with ribulose-1,5-bisphosphate (RuBP) as well as their specificities for CO_2 over the side-reaction substrate O_2 ($S_{C/O}$) at 25°C. From AncL to AncLS+AncSSU, the $K_m(CO_2)$ (the Michaelis constant for CO_2) decreased from 568 to 69 μM, the K_m(RuBP) increased from 92 to 544 μM, and the maximal rate of carboxylation decreased from 0.61 to 0.29 (Table 1). Overall, this resulted in an increased catalytic efficiency for the carboxylation reaction (1.1×10^3 to 4.2×10^3) as well as a faster carboxylation at physiologically relevant dissolved CO_2 concentrations <500 μM and saturating RuBP concentrations in AncLS (fig. S4E). Lastly, the $S_{C/O}$ increased from 21.9 to 47.3, which is comparable to the change in specificity from a form II to a cyanobacterial form I Rubisco (Table 1). Thus, the carboxylation efficiency and specificity of Rubisco improved when the canonical form I L8S8 assembly first evolved. Subsequently, extant form I Anaero Rubiscos appear to have reverted to low specificities ($S_{C/O}$ values between 12 and 26), consistent with their anaerobic habitat. This suggests that binding of the SSU alone is not the sole determinant of specificity.

The SSU quickly became essential

Our next aim was to determine to what extent the SSU was responsible for the functional changes that we observed. We sought to identify a Rubisco that can bind the SSU but does not yet depend on it for solubility and activity. We first tested whether AncL was already able to bind AncSSU. We produced AncL with untagged AncSSU and vice versa. In either case, the untagged protein did not coelute (fig. S4,

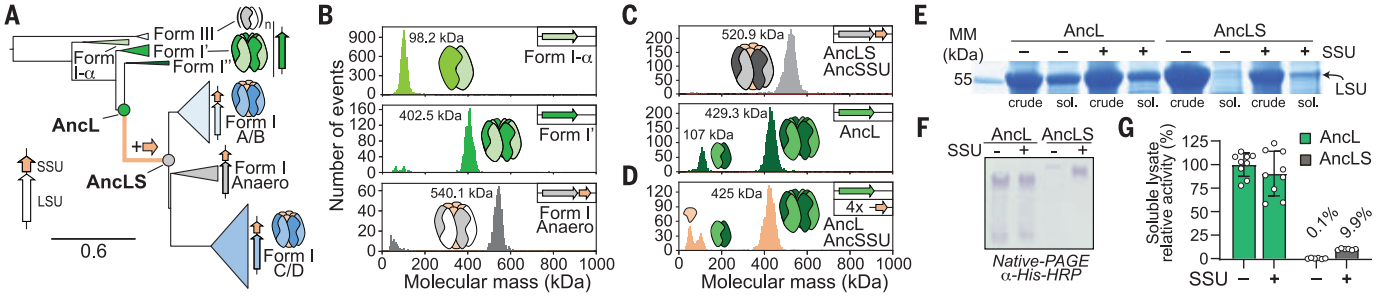

Fig. 1. The evolution of form I Rubiscos. (**A**) Reduced phylogeny of form I and related Rubiscos. Arrows depict operon structure. Complete phylogeny is shown in fig. S2. (**B**) MP spectra of metagenomic Rubiscos. Color scheme is according to (A). Inferred stoichiometries are depicted as cartoons. Representative spectra of two technical replicates. (**C**) MP spectra of ancestral Rubiscos AncL and AncLS+AncSSU. Representative spectra of more than five technical replicates. (**D**) MP spectrum of AncL after incubation with a fourfold molar excess of purified AncSSU. (**E**) Coomassie-stained SDS-PAGE of crude and soluble lysates of AncL and AncLS produced with or without AncSSU coproduction. MM, molecular mass; sol., soluble. Representative gel of more than five biological replicates. See fig. S5A for full gel. (**F**) Native PAGE and Western blot analyses of lysates from cultures producing AncL or AncLS with or without AncSSU coproduction. Loading control is shown in fig. S5B. HRP, horseradish peroxidase. (**G**) Relative Rubisco activities in soluble lysates of cultures producing AncL and AncLS with and without coproduction of AncSSU. Data are relative to measurements of AncL without AncSSU coproduction. For SDS-PAGE analysis of biological triplicates, see fig. S5C. $N = 9$ technical replicates for AncL, and $N = 6$ for AncLS. Error bars depict standard deviations (SDs).

Table 1. Kinetic characterization of ancestral and related extant Rubisco at 25°C. AncL+7 derives from AncL and contains seven substitutions at the LSU-SSU interface to enable SSU binding (Fig. 2). k_{catC} is the maximal rate of carboxylation under saturating substrate concentrations. $K_m(CO_2)$ and K_m(RuBP) are the Michaelis constants for CO_2 and RuBP, respectively. $S_{C/O} = [k_{catC}/K_m(CO_2)]/[k_{catO}/K_m(O_2)]$. *R. rubrum*, *Rhodospirillum rubrum*; *A. ferrooxidans*, *Acidithiobacillus ferrooxidans*; *Syn.*, *Synechococcus*; PCC, Pasteur Culture Collection. Values are means ± 95% confidence intervals with the number of technical replicates (*N*) indicated in parentheses. Extant form I Rubiscos were produced and measured with their native SSUs. Kinetic curves are shown in fig. S17. The $K_m(CO_2)$ measurement for RME08239 Rubisco was performed at 1 mM RuBP as opposed to 2.2 mM. n.d., not determined.

Rubisco name or identifier	k_{catC} (s^{-1})	$K_m(CO_2)$ (μM)	K_m(RuBP) (μM)	Specificity ($S_{C/O}$)	$k_{catC}/K_m(CO_2)$ (M^{-1} s^{-1})	$k_{catO}/K_m(O_2)$ (M^{-1} s^{-1})
AncL	0.61 ± 0.10 (2)	568 ± 177 (2)	92 (1)	21.9 ± 1.1 (9)	1.1×10^3	0.5×10^2
AncL+7	0.63 ± 0.11 (2)	499 ± 167 (2)	58 ± 18 (3)	25.3 ± 1.9 (5)	1.3×10^3	0.5×10^2
AncL+7 + 4x AncSSU	0.41 ± 0.02 (2)	148 ± 21 (2)	331 ± 76 (3)	29.6 ± 1.7 (4)	2.8×10^3	0.9×10^2
AncL+7 s437W	0.61 ± 0.11 (2)	460 ± 158 (2)	63 (1)	25.6 ± 1.4 (9)	1.3×10^3	0.5×10^2
AncL+7 s437W + 2x AncSSU	0.49 ± 0.02 (2)	162 ± 24 (2)	483 (1)	25.8 ± 2.2 (5)	3.0×10^3	1.2×10^2
AncL+7 e170N	0.55 ± 0.16 (2)	569 ± 300 (2)	28 (1)	25.6 ± 2.3 (6)	1.0×10^3	0.4×10^2
AncL+7 e170N + 4x AncSSU	0.47 ± 0.03 (4)	113 ± 29 (4)	203 (1)	38.7 ± 2.9 (6)	4.2×10^3	1.1×10^2
AncL+7 e170N s437W + 4x AncSSU	0.49 ± 0.02 (2)	119 ± 17 (2)	n.d.	40.7 ± 2.8 (4)	4.1×10^3	1.0×10^2
AncLS + AncSSU	0.29 ± 0.02 (2)	69 ± 16 (2)	544 (1)	47.3 ± 2.1 (9)	4.2×10^3	0.9×10^2
RME08239 + SSU (form I Anaero)	1.1 ± 0.12 (2)	200 ± 47 (2)	n.d.	12.2 ± 2.5 (2)	5.5×10^3	4.5×10^2
RMG64267 + SSU (form I Anaero)	1.94 ± 0.28 (2)	88 ± 53 (2)	67 (1)	26.4 (1)	2.2×10^4	8.4×10^2
R. rubrum (form II)	6.31 ± 0.56 (2)	116 ± 38 (2)	9 (1)	12.6 ± 0.5 (15)	5.4×10^4	4.3×10^3
A. ferrooxidans (form II)	n.d.	n.d.	n.d.	17.9 ± 0.5 (6)	n.d.	n.d.
Syn. PCC 6301 + SSU (form I)	n.d.	n.d.	n.d.	45.7 ± 1.7 (9)	n.d.	n.d.

F and G). Additionally, we purified AncL and AncSSU separately and used MP to probe the interaction, but we could not detect binding of AncSSU to AncL (Fig. 1D).

In parallel, we tested whether AncLS could still function without the SSU. We produced both ancestors with and without coproduction of AncSSU and quantified solubility using SDS–polyacrylamide gel electrophoresis (SDS-PAGE), Western blots, and Rubisco activities in clarified lysates. The yield of soluble AncLS was markedly reduced without AncSSU, whereas AncL titers were unchanged (Fig. 1, E, F, and G). The interaction with the SSU and a total dependence on it thus evolved in quick succession between AncL and AncLS. Interactions, dependencies, and catalytic properties of AncL and AncLS were qualitatively unchanged when validating their robustness to statistical uncertainty (*31*). Moreover, inferences of AncLS's stoichiometry and SSU dependence were unchanged when AncLS was reconstructed using an alternative phylogeny (*29*) (figs. S6, S7, and S8 and supplementary text).

Genetic basis of LSU-SSU interaction

Because AncL cannot yet interact with the SSU, and AncLS already cannot function without it, historical substitutions that separate the two constructs must be responsible for both creating the LSU-SSU interaction and making it essential. We reasoned that we might be able to construct a nonobligate LSU-SSU interaction by introducing only those substitutions into AncL that create the interaction.

To pinpoint relevant substitutions, we solved x-ray crystal structures of inhibitor-bound AncL and AncLS+AncSSU to 2.1- and 1.8-Å resolution, respectively (Fig. 2, A and B). AncL and AncLS differ by 95 substitutions, 14 of which are close to the SSU in the AncLS structure, and three insertions (Fig. 2, C and D, and fig. S4B). The 14 substituted sites make up only 22% of all interface sites and 25% of the total buried interface area in AncLS.

Next, we created AncL constructs containing single, double, or triple combinations of the 14 substitutions in proximity to the SSU (8, 28, and 10 variants, respectively). At least three substitutions were required to create a MP-detectable LSU-SSU interaction (fig. S9), although this interaction remained weak. To achieve tighter binding, we simultaneously introduced seven interface substitutions into AncL (Fig. 2D). This variant (AncL+7) was soluble without AncSSU and rapidly reconstituted an L8S8 heterocomplex upon mixing with purified AncSSU (Fig. 2E).

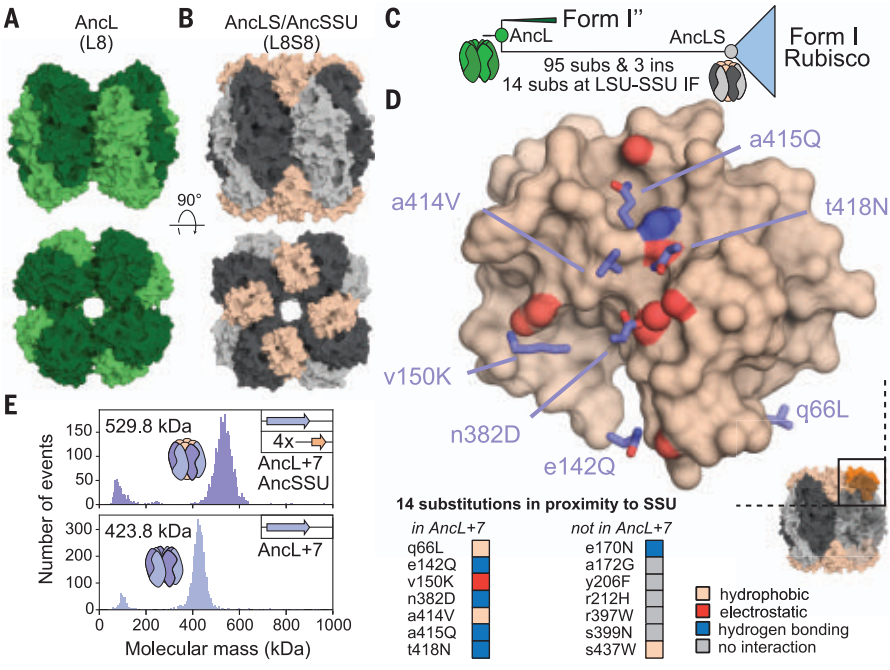

Fig. 2. A small set of substitutions can create the LSU-SSU interface. (**A**) Structure of CABP-bound AncL solved to 2.1 Å. (**B**) Structure of CABP-bound AncLS cocrystallized with AncSSU solved to 1.8 Å. LSU is shown in light and dark gray, and AncSSU is shown in beige. (**C**) Schematic phylogeny highlighting the differences between AncL and AncLS. subs, substitutions; ins, insertions; IF, interface. (**D**) Substitutions separating AncL from AncLS that occurred in proximity to the SSU. Small letters denote ancestral states, and capitalized letters denote derived states. Purple side chains depict substitutions that are transplanted into AncL+7. The SSU surface is depicted in beige. Heteroatoms within 3.8 Å of the substitutions are highlighted in red (oxygen) and blue (nitrogen). Water molecule is shown as a red sphere. (**E**) MP spectra of AncL+7 in isolation (bottom) or with a fourfold molar excess of purified AncSSU (top). Empirical masses and inferred stoichiometries are depicted in the histogram. Theoretical L8 mass: 428.0 kDa; theoretical L8S8 mass: 527.6 kDa. Data are from three technical replicates. Single-letter abbreviations for the amino acid residues are as follows: A, Ala; C, Cys; D, Asp; E, Glu; F, Phe; G, Gly; H, His; I, Ile; K, Lys; L, Leu; M, Met; N, Asn; P, Pro; Q, Gln; R, Arg; S, Ser; T, Thr; V, Val; W, Trp; and Y, Tyr.

SSU improved catalysis and specificity

We were now able to directly test how the interaction with the SSU affected Rubisco. To do this, we measured AncL+7's kinetic parameters in the presence or absence of AncSSU (the L8 and L8S8 forms of AncL+7, respectively). The carboxylation rate of AncL+7 decreased slightly when interacting with the SSU (k_{catC} values of 0.63 and 0.41, respectively), and the K_m(RuBP) increased sixfold. Notably, however, the $K_m(CO_2)$ was decreased threefold, which, in total, leads to a 2.2-fold improvement in carboxylation efficiency. Carboxylation is up to twofold faster at physiologically relevant dissolved CO_2 concentrations <500 μM in the L8S8 form at saturating RuBP concentrations (Fig. 3, A and B, and Table 1). We verified robustness of these inferences with an alternative SSU reconstruction, corresponding to a deeper but worse-reconstructed node on our SSU phylogeny (fig. S10).

Besides increasing carboxylation efficiency, the addition of AncSSU to AncL+7 markedly increased the temperature tolerance of catalysis from ~40°C up to 50° to 70°C, which results in an up to 12.5-fold improved carboxylation rate in the L8S8 form at 70°C (Fig. 3C). Yet, unexpectedly, AncSSU did not increase overall stability of AncL+7 toward denaturation: We found no difference in stability between the L8 and L8S8 forms upon exposure to elevated temperatures (Fig. 3D).

Next, we quantified how the SSU affected CO_2/O_2 specificity. The seven substitutions introduced at the LSU-SSU interface to create AncL+7 already caused a statistically significant increase in specificity from 21.9 to 25.3 (P = 0.0013, two-tailed t test; Fig. 3E and Table 1). This increase was amplified to 29.6 when the SSU was added. We could further improve specificity by introducing one more substitution at the LSU-SSU interface. Introducing e170N (where small letters denote ancestral states and capitalized letters denote derived states) into AncL+7 boosted specificity to 38.7 in the presence of AncSSU but did not improve AncL+7's specificity without AncSSU (Fig. 3E and Table 1). Together, eight substitutions and the presence of AncSSU almost doubled the specificity of AncL from 21.9 to 38.7, whereas no changes in or close to the active site were required. The SSU is thus directly and indirectly responsible for the key functional improvements associated with form I Rubiscos: The interaction directly improves

catalytic efficiency and catalysis at high temperatures. Its effect on specificity is (at least partly) indirect because it epistatically enhances the effect of substitution e170N, which has no influence on specificity without the SSU.

To elucidate the structural basis of the SSUs' effects on catalysis, we solved x-ray crystal structures of inhibitor-bound AncL+7 as well as AncL+7 e170N in their L8 and L8S8 forms (Fig. 3F and fig. S11A). In both complexes, individual monomers are virtually identical between the L8 and L8S8 forms [average root mean square deviation (RMSD) < 0.3 Å; fig. S11B]. The only observable structural difference is that the LSU octamer is slightly more compact in the L8S8 forms, but this does not translate into observable active site rearrangements (Fig. 3G and fig. S11, C and D). The high specificity–conferring e170N substitution at the LSU-SSU interface is far away from the active site, where it engages in a hydrogen-bonding interaction with Y83 and Q88 on the SSU (fig. S11E). The SSU thus improves catalysis through allosteric effects on either the open, non–inhibitor-bound state or protein dynamics.

A single substitution causes SSU dependence

All characterized form I Rubiscos depend on the SSU for solubility or catalysis (*15*, *21*, *22*), and our results indicate that this trait had already evolved by the time of AncLS. We therefore sought to discover how this dependence evolved. Drawing on prior work on how

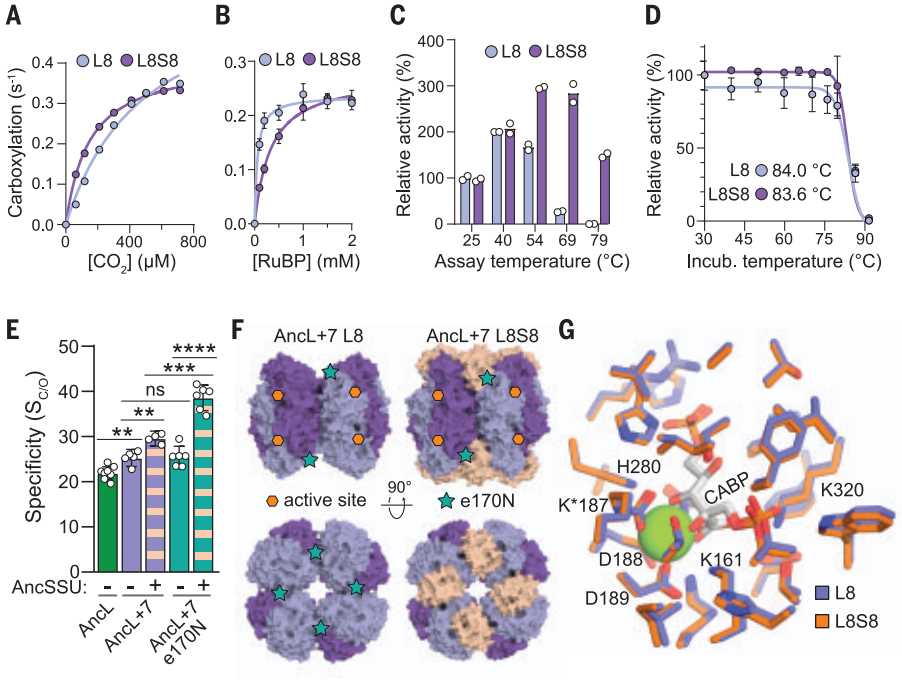

Fig. 3. The SSU allosterically enhances catalysis. (**A** and **B**) Kinetic characterization of AncL+7 with or without AncSSU (L8 and L8S8 forms, respectively). Data are the means of two (A) or three (B) technical replicates. Error bars indicate SDs. (**C**) Carboxylation rates of the L8 and L8S8 forms of AncL+7 at varying temperatures. Bars represent the means of two technical replicates. Activity is relative to the rate of catalysis at 25°C in L8 form. (**D**) Remaining activities of the L8 and L8S8 forms of AncL+7 after incubation at elevated temperatures, shown relative to incubation (Incub.) at 30°C. Curve is a sigmoidal fit (N = 3 technical replicates; error bars indicate SDs). (**E**) Specificity of AncL variants with and without AncSSU. Significance tested by two-tailed t test. ns, nonsignificant; $^{**}P < 0.01$; $^{***}P < 0.001$; $^{****}P < 0.0001$. N values are listed in Table 1, and error bars represent 95% confidence intervals. (**F**) Structures of CABP-bound AncL+7 crystallized as a homomer (left) or in complex with AncSSU (right) solved at 2.65 and 2.0 Å, respectively. LSU monomers are shown in light and dark purple, and AncSSU is shown in beige. (**G**) Active site residues of the L8 (purple) and L8S8 forms (orange) of AncL+7 with coordinated magnesium (green spheres) and bound CABPs (L8, light gray; L8S8, dark gray). K*187 marks the carbamylated active site lysine.

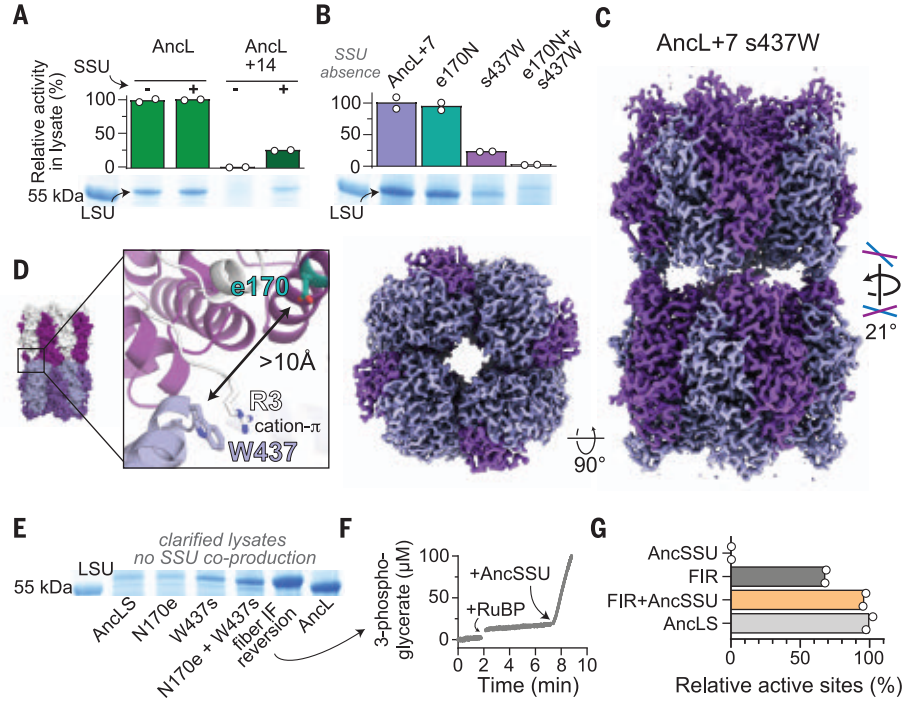

Fig. 4. Rubisco evolves to depend on the SSU for solubility and catalysis. (**A**) Relative Rubisco activities and SDS-PAGE analysis of soluble lysates from strains producing AncL and AncL+14 with or without AncSSU. LSU band is indicated. Full gel is shown in fig. S16A. N = 2 technical replicates. (**B**) Relative Rubisco activities and SDS-PAGE analysis of soluble lysates from strains producing AncL+7 and derivates thereof. Full gel is shown in fig. S16B, and crude lysate pictures are shown in fig. S16C. N = 2 technical replicates. (**C**) A 3.01-Å resolution cryo-EM density map of AncL+7 s437W fibrils. (**D**) Structural interactions across the fiber interface of sites that contain entrenching states. (**E**) Coomassie-stained SDS-PAGE of clarified lysates from cells producing AncLS and variants thereof. AncSSU was not coproduced. Genotype of the fiber IF reversion construct is listed in fig. S11H. Full gel is shown in fig. S16B. (**F**) 3-Phosphoglycerate production of fiber interface reversion is SSU-dependent, even though solubility is recovered. Arrows mark addition of RuBP and AncSSU (10-fold excess). (**G**) Relative active site contents of Rubisco LSU (0.2 nmol) and SSU (2 nmol) samples, as determined by ^{14}C-CABP binding assays. FIR, fiber interface reversion construct. Bars represent the means of two technical replicates.

interactions can become essential (*32*, *33*), we hypothesized that entrenching substitutions occurred near the SSU interface. To test this idea, we simultaneously transplanted all seven additional SSU-neighboring substitutions from AncLS into AncL+7. The resulting AncL+14 was only soluble when AncSSU was coproduced and formed an L8S8 heterocomplex (Fig. 4A and fig. S12A).

To pinpoint which changes cause SSU dependence, we introduced all 14 substitutions individually into AncL and tested their effect on solubility (fig. S12B and fig. S13). Substitution s437W reduced solubility of both AncL and AncL+7 by ~75%, as assessed by SDS-PAGE and relative Rubisco activities in clarified lysate (Fig. 4B). We examined the remaining six substitutions separating AncL+7 s437W from AncL+14 for their effect on solubility (fig. S12, C and D). Substitution e170N, which was also responsible for the specificity increase, had the most severe effect. When introduced into AncL+7 s437W, it caused a complete loss of solubility, which could be rescued by coproducing AncSSU. Notably, e170N alone had no negative effect on the solubility of AncL+7 (Fig. 4B). Thus, a single historical substitution (s437W) could make Rubisco become dependent on the SSU for solubility.

Introducing s437W had no measurable effect on most biochemical parameters of AncL+7 or on catalysis and specificity of AncL+7 e170N in the presence of AncSSU (fig. S14 and Table 1). Our results imply that Rubisco's dependence on the SSU for solubility is functionally neutral and is not required for the catalytic improvements associated with form I Rubiscos. This conclusion is further supported by the fact that most of the functional differences between AncL and AncLS are recapitulated in AncL+7 e170N+AncSSU, which does not depend on the SSU (Table 1).

Mechanisms of essentiality

To conclude our investigation, we sought to understand how these two substitutions make the LSU require the SSU for solubility. Rubiscos containing s437W formed higher-order oligomers in MP measurements and stacked into fibers in negative-stain electron microscopy images (fig. S12, E, F, and G). This led us to hypothesize that insolubility stems from LSU self-assembly into fibers (*34*), which can be prevented by the SSU.

To understand the molecular basis of fiber formation, we solved the structure of AncL+7 s437W fibers to 3.01 Å using cryo–electron microscopy (cryo-EM) (Fig. 4C and fig. S15). In fibers, LSU octamers interact at their apices, forming a helix with a twist of ~21° per octamer. The fiber-inducing W437 directly engages in a cation-π interaction with R3 of an adjacent LSU octamer at the fiber interface. N170, which exacerbates the effect of W437, seems to have a less direct mechanism of action, as it is >10 and >25 Å away from either of the fiber interfaces (Fig. 4D). The fiber interface partially overlaps with the LSU-SSU interface, which makes the cavity between interacting octamers too small to accommodate SSUs. Capping of LSU octamers by SSUs therefore makes fiber formation impossible (fig. S12, H and I).

We tested whether substitutions e170N and s437W remain the sole causes of insolubility in AncLS or whether additional entrenching substitutions accumulated at the SSU interface. Neither N170e nor W437s reversions, alone or as a pair, fully restored solubility without the SSU (Fig. 4E). Simultaneously reverting all 14 substitutions that occurred within 5 Å of the fiber interface fully recovered solubility in the absence of the SSU (Fig. 4E and fig. S12H). Hence, the region around the fiber interface remains the cause of insolubility, and additional entrenching substitutions beyond e170N and s437W accumulated after the gain of the SSU.

In the absence of SSUs, this so-called fiber interface reversion construct assembled into a conventional L8 complex but was only partially able to bind the active site inhibitor CABP and was barely active (~68% active site content; $k_{catC} < 0.05\ s^{-1}$). Addition of AncSSU quickly reconstituted an L8S8 complex, increased active site content to levels comparable to those of AncLS, and restored catalytic activity (Fig. 4, F and G, and fig. S12J). This indicated that even though we reverted the dependence on SSU for solubility, some of the remaining 81 substitutions separating AncL and the fiber interface reversion construct made Rubisco depend on the SSU for catalysis. This catalytic dependence is also present in the only form I Rubisco that is soluble without the SSU (*15*).

Conclusions

We show that the SSU modified the functional sequence space available to Rubisco. Consequently, certain substitutions became advantageous in the presence of the SSU that otherwise would not have been. However, it also enabled the accumulation of substitutions that created a dependence on the interaction. Rubisco is a slow-evolving (*35*), notoriously constrained enzyme (*36*, *37*), and the recruitment of an epistatic modifier like the SSU may have been the only way for it to access high specificity.

All features of modern form I Rubiscos—interaction with and dependence on the SSU, as well as high specificity—had already evolved by the time of AncLS. Notably, this timeline implies that high-specificity Rubiscos predate the GOE and may even predate the evolution of photosystem II, although the exact timing of this event is still contested (*25*–*28*, *38*). One possibility is that specificity first improved as a by-product of selection for decreasing $K_m(CO_2)$ alongside a drop in atmospheric CO_2 concentrations before the GOE (*39*). This would have fortuitously prepared Rubisco for the subsequent rise of atmospheric O_2 concentrations. However, there is also tentative evidence that O_2 (and, by implication, oxygenic photosynthesis) may have been present before the GOE (*28*, *38*, *40*–*42*), which could have directly selected for improved specificity. In either case, the evolution of the SSU facilitated Rubisco's coexistence with oxygenic photosynthesis, which helped set the stage for complex life in aerobic environments.

REFERENCES AND NOTES

1. I. Andersson, A. Backlund, *Plant Physiol. Biochem.* **46**, 275–291 (2008).
2. Y. M. Bar-On, R. Milo, *Proc. Natl. Acad. Sci. U.S.A.* **116**, 4738–4743 (2019).
3. F. R. Tabita, S. Satagopan, T. E. Hanson, N. E. Kreel, S. S. Scott, *J. Exp. Bot.* **59**, 1515–1524 (2008).
4. T. J. Erb, J. Zarzycki, *Curr. Opin. Biotechnol.* **49**, 100–107 (2018).
5. W. W. Cleland, T. J. Andrews, S. Gutteridge, F. C. Hartman, G. H. Lorimer, *Chem. Rev.* **98**, 549–562 (1998).
6. F. Flügel *et al.*, *Plant Cell* **29**, 2537–2551 (2017).
7. H. Bauwe, M. Hagemann, A. R. Fernie, *Trends Plant Sci.* **15**, 330–336 (2010).
8. J. A. Raven, C. S. Cockell, C. L. De La Rocha, *Phil. Trans. R. Soc. B* **363**, 2641–2650 (2008).
9. A. I. Flamholz *et al.*, *Biochemistry* **58**, 3365–3376 (2019).
10. R. J. Spreitzer, *Arch. Biochem. Biophys.* **414**, 141–149 (2003).
11. C. Iñiguez *et al.*, *Plant J.* **101**, 897–918 (2020).
12. B. Kacar, V. Hanson-Smith, Z. R. Adam, N. Boekelheide, *Geobiology* **15**, 628–640 (2017).
13. D. M. Banda *et al.*, *Nat. Plants* **6**, 1158–1166 (2020).
14. P. M. Shih *et al.*, *Nat. Commun.* **7**, 10382 (2016).
15. T. J. Andrews, *J. Biol. Chem.* **263**, 12213–12219 (1988).
16. T. J. Andrews, D. M. Greenwood, D. Yellowlees, *Arch. Biochem. Biophys.* **234**, 313–317 (1984).
17. S. Karkehabadi *et al.*, *Biochemistry* **44**, 9851–9861 (2005).
18. E. Martin-Avila *et al.*, *Plant Cell* **32**, 2898–2916 (2020).
19. M. T. Lin, W. D. Stone, V. Chaudhari, M. R. Hanson, *Nat. Plants* **6**, 1289–1299 (2020).
20. B. A. Read, F. R. Tabita, *Biochemistry* **31**, 519–525 (1992).
21. C. Liu *et al.*, *Nature* **463**, 197–202 (2010).
22. J. Joshi, O. Mueller-Cajar, Y.-C. C. Tsai, F. U. Hartl, M. Hayer-Hartl, *J. Biol. Chem.* **290**, 1066–1074 (2015).
23. M. van Lun, J. S. Hub, D. van der Spoel, I. Andersson, *J. Am. Chem. Soc.* **136**, 3165–3171 (2014).
24. G. K. A. Hochberg, J. W. Thornton, *Annu. Rev. Biophys.* **46**, 247–269 (2017).
25. P. M. Shih, J. Hemp, L. M. Ward, N. J. Matzke, W. W. Fischer, *Geobiology* **15**, 19–29 (2017).
26. B. E. Schirrmeister, J. M. de Vos, A. Antonelli, H. C. Bagheri, *Proc. Natl. Acad. Sci. U.S.A.* **110**, 1791–1796 (2013).
27. B. E. Schirrmeister, M. Gugger, P. C. J. Donoghue, *Palaeontology* **58**, 769–785 (2015).
28. N. J. Planavsky *et al.*, *Nat. Geosci.* **7**, 283–286 (2014).
29. J. A. West-Roberts *et al.*, bioRxiv 2021.08.23.457424 [Preprint] (2021). https://doi.org/10.1101/2021.08.23.457424.
30. Y. Sekiguchi *et al.*, *Int. J. Syst. Evol. Microbiol.* **53**, 1843–1851 (2003).
31. G. N. Eick, J. T. Bridgham, D. P. Anderson, M. J. Harms, J. W. Thornton, *Mol. Biol. Evol.* **34**, 247–261 (2017).
32. G. K. A. Hochberg *et al.*, *Nature* **588**, 503–508 (2020).
33. A. Stoltzfus, *J. Mol. Evol.* **49**, 169–181 (1999).
34. H. Garcia-Seisdedos, C. Empereur-Mot, N. Elad, E. D. Levy, *Nature* **548**, 244–247 (2017).
35. J. W. Bouvier, D. M. Emms, S. Kelly, bioRxiv 2022.07.06.498985 [Preprint] (2022). https://doi.org/10.1101/2022.07.06.498985.
36. G. G. B. Tcherkez, G. D. Farquhar, T. J. Andrews, *Proc. Natl. Acad. Sci. U.S.A.* **103**, 7246–7251 (2006).
37. J. W. Bouvier *et al.*, *Mol. Biol. Evol.* **38**, 2880–2896 (2021).
38. T. Cardona, J. W. Murray, A. W. Rutherford, *Mol. Biol. Evol.* **32**, 1310–1328 (2015).
39. A. M. Hessler, D. R. Lowe, R. L. Jones, D. K. Bird, *Nature* **428**, 736–738 (2004).
40. A. M. Satkoski, N. J. Beukes, W. Li, B. L. Beard, C. M. Johnson, *Earth Planet. Sci. Lett.* **430**, 43–53 (2015).
41. J. Jabłońska, D. S. Tawfik, *Nat. Ecol. Evol.* **5**, 442–448 (2021).
42. S. Kumar, G. Stecher, M. Suleski, S. B. Hedges, *Mol. Biol. Evol.* **34**, 1812–1819 (2017).
43. L. Schulz, G. Hochberg, T. Erb, Evolution of increased complexity and specificity at the dawn of Form I Rubiscos,

version 1.0, Edmond (Max Planck Digital Library, 2022); https://doi.org/10.17617/3.F9BWOU.

ACKNOWLEDGMENTS

The authors thank the Central Electron Microscopy Facility at the Max Planck Institute of Biophysics for expertise and access to their instruments. We acknowledge support from the European Synchrotron Radiation Facility (ESRF, Grenoble, France) and the EMBL Hamburg at the PETRA III storage ring (DESY, Hamburg, Germany). **Funding:** O.M.-C. is thankful for support from a Ministry of Education (MOE) of Singapore Tier 2 grant (MOE-T2EP30120-0005). J.M.S. is grateful for an Emmy Noether grant (SCHU 3364/1-1) from the Deutsche Forschungsgemeinschaft (DFG). L.S., J.Z., S.P., T.J.E., and G.K.A.H. are grateful for generous support from the Max Planck Society. L.S. thanks Refeyn Ltd. for a travel grant that funded the presentation of this work. **Author contributions:** L.S., T.J.E., and G.K.A.H. conceived the project, analyzed data, and planned experiments. L.S. performed molecular work, phylogenetics, ancestral sequence reconstruction, protein purification, cryo-EM and x-ray analysis, comparative in vitro biochemistry, and MP measurements. Z.G. performed enzyme kinetic analysis and specificity constant measurements. O.M.-C. supervised enzyme kinetic analysis and specificity constant measurements. W.S. analyzed x-ray structures. J.Z. collected, solved, refined, and analyzed x-ray structures and refined the cryo-EM structure. T.H. performed negative-stain EM. S.P. performed cryo-EM grid preparation and collected cryo-EM datasets, and J.M.S. processed the cryo-EM datasets. O.M.-C., T.J.E., and G.K.A.H. supervised the project. L.S., T.J.E., and G.K.A.H. wrote the manuscript with contributions and comments from all authors. **Competing interests:** O.M.-C. has consulted for FL79 Inc. This company did not fund and had no role in this research project. The authors declare no other competing interests. **Data and materials availability:** All raw data for MP spectra and kinetic traces as well as phylogenetic trees, alignments, and ancestral sequences are deposited on Edmond, the Open Research Data Repository of the Max Planck Society for public access (*43*). Atomic structures reported in this paper are deposited to the Protein Data Bank under accession codes 7QSV, 7QSW, 7QSX, 7QSY, 7QSZ, 7QT1, and 7QVI. The cryo-EM data were deposited to the Electron Microscopy Data Bank under EMD-14178.

SUPPLEMENTARY MATERIALS

science.org/doi/10.1126/science.abq1416
Materials and Methods
Supplementary Text
Figs. S1 to S18
Tables S1 to S7
References (*44*–*73*)
MDAR Reproducibility Checklist

Submitted 21 March 2022; accepted 26 August 2022
10.1126/science.abq1416

NEUROSCIENCE

In vivo direct imaging of neuronal activity at high temporospatial resolution

Phan Tan Toi[1,2]†, Hyun Jae Jang[3,4]†, Kyeongseon Min[5], Sung-Phil Kim[6], Seung-Kyun Lee[1,2]‡, Jongho Lee[5], Jeehyun Kwag[3,7]*, Jang-Yeon Park[1,2]*

There has been a long-standing demand for noninvasive neuroimaging methods that can detect neuronal activity at both high temporal and high spatial resolution. We present a two-dimensional fast line-scan approach that enables direct imaging of neuronal activity with millisecond precision while retaining the high spatial resolution of magnetic resonance imaging (MRI). This approach was demonstrated through in vivo mouse brain imaging at 9.4 tesla during electrical whisker-pad stimulation. In vivo spike recording and optogenetics confirmed the high correlation of the observed MRI signal with neural activity. It also captured the sequential and laminar-specific propagation of neuronal activity along the thalamocortical pathway. This high-resolution, direct imaging of neuronal activity will open up new avenues in brain science by providing a deeper understanding of the brain's functional organization, including the temporospatial dynamics of neural networks.

Advanced noninvasive neuroimaging methods provide valuable information on the brain's functional organization, but they have obvious pros and cons in terms of temporal and spatial resolution. Functional magnetic resonance imaging (fMRI) using the blood oxygenation level–dependent (BOLD) effect provides spatial resolution on the order of millimeters. However, its temporal resolution is limited by slow hemodynamic responses to neuronal activities such as spikes (*1*), whereas recent advances have been made in imaging subsecond oscillatory neuronal dynamics (*2*). Because there is no direct correspondence between BOLD signals and spiking activity (*3*–*5*), BOLD-fMRI provides indirect information about neuronal activity, intrinsically limiting the spatial and temporal precision (*5*, *6*). By contrast, electroencephalography (EEG) and magnetoencephalography (MEG) provide excellent temporal resolution in the millisecond range, but spatial information is limited to centimeter scales (*7*). Thus, while harnessing the high spatial resolution of MRI, enhancement of MRI-based temporal resolution up to that of EEG or MEG on the order of milliseconds is imperative to advance the understanding of the brain in vivo.

Many attempts have been made to use MRI to directly image neuronal activity (*8*). Most of them were based on the neuronal current models, where neuronal currents flowing along the axon produce an ultraweak circumferential magnetic field on the order of nanotesla (nT) (*9*, *10*), thereby locally changing the phase and magnitude of magnetic resonance (MR) signals. Phantom studies demonstrated small phase shifts (<1°) induced by magnetic field changes ≤1 nT when injecting electrical currents through wires in a gel phantom (*9*, *11*–*13*). In vitro studies using hemoglobin-free biological objects (*14*–*18*) also reported changes in the magnitude of MR signals (e.g., 0.01 to 5.5%) induced by the applied stimulus. Some studies have argued that they succeeded in directly detecting human brain activation in vivo (*19*–*24*), but these results have not been replicated in later attempts (*25*–*29*).

Other attempts have also been made to directly measure neuronal activity using biophysical changes at the cellular level or by using contrast agents. In diffusion fMRI, microstructural changes such as cell swelling, which may cause changes in water diffusion, have been proposed as possible signal sources for directly measuring neuronal activity (*30*–*33*). Although initial results were called into question (*32*), more recent work has shown encouraging evidence that diffusion fMRI provides faster and more-specific detection of neuronal activity than conventional fMRI on the basis of hemodynamic responses (*33*). Another approach is the development of contrast agents such as manganese that enable in vivo measurements of intracellular calcium in rodents (*34*) but are limited by toxicity and induced physiological effects, particularly in human studies.

We propose a method to enable direct imaging of neuronal activity (hereafter referred to as DIANA) for functional MRI. With DIANA, the temporal resolution is increased up to the temporal precision of neuronal activity in milliseconds while retaining the original benefit of the high spatial resolution of MRI.

Results

MRI of neuronal activity at millisecond temporal resolution

To implement high temporal resolution at the millisecond scale, we used a conventional two-dimensional (2D) gradient-echo imaging sequence with a short echo time (TE) and short

[1]Department of Biomedical Engineering, Sungkyunkwan University, Suwon 16419, Republic of Korea. [2]Department of Intelligent Precision Healthcare Convergence, Sungkyunkwan University, Suwon 16419, Republic of Korea. [3]Department of Brain and Cognitive Engineering, Korea University, Seoul 02841, Republic of Korea. [4]Division of Computer Engineering, Baekseok University, Cheonan 31065, Republic of Korea. [5]Department of Electrical and Computer Engineering, Seoul National University, Seoul 08826, Republic of Korea. [6]Department of Biomedical Engineering, Ulsan National Institute of Science and Technology, Ulsan 44919, Republic of Korea. [7]Department of Brain and Cognitive Sciences, Seoul National University, Seoul 08826, Republic of Korea.
***Corresponding author. Email: jyparu@skku.edu (J.-Y.P.); jkwag@snu.ac.kr (J.K.)**
†These authors contributed equally to this work.
‡Present address: GE Global Research, Niskayuna, NY 12309, USA.

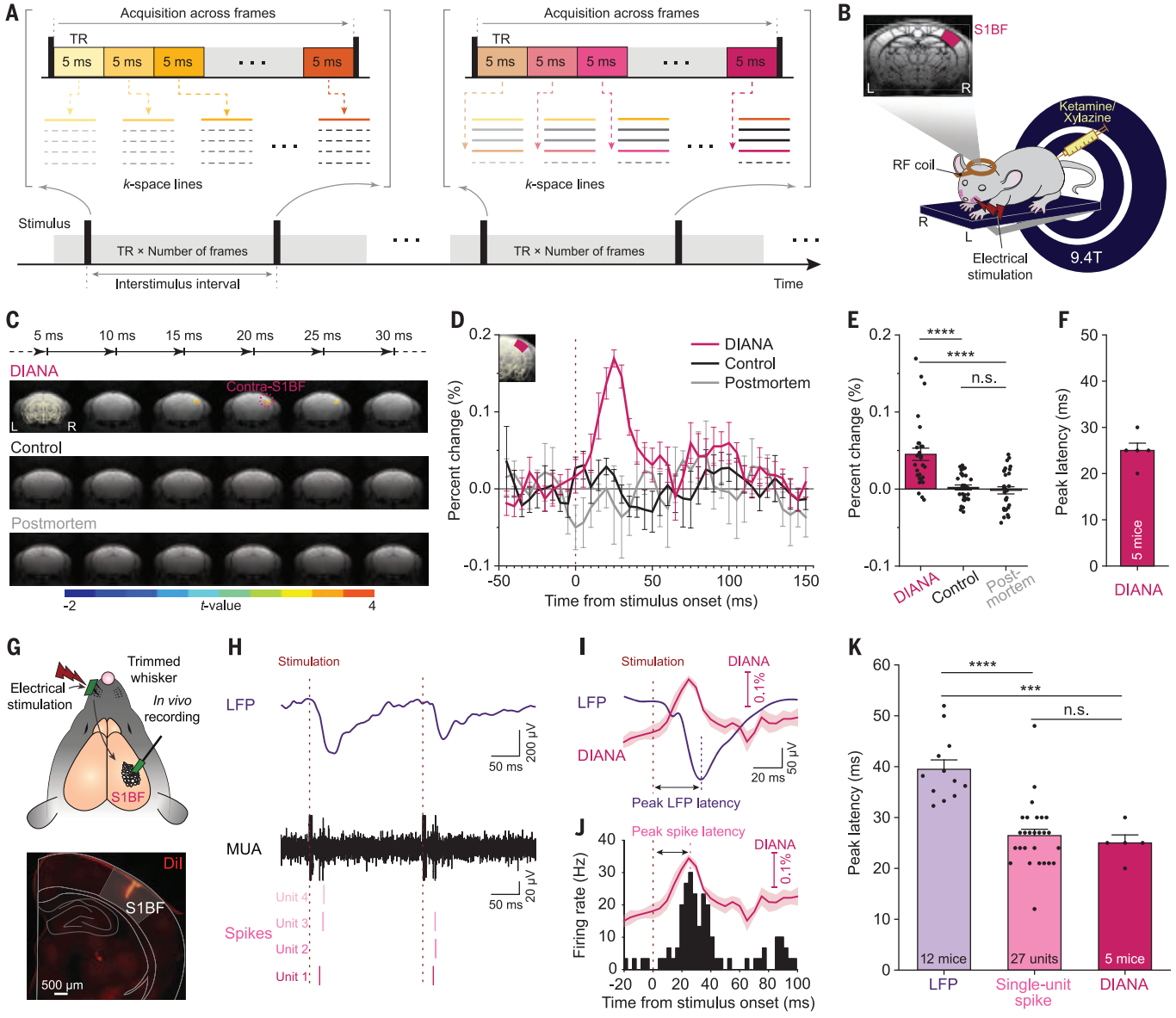

Fig. 1. Direct imaging of neuronal activity with high temporospatial resolution. (**A**) 2D fast line-scan DIANA (direct imaging of neuronal activity) acquisition scheme. (**B**) Illustration of the DIANA experiment used to image the S1BF by applying electrical stimulation to the left whisker pad in an anesthetized mouse on a 9.4-T scanner. L, left; R, right; RF, radiofrequency. (**C** to **E**) Time series of *t*-value maps at 5-ms temporal resolution (C), percent changes in DIANA signals (D), and mean signal changes during poststimulation (E) with electrical whisker-pad stimulation (magenta, n = 5 mice) and without stimulation (control, black, n = 5 mice) and in the postmortem condition (gray, n = 4 mice). In (D), the inset shows the contralateral S1BF. (**F**) Latency of the peak DIANA response. (**G**) Electrophysiological recording in mice in vivo with a 32-channel silicon probe implanted in the contralateral S1BF applying electrical whisker-pad stimulation (top) and electrode track marking using a fluorescent lipophilic dye (DiI) (bottom). (**H**) LFP signal (purple trace, top) and MUA (black trace, middle) from which single-unit spikes (bottom) were analyzed. Spikes of each single unit are displayed in different shades of magenta. (**I** and **J**) LFP (I) and PSTH of the whisker-pad stimulation-responsive single units over time in the contralateral S1BF (J) with DIANA signals superimposed (magenta trace) for comparison. (**K**) Bar graph showing the latencies of LFP (purple, n = 12 mice), the peak spike firing rate of whisker-pad stimulation-responsive single units (light magenta, n = 27 units from 10 mice), and the DIANA response (magenta, n = 5 mice). Vertical dashed lines indicate the electrical whisker-pad stimulation onset time [(D) and (H) to (J)] and latency of either peak LFP (I) or peak spike firing rate (J). All data are means ± SEM. ***$p < 0.001$, ****$p < 0.0001$, and n.s. is $p > 0.05$ for Kruskal-Wallis analysis of variance (ANOVA) with Dunn post hoc test (E) and one-way ANOVA with Bonferroni post hoc test (K).

repetition time (TR) of a few milliseconds by combining a line-scan acquisition strategy (*35*–*37*), which will be referred to as 2D fast line-scan, where a single line of *k*-space was repeatedly acquired during each interstimulus interval and different *k*-space lines were acquired in different periods. Each stimulation period adds one line of the *k*-space to all the time-series images within the period (Fig. 1A), and the TR exactly determines the temporal resolution of the dynamic imaging. This can be implemented simply by swapping the order of repetition and phase-encoding loops in a 2D gradient-echo imaging sequence (*35*, *36*). Electrical stimulation was repeatedly applied at 200-ms interstimulus intervals, determined by 5-ms TR multiplied by 40 frames in the time series. The TE for each line scan was set as short as 2 ms. We delivered electrical stimulation to the left whisker pad (strength, 0.5 mA; duration, 0.5 ms; frequency, 5 Hz) of anesthetized

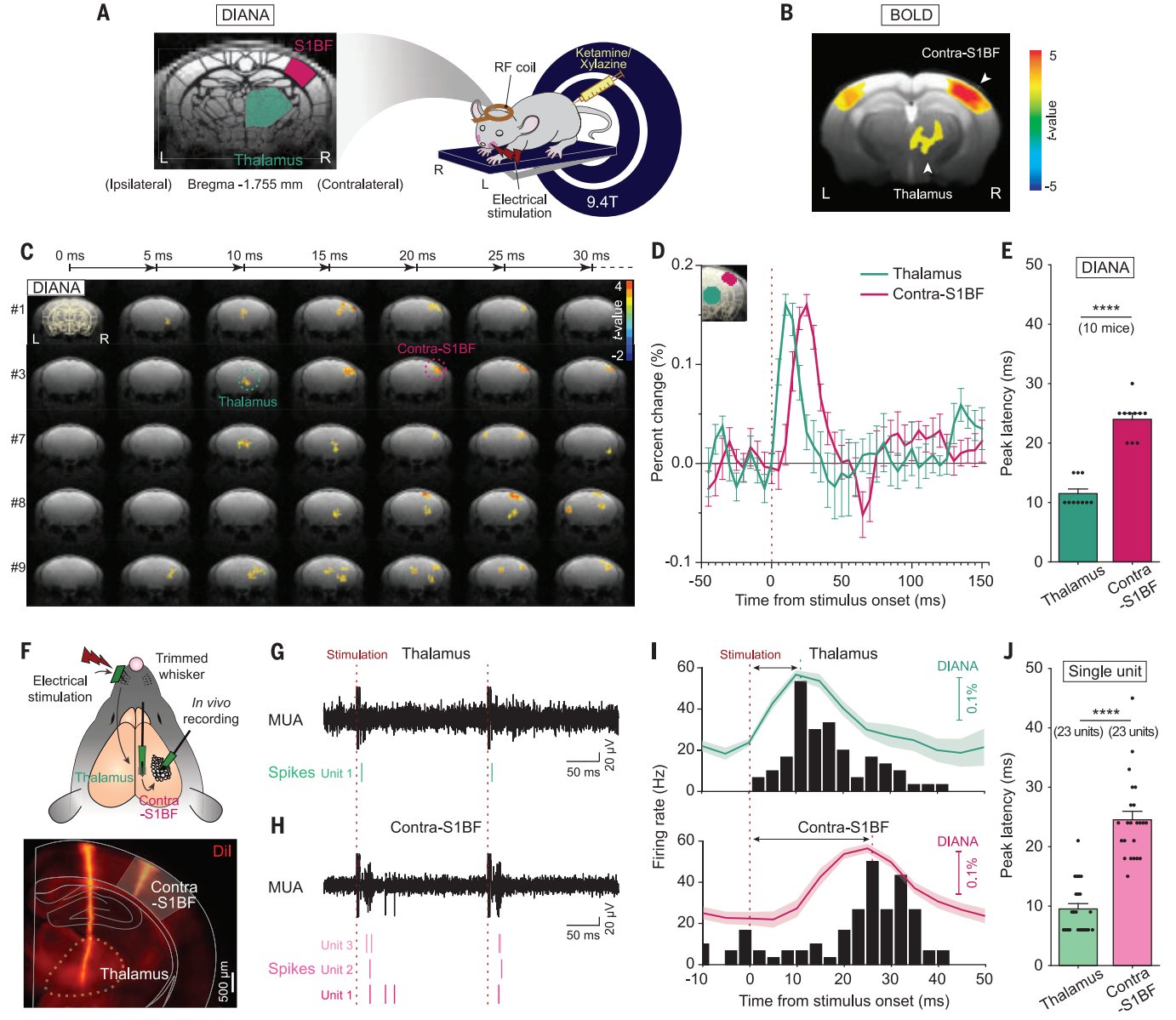

Fig. 2. High temporospatial resolution DIANA captures thalamocortical spike propagation. (**A**) Illustration of the DIANA experiment to image the contralateral S1BF and thalamus by applying electrical stimulation to the left whisker pad in an anesthetized mouse on a 9.4-T scanner (right) and brain imaging of a coronal slice containing both thalamus and S1BF regions (left). (**B**) BOLD activation map obtained as a reference (n = 10 mice). (**C** to **E**) Time series of t-value maps of DIANA for 30 ms after electrical whisker-pad stimulation in 5-ms temporal resolution from five mice (C), percent changes in DIANA signals (D), and a bar graph showing the mean latencies of peak DIANA responses from the thalamus (green) and contralateral S1BF (magenta) (E) (n = 10 mice, ****p < 0.0001 for paired Student's t test). (**F**) Illustration of electrophysiological recording in mice in vivo with silicon probes implanted in the thalamus and contralateral S1BF applying electrical whisker-pad stimulation (top) and electrode track marking using a fluorescent lipophilic dye (DiI) (bottom). (**G** and **H**) MUA (black trace, top) from which single-unit spikes (bottom) were analyzed in the thalamus (green) (G) and the contralateral S1BF (magenta) (H). (**I**) PSTH of the whisker-pad stimulation-responsive single units over time in the thalamus (top) and contralateral S1BF (bottom) with DIANA signals superimposed for comparison. (**J**) Bar graph showing the latencies of peak spike firing rates of whisker-pad stimulation-responsive single units recorded from the thalamus (light green, n = 23 units from 10 mice) and contralateral S1BF (light magenta, n = 23 units from five mice) (****p < 0.0001 for unpaired Student's t test). Vertical dashed lines indicate the electrical whisker-pad stimulation onset time (red) [(D) and (G) to (I)] and latency of peak spike firing rate (thalamus, green; contralateral S1BF, magenta) (I). All data are means ± SEM.

mice placed inside the 9.4-T scanner and imaged a single 1-mm coronal brain slice containing the right barrel field of the primary somatosensory cortex (S1BF) (Fig. 1B). In response to the electrical whisker-pad stimulation, a statistically significant increase in the DIANA signal was observed in the contralateral S1BF compared with the prestimulus signal (0.169 ± 0.011%, p < 0.001, five mice) (Fig. 1, C to E, and fig. S1), whereas there were no significant changes in unstimulated control mice or postmortem mice (Fig. 1, C to E, and fig. S1) or in sham experiments performed using an agar phantom (fig. S2). The peak DIANA signal occurred with a latency of 25.00 ± 1.58 ms after the electrical whisker-pad stimulation onset (Fig. 1, C, D, and F), indicating that 2D fast line-scan can detect whisker-pad stimulation-evoked responses by achieving high temporal resolution in the millisecond range. To find the neural correlates of the DIANA response in vivo,

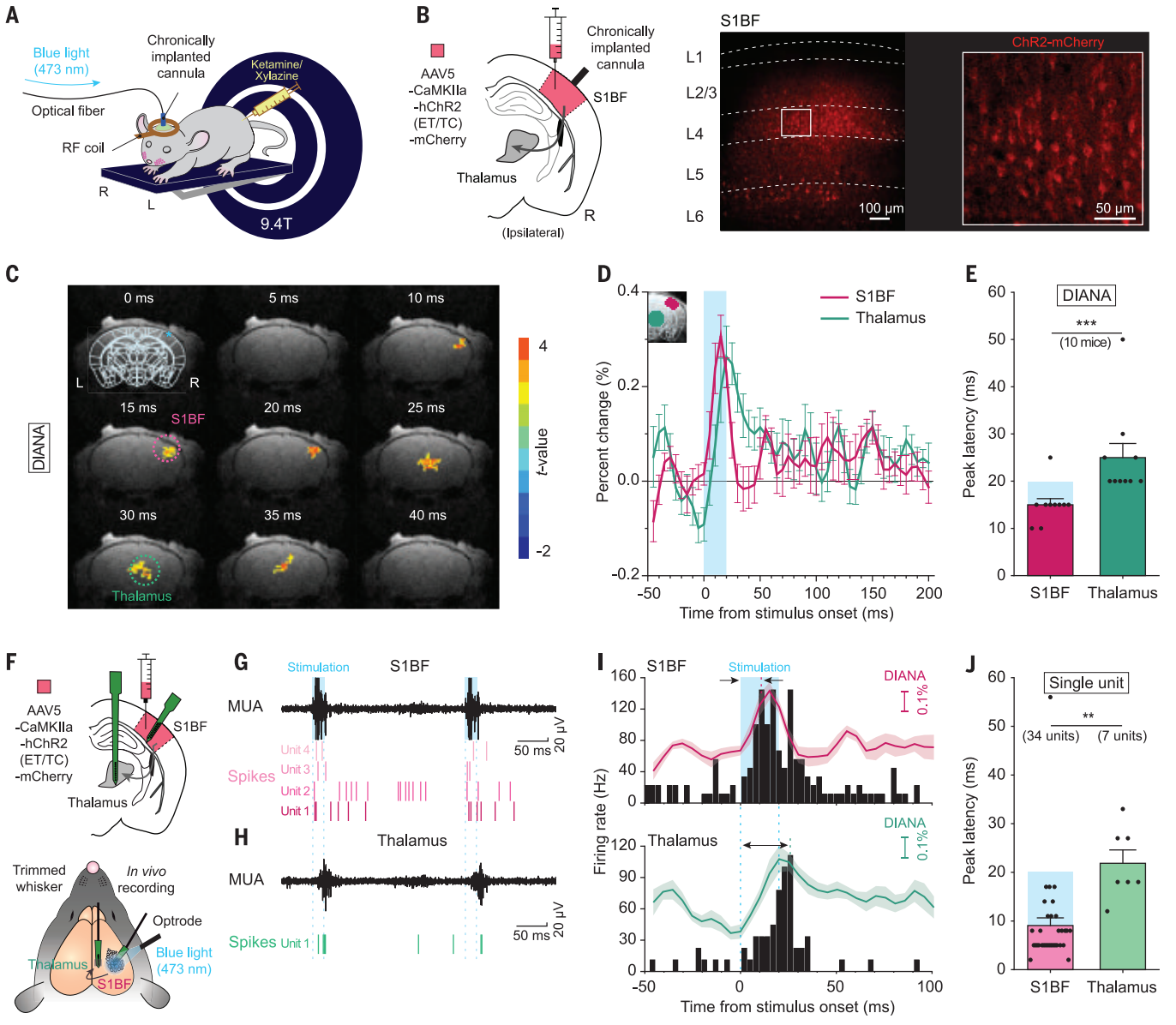

Fig. 3. Optogenetic DIANA experiment: DIANA responses directly detect optogenetic stimulation-evoked spikes. (**A**) Illustration of the optogenetic DIANA experiment where a fiberoptic cannula is implanted in the mouse S1BF for blue-light (473 nm) stimulation. (**B**) Illustration of injection of AAV5-CaMKIIa-hChR2 (ET/TC)-mCherry in S1BF (left), which expressed ChR2 to excitatory neurons across all layers of the S1BF. Confocal imaging of mCherry-expressing excitatory neurons (right). (**C**) Time series of *t*-value maps of DIANA from the S1BF and thalamus of a mouse (cluster size >5 voxels) imaged for 40 ms after blue-light stimulation onset (intensity, 50 mW/mm^2; duration, 20 ms). (**D** and **E**) Percent changes in DIANA signals (D) and bar graph showing the mean latencies of peak DIANA responses in the contralateral S1BF (magenta) and thalamus (green) (E) (n = 10 mice, ***p < 0.001 for paired Student's t test). Blue shading indicates the period of blue-light stimulation. (**F**) Illustration of simultaneous electrophysiological recordings in vivo in the thalamus and S1BF in mice injected with AAV5-CaMKIIa-hChR2(ET/TC)-mCherry in the S1BF, using the same blue-light stimulation as in the optogenetic DIANA experiment. (**G** and **H**) MUA (black trace, top) from which single-unit spikes (bottom) were analyzed in the contralateral S1BF (G) and the thalamus (H). (**I**) PSTH of the blue-light stimulation–responsive single units over time in the S1BF (top) and thalamus (bottom) with DIANA signals superimposed for comparison. (**J**) Bar graph showing the latencies of peak spike firing rates after the blue-light stimulation in the S1BF (n = 34 units from eight mice) and thalamus (n = 7 units from four mice) (**p < 0.01 for unpaired Student's t test). Blue shading and vertical dashed lines indicate the period of optogenetic stimulation in the S1BF [(D), (E), and (G) to (J)]. All data are means ± SEM.

the same electrical whisker-pad stimulation paradigm as in Fig. 1B was repeated but now in mice implanted with a 32-channel silicon probe in the S1BF (Fig. 1G) to record the local field potential (LFP) and single-unit spike activities (Fig. 1H), from which their latencies were analyzed (Fig. 1, I to K). The peak of whisker-pad stimulation-evoked LFP had a latency of 39.48 ± 1.84 ms (12 mice), which was significantly slower than the latency of the DIANA response (p < 0.001; Fig. 1, I and K). However, the peak spike firing rates of whisker-pad stimulation-responsive single units had a latency of 26.44 ± 1.24 ms (27 units from 10 mice) in the poststimulus time histogram (PSTH) (Fig. 1J), which was similar to the DIANA response latency (Fig. 1K). Other temporal spike characteristics such as time-to-first spike latency as well as median and mode of whisker-pad stimulation-responsive spike timings were also similar to the DIANA response

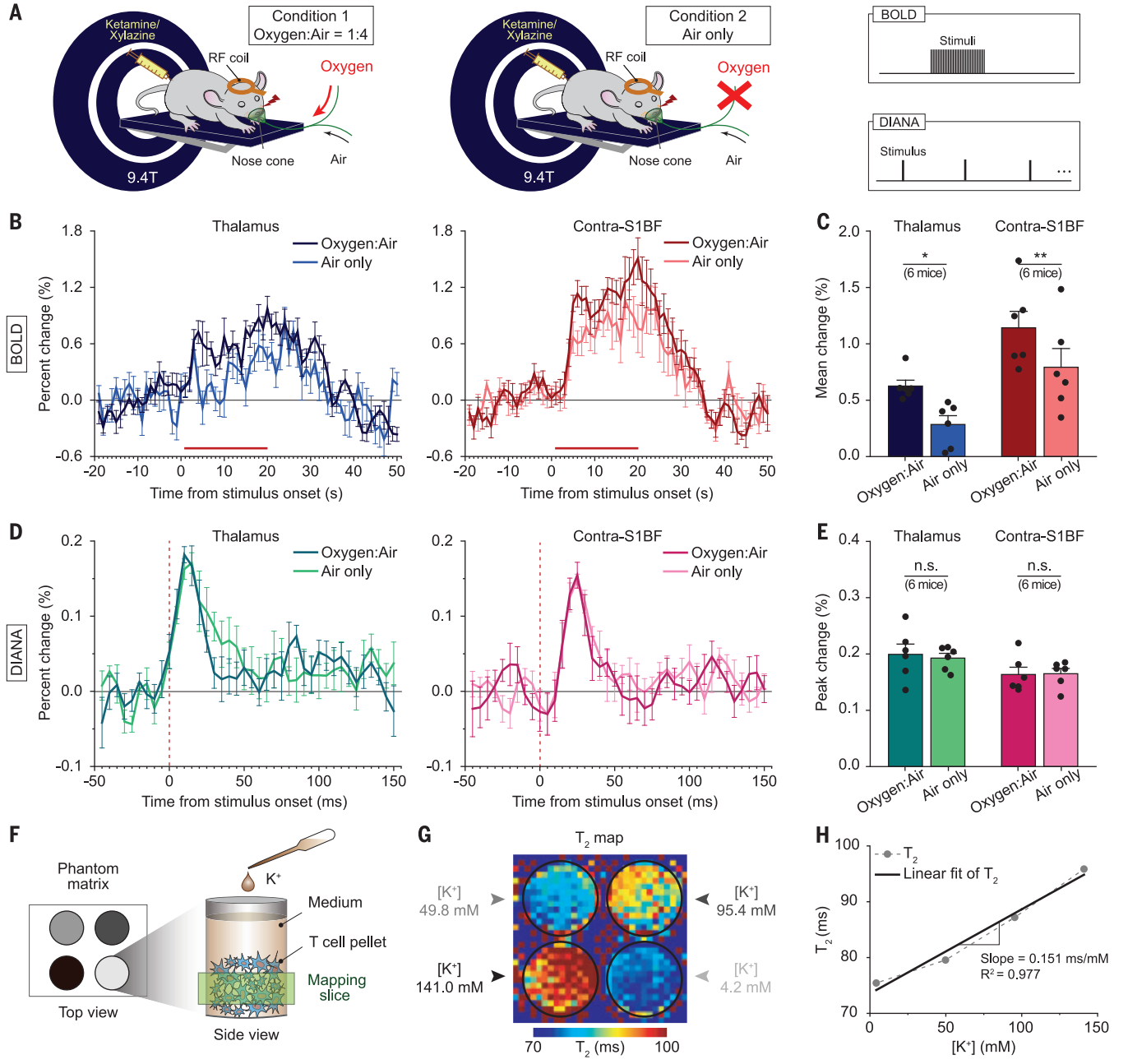

Fig. 4. BOLD-suppressed DIANA using 2D fast line-scan and its hypothesized contrast mechanism. (**A**) Illustration of oxygen challenge BOLD-fMRI and DIANA experiments to image contralateral S1BF and thalamus by applying electrical stimulation to the left whisker pad in an anesthetized mouse on a 9.4-T scanner under two conditions: one condition as a default with a mixture of extra oxygen and air (1:4) (left) and the other condition with air only (middle) at the same flow rate. The same whisker-pad electrical stimulus (strength, 0.5 mA; pulse duration, 0.5 ms) was used for both BOLD and DIANA stimulation paradigms (right). (**B** and **C**) Percent signal changes of BOLD responses obtained from the thalamus [(B), left] and contralateral S1BF [(B), right] under two conditions and the corresponding bar graph showing the mean signal changes of BOLD responses in the thalamus and contralateral S1BF [(C); n = 6 mice]. The horizontal red bar indicates the period of electrical stimulation in BOLD-fMRI. (**D** and **E**) Same as (B) and (C) but with responses acquired using DIANA (n = 6 mice). Vertical dashed lines indicate the stimulation onset time. (**F**) Illustration of a phantom experiment using T cells. (**G**) T_2 relaxation time maps acquired at different extracellular [K^+] from normal to depolarized states ranging from 4.2 to 141.0 mM. (**H**) Plot of T_2 (dashed line) changes with respect to [K^+]. The solid line is a linear fit to the T_2 values to calculate the correlation coefficient with respect to [K^+]. All data are means ± SEM. *p < 0.05, **p < 0.01, and n.s. is p > 0.05 for paired Student's t test.

latency (fig. S3). Both DIANA response amplitudes and spike firing rates increased with increasing strength of electrical whisker-pad stimulation, with little change in the latencies of their peaks (fig. S4).

Temporospatial imaging of neuronal activity propagation

Because somatosensory stimulus-evoked spikes propagate to the S1BF via the thalamus (*38*), we next explored whether the high temporospatial resolution (5 ms, 0.22 mm) of the 2D fast line-scan could also capture the propagation of spikes. When a 1-mm coronal brain slice containing both the thalamus and S1BF was imaged by applying electrical whisker-pad stimulation (Fig. 2A),

conventional BOLD-fMRI showed concomitant activation of the thalamus and contra- and ipsilateral S1BF (Fig. 2B and fig. S5). However, DIANA showed statistically significant responses that were sequentially activated in the order of the thalamus, contralateral S1BF, and ipsilateral S1BF (Fig. 2, C and D, and fig. S6, A and B) with latencies of 11.50 ± 0.76, 24.00 ± 1.00, and 28.50 ± 3.08 ms, respectively (Fig. 2E and fig. S6C; 10 mice). Further cross-correlation analysis of the time series confirmed that thalamic responses precede contra- and ipsilateral S1BF responses by 10 to 15 ms (fig. S7). To determine whether the temporospatial propagation of the DIANA response matches that of spikes in the thalamocortical pathway, we performed simultaneous single-unit recordings in the thalamus and S1BF using two silicon probes (Fig. 2, F to I). Latencies of peak spike firing rates of the whisker-pad stimulation-responsive single units occurred in the order of the thalamus (9.52 ± 0.90 ms, 23 units from 10 mice), contralateral S1BF (24.52 ± 1.43 ms, 23 units from five mice) (Fig. 2, I and J), and ipsilateral S1BF (30.00 ± 1.73 ms, three units from one mouse) (fig. S8). Such sequential propagation of spikes in the thalamus and S1BF was statistically similar to that observed from the DIANA response (Fig. 2E and fig. S9). LFPs also showed sequential propagation in the thalamus (31.78 ± 3.67 ms), contralateral S1BF (42.69 ± 3.04 ms), and ipsilateral S1BF (57.67 ± 5.33 ms), but they were significantly slower than the DIANA response (fig. S9).

Optogenetic DIANA experiment

Although the temporal characteristics of DIANA responses and electrophysiologically recorded spikes in vivo are statistically similar, these measurements are somewhat limited because they were not measured simultaneously. To more directly verify that DIANA using 2D fast line-scan is capable of imaging spike activity in vivo, we used an optogenetic fMRI scheme. DIANA responses were measured during optogenetic activation of channelrhodopsin2 (ChR2)–expressing excitatory neurons in the S1BF with 473-nm blue light delivered through a chronically implanted fiberoptic cannula (Fig. 3A). Immunostaining showed ChR2-mCherry expression in excitatory neurons across all cortical layers of the S1BF (Fig. 3B). During blue-light stimulation (intensity, 50 mW/mm^2; duration, 20 ms), DIANA responses were acquired as a time series of 50 images every 5 ms from a 1-mm coronal brain slice containing both the thalamus and S1BF (Fig. 3C). We found statistically significant DIANA signal changes in the S1BF with peak response latencies of 15.00 ± 1.29 ms, which were followed by significant DIANA signal changes in the thalamus with peak response latencies of 25.00 ± 2.98 ms after light stimulation onset (Fig. 3, D and E; 10 mice). Blue-light stimulation alone in control mice or ChR2 expression alone without blue-light stimulation did not change DIANA signals (fig. S10). When we recorded blue-light stimulation-evoked single-unit activities in the S1BF and thalamus of the same mice used for the optogenetic DIANA experiment (Fig. 3F), the peak spike firing rate of neurons in the S1BF occurred at 9.06 ± 1.59 ms after light stimulation onset (34 units from eight mice), followed by the thalamic peak spike firing rate occurring at 21.86 ± 2.76 ms (seven units from four mice) (Fig. 3, G to I), showing feedback spike propagation in the corticothalamic pathway. Both the DIANA response and the peak spike firing rate increased with increasing blue-light stimulation duration (fig. S11), indicating a similarity between the DIANA responses and single-unit activity. LFP also captured the blue-light stimulation-induced feedback activation in the corticothalamic pathway (fig. S12), with peak LFP latencies observed at 22.34 ± 0.87 ms in the S1BF and 77.47 ± 4.60 ms in the thalamus, respectively, after blue-light stimulation onset (fig. S12B). However, the peak LFP latencies were significantly slower than those in response to optogenetic DIANA (fig. S12B).

DIANA response as a non-BOLD effect

It could be possible that DIANA responses obtained from 2D fast line-scan involve hemodynamic responses such as the BOLD effect. To dissociate the BOLD effect from the DIANA response, BOLD-fMRI experiments were performed under two conditions: a default condition with an extra oxygen–to-air ratio of 1:4 (oxygen:air condition) and the other with air only (Fig. 4A). BOLD responses in the thalamus and S1BF after electrical whisker-pad stimulation in the air-only condition were significantly reduced compared with those in the oxygen:air condition (thalamus: 0.626 ± 0.052% to 0.284 ± 0.079%; contralateral S1BF: 1.142 ± 0.147% to 0.792 ± 0.166%; Fig. 4, B and C), consistent with the dependence of BOLD activation on oxygen supply (*39*, *40*). By contrast, there was little change in the DIANA response between the oxygen:air and air-only conditions (thalamus: 0.199 ± 0.018 to 0.193 ± 0.008%; contralateral S1BF: 0.164 ± 0.013% to 0.165 ± 0.009%; Fig. 4, D and E).

With respect to the data acquisition scheme, theoretical analysis revealed that the BOLD effect is suppressed by the TE/T_2* ratio because of the short TE compared with that of conventional BOLD-fMRI, where TE ≈ T_2* (T_2*, effective spin-spin relaxation time; see methods for details). For example, assuming that T_2* = 20 ms in the mouse brain and TE is set to 2 ms, the BOLD effect of the 2D fast line-scan experiment is reduced to 1/10 compared with that of BOLD-fMRI (fig. S13). The BOLD effect is further suppressed because of the fast, event-synchronized line-scan acquisition with a relatively short interstimulus interval compared with slow-varying hemodynamic responses of several seconds. In this case, the BOLD signal is suppressed by a factor of $(N - 1)/MN \approx 1/M$ (N, number of frames in interstimulus interval; M, number of phase-encoding steps) across all frames (see methods for details). For example, for $N = 40$ and $M = 54$, as in our DIANA experiment, the BOLD effect is further reduced by a factor of 0.018 (fig. S13). These theoretical analysis results were confirmed through numerical simulations (fig. S14). Furthermore, in terms of signal source, the BOLD signal is reported to be as small as ~0.021% during high-frequency stimulation that oscillates at 0.75 Hz at 7 T (*2*), which predicts that it might be much smaller and negligible for 5-Hz stimulation, as in this study.

What could be the possible signal source of the DIANA response? Electromagnetic effects based on popular neuronal current models cannot be a candidate because signal loss caused by the phase cancellation of proton spins under the neuronal current-induced magnetic field change has a negative value (*8*, *9*, *14*, *20*), whereas the DIANA response has a positive signal change in the main lobe.

Instead, because changes in neuronal membrane potential can induce reorientation of the membrane interfacial water (*41*), the DIANA response may arise from changes in MR relaxation times such as T_2 relaxation time during neuronal activity, which is closely related to the amount of water molecules in the hydration layer on the membrane surface (*42*–*45*) (see supplementary text 1 for details). Changes in T_2 relaxation time may also be attributed to rapid microstructural changes at the cellular level coupled with neural activity such as cell swelling (*46*), which has been postulated as one of the main signal sources for diffusion MRI (*47*–*50*). We performed phantom experiments using T cells to measure T_2 relaxation times while T cell membrane potentials were manipulated by different extracellular K^+ concentrations ([K^+]) (*51*) (4.2 to 141.0 mM in Fig. 4F and 1.0 to 4.2 mM in fig. S15A). We used T cells as the phantom because, unlike neurons, T cells are homogeneous and can survive without an oxygen supply in vitro in the scanner. The T_2 relaxation time map (Fig. 4G) and values showed a strong positive correlation with [K^+] [T_2 slope of 0.151 ms/mM, coefficient of determination (R^2) = 0.977; Fig. 4H]. Thus, it is possible that changes in membrane potential during neuronal activity may account for changes in T_2.

Based on these measurements of T_2 changes, Bloch simulation was performed to estimate DIANA signal changes and showed a positive signal change of 0.139% in the main lobe (fig. S15, B and C), which is in good agreement with the experimental results (Figs. 1 to 3). The T_2 dependence of the DIANA response

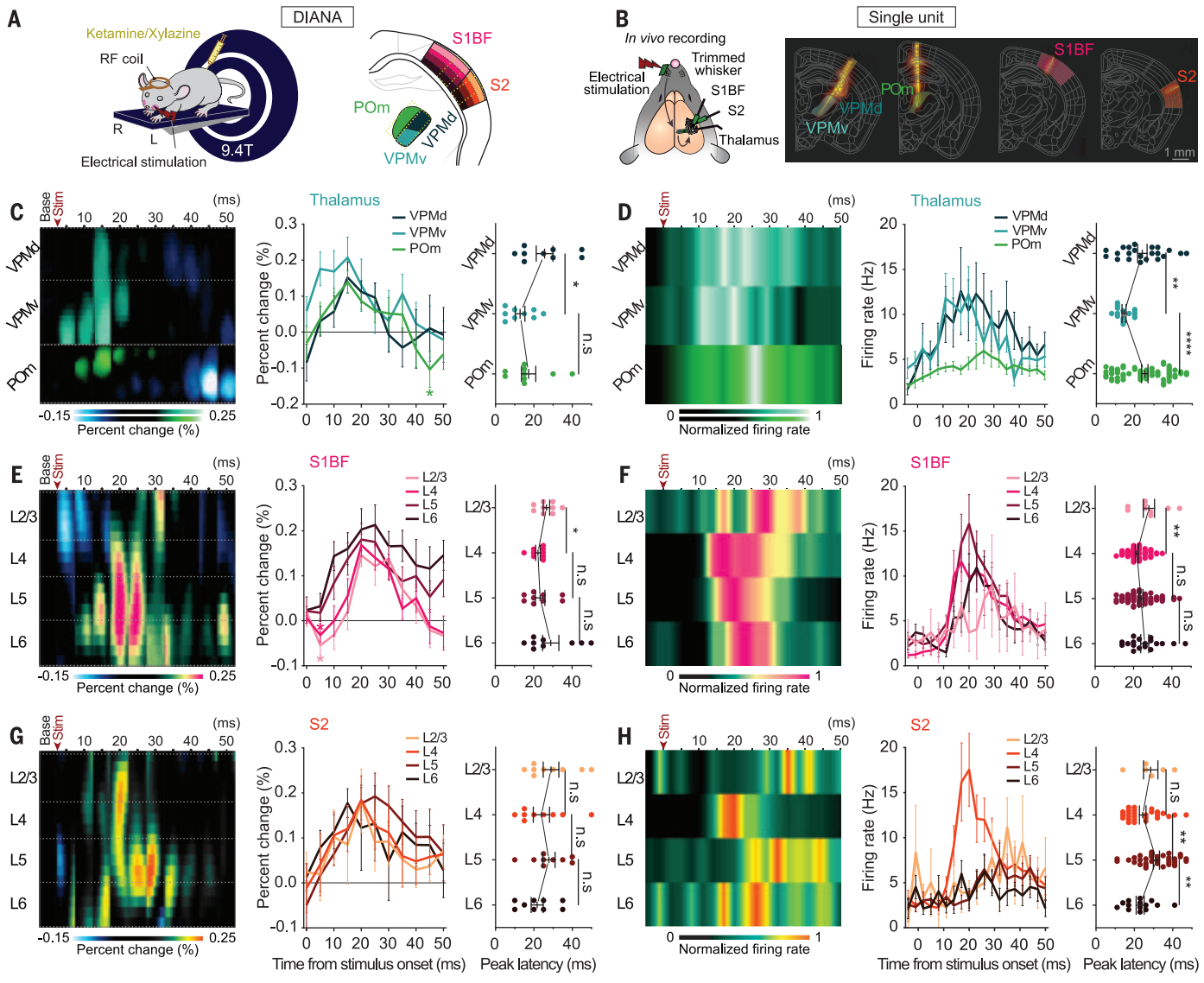

Fig. 5. Sublayer-specific DIANA responses reveal functionally distinct sublayer-specific microcircuits. (**A** and **B**) Illustration of the DIANA experiment (A) and in vivo spike recording (B) in the VPMd, VPMv, POm, S1BF, and S2 in response to electrical whisker-pad stimulation. Yellow dotted boxes in [(A), right] indicate extraction areas of DIANA heatmaps. (**C**) Heatmap (left) and temporal profile (middle) for the percent change in the DIANA signal, displayed with the mean latency of peak DIANA response from the VPMd (dark green), VPMv (green), and POm (light green) (right) (n = 9 mice). (**D**) Heatmap of in vivo–recorded single-unit spike firing rate normalized to the peak spike firing rate (left) and temporal profile of spike firing rate (middle), displayed with the mean latency of peak spike firing rate in the VPMd (dark green, n = 22 units from 16 mice), VPMv (green, n = 15 units from 16 mice), and POm (light green, n = 59 units from 14 mice) (right). (**E** and **F**) Same as (C) and (D) but for DIANA experiments (n = 9 mice) and spikes recorded from S1BF in L2/3 (light pink, n = 9 units from 28 mice), L4 (pink, n = 51 units from 28 mice), L5 (magenta, n = 60 units from 28 mice), and L6 (dark magenta, n = 18 units from 28 mice). (**G** and **H**) Same as (C) and (D) but for DIANA experiments (n = 9 mice) and spikes recorded from S2 in L2/3 (light orange, n = 6 units from 20 mice), L4 (orange, n = 27 units from 20 mice), L5 (brown, n = 35 units from 20 mice), and L6 (dark brown, n = 14 units from 20 mice). The base in DIANA heatmaps indicates the average of prestimulation frames. The asterisk in the middle panels of (C) and (E) indicates the statistically significant negative signal. All data are means ± SEM. *p < 0.05, **p < 0.01, ****p < 0.0001, and n.s. is p > 0.05 for paired Student's t test, unpaired Student's t test, and Welch's t test.

was further confirmed by modulating the T_2 weighting with different TEs in the DIANA experiment with the same electrical whisker-pad stimulation (fig. S16, A and B). By contrast, T_1-dependent changes in the DIANA signal were not observed in experiments where T_1 weighting was modulated with different flip angles (fig. S16, C and D). This is expected because it takes hundreds of milliseconds to several seconds for the T_1 change to manifest itself.

High temporospatial DIANA of neuronal activity propagation in thalamocortical microcircuits

Elucidating how sensory-evoked neural activities propagate across the microcircuits of multiple brain regions for sensory perception is one of the long-standing conundrums in sensory neuroscience. Because our 2D fast line-scan approach can directly image neural activities with not only high temporal resolution (5 ms) but also fine spatial resolution (0.22 mm) that can capture microstructures of the cortex and thalamus, we were able to address this question. We selected regions of interest (ROIs) from the thalamus, S1BF, and secondary somatosensory cortex (S2) (Fig. 5A). Within the ROIs,

the thalamus was subdivided into the posterior medial (POm) group, the ventral part of the ventral posteromedial nucleus (VPMv), and the dorsal part of the VPM (VPMd), whereas the S1BF and S2 were anatomically divided into cortical layers L2/3, L4, L5, and L6 (Fig. 5A). From these 11 ROIs, the DIANA data acquired during electrical whisker-pad stimulation were reanalyzed. For comparison, we also performed in vivo single-unit spike recordings in the corresponding thalamocortical microcircuits (Fig. 5B and fig. S17).

Heatmaps and percent changes of DIANA signals in response to electrical whisker-pad stimulation revealed distinct temporospatial neural activity propagation characteristics across the subdivisions of the thalamus and the cortical layers of the S1BF and S2 that were similar to those observed with single-unit spikes recorded in vivo (Fig. 5, C to H, and fig. S18). In the thalamus, both peak DIANA signals and peak spike firing rates were initiated from the VPMv, followed by the POm and VPMd (Fig. 5, C and D). In the S1BF, both peak DIANA signals and peak spike firing rates were initiated in L4 and L5, after which they propagated to L6 and L2/3 (Fig. 5, E and F), which is consistent with in vivo observations (*52*, *53*). In S2, for both peak DIANA signals and peak spike firing rates, L4 and L6 were the first layers to be activated, after which L5 and L2/3 were activated (Fig. 5, G and H), showing that neural activity propagation profiles are distinctively different between the S2 and S1BF.

To further investigate the correlation between the temporal dynamics of the DIANA response with neural activity, we analyzed the time point at which 30% of the peak DIANA response and peak spike firing rate occurred (fig. S19), but there were no significant differences (fig. S19). Also, the latencies of peak spike firing rates of multiunit activities (MUA) were similar to those of DIANA responses (fig. S20).

Although DIANA responses had high temporal correlations with spikes and MUA in all ROIs (Fig. 5 and fig. S20), they may not be detecting spikes per se but instead be detecting depolarizing membrane potential changes, as suggested by the T cell experiments in Fig. 4. Simultaneous intracellular recording of neurons during DIANA is technically difficult. However, current-source density (CSD) analysis allows the estimation of transmembrane current influx to neurons (current sink) in a layer-specific manner in the cortex (*54*). Indeed, CSD analysis from our data revealed that the latencies of the first current sink were similar to the latencies of the DIANA response in each layer of the S1BF and S2 (fig. S21), indicating that membrane depolarization caused by the influx of positive ions into neurons in each layer may have been manifested in positive DIANA responses.

The DIANA heatmap also showed two statistically significant negative DIANA percent signal changes that occurred before the peak positive DIANA responses in selected layers of the S1BF and S2 (Fig. 5, C to H, and fig. S22) and after the peak positive DIANA responses in the thalamus, S1BF, and S2 (fig. S22). Because DIANA using 2D fast line-scan can potentially image hyperpolarization of the neural network (fig. S15A), it is possible that γ-aminobutyric acid–containing (GABAergic) inhibitory interneuron-mediated hyperpolarization in excitatory neurons could have been manifested in DIANA responses. Based on the DIANA signals, the sensory input sequentially propagates through the VPMv, POm, and VPMd, after which they are inhibited to ensure that the initial epoch of sensory input can reliably propagate within cortical layers of the S1BF and S2 without being interrupted by other thalamic inputs (Fig. 5, C, E, and G). Also, thalamic input first inhibits L2/3 and L4 of the S1BF, whereas in the S2, L5 is inhibited first, which may contribute to the distinct laminar-specific signal propagation profiles observed in the S1BF and S2 (Fig. 5, C, E, and G). Thus, the DIANA signals observed here may provide the first experimental clues as to how spatiotemporally dynamic excitation and inhibition of neural circuits can route the flow of sensory-evoked signals.

Discussion

Together, our results demonstrate that a 2D fast line-scan approach enables direct mapping of spike activity in vivo with high temporal (5 ms) and spatial (0.22 mm) resolution, as confirmed through in vivo electrophysiology combined with optogenetics. Such high temporal resolution of the 2D fast line-scan DIANA allowed the detection of sequential propagation of neuronal activity through functionally defined neural networks in the thalamocortical and corticothalamic pathways. The 2D fast line-scan DIANA was also able to reveal the temporal neural network dynamics of multiple functionally connected brain regions—such as the thalamus, S1BF, and S2—at the subthalamic nucleus and cortical layer level.

In 2D fast line-scan DIANA, millisecond temporal resolution is a pivotal factor in direct measurement of neuronal activity because it helps to effectively capture the transient effects of neuronal activity in milliseconds. The DIANA response decreases with decreasing temporal resolution (fig. S23). This explains why the DIANA response has not been seen in previous fMRI studies with high temporal resolution, including line scan–based fMRI studies with the highest temporal resolution of 40 to 50 ms (fig. S24) (*35*, *55*). No DIANA response is shown even in single-shot single-slice echo planar imaging with the shortest achievable acquisition time of 20 to 30 ms (fig. S25). Another important feature of 2D fast line-scan DIANA is the ability to effectively suppress the BOLD effect (*2*) with its distinctive data acquisition scheme that uses the fast, event-synchronized line-scan with short TEs of a few milliseconds and a relatively short interstimulus interval (figs. S13 and S14).

The DIANA signal has a higher temporal correlation with the spikes than with the LFP (Figs. 1, I and J, 2I, and 3I), which suggests that DIANA might be detecting signals induced by flows of currents that evoke spikes rather than LFP. Typically, the LFP voltage is generated by the sum of influx and efflux currents across multiple neurons in the extracellular space, so the voltage is in the μV range (*54*). By contrast, the changes in membrane potential of individual neurons and their spikes are in the mV range, which is 10^3 times greater than that of the LFP. The DIANA signal could capture changes in membrane voltage on the mV scale, as shown in the T cell experiment in Fig. 4, where an extracellular $[K^+]$ change of 5 to 145 mM corresponds to a change in membrane potential from −40 to 10 mV (*51*). Moreover, both depolarizing and hyperpolarizing membrane potentiation changes could be detected as positive and negative signal changes in DIANA using 2D fast line-scan (Figs. 4 and 5 and fig. S15). CSD analysis revealed that latencies of the first current sinks had high correlations with latencies of peak positive DIANA responses (fig. S21). It is not possible to relate negative signal changes in DIANA to CSD analysis results (*54*). However, fast-spiking GABAergic interneurons and somatostatin-positive interneurons that hyperpolarize excitatory neurons have been reported to spike at two distinct time points during somatosensory information processing in the S1BF (*56*), similar to the two distinct time points observed from negative DIANA responses (fig. S22). The relationship between GABAergic interneuron activity and negative DIANA responses needs further investigation in the future. Nevertheless, these results together support our hypothesis that DIANA signals may be attributed to changes in neuronal membrane potential at the mV scale manifested by changes in transmembrane current flow.

DIANA using 2D fast line-scan has some limitations at this stage. Because 2D fast line-scan DIANA data are only generated in event-related responses to repetitive stimulation in the line-scan acquisition scheme, it is challenging to investigate brain function in the resting state or with a single stimulus. Moreover, 2D fast line-scan DIANA assumes that event-related responses in the brain are consistent across all responses without trial-by-trial variability, which can somewhat undermine the reliability of DIANA even with a modest change in neural spiking with each stimulation (*57*). Further investigation is also needed to fully elucidate the mechanism of the DIANA contrast

obtained from 2D fast line-scan. In other words, further validation with neurons in vivo is necessary because we hypothesized that the DIANA signal originates from changes in T_2 that are due to changes in membrane potential, which is supported by in vitro T cell experiments and simulations. Two possible mechanisms for these changes in T_2, that is, changes in hydration water of the plasma membrane and changes in microstructures at the cellular level such as cell swelling, require further investigation to assess their respective contributions.

There are interesting topics that can immediately be explored with DIANA. One is to test its feasibility for human fMRI and to translate DIANA into a clinical human system. Approximate predictions that only take into account neuronal density, magnetic field strength, and typical voxel size in the animal and human systems suggest that DIANA is likely to work in human studies as well (see supplementary text 2). More complicated feedforward and feedback responses are expected to be observed in human brain networks (*58*), which could make the DIANA response more challenging and even more interesting. However, motion artifacts can be more severe in humans than in anesthetized mice, leading to some inconsistencies in *k*-space and changes in the steady state of the magnetization.

Another interesting topic to investigate is the rapid dynamics of neural networks other than the somatosensory network presented here, such as the visual or auditory network, in multiple functionally connected distant brain regions (*59*). Because all experiments in this study were performed with electrical whisker-pad stimulation, which is an experimental paradigm that cannot be applied in human studies, the validation of DIANA experiments using standard visual or auditory stimulation is important to provide a realistic picture of how DIANA can contribute to human studies. A preliminary DIANA experiment with a flashing-light stimulus demonstrates the feasibility of visual stimuli DIANA experiments (fig. S26), exhibiting sequential propagation DIANA responses in the mouse cortex in the order of the superior colliculus (SC), primary visual cortex (V1), and lateral part of the secondary visual cortex (V2L). Although we presented the DIANA data that detect only fast-phasic neuronal activity here, by adjusting the interstimulus interval long enough to measure the neuronal activity of interest, DIANA could also be used to measure diverse temporal patterns of neuronal activity on various time scales such as sustained tonic neuronal activity over a longer period of time.

Overall, we expect high-resolution DIANA to open up new avenues in neuroimaging for a more accurate and deeper understanding of the brain's functional organization. In particular, the convergence of high temporal and spatial resolution realized through DIANA could help elucidate the causal relationship between temporal and spatial dynamics of neural networks and their functions.

REFERENCES AND NOTES

1. S. Ogawa, T. M. Lee, A. R. Kay, D. W. Tank, *Proc. Natl. Acad. Sci. U.S.A.* **87**, 9868–9872 (1990).
2. L. D. Lewis, K. Setsompop, B. R. Rosen, J. R. Polimeni, *Proc. Natl. Acad. Sci. U.S.A.* **113**, E6679–E6685 (2016).
3. A. Maier *et al*., *Nat. Neurosci.* **11**, 1193–1200 (2008).
4. Y. B. Sirotin, A. Das, *Nature* **457**, 475–479 (2009).
5. P. O'Herron *et al*., *Nature* **534**, 378–382 (2016).
6. Y. B. Sirotin, E. M. C. Hillman, C. Bordier, A. Das, *Proc. Natl. Acad. Sci. U.S.A.* **106**, 18390–18395 (2009).
7. D. Cohen, *Science* **161**, 784–786 (1968).
8. P. A. Bandettini, N. Petridou, J. Bodurka, *Appl. Magn. Reson.* **29**, 65–88 (2005).
9. J. Bodurka, P. A. Bandettini, *Magn. Reson. Med.* **47**, 1052–1058 (2002).
10. D. Konn, P. Gowland, R. Bowtell, *Magn. Reson. Med.* **50**, 40–49 (2003).
11. M. Singh, *IEEE Trans. Nucl. Sci.* **41**, 349–351 (1994).
12. J. Bodurka *et al*., *J. Magn. Reson.* **137**, 265–271 (1999).
13. P. Sundaram *et al*., *Neuroimage* **132**, 477–490 (2016).
14. N. Petridou *et al*., *Proc. Natl. Acad. Sci. U.S.A.* **103**, 16015–16020 (2006).
15. C. Park *et al*., *Neuroreport* **15**, 231–234 (2004).
16. T. S. Park, S. Y. Lee, J.-H. Park, M. H. Cho, S. Y. Lee, *Physiol. Meas.* **27**, 181–190 (2006).
17. Q. Luo *et al*., *Neuroimage* **47**, 1268–1276 (2009).
18. X. Jiang *et al*., *Magn. Reson. Med.* **72**, 1311–1319 (2014).
19. M. Joy, G. Scott, M. Henkelman, *Magn. Reson. Imaging* **7**, 89–94 (1989).
20. J. Xiong, P. T. Fox, J.-H. Gao, *Hum. Brain Mapp.* **20**, 41–49 (2003).
21. L. S. Chow, G. G. Cook, E. Whitby, M. N. J. Paley, *Neuroimage* **30**, 835–846 (2006).
22. L. S. Chow, G. G. Cook, E. Whitby, M. N. J. Paley, *Magn. Reson. Imaging* **24**, 681–691 (2006).
23. L. S. Chow, G. G. Cook, E. Whitby, M. N. J. Paley, *J. Magn. Reson. Imaging* **26**, 265–273 (2007).
24. L. S. Chow, A. Dagens, Y. Fu, G. G. Cook, M. N. J. Paley, *Magn. Reson. Med.* **60**, 1147–1154 (2008).
25. R. Chu *et al*., *Neuroimage* **23**, 1059–1067 (2004).
26. L. M. Parkes, F. P. de Lange, P. Fries, I. Toni, D. G. Norris, *Magn. Reson. Med.* **57**, 411–416 (2007).
27. L. Tang, M. J. Avison, J. C. Gatenby, J. C. Gore, *Magn. Reson. Imaging* **26**, 484–489 (2008).
28. J. Huang, *Magn. Reson. Med.* **71**, 756–762 (2014).
29. J. Huang, D. C. Zhu, *Int. J. Imaging Syst. Technol.* **25**, 172–178 (2015).
30. A. Darquié, J. B. Poline, C. Poupon, H. Saint-Jalmes, D. Le Bihan, *Proc. Natl. Acad. Sci. U.S.A.* **98**, 9391–9395 (2001).
31. D. Le Bihan, S. Urayama, T. Aso, T. Hanakawa, H. Fukuyama, *Proc. Natl. Acad. Sci. U.S.A.* **103**, 8263–8268 (2006).
32. K. L. Miller *et al*., *Proc. Natl. Acad. Sci. U.S.A.* **104**, 20967–20972 (2007).
33. D. Nunes, R. Gil, N. Shemesh, *Neuroimage* **231**, 117862 (2021).
34. A. Barandov *et al*., *Nat. Commun.* **10**, 897 (2019).
35. A. C. Silva, A. P. Koretsky, *Proc. Natl. Acad. Sci. U.S.A.* **99**, 15182–15187 (2002).
36. X. Yu *et al*., *Nat. Methods* **13**, 337–340 (2016).
37. L. Raimondo *et al*., *J. Cereb. Blood Flow Metab.* **41**, 2831–2843 (2021).
38. E. Ahissar, R. Sosnik, S. Haidarliu, *Nature* **406**, 302–306 (2000).
39. K. M. Sicard, T. Q. Duong, *Neuroimage* **25**, 850–858 (2005).
40. T. Q. Duong, *Brain Res.* **1135**, 186–194 (2007).
41. M. E. P. Didier, O. B. Tarun, P. Jourdain, P. Magistretti, S. Roke, *Nat. Commun.* **9**, 5287 (2018).
42. J. Monroe *et al*., *Annu. Rev. Chem. Biomol. Eng.* **11**, 523–557 (2020).
43. O. B. Tarun, C. Hannesschläger, P. Pohl, S. Roke, *Proc. Natl. Acad. Sci. U.S.A.* **115**, 4081–4086 (2018).
44. H. T. Edzes, E. T. Samulski, *J. Magn. Reson.* **31**, 207–229 (1978).
45. J. Cerbon, *Biochim. Biophys. Acta* **144**, 1–9 (1967).
46. J. V. Sehy, J. J. H. Ackerman, J. J. Neil, *Magn. Reson. Med.* **48**, 765–770 (2002).
47. I. Pál, G. Nyitrai, J. Kardos, L. Héja, *PLOS ONE* **8**, e57694 (2013).
48. A. El Hady, B. B. Machta, *Nat. Commun.* **6**, 6697 (2015).
49. Y. Yang *et al*., *ACS Nano* **12**, 4186–4193 (2018).
50. M. Koike-Tani, T. Tominaga, R. Oldenbourg, T. Tani, bioRxiv 523571 [Preprint] (2019); https://doi.org/10.1101/523571.
51. F. Mello de Queiroz, C. G. Ponte, A. Bonomo, R. Vianna-Jorge, G. Suarez-Kurtz, *BMC Immunol.* **9**, 63 (2008).
52. H. J. Jang *et al*., *Sci. Adv.* **6**, eaay5333 (2020).
53. C. M. Constantinople, R. M. Bruno, *Science* **340**, 1591–1594 (2013).
54. G. Buzsáki, C. A. Anastassiou, C. Koch, *Nat. Rev. Neurosci.* **13**, 407–420 (2012).
55. X. Yu, C. Qian, D. Y. Chen, S. J. Dodd, A. P. Koretsky, *Nat. Methods* **11**, 55–58 (2014).
56. J. Yu, H. Hu, A. Agmon, K. Svoboda, *Neuron* **104**, 412–427.e4 (2019).
57. E. Kheradpezhouh, M. Adibi, E. Arabzadeh, *Sci. Rep.* **7**, 11445 (2017).
58. O. Sporns, D. R. Chialvo, M. Kaiser, C. C. Hilgetag, *Trends Cogn. Sci.* **8**, 418–425 (2004).
59. I. Magrans de Abril, J. Yoshimoto, K. Doya, *Neural Netw.* **102**, 120–137 (2018).
60. P. T. Toi *et al*., Data for in vivo direct imaging of neuronal activity at high temporospatial resolution. Zenodo (2022); https://doi.org/10.5281/zenodo.7114876.

ACKNOWLEDGMENTS

We thank T.-N.-A. Dinh and G. Im for help in setting up mouse BOLD-fMRI experiments at the beginning of this study. We also thank S. Chung, J. Lee, C.-W. Woo, and S. Mangia for valuable scientific discussion; J.-K. Ryu and S. Han for pulse sequence support; C. Lee, J. W. Park, and E. Kim for MRI technical assistance; and S. Lee for administrative assistance. We acknowledge the Korea Institute of Radiological and Medical Sciences (no. 50539-2022) for providing a 9.4-T MRI facility to conduct additional experiments. **Funding:** P.T.T., S.-K.L., and J.-Y.P. acknowledge financial support from the Brain Research Program through the National Research Foundation of Korea funded by the Ministry of Science and ICT, under project ID NRF-2019M3C7A1031993. K.M. and J.L. acknowledge financial support from the same Brain Research Program, under project ID NRF-2019M3C7A1031994. H.J.J. and J.K. acknowledge financial support from the Brain Convergence Research Program through the National Research Foundation of Korea funded by the Ministry of Science and ICT, under project ID NRF-2019M3E5D2A01058328. **Author contributions:** P.T.T. and J.-Y.P. established the methodology for direct imaging of neuronal activity. P.T.T. prepared the pulse sequence and designed and conducted all animal MRI experiments. H.J.J. and J.K. designed all optogenetic experiments for MRI and electrophysiology. H.J.J. conducted the electrophysiological and optogenetic recordings and performed fluorescence and confocal imaging. H.J.J. and J.K. analyzed electrophysiological data. K.M., S.-K.L., and J.L. carried out MRI measurements of relaxation time changes in T cells and simulation. P.T.T., H.J.J., K.M., S.-P.K., S.-K.L., J.L., J.K., and J.-Y.P. contributed to data analysis and discussion. P.T.T., H.J.J., J.K., and K.M. prepared the figures and drafts. P.T.T. and J.-Y.P. wrote the paper. J.-Y.P. conceived of and supervised the project. All authors revised the manuscript. **Competing interests:** J.-Y.P. and S.-K.L. are listed as inventors on Korean patent "Methods for direct monitoring and spatial mapping of neuronal activity" (no. 10-2174092, registered on 29 October 2020). The authors declare no other competing interests. **Data and materials availability:** The data are stored and curated at Zenodo (*60*).

SUPPLEMENTARY MATERIALS

science.org/doi/10.1126/science.abh4340
Materials and Methods
Supplementary Text
Figs. S1 to S26
References (*61*–*81*)
MDAR Reproducibility Checklist

Submitted 11 March 2021; resubmitted 7 April 2022
Accepted 17 August 2022
10.1126/science.abh4340

THERMAL MANAGEMENT

Simultaneous electrical and thermal rectification in a monolayer lateral heterojunction

Yufeng Zhang[1]†, Qian Lv[2]†, Haidong Wang[1]*, Shuaiyi Zhao[1], Qihua Xiong[3,4,5,6], Ruitao Lv[2,7]*, Xing Zhang[1]*

Efficient waste heat dissipation has become increasingly challenging as transistor size has decreased to nanometers. As governed by universal Umklapp phonon scattering, the thermal conductivity of semiconductors decreases at higher temperatures and causes heat transfer deterioration under high-power conditions. In this study, we realized simultaneous electrical and thermal rectification (TR) in a monolayer $MoSe_2$-WSe_2 lateral heterostructure. The atomically thin $MoSe_2$-WSe_2 heterojunction forms an electrical diode with a high ON/OFF ratio up to 10^4. Meanwhile, a preferred heat dissipation channel was formed from $MoSe_2$ to WSe_2 in the ON state of the heterojunction diode at high bias voltage with a TR factor as high as 96%. Higher thermal conductivity was achieved at higher temperatures owing to the TR effect caused by the local temperature gradient. Furthermore, the TR factor could be regulated from maximum to zero by rotating the angle of the monolayer heterojunction interface. This result opens a path for designing novel nanoelectronic devices with enhanced thermal dissipation.

The size of silicon chips has continuously decreased in recent decades and is approaching its physical limits. The electronics industry has been faced with the arduous challenge of finding nanomaterials with intrinsic semiconductor characteristics (*1*). To date, semiconductor carbon nanotubes (*2*), graphene nanoribbons (*3*), and transition-metal dichalcogenide (TMD) monolayers (*4*–*13*) have been promising candidates for next-generation field-effect transistors beyond silicon. Compared with carbon-based semiconductors, monolayer TMD materials have a direct electronic bandgap and a high ON/OFF ratio. In particular, monolayer TMD lateral heterostructures can form an atomic-scale p-n node to minimize the size of the diode channel, which has great potential in highly integrated electronics to further push the limit of Moore's law (*6*–*15*). However, miniaturization and high integration will inevitably lead to an increase in the heat flux density and a rapid increase in node temperature (*16*). Generally, owing to Umklapp phonon-phonon scattering, the thermal conductivity of semiconductor materials dominated by phonon transport will decrease as the temperature increases, which accelerates the thermal failure of high–power density electronic devices (*17*–*19*). Designing a nanoscale electrical rectifier with a positive correlation between thermal conductivity and temperature that works above room temperature would be an ideal solution. Without external heat dissipation channels, more heat can be dissipated through the semiconductor material itself given its larger thermal conductivity at higher temperatures. However, no relevant experimental results have been reported thus far.

We fabricated a monolayer $MoSe_2$-WSe_2 lateral heterostructure device with simultaneous electrical rectification (ER) and thermal rectification (TR) characteristics, which were precisely measured by using a specially designed suspended H-type sensor. In the experiment, the monolayer $MoSe_2$-WSe_2 lateral heterojunction worked as an efficient electrical diode with a high ON/OFF ratio up to 10^4. In the OFF state, the reverse saturation current was small, and the joule heating effect was negligible. No heat flux or temperature gradient was formed in the heterojunction diode, so there was no preferred direction for phonon transport. In the ON state with a large bias voltage, the high current caused a substantial joule heating effect in the heterojunction area, and, consequently, a temperature gradient was formed from the high-resistivity $MoSe_2$ domain to the low-resistivity WSe_2 domain. This happened to be the preferred direction for both phonon transport and electron migration in the heterojunction diode. The thermal conductivity was increased by 96% at maximum in the preferred phonon transport direction from $MoSe_2$ to WSe_2. Benefiting from the simultaneous ER and TR characteristics of monolayer lateral heterojunction, the atomically thin working electrical diode can achieve larger thermal conductivity at higher temperature owing to the local temperature gradient.

The TR effect of the $MoSe_2$-WSe_2 lateral heterojunction rectifier was experimentally demonstrated to be angle dependent. The largest TR factor was realized when phonons vertically crossed the heterojunction interface. If the phonon transport direction was parallel to the heterojunction interface, the TR effect vanished. Our molecular dynamics (MD) simulation result was consistent with the experimental data and indicated that the asymmetric heterojunction interface transport behavior triggered by lattice anharmonicity should be responsible for TR in lateral heterostructures. The simultaneous ER and TR characteristics of the two-dimensional $MoSe_2$-WSe_2 lateral heterostructure put forward a new design principle and the possibility of developing highly integrated electronic devices with better thermal dissipation performance.

Growth and device fabrication of $MoSe_2$-WSe_2 lateral heterostructures

The $MoSe_2$-WSe_2 lateral heterostructure samples were synthesized by an atmospheric-pressure chemical vapor deposition (AP-CVD) route with the assistance of gold foil (*20*). To simultaneously measure the ER and TR characteristics of the same lateral heterostructure sample, we designed an H-type sensor, as previously reported (*20*, *21*). We supported the $MoSe_2$-WSe_2 heterostructure sample on a 300-nm-thick SiO_2 layer that bridges two gold nanosensors, forming an H-type structure (Fig. 1A). We used the gold sensor as an electrode, a joule heater, and a precise resistance thermometer simultaneously. We fully suspended the whole H-type sensing device from the silicon substrate to achieve the highest thermal measurement sensitivity. In the experiment, we could easily switch the electrical and thermal measurement modes by changing the outside electrical circuit.

We obtained atomic-resolution images of the $MoSe_2$, WSe_2, and interface domains, respectively, using high-angle annular dark-field scanning transmission electron microscopy (HAADF-STEM) (Fig. 1, B to D). The dark and bright dots in each HAADF-STEM image denote Mo and W atoms, respectively. We drew a polyline (indicated by the yellow dashed line) to indicate the shape of the heterojunction interface (Fig. 1D). We observed slight doping at the interface, which might be due to the relatively high energy at the interface region. By counting the number of Mo and W atoms in the HAADF-STEM image, we estimated the doping concentration to be ~10% for our tested samples. We selected six samples, labeled 1 to 6, for electrical and thermal measurements and showed their initial configurations (Fig. 1, E to J). With the help of a prefabricated micrometer-sized cross mark array and the automatic identification and positioning function of the electron beam lithography system,

[1]Key Laboratory for Thermal Science and Power Engineering of Ministry of Education, Department of Engineering Mechanics, Tsinghua University, Beijing 100084, China. [2]State Key Laboratory of New Ceramics and Fine Processing, School of Materials Science and Engineering, Tsinghua University, Beijing 100084, China. [3]State Key Laboratory of Low-Dimensional Quantum Physics and Department of Physics, Tsinghua University, Beijing 100084, China. [4]Frontier Science Center for Quantum Information, Beijing 100084, China. [5]Collaborative Innovation Center of Quantum Matter, Beijing 100084, China. [6]Beijing Academy of Quantum Information Sciences, Beijing 100193, China. [7]Key Laboratory of Advanced Materials (Ministry of Education), School of Materials Science and Engineering, Tsinghua University, Beijing 100084, China.
*Corresponding author. Email: hdwang@tsinghua.edu.cn (H.W.); lvruitao@tsinghua.edu.cn (R.L.); x-zhang@tsinghua.edu.cn (X.Z.)
†These authors contributed equally to this work.

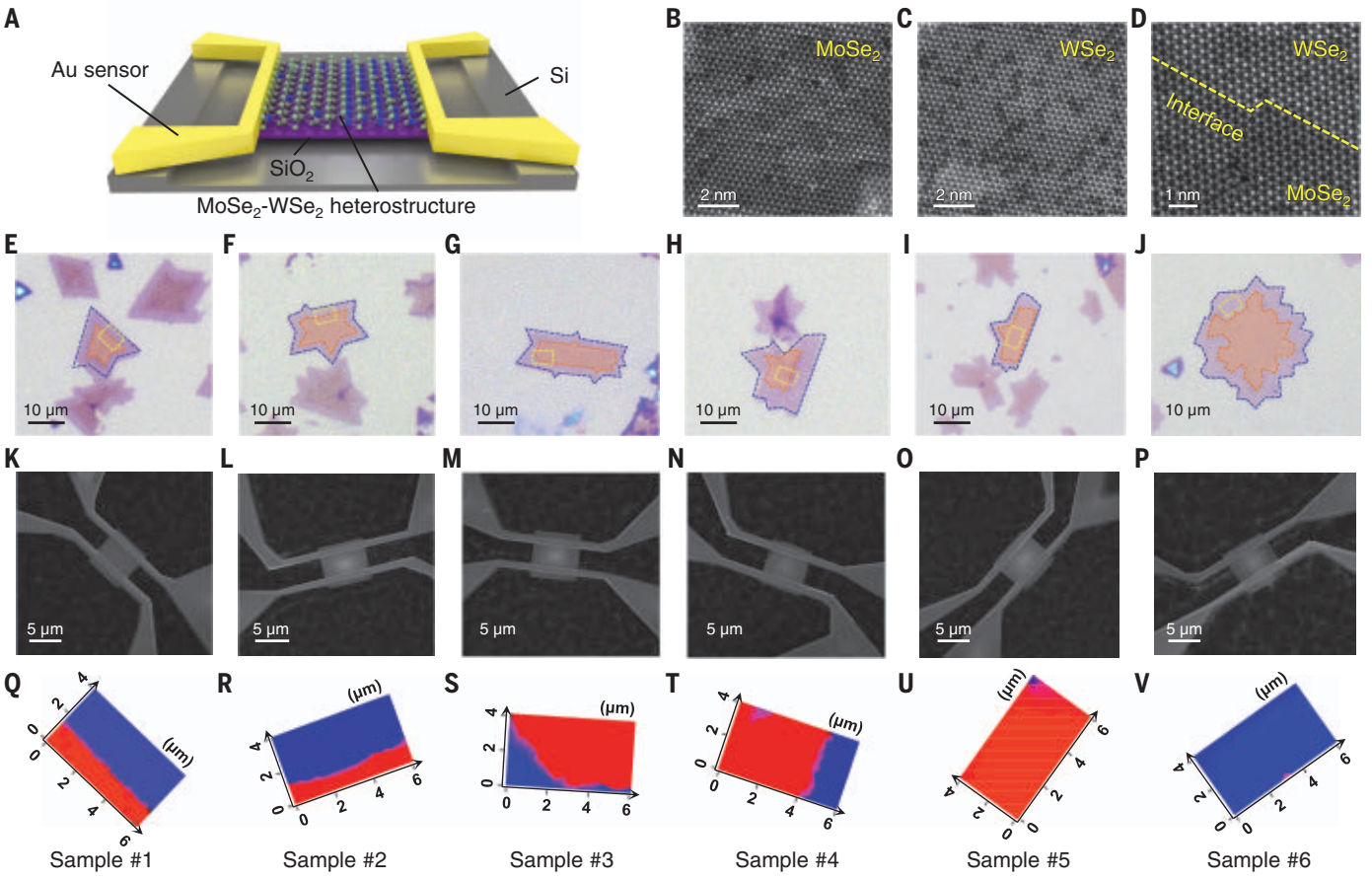

Fig. 1. Characterization of as-synthesized $MoSe_2$-WSe_2 lateral heterostructures and fabricated H-type sensing devices. (**A**) Schematic diagram of the suspended H-type sensing device. (**B** to **D**) Atomic-resolution HAADF-STEM images of $MoSe_2$, WSe_2, and the interface domain, respectively. (**E** to **J**) Optical micrograph images of samples 1 to 6 synthesized on SiO_2/Si substrates with $MoSe_2$ (dark contrast, outlined in orange dashed lines) surrounded by WSe_2 (bright contrast, outlined in blue dashed lines). The yellow dashed boxes show the sample areas prepared for characteristic measurement. (**K** to **P**) SEM images of samples 1 to 6 fabricated into H-type sensing devices, which are fully suspended from the silicon substrate with an etching depth of 8 μm to avoid heat loss into the substrate. (**Q** to **V**) Raman spatial mapping images of samples 1 to 6. The red, blue, and pink colors represent the $MoSe_2$, WSe_2, and interface domains, respectively. Raman spectra of the representative domains can be found in fig. S1.

we were able to precisely select the lateral heterojunction area and place it at the center between two gold nanosensors, with a spatial accuracy better than 100 nm. Each freestanding rectangle area between two sensors (Fig. 1, K to P) corresponds to the lateral heterojunction sample marked by yellow dashed boxes (Fig. 1, E to J). Using a high-resolution Raman spectrometer, we scanned all six suspended heterojunction samples and obtained Raman spectral mapping images (Fig. 1, Q to V, and fig. S1). We verified the uniformity of the as-synthesized heterostructure samples with the Raman mapping results. The shape of the $MoSe_2$-WSe_2 heterojunction interface is clearly illustrated in the Raman spectral mapping images, which are consistent with our initial optical micrograph images. We defined θ as the angle between the length directions of the interface and the elongated H-type sensors. When the interface is parallel to the sensor, θ = 0° (samples 1 and 2), and the electrons or phonons flow perpendicularly through the interface. Otherwise, when the interface and sensor are perpendicular to each other, θ = 90° (sample 4), and the electrons or phonons flow parallel to the interface. In addition to θ of 0° and 90°, sample 3 has an angle θ of 45° (fig. S2), and samples 5 and 6 are pure $MoSe_2$ and pure WSe_2, respectively. We measured these three samples to study the interface angle dependence and as control samples to verify the reliability of the experimental results.

Electrical characterization

We used the four-probe method to characterize the electrical transport across the interface (Fig. 2A). The measurement system included a precise dc voltage and current source (ADCMT, 6243), two high-precision digital multimeters (Keithley 2002, 8½-digits), and a vacuum thermoelectric heating and cooling stage (INSTEC, TP102SV-PM-F8, ±0.001 K). We measured the drain-source current–drain-source voltage (I_{ds}-V_{ds}) curves of four $MoSe_2$-WSe_2 lateral heterostructure samples and pure $MoSe_2$, pure WSe_2 samples under zero back-gate voltage (Fig. 2, B to F). The n-type $MoSe_2$ and p-type WSe_2 form a natural p-n junction with type-II band alignment at the interface. We show a sketch of the band alignment of $MoSe_2$ and WSe_2 domains when forming the heterojunction (Fig. 2B, inset). We obtained the bandgaps directly with the photoluminescence measurement (fig. S3). For samples 1, 2, and 3, the lateral p-n junction interface is located in the path of carrier transport from the source to the drain, and, as a consequence, the I_{ds}-V_{ds} curve shows a clear diode response. This electrical current rectification behavior cannot be attributed to the Schottky barriers of metallic electrode contacts, given the symmetric I_{ds}-V_{ds} curves of individual $MoSe_2$ and WSe_2 (Fig. 2F). The high ER ratio of 10^3 to 10^4 in samples 1 and 2 proves the high interface quality of the as-synthesized $MoSe_2$-WSe_2 lateral heterostructures. However, the ER ratio of sample 3 is substantially lower in comparison. This behavior is due to the tilted interface structure, which can be regarded as a parallel connection between a heterostructure and pure $MoSe_2$.

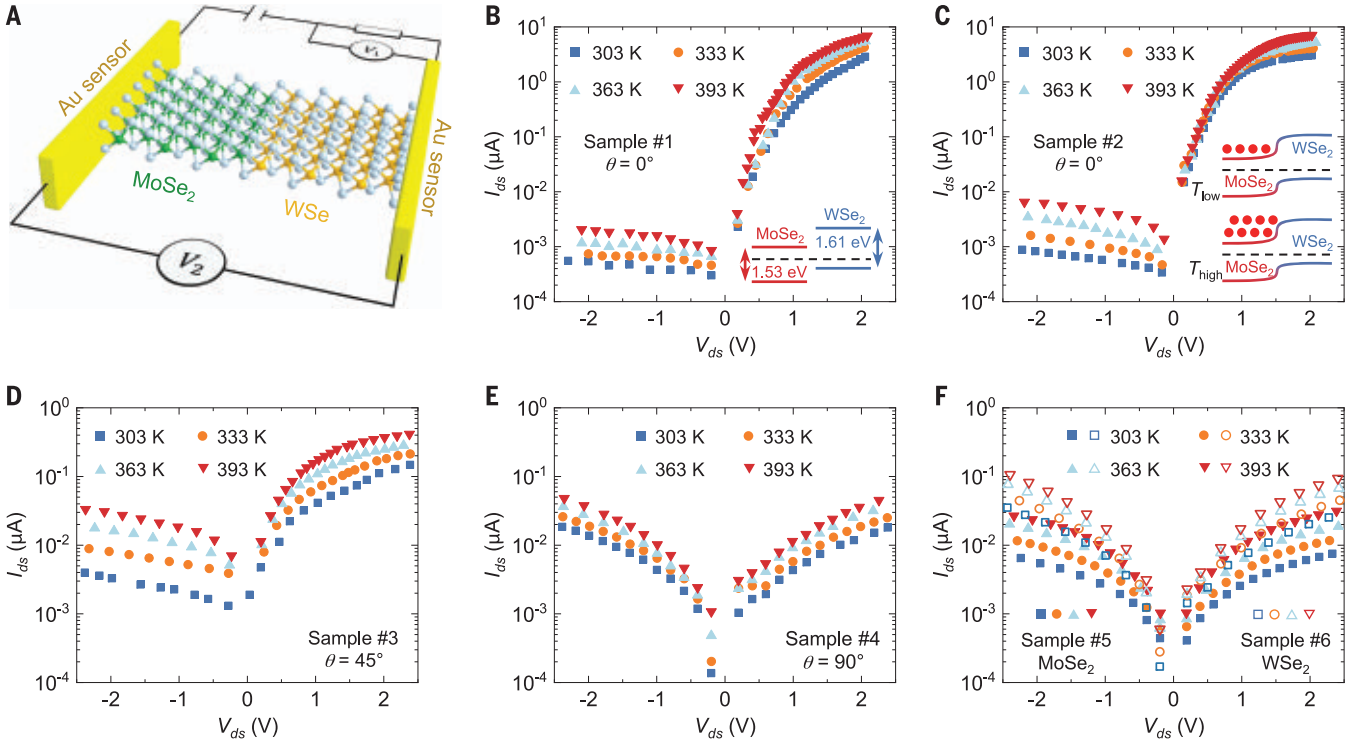

Fig. 2. External electrical measurement circuit and thermodynamic characterization of the electrical properties of $MoSe_2$-WSe_2 lateral heterostructures. (**A**) Schematic diagram of the electrical measurement circuit based on the H-type device, where the $MoSe_2$-WSe_2 heterostructure sample is in contact with two gold sensors, and one multimeter, V_1, is used to measure the voltage and another multimeter, V_2, is used to measure the current through the heterostructure sample. I_{ds}-V_{ds} characterization of (**B**) sample 1, (**C**) sample 2, (**D**) sample 3, (**E**) sample 4, and (**F**) samples 5 and 6 at different temperatures ranging from 303 to 393 K. Insets in (B) and (C) are sketches of the band alignments and the thermionic effect in the $MoSe_2$-WSe_2 lateral heterostructure, respectively.

Furthermore, we studied the thermodynamic behavior of charge carriers by varying the temperature from 303 to 393 K. A temperature dependence can be found in the I_{ds}-V_{ds} curves of all measured samples. Both the temperature-dependent current and rectification ratio are related to the interface angle. For heterostructure samples 1 to 3, forward current monotonically increases with temperature owing to the increase of thermionic emission. More electrons can contribute to the forward current when temperature is raised (Fig. 2C, inset). For the reverse bias conditions, more electron-hole pairs are generated in the depletion region because of the increase in kinetic energy at high temperature, thus leading to an increase trend of reverse current. In addition, the temperature influence on the reverse generation current is more pronounced than that on the forward current, resulting in a reduction of ER ratio. For samples 4 to 6 lacking the built-in potential, both the forward and reverse currents also increase with temperature because of the enhancement of carrier concentration. The symmetric I_{ds}-V_{ds} curves at different temperatures indicate the absence of an ER effect.

Thermal rectification measurement

We used the H-type sensor method to measure the thermal conductivities of the monolayer $MoSe_2$-WSe_2 lateral heterostructure in two opposite heat flow directions (*21*–*23*). We performed all the experiments in a high-vacuum chamber (pressure < 10^{-3} Pa), and the heat loss due to convection and thermal irradiation could be safely neglected [see (*20*) for detailed uncertainty analysis]. Furthermore, as seen in the scanning electron microscopy (SEM) images (Fig. 1, K to P), the geometric size of the gold sensor (0.8 μm in width, 15 μm in length, and 100 nm in thickness) was much smaller than that of the $MoSe_2$-WSe_2 heterostructure (6 μm in width and 4 μm in length) supported on a 300-nm-thick SiO_2 layer. The suspended gold sensor could offer high sensitivity in temperature measurement as a precise resistance thermometer. The influences of the contact thermal resistance between the gold sensor and two-dimensional (2D) material were carefully considered [see (*20*) for discussion]. Given the relatively large thermal resistance of the tested sample, we neglected the influence of the contact thermal resistance.

We heated one gold sensor and used the other one to detect the temperature rise (Fig. 3A). The heat flow direction can be reversed by exchanging the roles of "heater" and "detector" between the two sensors (*20*) (fig. S4). Because of the relatively weak mechanical strength of TMD materials (*24*), a thin supporting SiO_2 layer is essential to avoid device failure. We considered the influence of the supporting SiO_2 layer on the thermal property characterization of the $MoSe_2$-WSe_2 monolayer (*20*), which has no effect on the temperature difference between the two gold sensors in the experiment.

We plotted the measured thermal conductivities (table S1) of six samples (Fig. 3, B to F). The measured thermal conductivities (λ) of homogeneous $MoSe_2$ (sample 5) and WSe_2 (sample 6) are 45 and 40 W/(m·K) at room temperature, which is consistent with the literature values (*25*, *26*), proving the measurement accuracy of the H-type method. The flattened tendency of the thermal conductivity versus temperature curve was attributed to the atomic doping and SiO_2 substrate–induced phonon scattering, which is ubiquitous in monolayer 2D materials (*27*, *28*). The λ discrepancies of homogeneous $MoSe_2$ and WSe_2 in different heat flow directions are <3%, showing no TR effect, as expected. We show the thermal conductivities of $MoSe_2$-WSe_2 heterostructure samples 1 and 2, where the heterojunction interface is vertical to the heat flow direction (θ = 0°) (Fig. 3, B and C). In the heat flow direction from $MoSe_2$ to WSe_2 (the J^+ direction), sample 1 has a λ of ~30 W/(m·K) at 273 K, which is 96% higher than that in the opposite direction. Sample 2 has a TR factor

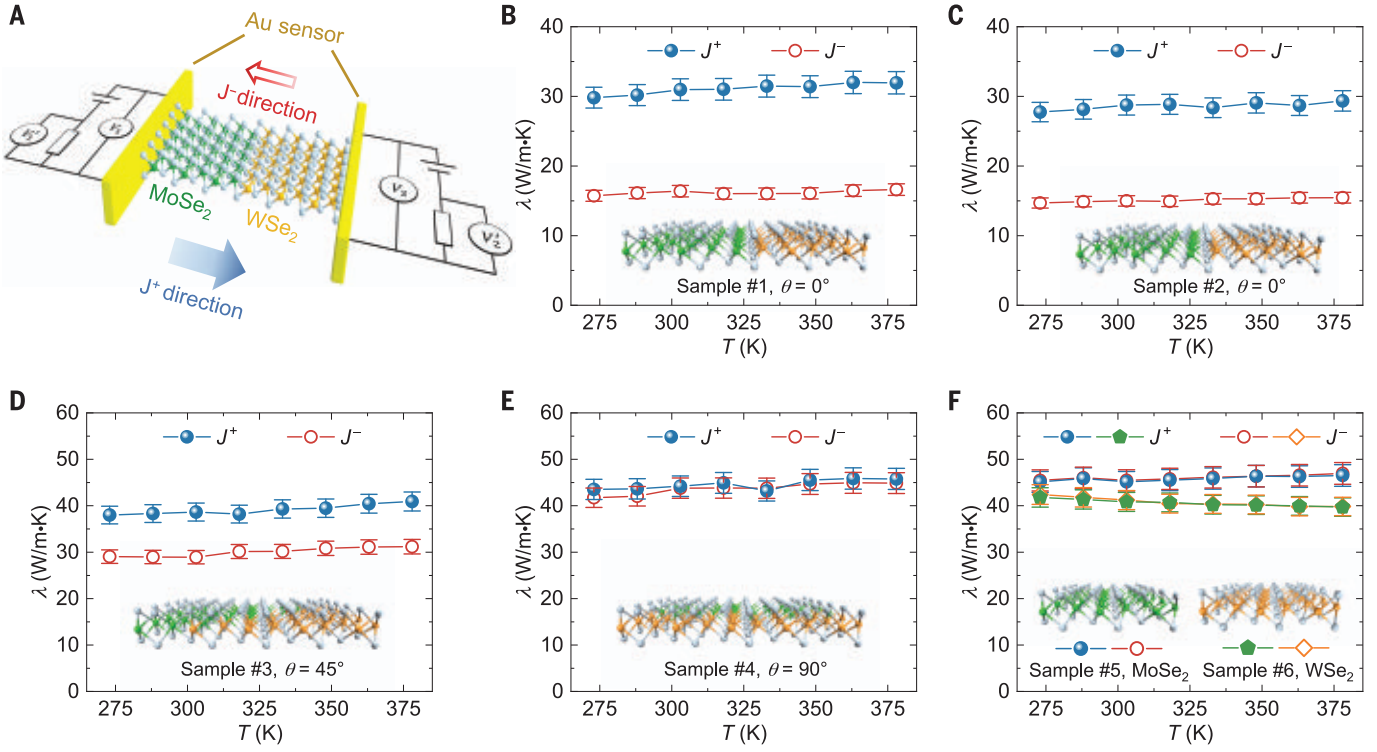

Fig. 3. External thermal measurement circuit and TR characteristics of $MoSe_2$-WSe_2 lateral heterostructures. (**A**) Schematic diagram of the thermal measurement circuit based on the H-type sensing device. Two precision dc power supplies, two standard resistors, and four high-precision digital multimeters are built in, where V_1 and V_2 are used to measure the voltages of the two gold sensors, and V_1' and V_2' are used to measure the current (divided by the standard resistance) in each loop. The blue solid arrow represents the high thermal conductivity direction J^+ from $MoSe_2$ to WSe_2, while the red hollow arrow represents the low thermal conductivity direction J^- from WSe_2 to $MoSe_2$. (**B** to **F**) The measured thermal conductivities of samples 1 to 6, respectively, in two opposite heat flow directions within a temperature range of 273 to 378 K. The insets show the atomic diagrams to demonstrate the interface morphology features at different angles. In each figure, the blue symbols represent the thermal conductivity in J^+ direction, while the red symbols represent the thermal conductivity in J^- direction. Error bars show experimental uncertainties of ±5%.

of 93%, consistent with the result of sample 1, owing to their similar heterojunction morphologies illustrated in the Raman spatial mapping images (Fig. 1, Q and R). For sample 3, the heat flows obliquely across the heterojunction interface at θ = 45°, and the TR factor is 32% (Fig. 3D). For sample 4, the heterojunction interface is parallel to the heat flow direction (θ = 90°), and the TR effect vanishes (Fig. 3E). The experimental results demonstrate that the TR effect is dependent on the angle between the heterojunction interface and heat flow direction. By simply adjusting the angle θ, the TR factor can be regulated between its maximum and zero. This provides an effective way to actively control phonon transport in monolayer heterostructures.

In reality, the existence of TR in the heterostructure could be directly proven from the original experimental data of the resistance of the H-type sensor in different heat flow directions (table S2). For monolayer heterostructure sample 1, the temperature of the detector sensor was 2.62 K higher in the J^+ direction than in the J^- direction at a fixed temperature rise of 30 K at the heater sensor (fig. S6). In contrast, for the homogeneous $MoSe_2$ sample 5, the temperature rise relationship between the detector sensor and heater sensor was the same in both the J^+ and J^- directions. This observation is solid proof of TR without any possible changes caused by finite element analysis or data postprocessing.

Furthermore, the thermal conductivities of heterostructure samples 1, 2, and 3 show a slight increasing trend with increasing temperature. This trend has been theoretically predicted to be the consequence of the increasing interfacial thermal conductance of a two-segment heterostructure system owing to the increase in phonon transmission caused by the enhanced anharmonicity at the inelastic interface (*29*). The agreement between the measurement and theoretical prediction further verifies the accuracy and reliability of our experimental data and proves the interface-dominated phonon transport in the $MoSe_2$-WSe_2 heterostructure.

Understanding the mechanisms of the TR effect

Given that previous experiments proved that the electron-dominated thermal rectifiers can have an ultrahigh TR ratio of up to 140 at low temperature (*30*, *31*), the intrinsic electrical diode effect of the lateral heterostructure prompted us to first look into the role of electrons. We performed a thorough examination and found that the electronic thermal conductivity is negligible in the $MoSe_2$-WSe_2 lateral heterostructure (*20*) (fig. S7), which means that phonons are the main heat carriers. We performed a nonequilibrium molecular dynamics (NEMD) simulation to reveal the physical mechanisms of TR. We started with a schematic diagram of the $MoSe_2$-WSe_2 lateral heterostructure divided into segments of pure materials (I and III) and interface (II) (Fig. 4A). Our simulation results indicate that heat preferentially flows from the $MoSe_2$ domain to the WSe_2 domain, consistent with the experimental results. Given the small contribution of the temperature-dependent thermal conductivities of individual $MoSe_2$ and WSe_2 to the TR effect (*20*), we turned to examine the phonon spectra mismatch of regions I and III in both the J^+ and J^- directions (Fig. 4B). When heat flows in the J^+ direction from $MoSe_2$ to WSe_2, the phonon spectra of the $MoSe_2$ and WSe_2 domains match

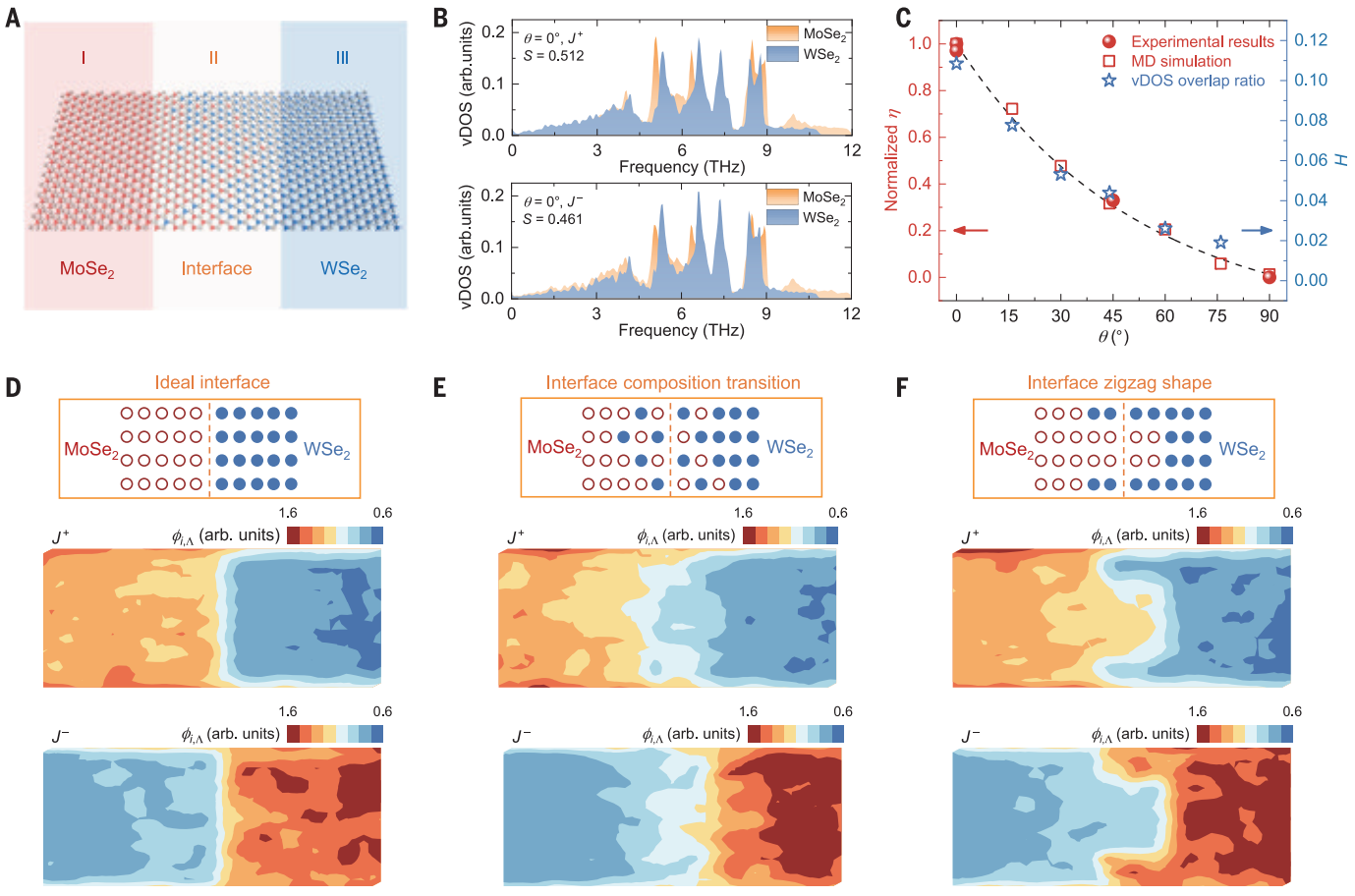

Fig. 4. MD simulation results revealing the physical mechanisms of TR. (**A**) Schematic diagram of the $MoSe_2$-WSe_2 lateral heterostructure models built for MD simulation with pure materials (I and III) and interface (II). (**B**) Vibrational density of states (vDOS) for θ = 0° in two directions. The larger spectra overlap (*S*) in the J^+ direction indicates higher thermal conductance across the interface. (**C**) Normalized TR ratio (η) and spectra overlap ratio (*H*) plotted with angle (θ). Schematic diagrams and distribution of localized phonon modes in forward and reverse directions for three different interface morphologies: (**D**) an ideal interface, (**E**) a composition transition interface, and (**F**) a zigzag-shaped interface. arb. units, arbitrary units.

well at low frequency (<4 THz). The coupling phonons with long wavelengths serving as the major force of heat conduction facilitate thermal transport across the interface. In contrast, the phonon spectra are staggered in the reverse J^- direction from WSe_2 and $MoSe_2$, which hinders the transmission of lattice vibrational energy across the interface. We further calculated the spectra overlap (*S*) to quantify the matching of the phonon bands. The overlap S^+ and S^- are 0.512 and 0.461 in the J^+ and J^- directions, respectively. A larger spectra overlap corresponds to a higher thermal conductivity, as observed in the experiment. A clearer physical picture of TR can be seen from the spatial energy distribution of propagating phonon modes (fig. S8).

In addition to the theory of phonon spectra overlap, another factor derived from the interface morphology also contributes to the TR effect. The HAADF-STEM image (Fig. 1D) shows the actual interface with a zigzag shape and compositional transition. A more precise model including region II was built, and the simulation results indicated that the real zigzag-shaped interface with local compositional transition enhances the TR effect (fig. S9). We also computed the distribution of localized phonon modes (Fig. 4, D to F), and the results demonstrated that the exchange between Mo and W atoms and narrow edges induced by the zigzag structure at the interface cause more localized phonon modes in the J^- direction (appearing dark red). This enhances the TR effect on the basis of the ideal sharp interface (Fig. 4D). The overlap of phonon spectra can be used to explain the mechanism of the TR effect caused by phonon anharmonicity of two dissimilar materials, while the composition transition and zigzag structure at the interface can further enhance the TR effect. The combination of these two mechanisms together results in a high TR ratio of 96% in monolayer $MoSe_2$-WSe_2 heterojunctions.

Our experimental results demonstrate that the TR ratio of the $MoSe_2$-WSe_2 heterostructure can be regulated by changing the angle between the directions of the interface and heat flow. To explain the angle-dependent TR effect, we set up seven different models with angle θ varying from 0° to 90° and separately calculated their TR ratios, phonon spectra, and spatial energy distribution (figs. S8, S10, and S11). The results show that the TR ratio monotonically decreases with increasing angle θ and finally disappears when the interface is parallel to the heat flow direction (Fig. 4C), consistent with the experimental results [see (*20*) for detailed discussion].

Numerous studies have demonstrated that the essence of TR is the asymmetry of phonon transport in the asymmetric structure (*21*, *32*–*45*). For homogeneous materials, TR can be achieved by artificially cutting or kneading the sample into asymmetric shapes, such as trapezoidal or T-shaped graphene (*21*, *43*) and diamond nanopyramids (*42*). In this case, TR originates from phonon lateral confinement and vanishes at the macroscale. The as-synthesized $MoSe_2$-WSe_2 heterostructure is a typical two-segment system with inherent

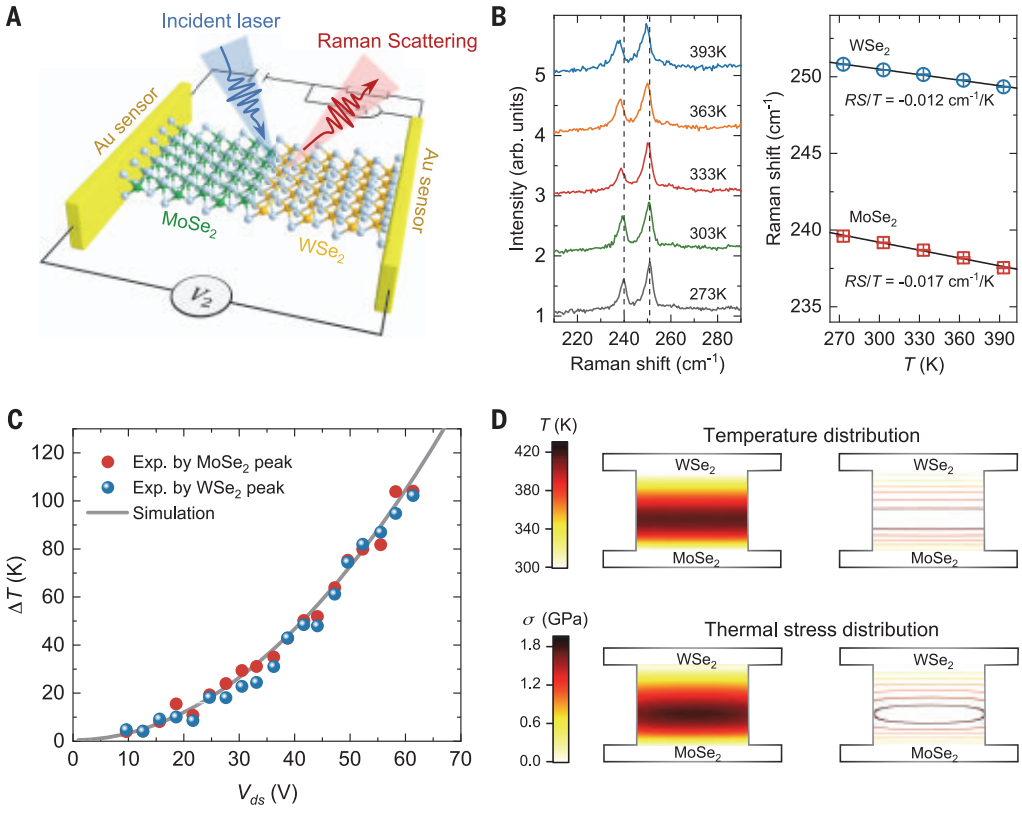

Fig. 5. High bias voltage experiment of the heterostructure with temperature characterization by Raman spectroscopy. (**A**) Schematic diagram of the temperature measurement. The $MoSe_2$-WSe_2 heterostructure was heated by an electrical current, and the temperature was measured by the Raman shift. (**B**) Calibration of the temperature-dependent Raman shift for WSe_2 and $MoSe_2$ segments from 273 to 393 K. The linearly fitted values of the slope are −0.012 cm^{-1}/K and −0.017 cm^{-1}/K for representative Raman peaks of WSe_2 and $MoSe_2$, respectively. Error bars show experimental uncertainties of eight individual measurements. (**C**) Temperature rise measured by experiment and calculated from finite element analysis. The laser beam was focused at the heterostructure interface, and the local temperature rise was obtained through the Raman shifts of both $MoSe_2$ and WSe_2 peaks. (**D**) Comparison of the asymmetric temperature and thermal stress distributions of the H-type device at V_{ds} = 60 V.

asymmetric structure, different from the previous examples. The interface formed by the covalent bonding between two materials acts as a sluice gate for both electron and phonon flows. When the size of the system increases, the role of the interface is suppressed, thus leading to a declining trend in the TR effect (fig. S12). However, the TR effect will not vanish in heterostructure as long as the interface exists.

Application

In practical applications, the applied bias voltage is much larger than that in our property measurements. To verify the upper limit of endurable bias voltage and corresponding temperature rise of the p-n heterojunction diode device, we measured the temperature rise at the interface by using noncontact Raman spectroscopy while continuously increasing the forward bias voltage to the $MoSe_2$-WSe_2 diode (Fig. 5A). The temperature dependence of the Raman shift was calibrated beforehand, and a small laser power was used so that the temperature rise caused by laser heating could be neglected. We show the A_{1g} mode peaks of both $MoSe_2$ and WSe_2, displaying a remarkable redshift with increasing temperature (Fig. 5B). We can fit the Raman shift versus temperature by a linear function with a slope of −0.017 cm^{-1}/K for the $MoSe_2$ A_{1g} mode and −0.012 cm^{-1}/K for the WSe_2 A_{1g} mode, agreeing well with the literature values (*25*, *26*). In the experiment, the bias voltage (V_{ds}) was gradually increased from 0 V to the maximum 61 V, at which point the diode device broke down. Figure 5C shows the measured temperature rise at the interface through the Raman shifts of both the $MoSe_2$ A_{1g} mode and WSe_2 A_{1g} mode peaks. The results from the two representative peak shifts show good agreement with each other, verifying the accuracy and reliability of Raman spectra measurement. Figure 5D depicts the asymmetric temperature and thermal stress distributions of the heterostructure device calculated by COMSOL.

The maximum current density of the monolayer heterojunction was estimated to exceed 2×10^7 A/cm^2, and the local temperature rise at the interface was measured to be 100 K before breakdown. The severe electromigration damage induced by high current density and high temperature at the interface is the main reason for the breakdown of the heterojunction device (*46*). The high local thermal stress further aggravates the damage. Therefore, decreasing the local temperature at heterojunction interface is the key factor to mitigate the electromigration damage and reduce the thermal stress, prolonging the life of the device. Benefiting from the TR effect, the lateral heterostructure has higher thermal conductivity in the ON state, which facilitates the heat dissipation and decreases the temperature at interface.

Conclusions

For highly integrated circuits at the nanoscale, efficient heat dissipation is crucial for better device performance and extended lifetime. Unfortunately, the universal Umklapp phonon-phonon scattering near room temperature causes a negative correlation between thermal conductivity and temperature, leading to heat transfer deterioration in high-power integrated circuits. In this work, we fabricated a monolayer $MoSe_2$-WSe_2 heterostructure device that possesses simultaneous ER and TR characteristics. This atomically thin electrical diode has a high ON/OFF ratio up to 10^4. When it works as a diode in the ON state with a large bias voltage, the thermal conductivity of device is increased by 96% in the heat flow direction from $MoSe_2$ to WSe_2. The monolayer lateral heterostructure has an enhanced capability to remove wasted heat by itself without external heat dissipation channels. This finding paves a new way for designing heterostructure devices with better electrical and thermal performances simultaneously.

REFERENCES AND NOTES

1. H. N. Khan, D. A. Hounshell, E. R. H. Fuchs, *Nat. Electron.* **1**, 14–21 (2018).
2. G. Hills *et al.*, *Nature* **572**, 595–602 (2019).
3. J. P. Llinas *et al.*, *Nat. Commun.* **8**, 633 (2017).

4. B. Radisavljevic, A. Radenovic, J. Brivio, V. Giacometti, A. Kis, *Nat. Nanotechnol.* **6**, 147–150 (2011).
5. J. G. Song *et al*., *ACS Nano* **7**, 11333–11340 (2013).
6. Y. Gong *et al*., *Nat. Mater.* **13**, 1135–1142 (2014).
7. X. Duan *et al*., *Nat. Nanotechnol.* **9**, 1024–1030 (2014).
8. Y. Gong *et al*., *Nano Lett.* **15**, 6135–6141 (2015).
9. M. Y. Li *et al*., *Science* **349**, 524–528 (2015).
10. P. K. Sahoo, S. Memaran, Y. Xin, L. Balicas, H. R. Gutiérrez, *Nature* **553**, 63–67 (2018).
11. J. Zhu *et al*., *J. Am. Chem. Soc.* **142**, 16276–16284 (2020).
12. Y. Yoo, Z. P. Degregorio, J. E. Johns, *J. Am. Chem. Soc.* **137**, 14281–14287 (2015).
13. C. Huang *et al*., *Nat. Mater.* **13**, 1096–1101 (2014).
14. Z. Zhang *et al*., *Science* **357**, 788–792 (2017).
15. S. Xie *et al*., *Science* **359**, 1131–1136 (2018).
16. A. L. Moore, L. Shi, *Mater. Today* **17**, 163–174 (2014).
17. N. Mingo, *Phys. Rev. B* **68**, 113308 (2003).
18. T. L. Feng, X. L. Ruan, *Phys. Rev. B* **93**, 045202 (2016).
19. T. L. Feng, L. Lindsay, X. L. Ruan, *Phys. Rev. B* **96**, 161201 (2017).
20. Materials and methods are available as supplementary materials.
21. H. Wang *et al*., *Nat. Commun.* **8**, 15843 (2017).
22. S. Fujiwara, X. Zhang, M. Fujii, *High Temp. High Press.* **33**, 271–278 (2001).
23. S. Y. Zhao, H. D. Wang, *ES Energy & Environment* **9**, 59–66 (2020).
24. K. Liu, J. Q. Wu, *J. Mater. Res.* **31**, 832–844 (2016).
25. X. Zhang *et al*., *ACS Appl. Mater. Interfaces* **7**, 25923–25929 (2015).
26. E. Easy *et al*., *ACS Appl. Mater. Interfaces* **13**, 13063–13071 (2021).
27. J. H. Seol *et al*., *Science* **328**, 213–216 (2010).
28. M. An, D. S. Chen, W. G. Ma, S. Q. Hu, X. Zhang, *Int. J. Heat Mass Transf.* **178**, 121630 (2021).
29. X. Liu, J. Gao, G. Zhang, Y. W. Zhang, *Nanoscale* **10**, 19854–19862 (2018).
30. F. Giazotto, F. S. Bergeret, *Appl. Phys. Lett.* **103**, 242602 (2013).
31. M. J. Martínez-Pérez, A. Fornieri, F. Giazotto, *Nat. Nanotechnol.* **10**, 303–307 (2015).
32. N. B. Li *et al*., *Rev. Mod. Phys.* **84**, 1045–1066 (2012).
33. N. A. Roberts, D. G. Walker, *Int. J. Therm. Sci.* **50**, 648–662 (2011).
34. C. W. Chang, D. Okawa, A. Majumdar, A. Zettl, *Science* **314**, 1121–1124 (2006).
35. B. Liang, X. S. Guo, J. Tu, D. Zhang, J. C. Cheng, *Nat. Mater.* **9**, 989–992 (2010).
36. W. Kobayashi, Y. Teraoka, I. Terasaki, *Appl. Phys. Lett.* **95**, 171905 (2009).
37. R. Shrestha *et al*., *Nat. Commun.* **11**, 4346 (2020).
38. X. Yang *et al*., *ACS Appl. Mater. Interfaces* **12**, 28306–28312 (2020).
39. B. Li, L. Wang, G. Casati, *Phys. Rev. Lett.* **93**, 184301 (2004).
40. B. Li, J. Lan, L. Wang, *Phys. Rev. Lett.* **95**, 104302 (2005).
41. N. Yang, N. Li, L. Wang, B. Li, *Phys. Rev. B* **76**, 020301 (2007).
42. J. Lee, V. Varshney, A. K. Roy, J. B. Ferguson, B. L. Farmer, *Nano Lett.* **12**, 3491–3496 (2012).
43. Y. Wang *et al*., *Nano Lett.* **14**, 592–596 (2014).
44. X. K. Chen, Z. X. Xie, W. X. Zhou, L. M. Tang, K. Q. Chen, *Carbon* **100**, 492–500 (2016).
45. Y. Y. Zhang, Q. X. Pei, C. M. Wang, C. H. Yang, Y. W. Zhang, *J. Phys. Chem. C* **122**, 22783–22789 (2018).
46. D. Lembke, A. Kis, *ACS Nano* **6**, 10070–10075 (2012).

ACKNOWLEDGMENTS

Funding: H.W. acknowledges financial support from the National Natural Science Foundation of China (51976096). X.Z. acknowledges financial support from the National Natural Science Foundation of China (51827807 and 52130602). R.L. acknowledges financial support from the National Key Research and Development Program of China (2021YFA1200800) and the National Natural Science Foundation of China (51972191). **Author contributions:** H.W., R.L., and X.Z. conceived of and designed the research. Q.L. grew the $MoSe_2$-WSe_2 lateral heterostructures and performed the high-resolution transmission electron microscopy characterization. H.W. designed and fabricated the H-type sensing devices. H.W. and Y.Z. performed the electrical and thermal property measurements and conducted Raman spectral mapping and high bias voltage measurements. Y.Z. conducted the molecular dynamics simulations. H.W. and S.Z. analyzed the data and performed the finite element simulations. H.W., Y.Z., and Q.L. wrote the manuscript with contributions from all authors. Q.X. provided valuable suggestions and revised the manuscript. **Competing interests:** The authors declare that they have no competing interests. **Data and materials availability:** All data are available in the main text or the supplementary materials.

SUPPLEMENTARY MATERIALS

science.org/doi/10.1126/science.abq0883
Materials and Methods
Supplementary Text
Figs. S1 to S14
Tables S1 to S4
References (*47*–*64*)

Submitted 17 March 2022; accepted 20 September 2022
10.1126/science.abq0883

PLANT SCIENCE

Peptide ligand-mediated trade-off between plant growth and stress response

Mari Ogawa-Ohnishi, Tomohide Yamashita, Mitsuru Kakita†, Takuya Nakayama, Yuri Ohkubo, Yoko Hayashi, Yasuko Yamashita, Taizo Nomura, Saki Noda, Hidefumi Shinohara‡, Yoshikatsu Matsubayashi*

Deciding whether to grow or to divert energy to stress responses is a major physiological trade-off for plants surviving in fluctuating environments. We show that three leucine-rich repeat receptor kinases (LRR-RKs) act as direct ligand-perceiving receptors for PLANT PEPTIDE CONTAINING SULFATED TYROSINE (PSY)-family peptides and mediate switching between two opposing pathways. By contrast to known LRR-RKs, which activate signaling upon ligand binding, PSY receptors (PSYRs) activate the expression of various genes encoding stress response transcription factors upon depletion of the ligands. Loss of PSYRs results in defects in plant tolerance to both biotic and abiotic stresses. This ligand-deprivation–dependent activation system potentially enables plants to exert tuned regulation of stress responses in the tissues proximal to metabolically dysfunctional damaged sites where ligand production is impaired.

Leucine-rich repeat receptor kinases (LRR-RKs) represent the largest family of transmembrane receptor-like kinases in plants; these proteins are involved in a variety of developmental processes from stem cell regulation to bacterial disease resistance. In *Arabidopsis*, 251 predicted LRR-RK genes have been identified and this family is further subdivided into 15 subfamilies based on phylogenetic analysis of the kinase domain (*1*, *2*). LRR-RKs are also classified into two types: ligand-perceiving receptors that directly interact with ligands and coreceptors that heterodimerize with ligand-perceiving receptors to facilitate signal transduction (*3*). Generally, most ligand-perceiving receptors belong to the subfamilies X, XI, and XII. In particular, LRR-RKs in subfamily XI play roles in the perception of various endogenous peptide hormones. Indeed, specific oligopeptides have been identified as cognate ligands for most of the members of subfamily XI (*4*). However, members of one distinct clade comprising three LRR-RKs belonging to subgroup XI remain orphan receptors, for which the cognate ligands have not yet been identified.

Genes encoding the precursors of small peptide hormones typically exist as multiple paralogous copies in the genome (*5*, *6*). Individual precursor polypeptides share a family-specific conserved domain close to the C terminus, from which mature functional peptide hormones are generated through posttranslational modification followed by proteolytic processing. One such peptide, *Arabidopsis* PLANT PEPTIDE CONTAINING SULFATED TYROSINE 1 (PSY1), is (in its mature form) a 18-amino acid peptide that is posttranslationally modified by tyrosine sulfation and hydroxyproline arabinosylation (*7*). PSY1 has been shown to promote root growth (*7*, *8*), increase cell size (*7*), promote seedling cuticle development (*9*), and activate the plasma membrane H^+-ATPase AHA2 by phosphorylation (*10*), but its direct ligand-perceiving receptor has yet to be identified.

PSY1-like sulfated peptide, RaxX, has also been found in the rice pathogen *Xanthomonas oryzae* pv. *oryzae* (*Xoo*) (*8*, *11*, *12*). RaxX triggers the immune response in rice by directly binding to the immune receptor XA21 (*11*, *12*). *Xoo* mutants lacking RaxX are, however, less virulent than wild-type (WT) *Xoo* on rice leaves in the absence of XA21, suggesting that RaxX is required for the full virulence of *Xoo* for infection

Graduate School of Science, Nagoya University, Nagoya 464-8602, Japan.
***Corresponding author. Email: matsu@bio.nagoya-u.ac.jp**
†Present address: Center for Research Administration and Collaboration, Tokushima University, Tokushima 770-8501, Japan.
‡Present address: Department of Bioscience and Biotechnology, Fukui Prefectural University, Eiheiji 910-1195, Japan.

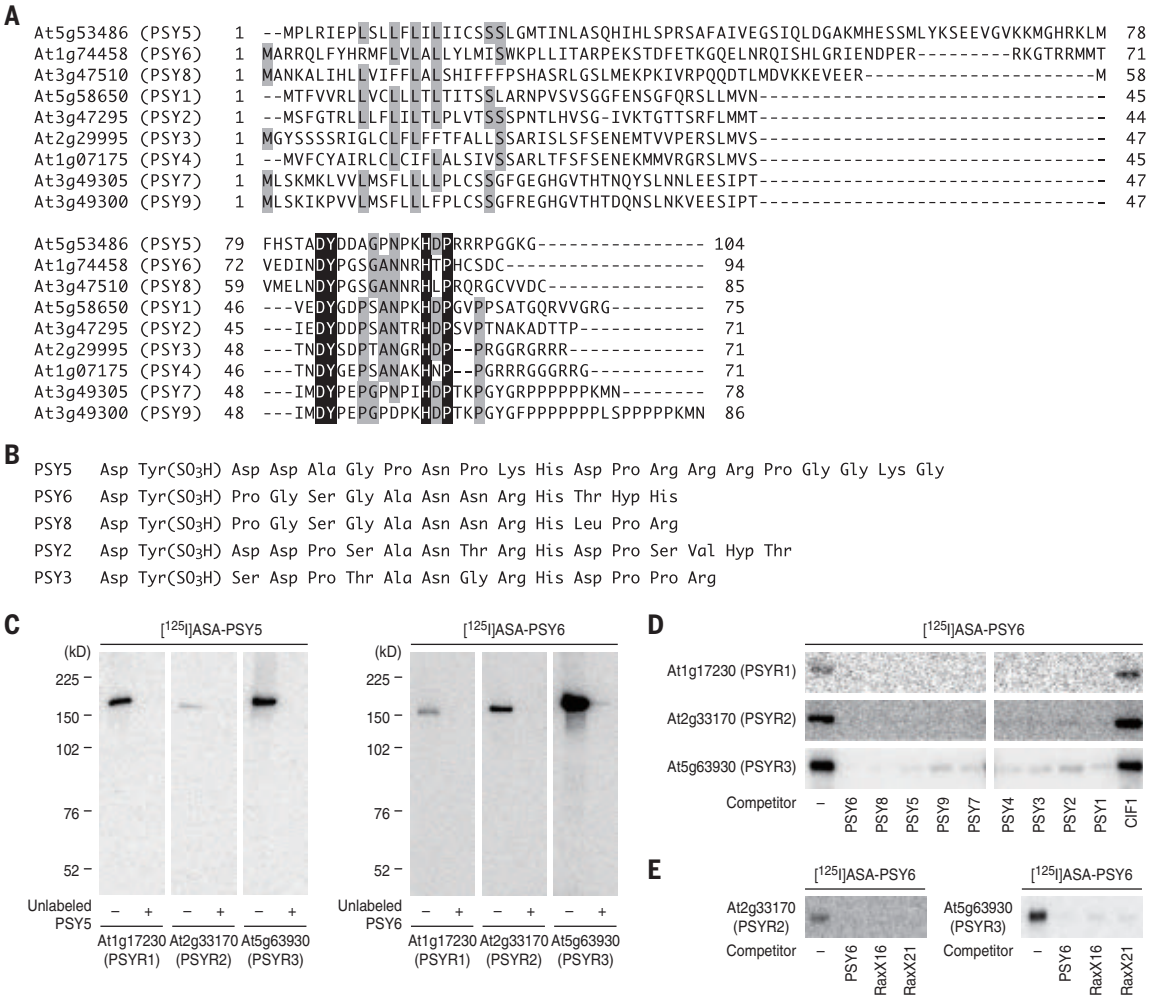

Fig. 1. PSY-family peptides bind directly to the three LRR-RKs. (**A**) Multiple sequence alignments of the primary PSY-family peptides. Identical amino acids are shaded in black and similar amino acids are shaded in gray. (**B**) Structures of the mature peptides of PSY5, PSY6, PSY8, PSY2, and PSY3. (**C**) Photoaffinity labeling of PSYR1 (At1g17230), PSYR2 (At2g33170), and PSYR3 (At5g63930) with [^{125}I]ASA-PSY5 and [^{125}I]ASA-PSY6. The labeled proteins were separated by SDS-PAGE and detected by autoradiography. (**D**) Competitive replacement of [^{125}I]ASA-PSY6 binding to PSYRs by 300-fold excess unlabeled PSY-family peptides. (**E**) Competitive replacement of [^{125}I]ASA-PSY6 binding to PSYR2 and PSYR3 by 300-fold excess unlabeled *Xoo* RaxX16 and RaxX21 peptides.

(*8*). One possible scenario is that activation of host PSY signaling is beneficial to infection and that pathogen–derived RaxX peptide is able to bind the host PSY receptor to activate downstream signaling (*13*); however, the fundamental roles of PSY signaling during plant growth and development remain unknown. We report that three current orphan LRR-RKs act as direct ligand-perceiving receptors for PSY-family sulfated peptides and mediate the trade-off between plant growth and stress and defense responses.

Results

The PSY family is a large group of structurally related tyrosine sulfated peptides

While screening uncharacterized peptide hormone candidates in *Arabidopsis* based on the above empirical rules (*6*), we focused on three closely related paralogous genes, *At5g53486*, *At1g74458*, and *At3g47510*, each of which encodes a polypeptide consisting of ≈90 amino acids characterized by a conserved domain at the C terminus (Fig. 1A). Because these polypeptides show sequence similarity with PSY1, recently At5g53486, At1g74458, and At3g47510 were designated PSY5, PSY6, and PSY8, respectively (*8*, *14*).

Nano-liquid chromatography-coupled tandem mass spectrometry (LC-MS/MS) analyses of the peptides secreted from *Arabidopsis* cells overexpressing PSY5, PSY6, or PSY8 showed that the mature forms of these peptides are 21-, 14- and 14-amino acid tyrosine-sulfated peptides derived from the conserved domain (Fig. 1B and fig. S1, A to C). By contrast to the PSY1 glycopeptide, PSY5, PSY6, and PSY8 lack hydroxyproline arabinosylation. We further determined that PSY2 and PSY3 are 17- and 15-amino acid tyrosine-sulfated peptides, respectively (Fig. 1B and fig. S1, D and E). To dissect the function of PSY-family peptides, we generated an *Arabidopsis psy5 psy6 psy8* triple mutant, but this line showed no apparent phenotype with respect to plant growth, suggesting that functional redundancy among PSY-family peptides prevents analysis of their specific roles from the ligand side (fig. S2, A to C).

Three related LRR-RKs directly recognize PSY-family peptides

To identify receptors that directly interact with these peptides, we chemically synthesized cross-linkable derivatives of PSY5 and PSY6 in which a photoactivatable 4-azidosalicylic acid (ASA) moiety was incorporated into residues not conserved among paralogs and performed radio-iodination (fig. S3, A and B). We carried out an exhaustive binding assay by photoaffinity labeling against an *Arabidopsis* receptor kinase expression library corresponding to subfamilies LRR X and LRR XI (*15*). We found that three related LRR-RKs (At1g17230,

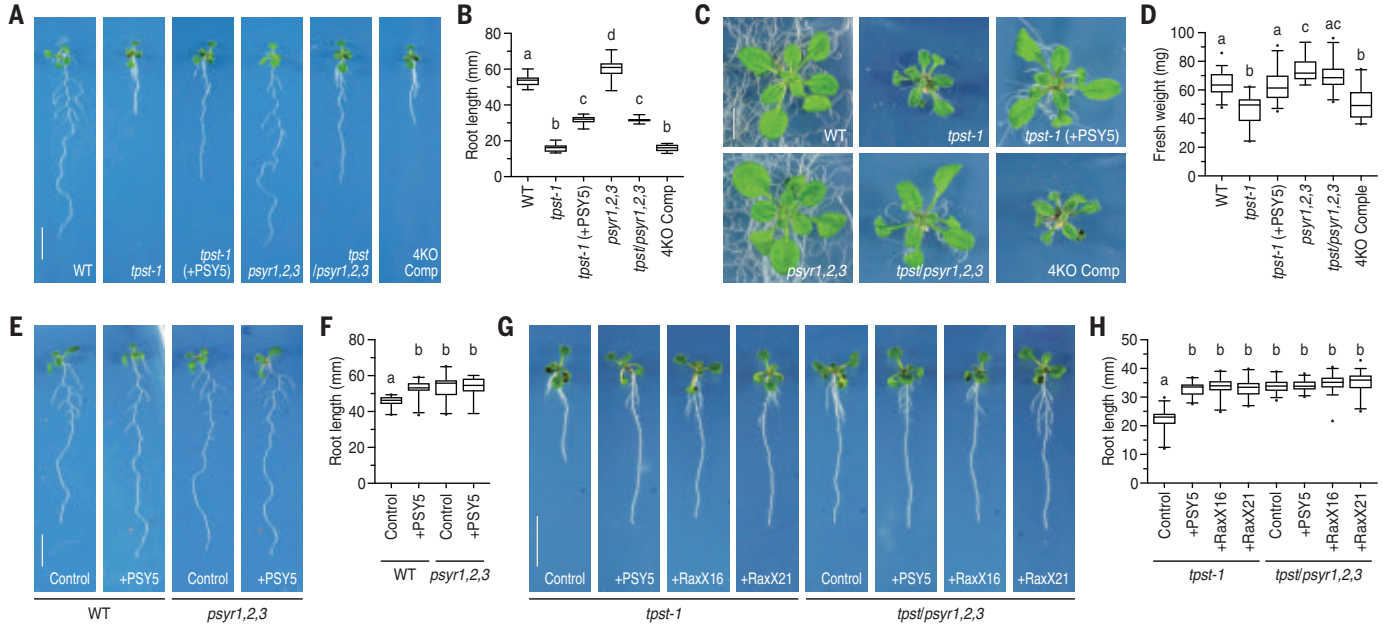

Fig. 2. PSY-family peptides repress PSYR signaling to allow for growth. (**A** and **B**) Effect of PSY5 treatment or *PSYR* disruption on root growth of *tpst-1* plants (mean ± s.d., $P < 0.05$, one-way analysis of variance (ANOVA) followed by Tukey's test, $n = 15$). Images were recorded 8 days after germination. (**C** and **D**) Effect of peptide treatment or receptor disruption on shoot growth of *tpst-1* ($n = 20$ to 39). Images were recorded 16 days after germination. (**E** and **F**) Effect of PSY5 treatment on root growth of WT and *psyr1,2,3* plants ($n = 18$ to 22). Images were recorded 9 days after germination. (**G** and **H**) Effect of PSY5, RaxX16 and RaxX21 treatment on root growth of *tpst-1* and *tpst/psyr1,2,3* plants ($n = 31$ to 39). Images were recorded 10 days after germination. Scale bar, 10 mm [(A), (C), (E), and (G)].

At2g33170, and At5g63930; all members of subfamily LRR XI) directly interacted with both the [^{125}I]ASA-PSY5 and [^{125}I]ASA-PSY6 peptides (Fig. 1C and fig. S3, C and D). This interaction was competitively inhibited by excess unlabeled ligand, indicating that this binding is specific (Fig. 1C). [^{125}I]ASA-PSY6 also interacted with GSO1 and GSO2, but this binding was not competitively antagonized by excess unlabeled PSY6, indicating that the observed binding is nonspecific (fig. S3E).

To dissect how sulfated peptides in the PSY family act as ligands for these LRR-RKs, we screened other PSY-family members using a competitive binding assay with [^{125}I]ASA-PSY6 as the radioligand. We found that all nine of these peptides were able to compete effectively with [^{125}I]ASA-PSY6 in binding to any of the three tested LRR-RKs (Fig. 1D). A control peptide, CIF1, displayed no measurable competition with PSY6 for receptor binding. These results indicated that all of the above-mentioned nine sulfated peptides act as ligands for the three tested LRR-RKs, which we therefore have designated PSYR1 (At1g17230), PSYR2 (At2g33170), and PSYR3 (At5g63930).

We noted that [^{125}I]ASA-PSY6 showed no direct interaction with At1g72300 (in subfamily LRR X), which has been reported to affect PSY1 responses in some experiments and is often called a PSY1 receptor (PSY1R) (fig. S3, C and D) (*7*, *9*, *10*, *16*). At1g72300 also did not directly recognize [^{125}I]ASA-PSY1, indicating that At1g72300 in the LRR X subfamily is not a direct ligand-perceiving receptor for PSY peptides (fig. S3, F and G).

PSYRs also recognize Xanthomonas RaxX peptide

The biotrophic pathogen *Xoo* secretes a sulfated peptide named RaxX, which shares high similarity with PSY family peptides (*8*, *11*). Synthetic sulfated RaxX peptides comprising 16 (RaxX16) or 21 (RaxX21) residues are known to promote root growth in *Arabidopsis* and rice in a manner similar to that triggered by PSY1 (*8*). Our competitive binding assay showed that both RaxX16 and RaxX21 compete effectively with [^{125}I]ASA-PSY6 in binding to PSYR2 and PSYR3, indicating that RaxX is also perceived by PSYRs in *Arabidopsis* (Fig. 1E).

Expression profiles for PSY and PSYR genes

In silico expression profiling of the *PSYR1*, *PSYR2*, and *PSYR3* genes based on publicly available large transcriptomic datasets from Genevestigator (*17*) showed that *PSYR* family receptor genes exhibit a largely ubiquitous expression pattern throughout *Arabidopsis* plants (fig. S4A). Specifically, the expression level of *PSYR1* was higher in shoots than in roots, whereas *PSYR3* expression was higher in roots than in shoots. Histochemical staining of transgenic plants expressing β-glucuronidase (GUS) under control of the promoter of each *PSYR* gene supported these transcript-based expression patterns (fig. S4B). We also examined the expression of *PSY* family peptide genes with Genevestigator and GUS reporter lines and found that members of this peptide family are, in general, expressed in various tissues including leaves, petioles, stems, hypocotyls, cotyledons, and roots (fig. S4, C and D). Expression of *PSYR*s and *PSY*s remained almost stable under various stress conditions, including cold, drought, heat, osmotic, salt, wounding, and microbial inoculation, suggesting that these genes are not stress inducible (fig. S4E). These results indicated that PSY-PSYR signaling typically is constitutively active at the whole-plant level.

Genotype-phenotype correlation analysis from both the ligand and receptor sides

To uncover the molecular mechanisms underlying PSY-PSYR signaling, we analyzed the genotype-phenotype correlation from both the ligand and receptor sides with a tyrosylprotein sulfotransferase mutant *tpst-1* and receptor triple mutant *psyr1-1 psyr2-1 psyr3-1* (*psyr1,2,3*) generated by crossing individual transfer DNA (T-DNA) insertion mutants (fig. S5, A and B). We first cultured the *tpst-1* seedlings in culture medium supplemented with synthetic mature PSY peptides. Because *tpst-1* is deficient in biosynthesis of all tyrosine sulfated peptides, this mutant serves as a substitute for a polymutant of the sulfated peptide hormones (*18*–*20*). The addition of 1 μM PSY2, PSY3, PSY5, PSY6, or PSY8 to the culture medium rescued the root growth defect otherwise seen in *tpst-1* with PSY5 being most potent; this peptide was selected as a representative of the PSY family (fig. S5C). The addition of 1 μM PSY5 to the culture medium rescued the cell elongation defect in the roots of *tpst-1*, along with slightly increasing root apical

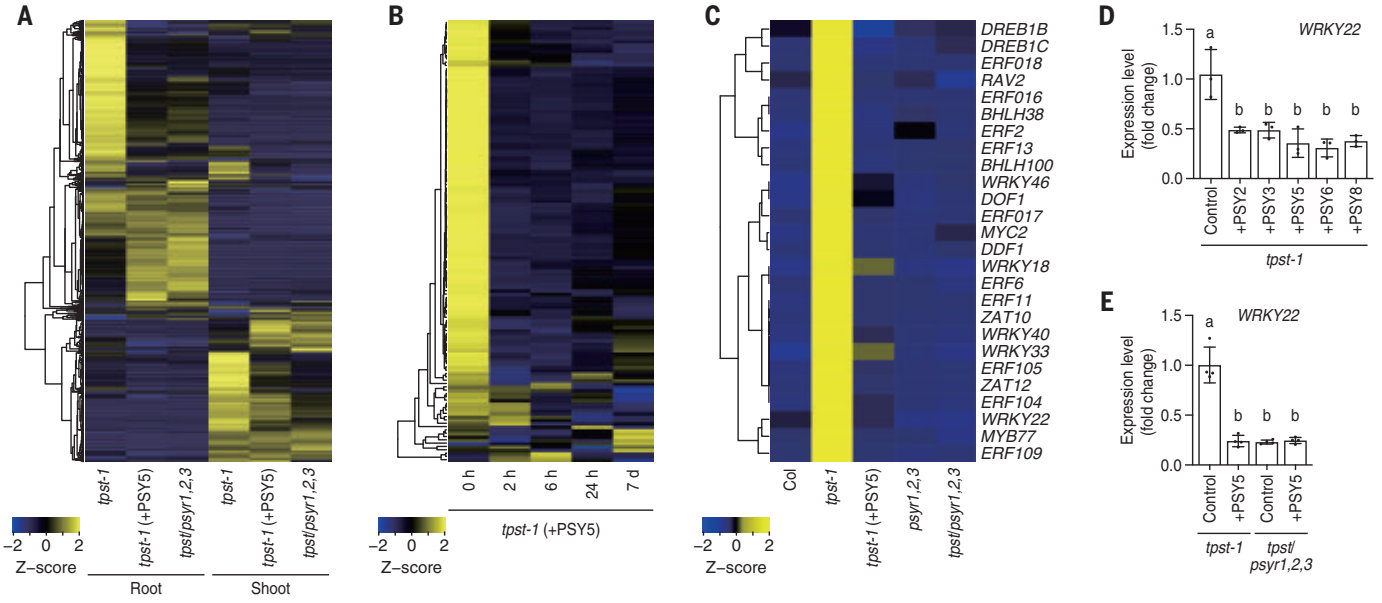

Fig. 3. PSY-PSYR signaling mediates the trade-off between plant growth and stress response. (**A**) Heat map of transcript levels of all genes differentially expressed in at least one of the comparisons in the root and shoot datasets (n = 3 for roots, n = 4 for shoots). (**B**) Heat map of changes in transcript levels of core DEGs in *tpst-1* whole plants following PSY5 treatment (n = 3). Plants were treated with PSY5 for indicated periods before harvest at 7 days. (**C**) Heat map of shoot transcript levels of 26 transcription factor genes enriched in core DEGs (n = 3). (**D**) Expression level of *WRKY22* in the roots of 7-day-old *tpst-1* plants grown on the medium containing various PSY-family peptides (n = 3). (**E**) Expression level of *WRKY22* in the roots of 10-day-old *tpst-1* and *tpst/psyr1,2,3* plants grown on the medium supplemented with or without PSY5 (n = 4).

meristem activity (Fig. 2, A and B, and fig. S5, D to G). Additionally, leaf cell size in *tpst-1* was restored to the WT level and accordingly the rosette size was recovered, though the previously reported increase in the AHA2 Thr^{881} phosphorylation level was not detected under our conditions (Fig. 2, C and D, and fig. S5, H to J) (*10*).

However, in contrast to our initial expectations based on the above peptide bioassays, the *psyr1,2,3* receptor triple mutant displayed a slightly elongated root phenotype compared with WT characterized by increased cortical root cell length (Fig. 2, A and B, and fig. S5, D and E). Nevertheless, no additional root growth in response to PSY5 treatment was observed for *psyr1,2,3*, indicating that this receptor mutant is nonresponsive to the ligand (Fig. 2, E and F).

We further generated a *tpst-1 psyr1-1 psyr2-1 psyr3-1* (*tpst/psyr1,2,3*) quadruple mutant to definitively confirm the receptor mutant phenotypes. Combining the *psyr1,2,3* mutations with *tpst-1* resulted in a 2.1-fold increase in root length compared with the parental *tpst-1*, an effect comparable to that seen in *tpst-1* roots treated with PSY5 peptide (Fig. 2, A and B). Cortical root cell length was also increased in the *tpst/psyr1,2,3* quadruple mutant, reaching a level exceeding that seen in WT plants (fig. S5, D and E). A similar result was obtained for the leaf mesophyll palisade cells and accordingly rosette leaf size was restored (Fig. 2, C and D, and fig. S5, H and I). Combining the *psyr1,2,3* mutations with *tpst-1* also had a minor but noticeable positive effect on root apical meristem activity (fig. S5, F and G). These cellular phenotypes in the roots of the *tpst/psyr1,2,3* quadruple mutant were reversed by complementation with a *PSYR3* genomic fragment (Fig. 2, A to D, and fig. S5, D to I). The flowering and seed sets were normal in both *psyr1,2,3* and *tpst/psyr1,2,3* mutants (fig. S5K).

The *tpst/psyr1,2,3* mutant showed no increase in primary root length following treatment with *Arabidopsis* PSY5 or *Xoo* RaxX peptides, although still responsive to other tyrosine-sulfated peptide hormones such as phytosulfokine (PSK) (*21*), RGF (*19*), and Casparian strip integrity factor (CIF) (*22*, *23*), confirming that the *tpst/psyr1,2,3* mutant is specifically nonresponsive to PSY family peptides (Fig. 2, G and H, and fig. S6, A to F). These results indicated that PSYR1, PSYR2, and PSYR3 are functionally redundant negative regulators of growth in the absence of the ligand, and that PSY-family peptides repress PSYR signaling to allow for growth.

Co-immunoprecipitation coupled with mass spectrometry (CoIP-MS) showed that PSYR3-GFP does not co-precipitate with known co-receptors, irrespective of PSY5 treatment, under the condition that RGFR1-GFP is co-precipitated with SERK1 and BAK1 in the presence of RGF1, suggesting the involvement of an atypical co-receptor system in PSYR signaling (fig. S7, A to C, and table S1) (*3*, *24*).

PSY–PSYR signaling mediates trade-off between growth and stress responses

To explore whether PSY peptide treatment phenocopies loss of PSYRs at a molecular level, we compared transcriptome profiles of roots among the *tpst-1* single mutant, the *tpst/psyr1,2,3* quadruple mutant and PSY5-treated *tpst-1* plants. A total of 1004 differentially expressed genes (DEGs) were identified in PSY5-treated *tpst-1* plants compared with untreated *tpst-1* (data S1 and S2). Of these DEGs, 656 (65.3%) were overlapped with DEGs detected in the *tpst/psyr1,2,3* quadruple mutant (compared with the *tpst-1* single mutant), indicating that *tpst/psyr1,2,3* and PSY5-treated *tpst-1* plants share highly similar transcriptional profiles (Fig. 3A, fig. S8A, and data S3 and S4). We also compared transcriptomes of the shoots of the above plants and found that 400 DEGs (68.3%) of a total 586 DEGs detected in PSY5-treated *tpst-1* plants overlapped with DEGs from the *tpst/psyr1,2,3* quadruple mutant (Fig. 3A, fig. S8A, and data S5 to S7). Therefore, we concluded that the *psyr1,2,3* triple mutant exhibits a constitutive PSY response phenotype, a response that appears to be opposite to that seen for other known LRR-RKs, which usually induce responses only when ligands are bound.

A comparative analysis of overlapping DEGs from the above two comparisons (*tpst-1* versus PSY5-treated *tpst-1* and *tpst-1* versus *tpst/psyr1,2,3* quadruple mutant) in roots and those in shoots uncovered 139 "core" DEGs shared by the root and shoot datasets, of which 135 DEGs were downregulated upon PSY5 treatment (fig. S8B and data S8).

Time course transcriptome analysis of *tpst-1* plants following PSY5 treatment under the culture condition of whole-plant submersion

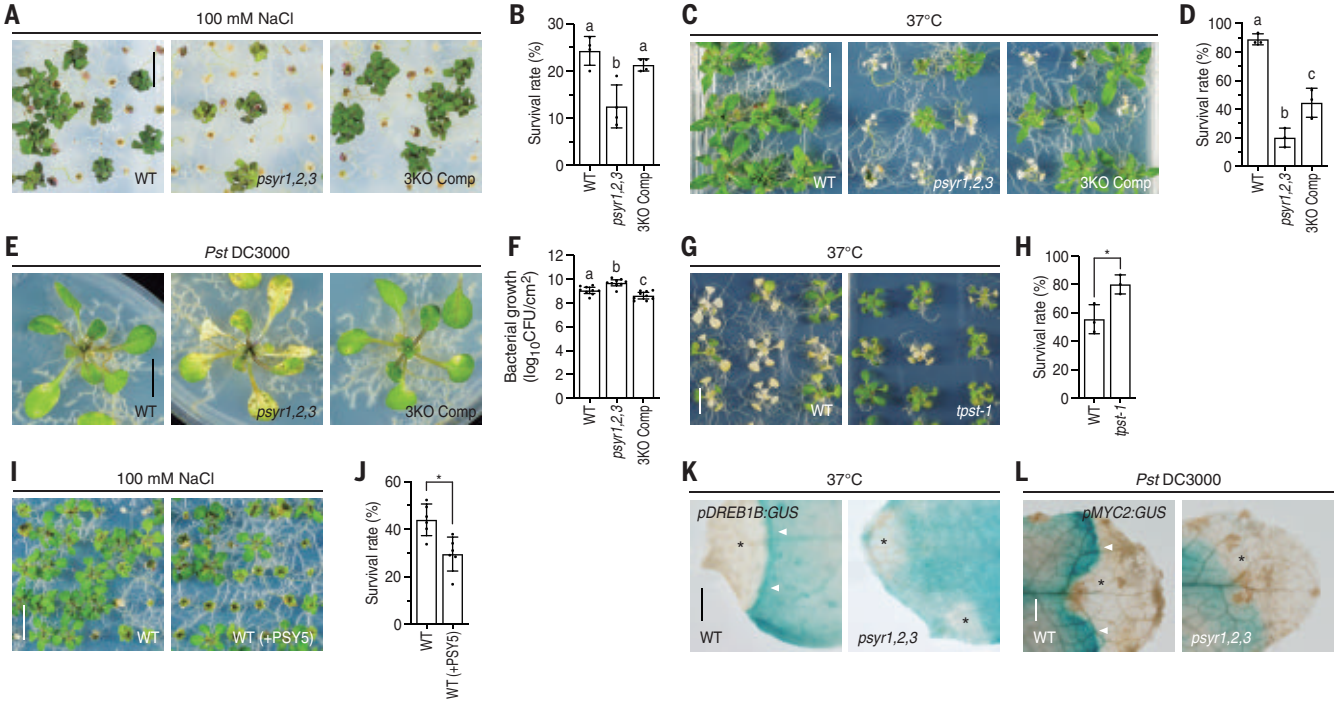

Fig. 4. Loss of PSYRs impairs tolerance to both biotic and abiotic stresses. (**A** and **B**) Salt tolerance of WT, the *psyr1,2,3* triple mutant, and the mutant complemented with *PSYR3*, as assessed following growth for 14 days in the presence of 100 mM NaCl (n = 4). (**C** and **D**) Thermotolerance of WT, the *psyr1,2,3* mutant and the complemented line. Ten-day-old seedlings were incubated at 37°C for 3 days and then allowed to recover at 22°C for 10 days (n = 3). (**E**) Disease resistance of WT, the *psyr1,2,3* and the complemented line, as assessed at 11 days after being challenged by flood inoculation with *Pst* DC3000. (**F**) Bacterial growth in each plant line (n = 9). (**G** and **H**) Thermotolerance of WT and *tpst-1* plants. Ten-day-old seedlings were transferred to 37°C for 4 days and then allowed to recover at 22°C for 3 days (n = 3). (**I** and **J**) Salt tolerance of WT plants grown in the presence of 100 mM NaCl with or without PSY5 for 23 days (n = 6). (**K**) Histochemical GUS staining of leaves of heat-stressed plants carrying *pDREB1B:GUS* reporter in WT and *psyr1,2,3* backgrounds. Ten-day-old seedlings were incubated at 37°C for 3 days and then allowed to recover at 22°C for 1 day before staining. Asterisks denote metabolically dysfunctional damaged sites. Arrowheads show up-regulation of *DREB1B* promoter activity in cell layers adjacent to damaged sites. (**L**) Histochemical GUS staining of leaves of WT and *psyr1,2,3* plants carrying *pMYC2:GUS* reporter at 10 days after inoculation of *Pst* DC3000. Asterisks denote damaged sites. Arrowheads show up-regulation of *MYC2* promoter activity in regions peripheral to the site of damage. Scale bar, 10 mm [(A), (C), (E), (G), and (I)], 0.5 mm [(K) and (L)].

showed that most core DEGs were early responsive genes that were down-regulated within 2 hours (Fig. 3B and data S9). Gene ontology terms for these 135 down-regulated DEGs were largely related to stress response, as exemplified by the enrichment for 26 transcription factor genes, among which almost all were stress-related genes including 10 *ERFs*, 5 *WRKYs*, 3 *DREBs*, and 1 *MYC* (Fig. 3C and fig. S8C). These transcription factors have been shown to play a role in conferring abiotic and biotic stress tolerance through direct binding to the cis elements in the promoter region of the stress resistance genes (*25*–*28*). This finding led us to interpret the growth-promoting effect of PSY-family peptides in the context of a trade-off between optimal growth and maximal stress tolerance (*29*). The stress signaling network actively represses cellular metabolic activities leading to severe constraints on plant growth (*30*). By contrast, growth-promoting pathways need to repress the stress response program. The decision of whether to grow or to restrict growth and divert resources to stress responses is a major physiological trade-off for plants attempting to adapt to fluctuating environments. However, the cell-to-cell communication mechanism underlying this decision remains largely unknown.

The transcript levels for all 26 of these transcription factor genes were highly elevated in *tpst-1* (i.e., plants deficient in PSY-family peptides) compared with the levels for those in WT plants (Fig. 3C and data S10). This observation suggested that stress responses are actively repressed by the almost constitutively expressed PSY-family peptides to allow for growth under normal growth conditions (Fig. 3C). We confirmed that when *tpst-1* was grown on a medium containing various PSY-family peptides (PSY2, PSY3, PSY6, or PSY8, in addition to PSY5), the levels of transcripts of representative genes (*WRKY22* in roots and *DREB1B* in shoots) were decreased (Fig. 3D and fig. S8D). By contrast, even in the absence of the ligands, loss of PSYRs resulted in decreased levels of the transcripts of stress response transcription factor genes as seen in the *tpst/psyr1,2,3* quadruple mutant (Fig. 3C). The *tpst/psyr1,2,3* mutant showed no further decrease in *WRKY22* transcript levels following treatment with PSY5 (Fig. 3E). This observation explained, in terms of the trade-off between growth and stress responses, why the *tpst/psyr1,2,3* quadruple mutant develops longer roots and larger shoots than the parental *tpst-1*. Collectively, our data suggested that PSYRs themselves induce stress response genes and restrict growth in the absence of ligands whereas this stress signaling is prevented in the presence of ligands thereby allowing growth to proceed.

Loss of PSYRs impairs tolerance to both biotic and abiotic stresses

We hypothesized that if PSYR signaling is involved in the regulation of stress response genes, *psyr1,2,3* triple-mutant plants—which are impaired for PSYR-mediated induction of stress response transcription factor genes—will show altered stress tolerance. To test this possibility we examined the response of *psyr1,2,3* mutant plants to various stresses such as high salinity, high temperature, and pathogen exposure. When germinated under 100 mM NaCl conditions, the *psyr1,2,3* mutant displayed

severe growth arrest, with an approximately twofold reduction in survival rate compared with WT plants at 28 days after germination (Fig. 4, A and B). For heat stress treatment, 10-day-old seedlings were incubated at 37°C for 3 days and then returned to 22°C for 10 days. The *psyr1,2,3* mutant exhibited early chlorosis and a severe reduction in survival rate compared with WT plants (Fig. 4, C and D). We also examined the susceptibility of 10-day-old plants to a bacterial pathogen, *Pseudomonas syringae* pv. tomato (*Pst*) DC3000, by flood inoculation. When the surfactant concentration was lowered to facilitate slow infection, typical lesions were seen at 11 days after inoculation in the WT plants. Under these conditions, the *psyr1,2,3* plants showed more severe disease symptoms than the WT plants, with larger chlorotic lesions forming on the leaves (Fig. 4E). Bacterial growth in the leaves of the WT and *psyr1,2,3* plants yielded 1.5×10^9 and 6.1×10^9 colony-forming units (CFU) per cm^2 at 11 days after inoculation, respectively, representing a 4.2-fold increase in bacterial growth in the mutant compared with WT (Fig. 4F). Complementation of *psyr1,2,3* with *PSYR3* rescued the above phenotypes of the mutant. The *tpst-1* mutant in which PSYR signaling is constitutively active exhibited enhanced tolerance to heat stress (Fig. 4, G and H). Conversely, treatment of WT plants with PSY5, which impedes PSYR signaling, caused a reduction in the survival rate of WT plants grown under 100 mM NaCl conditions, again indicating that constitutive blocking of PSYR signaling impairs stress tolerance (Fig. 4, I and J). Similarly, overexpression of *PSY6* decreased salt tolerance although growth was promoted (fig. S9, A to E). Together, these results showed that PSYRs are essential for resistance of plants to multiple environmental stresses.

PSY–PSYR signaling allows induction of stress responses specifically in regions peripheral to the site of damage

Finally, given that PSYR induces stress response genes when ligands are absent, we investigated how this mechanism contributes to the acquisition of tolerance to environmental stresses. With *DREB1B* and *MYC2* as examples, we compared the expression patterns of PSYR target genes between *psyr1,2,3* and WT plants following heat and biotic stresses. A *DREB1B* promoter-GUS reporter assay showed that when 10-day-old plants were incubated at 37°C for 3 days and then returned to 22°C for 1 day, the promoter activity of *DREB1B* was up-regulated in a few cell layers adjacent to the damaged regions in the WT plants (Fig. 4K). By contrast, no such region-specific GUS expression was observed in *psyr1,2,3* plants. Similar results were obtained with plants expressing *MYC2* promoter-GUS reporter at 10 days after inoculation with *Pst* DC3000 (Fig. 4L). These results suggested that, because an increase in metabolically dysfunctional damaged cells leads to a reduction in the extracellular PSY concentration within cell layers adjacent to the damaged sites (even if PSY signaling acts in an autocrine fashion to some extent), this ligand-deprivation–triggered activation of PSYR signaling potentially enables plants to induce stress responses specifically in regions peripheral to the site of damage.

Discussion

Plants, being sessile, must cope with various types of abiotic and biotic stresses, creating a definite trade-off between stress tolerance and growth. Previous work has led to the identification and extensive characterization of cell autonomous stress response systems in plants (*31*). The results of the present study demonstrate the existence of an additional, previously unknown, cell-to-cell communication pathway underlying a trade-off between growth and stress tolerance, shedding light on the mechanisms by which plants survive under diverse environmental stresses. The pattern of stress-induced tissue damage in the natural environment is often patchy, given the uneven distribution of the level of abiotic stresses and pathogen populations. To prevent further tissue damage, viable cells adjacent to the damaged areas need to acquire the ability to take the necessary precautions to minimize the spread of cell death. However, damaged cells are usually metabolically impaired and no longer able to produce positive signals that induce stress responses in viable neighboring cells. To overcome this paradox, plants appear to have evolved elaborate ligand-deprivation–dependent activation systems that potentially induce prophylactic stress responses within still viable cell layers adjacent to the damaged sites. This mechanism balances stress tolerance with associated energetic costs, allowing plants to achieve optimal growth even under stressful environmental conditions.

Our results also explain the physiological benefits of the PSY-mimic peptide RaxX to rice pathogen *Xoo* during infection. Bioinformatics and phylogenetic analysis have shown that rice has two PSYRs and eight PSY-family peptides (*8*). Pathogens invading tissues cause damage to host cells, which leads to the induction of stress/defense responses within cells adjacent to the damaged sites where extracellular PSY concentration is decreased. RaxX would possibly facilitate the invasion of a pathogen by hijacking the host PSY signaling pathway and suppressing the induction of the PSYR-mediated defensive stress response activated in cells peripheral to the invaded, metabolically impaired regions in the host.

REFERENCES AND NOTES

1. S. H. Shiu, A. B. Bleecker, *Proc. Natl. Acad. Sci. U.S.A.* **98**, 10763–10768 (2001).
2. J. Man, J. P. Gallagher, M. Bartlett, *New Phytol.* **226**, 1492–1505 (2020).
3. L. Xi, X. N. Wu, M. Gilbert, W. X. Schulze, *Front. Plant Sci.* **10**, 472 (2019).
4. V. Olsson *et al.*, *Annu. Rev. Plant Biol.* **70**, 153–186 (2019).
5. Y. Matsubayashi, *Annu. Rev. Plant Biol.* **65**, 385–413 (2014).
6. K. Ohyama, M. Ogawa, Y. Matsubayashi, *Plant J.* **55**, 152–160 (2008).
7. Y. Amano, H. Tsubouchi, H. Shinohara, M. Ogawa, Y. Matsubayashi, *Proc. Natl. Acad. Sci. U.S.A.* **104**, 18333–18338 (2007).
8. R. N. Pruitt *et al.*, *New Phytol.* **215**, 725–736 (2017).
9. J. De Giorgi *et al.*, *Dev. Cell* **56**, 3066–3081.e5 (2021).
10. A. T. Fuglsang *et al.*, *Plant J.* **80**, 951–964 (2014).
11. R. N. Pruitt *et al.*, *Sci. Adv.* **1**, e1500245 (2015).
12. D. D. Luu *et al.*, *Proc. Natl. Acad. Sci. U.S.A.* **116**, 8525–8534 (2019).
13. P. Ronald, A. Joe, *Ann. Bot. (Lond.)* **121**, 17–23 (2018).
14. A. S. Tost, A. Kristensen, L. I. Olsen, K. B. Axelsen, A. T. Fuglsang, *Genes* **12**, 218 (2021).
15. H. Shinohara, A. Mori, N. Yasue, K. Sumida, Y. Matsubayashi, *Proc. Natl. Acad. Sci. U.S.A.* **113**, 3897–3902 (2016).
16. K. Mahmood, R. Kannangara, K. Jørgensen, A. T. Fuglsang, *BMC Genomics* **15**, 441 (2014).
17. T. Hruz *et al.*, *Adv. Bioinforma.* **2008**, 420747 (2008).
18. R. Komori, Y. Amano, M. Ogawa-Ohnishi, Y. Matsubayashi, *Proc. Natl. Acad. Sci. U.S.A.* **106**, 15067–15072 (2009).
19. Y. Matsuzaki, M. Ogawa-Ohnishi, A. Mori, Y. Matsubayashi, *Science* **329**, 1065–1067 (2010).
20. C. Kaufmann, N. Stührwohldt, M. Sauter, *J. Exp. Bot.* **72**, 5508–5521 (2021).
21. Y. Matsubayashi, Y. Sakagami, *Proc. Natl. Acad. Sci. U.S.A.* **93**, 7623–7627 (1996).
22. V. G. Doblas *et al.*, *Science* **355**, 280–284 (2017).
23. T. Nakayama *et al.*, *Science* **355**, 284–286 (2017).
24. Y. Ou *et al.*, *Plant Physiol.* **189**, 165–177 (2022).
25. Z. Xie, T. M. Nolan, H. Jiang, Y. Yin, *Front. Plant Sci.* **10**, 228 (2019).
26. U. J. Phukan, G. S. Jeena, R. K. Shukla, *Front. Plant Sci.* **7**, 760 (2016).
27. C. Lata, M. Prasad, *J. Exp. Bot.* **62**, 4731–4748 (2011).
28. K. Kazan, J. M. Manners, *Mol. Plant* **6**, 686–703 (2013).
29. H. Zhang, Y. Zhao, J. K. Zhu, *Dev. Cell* **55**, 529–543 (2020).
30. M. Kasuga, Q. Liu, S. Miura, K. Yamaguchi-Shinozaki, K. Shinozaki, *Nat. Biotechnol.* **17**, 287–291 (1999).
31. H. Zhang, J. Zhu, Z. Gong, J. K. Zhu, *Nat. Rev. Genet.* **23**, 104–119 (2022).

ACKNOWLEDGMENTS

We thank M. Nomoto and Y. Tada at Nagoya University for technical advice for *Pst* DC3000 treatment. **Funding:** This work was funded by the following: Japan Society for the Promotion of Science (JSPS) Grant-in-Aid for Scientific Research (S) JP18H05274 (to Y.M.); JSPS Grant-in-Aid for Transformative Research Areas JP20H05907 (to Y.M.); and JSPS Grant-in-Aid for Research Activity Start-up JP21K20653 (to M.O.-O.). **Author contributions:** Conceptualization: Y.M. Investigation: M.O.-O., T.Y., M.K., T.Na., Y.O., Y.H., Y.Y., T.No., S.N., H.S., and Y.M. Funding acquisition: M.O.-O. and Y.M. Project administration: Y.M. Supervision: M.O.-O. and Y.M. Writing: M.O.-O. and Y.M. **Competing interests:** Authors declare that they have no competing interests. **Data and materials availability:** All data are available in the main text or the supplementary materials. The RNA-seq data have been deposited in the NCBI Gene Expression Omnibus (GEO) under accession number GSE208340. The raw mass spectrometry data have been deposited in the ProteomeXchange Consortium via PRIDE partner repository under accession number PXD035421.

SUPPLEMENTARY MATERIALS

science.org/doi/10.1126/science.abq5735
Materials and Methods
Figs. S1 to S9
Table S1 and S2
References (*32*–*39*)
MDAR Reproducibility Checklist
Data S1 to S10

Submitted 17 April 2022; accepted 14 September 2022
10.1126/science.abq5735

FUEL CELLS

Covalent organic framework–based porous ionomers for high-performance fuel cells

Qingnuan Zhang[1], Shuda Dong[1], Pengpeng Shao[1], Yuhao Zhu[1], Zhenjie Mu[1], Dafei Sheng[1], Teng Zhang[1], Xin Jiang[2], Ruiwen Shao[3], Zhixin Ren[1], Jing Xie[1], Xiao Feng[1]*, Bo Wang[1]*

Lowering platinum (Pt) loadings without sacrificing power density and durability in fuel cells is highly desired yet challenging because of the high mass transport resistance near the catalyst surfaces. We tailored the three-phase microenvironment by optimizing the ionomer by incorporating ionic covalent organic framework (COF) nanosheets into Nafion. The mesoporous apertures of 2.8 to 4.1 nanometers and appendant sulfonate groups enabled the proton transfer and promoted oxygen permeation. The mass activity of Pt and the peak power density of the fuel cell with Pt/Vulcan (0.07 mg of Pt per square centimeter in the cathode) both reached 1.6 times those values without the COF. This strategy was applied to catalyst layers with various Pt loadings and different commercial catalysts.

The oxygen reduction reaction (ORR) at the cathode in commercial proton-exchange membrane fuel cells (PEMFCs) is catalyzed by precious metals, which are usually platinum (Pt)–based materials. Reducing the Pt loading of PEMFCs while maintaining high power density and durability is still challenging (*1*–*3*). Although new catalysts have been prepared through alloying and nanostructuring strategies (*4*), their performance is often evaluated by the rotating disk electrode (RDE) technique and is hard to translate into a membrane electrode. In a catalyst layer (CL) of the membrane electrode assembly (MEA), the ORR happens at oxygen-water-catalyst three-phase interfaces. To react, oxygen must pass across a few-nanometer-sized ionomer component and encounters substantial mass transport resistance. Thus, optimizing the three-phase microenvironment becomes crucial to maximize the activity of the catalyst in PEMFCs.

Ionomers, which are the proton-conducting link between the proton-exchange membrane and Pt catalyst sites for the proton current flow, dominate the three-phase microenvironment in PEMFCs. Currently, perfluorosulfonic acid polymer (PFSA, or Nafion) is the most widely used ionomer (*5*, *6*). However, PFSA is inevitably tightly coated on the catalyst, which causes high gas diffusion resistance (*7*). The diffusion resistance from the ionomer and water accounts for 80% of total gas resistance, and the remainder mainly originates from secondary pores, which refer to the pores >20 nm that exist between aggregates of agglomerates (*7*). Moreover, the $-SO_3H$ groups in Nafion can strongly adsorb and occupy active sites on the Pt surface, which can decrease the Pt activity and thus reduce corresponding mass activity (MA) and power density (*8*, *9*).

Several approaches have been used to solve these problems. Efforts have been devoted to optimizing the ionomers or carbon supports. Embedding Pt in the channel of the carbon support could avoid direct interaction between Pt and the ionomer (*9*, *10*). The carbon supports can be tuned to adjust the ionomer coverage on their surface (*11*). Altering the side chain of the ionomers (*12*–*15*) can reduce the $-SO_3H$ inhibition effect. The incorporation of additives such as hydrophobic polytetrafluoroethylene (*16*, *17*) or pore-forming materials (*18*–*20*) can improve mass transfer. Nevertheless, it remains a substantial challenge to optimize gas diffusion without sacrificing proton conductivity in the CL to achieve highly efficient fuel

[1]Beijing Key Laboratory of Photoelectronic/Electrophotonic Conversion Materials, Key Laboratory of Cluster Science, Ministry of Education, Frontiers Science Center for High Energy Material, Advanced Technology Research Institute (Jinan), School of Chemistry and Chemical Engineering, Beijing Institute of Technology, Beijing 100081, P. R. China. [2]Orthopaedics Department, China-Japan Friendship Hospital, Beijing 100081, P. R. China. [3]Beijing Advanced Innovation Center for Intelligent Robots and Systems, School of Medical Technology, Beijing Institute of Technology, Beijing 100081, P. R. China.
*Corresponding author. Email: bowang@bit.edu.cn (B.W.); fengxiao86@bit.edu.cn (X.F.)

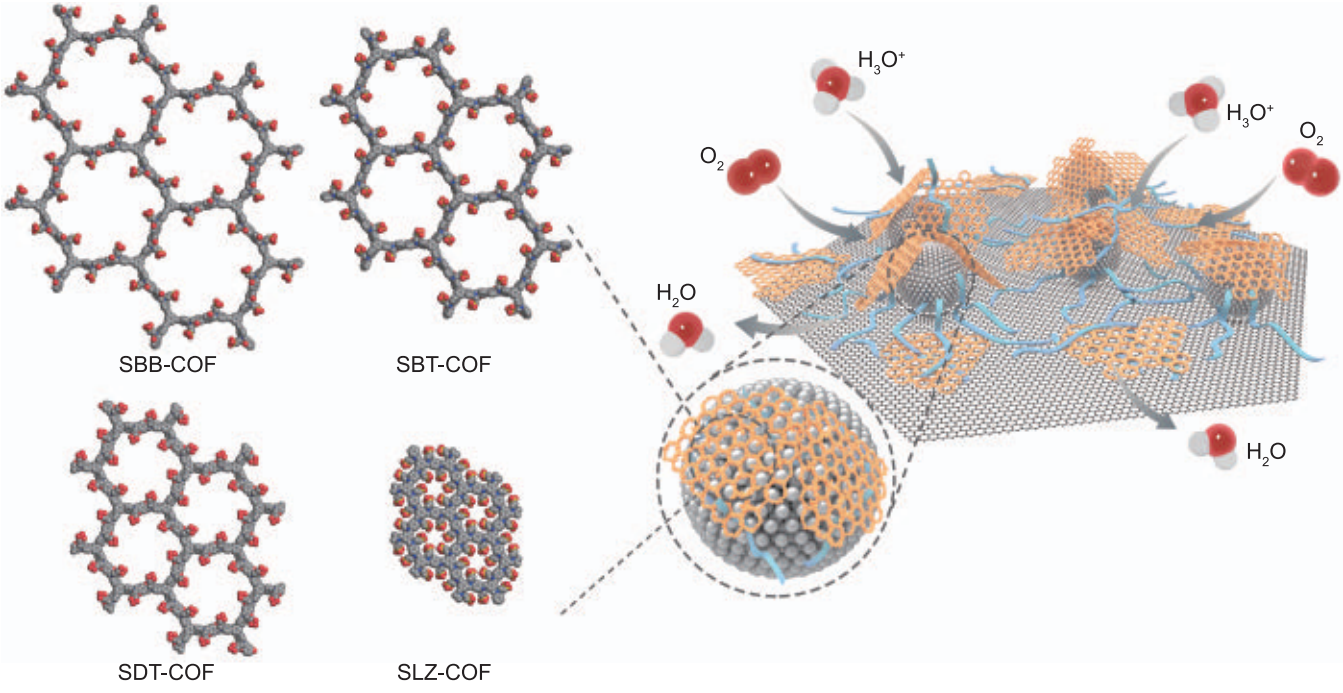

Fig. 1. Overview of Pt/C@COF-Nafion. Schematic illustration of the gas and proton transfer in Pt/C@COF-Nafion. Structure models of SLZ-COF, SDT-COF, SBT-COF, and SBB-COF with aperture sizes of 1.2, 2.8, 3.6, and 4.1 nm, respectively, are shown. Red, O; blue, N; gray, C; and yellow, S. Hydrogen is omitted for clarity.

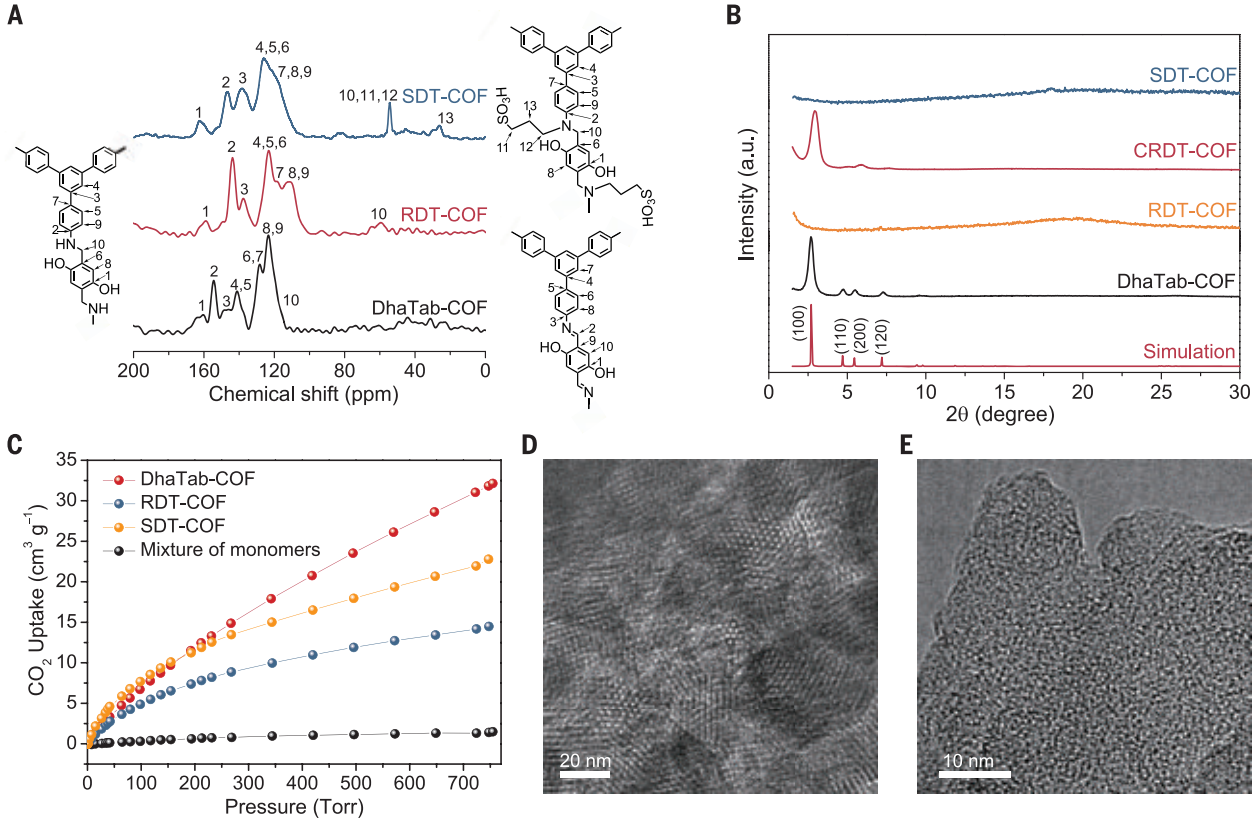

Fig. 2. Structural characterizations of SDT-COF. (**A**) ^{13}C ssNMR spectra of SDT-COF, RDT-COF, and DhaTab-COF. (**B**) Experimental PXRD patterns of SDT-COF, CRDT-COF, RDT-COF, and DhaTab-COF and the simulated PXRD pattern of DhaTab-COF (AA stacking). (**C**) CO_2 sorption isotherm profiles of DhaTab-COF, RDT-COF, SDT-COF, and the mixture of monomers. (**D** and **E**) HR-TEM images of (D) DhaTab-COF and (E) SDT-COF.

cells with low Pt loading. Covalent organic frameworks (COFs), which are an emerging class of crystalline porous polymers that are constructed by topological linking organic building units, show notable potential in mass transfer given their atomically pre-designable structure, high surface area, and ease of precise modification (*21*–*23*). They have been proposed as proton-exchange membranes in the forms of pressed pellets or assembled membranes (*24*, *25*) for the PEMFCs. However, their mechanical performances, as well as the H_2 crossover risk from anode to cathode in the fuel cell, present obstacles for their practical application.

Here, we fabricated high-performance fuel cells with commercial Pt/C (Pt/Vulcan) by incorporating a sulfonic acid functionalized DhaTab-COF (SDT-COF) into Nafion as a composite ionomer (the corresponding CL is denoted as Pt/C@SDT-Nafion) (Fig. 1). The SDT-COF has inherent hexagonal nanopores partitioned by molecular building units, which impart the CL with improved gas transport capability. The $-SO_3H$ group linking to the pore walls ensures the rapid proton conduction within the channels, whereas Nafion helps reduce interface impedance between the COF nanosheets. The rigidity and high porosity of SDT-COF also help weaken adsorption of the $-SO_3H$ group on Pt. The particular properties of this COF were demonstrated by performing control experiments with other COFs with different pore sizes (Fig. 1) as well as other rigid sulfonated materials. The addition of COFs with mesoporous apertures in the CL promoted ORR at the three-phase interface and improved Pt use to realize high power density for PEMFCs with low Pt loading.

Synthesis and characterizations of SDT-COF

We synthesized DhaTab-COF from its monomers, 2,5-dihydroxyterephthalaldehyde (Dha) and 1,3,5-tris(4-aminophenyl)benzene (Tab), which are linked by imine bonds. This crystalline COF has periodic and unidirectional columnar arrays of 3.4-nm hexagonal channels. Further reduction of its imine linkages to secondary amine linkages afforded reduced DhaTab-COF (RDT-COF) (figs. S1 to S3) to ensure its acid stability for fuel cell application (*26*–*28*). We then obtained SDT-COF by grafting propanesulfonic acid sodium salt to the pore walls of RDT-COF, followed by acidification. Their chemical compositions and structures were confirmed with the elemental analyses (supplementary materials), Fourier-transform infrared (FTIR) spectra (fig. S4 and table S1), the ^{13}C cross-polarization magic-angle spinning (CP-MAS) solid-state nuclear magnetic resonance (ssNMR) spectra (Fig. 2A), x-ray photoelectron spectroscopy (XPS) (figs. S5 and S6), powder x-ray diffractions (PXRDs) (Fig. 2B), and N_2 sorption isotherms (fig. S7).

Compared with DhaTab-COF, the crystallinity and the Brunauer-Emmett-Teller (BET) surface area of RDT-COF were greatly reduced, which we attributed to the conformational flexibility of the secondary amine linkages (fig. S2) (*29*). The retention of the extended framework linked by covalent bonding of RDT-COF was further confirmed by successfully converting it to crystalline and porous cyclic carbamate–linked COF (CRDT-COF) (Fig. 2B and figs. S8 to S10) (*29*). In the high-resolution transmission electron microscopy (HR-TEM) images, ordered mesopores and disordered pores can be observed in the DhaTab-COF and SDT-COF, respectively (Fig. 2, D and E). The RDT-COF and SDT-COF both showed CO_2 uptake ability (273 K) (Fig. 2C), whereas the physical mixture of the monomers did not show apparent adsorption. These results demonstrated that the polymeric layers of RDT-COF and SDT-COF can still create nanosized apertures that allow gas permeation. The grafting fraction of sulfonic acid groups based on the elemental

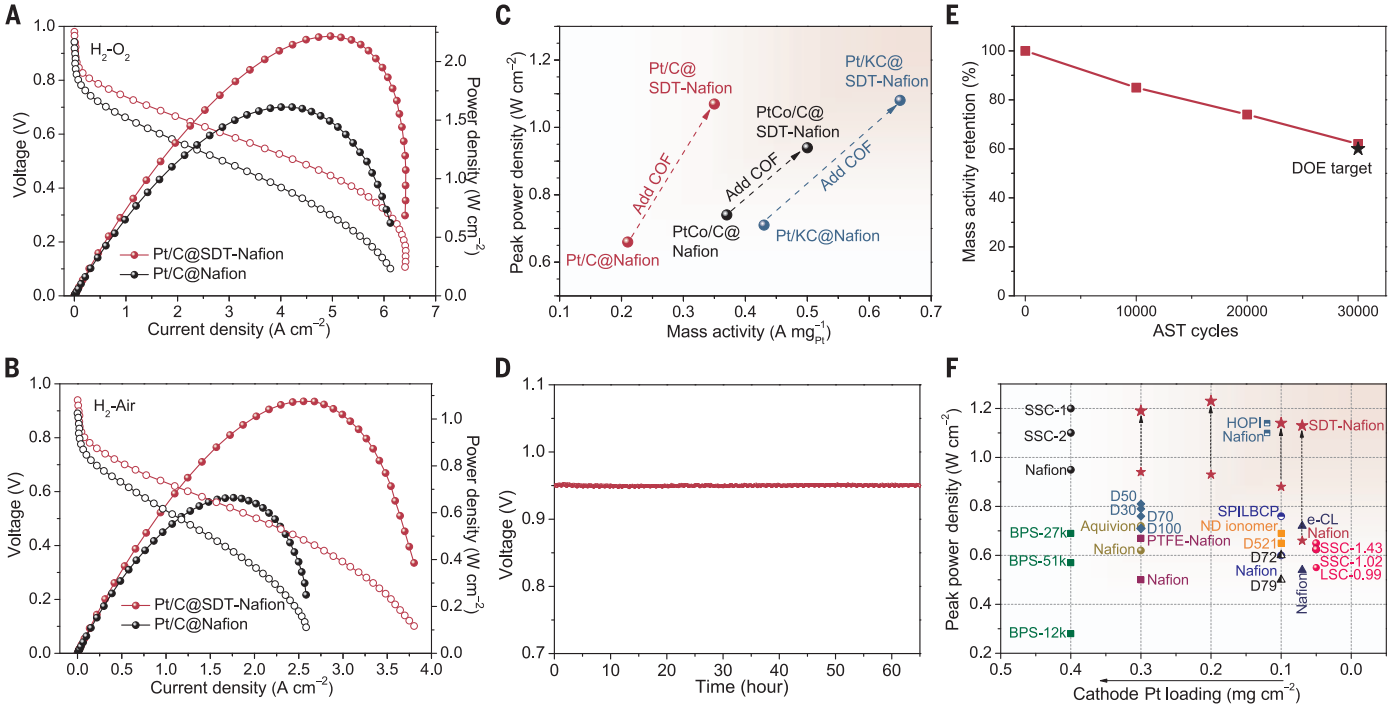

Fig. 3. Fuel cell performance and durability. (**A**) H_2-O_2 and (**B**) H_2-air fuel cell *I-V* polarization (without *iR* compensation; *i*, current; *R*, resistance) and power density plots of the cells with Pt/C@Nafion and Pt/C@SDT-Nafion measured at 80°C and 100% RH under 150 kPa abs. (**C**) Comparison of the MAs and peak power densities of MEAs evaluated under H_2-air conditions. (**D**) OCV test of the MEA with Pt/C@SDT-Nafion at 90°C lasted 65 hours. (**E**) Attenuation of the MA of Pt/C@SDT-Nafion in the AST with 30,000 cycles. (**F**) Comparing the cathode Pt loading and peak power density for MEAs based on commercial Pt/C catalyst in this study and previous reports (table S3). Smaller red stars indicate Pt/C@Nafion data; larger red stars are the Pt/C@SDT-Nafion data. BPS, sulfonated poly(arylene ether sulfone); HOPI, high oxygen permeability ionomer; ND, nanodispersion PFSA; PTFE, polytetrafluoroethylene; SPILBCP, sulfonated poly(ionic liquid) block copolymer; SSC, short-side-chain PFSA.

analysis was 60%. Thermogravimetric analysis (TGA) showed that the decomposition temperature of SDT-COF was 200°C (fig. S11).

After grafting, the SDT-COF could be dispersed in water and exhibited a Tyndall effect (fig. S12). The atomic force microscope also showed that SDT-COF adopted a nanosheet morphology with an average thickness of ~0.8 nm (fig. S13). The ion exchange capacity (IEC) of SDT-COF is 1.85 mequiv g^{-1} as calculated by means of elemental analysis and 1.70 mequiv g^{-1} as calculated by titrating with NaOH solution to a phenolphthalein end point, which is greater than that of the commercial Nafion DE2020 ionomer (1.03 to 1.12 mequiv g^{-1}). The temperature dependence of the proton conductivity was measured at 100% relative humidity (RH) (figs. S14 to S16), and the conductivity of the pressed SDT-COF tablet was 95.3 mS cm^{-1}. The proton transport property of Nafion DE2020 and SDT-COF/Nafion (ratio 1:1) thin films was also investigated by using gold interdigitated electrodes, and the result showed that the proton conductivities were increased slightly after adding SDT-COF (fig S17).

Fuel cell performance and durability

For PEMFC measurements, the ratio of total ionomer to carbon (I/C) was set at 0.8 (*30*). We then optimized the component proportions of SDT-COF and Nafion in the ionomer by using H_2–O_2 single-cell tests (5.0 cm^2 MEAs). Among the CLs that have been evaluated (fig. S18), including pure Pt/C, Pt/C@Nafion, Pt/C@SDT, and Pt/C@SDT-Nafion (mass ratio of SDT-COF and Nafion = 1:2, 1:1, or 2:1), Pt/C@SDT-Nafion (mass ratio = 1:1) had the largest current density and power density. After optimization, the Pt loadings were fixed at 0.07 and 0.05 mg_{Pt} cm^{-2} in the cathode and anode CLs, respectively.

The current-voltage (*I-V*) polarization and power density distributions of Pt/C@Nafion and Pt/C@SDT-Nafion fuel cells are shown in Fig. 3A, measured under 150 kPa absolute pressure (abs) (50 kPa back pressure) fully humidified O_2. The peak power density of Pt/C@SDT-Nafion fuel cell achieved 2.21 W cm^{-2}, which was 1.4 times of the controlled MEA without SDT-COF. Pt/C@SDT-Nafion exhibited an MA of 0.35 A mg_{Pt}^{-1} in the H_2-O_2 test versus 0.21 A mg_{Pt}^{-1} for Pt/C@Nafion (Fig. 3C). The electrochemical active surface area (*31*) of Pt/C@SDT-Nafion (67.4 m^2 g_{Pt}^{-1}) was also higher than that of the Pt/C@Nafion (41.4 m^2 g_{Pt}^{-1}) (fig. S19 and table S2). A similar trend was observed under the H_2-air condition. Under the 150 kPa abs fully humidified air condition, the PEMFC with Pt/C@SDT-Nafion reached a peak power density of 1.08 W cm^{-2}, which was 1.6 times of the Nafion-based MEA. At 0.7 V, the power density was 2.4 times greater than the value without SDT-COF (Fig. 3B). The peak power density and limiting current densities reported here exceed those reported for other low Pt-loading cathodes (≤0.1 mg_{Pt} cm^{-2}) obtained with commercial Pt/C (Fig. 3F and table S3). These results showed that the SDT-COF in the CL enabled the exposure of more active sites of Pt.

The accelerated stress tests (ASTs) were conducted according to the US Department of Energy (DOE) catalyst stability evaluation protocols (figs. S20 to S22). After 30,000 cycles, the MA decreased by 38%, which meets the requirement of the DOE 2025 technical target of 40% (Fig. 3E) (*32*). The open circuit voltage (OCV) was maintained at 90°C for 65 hours, which also shows the electrochemical stability of SDT-COF (Fig. 3D). Because peroxide byproduct is the main source of the attack on the CL (*3*), the chemical stability of SDT-COF was further proved by soaking it in 1% hydrogen peroxide for 5 hours; no degradation was observed, as evidenced by the IR spectra (fig. S23).

In addition, to meet different MEA requirements for various practical fuel cell stacks,

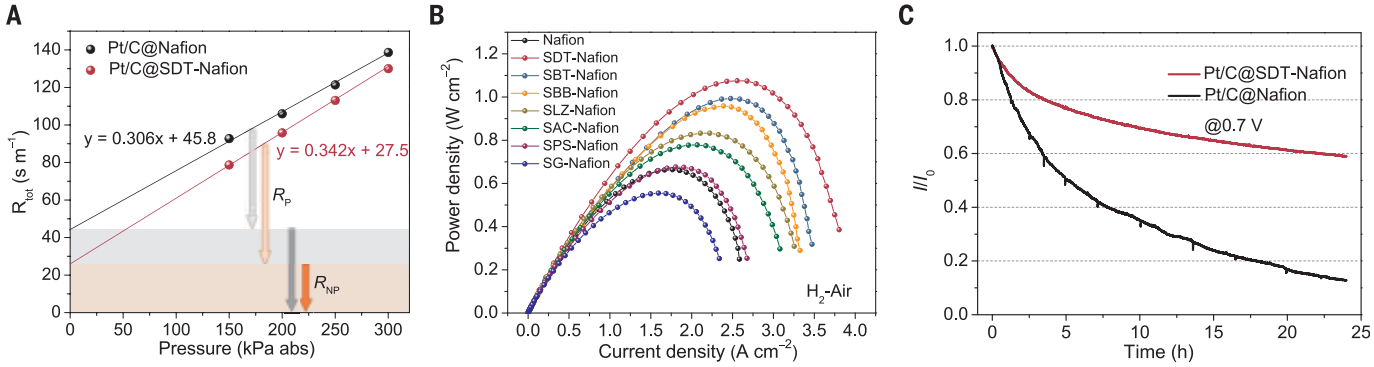

Fig. 4. Mass transport. (**A**) R_{tot} of Pt/C@Nafion and Pt/C@SDT-Nafion plotted versus the absolute pressure. (**B**) Comparison of the power density of MEAs with different ionomers in CLs under H_2-air condition. (**C**) Twenty-four–hour continuous working tests for Pt/C@SDT-Nafion and Pt/C@Nafion without water management.

we tested the MEA performance with cathode to anode loadings of 0.1/0.1 mg_{Pt} cm^{-2}, 0.2/0.2 mg_{Pt} cm^{-2}, and 0.3/0.3 mg_{Pt} cm^{-2}, respectively (figs. S24 to S28). The power densities were all improved after the addition of SDT-COF, irrespective of the Pt loadings (Fig. 3F). To further demonstrate the applicability of this strategy, we evaluated the PEMFC performance by using commercial PtCo/C and Pt/Ketjenblack (Pt/KB) catalysts with the addition of SDT-COF/Nafion composite ionomer (Fig. 3C and figs. S29 to S31). The parameter improvements of the PEMFC performance by using our porous ionomer design strategy are summarized in table S2. The MA of PtCo/C and Pt/KB catalysts in MEA with SDT-COF reached 0.50 A mg_{Pt}^{-1} and 0.65 A mg_{Pt}^{-1}, respectively, which surpassed the DOE 2025 technical target (0.44 A mg_{Pt}^{-1}).

Mechanism discussions

The ORR performance in the CL depends on the O_2 transfer resistance, proton accessibility, and RH. The mass transfer resistance of O_2 in the H_2-air cell is calculated based on the limiting current density (fig. S32). (*17*, *33*). The apparent value obtained is the total mass transport resistance (R_{tot}), which includes pressure-dependent resistance (R_P) and pressure-independent resistance (R_{NP}). Flow field channels and the gas diffusion layer govern the R_P, whereas the Knudsen mass transport and the resistance derived from the Pt-ionomer-water interface dominate the mass transport resistance of R_{NP} (*10*). The slope and intercept in Fig. 4A indicate the O_2 diffusion resistances R_P and R_{NP}, respectively. The R_{NP} were 45.8 and 27.5 s m^{-1} for the Pt/C@Nafion and Pt/C@SDT-Nafion, respectively, which reflects the positive effect of SDT-COF on gas diffusion.

Electrochemical impedance spectroscopy (EIS) can also be used assess the individual contributions of the transport and kinetic processes to the PEMFCs (figs. S33 and S34). The EIS data were fitted to a modified Randles cell equivalent circuit model (table S4) to monitor the ohmic resistance (R_{ohm}), polarization resistances (Z_{ct}, Z_{ox}, Z_{mass}), and capacitances (C_1, CPE1, and CPE2) (*34*). The total mass transfer resistance of O_2 was reduced after adding SDT-COF for both the H_2–O_2 cell (from 0.027 to 0.0068 ohms) and the H_2-air cell (from 0.055 to 0.032 ohms).

To further investigate the relation between COF structure and CL performance, we prepared COFs with the same topology but different aperture sizes, which included sulfonated LZU-1 (SLZ-COF), sulfonated DbdTab-COF (SBT-COF), and sulfonated DbdBtt-COF (SBB-COF) with aperture sizes of 1.2, 3.6, and 4.1 nm, respectively (Fig. 1 and figs. S35 to S44). Furthermore, sulfonated graphene (SG) (nonporous), sulfonated activated carbon (SAC) (pore size: 0.9 nm), and sulfonated polystyrene spheres (SPSs) (nonporous) were also used as the controls. SPSs and SG both increased the heterogeneity of the interface yet did not improve MEA performance (Fig. 4B and figs. S45 to S48). Even for the sulfonated porous structure with micropores such as SAC and SLZ-COF, only slight performance improvements were observed.

By contrast, SDT-COF, SBT-COF, and SBB-COF with aperture sizes of 2.8, 3.6, and 4.1 nm, respectively, could boost the power density of the fuel cells (Fig. 4B and figs. S49 to S52), which indicates that the intrinsic mesopores of the frameworks were critical for promoting oxygen permeation. We also measured O_2 gas transport with additive-Nafion mixed membranes, in which the ratio of additive/Nafion was set as 2:8 to ensure the compactness and integrity of the resultant membrane. Oxygen permeability was directly related to the pore structure of these additives (figs. S53 to S56 and table S5). In addition, we tested the O_2 permeability of Nafion membrane and SDT-COF–Nafion membrane under 100% RH. The O_2 permeability of SDT-COF/Nafion (2:8) under the humid condition had a permeability of 36 Barrer, whereas that of Nafion decreased to 0 Barrer.

To further exclude the influence of secondary large pores (fig. S57) on the cell performance, we measured gas sorption isotherms and deduced the corresponding pore size distributions of the Pt/C@additive-Nafion (fig. S58). The results showed that only the addition of COF led to the exposure of the mesopores in the Pt/C, revealing that the gas molecules could reach the catalyst through the apertures in the COF framework. The interface heterogeneity induced by other rigid-structured nanomaterials (SG and SPSs) could not improve gas permeation to the catalyst surface, whereas Nafion blocked the mesopores of Pt/C. These results showed that only the COF-Nafion membrane allowed relatively rapid gas permeation, whereas the Nafion membranes with nonporous additives did not boost the permeation of gas molecules. As for PEMFCs, both proton conductivity and O_2 gas transport ability together affect cell performance. Because the proton conductivity did not markedly increase after adding SDT-COF, the O_2 gas transport ability dominated the performance.

The dry proton accessibility to the Pt sites increased from 0.61 to 0.76 after adding SDT-COF (fig. S59) (*9*). We then performed 24-hour continuous H_2-air fuel cell tests under 0.7 V constant voltage without scheduled refreshing (Fig. 4C and fig. S60). The currents dropped 41 and 87% for Pt/C@SDT-Nafion and Pt/C@Nafion, respectively, which indicates that the porous ionomer improved resistance to flooding. We measured the static and dynamic water vapor sorptions (figs. S61 to S63). Compared with Nafion, the water desorption of SDT-COF exhibited obvious hysteresis phenomena. We also conducted the fuel cell measurements under 30% RH and 60% RH conditions. Along with reducing RH, the decreasing degree of the cell performance was reduced after adding SDT-COF (fig. S64). Thus, SDT-COF facilitated the mass transfer with or without accumulated water.

The RDE measurement could reveal the inhibitory effect of ionomer on a Pt surface and the mass transfer resistance between the Pt particles and ionomer. As shown in the linear sweep voltammetry (LSV) curves (Fig. 5A), the

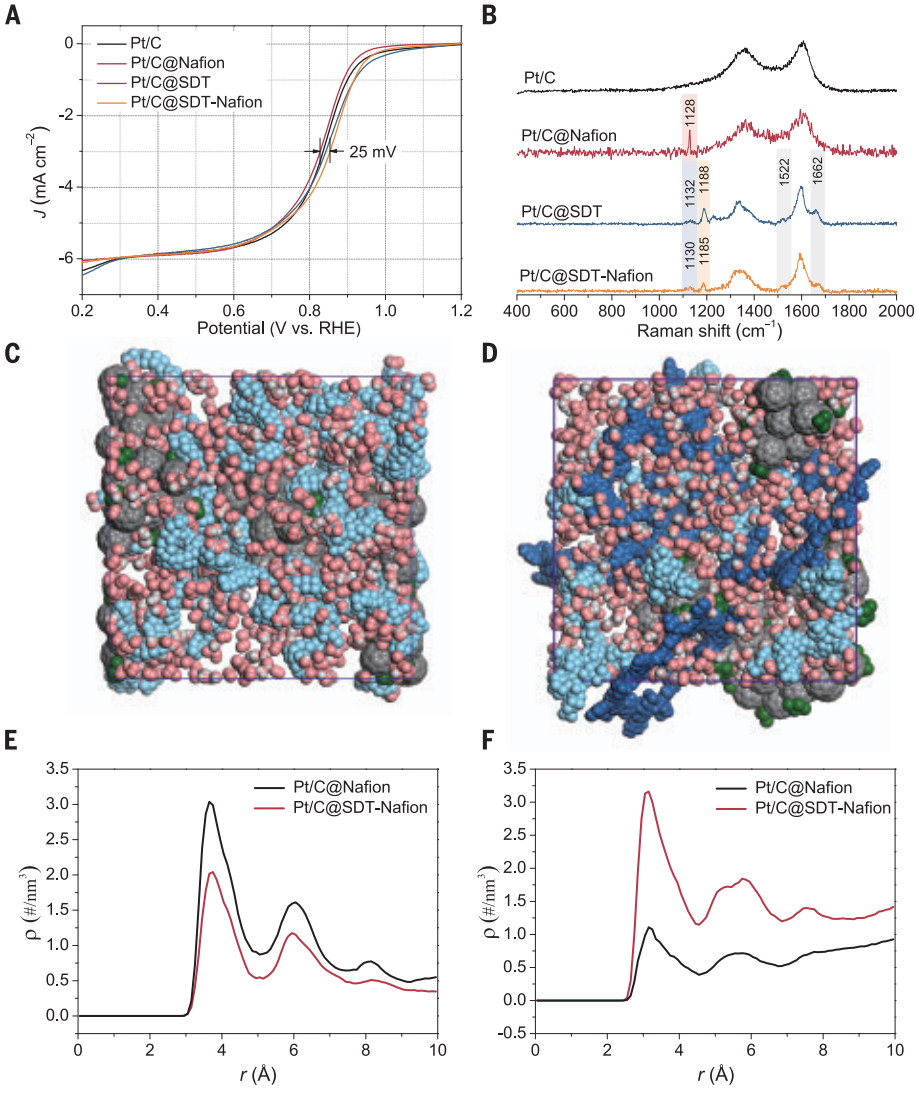

Fig. 5. Poisoning effect. (**A**) LSV and (**B**) Raman spectra of Pt/C catalysts with different ionomers. RHE, reversible hydrogen electrode. (**C** and **D**) Molecular models of the multicomponent CL with Nafion (C) and the combination of SDT-COF and Nafion (D). Light blue, Nafion; dark blue, SDT-COF; green, Pt; pink, O; white, H; gray, C. (**E** and **F**) Comparison of the atom density profiles of (E) Pt–S and (F) Pt–O (O from O_2).

halfwave potential increased in the order of Pt/C@Nafion < Pt/C ≤ Pt/C@SDT < Pt/C@SDT-Nafion. This result suggested that SDT-COF could weaken the Nafion inhibition. The XPS analysis showed that $-SO_3H$ groups did not change the valence state of Pt but could strongly adsorb onto Pt and occupy the active sites (figs. S65 and S66). In the Raman spectrum of Pt/C@Nafion, the peak at 1128 cm^{-1} was caused by the adsorption of sulfonic acid groups on the surface of Pt atoms [δ(Pt-SO_3)] (*9*, *35*). In comparison, the peak assigned to δ(Pt-SO_3) was greatly weakened for Pt/C@SDT-Nafion (Fig. 5B and figs. S67 and S68). The rigid framework structure of SDT-COF helped decrease the interaction of flexible sulfonic acid groups to Pt, which was beneficial to improving the MA of the catalysts. The peaks at 1132 and 1188 cm^{-1} represented the stretching vibration of the sulfonic acid group, and both peaks had a slight red shift when SDT-COF was mixed with Nafion. The Raman spectra of physically mixed pure Pt nanoparticles with SDT-COF (fig. S69) also showed that the sulfonic acid groups located in the pores of the rigid COF framework could avoid direct contact with the Pt particles.

We performed TEM, energy dispersive x-ray spectroscopy (EDS) mapping (figs. S70 to S73), and three-dimensional TEM (movies S1 and S2) and found uniform wrapping of SDT-COF and Nafion on the surface of the Pt/C catalyst. Molecular dynamics simulations were further performed. The structures of Pt/C@Nafion and Pt/C@SDT-Nafion were built in a simplified model (Fig. 5, C and D; fig. S74; and table S6). We calculated the radial density distributions for $-SO_3H$ coordinating to Pt [$\rho_{Pt-S}(r)$] (Fig. 5E), and we compared the intensity of the first peak. The atom density profile of Pt–S decreased 0.6-fold after adding SDT-COF, which we attribute to the steric hindrance of SDT-COF. The height of the first peak of $\rho_{Pt-O}(r)$ increased 2.7-fold after the addition of SDT-COF (Fig. 5F), which revealed that more O_2 molecules can interact with the Pt catalyst. The simulation snapshots (figs. S75 and S76) showed that the ionomer chains took the chance to penetrate into mesopore apertures and interacted with the pore skeleton through hydrogen bond and van der Waals force, yet there remained apertures for water and oxygen molecules to pass through.

Conclusions

By introducing COFs, the MA, durability, and rate powder density can surpass and/or approach the DOE target (table S2) with unmodified commercial Pt/C, PtCo/C, or Pt/KB catalysts under low Pt loadings (0.07 mg_{Pt} cm^{-2}). The DOE 2025 target is to reduce the Pt group metal total content to 0.1 g kW^{-1} from the current level of 0.79 g kW^{-1} (at 0.7 V). After using SDT-COF, the MEA with those commercial catalysts (0.32 g kW^{-1} at 0.7 V and 0.16 g kW^{-1} at 0.6 V) could approach this requirement. Moreover, the cost deduced from the whole CL is calculated to be $19.5 per kilowatt, which can further reduce the cost of the conventional CL (~$29 per kilowatt) by one-third. This strategy, together with the development of advanced catalysts, leads to efficient clean-energy storage opportunities. In addition, we used polystyrene sulfonic acid (PSA) to replace Nafion in the catalytic layer, and without further optimization, the performance of MEA by using the PSA-COF ionomer rivals the performance of pure Nafion (fig. S77). For the ionomer design principles, we introduced rigid network nanosheets with mesoporous apertures into the linear ionomer without sacrificing the proton conductivity. The thermal stability and structural designability of ionic COFs also make them promising in high-temperature fuel cells and alkaline fuel cells.

REFERENCES AND NOTES

1. L. Chong *et al.*, *Science* **362**, 1276–1281 (2018).
2. X. X. Wang, M. T. Swihart, G. Wu, *Nat. Catal.* **2**, 578–589 (2019).
3. C. Y. Ahn *et al.*, *Chem. Rev.* **121**, 15075–15140 (2021).
4. X. Tian *et al.*, *Science* **366**, 850–856 (2019).
5. A. Kusoglu, A. Z. Weber, *Chem. Rev.* **117**, 987–1104 (2017).
6. S. H. Kwon *et al.*, *Sci. Rep.* **11**, 8702 (2021).
7. S. Salari, M. Tam, C. McCague, J. Stumper, M. Bahrami, *J. Power Sources* **449**, 227479 (2020).
8. K. Shinozaki, Y. Morimoto, B. S. Pivovar, S. S. Kocha, *J. Power Sources* **325**, 745–751 (2016).
9. S. Ott *et al.*, *Nat. Mater.* **19**, 77–85 (2020).
10. Y. C. Park, H. Tokiwa, K. Kakinuma, M. Watanabe, M. Uchida, *J. Power Sources* **315**, 179–191 (2016).
11. V. Yarlagadda *et al.*, *ACS Energy Lett.* **3**, 618–621 (2018).
12. K. Kodama *et al.*, *ACS Catal.* **8**, 694–700 (2018).

13. K. Talukdar, P. Gazdzicki, K. A. Friedrich, *J. Power Sources* **439**, 227078 (2019).
14. S. So, H. Kang, D. Choi, K. H. Oh, *Int. J. Hydrogen Energy* **45**, 19891–19899 (2020).
15. H. Ren *et al*., *J. Power Sources* **506**, 230186 (2021).
16. S. Wang *et al*., *J. Power Sources* **379**, 338–343 (2018).
17. Z. Q. Tian, X. L. Wang, H. M. Zhang, B. L. Yi, S. P. Jiang, *Electrochem. Commun.* **8**, 1158–1162 (2006).
18. A. Fischer, J. Jindra, H. Wendt, *J. Appl. Electrochem.* **28**, 277–282 (1998).
19. K. Gu *et al*., *Mater. Today Energy* **19**, 100560 (2021).
20. E. Şengül, S. Erkan, I. Eroglu, N. Bac, *Chem. Eng. Commun.* **196**, 161–170 (2009).
21. S. Zhao *et al*., *Nat. Mater.* **20**, 1551–1558 (2021).
22. C. S. Diercks, O. M. Yaghi, *Science* **355**, eaal1585 (2017).
23. J. Li, S. Zhao, B. Wang, X. Feng, *Sci. China Chem.* **65**, 836–839 (2022).
24. Y. Yang *et al*., *Angew. Chem. Int. Ed.* **59**, 3678–3684 (2020).
25. L. Cao *et al*., *Adv. Mater.* **32**, e2005565 (2020).
26. S. Kandambeth *et al*., *Nat. Commun.* **6**, 6786 (2015).
27. X. Huang, C. Sun, X. Feng, *Sci. China Chem.* **63**, 1367–1390 (2020).
28. H. Liu *et al*., *Chem* **4**, 1696–1709 (2018).
29. S. J. Lyle *et al*., *J. Am. Chem. Soc.* **141**, 11253–11258 (2019).
30. A. Suzuki *et al*., *Int. J. Hydrogen Energy* **36**, 2221–2229 (2011).
31. M. R. Lee *et al*., *Fuel Cells (Weinh.)* **18**, 129–136 (2018).
32. The US DOE Fuel Cell Technologies Office (FCTO), Fuel cell technical team roadmap (DOE, 2017); https://www.energy.gov/sites/default/files/2017/11/f46/FCTT_Roadmap_Nov_2017_FINAL.pdf.
33. Y. V. Yakovlev *et al*., *J. Power Sources* **490**, 229531 (2021).
34. S. M. Alia, K. S. Reeves, J. S. Baxter, D. A. Cullen, *J. Electrochem. Soc.* **167**, 144512 (2020).
35. A. S. Rad, *J. Theor. App. Phys.* **10**, 307–313 (2016).

ACKNOWLEDGMENTS

This research was supported by the Analysis and Testing Center of the Beijing Institute of Technology for basic characterization. We thank G. Feng from Huazhong University of Science and Technology for his assistance in simulation calculations. We thank Y. Li, H. Wang, Y. Zhang, C. Hou, W. Zhang, W. Dong, C. Li, and L. Bao from Beijing Institute of Technology and J. Wang from Tsinghua University for their experimental assistance. **Funding:** This work was supported by the National Key Research and Development Program of China (2020YFB1506300); National Natural Science Foundation of China (grants no. 21922502, 22171022, 21805292, 21625102, and 21971017); Beijing Municipal Science and Technology Project (Z211100002421013); and China Postdoctoral Science Foundation (grants no. 2020T130055 and 2020M670143). **Author contributions:** Conceptualization: B.W. and X.F.; Supervision: X.F. and B.W.; Methodology: X.F. and Q.Z.; Funding acquisition: X.F., Q.Z., and B.W.; Investigation: Q.Z., S.D., Y.Z., Z.M., P.S., D.S., X.J., T.Z., Z.R., J.X., and R.S.; Visualization: X.F., Q.Z., P.S., Y.Z., S.D., D.S., J.X., and R.S.; Writing – original draft: Q.Z., X.F., S.D., Z.M., and Y.Z.; Writing – review and editing: X.F., B.W., Q.Z., and P.S. **Competing interests:** B.W., X.F., and Q.Z. are inventors on patent application no. CN114361469A submitted by Beijing Institute of Technology, which covers COF-based porous ionomer for fuel cell. **Data and materials availability:** All data are available in the main text or the supplementary materials.

SUPPLEMENTARY MATERIALS

science.org/doi/10.1126/science.abm6304
Materials and Methods
Figs. S1 to S77
Tables S1 to S6
References (*36*–*48*)
Movies S1 and S2

Submitted 3 October 2021; resubmitted 26 April 2022
Accepted 26 August 2022
10.1126/science.abm6304

PEPTIDE SEQUENCING

Real-time dynamic single-molecule protein sequencing on an integrated semiconductor device

Brian D. Reed[1]*, Michael J. Meyer[1], Valentin Abramzon[1], Omer Ad[1], Pat Adcock[1], Faisal R. Ahmad[1], Gün Alppay[1], James A. Ball[1], James Beach[1], Dominique Belhachemi[1], Anthony Bellofiore[1], Michael Bellos[1], Juan Felipe Beltrán[1], Andrew Betts[1], Mohammad Wadud Bhuiya[1], Kristin Blacklock[1], Robert Boer[1], David Boisvert[1], Norman D. Brault[1], Aaron Buxbaum[1], Steve Caprio[1], Changhoon Choi[1], Thomas D. Christian[1], Robert Clancy[1], Joseph Clark[1], Thomas Connolly[1], Kathren Fink Croce[1], Richard Cullen[1], Mel Davey[1], Jack Davidson[1], Mohamed M. Elshenawy[1], Michael Ferrigno[1], Daniel Frier[1], Saketh Gudipati[1], Stephanie Hamill[1], Zhaoyu He[1], Sharath Hosali[1], Haidong Huang[1], Le Huang[1], Ali Kabiri[1], Gennadiy Kriger[1], Brittany Lathrop[1], An Li[1], Peter Lim[1], Stephen Liu[1], Feixiang Luo[1], Caixia Lv[1], Xiaoxiao Ma[1], Evan McCormack[1], Michele Millham[1], Roger Nani[1], Manjula Pandey[1], John Parillo[1], Gayatri Patel[1], Douglas H. Pike[1], Kyle Preston[1], Adeline Pichard-Kostuch[2], Kyle Rearick[1], Todd Rearick[1], Marco Ribezzi-Crivellari[2], Gerard Schmid[1], Jonathan Schultz[1], Xinghua Shi[1], Badri Singh[1], Nikita Srivastava[1], Shannon F. Stewman[1], T. R. Thurston[1], Philip Trioli[1], Jennifer Tullman[1], Xin Wang[1], Yen-Chih Wang[1], Eric A. G. Webster[1], Zhizhuo Zhang[1], Jorge Zuniga[1], Smita S. Patel[3], Andrew D. Griffiths[2], Antoine M. van Oijen[4], Michael McKenna[1], Matthew D. Dyer[1], Jonathan M. Rothberg[1]

Studies of the proteome would benefit greatly from methods to directly sequence and digitally quantify proteins and detect posttranslational modifications with single-molecule sensitivity. Here, we demonstrate single-molecule protein sequencing using a dynamic approach in which single peptides are probed in real time by a mixture of dye-labeled N-terminal amino acid recognizers and simultaneously cleaved by aminopeptidases. We annotate amino acids and identify the peptide sequence by measuring fluorescence intensity, lifetime, and binding kinetics on an integrated semiconductor chip. Our results demonstrate the kinetic principles that allow recognizers to identify multiple amino acids in an information-rich manner that enables discrimination of single amino acid substitutions and posttranslational modifications. With further development, we anticipate that this approach will offer a sensitive, scalable, and accessible platform for single-molecule proteomic studies and applications.

Measurements of the proteome provide deep and valuable insight into biological processes. However, methods with higher sensitivity are needed to fully understand the complex and dynamic states of the proteome in cells and changes to the proteome that occur in disease states and to make this information more accessible. The complex nature of the proteome and the chemical properties of proteins present several fundamental challenges to achieving sensitivity, throughput, cost, and adoption on par with DNA sequencing technologies (*1*, *2*). These challenges include the large number of different proteins per cell (>10,000) and yet larger number of proteoforms (*3*); the very wide dynamic range of protein abundance in cells and biological fluids (*4*, *5*) and lack of correlation with transcript levels (*6*); the costs and high detection limits of current methods of mass spectrometry (*2*); and the inability to copy or amplify proteins. Methods to directly sequence single protein molecules offer the maximum possible detection sensitivity, with the potential to enable single-cell inputs, digital quantification based on read counts, detection of posttranslational modifications (PTMs) and low-abundance or aberrant proteoforms, and cost and throughput levels that favor broad adoption.

Here, we present a single-molecule protein sequencing approach and integrated system for proteomic studies. We immobilize peptides in nanoscale reaction chambers on a semiconductor chip and detect N-terminal amino acids (NAAs) with dye-labeled NAA recognizers in real time. Aminopeptidases sequentially remove individual NAAs to expose subsequent amino acids for recognition, eliminating the need for complex chemistry and fluidics (Fig. 1). We built a benchtop device with a 532-nm pulsed laser source for fluorescence excitation and electronics for signal processing (fig. S1A). Our semiconductor chip uses fluorescence intensity and lifetime, rather than emission wavelength, for discrimination of dye labels. Our recognizers detect one or more types of NAAs and provide information for peptide identification based on the temporal order

[1]Quantum-Si, Inc., Guilford, CT 06437, USA. [2]Laboratoire de Biochimie, ESPCI Paris, Université PSL, CNRS UMR 8231, Paris, France. [3]Department of Biochemistry and Molecular Biology, Rutgers University, Piscataway, NJ 08854, USA. [4]Molecular Horizons, University of Wollongong, Wollongong, NSW 2522, Australia.
*Corresponding author. Email: breed@quantum-si.com

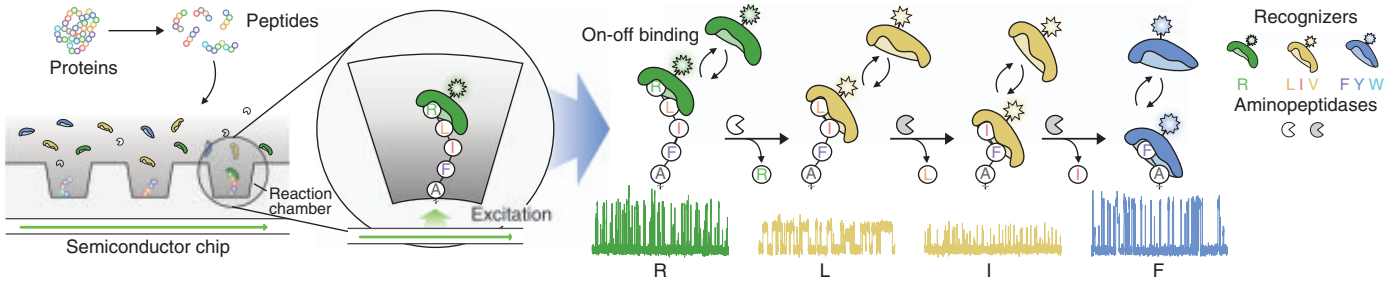

Fig. 1. Overview of real-time dynamic protein sequencing. Protein samples are digested into peptide fragments, immobilized in nanoscale reaction chambers, and incubated with a mixture of freely diffusing NAA recognizers and aminopeptidases that carry out the sequencing process. The labeled recognizers bind on and off to the peptide when one of their cognate NAAs is exposed at the N terminus, thereby producing characteristic pulsing patterns. The NAA is cleaved by an aminopeptidase, exposing the next amino acid for recognition. The temporal order of NAA recognition and the kinetics of binding enable peptide identification and are sensitive to features that modulate binding kinetics, such as PTMs.

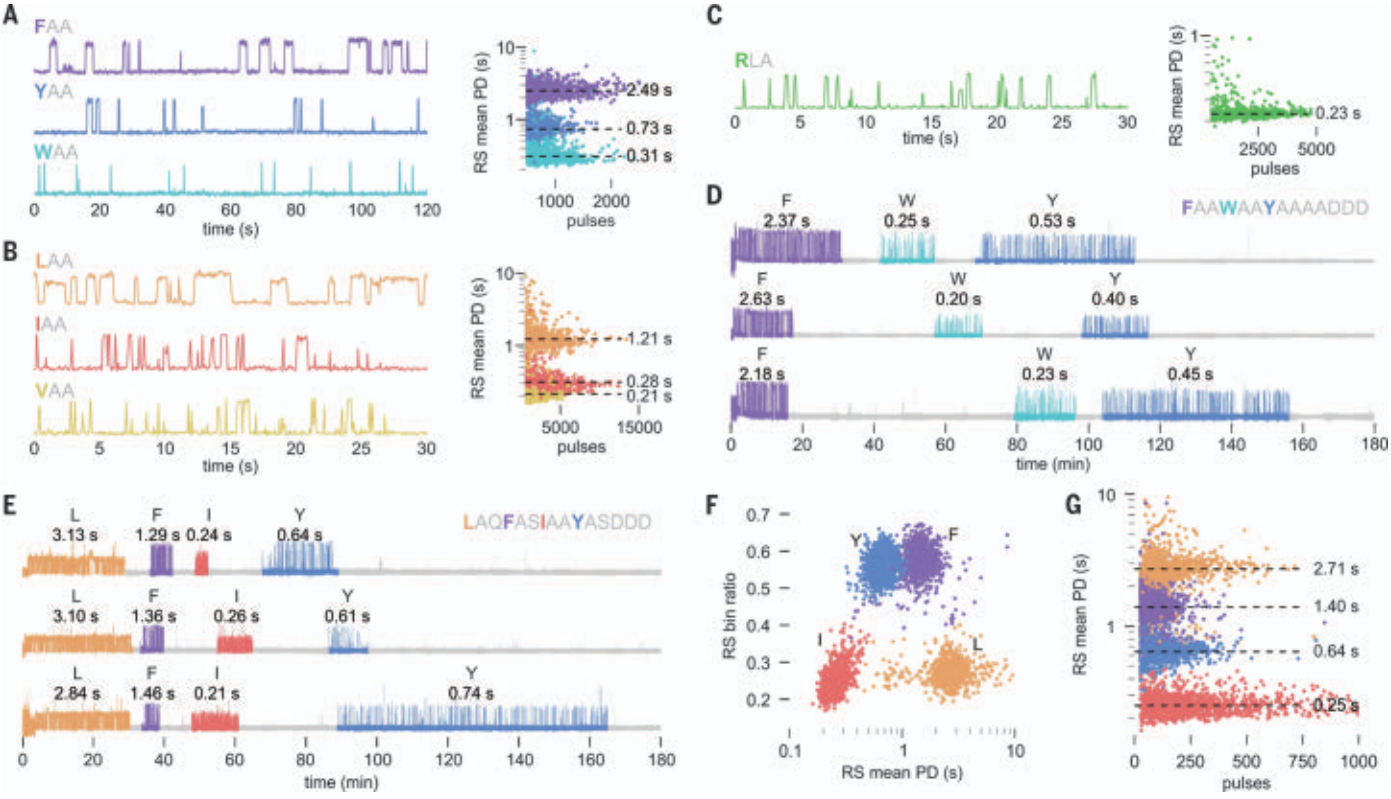

Fig. 2. NAA recognition and dynamic sequencing. (**A** to **C**) Example traces demonstrating single-molecule N-terminal recognition by PS610 (A), PS961 (B), and PS691 (C). Scatterplots of the number of pulses per RS versus RS mean PD are displayed for each peptide in (A) to (C), with median PD indicated. (**D**) Example traces from dynamic sequencing of the synthetic peptide FAAWAAYAADDD. Median PD is indicated above each RS. (**E** to **G**) Dynamic sequencing of the synthetic peptide LAQFASIAAYASDDD using PS610 and PS961. Example traces are shown in (E). A scatterplot of RS mean PD versus bin ratio illustrating discrimination of recognizers by bin ratio and NAAs by PD is shown in (F). A scatterplot of the number of pulses per RS versus RS mean PD, grouped by the amino acid label assigned to the RS, is shown in (G).

of NAA recognition and the kinetics of on-off binding.

A complementary metal-oxide semiconductor chip and integrated system for single-molecule measurements

We used complementary metal-oxide semiconductor fabrication technology to build a custom time domain–sensitive semiconductor chip with nanosecond precision, containing fully integrated components for single-molecule detection, including photosensors, optical waveguide circuitry, and reaction chambers for biomolecule immobilization (fig. S1, B and C). We achieve observation volumes of <5 attoliters through evanescent illumination at reaction-chamber bottoms from the nearby waveguide, enabling sensitive single-molecule detection in the context of high concentrations (>1 μM) of freely diffusing dye.

The semiconductor chip uses a filterless system that excludes excitation light on the basis of photon arrival time, achieving >10,000-fold attenuation of incident excitation light.

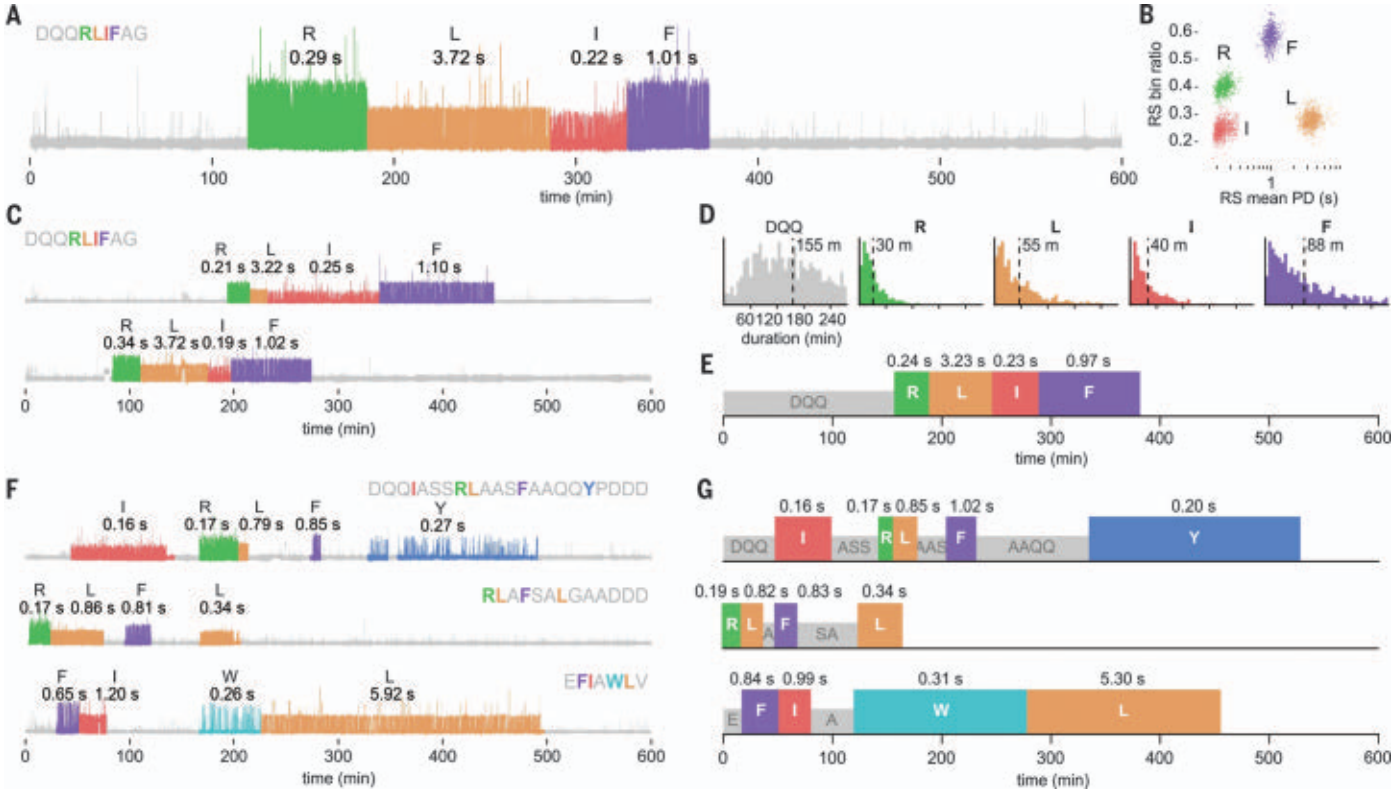

Fig. 3. Dynamic sequencing of diverse peptides with high-precision kinetic outputs. (**A** to **E**) Dynamic sequencing of the peptide DQQRLIFAG. An example trace is shown in (A). A scatterplot of RS mean PD versus bin ratio is shown in (B). Shown in (C) are additional example traces of dynamic sequencing of DQQRLIFAG peptide. Shown in (D) are distributions of the duration of each RS and NRS acquired during sequencing, with mean durations indicated. Kinetic signature plots summarizing the characteristic sequencing behavior of DQQRLIFAG peptide are shown in (E). (**F** to **G**) Dynamic sequencing of the synthetic peptides DQQIASSRLAASFAAQQYPDDD (top), RLAFSALGAADDD (middle), and EFIAWLV (bottom). Example traces for each peptide are shown in (F). Corresponding kinetic signature plots are shown in (G).

Elimination of an integrated optical filter layer increases the efficiency of fluorescence collection and enables scalable manufacturing of the chip. To discriminate fluorescent dye labels attached to NAA recognizers by fluorescence lifetime and intensity, the chip rapidly alternates between early and late signal collection windows associated with each laser pulse, thereby collecting different portions of the exponential fluorescence lifetime decay curve. The relative signal in these collection windows (termed "bin ratio") provides a reliable indication of fluorescence lifetime (fig. S1, D to H, and materials and methods).

Ordered recognition and cleavage of NAAs on single peptide molecules in real time

For NAA binding proteins to function as recognizers, the recognizer-peptide complex must remain bound long enough (typically >120 ms on average) to generate detectable single-molecule binding events. We first focused on proteins from the N-end rule adapter family ClpS that naturally bind to N-terminal phenylalanine, tyrosine, and tryptophan (*7*–*9*). Using PS610, a recognizer we derived from ClpS2 from *Agrobacterium tumefaciens* (table S1), we established that this recognizer binds detectably to immobilized peptides with these NAAs. We also determined that the kinetics of binding differ for each NAA. To demonstrate these properties, we incubated immobilized peptides containing the initial N-terminal sequences FAA, YAA, or WAA (A, alanine; F, phenylalanine; W, tryptophan; Y, tyrosine) on separate chips with PS610 and collected data for 10 hours (see materials and methods). We observed NAA recognition by PS610, characterized by continuous on-off binding during the incubation period, with a distinct pulse duration (PD) for each peptide (Fig. 2A). Median PDs were 2.49, 0.73, and 0.31 s for FAA, YAA, and WAA, respectively. These values reflect differences in binding affinity driven by different dissociation rates for each type of protein-NAA interaction (*7*) (fig. S2, A and B).

To expand the set of recognizable NAAs, we further investigated N-end rule pathway proteins as a source of additional recognizers. In a comprehensive screen of diverse ClpS family proteins, we discovered a group of ClpS proteins from the bacterial phylum Planctomycetes with native binding to N-terminal leucine, isoleucine, and valine. We applied directed evolution techniques to generate a Planctomycetes ClpS variant—PS961 (table S1)—with submicromolar affinity to N-terminal leucine, isoleucine, and valine, and demonstrated recognition of these NAAs (Fig. 2B). The median PD of binding to peptides with N-terminal LAA, IAA, and VAA (I, isoleucine; L, leucine; V, valine) was 1.21, 0.28, and 0.21 s, respectively, in agreement with bulk characterization (fig. S2C).

In a separate screen, we investigated a diverse set of UBR-box domains from the UBR family of ubiquitin ligases that natively bind N-terminal arginine, lysine, and histidine (*10*). The UBR-box domain from the yeast *Kluyveromyces marxianus* UBR1 protein (table S1) exhibited the highest affinity for N-terminal arginine, and we used this protein to generate an arginine recognizer, PS691. PS691 recognized arginine in a peptide with N-terminal RLA (R, arginine) with a median PD of 0.23 s (Fig. 2C). Lower-affinity binding to N-terminal lysine and histidine (fig. S2, D and E) was insufficient for single-molecule detection.

To demonstrate that amino acids in a single peptide molecule can be sequentially exposed by aminopeptidases and recognized in real time with distinguishable kinetics, we incubated

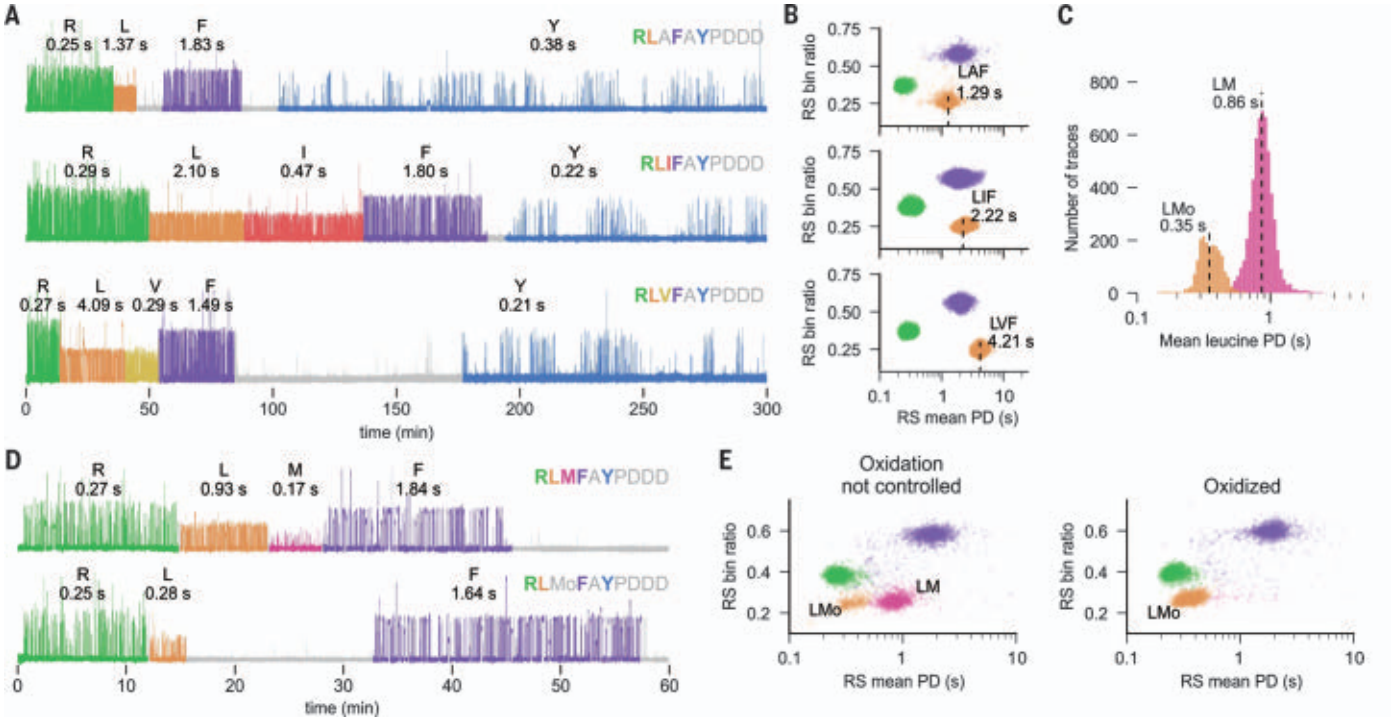

Fig. 4. Detection of single amino acid changes and PTMs. (**A** and **B**) Dynamic sequencing of synthetic peptides that differ by a single amino acid: RLAFAYPDDD (top), RLIFAYPDDD (middle), and RLVFAYPDDD (bottom). Example traces are shown in (A). Scatterplots of RS mean PD versus bin ratio are shown in (B). (**C** and **D**) Detection of oxidized methionine in the peptide RLMFAYPDDD. Distributions of mean PD for leucine are shown in (C); labels indicate populations with leucine followed by methionine (LM) or methionine sulfoxide (LMo). Shown in (D) are example traces in which methionine is recognized by PS961 and leucine exhibits a long PD (top) or in which methionine is not recognized, owing to oxidation, and in which leucine exhibits a short PD (bottom). (**E**) Scatterplots of RS mean PD versus bin ratio for runs in which oxidation was not controlled (left) or in which methionine was fully oxidized (right).

an immobilized peptide containing the initial sequence FAAWAAYAA with PS610 for 15 min, followed by the addition of PhTET3, an aminopeptidase from *Pyrococcus horikoshii* (*11*). The collected traces consisted of regions of distinct pulsing, which we refer to as recognition segments (RSs), separated by regions lacking recognition pulsing [nonrecognition segments (NRSs)]. We developed analysis software to automatically identify pulsing regions and transition points within traces on the basis of fluorescence properties and pulsing kinetics (see materials and methods). Traces began with the recognition of phenylalanine with a median PD of 2.36 s (Fig. 2D), in agreement with the PD observed for FAA in recognition-only assays. This pattern terminated after aminopeptidase addition (on average, 11 min after addition) and was followed by the ordered appearance of two RSs with median PDs of 0.25 and 0.49 s (Fig. 2D), corresponding to the short and medium PDs obtained in our YAA and WAA recognition-only assays. Thus, the introduction of aminopeptidase activity to the reaction resulted in the sequential appearance of discrete RSs with the expected kinetic properties in the correct order.

To demonstrate dynamic sequencing with two NAA recognizers, we labeled PS610 and PS961 with the distinguishable dyes atto-Rho6G and Cy3, respectively, and exposed an immobilized peptide of sequence LAQFASIAAYASDDD (D, aspartate; Q, glutamine; S, serine) to a solution containing both recognizers. After 15 min, we added two *P. horikoshii* aminopeptidases with combined activity covering all 20 amino acids—PhTET2 and PhTET3 (*11*, *12*). The collected traces displayed discrete segments of pulsing alternating between PS961 and PS610 according to the order of recognizable amino acids in the peptide sequence (Fig. 2E). The average bin ratio and average PD associated with each RS readily distinguished the two dye labels and four types of recognized NAAs (Fig. 2F). Median PDs were 2.71, 1.40, 0.25, and 0.64 s for N-terminal LAQ, FAS, IAA, and YAS, respectively (Fig. 2G).

Previous studies have shown that NAA-bound ClpS and UBR proteins also make contacts with the residues at position 2 (P2) and position 3 (P3) from the N terminus that influence binding affinity (*9*, *13*, *14*). These influences are reflected in the modulation of PD depending on the downstream P2 and P3 residues, as we observed above for LAA (1.21 s) compared with LAQ (2.70 s). We find that these influences on PD vary within informatically advantageous ranges and can be determined empirically or approximated in silico to model peptide sequencing behavior a priori (fig. S2, F to H). A powerful feature of this recognition behavior with respect to peptide identification is that each RS contains information about potential downstream P2 and P3 residues or PTMs, regardless of whether these positions are the targets of an NAA recognizer.

Principles of dynamic protein sequencing illustrated with model peptides

To evaluate the kinetic principles of our dynamic sequencing method when applied to diverse sequences, we first characterized the synthetic peptide DQQRLIFAG (G, glycine), corresponding to a segment of human ubiquitin (Fig. 3, A to E). We performed sequencing reactions through a combination of three differentially labeled recognizers—PS610, PS961, and PS691—and two aminopeptidases—PhTET2 and PhTET3 (see materials and methods). The example trace in Fig. 3A starts with an NRS that corresponds to the time interval during which residues in the initial DQQ motif are present at the N terminus. The first RS starts at 120 min, upon exposure of N-terminal arginine to recognition by PS691. Subsequent cleavage events sequentially expose N-terminal leucine, isoleucine, and phenylalanine to their corresponding recognizers, with fast transitions (average <10 s) from one RS to the next. The transition from leucine to isoleucine recognition by PS961 is

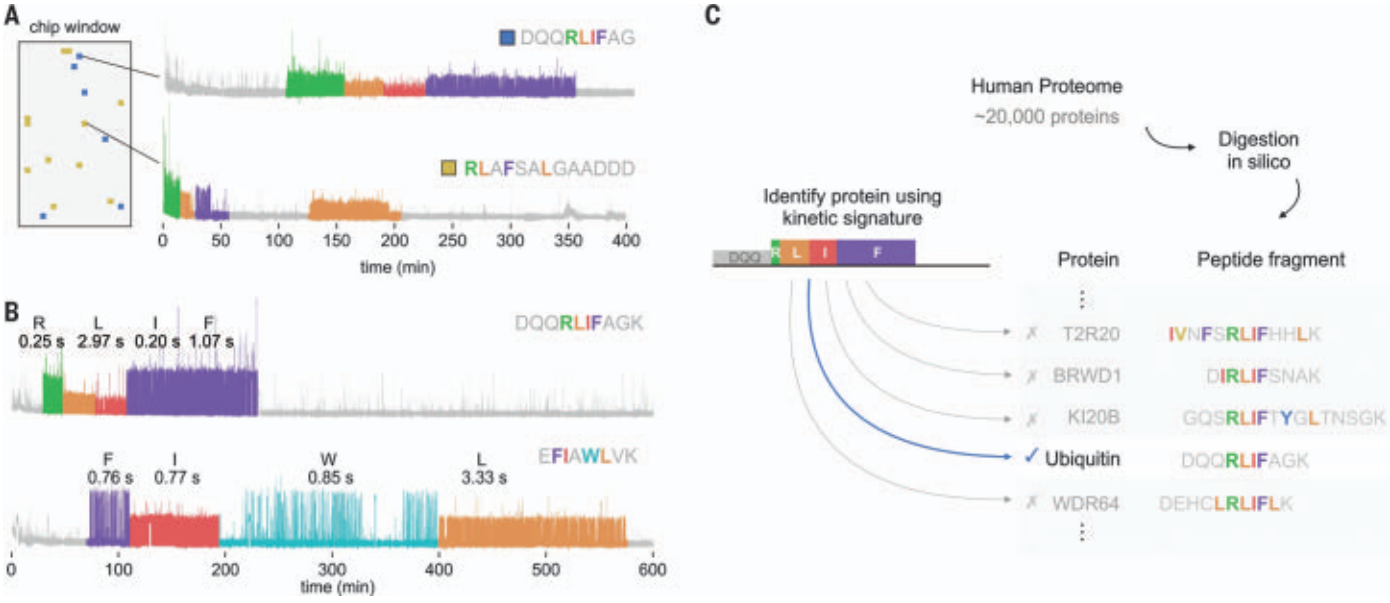

Fig. 5. Discrimination of peptides in mixtures and mapping peptides to the human proteome. (**A**) Example traces from sequencing a mixture of the peptides DQQRLIFAG and RLAFSALGAADDD on the same chip; the chip window indicates the location of reaction chambers producing a sequencing readout for each peptide. (**B**) Example traces from the dynamic sequencing of two peptides, DQQRLIFAGK (top) and EFIAWLVK (bottom), isolated from the recombinant human proteins ubiquitin and GLP-1, respectively. (**C**) Diagram illustrating the identification of the protein ubiquitin as a match to the kinetic signature from DQQRLIFAGK peptide in an in silico digest of the human proteome based on kinetic information.

readily identified as a sharp change in average PD. This overall pattern is replicated across many instances of sequencing of the same peptide, with similar PD statistics across traces, as each peptide molecule follows the same reaction pathway over the course of the sequencing run (Fig. 3, B and C). Owing to the stochastic timing of cleavage events, each trace displays distinct start times and durations for each RS (Fig. 3C).

This approach reports the binding kinetics at each recognizable amino acid position and the kinetics of aminopeptidase cleavage along the peptide sequence. High-precision kinetic information on binding is obtained from a single trace because each RS typically contains tens to hundreds of on-off binding events, resulting in a distribution of PD and interpulse duration (IPD) measurements that can be analyzed statistically. The repetitive probing of each NAA also provides accurate recognizer calling because calls are not based on the error-prone detection of a single event associated with one fluorophore molecule (fig. S1F). Recognizer on-rate and concentration govern IPD for each RS; higher recognizer concentrations result in shorter average IPDs and faster rates of pulsing (fig. S3, A and B). Higher recognizer concentrations, however, increase the fluorescence background from freely diffusing recognizers, resulting in lower pulse signal-to-noise ratios, and can compete with aminopeptidases for N-terminal access. In practice, IPDs in the range of ~2 to 10 s provide a favorable balance among these factors.

The distribution of RS durations across an ensemble of replicate traces defines the rate of cleavage of each recognizable NAA. For DQQRLIFAG peptide, we observed average cleavage times of 30, 55, 40, and 88 min for N-terminal arginine, leucine, isoleucine, and phenylalanine, respectively, with approximate single-exponential decay statistics for each position (Fig. 3D and fig. S3C). The distribution of NRS durations reports the cleavage rate of a run of one or more nonrecognized NAAs. The average NRS duration for the initial DQQ motif was 155 min (Fig. 3D). Average cleavage rates are a key parameter and are controlled by the aminopeptidase concentration in the assay (fig. S3, D and E). Given the exponential behavior, we target average RS durations of 10 to 40 min to provide sufficient time for pulsing data collection, avoid missed RSs due to rapid cleavage, and minimize excessively long RS durations. We found it helpful to visualize the sequencing profiles of peptides as kinetic signature plots—simplified trace-like representations of the time course of complete peptide sequencing containing the median PD for each RS and the average duration of each RS and NRS (Fig. 3E). These highly characteristic features provide a wealth of sequence-dependent information for mapping traces from peptides to their proteins of origin.

To demonstrate that this core methodology and its kinetic principles apply to a wide range of peptide sequences, we sequenced the synthetic peptides DQQIASSRLAASFAAQQYPDDD, RLAFSALGAADDD, and EFIAWLV (E, glutamate; P, proline)—a segment of human glucagon-like peptide–1 (GLP-1)—under the same sequencing conditions used for DQQRLIFAG (Fig. 3F). Each peptide generated a characteristic kinetic signature in accordance with its sequence (Fig. 3G). We obtained readouts as far as position 18 (the furthest recognizable amino acid) in the peptide DQQIASSRLAASFAAQQYPDDD, illustrating that the method is compatible with long peptides and capable of deep access to sequence information in peptides.

Distinctive kinetic signatures from single amino acid changes and PTMs

To illustrate how the kinetic parameters acquired from sequencing are sensitive to changes in sequence composition, we performed sequencing with a set of three peptides—RLAFAYPDDD, RLIFAYPDDD, and RLVFAYPDDD—that differ only at a single position, located immediately downstream from the PS961 N-terminal target leucine (Fig. 4A). Each type of amino acid at this position had a distinct effect on the PD acquired during recognition of N-terminal leucine by PS961. We observed median PDs of 1.29, 2.22, and 4.21 s for LAF, LIF, and LVF, respectively (Fig. 4B). In addition to differences in PD for leucine, each peptide displayed a characteristic RS or NRS in the interval between leucine and phenylalanine recognition (Fig. 4A and fig. S4A). These results demonstrate the sensitivity of the sequencing readout to variation at a single position and illustrate that both directly recognized NAAs and adjacent residues can influence the full kinetic signature obtained from sequencing.

Because the aminoacyl-proline bond of the YP motif in peptides such as RLIFAYPDDD cannot be cleaved by the PhTET aminopeptidases (*11*, *12*), observation of YP pulsing at the end of a trace ensures that cleavage has progressed completely from the first to last recognizable amino acid. The sequencing output from RLIFAYPDDD, therefore, provided a convenient dataset for examining biochemical sources of nonideal behavior that could lead to errors in peptide identification. The main sources of incomplete information in traces were deletions of expected RSs due to the stochastic occurrence of rapid sequential cleavage events (fig. S4B) and early termination of reads resulting from photodamage or surface detachment (fig. S4C).

In addition to changes in amino acid sequence composition, sequencing readouts are sensitive to changes due to PTMs. As an example, we examined methionine oxidation. The thioether moiety of the methionine side chain is susceptible to oxidation during peptide synthesis and sequencing. We determined that PS961 binds a peptide with N-terminal methionine with a dissociation constant (K_d) of 947 ± 47 nM (fig. S4D) and hypothesized that oxidation, resulting in a polar methionine sulfoxide side chain, would eliminate binding and reduce NAA binding affinity when located at P2. We determined computationally that methionine sulfoxide is highly unfavorable in the PS961 NAA binding pocket and that nonpolar residues are preferred at P2 (fig. S4E and fig. S2H). We sequenced the synthetic peptide RLMFAYPDDD (M, methionine) and observed two populations of traces with distinct kinetic signatures—a first population containing leucine recognition with a median PD of 0.86 s and a second population with a median PD of 0.35 s (Fig. 4C). Traces from the first population also displayed methionine recognition with a short PD in the time interval between leucine and phenylalanine recognition (Fig. 4D). Methionine recognition was absent in traces from the second population (Fig. 4D), indicating that the methionine side chain in these peptides was not capable of recognition by PS961. When we fully oxidized methionine by preincubation with hydrogen peroxide (see materials and methods), we observed elimination of both methionine recognition and the leucine recognition cluster with a long median PD, as expected (Fig. 4E). These results demonstrate the capability for extremely sensitive detection of PTMs owing to their kinetic effects on recognition.

Sequencing peptide mixtures and mapping peptides derived from human proteins

Proteomics applications require identification of peptides in mixtures derived from biological sources. To extend our results to peptide mixtures and biologically derived peptides, we performed two experiments. First, we mixed DQQRLIFAG and RLAFSALGAADDD peptides, immobilized them on the same chip, and performed a sequencing run. Data analysis (see materials and methods) identified two populations of traces corresponding to each peptide, with kinetic signatures in close agreement with those identified in runs with individual peptides (Fig. 5A and fig. S4F). Second, to demonstrate that our method extends to biologically derived peptides, we performed sequencing runs with peptide libraries generated using a simple workflow from recombinant human ubiquitin (76 amino acids) and GLP-1 (37 amino acids) proteins digested with AspN/LysC and trypsin, respectively (see materials and methods). For both libraries, data analysis readily identified traces matching the expected recognition pattern for the protease cleavage products DQQRLIFAGK and EFIAWLVK (K, lysine) for ubiquitin and GLP-1, respectively, and produced kinetic signatures in agreement with synthetic versions of these peptides (Fig. 5B and fig. S4G). We identified matches to the kinetic signature of the ubiquitin peptide DQQRLIFAGK across the human proteome, taking advantage of simple sequence constraints provided by kinetic information (see materials and methods). We found only one protein other than ubiquitin that contained a peptide that could potentially match this signature (Fig. 5C); thus, even short signatures can exhibit proteome abundance of <1 in 10^4 proteins. These results illustrate the potential of the full kinetic output from sequencing to enable digital mapping of peptides to their proteins of origin.

Conclusions

Our simple, real-time dynamic approach differs markedly from other recently described single-molecule approaches that rely on complex, iterative methods involving stepwise Edman chemistry or hundreds of cycles of epitope probing (*15*–*17*). Nanopore approaches offer the potential for real-time readouts and simplicity but face substantial challenges related to the size and biophysical complexity of polypeptides (*18*–*20*). Our sequencing technology is readily expanded in its capabilities, and there are multiple areas for improvement. Expansion of proteome coverage can be achieved through directed evolution and engineering of recognizers. The NAA targets demonstrated here make up ~35.6% of the human proteome, but lower-affinity NAA targets require longer PDs to enable detection in all sequence contexts. Recognizers for new amino acids or PTMs can be evolved from current recognizers or identified in screens of other scaffolds, such as other types of NAA- or PTM-binding proteins or aptamers. Extension to detection of all 20 natural amino acids and multiple PTMs is feasible for de novo sequencing; however, partial sequences are sufficient for most proteomics applications, which rely on mapping to predefined sets of candidate proteins (*21*). Aminopeptidases can be engineered to optimize cleavage rates and minimize RS deletions from rapid sequential cleavage. We envision that the dynamic range of samples and the applications most suitable for the system will tend to scale with the number of reaction chambers on the chip and that compression of dynamic range will be necessary for certain applications. We anticipate that future developments of the platform will increase the accessibility of proteomics studies and enable discoveries in biological and clinical research.

REFERENCES AND NOTES

1. S. Goodwin, J. D. McPherson, W. R. McCombie, *Nat. Rev. Genet.* **17**, 333–351 (2016).
2. W. Timp, G. Timp, *Sci. Adv.* **6**, eaax8978 (2020).
3. R. Aebersold *et al.*, *Nat. Chem. Biol.* **14**, 206–214 (2018).
4. M. Beck *et al.*, *Mol. Syst. Biol.* **7**, 549 (2011).
5. N. L. Anderson, N. G. Anderson, *Mol. Cell. Proteomics* **1**, 845–867 (2002).
6. Y. Liu, A. Beyer, R. Aebersold, *Cell* **165**, 535–550 (2016).
7. J. Tullman, N. Callahan, B. Ellington, Z. Kelman, J. P. Marino, *Appl. Microbiol. Biotechnol.* **103**, 2621–2633 (2019).
8. D. A. Dougan, B. G. Reid, A. L. Horwich, B. Bukau, *Mol. Cell* **9**, 673–683 (2002).
9. B. J. Stein, R. A. Grant, R. T. Sauer, T. A. Baker, *Structure* **24**, 232–242 (2016).
10. T. Tasaki, Y. T. Kwon, *Trends Biochem. Sci.* **32**, 520–528 (2007).
11. M. A. Durá *et al.*, *Mol. Microbiol.* **72**, 26–40 (2009).
12. M. A. Durá *et al.*, *Biochemistry* **44**, 3477–3486 (2005).
13. W. S. Choi *et al.*, *Nat. Struct. Mol. Biol.* **17**, 1175–1181 (2010).
14. J. Muñoz-Escobar, E. Matta-Camacho, C. Cho, G. Kozlov, K. Gehring, *Structure* **25**, 719–729.e3 (2017).
15. J. Swaminathan *et al.*, *Nat. Biotechnol.* **36**, 1076–1082 (2018).
16. J. D. Egertson *et al.*, bioRxiv 2021.10.11.463967 [Preprint] (2021); https://doi.org/10.1101/2021.10.11.463967.
17. M. Chee, K. Gunderson, M. P. Weiner, Macromolecule analysis employing nucleic acid encoding (2019); https://pdfaiw.uspto.gov/.aiw?Docid=20190145982.
18. S. Zhang *et al.*, *Nat. Chem.* **13**, 1192–1199 (2021).
19. H. Brinkerhoff, A. S. W. Kang, J. Liu, A. Aksimentiev, C. Dekker, *Science* **374**, 1509–1513 (2021).
20. J. A. Alfaro *et al.*, *Nat. Methods* **18**, 604–617 (2021).
21. J. Swaminathan, A. A. Boulgakov, E. M. Marcotte, *PLOS Comput. Biol.* **11**, e1004080 (2015).
22. B. D. Reed, M. J. Meyer, J. F. Beltrán, Code and data for "Real-time dynamic single-molecule protein sequencing on an integrated semiconductor device." Zenodo (2022); https://doi.org/10.5281/zenodo.7017750.

ACKNOWLEDGMENTS

We thank E. Chen for helpful discussions in preparing the manuscript. **Funding:** This work was funded by Quantum-Si, Inc. **Author contributions:** A.D.G., A.L., A.M.v.O., A.P.-K., B.D.R., B.S., C.L., D.H.P., E.M., F.L., G.P., H.H., J.A.B., J.P., J.T., J.Z., K.B., K.F.C., M.Mi., M.M.E., M.P., M.R.-C., M.W.B., N.D.B., N.S., O.A., R.B., R.N., S.Ha., S.G., S.S.P., T.D.C., X.S., and Y.-C.W. developed methods and reagents for protein sequencing; A. Bu., D. Be., D.F., G.A., G.K., J.F.B., M.D., M.J.M., S.F.S., S.L., V.A., and Z.Z. developed software; and A. Bel., A. Bet., A.K., B.L., C.C., D.Bo., E.A.G.W., F.R.A., G.S., J.B., J.C., J.D., J.S., K.P., K.R., L.H., M.B., M.F., P.A., P.L., P.T., R.Cl., R.Cu., S.Ho., S.C., T.C., T.R., T.R.T., X.M., X.W., and Z.H. developed semiconductor chips, nanophotonics, lasers, and instruments. J.M.R., M.Mc., T.R., B.D.R., M.D., G.S., M.F., P.L., and M.D.D. supervised and/or acquired resources and funding. B.D.R., M.J.M., M.P., and B.S. designed experiments and/or generated the single-molecule recognition and sequencing data presented in the figures. B.D.R., M.J.M., and J.F.B. analyzed sequencing data and prepared the figures. M.P. and G.P. characterized recognizer ensemble kinetic properties. O.A. generated libraries from recombinant proteins. H.H. and Y.-C.W. generated model

peptides. D.H.P. performed computational modeling. B.D.R. led the study and wrote the manuscript with review and commentary from coauthors. All authors met the criteria for authorship and contributed critically to the development of the sequencing method and platform by conducting experiments, developing methods and concepts, analyzing and interpreting data, developing software, supervising research, or acquiring funding. **Competing interests:** All authors affiliated with Quantum-Si, Inc., along with A.D.G. and A.M.v.O., are shareholders and/or are listed as inventors on patents owned by Quantum-Si, Inc.; A.D.G. and A.M.v.O. are on the scientific advisory board of Quantum-Si, Inc., and are paid consultants. The technology presented in this paper is the subject of numerous pending or awarded patents filed by Quantum-Si, Inc., with the US Patent and Trademark Office and international offices. **Data and materials availability:** Data and custom code used in this paper are available for download online at Zenodo (*22*). Sequencing reagents and instruments are available from Quantum-Si, Inc., under a material transfer agreement.

SUPPLEMENTARY MATERIALS

science.org/doi/10.1126/science.abo7651
Materials and Methods
Figs. S1 to S4
Table S1
References (*23*–*27*)

Submitted 28 February 2022; accepted 13 September 2022
10.1126/science.abo7651

CELL BIOLOGY

Sentinel *p16*$^{INK4a+}$ cells in the basement membrane form a reparative niche in the lung

Nabora S. Reyes[1], Maria Krasilnikov[1], Nancy C. Allen[1], Jin Young Lee[1], Ben Hyams[1], Minqi Zhou[1], Supriya Ravishankar[1], Monica Cassandras[1], Chaoqun Wang[1], Imran Khan[1], Peri Matatia[3], Yoshikazu Johmura[4], Ari Molofsky[3], Michael Matthay[1], Makoto Nakanishi[4], Dean Sheppard[1], Judith Campisi[5], Tien Peng[1,2]*

We engineered an ultrasensitive reporter of *p16*^{INK4a}, a biomarker of cellular senescence. Our reporter detected *p16*^{INK4a}-expressing fibroblasts with certain senescent characteristics that appeared shortly after birth in the basement membrane adjacent to epithelial stem cells in the lung. Furthermore, these *p16*$^{INK4a+}$ fibroblasts had enhanced capacity to sense tissue inflammation and respond through their increased secretory capacity to promote epithelial regeneration. In addition, *p16*^{INK4a} expression was required in fibroblasts to enhance epithelial regeneration. This study highlights a role for *p16*$^{INK4a+}$ fibroblasts as tissue-resident sentinels in the stem cell niche that monitor barrier integrity and rapidly respond to inflammation to promote tissue regeneration.

p16^{INK4a} is a tumor suppressor encoded in the cyclin-dependent kinase 2a (*Cdkn2a*) locus that is increased in cultured cells in vitro undergoing cellular senescence (*1*), defined as a form of irreversible cell cycle arrest often induced by stress and associated with a secretory profile (*2*). Mouse reporters using *p16*^{INK4a} promoter to drive luciferase expression have demonstrated increased transcription of *p16*^{INK4a} associated with aging and wound repair (*3*–*5*). On the basis of these and other studies quantifying *p16*^{INK4a} transcripts in whole tissues, cells expressing *p16*^{INK4a} (*p16*$^{INK4a+}$) are thought to be rare or absent in young and healthy tissues. However, the use of luciferase combined with whole-body bioluminescence imaging precludes studying *p16*$^{INK4a+}$ cells at cellular resolution. Genetic models have demonstrated the beneficial effects of killing *p16*$^{INK4a+}$ cells in models of aging-related pathologies (*6*–*12*), but the identity and behavior of living *p16*$^{INK4a+}$ cells in their cellular ecosystem within tissues remain largely undefined (*13*). Recent advances have been made using Cre to identify and delete *p16*$^{INK4a+}$ cells, but this approach only identifies cells with high *p16*^{INK4a} expression, which is rare in young adult tissue (*14*, *15*). Although *p16*$^{INK4a+}$ senescent cells have been described as having a rigid and nonresponsive cell state (*16*), the presence of *p16*$^{INK4a+}$ cells in young tissue might indicate that they have some normal physiological function. We examined the role and function of *p16*$^{INK4a+}$ cells in non-aged tissue with a reporter that has improved sensitivity for *p16*^{INK4a}.

[1]Department of Medicine, Pulmonary and Critical Care Division, University of California San Francisco, San Francisco, CA, USA. [2]Bakar Aging Research Institute, University of California San Francisco, San Francisco, CA, USA. [3]Department of Laboratory Medicine, University of California San Francisco, San Francisco, CA, USA. [4]Division of Cancer Cell Biology, University of Tokyo, Tokyo, Japan. [5]Buck Institute for Research on Aging, Novato, CA, USA.
***Corresponding author. Email: tien.peng@ucsf.edu**

High-sensitivity fluorescent reporter of *p16*^{INK4a} in vivo

To build a sensitive reporter for *p16*$^{INK4a+}$ in tissues, we constructed a bacterial artificial chromosome (BAC) in which tandem cassettes of fused histone H2B–green fluorescent protein (H2B-GFP) is expressed in-frame with the *p16*^{INK4a} gene product in the murine *Cdkn2a* locus, thus using the *p16*^{INK4a} promoter to drive the expression of multiple copies of a stable fluorescent protein that would be incorporated into the nucleosome. The BAC was injected into mouse embryos to create a transgenic mouse model named INKBRITE (INK4a H2B-GFP reporter-in-tandem) (Fig. 1A). Flow cytometry analysis of cells from lungs of healthy, young [postnatal day 60 (PND60)] INKBRITE mice showed highly fluorescent cells not observed in wild-type (WT) lungs, and sorted GFP$^+$ cells were significantly enriched for the *p16*^{INK4a} transcript, as detected by quantitative reverse transcription polymerase chain reaction (qRT-PCR) (Fig. 1B). Flow cytometry with lineage markers showed that most of the GFP$^+$ cells were immune cells [protein tyrosine phosphatase receptor type C–positive (CD45$^+$)] and fibroblasts [platelet-derived growth factor receptor alpha–positive (PDGFRα$^+$)] (fig. S1A). We failed to detect *p16*$^{INK4a+}$ cells in the lung during embryogenesis, but *p16*$^{INK4a+}$ cells started appearing in the basement membrane shortly after birth (fig. S1, B to E), when the oxygen environment changes in the lung before the onset of alveologenesis starting at PND3 through PND5. PND4 INKBRITE pups subjected to hyperoxia demonstrated a small, not statistically significant increase in GFP$^+$ cells in the lung (fig. S1F). Thick section images of PND60 lungs showed nuclear GFP staining surrounded by a laminin-positive basement membrane beneath the airway epithelium [secretoglobin 1A1 (SCGB1A1) marks airway stem cells; Fig. 1C]. We observed these *p16*$^{INK4a+}$ cells in similar positions in other barrier organs such as the small intestine, colon, and skin (fig. S1, G to I).

To determine whether *p16*$^{INK4a+}$ fibroblasts divide more slowly than *p16*$^{INK4a-}$ fibroblasts, we administered bromodeoxyuridine (BrdU) continuously to separate cohorts of INKBRITE animals during the alveologenesis phase (PND5 to PND45) or the adult homeostasis phase (PND60 to PND90) of postnatal lung development and maintenance, respectively. Examining PDGFRα$^+$ fibroblasts in the subairway epithelial compartment, we found a significant reduction of BrdU incorporation in the *p16*$^{INK4a+}$ fibroblasts during alveologenesis, but no statistically significant reduction during adult homeostasis compared with *p16*$^{INK4a-}$ fibroblasts (Fig. 1, D to F). To trace the fate of *p16*$^{INK4a+}$ cells over a longer period during homeostasis, we administered tamoxifen to *p16*^{creERT}:*Rosa*^{tdTomato} animals to permanently activate *tdTomato* expression in *p16*$^{INK4a+}$ cells, followed by a chase period off of tamoxifen to study the behavior of tdTomato$^+$ cells (*15*). Histology analysis of tdTomato$^+$ cells confirmed their localization in the subepithelial

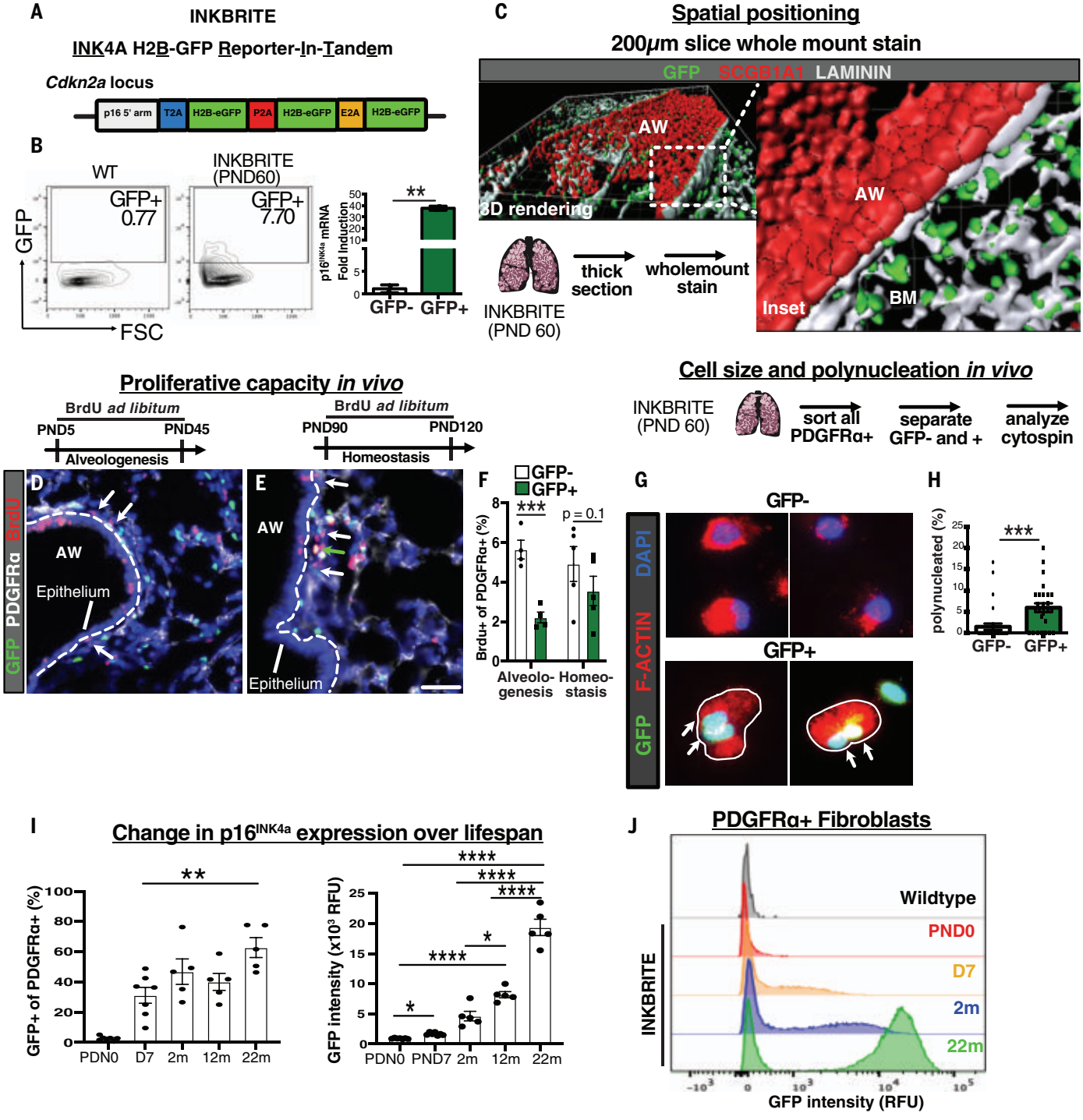

Fig. 1. INKBRITE identifies *p16*$^{INK4a+}$ cells with senescent characteristics in vivo. (**A**) Target construct design for INKBRITE. (**B**) FACS analysis of GFP$^+$ cells from INKBRITE lungs and qRT-PCR of sorted GFP$^+$ and GFP$^-$ cells (n = 2). (**C**) Whole-mount image of the airway from thick-sectioned INKBRITE lung rendered on Imaris. (**D** to **F**) IHC and quantification of BrdU incorporation into PDGFRα$^+$ and GFP$^-$ cells (white arrows) or PDGFRα$^+$ and GFP$^+$ cells (green arrows) during alveologenesis or homeostasis (n = 4 alveologenesis, n = 5 homeostasis). (**G** and **H**) IHC and quantification of freshly sorted of GFP$^+$ and GFP$^-$ fibroblasts for polynucleation (n = 2 experiments, n = 29 to 31 images per cell type). (**I**) FACS data with quantification of the percentage of GFP$^+$ cells and mean GFP$^+$ intensity of PDGFRα$^+$ fibroblasts over the life span of INKBRITE animals (n = 7 PND0; n = 7 PND7; n = 5 2m; n = 5 22m). (**J**) Histogram displaying the GFP intensity in PND0, PND7, 2m, and 22m PDGFRα$^+$ lung fibroblasts (n = 5 per time point, n = 2 experiments). AW, airway, BM, basement membrane. Scale bars, 100 μm. Each point in the graph represents one animal or one distinct image for in vitro studies with mean ± SEM. All P values were determined by one-tailed t test or two-way ANOVA when applicable. *P < 0.05, **P < 0.01, ***P < 0.001, ****P < 0.0001.

compartment in the airway, and tdTomato$^+$ fibroblasts demonstrated a significant reduction in 5-ethynyl-2-deoxyuridine (EdU) incorporation over a 60-day chase period (PND60 to PND120) relative to tdTomato$^-$ fibroblasts (fig. S2, A and B). Long-term trace of tdTomato$^+$ fibroblasts demonstrated their persistence in the lung 7 months after animals were treated with tamoxifen to activate *tdTomato* expression (fig. S2C). These studies demonstrate that *p16*$^{INK4a+}$ fibroblasts constitute a stable, tissue-resident population with slower replication within the basement membrane during postnatal development and homeostasis.

Polynucleation is a feature of cellular senescence in cultured fibroblasts (*1*, *17*), but it has not been observed in intact tissues. Using nuclear and actin filament (F-actin) staining to define the morphology of freshly isolated fibroblasts from INKBRITE lungs (>PND60), we detected bi- and trinucleated fibroblasts that were more prevalent in *p16*$^{INK4a+}$ fibroblasts (Fig. 1, G and H). *p16*$^{INK4a+}$ fibroblasts also demonstrated other features of senescent cells when cultured ex vivo, including an increase in size and in the presence of γhistone2AX (γH2AX) and senescence-associated β-galactosidase (fig. S2, D to F).

To examine the proportion of lung fibroblasts that express *p16*^{INKa} over a mouse's life span, we collected INKBRITE lungs at PND0, PND7, 2 months (2m), 12m, and 22m of age for fluorescence-activated cell sorting (FACS). The proportion of fibroblasts expressing *p16*^{INK4a} increased in the first week of life, followed by stability between PND7 and 12m, with the highest proportion of *p16*$^{INK4a+}$ fibroblasts present at 22m (Fig. 1I). Although the proportion of fibroblasts expressing GFP increased by approximately twofold with age, we observed a larger, age-dependent increase in GFP intensity in GFP$^+$ fibroblasts (Fig. 1, I and J), as indicated by the INKBRITE reporter and confirmed by qRT-PCR analysis of *p16*^{INK4a} from GFP$^+$ cells collected from young and aged animals (fig. S2G). Therefore, *p16*$^{INK4a+}$ fibroblasts in vivo exhibit features previously ascribed to senescent cells in vitro. This indicates that *p16*$^{INK4a+}$ cells are not absent or particularly rare in healthy, young tissue, but are present in relative abundance at the epithelial-mesenchymal interface, where *p16*^{INK4a} expression is increased throughout the life span.

Variable *p16*^{INK4a} expression correlates with proliferative cell cycle arrest

We observed a broad range of GFP intensity in the GFP$^+$ fibroblasts across the life span, and further sorting of GFP$^+$ fibroblasts into GFP^{hi} (top 50 percentile fluorescent intensity) and GFP^{lo} (bottom 50 percentile) confirmed the correlation of GFP intensity with *p16*^{INK4a} expression (Fig. 2, A and B). *p16*^{INK4a} expression was distributed across fibroblast subsets in the lung (*18*), with an enrichment of GFP^{hi} fibroblasts in the adventitial fibroblast lineage associated with the airway and vasculature (fig. S3, A and B). To determine whether high *p16*^{INK4a} expression correlates with cell cycle arrest in response to proliferative stimuli, which is the canonical definition of senescence (*19*), we applied a chemical cell trace to *p16*$^{INK4a+}$ cells that allowed quantification of proliferative history using flow cytometry. We treated lung fibroblasts isolated from INKBRITE lungs with CellTrace Far Red (CTFR), a fluorescent cell dye that is diluted with each cell division, and grew them in culture. Serum-deprived fibroblasts retained CTFR, as demonstrated by a narrow, bright CTFR peak on FACS indicative of cell cycle arrest (Fig. 2C, red histogram). In serum-enriched growth medium, we observe a broad range of CTFR intensity in cultured fibroblasts, with a significant enrichment of CTFR-retaining cells (i.e., the percentage of cells with a CTFR intensity similar to that of serum-deprived cells) in GFP$^+$ fibroblasts. Further segregation on the basis of GFP intensity showed that GFP^{hi} fibroblasts had increased CTFR retention relative to GFP^{lo} (Fig. 2, C and D). Analysis of CFTR-retaining fibroblasts also confirmed that they were enriched for other senescence characteristics such as polyploidy, increased cell size, and DNA damage (fig. S3, B to E). We saw similar results when we isolated adventitial fibroblasts (fig. S3F). To confirm this behavior in vivo, we treated freshly isolated INKBRITE lung fibroblasts with CTFR and transplanted them into injured host lungs without endogenous fluorescence to induce fibroblast proliferation (*18*). Four days after CTFR treatment and transplantation, we observed a broad range of CTFR retention in adoptive transferred fibroblasts (CTFR$^+$). Segregation of GFP intensity showed the highest CTFR retention in GFP^{hi} fibroblasts, followed by GFP^{lo} and GFP$^-$ (Fig. 2, E to I). We applied this technique to adult human lung fibroblasts (HLFs) freshly isolated from deceased donors without prior history of lung disease (*20*). This confirmed the presence of CTFR-retaining HLFs that were enriched for *p16*^{INK4a} expression, along with other characteristics of senescent cells (fig. S3, G to J), revealing a technique to isolate senescent cells from human tissues.

In a quiescent organ, cell cycle arrest can be attributed to either senescence or quiescence. Such cells differ in their response to a proliferative stimulus. Therefore, evaluating senescence requires the introduction of a proliferative stimulus to cells in vivo. To add a mitogenic stimulus to the lung, which normally exhibits very low cell turnover (*21*), we administered naphthalene to injure the lung of INKBRITE animals, followed by continuous BrdU administration. Naphthalene induces damage to the airway epithelium accompanied by an increase in the proliferation of airway stem cells and fibroblasts during repair within 2 weeks of injury (*22*, *23*). Here, naphthalene injury increased GFP$^+$ cells in the lung (fig. S3K), but this appeared to result from an increase in GFP$^+$ immune cells, because the fraction of GFP$^-$, GFP^{lo}, and GFP^{hi} fibroblasts remained constant (fig. S3B) and the percentage of GFP$^+$ immune cells increased with injury (fig. S3L), with a skewing toward myeloid lineages in GFP^{hi} immune cells (fig. S3M). There was minimal BrdU incorporation of PDGFRα$^+$ fibroblasts that were GFP$^+$ or GFP$^-$ over 2 weeks without injury. However, naphthalene injury was accompanied by an increase in BrdU incoporation that was almost exclusively in the *p16*$^{INK4a-}$ fibroblasts, with little to no BrdU incorporation in the *p16*$^{INK4a+}$ fibroblasts (Fig. 2, J to L). To compare proliferative changes on the basis of GFP intensity, we repeated the BrdU experiment with EdU, which allows for FACS quantification concurrent with GFP measurement. There was no difference in EdU uptake between groups after 2 weeks of EdU administration in vehicle-treated controls, but a significant difference appeared when the lung was injured with naphthalene, with the least EdU incorporation in GFP^{hi} fibroblasts (Fig. 2, M and N).

To evaluate the propensity of *p16*$^{INK4a+}$ fibroblasts to undergo cell cycle arrest as *p16*^{INK4a} expression increases with age, we isolated GFP$^+$ lung fibroblasts of animals at 2m, 12m, and 25m for CTFR treatment and cell culture. We observed an age-dependent increase in the fraction of arrested (CTFR-retaining) fibroblasts in proliferative conditions (Fig. 2O). These experiments suggest that a physiologic increase in *p16*^{INK4a} expression correlates with increased senescent characteristics in vivo during organ aging.

p16^{INK4a+} fibroblasts develop a secretory phenotype after epithelial injury

To profile the transcriptomic signature of *p16*$^{INK4a+}$ fibroblasts, we performed bulk RNA sequencing on sorted GFP$^+$ or GFP$^-$ and PDGFRα$^+$ fibroblasts from uninjured [0 days postinjury (0 dpi)] and naphthalene-injured (7, 14, and 28 dpi) INKBRITE lungs (Fig. 3A). Differentially expressed gene (DEG) analysis (*p16*$^{INK4a+}$ versus *p16*$^{INK4a-}$) showed that *Cdkn2a*, the gene that encodes *p16*^{INK4a}, was highly up-regulated at all time points in the *p16*$^{INK4a+}$ fibroblasts (Fig. 3B and fig. S4A). A key feature of senescent cells is the ability to up-regulate a senescence-associated secretory phenotype (SASP) to modify the extracellular environment (*24*). To identify potential SASP factors in *p16*$^{INK4a+}$ fibroblasts, we compared DEGs overexpressed in *p16*$^{INK4a+}$ and *p16*$^{INK4a-}$ fibroblasts ($P < 0.05$) with a list of SASP factors previously identified in vitro (*24*). Gene-overlap analysis showed a significant time-dependent increase in SASP factor expression in *p16*$^{INK4a+}$ but not

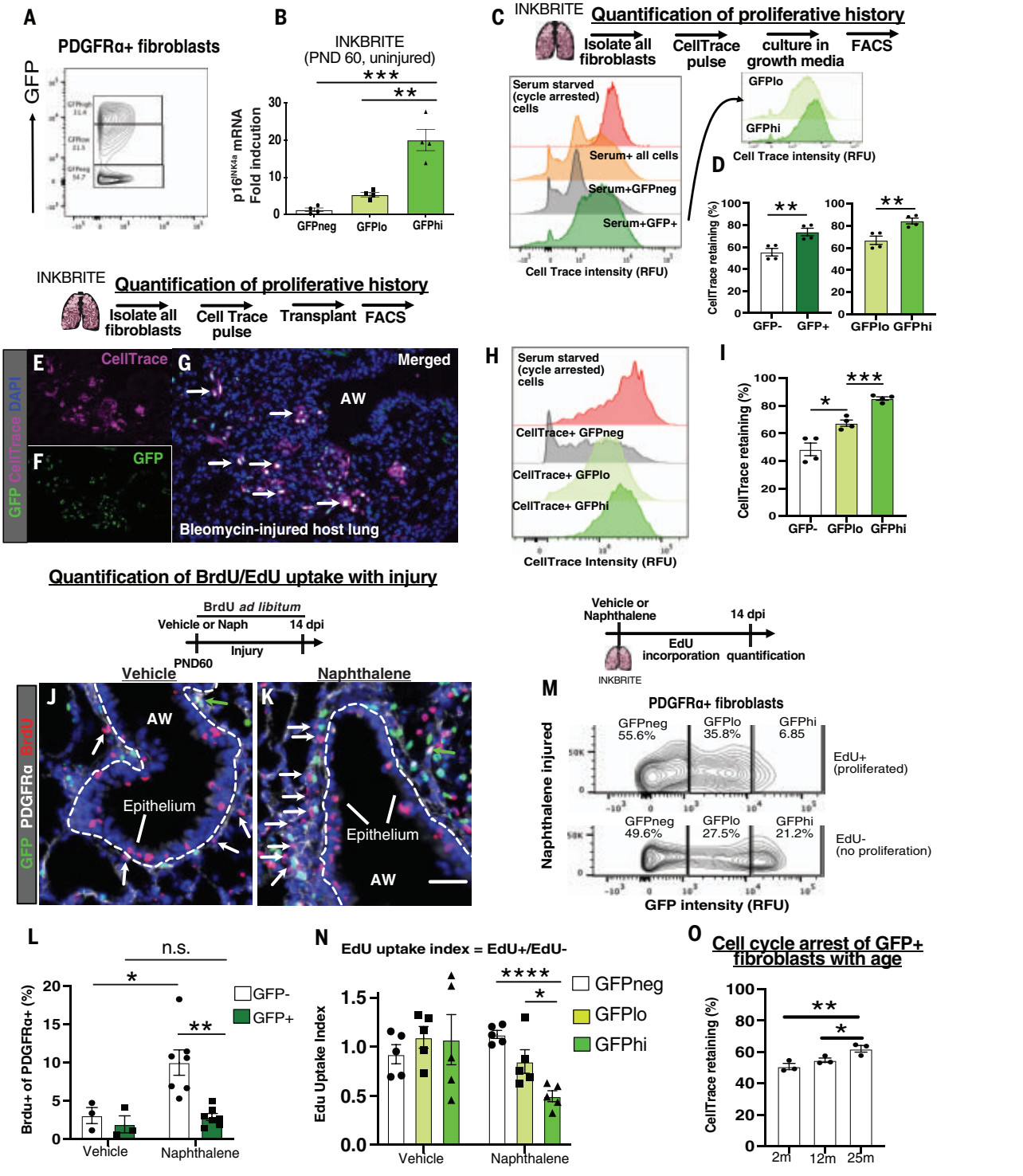

Fig. 2. Range of *p16*^{INK4a} expression correlates with proliferative cell cycle arrest. (**A**) Sorting strategy for GFP$^{hi/lo/-}$ fibroblasts from uninjured INKBRITE lungs using GFP fluorescence intensity. (**B**) qRT-PCR of *p16*^{INK4a} transcript in GFP$^{hi/lo/-}$ populations (n = 4, n > 2 experiments). (**C**) Histogram of CTFR intensity in INKBRITE lung fibroblasts. (**D**) Quantification of percent cell cycle arrest based on the percentage of cells with CTFR intensity of serum-deprived cells (n = 4, n > 2 experiments). (**E** to **I**) Histology, FACS, and quantification of CTFR^{+} transplanted INKBRITE fibroblasts into bleomycin-injured NGS mice (n = 4, n = 2 experiments). (**J** to **L**) IHC and quantification of BrdU incorporation into PDGFRα^{+} and GFP^{-} cells (white arrows) or PDGFRα^{+} and GFP^{+} cells (green arrows) in vehicle or naphthalene-injured (14 dpi) lungs (n = 3 for vehicle, n = 6 for naphthalene). (**M**) GFP intensity distribution of EdU^{+} and EdU^{-} fibroblasts isolated from naphthalene-injured lungs (14 dpi). (**N**) EdU uptake index (%EdU^{+}/%EdU^{-}) of GFP$^{hi/lo/-}$ fibroblast populations in vehicle- and naphthalene-treated (14 dpi) fibroblasts (n = 5 per condition, n = 2 experiments). (**O**) CTFR retention in GFP^{+} fibroblasts of 2m, 12m, and 25m INKBRITE lungs (n = 3 per time point, n = 2 experiments). Each point in the graph represents one animal with mean ± SEM. All P values were determined by one-tailed t test or two-way ANOVA when applicable. *P < 0.05, **P < 0.01, ***P < 0.001, ****P < 0.0001.

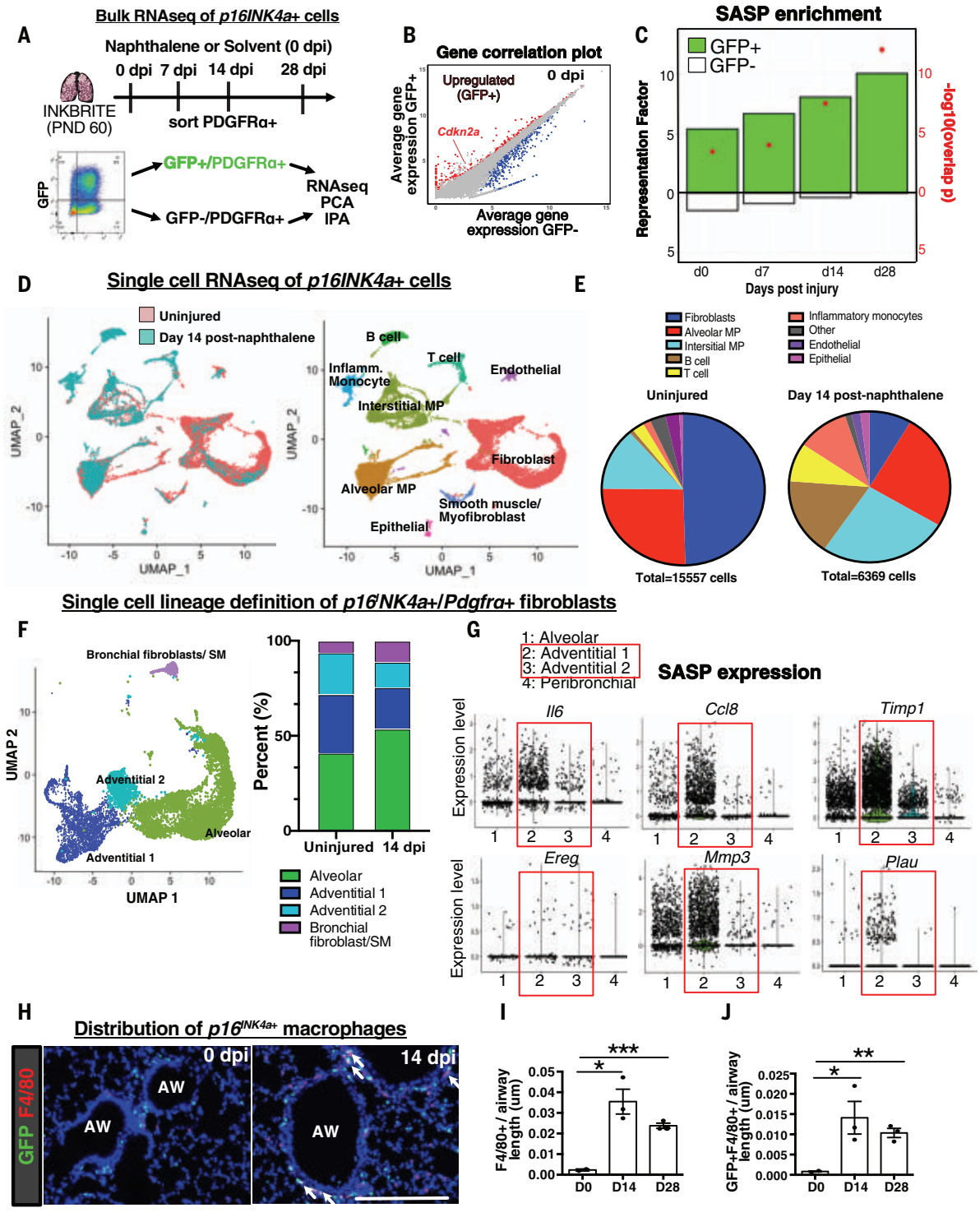

Fig. 3. scRNAseq and bulk RNA-sequencing analysis of $p16^{INK4a+}$ cells in the lung. (**A**) Bulk RNA-sequencing analysis of $p16^{INK4a+}$ and $p16^{INK4a-}$ fibroblasts during homeostasis (0 dpi) and injury (7, 14, and 28 dpi) (n = 3 animals per time point). (**B**) Gene correlation plot showing *Cdkn2a* expression. (**C**) Hypergeometric probability test for enrichment of DEGs between GFP^+ and GFP^- fibroblasts at each time point with SASP genes as quantified by representation factor and P value. (**D** and **E**) scRNAseq of all $p16^{INK4a+}$ cells in 0 and 14 dpi INKBRITE lungs. (**F**) Clustering of $p16^{INK4a+}$ fibroblasts into distinct subsets in 0 and 14 dpi INKBRITE lungs. (**G**) SASP gene expression at the single-cell level in the four-fibroblast subsets. (**H** to **J**) Histologic analysis of $F4/80^+$ and GFP^+ and $F4/80^+$ macrophage/monocyte population in 0 and 14 dpi INKBRITE lungs (0, 14, and 28 dpi, n = 3). Each point in the graph represents one animal with mean ± SEM. All P values were determined by one-tailed t test. $^*P < 0.05$, $^{**}P < 0.01$, $^{***}P < 0.001$, $^{****}P < 0.0001$.

$p16^{INK4a-}$ fibroblasts after injury (Fig. 3C; fig. S4, B and C; and table S1).

To assess the heterogeneity of $p16^{INK4a+}$ cells in the lung, we performed single-cell RNA sequencing (scRNAseq) on sorted GFP^+ cells from healthy and naphthalene-injured (14 dpi) adult (2m) INKBRITE lungs by droplet capture (10X Chromium Single Cell 3′v2). Cluster analysis confirmed our flow cytometry and immunohistochemistry (IHC) analysis, showing that most GFP^+ cells are *Pdgfra*$^+$ fibroblasts and *Ptprc*$^+$ ($CD45^+$) immune cells (Fig. 3, D and E). scRNAseq of GFP^- cells in age-matched lungs (2m) showed fewer fibroblasts and more T cells in the immune population compared with GFP^+ cells (fig. S5A). Airway injury with naphthalene increased the fraction of immune $p16^{INK4a+}$ cells relative to $p16^{INK4a+}$ fibroblasts. Notably increased were infiltrating immune subsets associated with tissue injury, such as inflammatory monocytes and monocyte-derived interstitial macrophages (*25*) (Fig. 3, D and E). Further clustering of the fibroblasts according to previously annotated markers (*18*) confirmed our FACS analysis, showing that most $p16^{INK4a+}$ fibroblasts cluster within fibroblasts with adventitial markers (*Pi16* and *Adh7*) predominantly found in connective tissue around the blood vessel, and the cluster distribution did not change significantly with injury or age (Fig. 3F and fig. S5, B and C). SASP factors that were up-regulated in $p16^{INK4a+}$ fibroblasts with injury, as shown by bulk RNAseq (Fig. 3C and fig. S4B), were expressed in the adventitial fibroblasts (Fig. 3G) that are found in various barrier organs (*26*). This suggests that $p16^{INK4a+}$ adventitial fibroblasts respond to airway injury by increasing SASP. IHC of the airway confirmed the scRNAseq finding that infiltrating immune cells such as $p16^{INK4a+}$ macrophages with interstitial subtype marker (*Adgre1* encoding the F4/80 antigen) are increased in the adventitial space adjacent to the airway and blood vessels after injury (Fig. 3, H to J). Finally, scRNAseq analysis of $p16^{INK4a+}$ cells in aged INKBRITE lungs (30m) showed an increased number of cells from myeloid lineages (e.g., monocytes and interstitial macrophages) similar to those seen in young, injured lungs (fig. S5C). This suggests that an increase in the number of $p16^{INK4a+}$ myeloid cells is a feature of both tissue injury and aging in the lung.

$p16^{INK4a+}$ fibroblasts promote epithelial stem cell regeneration

$p16^{INK4a+}$ fibroblasts had increased SASP after epithelial injury that might alter epithelial stem cell behavior. To determine the effect of $p16^{INK4a+}$ fibroblasts on airway stem cells responding to injury, we co-cultured airway stem cells with GFP^{hi}, GFP^{lo}, or GFP^- fibroblasts ($PDGFR\alpha^+$) isolated from uninjured (0 dpi) or naphthalene-injured (14 dpi) INKBRITE lungs in a three-dimensional (3D) cell culture. When cultured with *Scgb1a1*$^+$ airway stem cells (isolated from a *Scgb1a1* reporter mouse), both uninjured GFP^{hi} and GFP^{lo} fibroblasts increased the number of *Scgb1a1*$^+$ organoids more than GFP^- fibroblasts did (Fig. 4, A and B). Naphthalene injury further increased the capacity of both GFP^{hi} and GFP^{lo} fibroblasts to increase the number of *Scgb1a1*$^+$ organoids relative to GFP^- fibroblasts (Fig. 4, A and B). Naphthalene-injured GFP^{hi} and GFP^{lo} fibroblasts also increased the size of the organoids relative to GFP^- fibroblasts (Fig. 4C). To determine whether $p16^{INK4a}$ expression is associated with an enhanced ability to promote epithelial growth in human lung, we isolated $p16^{INK4a\text{-}hi}$ and $p16^{INK4a\text{-}lo}$ HLFs on the basis of CTFR retention on FACS (fig. S3G) and co-cultured them with airway stem cells isolated from donor lungs (*27*). $p16^{INK4a\text{-}hi}$ HLFs enhanced airway stem cell organoid growth (fig. S6, A and B), demonstrating that the capacity for $p16^{INK4a+}$ fibroblasts to promote epithelial stem cell growth is conserved in mouse and human lungs.

One of the genes found to be up-regulated in $p16^{INK4a+}$ fibroblasts after injury is *Ereg*, which encodes epiregulin (fig. S4A), a growth factor that signals through the epidermal growth factor receptor (EGFR) (*28*–*30*). qRT-PCR analysis of sorted lung fibroblasts at 0 and 14 dpi confirmed that the *Ereg* transcript was more abundant in $p16^{INK4a+}$ fibroblasts after injury than in $p16^{INK4a-}$ fibroblasts at 14 dpi and $p16^{INK4a+}$ fibroblasts at 0 dpi (Fig. 4D). scRNAseq analysis of *Ereg* expression demonstrated preferential expression in the adventitial fibroblasts (Fig. 3G) and alveolar macrophages (fig. S6C). To determine the effect of fibroblast-derived EREG on club cell growth, we isolated fibroblasts from naphthalene-injured lungs (14 dpi) of Ereg-null [knockout (KO)] and WT animals for the 3D organoid assay, which showed a reduced capacity of the *Ereg* KO fibroblasts to promote airway stem cell growth (fig. S6, D and E). Furthermore, organoids cultured with *Ereg* KO fibroblasts exhibited reduced phosphorylated extracellular signal-related kinase (pERK), a readout of EGFR activation (*31*) (fig. S6F). Although Ereg KO animals had a normal number of $SCGB1A1^+$ cells in the airway before injury (fig. S6G), they exhibited a significant deficit in $SCGB1A1^+$ cell regeneration in response to naphthalene in vivo (Fig. 4, E and F).

To determine whether $p16^{INK4a+}$ cells are required for airway stem cell regeneration in vivo, we treated INKBRITE animals with naphthalene and then the senolytics dasatnib and quercetin (DQ), a combination that kills senescent cells (*32*). DQ treatment reduced the number of GFP^+ cells in the lung after naphthalene injury (Fig. 4, G to I). DQ-treated lungs had a significant deficit in $SCGB1A1^+$ cell regeneration (Fig. 4, J to L). Furthermore, pERK was less abundant in $SCGB1A1^+$ airway stem cells in DQ-treated lungs (Fig. 4, M to O). These experiments demonstrated that $p16^{INK4a+}$ fibroblasts adjacent to airway stem cells promote epithelial regeneration after injury by secreting a growth factor that enhances airway barrier repair.

$p16^{INK4a+}$ fibroblasts sense inflammatory stimuli to augment epithelial repair

Ingenuity pathway analysis of the DEGs in $p16^{INK4a+}$ fibroblasts demonstrated a time-dependent activation of upstream regulators associated with nuclear factor κB (NF-κB) signaling (fig. S7A). NF-κB responds to inflammatory stimuli to regulate SASP (*33*, *34*). To determine whether $p16^{INK4a+}$ fibroblasts can directly sense inflammatory stimuli, we examined NF-κB activation in $p16^{INK4a+}$ and $p16^{INK4a-}$ fibroblasts in response to lipopolysaccharide (LPS), a bacterial wall component. There was an increase in baseline nuclear localization of p65/RelA, a component of the NF-κB transcriptional complex, in live sorted and unstimulated $p16^{INK4a+}$ fibroblasts compared with $p16^{INK4a-}$ fibroblasts from uninjured INKBRITE lungs (Fig. 5, A and B). Upon LPS induction in vitro, there was a further increase in the nuclear localization of p65/RelA in $p16^{INK4a+}$ fibroblasts (Fig. 5, A and B). Examining the transcriptional response of GFP^{hi}, GFP^{lo}, and GFP^- fibroblasts to LPS stimulation in vitro, we found that many of the SASP factors in $p16^{INK4a+}$ fibroblasts were more abundantly expressed in the GFP^{hi} subset than in GFP^{lo} and GFP^- (Fig. 5C). Similar to murine $p16^{INK4a\text{-}hi}$ fibroblasts, $p16^{INK4a\text{-}hi}$ HLFs also demonstrated increased expression of SASP factors such as *EREG* and interleukin-6 (*IL6*) in response to LPS (fig. S7B). To test the ability of $p16^{INK4a+}$ fibroblasts to respond to LPS in vivo, we administered LPS by intranasal inhalation, which promotes an inflammatory response that mimics gram-negative bacterial infection (*35*), into INKBRITE animals and isolated GFP^+ and GFP^- fibroblasts at 3 dpi for the 3D organoid assay. The 3D airway stem cell organoid growth was enhanced when cultured with $p16^{INK4a+}$ fibroblasts from LPS-treated lungs, and this was attenuated with the NF-κB inhibitor BAY11-7082 (Fig. 5, D and E). qRT-PCR analysis of $p16^{INK4a+}$ fibroblasts isolated from LPS-treated lungs demonstrated a significant increase in *Ereg* expression (fig. S7C).

To define the potential source and identity of NF-κB activators during tissue repair, we performed an interactome analysis (NicheNet) of our scRNAseq of $p16^{INK4a+}$ cells to evaluate potential ligand-receptor interactions (*36*). We found that the IL-1 family cytokines were particularly enriched in monocytes and monocyte-derived interstitial macrophages (Fig. 5, F and

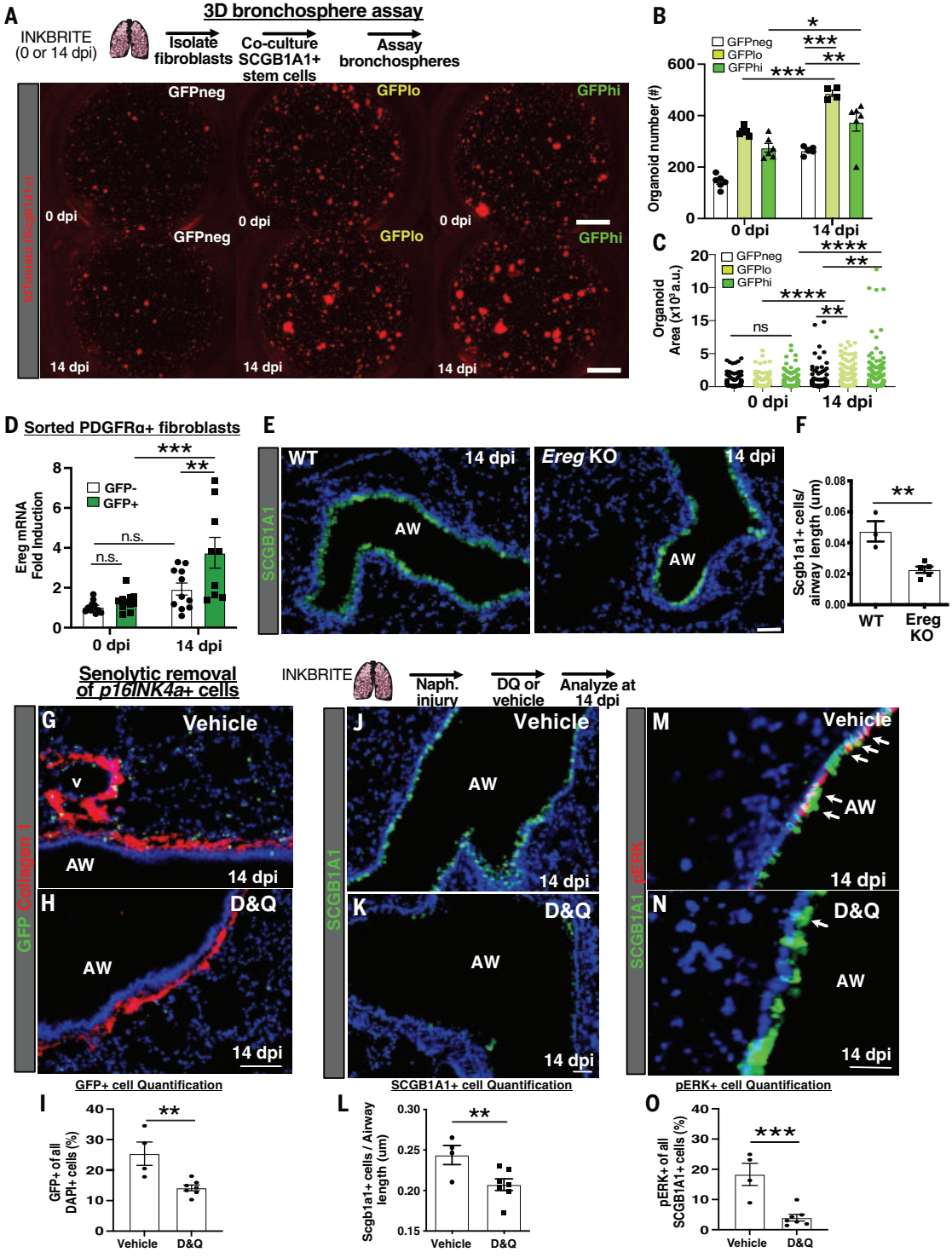

Fig. 4. Injured *p16*$^{INK4a+}$ fibroblasts enhance epithelial progenitor proliferation ex vivo. (**A**) 3D organoid assay combining uninjured *Scgb1a1*$^{+}$ airway stem cells (tdTomato^{+}) with *p16*$^{INK4ahi/lo/-}$ fibroblasts isolated from INKBRITE lungs at 0 or 14 dpi. (**B** and **C**) Quantification of *Scgb1a1*$^{+}$ organoid numbers (B) and size (C) (n = 3 triplicate wells per condition, n > 2 experiments). (**D**) qRT-PCR of *Ereg* on sorted GFP^{+} or GFP^{-} fibroblasts from INKBRITE lungs at 0 or 14 dpi (n = 9 per time point, n > 2 experiments). (**E** and **F**) Histologic quantification of airway stem cell regeneration in *Ereg* KO versus WT lungs at 14 dpi (n = 4 per genotype, n = 2 experiments). IHC quantification is shown for GFP^{+} cells (**G** to **I**), SCGB1A1^{+} cells (**J** to **L**), and pERK^{+}SCGB1A1^{+} cells (**M** to **O**) in vehicle- versus DQ-treated INKBRITE lungs after naphthalene injury (14 dpi, n = 4 vehicle; n = 7 DQ; n = 2 experiments). Each point in the graph represents one technical replicate (bronchosphere) or one animal with mean ± SEM. All P values were determined by one-tailed t test or two-way ANOVA when applicable. *P < 0.05, **P < 0.01, ***P < 0.001, ****P < 0.0001.

G), which were found to be increased in the adventitial space after injury (Fig. 3, H to I), corresponding to an enrichment of *Il1r1* (the receptor for IL-1A and IL-1B) in *p16*$^{INK4a+}$ fibroblasts (Fig. 5, F and G). To test the ability of monocytes to directly activate *p16*$^{INK4a+}$ fibroblasts, we cultured inflammatory monocytes with lung fibroblasts isolated from INKBRITE lungs (plus macrophage colony-stimulating factor to maintain monocyte survival). After 24 hours in co-culture, the monocytes increased the abundance of SASP factors including *Ereg*, and the expression was highest in GFP^{hi} fibroblasts (fig. S7D). Induction with recombinant IL-1B produced an almost identical phenotype in INKBRITE lung fibroblasts (fig. S7E). Finally, to test the ability of *p16*$^{INK4a+}$ fibroblasts to sense IL-1B in vivo, we administered recombinant IL-1B to the INKBRITE lung for the 3D organoid assay. Similar to LPS injury, exposure to IL-1B in vivo primed the isolated *p16*$^{INK4a+}$ fibroblasts to enhance airway stem cell organoid formation compared with *p16*$^{INK4a-}$ fibroblasts (Fig. 5, H and I). These data highlight a role for *p16*$^{INK4a+}$ in sensing and responding to inflammatory signals during injury through NF-κB, which

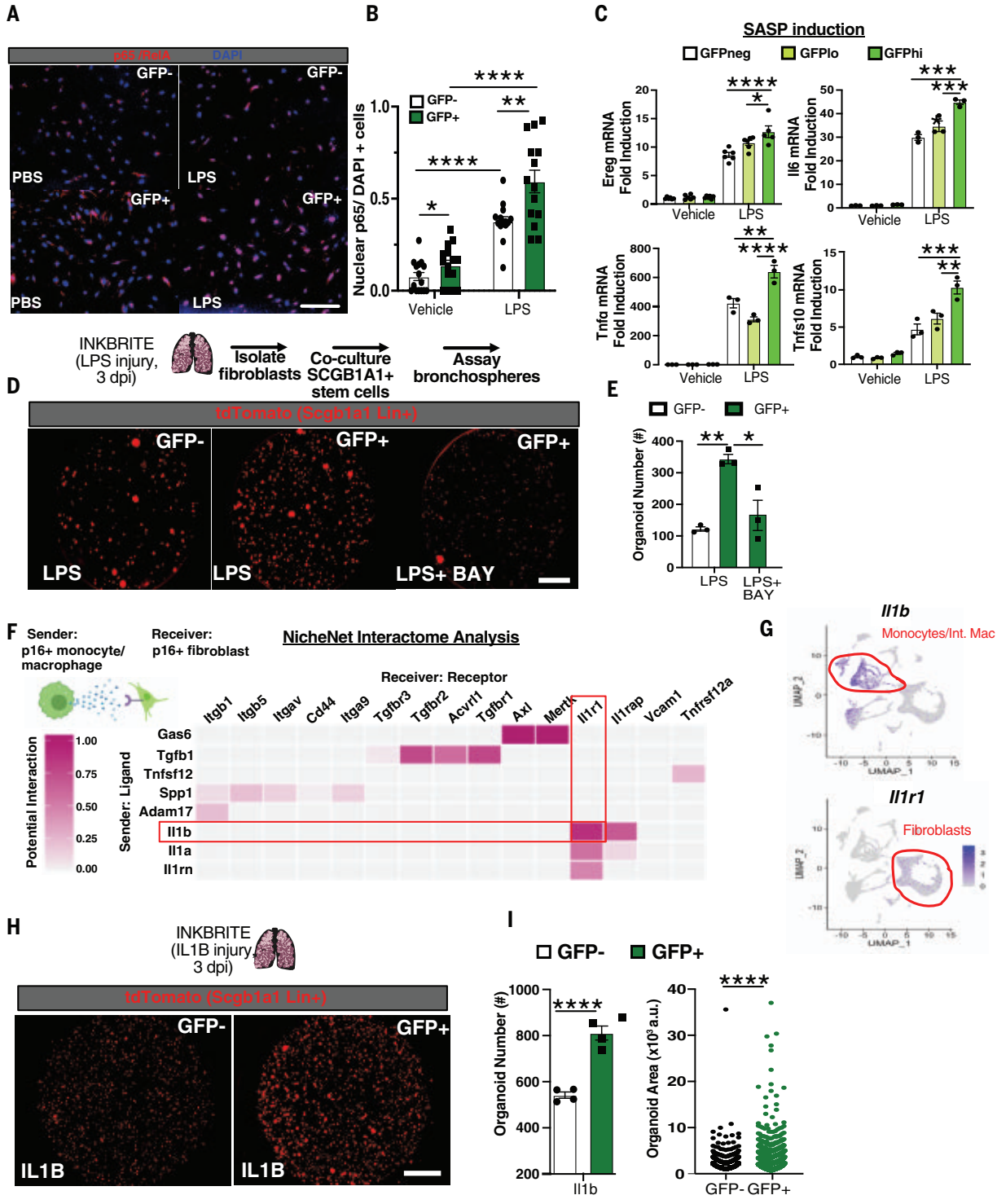

Fig. 5. *p16*$^{INK4a+}$ fibroblasts sense inflammatory stimuli to augment epithelial regeneration. (**A** and **B**) Quantification of nuclear p65/RelA in *p16*$^{INK4a+}$ or *p16*$^{INK4a-}$ fibroblasts from uninjured INKBRITE lungs (PND60) after 1 hour of vehicle or LPS treatment (n = 3 wells, n = 14 to 15 images per condition). (**C**) SASP gene expression in *p16*$^{INK4ahi/lo/-}$ fibroblasts from uninjured INKBRITE lungs after 6 hours of phosphate-buffered saline (PBS) or LPS treatment (n = 3 wells per condition, n = 2 experiments). (**D** and **E**) *Scgb1a1*$^{+}$ 3D organoid assay with *p16*$^{INK4a+}$ or *p16*$^{INK4a-}$ fibroblasts isolated from LPS-injured INKBRITE lungs and treated with vehicle or BAY11-7082 (n = 3 wells per condition, n = 2 experiments). (**F**) NicheNet interactome analysis of *p16*$^{INK4a+}$ fibroblasts and monocytes or interstitial monocytes from scRNAseq of injured INKBRITE lungs (14 dpi). (**G**) Expression of *Il1b* and *Il1r1* in *p16*$^{INK4a+}$ cells in the lung. (**H** and **I**) Quantification of *Scgb1a1*$^{+}$ organoids co-cultured with *p16*$^{INK4a+}$ or *p16*$^{INK4a-}$ fibroblasts from IL-1B–treated INKBRITE lungs (n = 4 wells per condition). Scale bars, 100 μm. Each point in the graph represents one triplicate well or distinct image with mean ± SEM. All P values were determined by one-tailed t test or two-way ANOVA when applicable. *P < 0.05, **P < 0.01, ***P < 0.001, ****P < 0.0001. Scale bars, 100 μm.

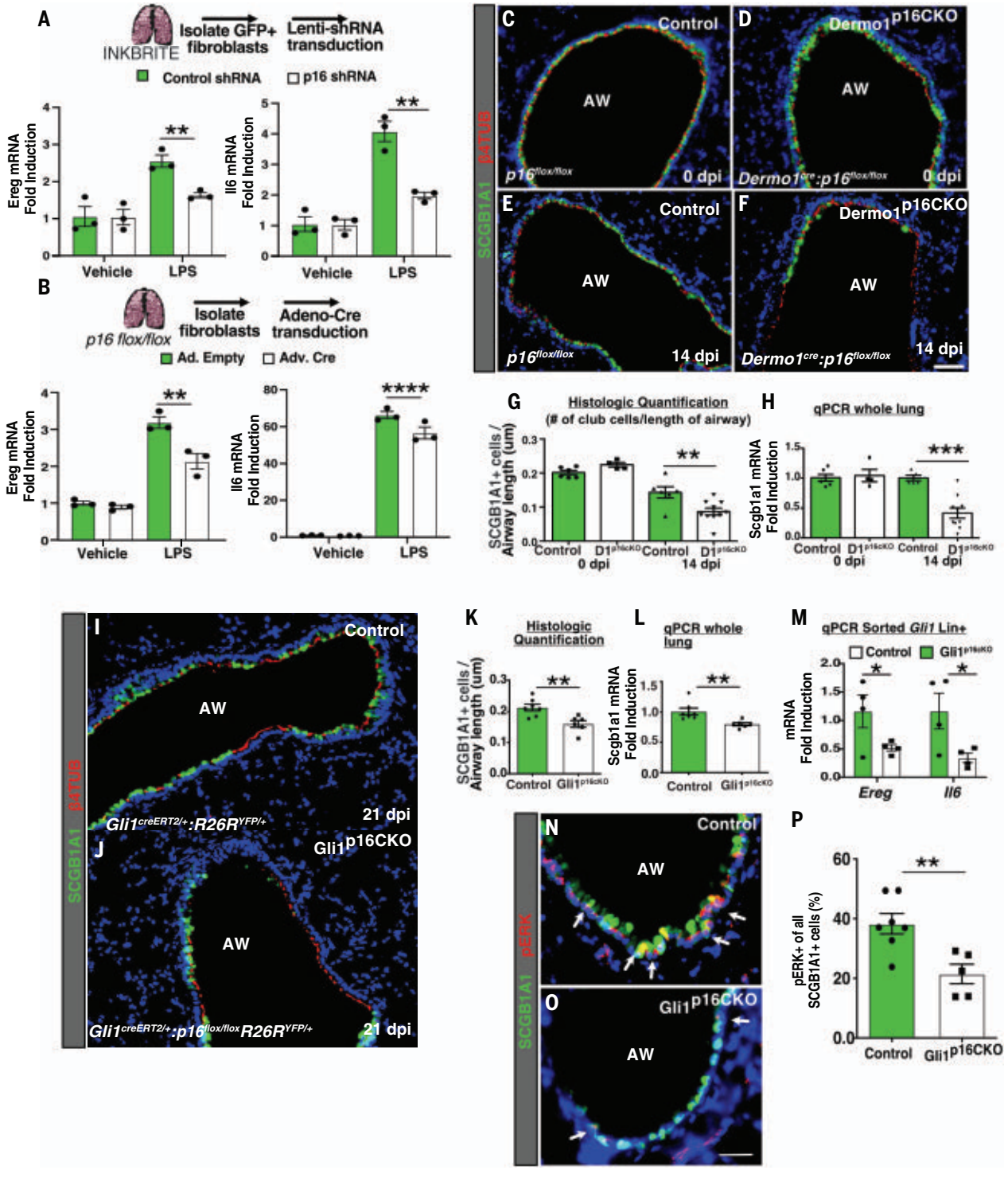

Fig. 6. Mesenchymal *p16*^{INK4a} expression is required for epithelial regeneration in vivo. (**A**) qRT-PCR of *Ereg* and *Il6* in control or *p16*^{INK4a} shRNA-treated GFP^{+} fibroblasts after stimulation with vehicle or LPS for 6 hours (n = 3 wells per condition, n = 2 experiments). (**B**) qRT-PCR of *Ereg* and *Il6* in adeno-control– or adeno-Cre–treated *p16*$^{flox/flox}$ fibroblasts after stimulation with vehicle or LPS (n = 3 wells per condition, n > 2 experiments). (**C** to **G**) Images and quantification of the airways of control and *Dermo1*^{p16CKO} lungs with and without naphthalene injury. (**H**) qRT-PCR of *Scgb1a1* of whole-lung RNA (uninjured: n = 6 control, n = 5 *Dermo1*^{p16CKO}; injured: n = 6 control, n = 10 *Dermo1*^{p16CKO}; n = 2 experiments). (**I** to **L**) Images and histological quantification of SCGB1A1 club cells and qRT-PCR of *Scgb1a1* in control and *Gli1*^{p16CKO} lungs after naphthalene injury (n = 7 control, n = 6 *Gli1*^{p16CKO}). (**M**) qRT-PCR of *Ereg* and *Il6* of sorted *Gli1* Lin^{+} cells after naphthalene injury (n = 4 control; n = 4 *Gli1*^{p16CKO}). (**N** to **P**) Images and histological quantification of pERK^{+} and SCGB1A1^{+} cells in control and *Gli1*^{p16CKO} lungs after naphthalene injury (n = 7 control, n = 6 *Gli1*^{p16CKO}). Scale bars, 100 μm. Each point in the graph represents one animal with mean ± SEM. All P values were determined by one-tailed t test or two-way ANOVA when applicable. *P < 0.05, **P < 0.01, ***P < 0.001, ****P < 0.0001.

regulates a secretory program that enhances stem cell repair.

Modulation of *p16*^{INK4a} in fibroblasts alters epithelial regeneration

To determine whether the modulation of *p16*^{INK4a} expression alters SASP factors that induce epithelial proliferation, we designed a lentivirus expressing short hairpin RNA (shRNA) targeting *p16*^{INK4a} (Lenti-shp16), and infected GFP$^+$ fibroblasts isolated from INKBRITE lungs. Infection of Lenti-shp16 suppressed the expression of *Ereg* and *Il6* in GFP$^+$ fibroblasts after LPS stimulation (Fig. 6A), increased fibroblast proliferation (fig. S8A), and suppressed *p16*^{INK4a} transcript (fig. S8B). We also knocked down *p16*^{INK4a} by treating lung fibroblasts isolated from *p16*$^{flox/flox}$ animals with adenovirus expressing Cre recombinase (adeno-cre) followed by LPS stimulation, which demonstrated a similar attenuation of *Ereg* and *Il6* expression after LPS treatment (Fig. 6B). Conversely, we designed a dual lentiviral system (Lenti-tTS/rTTA + Lenti-TRE-p16-2A-tdTomato) to overexpress *p16*^{INK4a} in GFP$^-$ fibroblasts in a doxycycline-dependent manner, which did not change baseline SASP expression but did increase the expression of *Ereg* and other NF-κB–responsive genes in response to LPS (fig. S8C). To determine whether fibroblast-specific *p16*^{INK4a} expression is necessary for epithelial regeneration in vivo, we deleted *p16*^{INK4a} with a mesenchymal-specific Cre-driver (*Dermo1*$^{Cre/+}$) (*37*). Mesenchymal-specific deletion of *p16*^{INKa} (*Dermo1*$^{Cre/+}$:*p16*$^{flox/flox}$, referred to as *Dermo1*^{p16CKO}) did not alter the gross morphology of the uninjured adult lung (Fig. 6, C and D). However, after injury with naphthalene, *Dermo1*^{p16CKO} airways demonstrated reduced epithelial repair, as quantified by the number of SCGB1A1$^+$ club cells present and by qRT-PCR of *Scgb1a1* transcripts in the whole lung (Fig. 6, E to H). Airway injury in *Dermo1*^{p16CKO} also resulted in increased airway fibrosis, as demonstrated by increased fibrotic markers and collagen deposition along the airway (fig. S8, D to F). To confirm the epithelial-regenerative defect, we also deleted *p16*^{INK4a} with *Gli1*^{CreERT2} to specifically target *Gli1*$^+$ adventitial fibroblasts that are enriched for GFP^{hi} fibroblasts surrounding the airway (fig. S8G to I). Tamoxifen treatment of *Gli1*$^{CreERT2/+}$:*p16*$^{flox/flox}$:*R26R*$^{YFP/+}$ (referred to as *Gli1*^{p16CKO}) animals, followed by naphthalene injury, significantly attenuated SCGB1A1$^+$ airway stem cell recovery compared with controls (*Gli1*$^{CreERT2/+}$:*R26R*$^{YFP/+}$) (Fig. 6, I to L). Analysis of *Gli1* lineage–traced (*Gli1* Lin$^+$) fibroblasts in vivo demonstrated an increase in BrdU incorporation after inducible *p16*^{INK4a} deletion and injury (fig. S8, J to M) and a reduction in *Ereg* and *Il6* expression (Fig. 6M) that was similar to that observed with in vitro knockdown of *p16*^{INKa}. The regenerating airway epithelium of *Gli1*^{p16CKO} animals demonstrated a significant reduction in pERK$^+$ airway stem cells (Fig. 6, N to P). These data show that *p16*^{INKa} is required to maintain cell cycle arrest and promote the SASP in response to inflammation in senescent fibroblasts in vivo, and its absence disrupts mesenchymal signals to progenitors required for the repair of the barrier epithelia.

Discussion

We generated an ultrasensitive reporter mouse to isolate and localize *p16*$^{INK4a+}$ cells in tissues. We focused on *p16*^{INK4a} because of the reported benefits of eliminating *p16*$^{INK4a+}$ cells from aging tissues. Proposals that *p16*$^{INK4a+}$ cells are in a rigid cellular state may be inaccurate, because we found that some *p16*$^{INK4a+}$ cells remained responsive to physiological cues and dynamically increased their secretory capacity in the reparative niche to enhance stem cell repair. We also show that physiological heterogeneity exists within a given *p16*$^{INK4a+}$ cellular population in vivo, because not all *p16*$^{INK4a+}$ cells exhibited uniform senescent characteristics. Thus, not all *p16*$^{INK4a+}$ cells may be senescent, and expression of other biomarkers (e.g., *Cdkn1a* and *Cdkn1b*) may contribute to senescent characteristics in vivo. However, we have demonstrated that cells within a range of *p16*^{INK4a} expression levels can account for this heterogeneity in vivo, with a direct correlation of *p16*^{INK4a} level with cell cycle arrest, response to inflammation, and SASP. Furthermore, we have shown that *p16*^{INK4a} expression increases throughout the life span of *p16*$^{INK4a+}$ fibroblasts.

Our data show that *p16*$^{INK4a+}$ fibroblasts, some with senescent characteristics, arise normally during postnatal tissue maturation in the basement membrane, persist within the stem cell niche, and are activated upon barrier injury to promote epithelial repair (fig. S9). *p16*$^{INK4a+}$ fibroblasts can sense the presence of infiltrating immune cells that appear during tissue injury and rapidly integrate inflammatory stimuli through NF-κB activation to induce SASP to restore barrier integrity. We uncovered EREG as a SASP component, the induction of which is regulated by *p16*^{INK4a} to promote regional repair in the airway stem cell niche, but there are likely to be many SASP factors that function in other regional stem cell niches that are specific to the requirement of the resident stem cell. The enrichment of *p16*^{INK4a} expression in the adventitial fibroblast subset suggests a cross-tissue role, because *p16*$^{INK4a+}$ adventitial fibroblasts can serve as tissue sentinels at the barrier interface across multiple organs.

REFERENCES AND NOTES

1. F. Zindy, D. E. Quelle, M. F. Roussel, C. J. Sherr, *Oncogene* **15**, 203–211 (1997).
2. V. Gorgoulis *et al.*, *Cell* **179**, 813–827 (2019).
3. S. Takeuchi *et al.*, *Cancer Res.* **70**, 9381–9390 (2010).
4. C. E. Burd *et al.*, *Cell* **152**, 340–351 (2013).
5. M. Demaria *et al.*, *Dev. Cell* **31**, 722–733 (2014).
6. D. J. Baker *et al.*, *Nature* **479**, 232–236 (2011).
7. D. J. Baker *et al.*, *Nature* **530**, 184–189 (2016).
8. J. Chang *et al.*, *Nat. Med.* **22**, 78–83 (2016).
9. B. G. Childs *et al.*, *Science* **354**, 472–477 (2016).
10. M. P. Baar *et al.*, *Cell* **169**, 132–147.e16 (2017).
11. O. H. Jeon *et al.*, *Nat. Med.* **23**, 775–781 (2017).
12. T. J. Bussian *et al.*, *Nature* **562**, 578–582 (2018).
13. J. M. van Deursen, *Science* **364**, 636–637 (2019).
14. L. Grosse *et al.*, *Cell Metab.* **32**, 87–99.e6 (2020).
15. S. Omori *et al.*, *Cell Metab.* **32**, 814–828.e6 (2020).
16. M. Scudellari, *Nature* **550**, 448–450 (2017).
17. P. A. Benn, *Am. J. Hum. Genet.* **28**, 465–473 (1976).
18. T. Tsukui *et al.*, *Nat. Commun.* **11**, 1920 (2020).
19. L. Hayflick, P. S. Moorhead, *Exp. Cell Res.* **25**, 585–621 (1961).
20. C. Wang *et al.*, *J. Clin. Invest.* **128**, 4343–4358 (2018).
21. M. C. Basil *et al.*, *Cell Stem Cell* **26**, 482–502 (2020).
22. K. U. Hong, S. D. Reynolds, A. Giangreco, C. M. Hurley, B. R. Stripp, *Am. J. Respir. Cell Mol. Biol.* **24**, 671–681 (2001).
23. T. Peng *et al.*, *Nature* **526**, 578–582 (2015).
24. J. P. Coppé, P. Y. Desprez, A. Krtolica, J. Campisi, *Annu. Rev. Pathol.* **5**, 99–118 (2010).
25. S. Chakarov *et al.*, *Science* **363**, eaau0964 (2019).
26. M. B. Buechler *et al.*, *Nature* **593**, 575–579 (2021).
27. L. R. Bonser *et al.*, *Am. J. Respir. Cell Mol. Biol.* **64**, 308–317 (2021).
28. N. Toyoda, M. J. Berry, J. W. Harney, P. R. Larsen, *J. Biol. Chem.* **270**, 12310–12318 (1995).
29. B. K. Draper, T. Komurasaki, M. K. Davidson, L. B. Nanney, *J. Cell. Biochem.* **89**, 1126–1137 (2003).
30. S. Li *et al.*, *Proc. Natl. Acad. Sci. U.S.A.* **105**, 3539–3544 (2008).
31. M. Iijima, M. Anai, T. Kodama, Y. Shibasaki, *Biochem. Biophys. Res. Commun.* **489**, 83–88 (2017).
32. Y. Zhu *et al.*, *Aging Cell* **14**, 644–658 (2015).
33. R. M. Laberge *et al.*, *Nat. Cell Biol.* **17**, 1049–1061 (2015).
34. Y. Chien *et al.*, *Genes Dev.* **25**, 2125–2136 (2011).
35. D. D. Bannerman, S. E. Goldblum, *Am. J. Physiol. Lung Cell. Mol. Physiol.* **284**, L899–L914 (2003).
36. R. Browaeys, W. Saelens, Y. Saeys, *Nat. Methods* **17**, 159–162 (2020).
37. D. Šošić, J. A. Richardson, K. Yu, D. M. Ornitz, E. N. Olson, *Cell* **112**, 169–180 (2003).

ACKNOWLEDGMENTS

We thank the Parnassus Flow Cytometry Core for assistance with cell sorting for bulk and scRNAseq, Biological Imaging Development Core members, and E. Wan and the Institute for Human Genetics Core for processing of single-cell RNA samples and high-throughput sequencing. **Funding:** This work was supported by the National Institutes of Health (grants DP2AG056034, R01HL142552, and R01HL155622 to T.P.; grant F32HL14226 to N.R.; grant P30DK06372 to P.F.C.C.; and grant P30DK063720 to B.I.D.C.), the Tobacco Related Disease Research Program (New Investigator Award to T.P.), and the Pulmonary Hypertension Association (T.P.). **Author contributions:** T.P. conceived and surpervised the study. N.R., M.K., N.A., J.L., M.C., M.Z., B.H., S.R., C.W., P.M., and I.K. performed the experiments. P.M. visualized the data. M.M., M.N., and Y.J. contributed reagents. T.P. and N.R. acquired funding. T.P. and N.R. wrote the original draft. T.P., D.S., J.C., and N.R. provided editorial comments. **Competing interests:** The authors declare no competing interests. **Data and materials availability:** All data are available in the main text or the supplementary materials. The sequencing data have been deposited in NCBI Gene Expression Omnibus (GEO) under accession number GSE140654. Materials are available upon request to the corresponding author with a signed material transfer agreement.

SUPPLEMENTARY MATERIALS

science.org/doi/10.1126/science.abf3326
Materials and Methods
Figs. S1 to S9
Table S1
MDAR Reproducibility Checklist

Submitted 26 October 2020; resubmitted 3 December 2021
Accepted 14 September 2022
10.1126/science.abf3326

REPORTS

ELECTRON HOLOGRAPHY

Direct identification of the charge state in a single platinum nanoparticle on titanium oxide

Ryotaro Aso[1]*, Hajime Hojo[2], Yoshio Takahashi[3], Tetsuya Akashi[3], Yoshihiro Midoh[4], Fumiaki Ichihashi[3], Hiroshi Nakajima[1], Takehiro Tamaoka[5], Kunio Yubuta[1], Hiroshi Nakanishi[6], Hisahiro Einaga[2], Toshiaki Tanigaki[3], Hiroyuki Shinada[3], Yasukazu Murakami[1,5]*

A goal in the characterization of supported metal catalysts is to achieve particle-by-particle analysis of the charge state strongly correlated with the catalytic activity. Here, we demonstrate the direct identification of the charge state of individual platinum nanoparticles (NPs) supported on titanium dioxide using ultrahigh sensitivity and precision electron holography. Sophisticated phase-shift analysis for the part of the NPs protruding into the vacuum visualized slight potential changes around individual platinum NPs. The analysis revealed the number (only one to six electrons) and sense (positive or negative) of the charge per platinum NP. The underlying mechanism of platinum charging is explained by the work function differences between platinum and titanium dioxide (depending on the orientation relationship and lattice distortion) and by first-principles calculations in terms of the charge transfer processes.

Metal nanoparticles (NPs) supported on oxide surfaces can act as heterogeneous catalysts for fuel chemical production and pollution cleanup (*1*). The catalytic properties can be tuned not only by the geometric structures of the NPs such as size, shape, and composition, but also by their interaction with the oxide support (*1*–*3*), such as through electronic metal–support interactions (EMSIs) (*4*–*7*). Charge transfer from the support can electrically charge the metal NPs, which could affect the adsorption and desorption of molecules onto or off of the catalyst surface through a shift of the *d*-band center (*8*–*11*). Lattice strain can also change the electronic states of catalytic metals (*12*). Thus, it is important to determine both the charge state and distribution on single NPs and to look for any changes in the NP structure and its orientation to the oxide.

Resonance x-ray photoemission has been used to determine the amount of charge transfer across the Pt/CeO_2 interface as ~1 electron/nm^2 (depending on the NP diameter), although this result was the average from many NPs (*13*). Probe microscopy of individual NPs has provided critical information about the catalytically active sites through measurements of the surface structure, surface potential, or both (*14*–*17*). Nonetheless, direct counting of charges remains a challenge. Electron holography, a method related to transmission electron microscopy (TEM), offers an ideal solution to this problem because it can reveal both the structure and the electrostatic potential in individual NPs by measuring the phase shift of an incident electron wave. In conjunction with an improvement in the lateral resolution of TEM during the past two decades (*18*, *19*), electron holography has enabled the detection of weak artificial charging in noncatalytic model specimens such as Si and MgO subjected to electron exposure (*20*, *21*).

However, examining small-scale intrinsic charging in a single supported NP, which requires a short electron exposure time to suppress undesired radiation-induced phenomena, requires further improvements in electron holography. Indeed, the sensitivity during phase analysis depends on the image quality of holograms composed of the interference fringes of electron waves (*22*). To solve this problem, we used several methods, including hologram acquisition with negligible mechanical and electrical disturbances using a sophisticated 1.2-MV atomic-resolution holography microscope (*23*) with an aberration corrector and reduction of the statistical noise using a wavelet hidden Markov model (WHMM) (*24*, *25*). As described below in detail, the holography observations enabled counting of just a few charges responsible for the electric charging in a single supported NP.

We prepared Pt NPs supported on a rutile TiO_2 foil (Pt/TiO_2) using a photoreduction method (see the supplementary materials). Pt/TiO_2 is a typical catalyst system applied to the purification of air and water (*1*). Our specimen contained Pt NPs deposited onto the foil edge composed of TiO_2 (110) facets (fig. S1) that protruded into the vacuum region (Fig. 1). We estimated the average diameter of the Pt NPs to be ~10 nm by measuring 65 individual NPs (fig. S2).

The protrusions provided an ideal geometry in the hologram acquisition and analysis because the electrostatic potential could be observed both outside and inside the Pt NPs (Fig. 1A). A typical electron hologram with a fringe pitch of 0.048 nm (Fig. 1B) enabled a spatial resolution of 0.16 nm in the phase analysis (Fig. 1C). The phase shift within the NP originated mostly from the mean inner potential of the Pt crystal, whereas the contribution from the electric charging must be orders of magnitude smaller. In addition, an additional phase shift caused by dynamical electron scattering made a precise charge measurement at the interior particle region difficult. By contrast, as demonstrated in Fig. 1D, the region outside of the NP (the vacuum region) provided charge-state information that was free from disturbance by the mean inner potential and the dynamical electron scattering. Although the original phase image in Fig. 1D is still noisy, the application of WHMM satisfactorily reduced the noise (Fig. 1E). Thus, in the following discussion, we analyze the phase shift outside of the NP to locate the charges.

Particle-by-particle observations allowed us to observe two distinct charge states of both negatively and positively charged NPs. Figure 2, A and B, shows a TEM image of Pt/TiO_2 and a phase shift in the vacuum region subjected to the noise reduction, respectively. In principle, the observed phase shift can be explained by the contact potential caused by the difference in work function between Pt and TiO_2, which is accompanied by charge transfer. The negative phase shift in the vacuum region (i.e., the decrease in phase toward the NP) explicitly indicated that this Pt NP was negatively charged. Figure 2, C to E, shows plots of the phase shift measured along lines X_1–Y_1, X_2–Y_2, and X_3–Y_3, respectively.

Extrapolations of these three lines cross a central point of the Pt NP, so curve fitting of the phase plots can be used to estimate the value of a point charge (assumed to exist at the NP center) representing all of the charges within the NP (*26*, *27*) (see the supplementary materials). The precision in the phase analysis was 1.6 to 3.6×10^{-3} rad (deduced from the root-mean-squared error of the curve fitting in Fig. 2) (*21*), which enabled the total charge (Q) to be counted with an accuracy better than ±1 electron charge (q_e). In the framework of the approximation by classical electromagnetism,

[1]Department of Applied Quantum Physics and Nuclear Engineering, Kyushu University, Nishi-ku, Fukuoka 819-0395, Japan. [2]Department of Advanced Materials Science and Engineering, Faculty of Engineering Sciences, Kyushu University, Kasuga, Fukuoka 816-8580, Japan. [3]Research and Development Group, Hitachi, Ltd., Hatoyama, Saitama 350-0395, Japan. [4]Graduate School of Information Science and Technology, Osaka University, Suita, Osaka 565-0871, Japan. [5]The Ultramicroscopy Research Center, Kyushu University, Nishi-ku, Fukuoka 819-0395, Japan. [6]National Institute of Technology, Akashi College, Akashi, Hyogo 674-8501, Japan.
*Corresponding author. Email: aso.ryotaro.072@m.kyushu-u.ac.jp (R.A.); murakami.yasukazu.227@m.kyushu-u.ac.jp (Y.M.)

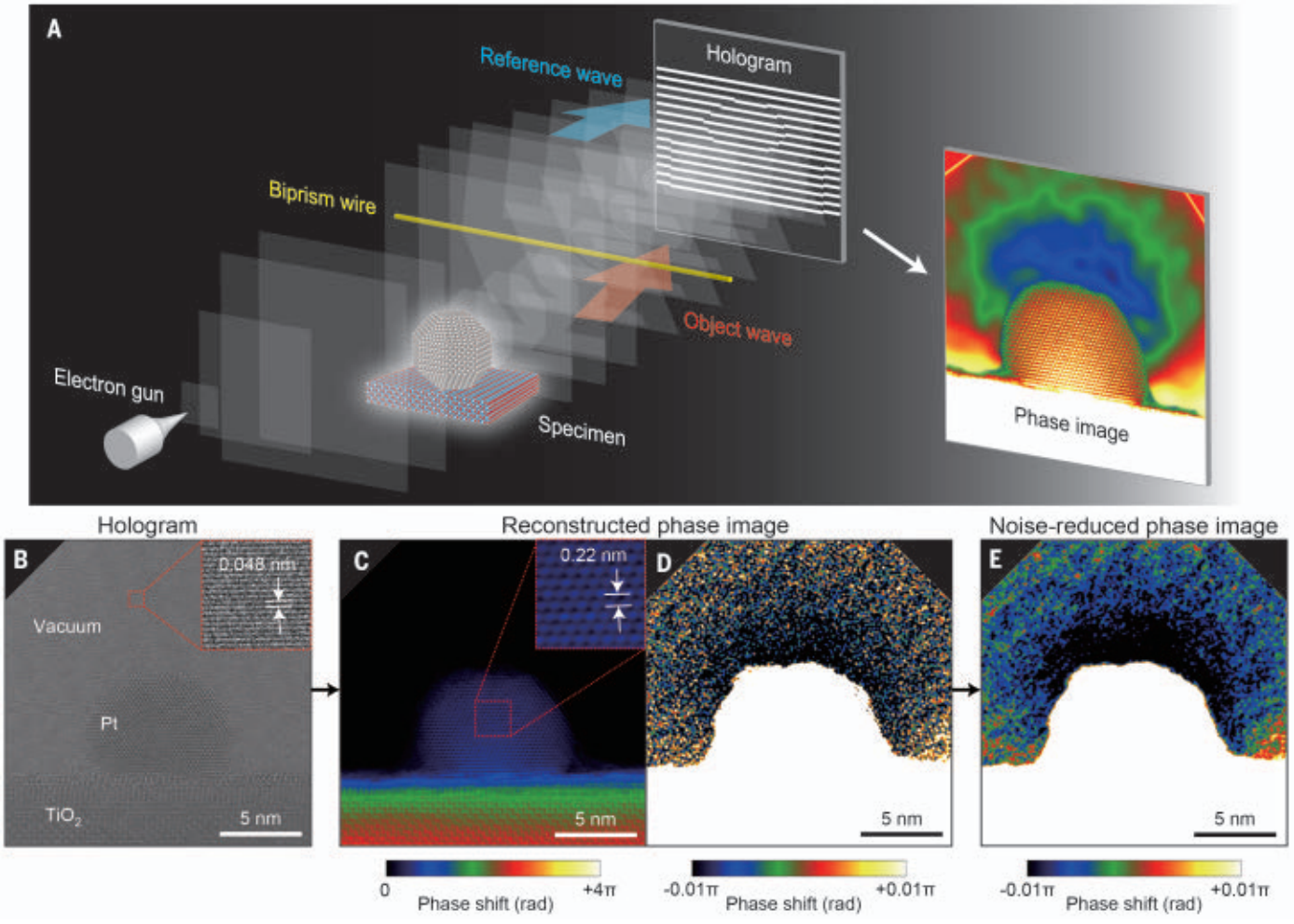

Fig. 1. Visualization of a local electric field around a supported NP. (**A**) Schematic of atomic-resolution electron holography. (**B**) Hologram image of a Pt NP on a TiO_2 support. The inset shows the interference fringe pitch. (**C** and **D**) Reconstructed phase images from (B). The image in (C) reveals the phase shift within Pt and TiO_2 crystals, where the atomic arrangement of Pt is revealed by the phase reconstruction; that is, the lattice spacing of 0.22 nm corresponds to the (111) planes of Pt. The weak signal in the vacuum region (outside of the crystals) in (C) is unclear. The image in (D) highlights the weak phase shift in the vacuum region, although this contrast (brightness) adjustment made the phase shift within Pt and TiO_2 crystals invisible. The inset in (C) shows the lattice fringes of the Pt NP. (**E**) Noise-reduced phase image. A noise reduction method (WHMM) was applied to the original phase image in (D).

least-squares fitting predicted a charge amount of $-5.6\ q_e$ for line X_1–Y_1, $-6.6\ q_e$ for line X_2–Y_2, and $-5.0\ q_e$ for line X_3–Y_3. The scatter (i.e., -6.6 to $-5.0\ q_e$) was most likely caused by the position-dependent surface potential of the Pt NP, which could not be incorporated into the classical analysis. Indeed, the value of the work function depended on the crystal surfaces (*28*), the effect of which is superposed on the phase plots in Fig. 2, C to E. Surface reconstruction, the presence of different indices of the crystal planes, and molecular absorption (contamination) related to charge compensation are other sources of slight variations in the results for the net charge deduced from the phase plots because these factors affect the surface potential of a NP. Nevertheless, this electron holography study has demonstrated the detection of extremely small charging induced in the Pt/TiO_2 specimen.

The images in Fig. 2, F and G, which were acquired from another Pt NP, represent the state of positive charging. From curve fitting of the phase plots (Fig. 2, H to J), we determined the charge amount to be $+2.6\ q_e$ for line X_4–Y_4, $+2.6\ q_e$ for line X_5–Y_5, and $+0.6\ q_e$ for line X_6–Y_6. To rule out artifacts generated by electron radiation, which make the specimen positively charged through secondary electron emission and other effects, we carefully examined in advance the relation between the magnitude of the phase shift and the electron beam exposure time. As shown in fig. S4, the phase shifts observed at the top of the Pt NPs increased linearly with increasing exposure time. After this examination, we obtained the results shown in Fig. 2 for both negative and positive charging under conditions optimized to suppress the radiation effect and improve the image contrast in holograms (see the supplementary materials for details of the data collection conditions). Thus, the positive charging shown in Fig. 2G is not a radiation-induced phenomenon but rather an intrinsic charge state of this NP.

Nanostructural analysis provided additional understanding of the two charge states. We analyzed the crystal structure of 65 Pt NPs supported on the TiO_2 foil (fig. S2). Although the electron microscopy images are projections, the digital diffractograms provide useful information about the average structure, including whether the NP shows an ideal face-centered cubic (fcc) lattice or distorted lattice. Although 92% of the NPs were identified as fcc, the others exhibited substantial lattice distortion. Unexpectedly, some of the distorted NPs showed a lattice analogous to a hexagonal close-packed (hcp) structure. The hcp-like configuration in Pt NPs is anomalous, although

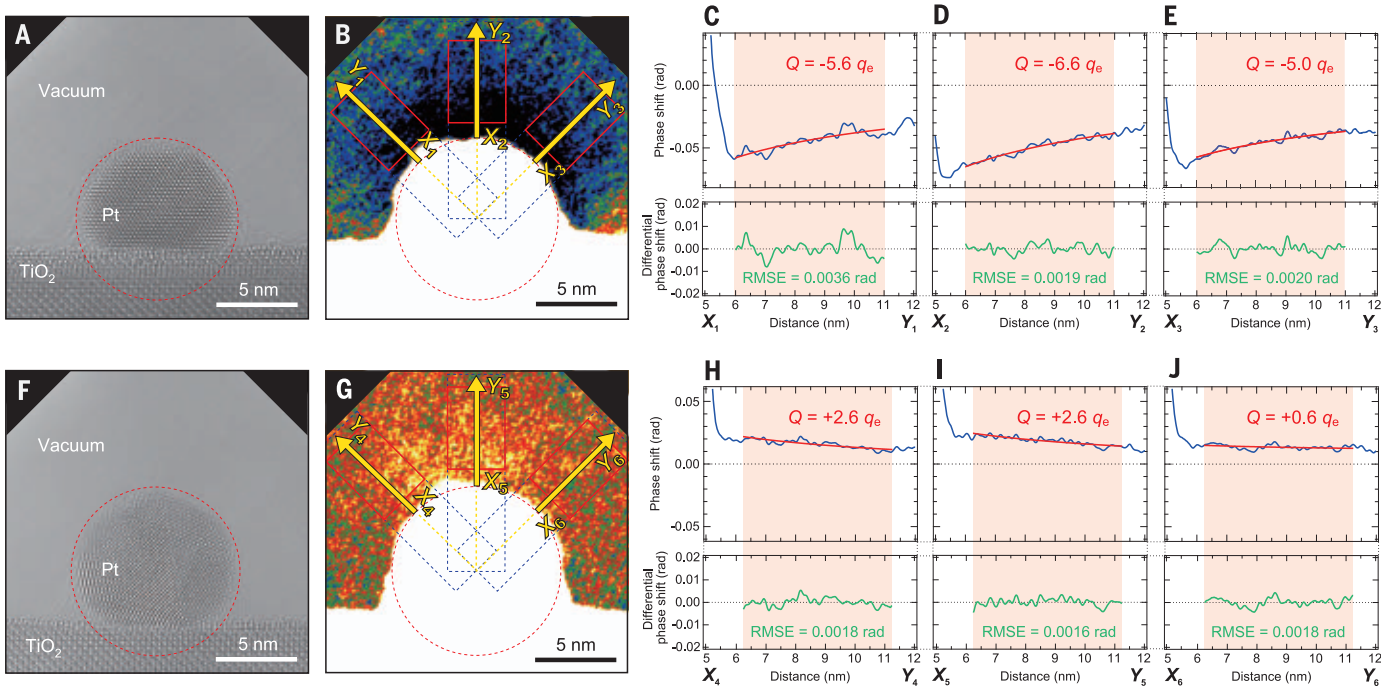

Fig. 2. Quantification of charges on supported NPs. (**A**) Reconstructed amplitude image (identical to TEM image) of a negatively charged Pt NP. (**B**) Noise-reduced phase image obtained from the specimen shown in (A). (**C** to **E**) Plots of the phase shift along lines X_1–Y_1 (C), X_2–Y_2 (D), and X_3–Y_3 (E). The top panels provide the phase plots, in which the red lines show the results of curve fitting (applied to the hatched (vacuum) region) to evaluate the net charges Q of the Pt NPs. The bottom panels show the difference between observations and curve-fitting results. Root-mean-squared error (RMSE) was used as a measure of the precision in the phase analysis. (**F**) Reconstructed amplitude image (identical to TEM image) of a positively charged Pt NP. (**G**) Noise-reduced phase image obtained from the specimen shown in (F). (**H** to **J**) Plots of the phase shift along lines X_4–Y_4 (H), X_5–Y_5 (I), and X_6–Y_6 (J). The top panels provide the phase plots, where the red lines show the results of curve fitting applied to the vacuum (hatched) region to evaluate the net charges Q of the Pt NPs. The bottom panels show the difference between observations and the curve-fitting results. RMSE was used as a measure of the precision in the phase analysis.

other researchers have reported a hcp lattice in Ru catalyst NPs (*29*). Figure 3, A to E, shows lattice images (reconstructed amplitude images) acquired from five Pt NPs on the TiO_2 (110) surface. For convenience, the Pt lattice is labeled in green for fcc and in red for distorted fcc or hcp-like configuration, consistent with the digital diffractograms in Fig. 3, F to J. Figure 3, K to O, shows the denoised phase maps particularly focused on the phase gradient outside of the NPs. Although Fig. 3, K to M, indicates negative charging of the NPs in Fig. 3, A to C, the other two panels (Fig. 3, N and O) indicate positive charging of the NPs (Fig. 3, D and E). With reference to the full fcc state shown in Fig. 3C, the amount of charging changes with increasing volume fraction of the distorted lattice irrespective of the sense (positive or negative) of charging. Thus, the charge amount can be related to the lattice distortion (see the supplementary materials for further details of the strain analysis).

The sense of charging appears to be related to the lattice distortion because it can affect the interplanar distance of the bottom crystal planes of Pt facing the TiO_2 (110) surface. As the enlarged views of the interface regions indicate, for the positively charged NPs (Fig. 3, D and E, bottom panels), the bottom crystal planes in Pt were those with small interplanar distances ranging from 0.13 to 0.14 nm. The negatively charged Pt NPs shown in Fig. 3, A to C, have distinct bottom crystal planes with interplanar distances ranging from 0.20 to 0.22 nm, larger than the interplanar distances of the planes with positively charged Pt NPs. With reference to the fcc lattice in Pt (a = 0.393 nm), spacings of 0.14, 0.20, and 0.23 nm corresponded to the (220), (002), and (111) planes, respectively.

The work function of bulk fcc Pt (φ_{Pt}) depended on the crystal planes: 5.4 eV for {110}, 5.5 eV for {100}, and 6.0 eV for {111} (*28*). The value of the work function changed in conjunction with the degree of atom packing within these planes. Assuming a stoichiometric TiO_2 (110) surface for the observations shown in Fig. 3, the work function of TiO_2 (φ_{TiO2}) should be in the range of 5.5 to 5.8 eV (*30*). In the framework of solid-state physics related to junction planes, for the condition $\varphi_{Pt} > \varphi_{TiO2}$, electrons transfer from the TiO_2 support to the Pt NP, resulting in negative charging of the Pt NPs. This result was consistent with the observations shown in Fig. 3, A to C, in which the bottom crystal planes have a spacing similar to that of the (111) plane of an fcc Pt lattice. For the other condition, $\varphi_{Pt} < \varphi_{TiO2}$, electrons transfer from the Pt NP to the TiO_2 support. This charge transfer explained the positive charging in the Pt NP (Fig. 3E), the bottom crystal plane of which can be approximated by the (220) plane of the fcc Pt lattice.

For a further explanation of the different charge states (positive and negative charging) observed by electron holography, we performed density functional theory (DFT) calculations (see the supplementary materials). In this case, the charge transfer was examined in terms of the reduction state of the TiO_2 surface because it can affect the effective work function. For this purpose, two structural models were constructed: Pt NPs 1 nm in diameter with a bottom crystal plane (100) supported on either a stoichiometric (Fig. 4A) or an oxygen-deficient TiO_2 (110) surface (Fig. 4E). The oxygen-deficient model approximates a reduced state in which the work function of the TiO_2 (110) surface becomes smaller than that of the stoichiometric TiO_2 (110) surface (*31*).

Figure 4 summarizes the calculations for both the stoichiometric model (Fig. 4, B to D) and the oxygen-deficient model (Fig. 4, F to H). The atomic charging can be substantial in a limited region near the Pt/TiO_2 interface. With respect to the net charges of Pt NPs in the stoichiometric model, a Bader charge analysis

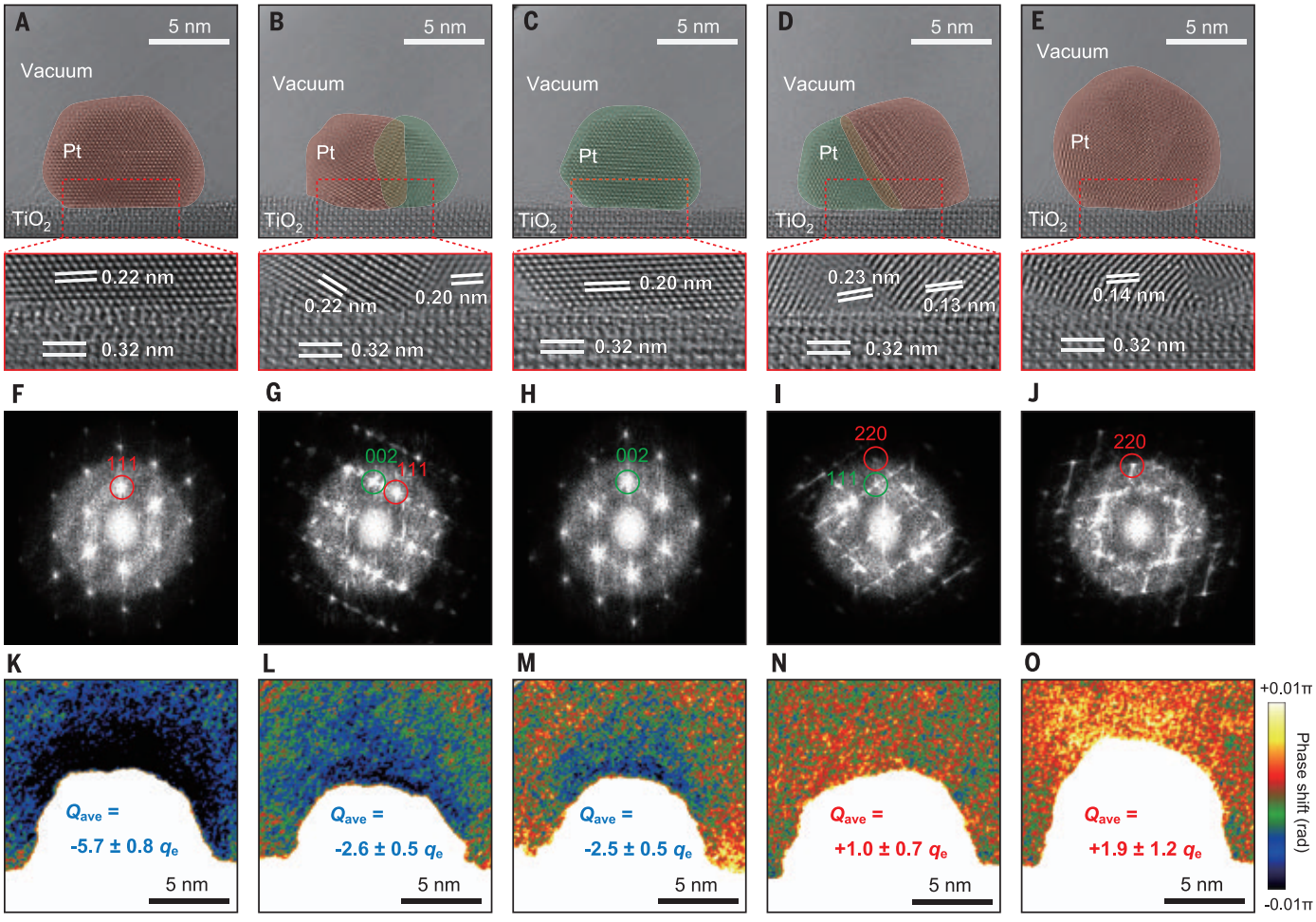

Fig. 3. Characterization of charging on supported NPs. (**A** to **E**) Reconstructed amplitude images representing the crystal structure and orientation of five Pt NPs supported on a TiO_2 (110) surface (top panels). Depending on the lattice distortion, Pt crystal grains were tentatively classified as fcc (green) or distorted fcc or hcp-like configuration (red). The bottom panels represent the magnified images of the heterointerface of each NP. (**F** to **J**) Digital diffractograms of the NPs in (A) to (E), respectively. For simplicity, the spots are indexed by assuming an fcc lattice. (**K** to **O**) Noise-reduced phase images corresponding to (A) to (E), respectively. The average total charges Q_{ave} estimated by curve fitting are shown.

(Fig. 4C) predicted positive charging through the charge accumulation of +0.432 q_e (induced by electron transfer from Pt to TiO_2), although the calculation assumes a small Pt diameter of 1 nm. Conversely, for the oxygen-deficient model (Fig. 4G), the calculation predicted negative charging by the charge depletion of −1.259 q_e. That is, the surface reduction of the TiO_2 support also explains the presence of two charge states (i.e., positive and negative charging). Nevertheless, this point is consistent with the arguments of charge transfer based on the work function, which is affected by the surface stoichiometry.

As the density of states calculation shown in Fig. 4, D and H, indicates, the *d*-band center responsible for catalytic reactions is shifted from −2.2 to −2.3 eV because of the slight charge transfer across the Pt/TiO_2 interface (see the supplementary materials for the detailed analysis based on *d*-band theory). Because of computational constraints, the calculations for a large NP similar in size to those in the observations were difficult. Nevertheless, the prediction by electron holography (one to six electrons per NP) was consistent with the values deduced from resonant x-ray photoemission studies of the Pt/CeO_2 system (*13*).

The local charge state of supported metal catalysts is critically important in catalysis research because it provides a key for understanding the activation sites in chemical reactions (*2*, *8*, *32*). Our electron microscopy study using Pt/TiO_2 as a model catalyst has revealed essential features of the supported metal catalysts. The supported Pt NP could be charged both positively and negatively. This result can be explained by the difference in the work function between Pt and TiO_2, although the lattice distortion is another factor that can affect the amount of charging. This scenario (i.e., charge transfer due to the difference in work function) is consistent with the results of the DFT calculations performed using two distinct interface models. That is, the framework of solid-state physics related to metal/oxide junction planes (established in many bulk crystals) can be valid for understanding the charge transfer across a nanometer-scale heterointerface of supported metal catalysts.

In addition, our particle-by-particle analysis using ultrahigh sensitivity and precision electron holography can be highly complementary to analyses by x-ray photoelectron spectroscopy (to determine the average charge state of numerous NPs) and probe microscopy (to examine the surface potential of limited numbers of NPs). The sophisticated process of data acquisition and analysis in electron holography achieved ultrahigh precision (on the order of the elementary charge q_e) in the charge analysis of a nanometer-sized area and succeeded in determining the small amount of charge (−5.7 to +1.9 q_e) per Pt NP.

Surface catalysis is well known to be affected by even the small charge transfer responsible

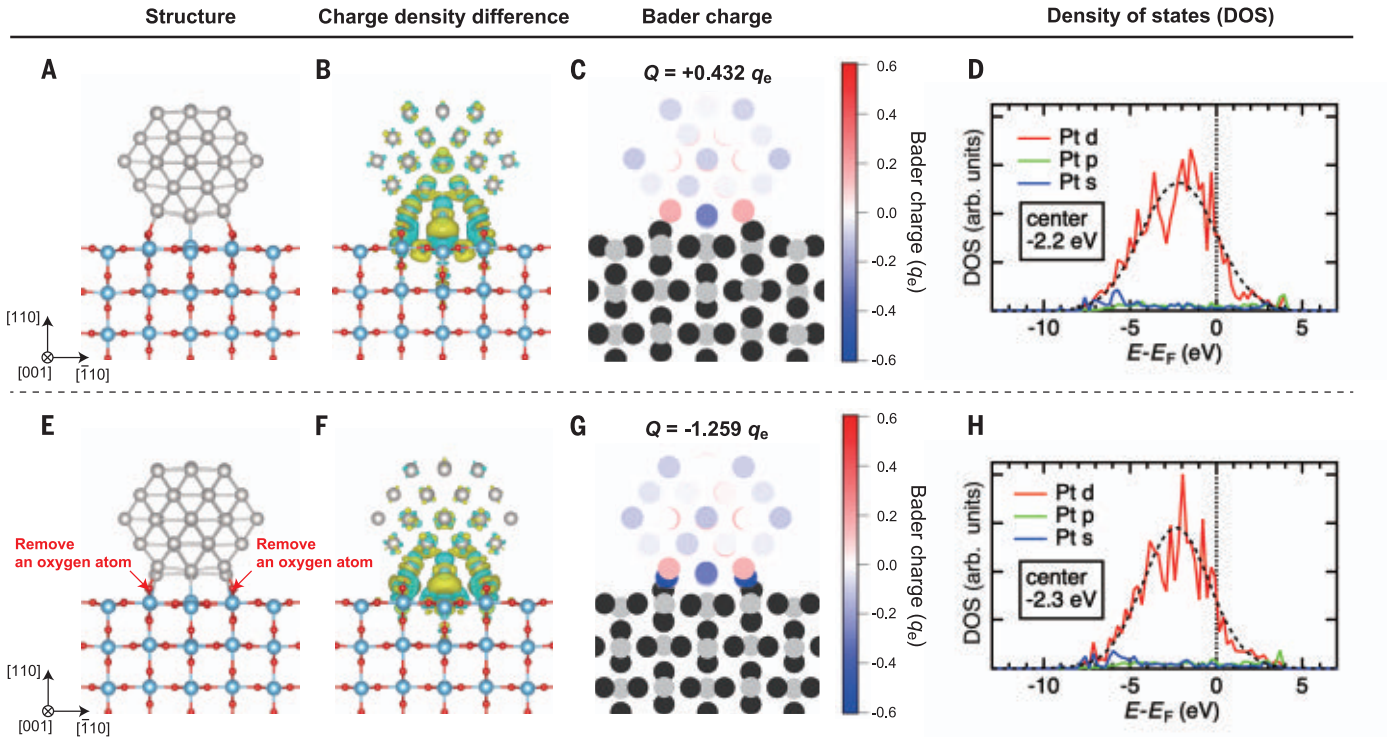

Fig. 4. Charge analysis by DFT calculations. (**A** to **C**) Structures (A), charge-density difference plots (B), and Bader charge distributions (C) for a Pt NP on stoichiometric TiO_2 (110) surfaces. (**D**) Density of states (DOS) for the first Pt layer in direct contact with TiO_2 in (A). (**E** to **G**) Structures (E), charge-density difference plots (F), and Bader charge distributions (G) for a Pt NP on oxygen-deficient TiO_2 (110) surfaces. (**H**) DOS for the first Pt layer in direct contact with TiO_2 in (E). The structures in (A), (B), (E), and (F) are displayed along the $[001]_{TiO2}$ direction, where the Pt atoms, Ti atoms, and O atoms are shown in gray, blue, and red, respectively. The yellow and cyan surfaces in the charge-density difference plots [(B) and (F)] correspond to the charge gain (accumulation) and loss (depletion) regions, respectively. The red and blue in the Bader charge distributions [(C) and (G)] for the Pt NP indicate the extent of charge accumulation (positive) and depletion (negative), respectively. The position of the Pt *d*-band center in the DOS [(D) and (H)] is determined by fitting with a Voigt function, as shown by dashed lines.

for the metal *d*-band state. For example, in the oxygen reduction reaction using Pt-alloy catalysts, the activity depends on slight differences of <1 eV in the position of the metal *d*-band center (*11*). Therefore, the present study on the charge state controlled by the lattice distortion and orientation relationship of supported catalytic NPs using ultrahigh sensitivity and precision electron holography provides new insights for understanding surface catalytic reactions. In terms of the future prospects of electron holography, we believe that a critical topic is data collection in a gas atmosphere, which can be achieved in conjunction with environmental TEM. However, precise analysis requires solutions to technical problems such as the deterioration of the hologram contrast as a result of electron scattering by the environmental gas molecules.

REFERENCES AND NOTES

1. L. Liu, A. Corma, *Chem. Rev.* **118**, 4981–5079 (2018).
2. T. W. van Deelen, C. Hernández Mejía, K. P. de Jong, *Nat. Catal.* **2**, 955–970 (2019).
3. M. S. Chen, D. W. Goodman, *Science* **306**, 252–255 (2004).
4. C. T. Campbell, *Nat. Chem.* **4**, 597–598 (2012).
5. A. Bruix *et al.*, *J. Am. Chem. Soc.* **134**, 8968–8974 (2012).
6. T. Binninger, T. J. Schmidt, D. Kramer, *Phys. Rev. B* **96**, 165405 (2017).
7. J. A. Farmer, C. T. Campbell, *Science* **329**, 933–936 (2010).
8. G. Pacchioni, H. J. Freund, *Chem. Soc. Rev.* **47**, 8474–8502 (2018).
9. L. Rößner, M. Armbrüster, *ACS Catal.* **9**, 2018–2062 (2019).
10. A. Garg *et al.*, *ACS Catal.* **9**, 7090–7098 (2019).
11. V. Stamenkovic *et al.*, *Angew. Chem. Int. Ed.* **45**, 2897–2901 (2006).
12. M. Mavrikakis, B. Hammer, J. K. Norskov, *Phys. Rev. Lett.* **81**, 2819–2822 (1998).
13. Y. Lykhach *et al.*, *Nat. Mater.* **15**, 284–288 (2016).
14. J. H. K. Pfisterer, Y. Liang, O. Schneider, A. S. Bandarenka, *Nature* **549**, 74–77 (2017).
15. T. Zambelli, J. Wintterlin, J. Trost, G. Ertl, *Science* **273**, 1688–1690 (1996).
16. T. Kittel, E. Roduner, *J. Phys. Chem. C* **120**, 8907–8916 (2016).
17. A. Sasahara, K. Hiehata, H. Onishi, *Catal. Surv. Asia* **13**, 9–15 (2009).
18. M. Haider *et al.*, *Nature* **392**, 768–769 (1998).
19. P. E. Batson, N. Dellby, O. L. Krivanek, *Nature* **418**, 617–620 (2002).
20. C. Gatel, A. Lubk, G. Pozzi, E. Snoeck, M. Hÿtch, *Phys. Rev. Lett.* **111**, 025501 (2013).
21. T. Suzuki *et al.*, *Ultramicroscopy* **118**, 21–25 (2012).
22. H. Lichte, M. Lehmann, *Rep. Prog. Phys.* **71**, 016102 (2008).
23. T. Akashi *et al.*, *Appl. Phys. Lett.* **106**, 074101 (2015).
24. Y. Midoh, K. Nakamae, *Microscopy (Oxf.)* **69**, 123–131 (2020).
25. T. Tamaoka *et al.*, *AIP Adv.* **11**, 025135 (2021).
26. C.-W. Lee, D. Shindo, K.-N. Kijiro, *Mater. Trans.* **42**, 1882–1885 (2001).
27. A. Tonomura, L. F. Allard, G. Pozzi, D. C. Joy, Y. A. Ono, *Electron Holography* (Elsevier, 1995).
28. R. Vanselow, X. Q. D. Li, *Surf. Sci.* **264**, L200–L206 (1992).
29. C. Song *et al.*, *Sci. Rep.* **6**, 31400 (2016).
30. K. Onda, B. Li, H. Petek, *Phys. Rev. B* **70**, 045415 (2004).
31. Y. W. Chung, W. J. Lo, G. A. Somorjai, *Surf. Sci.* **64**, 588–602 (1977).
32. Q. Fu, T. Wagner, *Surf. Sci. Rep.* **62**, 431–498 (2007).
33. Y. Midoh, "Code for denoising using a wavelet hidden Markov model (WHMM)" (2022); http://www-ise3.ist.osaka-u.ac.jp/whmm/.

ACKNOWLEDGMENTS

Funding: This work was supported in part by CREST grant JPMJCR1664 from the Japan Science and Technology Agency and by KAKENHI grants JP18H03845 and JP21H04623 from the Japan Society for the Promotion of Science. **Author contributions:** Y.Mu. conceived the idea and initiated the project. H.H. fabricated the samples. Y.T., T.A., F.I., and T.Tan. performed holography experiments. R.A. collected the TEM and STEM data. R.A. and Y.Mi. developed and used WHMM to improve the hologram data. H.H. and H.Nakan. performed DFT calculations. R.A., Y.T., H.Nakaj., T.Tam., K.Y., and T.Tan. analyzed the hologram data. H.E., T.Tan., H.S., and Y.Mu. supervised the project. All authors discussed the experimental data and co-wrote the manuscript. **Competing interests:** The authors declare no competing interests. **Data and materials availability:** All data are available in the main text or the supplementary materials. The code for denoising is available at Osaka University (*33*).

SUPPLEMENTARY MATERIALS

science.org/doi/10.1126/science.abq5868
Materials and Methods
Figs. S1 to S10
Table S1
References (*34*–*49*)

Submitted 18 April 2022; accepted 5 August 2022
10.1126/science.abq5868

PLASTIC WASTE

Mixed plastics waste valorization through tandem chemical oxidation and biological funneling

Kevin P. Sullivan[1,2]†, Allison Z. Werner[1,2]†, Kelsey J. Ramirez[1,2]†, Lucas D. Ellis[1,2]†‡, Jeremy R. Bussard[1,2], Brenna A. Black[1,2], David G. Brandner[1,2], Felicia Bratti[1,2], Bonnie L. Buss[1,2]§, Xueming Dong[1,2], Stefan J. Haugen[1,2], Morgan A. Ingraham[1,2], Mikhail O. Konev[1,2], William E. Michener[1,2], Joel Miscall[1,2], Isabel Pardo[1,2]¶, Sean P. Woodworth[1,2], Adam M. Guss[2,3], Yuriy Román-Leshkov[4], Shannon S. Stahl[5]*, Gregg T. Beckham[1,2]*

Mixed plastics waste represents an abundant and largely untapped feedstock for the production of valuable products. The chemical diversity and complexity of these materials, however, present major barriers to realizing this opportunity. In this work, we show that metal-catalyzed autoxidation depolymerizes comingled polymers into a mixture of oxygenated small molecules that are advantaged substrates for biological conversion. We engineer a robust soil bacterium, *Pseudomonas putida*, to funnel these oxygenated compounds into a single exemplary chemical product, either β-ketoadipate or polyhydroxyalkanoates. This hybrid process establishes a strategy for the selective conversion of mixed plastics waste into useful chemical products.

Plastics have revolutionized modern life because of their low cost and utility in a vast range of applications. However, the accumulation of synthetic polymers in landfills and the environment has created a global pollution crisis that the existing reclamation and recycling infrastructure is not equipped to resolve (*1*–*3*). This challenge has accelerated investigation into new chemical recycling technologies that could enable the conversion of plastic waste streams into valuable chemicals and support the creation of a circular plastics economy (*3*–*11*). Many chemical recycling approaches focus on selective depolymerization of single plastic streams. However, plastics chemistry is diverse in both monomer and bond type, and plastics in postconsumer waste are physically mixed and include complex materials, such as multilayer packaging. These features complicate and increase the cost of separation methods required to isolate individual polymers for recycling (*3*). Chemical recycling processes that enable the deconstruction of mixed plastics into valuable products without requiring sorting could bypass this limitation and substantially enhance plastics reclamation and recycling infrastructure.

In this work, we present a strategy whereby mixed plastics are converted into single products through a tandem catalytic and biological process (Fig. 1). The initial catalytic step uses metal-promoted autoxidation to depolymerize mixed plastics into oxygenated intermediates that represent advantaged substrates for subsequent bioconversion (*12*). The biological step uses a robust engineered bacterial strain to funnel the mixed oxygenates into the target product, in this case illustrated by either β-ketoadipate or polyhydroxyalkanoates. This approach is demonstrated with mixtures of high-density polyethylene (HDPE), polystyrene (PS), and poly(ethylene terephthalate) (PET), which are among the most abundant components of postconsumer plastics waste.

Autoxidation is a complex chemical process in which initiation reactions generate organic radicals that react with O_2 and undergo chain propagation to generate oxygenated products. A notable example of industrial autoxidation is the conversion of *p*-xylene to terephthalic acid in the Amoco process, which operates at ~80 million metric tons per year, where acetate salts of Co and Mn are used as catalysts with Br radicals to promote reaction of the hydrocarbon with O_2 (*13*). Partenheimer has shown that similar conditions support depolymerization of several pristine polymers (*14*). Autoxidation of polymers is initiated by H-atom transfer from C-H bonds in the polymer backbone to generate alkyl radicals, which react at diffusion-controlled rates with O_2 to form peroxide intermediates (Fig. 2A). Homolytic cleavage of the O-O bond, aided by the Co and Mn catalysts, forms alkoxyl radicals that can undergo C-C cleavage through β-scission steps. This collection of H-atom transfer, radical trapping by O_2, and C-C cleavage steps ultimately affords a mixture of low–molecular weight oxygenated products (*14*). This precedent from Partenheimer, among other studies (*15*–*17*), prompted us to explore a similar approach as the initial stage of our mixed plastics valorization process.

Autoxidation studies began with single-component commercial polymer resins including HDPE beads, PS beads, or PET powder. Use of bromide as a cocatalyst was avoided in our studies because it is corrosive and requires specialized reactor materials. *N*-hydroxyphthalimide (NHPI) has precedent as an initiator and cocatalyst in autoxidation (*18*) and proved to be an effective alternative to bromide.

Under autoxidation conditions, depolymerization of PS yields benzoic acid (62.9 ± 1.1 mol %), HDPE yields a distribution of C_4 to C_{22} α,ω-dicarboxylic acids (34.2 ± 0.7 mol %), and PET generates terephthalic acid (67.6 ± 1.4 mol %) (Fig. 2B, figs. S1 to S12, and tables S1 to S3). To compare results more easily between different polymers, molar yields were determined in terms of moles of carbon in the isolated product relative to the starting polymer, such that the maximum theoretical yield is 87.5% for PS, 100% for PE, and 80% for PET. This difference accounts for the loss of the methylene carbon in PS and the ethylene glycol carbons in PET. The molecular weight of the starting polymer had little influence on the product yields (fig. S3A and fig. S8A), which suggests that depolymerization occurs through random chain scission. The yields obtained for the single-component substrates in this study are comparable to those observed previously by Partenheimer when using bromide-containing systems (*14*) and generated the expected products from the polymer precursor. Depolymerization of PS and PET affords a single major product—benzoic acid and terephthalic acid, respectively—whereas HDPE depolymerization led to a more complex product mixture, including dicarboxylic acids and five-membered lactone-containing products (figs. S13 to S16 and tables S3 and S4). Experiments with PS and PET demonstrate that product yields are similar over a range of 1 to 10 wt % loadings, whereas higher HDPE loadings afford lower yields (fig. S17) that are attributed to in situ degradation of the dicarboxylic acid products.

We then shifted our efforts to reactions of mixed plastics, including binary mixtures of PS and HDPE and ternary mixtures of PS, HDPE, and PET, for both commercial resins and postconsumer plastics. The latter were derived from expanded PS (EPS) cups (e.g., Styrofoam), HDPE bottles (e.g., milk containers), or PET bottles (e.g., single-use beverage bottles). Depolymerization of PS and PET is favored at higher temperatures (180° and 210°C, respectively) and longer reaction times (5.5 hours) relative to HDPE (160°C, 2.5 hours) (Fig. 2B and figs. S1, S6, and S9) because HDPE generates products that degrade at higher temperatures (*14*, *19*). Despite these differences, we identified conditions that support effective autoxidative depolymerization of mixed PS and HDPE as well as mixed PS, HDPE, and PET. Treatment of the mixed PS and HDPE commercial resins at 180°C for 5.5 hours led to benzoic acid (68.9 ± 0.6 mol %) and dicarboxylic

[1]Renewable Resources and Enabling Sciences Center, National Renewable Energy Laboratory, Golden, CO, USA. [2]BOTTLE Consortium, Golden, CO, USA. [3]Biosciences Division, Oak Ridge National Laboratory, Oak Ridge, TN, USA. [4]Department of Chemical Engineering, Massachusetts Institute of Technology, Cambridge, MA, USA. [5]Department of Chemistry, University of Wisconsin Madison, Madison, WI, USA.
***Corresponding author. Email: gregg.beckham@nrel.gov (G.T.B.); stahl@chem.wisc.edu (S.S.S.)**
†These authors contributed equally to this work.
‡Present address: School of Chemical, Biological and Environmental Engineering, Oregon State University, Corvallis, OR, USA.
§Present address: Department of Chemistry and Biochemistry, University of Northern Colorado, Greeley, CO, USA.
¶Present address: Centro de Investigaciones Biológicas Margarita Salas (CIB), CSIC, Madrid, Spain.

acids (22.5 ± 0.5 mol %) (Fig. 2C and figs. S18 to S22). Very similar results were obtained from reactions of mixed PS and HDPE postconsumer plastics, showing a slight increase in benzoic acid (71.0 ± 0.1 mol %) and similar dicarboxylic acid (22.1 ± 0.3 mol %) yields. Analogous results were obtained from the PS, HDPE, and PET mixture of commercial resins and postconsumer plastics (Fig. 2C). These reactions were conducted at elevated temperature (210°C) to facilitate PET depolymerization, but despite this adjustment, autoxidation of these mixtures afforded the same products in similar (benzoic acid, 59.5 ± 2.3 mol %) or moderately reduced (dicarboxylic acids, 20.4 ± 1.1 mol %; terephthalic acid, 62.9 ± 1.4 mol %) yields relative to those observed from depolymerization of the individual polymers (Fig. 2, B and C).

The mixture of oxygenates obtained from autoxidation of mixed plastics is sufficiently complex that it would require advanced separation methods to isolate and purify individual products suitable for downstream application. This challenge is akin to that encountered in thermal treatments of mixed plastics waste, such as pyrolysis. The autoxidation products are appealing, however, because they have enhanced water solubility that make them advantaged feedstocks for biological funneling, wherein an engineered microbe converts diverse chemicals to a single product (*20*). To pursue this opportunity, we engineered two strains of *Pseudomonas putida* (*21*, *22*): first, to convert acetate, C_4 to C_{17} dicarboxylates, benzoate, and terephthalate to polyhydroxyalkanoates, a natural polyester with growing industrial applications (*23*), and second,

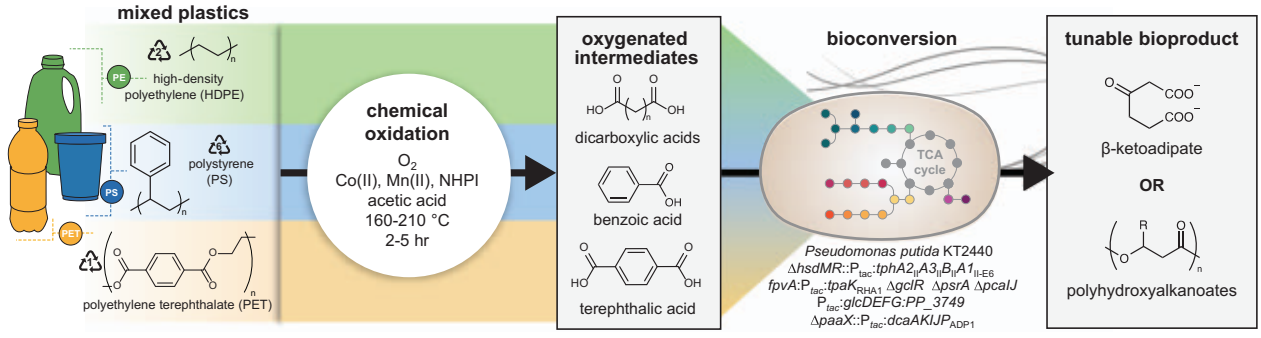

Fig. 1. Concept for the upcycling of mixed plastic waste through tandem chemical oxidation and bioconversion. Metal-promoted autoxidation simultaneously deconstructs multiple polymers, generating a mixture of oxygenated intermediates that are advantaged substrates for bioconversion. An engineered *P. putida* strain funnels the heterogeneous mixture of oxygenates into a single target product. TCA cycle, tricarboxylic acid cycle.

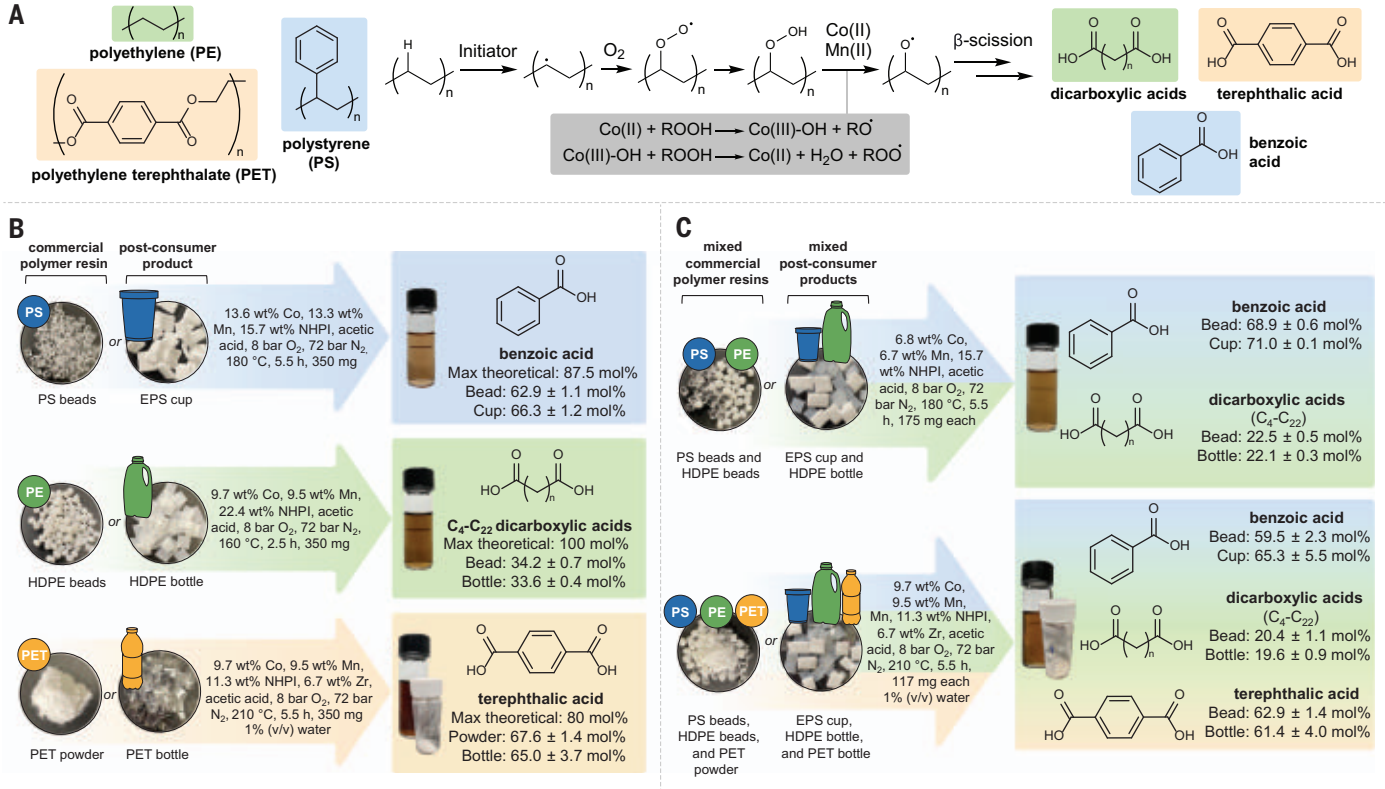

Fig. 2. Oxidative depolymerization of mixed plastics. (**A**) Autoxidation scheme, illustrated for HDPE, with primary products for all polymers shown. (**B**) Oxidation of single-component commercial polymer resins and postconsumer plastics. (**C**) Oxidation of mixed plastic substrates. Experimental details are in the supplementary materials. Data are means ± SDs; *N* = 3 trials. Mole % values indicate mole % carbon in isolated products relative the total carbon in the starting polymer, and weight % values are relative to the total plastics loading. Tabulated values are included in data S1.

to use acetate and dicarboxylates for growth while converting benzoate and terephthalate to β-ketoadipate, a monomer for performance-advantaged polymers (*24*, *25*) (Fig. 3).

P. putida natively uses acetate, benzoate, and C_4 and C_5 dicarboxylates as carbon sources, and we had previously engineered a strain of *P. putida* to use terephthalate and ethylene glycol (*26*), which was used a base strain for further engineering in the present study (figs. S23 and S24). Ackermann *et al.* have enabled adipate (C_6) utilization in *P. putida* by combining the native phenylacetate pathway with select transport and β-oxidation reactions from *Acinetobacter baylyi* ADP1 (fig. S25) (*27*). We took a similar approach by heterologously expressing the *A. baylyi dcaAKIJP* operon (*28*) and deleting genes encoding two native repressors of phenylacetate catabolism and β-oxidation, PaaX and PsrA, respectively (*29*, *30*). The resulting strain, AW162, grew on C_4 to C_{10} dicarboxylates when each was tested as a sole carbon source and simultaneously used C_4 to C_{14} dicarboxylates when tested in a mixture (figs. S24 to S31 and tables S5 to S8). Additionally, the strain was not inhibited by trace catalyst, initiator, or lactone acid species (figs. S32 to S37).

Metal catalysts were recovered from crude, deconstructed polymers by suspension in water, NaOH addition, and filtration to remove the precipitated metal hydroxides (fig. S38). The resulting filter-sterilized solutions contained substrates congruent with the feedstocks, trace (<5 μM) Co and Mn metals, and acetate (tables S9 to S12). These so-called effluent streams were used directly in microbial cultivations.

We next engineered and demonstrated biological funneling of intermediates from both commercial polymer resins and postconsumer plastics to polyhydroxyalkanoates and, separately, to β-ketoadipate. AW162 grew on effluent from mixed PS and HDPE commercial polymer resin as well as effluent from mixed EPS and HDPE postconsumer products, with simultaneous utilization of benzoate and C_4 to C_{17} dicarboxylates (Fig. 4, A to C, and fig. S39). In effluent from mixed PS, HDPE, and PET commercial polymer resin, AW162 cultivations simultaneously used the aromatic and aliphatic substrates during growth (Fig. 4, D and E, and fig. S40). AW162 was also used for polyhydroxyalkanoates production by cultivation in nitrogen-limited medium: Polyhydroxyalkanoates were produced from both effluent from mixed PS beads and HDPE beads as well as effluent from mixed postconsumer EPS cups and HDPE bottles; polyhydroxyalkanoates primarily comprised 3-hydroxydodecanoic acid and 3-hydroxydecanoic acid (Fig. 4F and figs. S41 and S42). In previous work, deletion of *pcaIJ* in *P. putida* has enabled the conversion of 4-hydroxybenzoate to β-ketoadipate at 41 g/liter, 0.8 g/liter per hour, and quantitative yield in bioreactors (*24*). In this case, *pcaIJ* was deleted in strain AW162, resulting in strain AW307, to enable the conversion of benzoate and terephthalate to β-ketoadipate (Fig. 3 and Fig. 4G). β-ketoadipate production by AW307 was evaluated, with aliphatic substrates supporting growth and conversion of aromatic substrates to β-ketoadipate. Yields are reported as mole β-ketoadipate per mole aromatic monomer, where the theoretical yield is 1 mol/mol (see table S13 for consideration of aliphatic carbon that is used as the substrate for cellular growth). In effluent from mixed PS and HDPE commercial

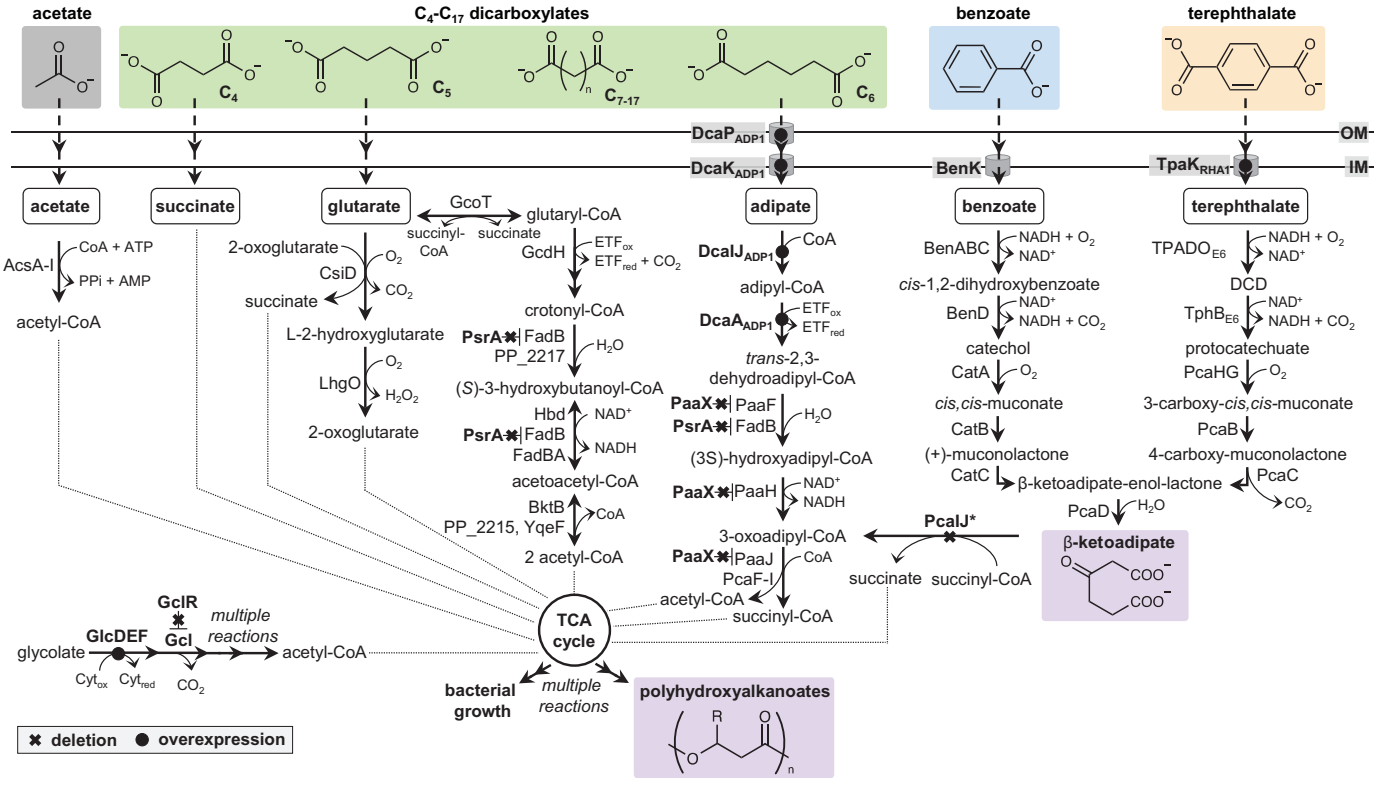

Fig. 3. Engineered metabolic pathways for biological funneling of PS-, HDPE-, and PET-derived oxygenated intermediates to β-ketoadipate or polyhydroxyalkanoates. Engineered expression changes to genes encoding the corresponding proteins are depicted in bold font, where gene deletion is indicated by an "×" and gene overexpression is indicated by a circle. Subscripts indicate a protein of heterologous origin, where ADP1 indicates *A. baylyi* ADP1, RHA1 indicates *R. jostii* RHA1, and E6 indicates *Comamonas* sp. E6. AW162: *P. putida* Δ*hsdMR*::P_{tac}:*tphA2*$_{II}$*A3*$_{II}$*B*$_{II}$*A1*$_{II\text{-}E6}$*fpvA*:P_{tac}:*tpaK*$_{RHA1}$ Δ*glcR* P_{tac}:*glcDEFG*:*PP_3749* Δ*paaX*::P_{tac}:*dcaAKIJP*$_{ADP1}$ Δ*psrA*. AW307: AW162 Δ*pcaIJ*. Genotypes and strain construction details are provided in tables S5 to S8. CoA, coenzyme-A; ATP, adenosine 5′-triphosphate; AMP, adenosine 5′-monophosphate; ADP, adenosine 5′-diphosphate; PPi, pyrophosphate; ETF_{ox}, an oxidized electron-transfer flavoprotein; ETF_{red}, a reduced electron-transfer flavoprotein; NAD^+, oxidized nicotinamide adenine dinucleotide; NADH, reduced nicotinamide adenine dinucleotide; TCA cycle, tricarboxylic acid cycle; Cyt_{ox}, an electron-transfer quinone; Cyt_{red}, an electron-transfer quinol; DCD, 1,2-dihydroxy-3,5-cyclohexadiene-1,4-dicarboxylate. GcoT is also referred to as GcdG (PP_0159); all enzyme names and corresponding genes can be found in the BioCyc Database.

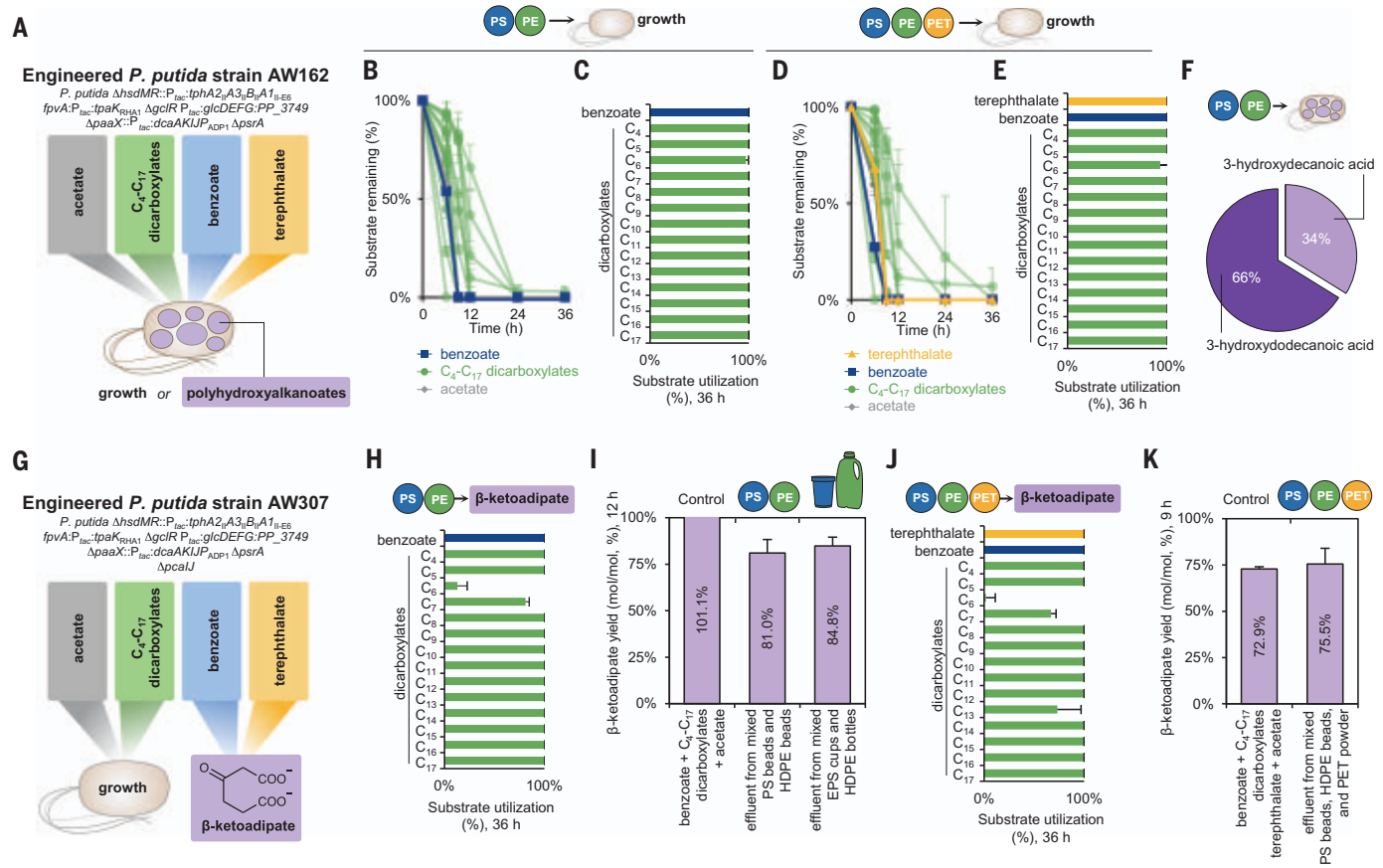

Fig. 4. Bioconversion of effluent from mixed plastics to target products. (**A**) AW162 was engineered to use all intermediates as substrates for growth or polyhydroxyalkanoates production. (**B** to **E**) Utilization of intermediates in effluent from mixed PS beads and PE beads [(B) and (C)] or in effluent from mixed PS beads, HDPE beads, and PET powder by AW162 [(D) and (E)]. (**F**) Composition of polyhydroxyalkanoates produced from effluent from mixed PS beads and HDPE beads by AW162. (**G**) AW307 was engineered to use acetate and dicarboxylates for growth and convert benzoate and terephthalate to β-ketoadipate. (**H**) Utilization of intermediates in effluent from mixed PS beads and HDPE beads by AW307. (**I**) β-ketoadipate yields (percentage of theoretical maximum) from control mixtures, effluent from mixed PS beads and HDPE beads, or effluent from mixed postconsumer EPS cups and HDPE bottles by AW307. (**J** and **K**) Utilization of intermediates in effluent from mixed PS beads, HDPE beads, and PET powder by AW307 (J) and β-ketoadipate yields from the same or control mixtures (K). Data are means ± SDs; $N = 3$ trials. Genotypes and strain construction details are provided in tables S5 to S8.

polymer resins, all dicarboxylates except C_6 and C_7 were completely used, and benzoate was converted to β-ketoadipate at an 81.0 ± 7.2% molar yield (Fig. 4, H and I, and fig. S43B). AW307 cultivations in effluent from mixed postconsumer EPS cups and HDPE bottles displayed similar growth and substrate utilization, generating β-ketoadipate at 84.8 ± 4.7% molar yield (Fig. 4I and fig. S43C). Incomplete utilization of C_6 and C_7 dicarboxylates was observed, and β-ketoadipate decreased at extended time points (fig. S43), which may indicate promiscuous activity of PcaIJ on C_6 and C_7 dicarboxylates and/or DcaIJ on β-ketoadipate. In effluent from mixed PS, HDPE, and PET commercial polymer resins, β-ketoadipate was produced at a 75.5 ± 8.5% molar yield (Fig. 4, J and K, and figs. S44 and S45). Assuming that no losses occurred during the processing of samples between the chemical and biological processes, overall molar β-ketoadipate yields from the aromatic constituents of the original plastics were 64% for mixed PS and HDPE commercial polymer resins; 69% for mixed PS and HDPE postconsumer plastics; and 57% for mixed PS, HDPE, and PET commercial polymer resins (tables S13 and S14).

This work demonstrates a process concept for pairing chemical and biological catalysis to convert mixed plastics into valuable products. Metal-catalyzed autoxidation offers a feedstock-agnostic approach for mixed-polymer deconstruction into oxygenated small molecules, with advantages for biological funneling owing to their solubility in water and known catabolic pathways. Extensions from the individual and mixed PS, HDPE, and PET materials demonstrated in this work to other polymers susceptible to autoxidation, including polypropylene and polyvinyl chloride (*14*), are readily envisioned. Continuous reactor systems, such as those used in the Amoco process, should support higher polymer loadings by improving oxygen delivery and continuous removal of products to limit in situ degradation. Improvements in process integration will increase recovery of acetic acid and catalysts between the chemical and biological steps. Separations could also enable the isolation of valuable autoxidation products before bioconversion. Further metabolic engineering will enable bioprocess improvements to access higher titers and rates and production of other products (*31*) beyond the two examples we have demonstrated here. Ideal targets include the synthesis of monomers for intrinsically circular polymers (*10*, *32*). Techno-economic analysis and life cycle assessment will be necessary to guide future progress toward economical and sustainable processes (*11*).

REFERENCES AND NOTES

1. S. B. Borrelle *et al.*, *Science* **369**, 1515–1518 (2020).
2. A. Milbrandt, K. Coney, A. Badgett, G. T. Beckham, *Resour. Conserv. Recycling* **183**, 106363 (2022).
3. K. Ragaert, L. Delva, K. Van Geem, *Waste Manag.* **69**, 24–58 (2017).
4. A. Rahimi, J. M. García, *Nat. Rev. Chem.* **1**, 0046 (2017).
5. G. W. Coates, Y. D. Y. L. Getzler, *Nat. Rev. Mater.* **5**, 501–516 (2020).
6. I. Vollmer *et al.*, *Angew. Chem. Int. Ed.* **59**, 15402–15423 (2020).
7. L. D. Ellis *et al.*, *Nat. Catal.* **4**, 539–556 (2021).
8. S. C. Kosloski-Oh, Z. A. Wood, Y. Manjarrez, J. P. de Los Rios, M. E. Fieser, *Mater. Horiz.* **8**, 1084–1129 (2021).
9. A. J. Martín, C. Mondelli, S. D. Jaydev, J. Pérez-Ramírez, *Chem* **7**, 1487–1533 (2021).

10. C. Jehanno *et al.*, *Nature* **603**, 803–814 (2022).
11. S. R. Nicholson *et al.*, *Annu. Rev. Chem. Biomolec. Eng.* **13**, 301–324 (2022).
12. R. Wei *et al.*, *Nat. Catal.* **3**, 867–871 (2020).
13. R. A. F. Tomás, J. C. M. Bordado, J. F. P. Gomes, *Chem. Rev.* **113**, 7421–7469 (2013).
14. W. Partenheimer, *Catal. Today* **81**, 117–135 (2003).
15. A. Pifer, A. Sen, *Angew. Chem. Int. Ed.* **37**, 3306–3308 (1998).
16. E. Bäckström, K. Odelius, M. Hakkarainen, *Ind. Eng. Chem. Res.* **56**, 14814–14821 (2017).
17. M. W. Guzik *et al.*, *Waste Manag.* **135**, 60–69 (2021).
18. Y. Ishii, S. Sakaguchi, *Catal. Today* **117**, 105–113 (2006).
19. F. Gugumus, *Polym. Degrad. Stabil.* **76**, 329–340 (2002).
20. J. G. Linger *et al.*, *Proc. Natl. Acad. Sci. U.S.A.* **111**, 12013–12018 (2014).
21. I. Poblete-Castro, J. Becker, K. Dohnt, V. M. dos Santos, C. Wittmann, *Appl. Microbiol. Biotechnol.* **93**, 2279–2290 (2012).
22. P. I. Nikel, V. de Lorenzo, *Metab. Eng.* **50**, 142–155 (2018).
23. M. P. Mezzina, M. T. Manoli, M. A. Prieto, P. I. Nikel, *Biotechnol. J.* **16**, 2000165 (2021).
24. C. W. Johnson *et al.*, *Joule* **3**, 1523–1537 (2019).
25. N. A. Rorrer *et al.*, *Cell Rep. Phy. Sci.* **3**, 100840 (2022).
26. A. Z. Werner *et al.*, *Metab. Eng.* **67**, 250–261 (2021).
27. Y. S. Ackermann *et al.*, *Metab. Eng.* **67**, 29–40 (2021).
28. D. Parke, M. A. Garcia, L. N. Ornston, *Appl. Environ. Microbiol.* **67**, 4817–4827 (2001).
29. M. G. Thompson *et al.*, *Appl. Environ. Microbiol.* **86**, e01665-20 (2020).
30. C. Fernández, E. Díaz, J. L. García, *Environ. Microbiol. Rep.* **6**, 239–250 (2014).
31. S. Y. Lee *et al.*, *Nat. Catal.* **2**, 18–33 (2019).
32. C. Shi *et al.*, *Chem* **7**, 2896–2912 (2021).

ACKNOWLEDGMENTS

We thank R. Allen, A. Cuthbertson, S. Hesse, K. Knauer, J. Kruger, C. Lahive, D. Moore, N. Rorrer, C. Tassone, N. Wierckx, Y. Ackermann, W. McNeary, H. Alt, and members of the BOTTLE Consortium for helpful discussions. We thank K. Beers and S. V. Orski at the National Institute of Standards and Technology for supplying a 1475A HDPE standard. **Funding:** Funding was provided by the US Department of Energy, Office of Energy Efficiency and Renewable Energy, Advanced Manufacturing Office (AMO), and Bioenergy Technologies Office (BETO). This work was performed as part of the BOTTLE Consortium and was supported by AMO and BETO under contract no. DE-AC36-08GO28308 with the National Renewable Energy Laboratory (NREL), operated by the Alliance for Sustainable Energy, LLC. The BOTTLE Consortium includes members from MIT, funded under contract no. DE-AC36-08GO28308 with NREL. Contributions by S.S.S. were supported by the US Department of Energy, Office of Basic Energy Sciences, under award no. DEFG02-05ER15690. **Author contributions:** Conceptualization: G.T.B., K.P.S., A.Z.W., K.J.R., L.D.E., and S.S.S. Investigation: K.P.S., A.Z.W., K.J.R., L.D.E., J.B., B.A.B., X.D., and I.P. Visualization: A.Z.W. and K.P.S. Funding acquisition: G.T.B., A.M.G., and Y.R.-L. Resources: D.G.B., F.B., B.L.B., S.J.H., M.A.I., M.O.K., W.E.M., J.M., and S.P.W. Supervision: G.T.B., S.S.S., and Y.R.-L. Writing – original draft: K.P.S., A.Z.W., and G.T.B. Writing – review & editing: All authors have reviewed and approved of the manuscript. **Competing interests:** G.T.B., L.D.E., K.P.S., and A.Z.W. have filed a patent application on this concept, PCT/US2021/063725 "Upcycling Mixed Waste Plastic Through Chemical Depolymerization and Biological Funneling." The patent filer is the Alliance for Sustainable Energy, LLC. The authors declare no other competing interests. **Data and materials availability:** All data are available in the main text or the supplementary materials. Strains and plasmids are available upon request through a material transfer agreement with NREL.

SUPPLEMENTARY MATERIALS

science.org/doi/10.1126/science.abo4626
Materials and Methods
Supplementary Text
Figs. S1 to S45
Tables S1 to S14
References (*33*–*56*)
Data S1

Submitted 12 February 2022; resubmitted 7 July 2022
Accepted 19 August 2022
10.1126/science.abo4626

POLYMERS

Polymeric multimaterials by photochemical patterning of crystallinity

Adrian K. Rylski[1], Henry L. Cater[1]†, Keldy S. Mason[1]†, Marshall J. Allen[1,2]†, Anthony J. Arrowood[2], Benny D. Freeman[2], Gabriel E. Sanoja[2], Zachariah A. Page[1]*

An organized combination of stiff and elastic domains within a single material can synergistically tailor bulk mechanical properties. However, synthetic methods to achieve such sophisticated architectures remain elusive. We report a rapid, facile, and environmentally benign method to pattern strong and stiff semicrystalline phases within soft and elastic matrices using stereo-controlled ring-opening metathesis polymerization of an industrial monomer, *cis*-cyclooctene. Dual polymerization catalysis dictates polyolefin backbone chemistry, which enables patterning of compositionally uniform materials with seamless stiff and elastic interfaces. Visible light–induced activation of a metathesis catalyst results in the formation of semicrystalline *trans* polyoctenamer rubber, outcompeting the formation of *cis* polyoctenamer rubber, which occurs at room temperature. This bottom-up approach provides a method for manufacturing polymeric materials with promising applications in soft optoelectronics and robotics.

Multimaterial structures that synergistically combine stiff and elastic components are ubiquitous in living systems, providing unparalleled combinations of mechanical properties (e.g., strength, toughness, and durability) (*1*–*3*). However, creating synthetic materials with integrated stiff and elastic domains remains an ongoing challenge (*4*–*6*). A scalable solution to achieving such structures would prove transformative for fundamental and applied research in soft materials and in advanced technologies that benefit from compliant, tough, and lightweight objects, such as programmable actuators (*7*) and bioelectronics (*8*). State-of-the-art strategies to pattern stiffness rely on spatially varying the cross-link density of polymer networks using orthogonal two-stage and/or wavelength-selective lithographic curing processes (*9*–*14*). However, costly fabrication, material waste, brittle failure, and/or incumbent interfacial stress preclude access to synthetic materials and structures that mimic those found ubiquitously in nature. Herein, we overcome these limitations using a single, inexpensive feedstock to photopattern stiff and strong domains within a soft and elastic matrix using dual-initiated, stereo-controlled ring-opening metathesis polymerization (ROMP) of an olefinic monomer, *cis*-cyclooctene (COE) (Fig. 1A).

Twelve ruthenium (Ru)–based catalysts were screened and characterized in terms of reactivity and stereochemical control during ROMP (Fig. 1B and fig. S11). The use of COE as a low-viscosity liquid enabled bulk polymerizations (>99 vol % COE), minimizing hazardous solvent waste and postprocessing requirements. The *trans:cis* alkene ratios were characterized using ^{1}H nuclear magnetic resonance (NMR) spectroscopy, integrating the two peaks between ~5.3 and 5.4 parts per million (ppm), narrowing the catalyst scope to those that resulted in either high *trans*- or *cis*-alkene content (Fig. 1C, table S1, and fig. S12). Three representative catalysts were selected for further study: (i) Grubbs second generation (G2) as a control, (ii) a thermally latent *bis*-*N*-heterocyclic carbene (*bis*-NHC) catalyst (*15*) (Ru-1), and (iii) a stereoretentive catalyst (*16*) (Ru-2) (tables S1 to S3 and fig. S13). The use of G2 (50 ppm relative to COE, ~23°C, <5 min) resulted in complete COE consumption to produce *trans* polyoctenamer rubber (TOR) with ~85% *trans*-alkene content, whereas Ru-1 (50 ppm relative to COE, ~100°C, 60 min) resulted in ~78% *trans*-alkene content. This result suggested that latent activation of Ru-1 could enable selective TOR synthesis.

To facilitate spatial control over the stereochemistry of polyoctenamer, Ru-1 was examined for photolatency (figs. S14 and S15). Inspired by the work of Rovis and co-workers (*17*) on the use of pyrylium photoredox catalysis for ROMP, a pyrylium derivative, 2,4,6-tris(4-dodecylphenyl) pyrylium tetrafluoroborate (hereafter pyr.) (Fig. 1B), was synthesized to provide solubility in COE (figs. S16 to S23) and used to activate *bis*-NHC catalysts bearing indenylidene (Ru-1), benzylidene, or alkenylcarbene groups with visible light. Of the three derivatives, only Ru-1 was inactive in the absence of light (<1% conversion of COE, 50 ppm catalyst, 75 ppm pyr., ~23°C, 1 hour), which is attributed to the steric hindrance and Lewis basicity of indenylidene (*18*). Irradiation with a blue LED resulted in quantitative COE consumption, indicating excellent temporal control (~460 nm, 170 mW/cm^2, ~23°C, 5 min) (Fig. 1C and table S1). The resulting TOR polymers had a *trans* content of 91%, a

[1]Department of Chemistry, The University of Texas at Austin, Austin, TX 78712, USA. [2]McKetta Department of Chemical Engineering, The University of Texas at Austin, Austin, TX 78712, USA.
***Corresponding author. Email: zpage@utexas.edu**
†These authors contributed equally to this work.

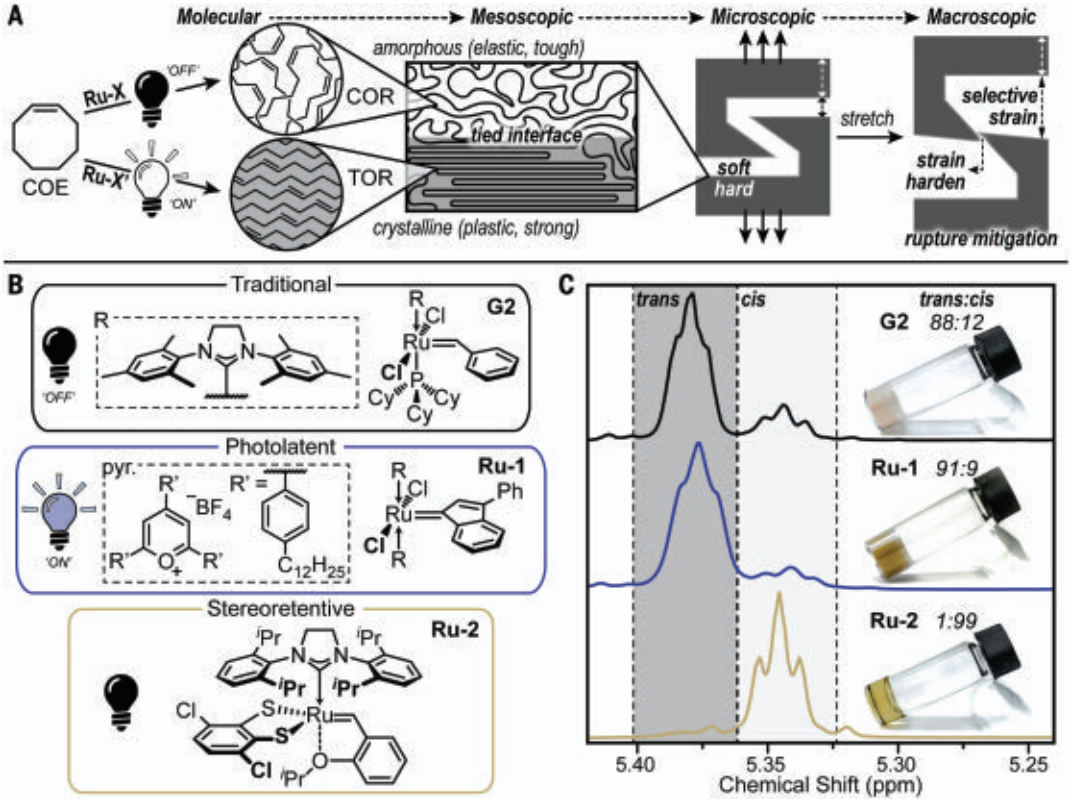

Fig. 1. Control over polyoctenamer stereochemistry. (**A**) Bottom-up design of synthetic materials with patterned crystallinity from a single feedstock, COE, to provide TOR or COR. (**B**) Chemical structures for Ru-alkylidene catalysts examined for ROMP of approximately neat COE. (**C**) ^{1}H NMR spectra for polyoctenamer produced using G2, Ru-1 + pyr. + light, and Ru-2 (<100 ppm catalyst) showing the signals corresponding to *trans* and *cis* isomers. Insets: *trans:cis* ratios and representative images of polyoctenamer.

modest increase relative to those obtained through thermal activation (78% *trans*), possibly arising from a decrease in polymerization temperature.

Polyoctenamers with high *cis*-alkene content, *cis* polyoctenamer rubber (COR), were achieved by examining four commercial stereoregulating catalysts (Fig. 1B and fig. S11) (*16*, *19*). The stereoselective catalysts (i.e., double-bond configuration defined by the catalyst) were unable to reach high conversions of COE at both room and elevated temperatures (<30%, 100°C, 18 hours). Conversely, low concentrations (20 ppm relative to COE) of the stereoretentive catalysts (i.e., double-bond configuration defined by the monomer) proved effective at reaching high conversions of COE (>99%, ~23°C, <2 hours) to produce COR with a *cis* content of ~99% (Fig. 1C and table S1).

The mechanical properties of TOR and COR were examined under uniaxial tension until failure (Fig. 2A, table S5, and figs. S24 to S27). Five different polymerization conditions were analyzed: (i) G2 (50 ppm) with trimethyl phosphite (50 ppm) (*20*) to facilitate thermally latent casting (80°C, 1 hour); (ii) Ru-1 (50 ppm) and pyr. (75 ppm) with blue light irradiation (~460 nm, ~170 mW/cm^2, 5 min); (iii) Ru-2 (20 ppm, room temperature, 1 hour); and (iv and v) Ru-1 (50 ppm), pyr. (75 ppm), and Ru-2 (20 ppm) with (5 min) (iv) or without (60 min) (v) light irradiation. Conditions that produced TOR (conditions i, ii, and iv) gave strong, stiff materials with a maximum stress (σ_m) from ~23 to 27 MPa and a Young's modulus (E) from ~800 to 1000 MPa. By contrast, conditions that produced COR (conditions iii and v) provided a soft and stretchable material, with $\sigma_m \approx 12$ MPa, $E \approx 3$ MPa, and strain at failure (ε_f) of ~800%. This mechanical behavior resembles that of conventional thermoplastic elastomers such as self-assembled polyolefin block copolymers (*21*, *22*); however, the composition and architecture of COR are those of a simple rubbery homopolymer. Specifically, at small strains, (≲100%) the hysteresis of COR was low and comparable to that of natural rubber (fig. S25), whereas at large strains, COR yields and plastically deforms (ε>100%; Fig. 2A), similar to other thermoplastics such as styrene-isoprene-styrene of low styrene fraction. Therefore, the mechanical properties of polyoctenamer could be substantially varied with mixtures of Ru-1 and Ru-2 catalysts by simply toggling visible light-emitting diode (LED) irradiation.

This difference in mechanical properties was hypothesized to stem from backbone stereochemistry and crystallization. TOR is opaque with visible light transmittance <1%, whereas COR is transparent (fig. S28), indicating that high *trans* content leads to more crystalline polymer domains. Differential scanning calorimetry was used to characterize the melting temperature (T_m) and degree of crystallinity (Fig. 2B and figs. S29 and S30). Using a modulated heat ramp and integrating the change in enthalpy versus "100%" crystalline polyoctenamer (216 J/g) (*23*) provided a $T_m \approx 72$°C and ~65% crystallinity for TOR and a $T_m \approx 16$°C and ~20% crystallinity for COR. In addition, a $T_g \approx -80$°C was identified for both TOR and COR (fig. S31), confirming that at room temperature, TOR is a semicrystalline thermoplastic with mechanical properties strongly influenced by the crystalline domains, and COR is an amorphous polymer melt.

The observation that COR was fracture resistant prompted the characterization of its fracture energy (i.e., toughness) as measured by the critical energy release rate (G_c). Precracked, pure-shear specimens of polyoctenamers were uniaxially stretched until failure, and G_c was calculated as $W_{PS} \times h_0$ (*24*), where W_{PS} is the strain energy density in the bulk at the critical stretch of crack propagation and h_0 is the initial specimen height (Fig. 2C , fig. S32, and table S6). This analysis revealed G_c values of 150 ± 40 kJ/m^2 (Ru-2, dark) and 190 ± 40 kJ/m^2 (Ru-1+Ru-2, dark) for COR and 10 ± 3 kJ/m^2 (Ru-1+Ru-2, light) for TOR (Fig. 2D). Compared with commercial materials, COR was an order of magnitude tougher than soft elastomers (E < 10 MPa), such as rubbers and polyurethanes 40A and 90A, and equivalent to the polyurethane Elastollan (G_c = 138 ± 13 kJ/m^2 and E = 7 MPa) (*25*). Conversely, TOR had a toughness between that of other stiff plastics such as acrylonitrile butadiene styrene (ABS) and high-density polyethylene (HDPE) (Fig. 2D, fig. S32, and table S6). Furthermore, lowering the Ru-2 catalyst concentration from

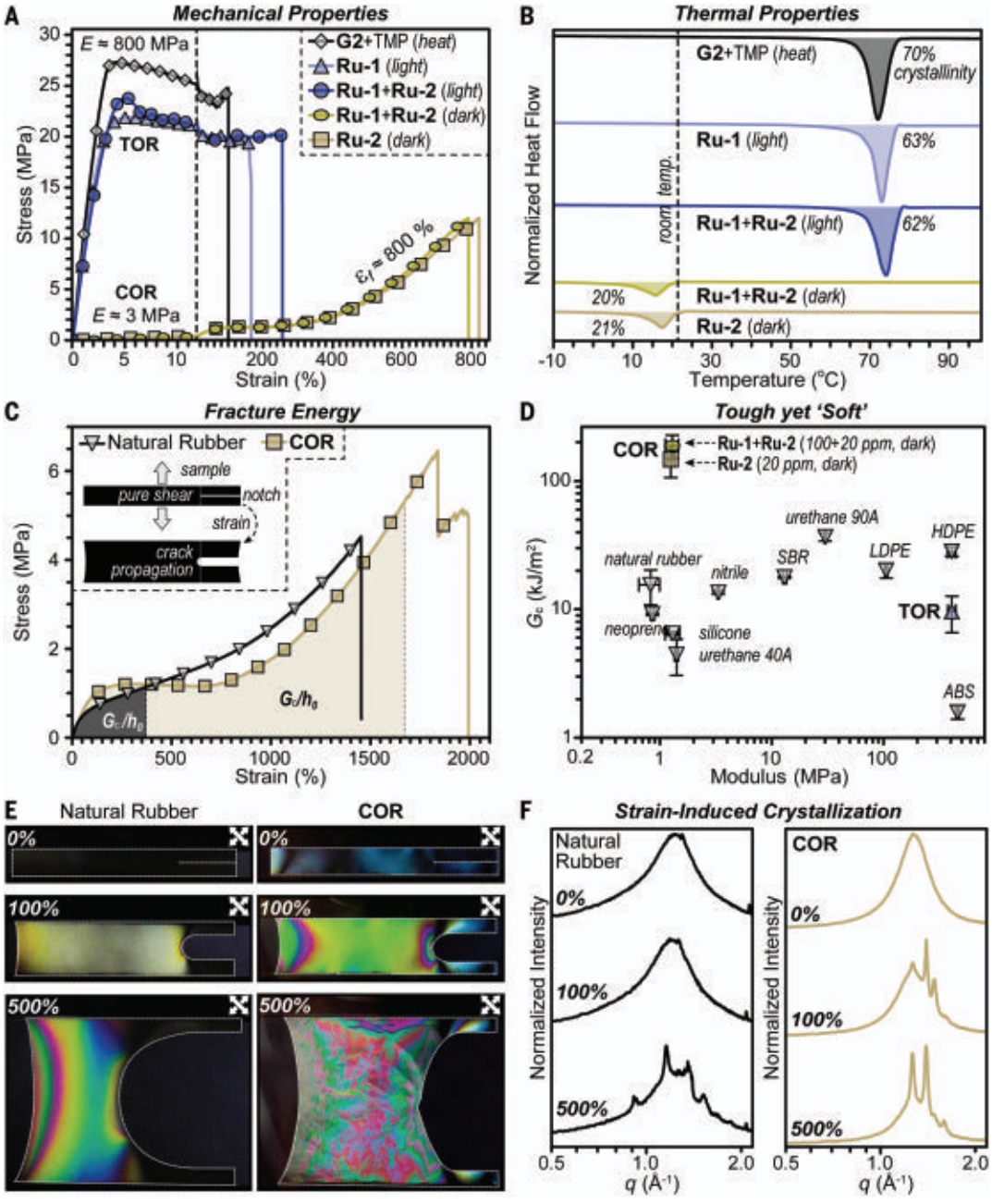

Fig. 2. Bulk thermomechanical analyses of polyoctenamer rubbers. (**A**) Stress-strain curves from uniaxial elongation until failure, with representative E and ε_f values indicated. Scale was expanded for the low-deformation range, and symbols are indexed for clarity. (**B**) Differential scanning calorimetry to characterize melting temperature and percent crystallinity. Parenthetical terms "heat," "light," and "dark" indicate fabrication conditions. (**C**) Representative stress-strain curves for COR and natural rubber used to calculate G_c, as defined in the shaded regions. Symbols are indexed for clarity. (**D**) Comparison of COR and TOR with commercial rubbers and plastics as a function of G_c and modulus. Data points represent an average of at least three notched and three notch-free samples with error bars of ±1 SD from the mean. (**E**) Strain-induced crystallization for natural rubber and COR as visualized through crossed polarizers and (**F**) measured using WAXS.

20 to 3.3 ppm increased the G_c to 280 ± 17 kJ/m^2 (figs. S33 to S35), which is postulated to arise from the increased COR molecular weight (figs. S36 to S38). Thus, stereoregulated ROMP of COE provides a facile pathway to designing soft and tough materials for applications that require large deformations at "soft/hard" interfaces, such as wearable electronics (*26*).

The role of crystallinity on the mechanical properties of polyoctenamers was further assessed and compared with natural rubber using a combination of birefringence (Fig. 2E and fig. S39) and wide-angle x-ray scattering (WAXS) (Fig. 2F and figs. S40 to S44). At low strains (100%), both natural rubber and COR showed a stress concentration in the vicinity of the crack tip, whereas at larger strains (500%), COR distinctly delocalized the stress and dissipated energy by undergoing plastic deformation throughout the bulk (movies S1 and S2). Characterization with WAXS confirmed that at room temperature, COR was amorphous before stretching but crystallized when deformed above 100% (Fig. 2F). Thus, like natural rubber, COR is first toughened by strain-induced crystallization but then dissipates elastic energy both in the vicinity of the crack tip and in the bulk to erase the stress concentration that constitutes a driving force for fracture.

The ability to control the stereochemistry and mechanical properties of polyoctenamers enabled photopatterning TOR and COR from COE using a mixed-catalyst system with Ru-1 (50 ppm + 75 ppm pyr.) and Ru-2 (20 ppm). ROMP kinetics for different catalyst systems were characterized by ^{1}H NMR spectroscopy (Fig. 3A and figs. S20 to S23). Blue light irradiation (~460 nm, ~170 mW/cm^2) of the mixed-catalyst system in COE resulted in ~90% conversion to TOR in ~5 min, comparable to the control without Ru-2. By contrast, the mixed-catalyst system in the dark resulted in relatively slow COR formation: <10% conversion in ~5 min. However, after ~60 min in the dark,

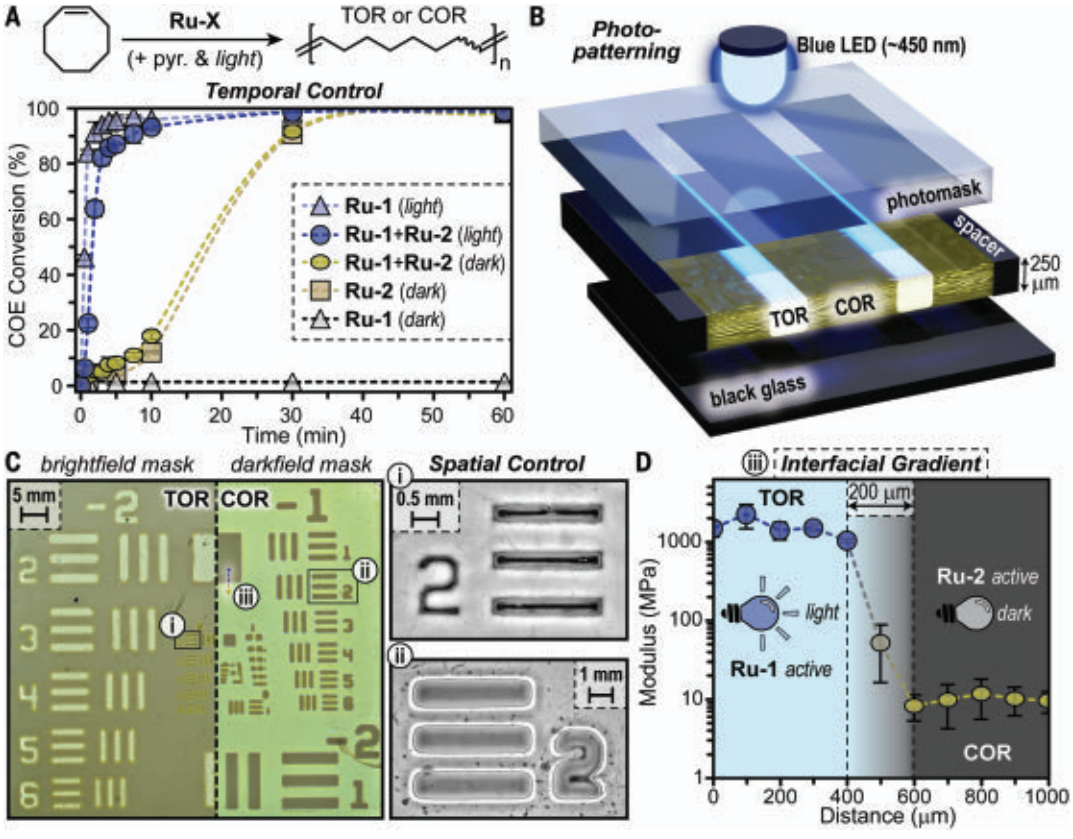

Fig. 3. Spatiotemporal control over polyoctenamer stereochemistry. (**A**) Polymerization kinetics of COE with various catalyst systems. pyr. is present in all examples containing Ru-1. Data points represent an average of three independent polymerizations with error bars of ±1 SD from the mean. (**B**) Illustration of photopatterning setup. (**C**) Images of photopatterned TOR and COR prepared using 1951 USAF bright-field and dark-field photomasks. Leftmost patterns are two backlit images of separate films digitally stitched together to show the effect of inverting the majority phase from TOR (left of dashed line) to COR (right of dashed line). Regions (i) and (ii) were examined with a backlit digital microscope, providing the magnified images shown to the right. The arrow labeled (iii) represents the position and direction of nanoindentation testing, providing modulus as a function of position across the TOR/COR interface (**D**). Data points represent an average of six indentations with error bars of ±1 SD from the mean.

COE was fully consumed, forming COR, and this was comparable to what happened in the control without Ru-1 and pyr. present. This method also enabled fabrication of thick TOR specimens with *trans*-alkene contents of ~80% up to a depth of ~4 mm (fig. S45), likely due to the low concentration and photobleaching of pyr. (75 ppm) during photoinduced ROMP. These distinct differences in light versus dark ROMP kinetics enabled photopatterning of stiff TOR domains in a soft COR matrix.

To pattern TOR domains in a COR matrix, the mixed-catalyst system in COE was loaded between a photomask and black glass separated by 250-μm shims and irradiated with blue light for 5 min (Fig. 3B and figs. S46 and S47). Pattern fidelity was characterized using both bright-field and dark-field 1951 USAF standardized photomasks, which define resolution as the smallest discernible line pair (Fig. 3C). The resolution for bright-field (majority TOR) and dark-field (majority COR) was ~9.0 line pairs/mm (~55 μm) and ~1.3 line pairs/mm (~400 μm), respectively, with differences hypothesized to arise from crystal growth outside of irradiated areas, as evidenced by features smaller (Fig. 3Ci) and larger (Fig. 3Cii) than those on the mask. Nanoindentation at a TOR/COR interface (Fig. 3Ciii) also revealed a change in E from ~1000 to ~10 MPa over ~200 μm, consistent with differences in polyoctenamer stereochemistry and crystallinity and the mechanical properties of TOR and COR (Fig. 3D and fig. S48).

As a final proof of concept, patterns were designed to access unusual bulk mechanical behaviors (i.e., metamaterials) that require synergy between stiff and soft domains (Fig. 4). First, selective straining was demonstrated with a square array of TOR patterned into a continuous COR matrix, a construct with potential utility as a substrate for stretchable electronics (*27*). Cycling these specimens to 100% strain qualitatively showed that deformation was localized in the soft COR domains (Fig. 4A and movie S3). Quantification of this behavior using digital image correlation on a specimen containing 5-mm-wide lines revealed <1% strain in the TOR domains relative to the bulk (Fig. 4B, figs. S49 to S51, and movie S4). Thus, TOR may act as a support structure (i.e., substrate) for brittle (electronic) components in stretchable devices. Moreover, the mitigation of interfacial failure upon application of substantial global stress (>4 MPa) suggests the presence of strongly interwoven domains, which may result from a combination of tie chains and physical entanglements between TOR and COR and/or continuity of TOR/COR polymer backbones as a result of cross-metathesis.

More sophisticated sutures were also examined as a means to control strain stiffening, a common mechanism used by natural tissue to prevent rupture (*28*) (Fig. 4C). Three patterns holding constant COR:TOR ratios (~0.35:0.65) were characterized by uniaxial tension between crossed polarizers. Straight-line (control), antitrapezoidal, and rectangular sutures showed stress-strain localization on COR. Distinct strain-stiffening behavior was apparent for each suture pattern due to the increase in stress that occurs as regions of TOR approach each other at specific global strain values (Fig. 4D, fig. S52, and movies S5 to S7). Thus, photopatterning of polyoctenamer stereochemistry enables the bulk preparation of mechanical metamaterials.

This report describes a simple and scalable synthetic method to prepare polymeric multimaterials with stiff (TOR) and elastic (COR) domains. Specifically, a mixed-catalyst system sensitive to visible light enables ROMP of COE with spatiotemporal control over the resultant polyoctenamer backbone stereochemistry. Polyolefins with a combination of toughness, elasticity, and moduli were patterned with microscopic precision, providing access to materials with mechanically robust "hard/soft" interfaces.

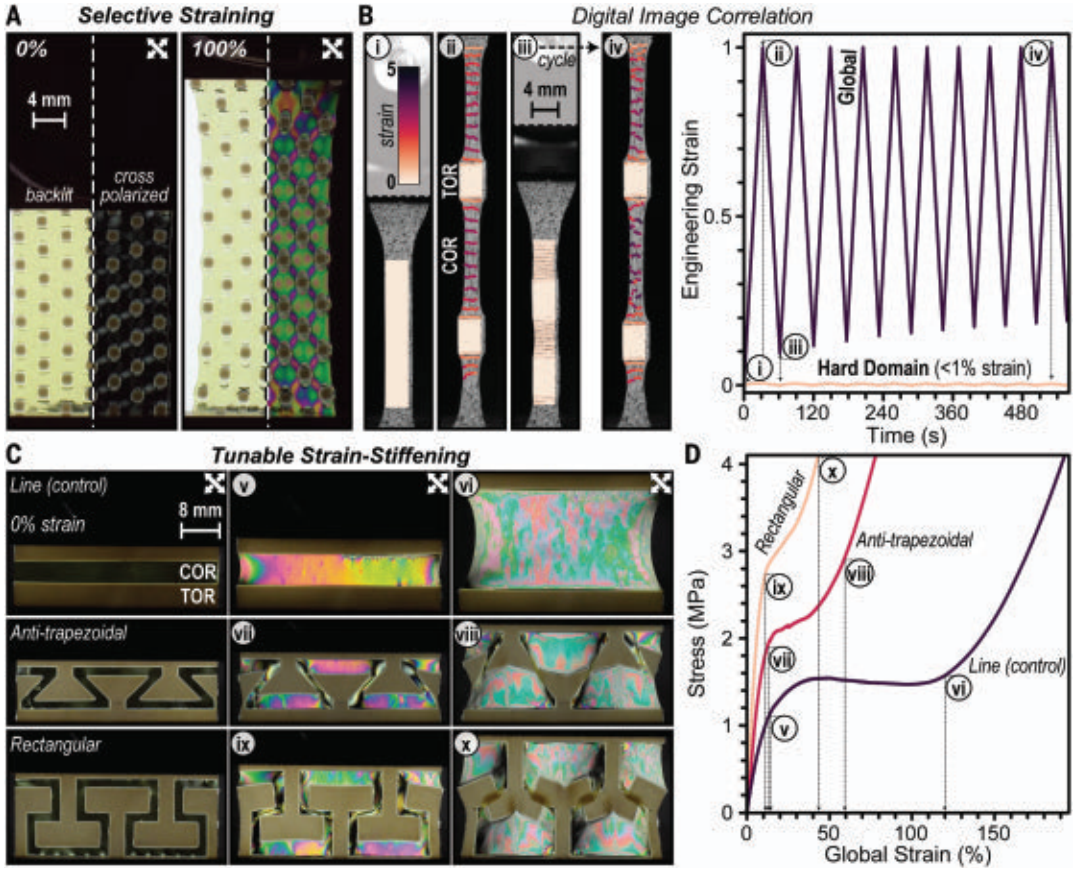

Fig. 4. Mechanical metamaterial characterization. (**A**) Images of backlit array of TOR squares in a COR matrix with and without crossed polarizers at 0 and 100% strain. (**B**) Images of a patterned sample during the first and last strain cycles used for digital image correlation analysis. (**C** and **D**) Images of backlit samples between crossed polarizers during uniaxial tension applied vertically, showing the effect of suture design on strain-stiffening behavior (C) and corresponding stress-strain curves (D).

REFERENCES AND NOTES

1. W. Huang *et al*., *Adv. Mater.* **31**, e1901561 (2019).
2. F. Barthelat, Z. Yin, M. J. Buehler, *Nat. Rev. Mater.* **1**, 16007 (2016).
3. N. Reznikov, M. Bilton, L. Lari, M. M. Stevens, R. Kröger, *Science* **360**, eaao2189 (2018).
4. M. S. Ganewatta, Z. Wang, C. Tang, *Nat. Rev. Chem.* **5**, 753–772 (2021).
5. Y. Fang *et al*., *Chem. Rev.* **122**, 5233–5276 (2022).
6. X. Zhao *et al*., *Chem. Rev.* **121**, 4309–4372 (2021).
7. M. Li, A. Pal, A. Aghakhani, A. Pena-Francesch, M. Sitti, *Nat. Rev. Mater.* **7**, 235–249 (2022).
8. T. Someya, Z. Bao, G. G. Malliaras, *Nature* **540**, 379–385 (2016).
9. L. M. Cox *et al*., *Adv. Eng. Mater.* **21**, 1900578 (2019).
10. S. Bialas *et al*., *Adv. Mater.* **31**, e1807288 (2019).
11. N. D. Dolinski *et al*., *Adv. Mater.* **30**, e1800364 (2018).
12. J. J. Schwartz, A. J. Boydston, *Nat. Commun.* **10**, 791 (2019).
13. Y. Ma *et al*., *J. Am. Chem. Soc.* **143**, 21200–21205 (2021).
14. Z. Wang *et al*., *Proc. Natl. Acad. Sci. U.S.A.* **116**, 5967–5972 (2019).
15. O. Eivgi, R. S. Phatake, N. B. Nechmad, N. G. Lemcoff, *Acc. Chem. Res.* **53**, 2456–2471 (2020).
16. J. A. Song *et al*., *J. Am. Chem. Soc.* **142**, 10438–10445 (2020).
17. C. Theunissen, M. A. Ashley, T. Rovis, *J. Am. Chem. Soc.* **141**, 6791–6796 (2019).
18. F. Boeda, H. Clavier, S. P. Nolan, *Chem. Commun.* **24**, 2726–2740 (2008).
19. K. Endo, R. H. Grubbs, *J. Am. Chem. Soc.* **133**, 8525–8527 (2011).
20. I. D. Robertson *et al*., *ACS Macro Lett.* **6**, 609–612 (2017).
21. A. Hotta *et al*., *Proc. Natl. Acad. Sci. U.S.A.* **103**, 15327–15332 (2006).
22. C. Creton, G. Hu, F. Deplace, L. Morgret, K. R. Shull, *Macromolecules* **42**, 7605–7615 (2009).
23. W. A. Schneider, M. F. Müller, *J. Mol. Catal.* **46**, 395–403 (1988).
24. R. S. Rivlin, A. G. Thomas, *J. Polym. Sci.* **10**, 291–318 (1953).
25. G. Scetta, N. Selles, P. Heuillet, M. Ciccotti, C. Creton, *Polym. Test.* **97**, 107140 (2021).
26. S. Wang, J. Y. Oh, J. Xu, H. Tran, Z. Bao, *Acc. Chem. Res.* **51**, 1033–1045 (2018).
27. R. Libanori *et al*., *Nat. Commun.* **3**, 1265 (2012).
28. Z. Liu, Z. Zhang, R. O. Ritchie, *Adv. Funct. Mater.* **30**, 1908121 (2020).

ACKNOWLEDGMENTS

We thank Umicore for supplying ruthenium catalysts M320, M800 (Ru-1), M2001, and M2002 and C. Tagnon for assistance with the preparation of Fig. 3B. **Funding:** This work was supported primarily by the National Science Foundation (grant no. DMR-2045336 to A.K.R., H.L.C., K.S.M., and Z.A.P. and a graduate research fellowship under grant no. DGE-1610403 to M.J.A.; film fabrication, catalyst system development, characterization, and supervision). This work was supported in part by the U.S. Department of Energy, Office of Science, Basic Energy Sciences, Energy Frontier Research Center, Center for Materials for Water and Energy Systems (M-WET) (grant no. DE-SC0019272 to M.J.A. and B.D.F.; supervision); the Robert A. Welch Foundation (grant no. F-2007 to Z.A.P.; materials and supplies); the American Chemical Society Petroleum Research Fund (grant no. 60802-DNI7 to Z.A.P.; materials and supplies); and the UT Cockrell School of Engineering (A.J.A. and G.E.S.; mechanical testing). The authors acknowledge use of the UT NMR facilities (NIH grant no. 1 S10 OD021508-01). **Author contributions:** Conceptualization (A.K.R., M.J.A., Z.A.P.); Funding acquisition (B.D.F., G.E.S., Z.A.P.); Investigation (A.K.R., H.L.C., K.S.M., M.J.A., A.J.A.); Methodology (A.K.R., H.L.C., K.S.M., M.J.A., A.J.A., G.E.S., Z.A.P.); Project administration (Z.A.P.); Supervision (B.D.F., G.E.S., Z.A.P.); Visualization (A.K.R., H.L.C., K.S.M., M.J.A., A.J.A., Z.A.P.); Writing – original draft (A.K.R., Z.A.P.); Writing – review and editing (A.K.R., H.L.C., K.S.M., M.J.A., A.J.A., B.D.F., G.E.S., Z.A.P.). **Competing interests:** US provisional patent application no. 63/351,868 ("Cyclic olefin polymer having high Cis double bond content") was filed 14 June 2022 by Z.A.P. and A.K.R. The remaining authors declare no competing interests. **Data and materials availability:** All data are available in the main text or the supplementary materials.

SUPPLEMENTARY MATERIALS

science.org/doi/10.1126/science.add6975
Materials and Methods
Supplementary Text
Figs. S1 to S55
Tables S1 to S6
References (*29*–*38*)
Movies S1 to S8
AutoCAD Data S1

Submitted 28 June 2022; accepted 21 September 2022
10.1126/science.add6975

Biology

KOCH INSTITUTE for Integrative Cancer Research at MIT

Tenure-track Assistant Professor

The **Koch Institute for Integrative Cancer Research** together with the **Department of Biology** at the Massachusetts Institute of Technology (Cambridge, Massachusetts) invites applications for a tenure-track appointment at the Assistant Professor level.

The Koch Institute is an NCI-designated Cancer Center, featuring a broad spectrum of cancer relevant research ranging from discovery and mechanistic analysis through to applied science. We are interested in candidates who have a Ph.D. in the Biological Sciences or M.D., or equivalent, by the start of employment. This is an open search with regard to field of study and specific research focus, but we are particularly interested in candidates who are pursuing innovative approaches to fundamental problems in molecular, cellular, or organismal biology.

The successful candidate will be provided with lab and office space in the Koch Institute, a generous start-up package, and access to state-of-the-art core facilities and is expected to develop and lead a vibrant, independent research program. Faculty duties include teaching courses in Biology and related topics; conducting research; and advising students. We seek colleagues who share our commitment to undergraduate and graduate education, and who will develop and teach courses, supervise graduate and undergraduate research, and mentor trainees at all levels. We are particularly interested in candidates who will help promote and provide diversity, equity, and inclusion. We are committed to providing our faculty with a supportive environment that emphasizes mentoring and is mindful of diverse backgrounds.

Applicants should submit a cover letter, curriculum vitae, summary of current and proposed research (≤5 pgs), statement on teaching philosophy (~1 pg), and a statement on mentoring, diversity, and outreach (~2 pgs) that describes the candidate's experience in these areas and/or how they envision contributing to our ongoing efforts. Letters of recommendation should be sent separately from at least three individuals able to evaluate the candidate's accomplishments and future potential. Application materials should be submitted to Academic Jobs Online link **https://academicjobsonline.org/ajo/jobs/22825**.

Completed applications will begin to be considered on 10/24/2022.

MIT Biology has additional open positions. Candidates may apply to any or all openings, but must submit a separate application for each position.

MIT is an equal opportunity employer. We value diversity and strongly encourage applications from individuals from all identities and backgrounds. All qualified applicants will receive equitable consideration for employment based on their experience and qualifications, and will not be discriminated against on the basis of race, color, sex, sexual orientation, gender identity, religion, disability, age, genetic information, veteran status, ancestry, or national or ethnic origin. MIT's full policy on Nondiscrimination can be found at ***https://policies.mit.edu/policies-procedures/90-relations-and-responsibilities-within-mit-community/92-nondiscrimination***

http://web.mit.edu

SAINT LOUIS UNIVERSITY
SCHOOL OF MEDICINE

FACULTY POSITIONS

EDWARD A. DOISY DEPARTMENT OF BIOCHEMISTRY AND MOLECULAR BIOLOGY
SAINT LOUIS UNIVERSITY SCHOOL OF MEDICINE

Saint Louis University, a Catholic Jesuit institution dedicated to education, research, health care, and service, is seeking outstanding applicants for tenure-track faculty positions at the **Assistant, Associate, or Full Professor** level in the Department of Biochemistry and Molecular Biology (**https://biochem.slu.edu/**). The Department, founded by Nobel Laureate Edward A. Doisy, is growing the number of faculty to celebrate its forthcoming centennial in 2024. Candidates with an outstanding track record of training and scholarly work in biochemistry, structural and/or molecular biology with emphasis on uncovering the molecular bases of human disease are strongly encouraged to apply. Please submit a cover letter, curriculum vitae, description of future research plans and addresses of three references to **https://slu.wd5.myworkdayjobs.com/Careers, Job #2022-04660**. A detailed 3-year budget is optional for initial submission.

Saint Louis University is an equal opportunity/affirmative action employer. All qualified candidates will receive consideration for the position applied for without regard to race, color, religion, sex, age, national origin, disability, marital status, sexual orientation, military/veteran status, gender identity, or other non-merit factors. We welcome and encourage applications from minorities, women, protected veterans, and individuals with disabilities (including disabled veterans). If accommodations are needed for completing the application and/or with the interviewing process, please contact Human Resources at 314-977-5847.

THE GEORGE WASHINGTON UNIVERSITY
WASHINGTON, DC

TENURE-TRACK FACULTY POSITION, BIOCHEMISTRY & MOLECULAR MEDICINE

The Department of Biochemistry and Molecular Medicine, at The George Washington University School of Medicine and Health Sciences invites applications for a tenure-track faculty position to be filled at the **assistant** or **associate professor level** at a salary commensurate with experience. Areas of relevant research interest include but are not limited to inflammation and metabolic dysfunction. Additional responsibilities include engaging in the educational programs of the department and service to the institution.

The current research programs in the department combine multifaceted experimental approaches (e.g., biochemistry, molecular genetics, bioinformatics, transcriptomics, proteomics, and glycomics) to address important biological problems with relevance to human health and pathogenesis. Our institution's close location to the NIH, Children's National Health System, and other institutions in the Washington DC metropolitan area provides outstanding opportunities for collaboration. Opportunities are also available to collaborate with colleagues in the George Washington University Cancer Center.

BASIC QUALIFICATIONS: Applicants must hold a PhD and/or MD or equivalent in an appropriate discipline with a demonstrable strong publication record.

APPLICATION PROCESS: To be considered, please complete an online faculty application at **http://www.gwu.jobs/postings/96292** and upload a current CV, cover letter, and a statement of current and future research interests (3-page limit). You will also be asked to provide the names and contact information for references. Review of applications will begin on **October 24, 2022** and will continue until the position is filled. Only complete applications will be considered. Employment offers are contingent on the satisfactory outcome of a standard background screening.

The university is an Equal Employment Opportunity/Affirmative Action employer that does not unlawfully discriminate in any of its programs or activities on the basis of race, color, religion, sex, national origin, age, disability, veteran status, sexual orientation, gender identity or expression, or on any other basis prohibited by applicable law.

Assistant Professor of Molecular and Cellular Biology

Harvard University, Faculty of Arts and Sciences
Department of Molecular and Cellular Biology

MCB
Department of Molecular and Cellular Biology

We seek applications for a tenure-track faculty position in the **Department of Molecular and Cellular Biology**.
MCB is a tight-knit, supportive and collaborative research community with interests in a broad range of topics, including cell biology, systems biology, biophysics, biochemistry, developmental biology, neurobiology, genetics, microbiology, computational biology, and structural biology. Junior faculty are assigned a mentoring committee that advises them on all aspects of setting up a successful research group. They also receive grant writing and submission support, and can recruit from a diverse pool of PhD students from various programs across the University. The appointment provides access to state of the art animal facilities and core facilities for imaging, proteomics, genomics and bioinformatics. The Department is also closely associated with science initiatives at Harvard such as the **Center for Brain Science**, **Harvard Quantitative Biology**, the **Harvard Stem Cell Institute**, the **Broad Institute**, and the **Center for Nanoscale Systems**, and provides opportunities for interactions with the broader Harvard community. The tenure-track professor will be responsible for teaching at least one course per year at the undergraduate and/or graduate levels, in subject(s) to be decided based on the professor's expertise and the department's curricular needs.
The appointment is expected to begin in the Summer of 2023 (later is possible if circumstances warrant).

MCB celebrates the multiple dimensions of diversity that each member of our community offers, including, but not limited to, race, ethnicity, sex, gender identity, sexual orientation, socioeconomic circumstance, national origin, geographic background, immigration status, ability and disability, physical characteristics, veteran status, political ideology, religious belief and age. As a department, we are committed to diversifying our faculty and providing a supportive environment for success. We strongly welcome applications from women, persons with disabilities, protected veterans, and underrepresented minorities.

Basic Qualifications: Doctorate or terminal degree in relevant field or related discipline required by the time the appointment begins.
Additional Qualifications: Demonstrated strong commitment to teaching and advising is desired.
We anticipate conducting in-person interviews in January-February of 2023.

Please submit through the ARIeS portal: **https://academicpositions.harvard.edu/postings/11703**
Complete applications, including letters of recommendation, should be received no later than **November 1, 2022**.

For information contact Polina Kehayova | kehayova@fas.harvard.edu | **www.mcb.harvard.edu**

HARVARD UNIVERSITY

Harvard is an equal opportunity employer and all qualified applicants will receive consideration for employment without regard to race, color, sex, gender identity, sexual orientation, religion, creed, national origin, ancestry, age, protected veteran status, disability, genetic information, military service, pregnancy and pregnancy-related conditions, or other protected status.

MIT Biology

Tenure-track Assistant Professor Department of Biology

The **Department of Biology** at the Massachusetts Institute of Technology (Cambridge, Massachusetts) invites applications for a tenure-track appointment at the Assistant Professor level.

For this position, we seek candidates who have a Ph.D. in Biology or a related field, or M.D., or equivalent, and are using data-driven techniques from machine learning and statistics to model and explore biological problems. Ph.D., M.D., or equivalent is required by the start of employment. Scientists using and/or developing such innovative, data-driven approaches to deepen our understanding of molecular, cellular, or organismal biology are encouraged to apply.

The successful candidate will be provided with lab and office space, a generous start-up package, access to state-of-the-art core facilities and computation resources, and opportunities to engage the broad scientific and computational community at MIT. This includes interaction with the MIT College of Computing and its extensive faculty and student community at MIT, and the Computational and Systems Biology program.

We seek colleagues who share our commitment to undergraduate and graduate education, and who will develop and teach courses, supervise graduate and undergraduate research, and mentor trainees at all levels. Faculty duties include teaching courses in Biology and related topics; conducting research; and advising students. We are particularly interested in candidates who will help promote and provide diversity, equity, and inclusion. We are committed to providing our faculty with a supportive environment that emphasizes mentoring and is mindful of diverse backgrounds.

Applicants should submit a cover letter, curriculum vitae, summary of current and proposed research (≤5 pgs), statement on teaching philosophy (~1 pg), and a statement on mentoring, diversity, and outreach (~2 pgs) that describes the candidate's experience in these areas and/or how they envision contributing to our ongoing efforts. Letters of recommendation should be sent separately from at least three individuals able to evaluate the candidate's accomplishments and future potential. Application materials should be submitted to **Academic Jobs Link https://academicjobsonline.org/ajo/jobs/22826**.

Completed applications will begin to be considered on 10/24/2022.

MIT Biology has additional open positions. Candidates may apply to any or all openings, but must submit a separate application for each position.

MIT is an equal opportunity employer. We value diversity and strongly encourage applications from individuals from all identities and backgrounds. All qualified applicants will receive equitable consideration for employment based on their experience and qualifications, and will not be discriminated against on the basis of race, color, sex, sexual orientation, gender identity, religion, disability, age, genetic information, veteran status, ancestry, or national or ethnic origin. MIT's full policy on Nondiscrimination can be found at ***https://policies.mit.edu/policies-procedures/90-relations-and-responsibilities-within-mit-community/92-nondiscrimination***

http://web.mit.edu

By **Arijit Mukherjee**

Expanding my horizons

As the pandemic started, so, too, did my journey as a Ph.D. student in a new country. Lockdown and homesickness combined to leave me feeling isolated and desperate to meet people. So, when I received an email one morning inviting volunteers to join the university's graduate students' society, I was intrigued. I worried that getting involved in extracurriculars would be a distraction from my Ph.D. work; I thought doing experiments and reading papers were supposed to be my sole priorities. But maybe this was my chance to make friends and find the connections I was missing.

I looked through the descriptions of open volunteer roles in the recruitment email, searching for opportunities that would involve teamwork and engagement both within and outside the university. A newly fledged venture matching graduate students with jobs and internships caught my eye. The program needed placement coordinators who would lead teams of graduate student volunteers to help bring in industry partners, determine logistics, and work with the university administration and student applicants. The opportunity to interact with all these different groups was enticing. I had no relevant experience, but I decided I might as well go for it and apply. I was nervous for the interview, but my enthusiasm seemed to carry the day.

"Maybe this was my chance to make friends and find the connections I was missing."

The first few weeks in my new role were daunting. Along with my routine Ph.D. work, I was suddenly managing a team of four volunteers and arranging virtual meetings with industry professionals and startup founders. Luckily my supervisor was supportive, and I decided I would just give it a try and do my best.

I found I was busier than ever before, but I enjoyed the daily mix of activities. It was an antidote to isolation, bringing me into contact with people from a variety of domains, positions, and backgrounds. At first I was intimidated in meetings with industry professionals, feeling I wasn't prepared or polished enough. But as I gained experience and confidence, the interactions became truly enjoyable and rewarding. Sometimes the conversations went beyond regular business to touch on career paths, personal challenges, travel, and more. A few even led to sustained connections, and I began to feel less lonely and more invigorated about my work and life.

I also learned about leadership. At the start, things seemed to go well with my team of graduate students. We were accomplishing our goals, and I thought that was all that mattered—until one of my team members came to me upset I wasn't including her more fully in decision-making. I was frustrated; didn't she trust my leadership? But after I calmed down, I saw that maybe she had a point. I reached out to my other team members, and another gave me similar feedback. So I began to ask team members to lead some of our meetings, encouraged them to express their views, and made sure to include them consistently. This new approach allowed us to meet our targets while helping everyone feel more invested, fulfilled, and connected—as colleagues, but also as friends.

Beyond building relationships and skills, my work with the graduate students' society unexpectedly opened my horizons about my own professional future. Before I joined, I had only been exposed to academic career paths, and I assumed that was my future. But when a startup founder asked me during one of our meetings what I hope to achieve, I began to think about what is most important to me. Recalling the happy faces of the students who receive offers through our endeavor, I realized I particularly enjoy feeling part of a team and affecting the lives of others. I now know I want to collaborate, share credit, and make a direct, measurable impact. And thanks to my experience, I know I can best find those opportunities outside academia. As I get closer to completing my Ph.D., I'm approaching job searches with a good idea of what I want.

Contrary to my initial concerns, getting involved in this role wasn't a distraction at all. It has helped me grow and identify my professional needs—and make friends along the way. ■

Arijit Mukherjee is a Ph.D. candidate at the National University of Singapore. Send your career story to SciCareerEditor@aaas.org.

ILLUSTRATION: ROBERT NEUBECKER

AAAS.ORG/COMMUNITY

AAAS' Member Community is a one-stop destination for scientists and STEM enthusiasts alike. It's "Where Science Gets Social": a community where facts matter, ideas are big and there's always a reason to come hang out, share, discuss and explore.

Member COMMUNITY
AAAS

AMERICAN ASSOCIATION FOR THE ADVANCEMENT OF SCIENCE

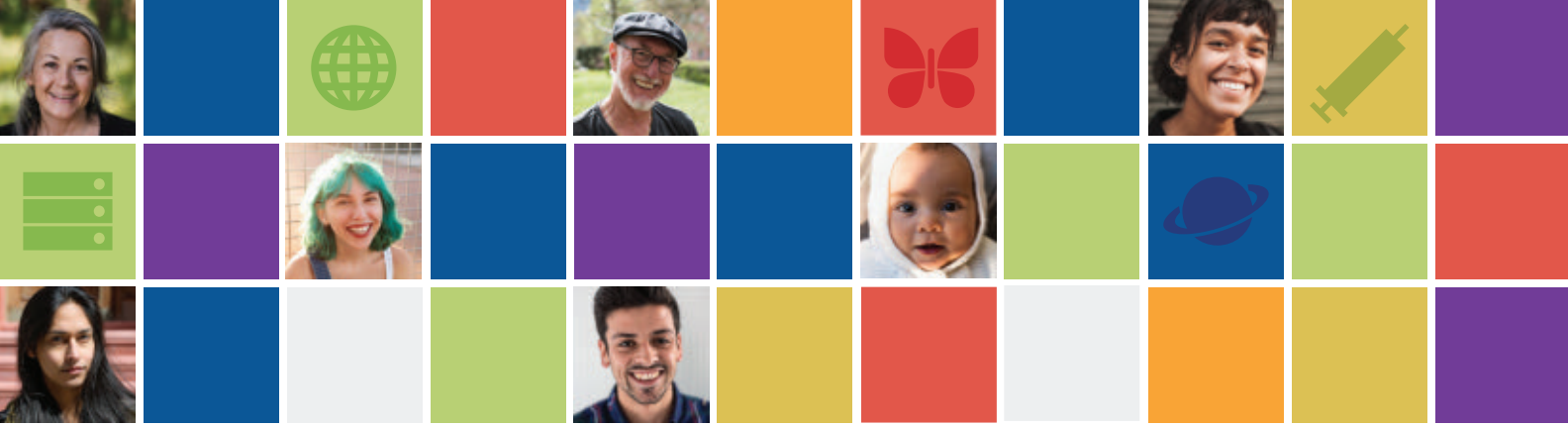

SCIENCE FOR HUMANITY

AAAS | ANNUAL MEETING
Washington, D.C. | March 2–5, 2023

REGISTER NOW FOR THE 2023 AAAS ANNUAL MEETING!

Be a part of the interdisciplinary meetings, set to take place online and in **Washington, D.C., March 2–5, 2023.**

At this year's meeting, you will access groundbreaking research that advances knowledge and responds to the needs of humanity. Choose to attend **plenaries, scientific sessions, workshops, topical lectures, e-poster presentations, and more.**

Join us in-person in Washington or online through the meeting platform.

aaas.org/meetings | #AAASmtg

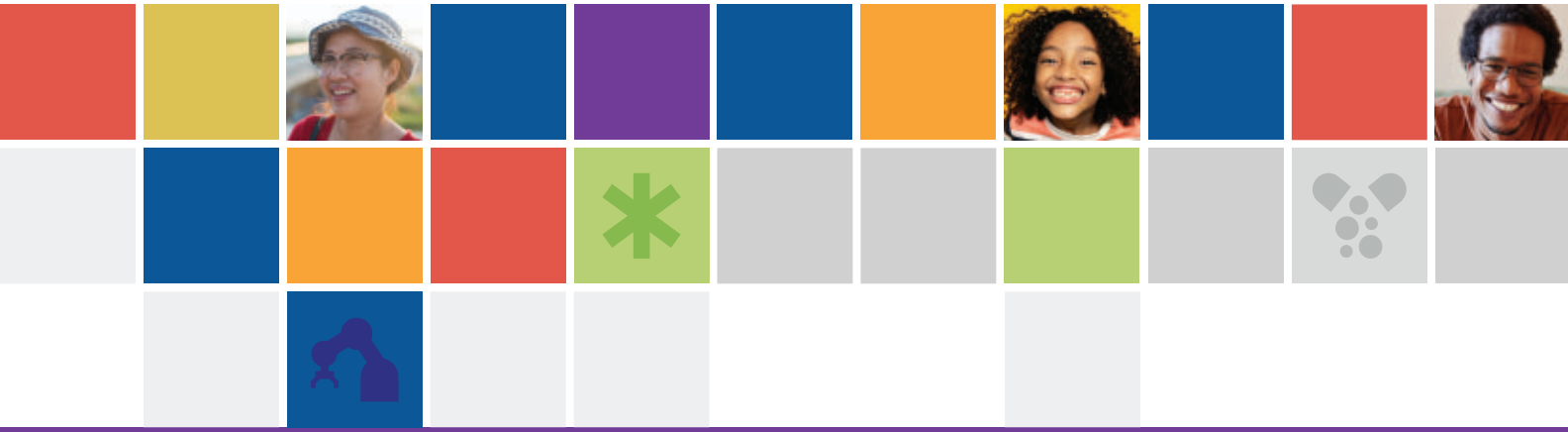

AMERICAN ASSOCIATION FOR THE ADVANCEMENT OF SCIENCE